NASA Conference Publication 10065
Part 2

4th NASA Workshop on Computational Control of Flexible Aerospace Systems

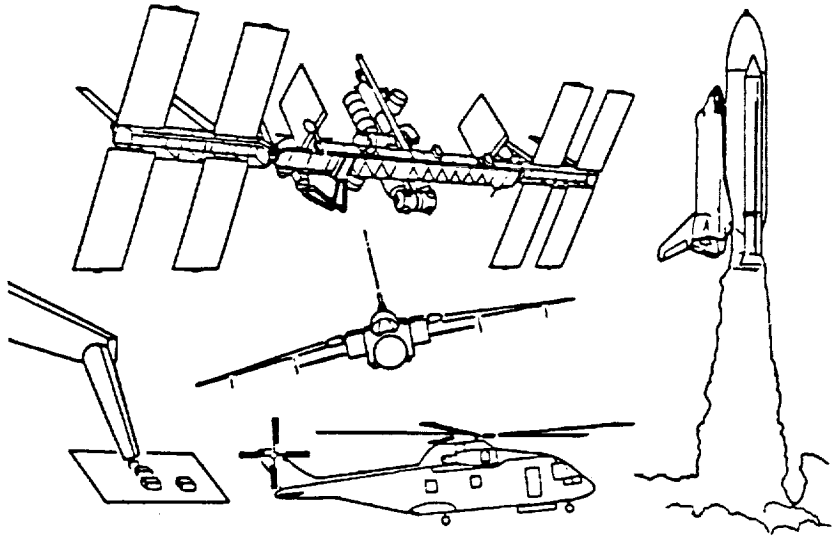

Compiled by
Lawrence W. Taylor, Jr.
Langley Research Center
Hampton, Virginia

Proceedings of a workshop sponsored by the National Aeronautics and Space Administration and held at the Kingsmill Resort Williamsburg, Virginia July 11, 1990

MARCH 1991

National Aeronautics and Space Administration

Langley Research Center
Hampton, Virginia 23665-5225

Foreword

The practice of modeling and controlling flexible aerospace systems grows in importance as the performance needed of active control systems increases. As the size of spacecraft increases and the demands of control systems become more exacting, the accuracy required of the models used for analysis also increases.

The increased complexity, the increased model accuracy, and the demands for more precise and higher control system performance result in an increased burden on the part of the analyst. Although this burden is somewhat alleviated by advances in software, there remains the pressure for assuring system stability and performance under conditions of plant uncertainty. Although robust considerations are included in many synthesis techniques, the price in terms of reduced system performance is often prohibitive.

Because similar difficulties and concerns are encountered for different applications, it is valuable to enhance the exchange of information with regard to aircraft, spacecraft and robotic applications. This is the fourth workshop in a series which has emphasized the computational aspects of controlling flexible aerospace systems. It is hoped that the reports contained in this proceedings will be useful to practicioners of modeling and controlling flexible systems.

Lawrence W. Taylor, Jr.
NASA Langley Research Center

TABLE of CONTENTS - Part 1*

* Published under separate cover

Table of Contents - Continued

Table of Contents - Continued

Table of Contents - Part 2

Table of Contents - Continued

Table of Contents - Continued

AN OVERVIEW OF THE ACTIVE FLEXIBLE WING PROGRAM

Stanley R. Cole
Boyd Perry III
NASA Langley Research Center

and
Gerald Miller
Rockwell International

Fourth Workshop on Computational Control
of Flexible Aerospace Systems
Williamsburg, VA
July 11-13, 1990

OUTLINE

This presentation is an overview of the Active Flexible Wing (AFW) project and will serve as an introduction to an entire session of the Computational Control Workshop. Background information concerning the AFW project will first be presented. This will be followed by a description of the AFW wind-tunnel model and results from the initial wind-tunnel test of the AFW model under the current project. Additionally, this presentation will emphasize major project accomplishments and briefly introduce the topics of the following five workshop presentations during the session. Summary remarks and project plans will conclude this presentation.

OUTLINE

- Project Background
- Model Description
- Test Results
- Session Overview
- Summary

ACTIVE FLEXIBLE WING PROJECT

The AFW project is a joint NASA/Rockwell International effort to demonstrate aeroelastic control through the application of digital active controls technology. The testbed for this effort is a sophisticated aeroelastically-scaled wind-tunnel model of an advanced fighter concept. The model was built by Rockwell International and had been previously tested under a separate, but closely related, research project. Two primary aspects of aeroelastic control are being examined under the current project. The first is active flutter suppression and the second is active control of maneuver loads during high-speed rolling maneuvers.

The anticipated benefits of this project include the validation of modelling, analysis, and design methods utilized in aeroservoelastic applications and the development of an experimental data base for future research efforts. Other possible benefits from the project may be an enhanced simulation technology for use in aeroservoelastic work and an increased experience base in developing and implementing digital control systems.

ACTIVE FLEXIBLE WING PROJECT

A JOINT NASA / ROCKWELL INTERNATIONAL EFFORT

Goal: **Demonstrate** Aeroelastic Control Through the Application of Active Controls Technology

- Flutter Suppression
- Rolling Maneuver Load Alleviation

Using a Sophisticated Aeroelastic Wind-Tunnel Model

Anticipated Benefits:

- Validation of Modelling, Analysis, and Design Methods
- Experience with Digital Control Systems
- Enhanced Simulation Technology
- Experimental Data Base

AFW HISTORY

The AFW wind-tunnel model was originally built by Rockwell International under a joint Rockwell International/United States Air Force/NASA project. Under this initial project effort, the model was tested twice in the NASA Langley Research Center Transonic Dynamics Tunnel. The first test, conducted in 1986, was a static data acquisition effort in which force and moment loads and control-surface effectiveness measurements were made. The second test entry, in 1987, was to obtain wing static pressure measurements and to conduct active controls tests for active roll control, structural mode control, and symmetric maneuver load alleviation.

The current project was officially started in October, 1987 as a new joint initiative involving the NASA Langley Research Center and Rockwell International. The primary goals of this project, as previously described, are to demonstrate active flutter suppression and rolling maneuver load alleviation (RMLA). The first test under the current project was completed during November, 1989. Active flutter suppression was demonstrated during this test. A second test is planned for February, 1991. A major goal of the second entry is to demonstrate active flutter suppression and RMLA simultaneously.

AFW PROGRAM: PAST, PRESENT, and FUTURE

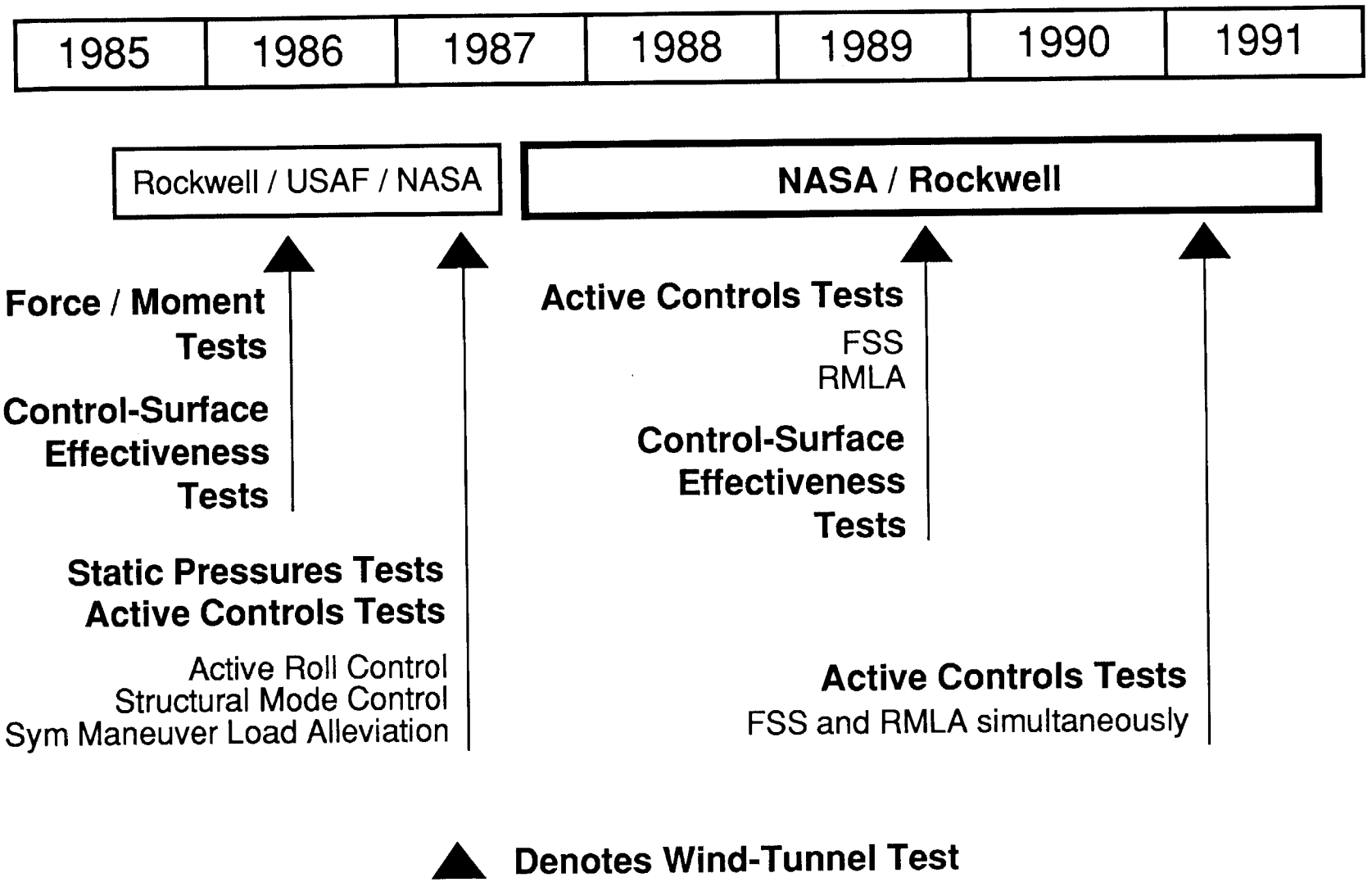

PROJECT ORGANIZATION

The AFW project has extensive support from various NASA Langley organizations and from Rockwell International. The chart shows the many organizations providing critical support to the project, lists individual members of the AFW team, and shows many of these same personnel in the photograph inset.

Primary work at the NASA Langley Research Center has spanned three of the seven center directorates. The Electronics Directorate has been responsible for coordination of computer allocations for real-time simulation and personnel support to implement and conduct simulation tests with the computer hardware associated with the AFW project. The Flight Systems Directorate has provided several control law designers to develop active flutter suppression system (FSS) control laws and has also conducted the code generation for creating the plant math model on the simulation computers. The Structures Directorate has generated the baseline equations of motion, conducted extensive flutter analyses, designed control laws for both FSS and RMLA, and led the ground and wind-tunnel testing of the AFW model. Additionally, personnel from the Structures Directorate are involved in aeroelastic calculations using advanced nonlinear unsteady aerodynamic codes.

Rockwell International has supported numerous aspects of the project dealing with the physical wind-tunnel model and has provided a finite element model to assist in the development of the AFW equations of motion. Rockwell personnel are also developing a flutter suppression system and rolling maneuver load control laws for testing during the February, 1991 wind-tunnel test.

ORIGINAL PAGE
BLACK AND WHITE PHOTOGRAPH

PROJECT ORGANIZATION

NASA Langley Research Center

Electronics
Analysis and Computation Division
Graham Wood
Houck

Flight Systems
Guidance and Control Division
Adams Kumar Waszak
Buttrill Christhilf

Unsteady Aerodynamics Branch
Bennett

Configuration Aeroelasticity Branch
Cole
Eckstrom
Matthews

Structures
Structural Dynamics Division

Aeroservoelasticity Branch
Heeg Hoadley Mukhopadhyay Noll
Perry McGraw Wieseman
Silva Pototzky Woods

Rockwell International

Advanced Design and Technology
Brosnan
Carroll
Klepl
Miller
Moore

WIND-TUNNEL MODEL PHOTO

TEST APPARATUS

WIND TUNNEL

The AFW model was tested in the NASA Langley Research Center Transonic Dynamics Tunnel (TDT). The TDT is a closed-circuit, continuous-flow wind tunnel capable of testing at stagnation pressures from near zero to atmospheric and over a Mach number range from zero to 1.2. The test section of the TDT is 16.0 ft. square with cropped corners. The TDT has several model support options. The AFW model was sting supported on the tunnel centerline. The TDT is capable of testing with either an air or a heavy gas test medium. The AFW model was tested in air under the present project.

A feature of the TDT which is particularly useful for aeroelastic testing is a group of four bypass valves connecting the test section area (plenum) of the tunnel to the return leg of the wind-tunnel circuit. In the event of a model instability, such as flutter, these quick-actuating valves are opened. This causes a rapid reduction in the test section Mach number and dynamic pressure which may result in stabilizing the model. During the AFW test, instrumentation on the model was monitored using electronic equipment that could automatically command the bypass valves to open if model response exceeded a predetermined criteria of amplitude and frequency.

WIND-TUNNEL MODEL

The wind-tunnel model is shown mounted in the TDT. The AFW wind-tunnel model is a full-span, aeroelastically-scaled representation of a fighter aircraft concept. It has a low-aspect ratio wing with a span of 8.67 ft. The fuselage of the model is designed to be rigid. It is constructed from aluminum stringers and bulkheads with a fiberglass skin providing the appropriate external shape. The model is supported on the wind-tunnel test section centerline by a sting mount specifically constructed for testing the AFW model. This sting utilizes an internal ballbearing arrangement to allow the model freedom to roll about the sting axis. The fuselage is connected to the sting through a pivot arrangement so that the model can be remotely pitched from approximately -1.5 degrees to +13.5 degrees angle of attack.

Wing Structure

The wing of the model is constructed from an aluminum honeycomb core co-cured with tailored plies of a graphite/epoxy composite material. The plies were oriented to permit desired amounts of bending and twist under aerodynamic loads. The surfaces of the graphite/epoxy material were covered by a semi-rigid polyurethane foam to provide the airfoil shape without significantly affecting the wing stiffness.

Control Surfaces

The model has two leading-edge and two trailing-edge control surfaces on each wing panel. These control surfaces are constructed of polyurethane foam cores with graphite/epoxy skins. Each control surface has a chord and span of 25 percent of the local wing chord and 28 percent of the wing semispan, respectively. The control surfaces are connected to the wing by hinge-line-mounted, vane-type rotary actuators powered by an onboard hydraulic system. Two actuators are used to drive most of the control surfaces. Only the outboard, trailing-edge control surfaces are driven by a single actuator. This was required due to limited internal space in this region of the wing. The actuators are connected to the wing structure by cylindrical rods which are fitted in titanium inserts in the wing. This arrangement is designed to provide the shear and torsion requirements placed on the wing-to-control surface connections and yet allow for bending freedom of the wing. This also minimizes the contribution of the control surfaces to the wing stiffness. Deflection limits are imposed on the various control surfaces to avoid exceeding hinge-moment and wing-load limitations.

ORIGINAL PAGE
BLACK AND WHITE PHOTOGRAPH

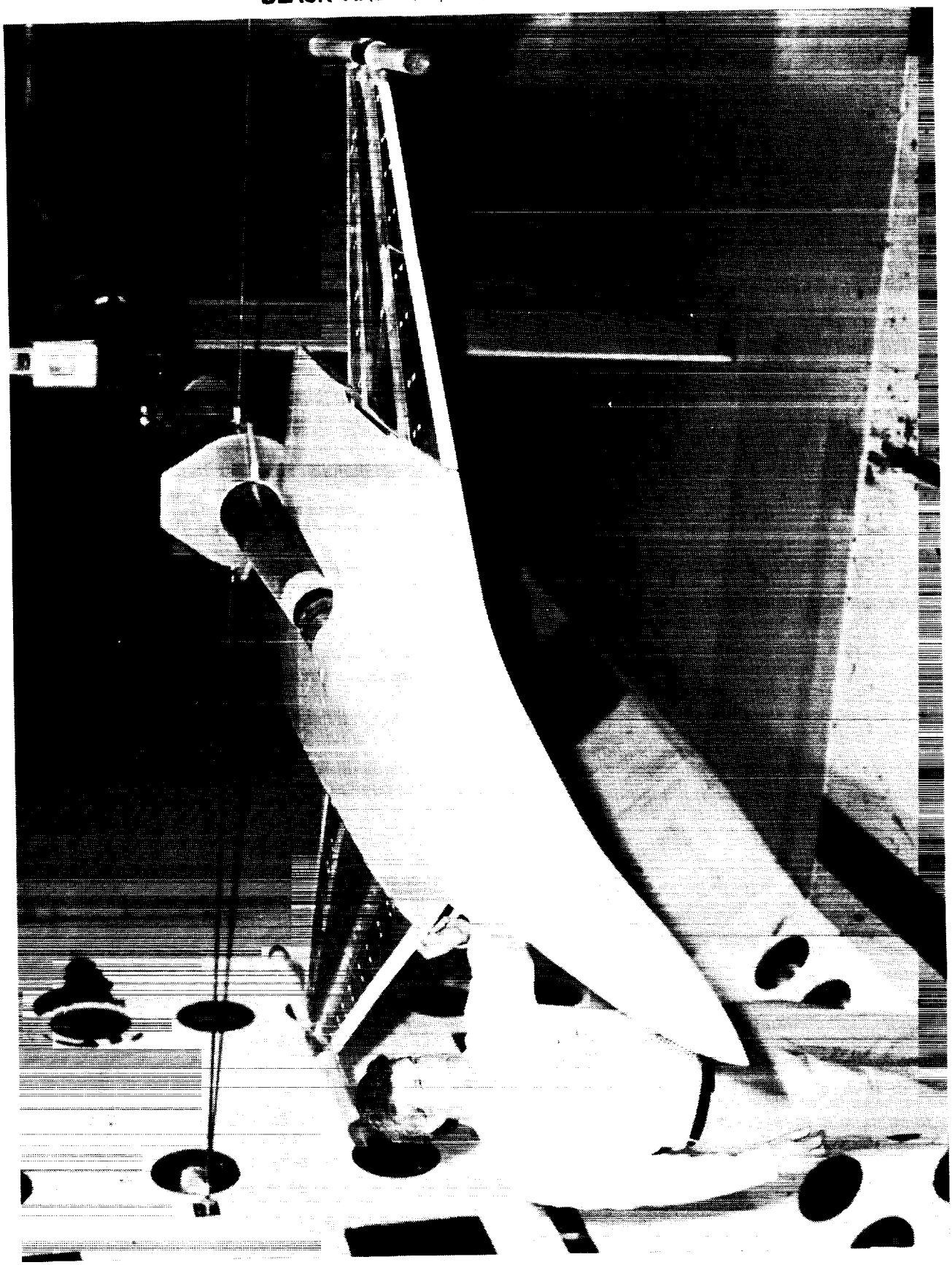

INSTRUMENTATION

The AFW model was instrumented with a six-component force-and-moment balance, accelerometers, strain-gauge bridges, rotary variable differential transducers (to measure control surface deflection angles), a roll potentiometer, and a roll-rate gyro.

AFW WIND-TUNNEL MODEL INSTRUMENTATION

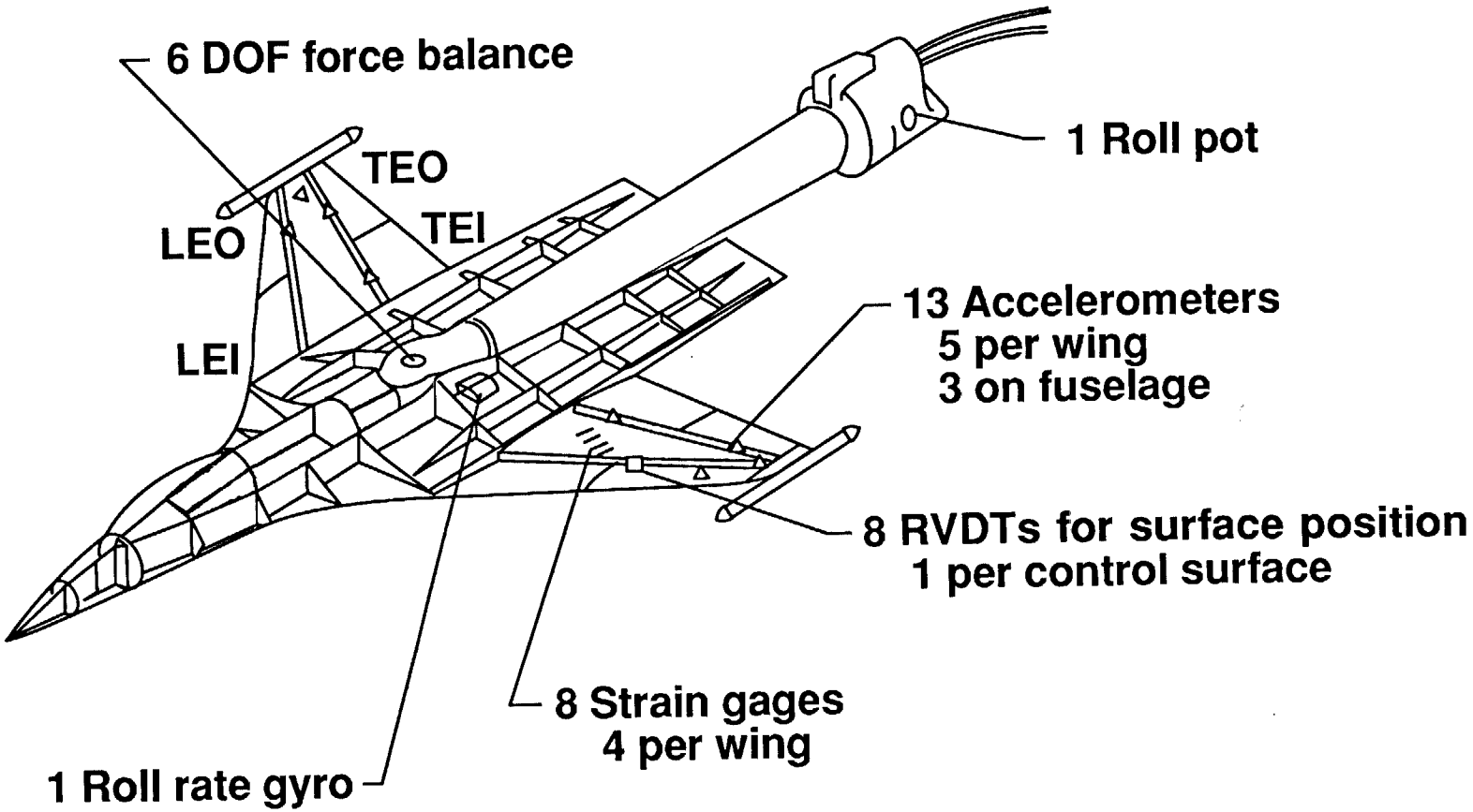

AFW MODEL DETAILS

Some of the special features of the AFW model are shown in the figure. In each of the photographs, the freestream flow direction is indicated to assist in orientation.

The photograph in the upper-left corner of the figure shows a view from upstream and above the model mounted in the TDT. The upper fuselage skin is removed to show the internal complexity of the model. Key features shown are the eight wing control surfaces, the roll brake mechanism located on the sting, and the wing tip ballast mechanism. The roll brake mechanism is designed to hold the model in place for "fixed-vehicle" testing and to stop the roll motion of the model if necessary during rolling maneuver testing. The importance of the wing tip ballast mechanism will be discussed later.

The lower, left photograph is a close-up view of internal fuselage details. Major features shown include the onboard hydraulic pump which supplies pressure to the fourteen control surface actuators and to the model pitch actuator, the pitch actuator itself, and the pitch pivot through which the model is attached to the support sting.

The lower, right photograph is a close-up view from above the trailing-edge-inboard region of the right wing with the right, trailing-edge-inboard control surface removed to show the hydraulic actuators that drive the control surfaces.

AFW MODEL DETAILS

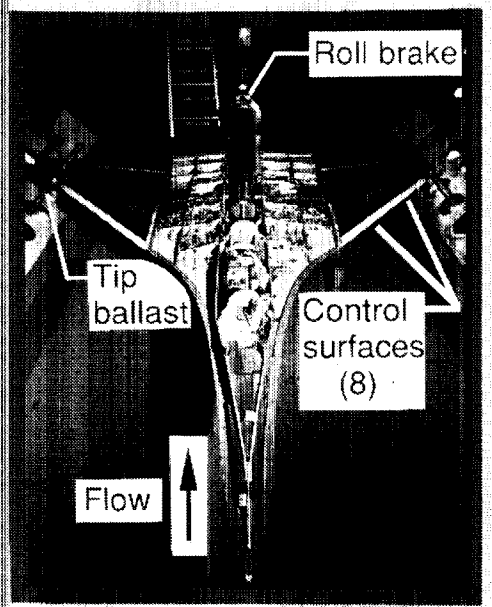

Instrumentation

- 13 accelerometers
- 8 strain gauges
- 8 RVDT
- 1 six-component balance
- 1 roll potentiometer
- 1 roll rate gyro

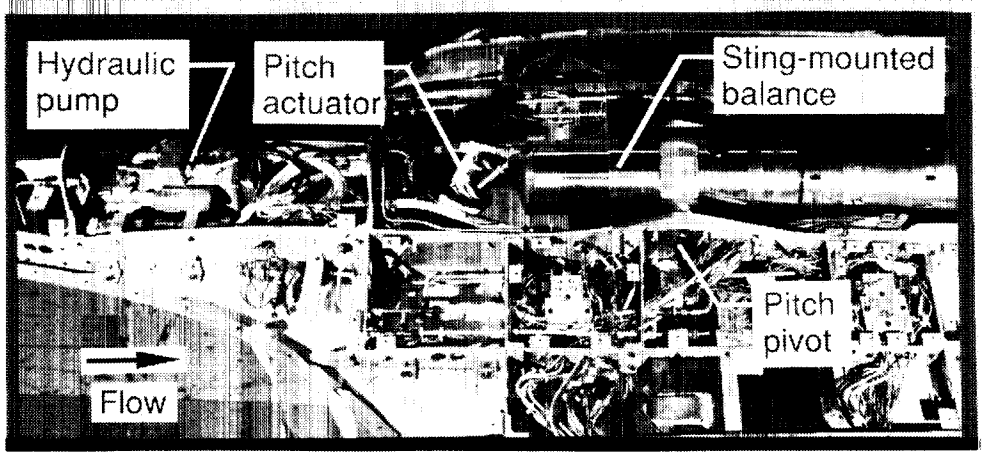

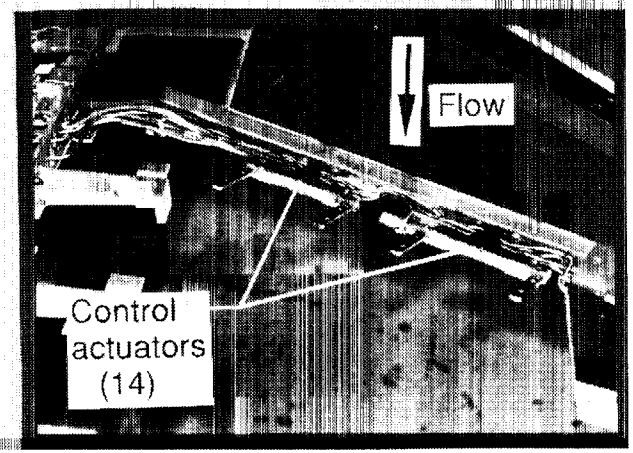

ROLL PHOTO

A special capability of the AFW wind-tunnel model is the ball-bearing mechanism built into the support sting which allows the model to have a rigid-body roll degree of freedom. This feature allows for the testing of rolling maneuver load alleviation control laws. The figure is a multiple-exposure photograph showing the model at roll angles of zero (wings level), -30, -60, and -90 degrees. The model is capable of rolling from approximately -135 degrees to +135 degrees.

ORIGINAL PAGE
BLACK AND WHITE PHOTOGRAPH

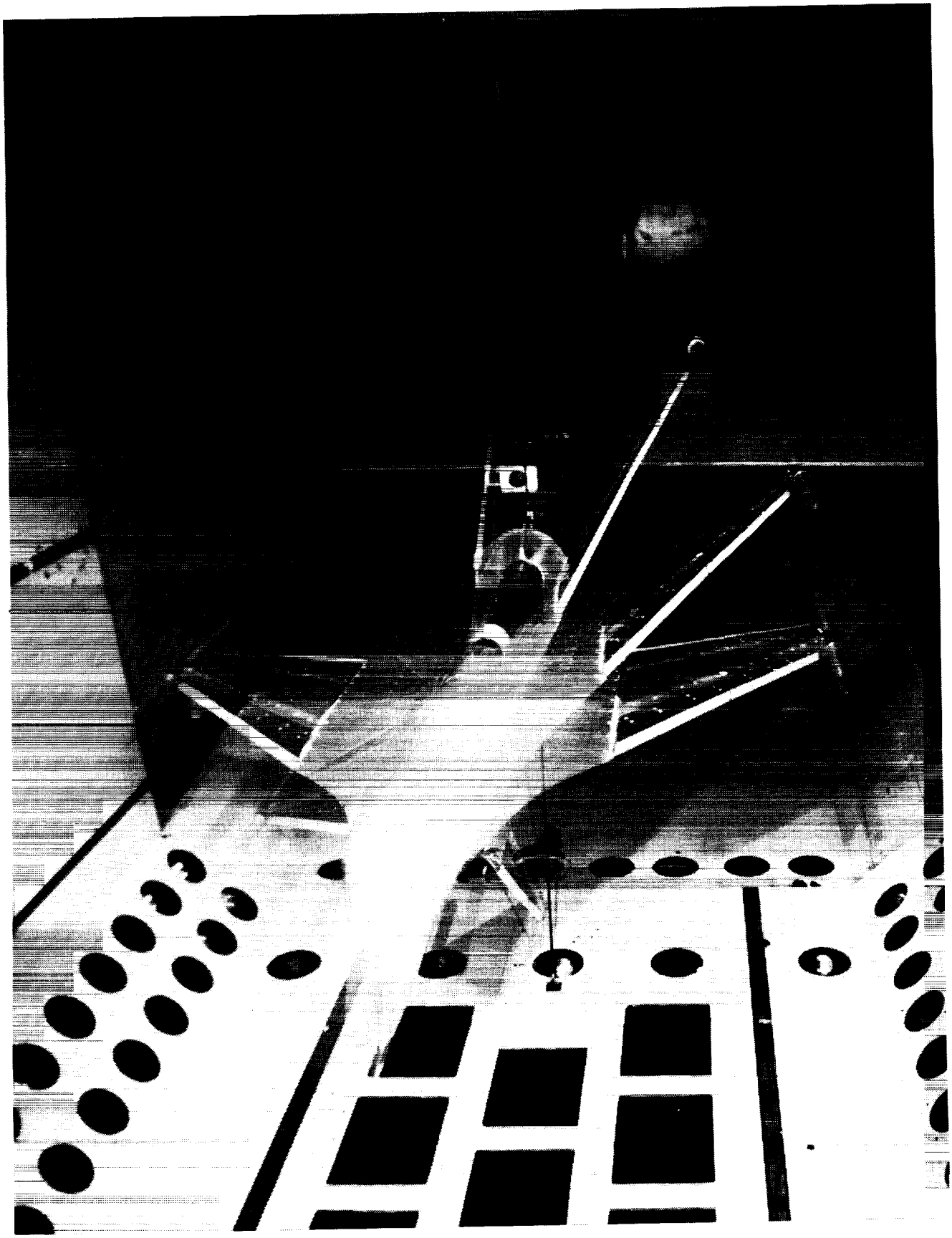

Flutter

Flutter is a dynamic aeroelastic instability of an elastic body in an airstream. Flutter onset occurs at a flow condition for which the exciting forces acting on a body are equal to the restoring forces. These exciting forces are generally unsteady aerodynamic loads and the restoring forces are usually a combination of structural forces generated through the stiffness of the body and aerodynamic forces. Flutter is characterized as a self-excited, self-sustained oscillation that occurs at a specific dynamic pressure with a specific frequency for a given Mach number condition.

Classical wing flutter occurs through the coupling of, primarily, the first wing bending and first wing torsion vibration modes. This was the type of flutter encountered for the AFW wind-tunnel model. The root locus plot shown in the figure represents a typical mapping of the poles for a bending and a torsion mode of a wing. The arrow heads indicate the direction of increasing dynamic pressure. This plot shows that the frequencies of the two modes migrate toward a common frequency, ω_f, and that the bending mode (lower path on figure) passes into the positive half of the complex plane as the dynamic pressure is increased, indicating that the flutter condition has occurred. The lower-right diagram in the figure shows a typical time history trace of wing acceleration at the flutter condition. This trace characterizes typical flutter in that it indicates a divergent instability (acceleration dynamically increasing with time) at a constant frequency ω_f.

FLUTTER

- Dynamic instability of an elastic body in an airstream
- Exciting forces equal restoring forces
- Self excited, self sustained oscillation
- Defined by critical dynamic pressure, mode frequency

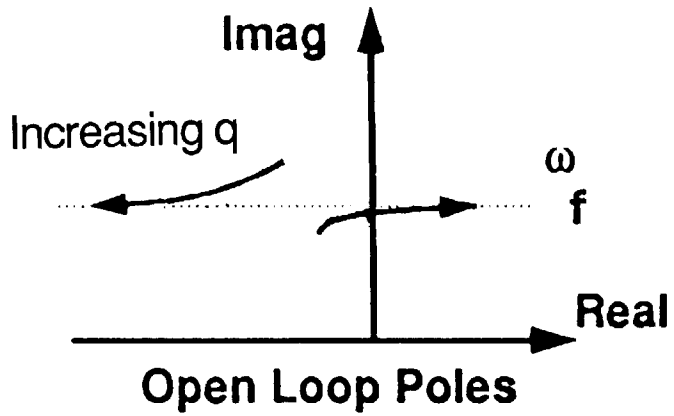

Open Loop Poles

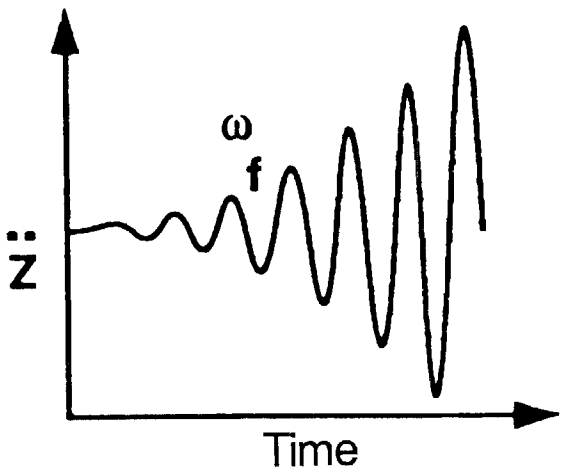

Unstable Time History

MODIFICATION OF MODEL FLUTTER BOUNDARY

The AFW model was modified for the current project so that flutter would occur within the operating envelope of the TDT. This modification consisted of adding a tip-ballast store to each wing panel. A drawing of the tip store is shown in the figure. The store is basically a thin, hollow aluminum tube with distributed internal ballast to lower the basic wing flutter boundary to a desired dynamic pressure range. Additionally, the store provides a model safety feature. Instead of a hard attachment, the store is connected to the wing by a pitch-pivot mechanism. The pivot allows freedom for the tip store to pitch relative to the wing surface. When testing for flutter, an internal hydraulic brake held the store to prevent such rotation (coupled configuration). In the event of a flutter instability, this brake was released. In the released configuration (decoupled configuration), the pitch stiffness of the store is provided by a spring element internal to the store as shown in the figure. The reduced pitch stiffness of the spring element (as compared to the hydraulic brake arrangement) significantly increases the frequency of the first torsion mode of the wing. This behavior is related to the concept of the decoupler pylon as discussed in reference 2. The raised torsional frequency leads to a significant increase in the model's flutter dynamic pressure which quickly suppressed the motion of the model on numerous occasions during the test.

MODIFICATION OF MODEL FLUTTER BOUNDARY

Goal: Demonstrate Increase in Flutter Dynamic Pressure

Problem: Basic AFW Flutter Boundary Beyond the TDT Operating Limits

Solution: Add Wing Tip Ballast to Lower Flutter Boundary

Benefit: Tip Ballast Designed as Flutter Stopper for Safety

479

FLUTTER BOUNDARIES

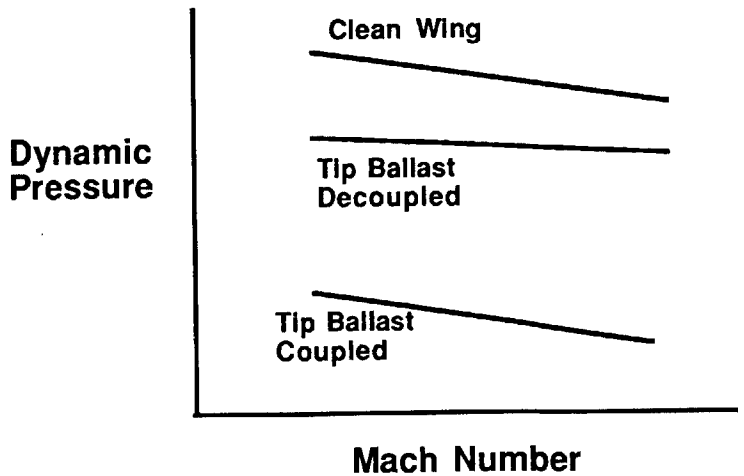

WING-TIP BALLAST

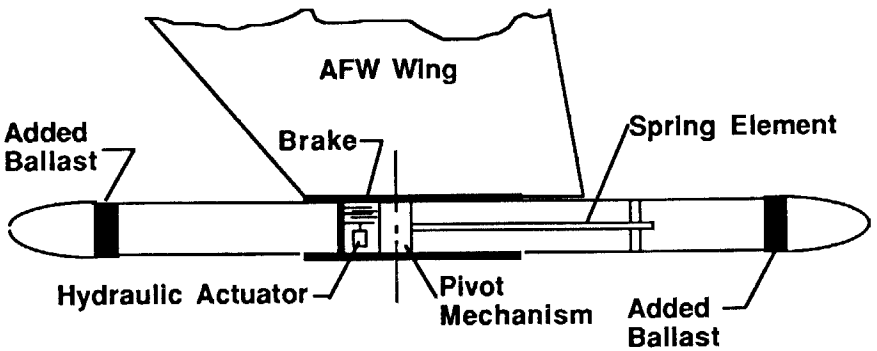

GROUND TESTS

A series of ground tests were conducted on the AFW model including actuator characterization tests, ground vibration tests, and end-to-end tests. The model and sting assembly were cantilever mounted from a backstop for these tests. Hydraulic pressure was supplied to the onboard hydraulic system so that the model would more closely match the wind-tunnel test configuration and so that control surfaces could be actuated. The measurements were made for both the coupled and the decoupled modes of the wing-tip ballast. The decoupled mode refers to the hydraulic brake within the tip ballast store being off and, therefore, the structural pitch stiffness of the tip store being provided through the internal spring mechanism.

GROUND TESTS

- Actuator Characterization
- Ground Vibration Tests
- End-to-End Tests

ACTUATOR CHARACTERIZATION

The control surface actuators were experimentally characterized for correlation with the AFW math model by conducting actuator transfer function measurements. The transfer function measurements were obtained by commanding the actuators with a constant amplitude, sinusoidal signal and sweeping the signal frequency from approximately 4 Hz to 50 Hz. The figure shows typical transfer function measurements (control surface deflection to commanded deflection) for one of the control surfaces at three different command amplitudes. The control surface pairs were oscillated both symmetrically and antisymmetrically for these measurements. The command signal and signals from most of the onboard instrumentation were stored on FM analog tape so that various combinations of transfer functions could be determined at a later time.

ACTUATOR CHARACTERIZATION

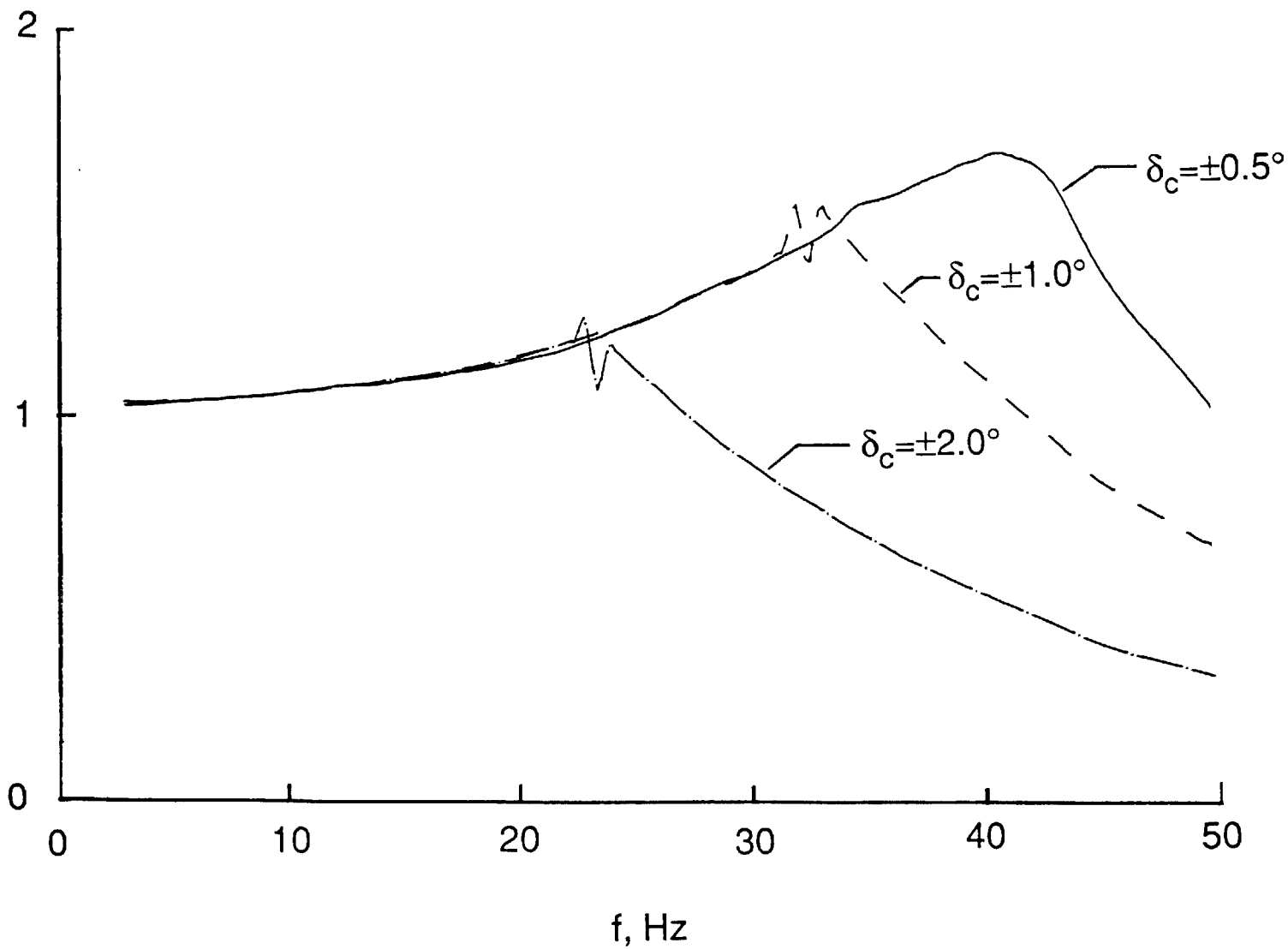

GROUND VIBRATION TESTS

A ground vibration test (GVT) was conducted on the AFW model to determine its natural frequencies, mode shapes, and damping for a number of primary vibration modes. The GVT measurements were made through the use of externally mounted accelerometers. The model was excited by a pair of electromagnetic shakers mounted under the wing surface. The shakers were driven symmetrically or antisymmetrically to obtain the appropriate results. Initial structural mode frequencies were determined using sine sweep commands to the shakers. Damping values were also assessed from transfer function measurements during the sine sweeps. Following this initial determination, sine-dwell excitation was utilized to determine the final frequencies and mode shapes. The figure shows typical experimental results for the symmetric, coupled tip ballast configuration. Measured natural frequencies and node lines are compared with analytically predicted results.

GVT RESULTS

Symmetric Coupled

—— Analysis ------ Measured

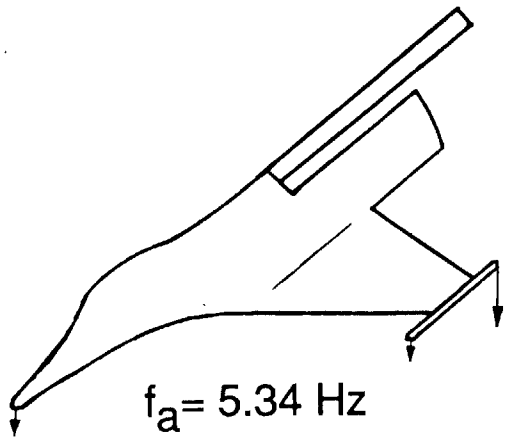

f_a= 5.34 Hz
f_m= 5.77 Hz

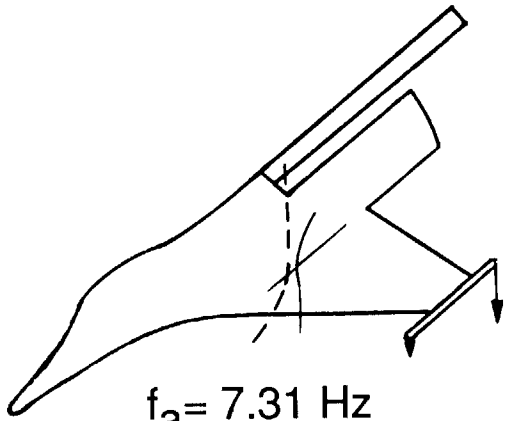

f_a= 7.31 Hz
f_m= 7.22 Hz

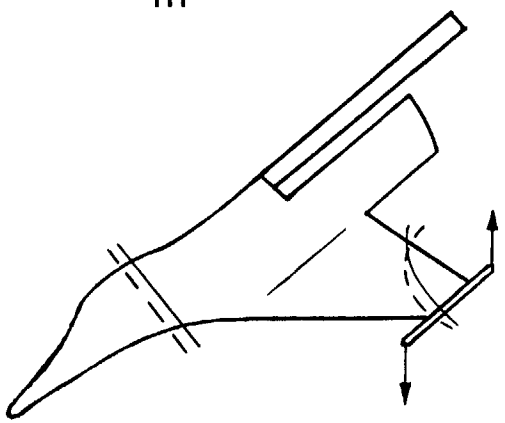

f_a= 12.85 Hz
f_m= 13.13 Hz

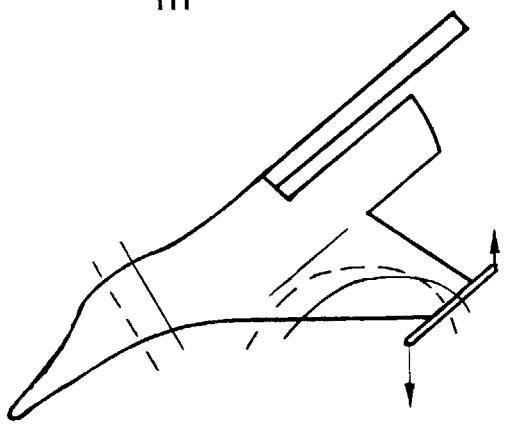

f_a= 14.79 Hz
f_m= 14.65 Hz

END-TO-END TESTS

Prior to installation of the AFW model in the wind-tunnel, a series of tests were conducted in which the digital computer hardware was in the loop with the wind-tunnel model. The purposes of these tests were to verify the hardware connectivity, to check numerical sign correlation between model electronics and software setups, to compare wind-off, open-loop control law measurements with analysis, and to verify the capability of sending wind-tunnel flow parameters from the TDT data acquisition system to the AFW digital computer system. The figure gives an indication of the types of equipment which were interconnected for these end-to-end verifications prior to the wind-tunnel test.

END-TO-END TESTS

- Verify hardware connectivity
- Compare wind-off, open-loop control law measurements with analysis
- Check numerical sign correlation
- Check for software factor errors
- Verify communication with TDT DAS

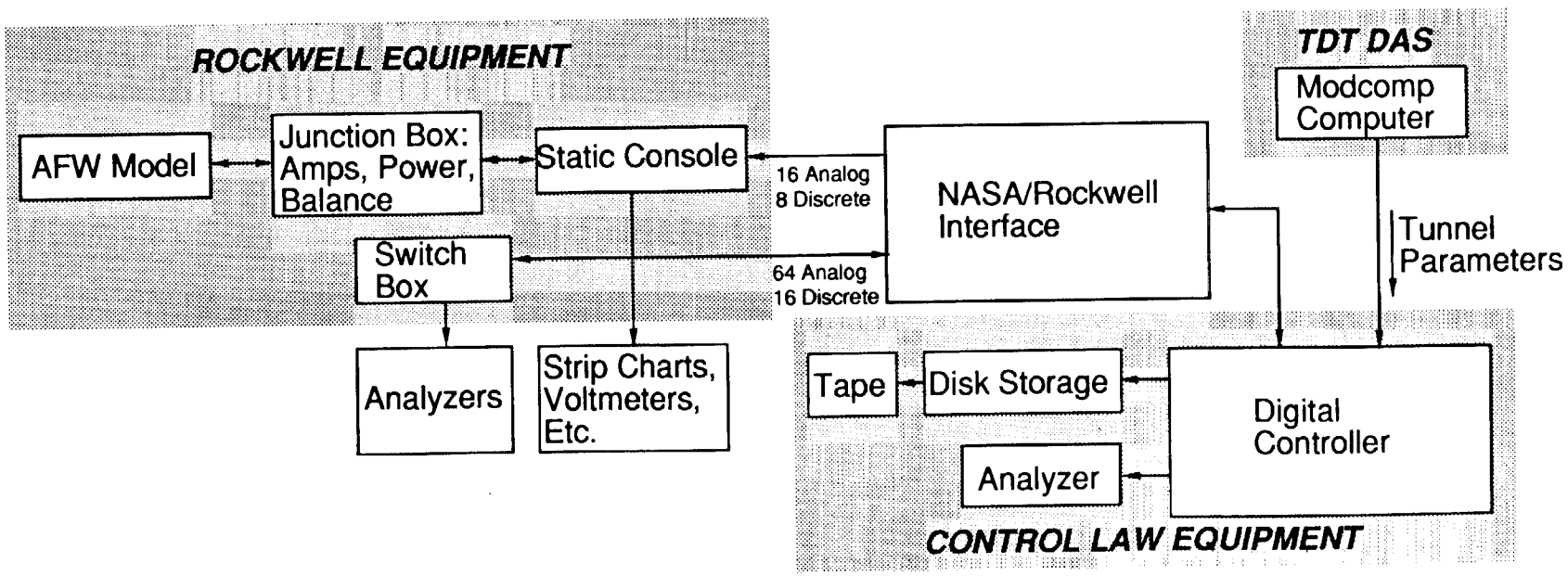

TIP BALLAST EFFECTIVENESS

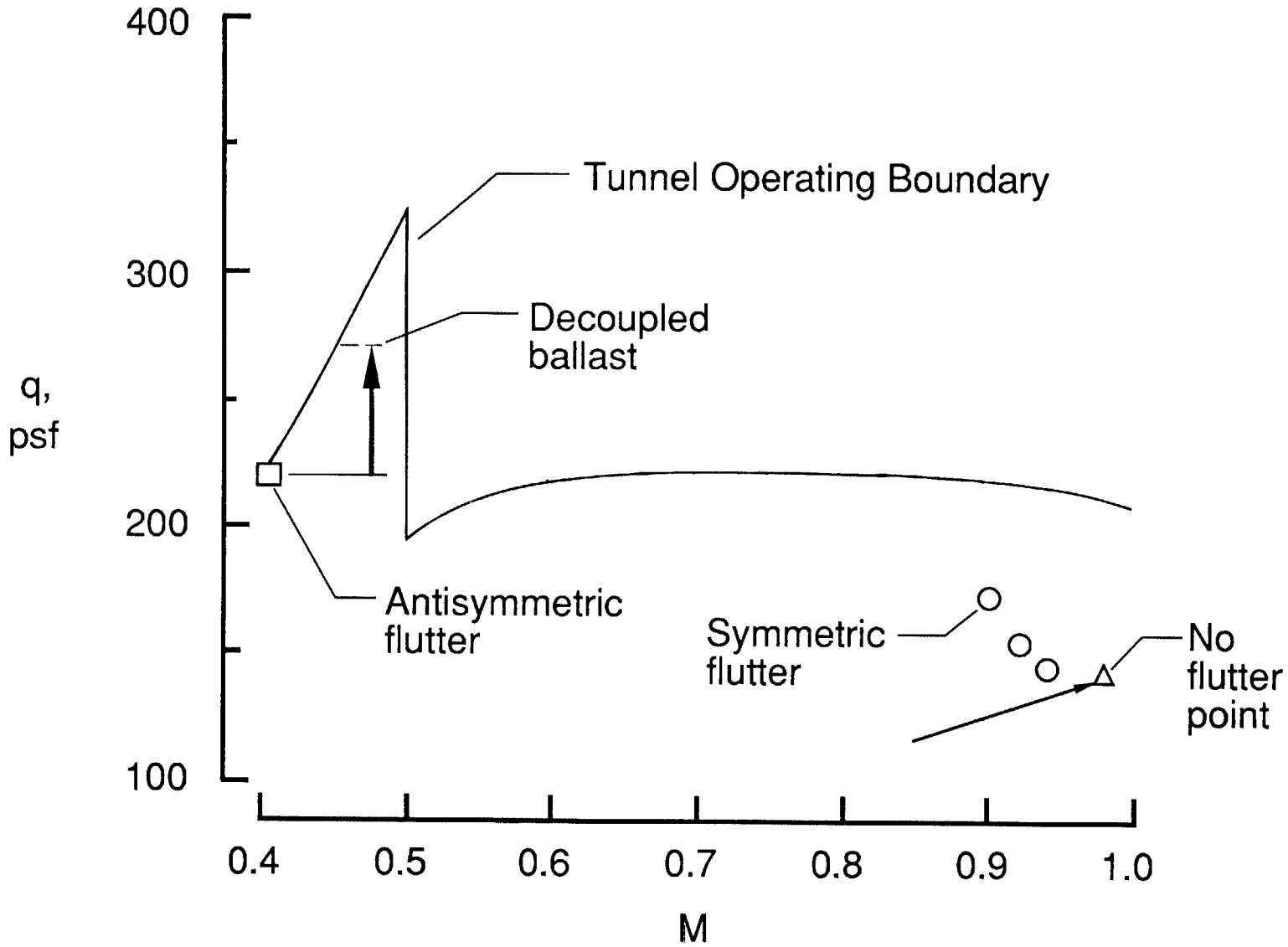

TIP BOOM EFFECTIVENESS

This figure shows experimental results which demonstrate the effectiveness of the tip ballast mechanism. Coupled-ballast flutter conditions (indicated by symbols in the figure) were found to occur within the operating capabilities of the TDT. Prior to the addition of the tip ballast, flutter could not have been encountered in the tunnel. In the decoupled configuration, the figure shows that the subsonic flutter condition was raised to dynamic pressures well beyond the coupled flutter boundary as indicated by the dashed-line boundary to which the decoupled ballast was tested. No flutter points were determined in the decoupled configuration.

TEST TIME HISTORIES

This figure shows both an open-loop and a closed-loop time history trace obtained for the AFW model during the wind-tunnel test. The open-loop trace is the antisymmetric flutter condition as measured by a wing accelerometer at tunnel conditions of M=0.40, q=221 psf. The trace shows an increasing amplitude dynamic response indicative of flutter onset. During the wind-tunnel test, this motion caused the automatic safety monitoring system to activate a number of passive flutter suppression systems (including the tip ballast decoupling) to stop the oscillation and save the model. Subtle changes in the character of the wing accelerations can be seen in the time history trace following the flutter-onset condition.

The closed-loop time history included in the figure (from the same wing accelerometer) shows that at a flow condition slightly above the open-loop flutter boundary there are no signs of an organized sinusoidal oscillation that would indicate a flutter condition.

TEST TIME HISTORIES

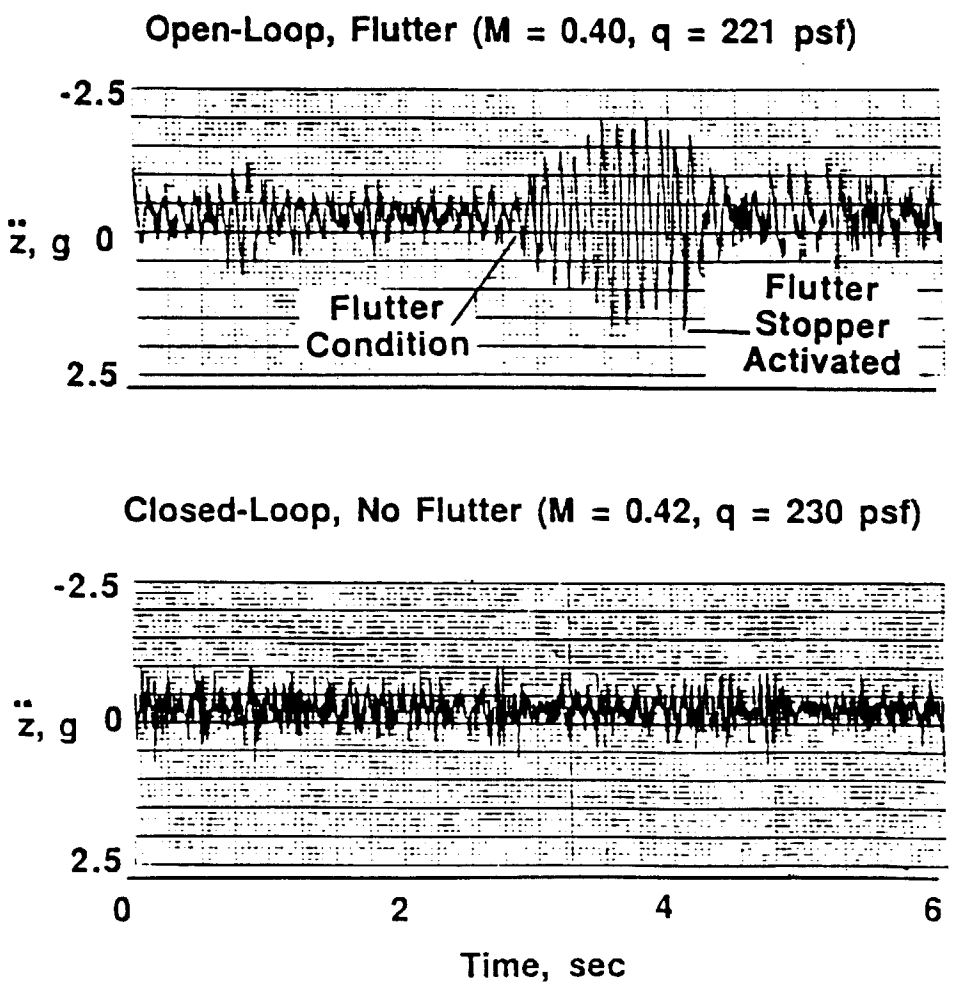

SESSION OVERVIEW

This presentation has served as an overview of the Active Flexible Wing project and has given background material concerning the wind-tunnel model and the wind-tunnel test. The five remaining presentations in this session of the Fourth Workshop on Computational Control of Flexible Aerospace Systems cover more specific aspects of the project. The figure lists the topic and authors for each of these remaining presentations in this session. The author giving the presentation is underlined.

The first of the remaining presentations covers the work that was accomplished to generate a math model of the AFW for flutter suppression system design and simulation. This presentation will also cover other flutter analyses that were accomplished using an advanced nonlinear unsteady aerodynamics computer code.

The next presentation covers the three flutter suppression systems that were designed and tested on the AFW model. The different design methodologies and performances are discussed in detail.

Following the flutter suppression system presentation, the work accomplished toward demonstrating rolling maneuver load alleviation is discussed. This presentation also touches on some of the flutter suppression system design work being done at Rockwell International in preparation for the next AFW wind-tunnel test.

The fifth presentation in this session covers the development, simulation verification, and testing of the digital controller system which was assembled for carrying out the active control law testing on the AFW model.

The last topic presents a controller performance evaluation capability which was developed specifically for testing on the AFW, but which is applicable to other multiple-input, multiple-output (MIMO) control systems. This capability was very important in predicting closed-loop stability while still in an open-loop condition and in accessing the open-loop instability condition while testing closed-loop.

SESSION OVERVIEW

- Math Modelling of the AFW (Silva, Heeg, Bennett)
- Active flutter suppression tests (Christhilf, Adams, Waszak, Srinathkumar, Mukhopadhyay)
- Rolling maneuver load alleviaton (Miller, Klepl, Moore)
- Digital controller system (Hoadley, Buttrill, McGraw, Houck)
- Controller performance evaluation (Pototzky, Wieseman, Hoadley, Mukhopadhyay)

CONCLUDING REMARKS

Some of the key accomplishments of the October, 1989 wind-tunnel test are shown on the attached figure. As presented, an assessment of the open-loop flutter boundary was accomplished near M=0.4 and M=0.9. The tip ballast was shown to provide a safety margin in terms of where the flutter conditions occurred between the coupled and decoupled ballast modes. Additionally, the tip ballast was remotely decoupled several times while experiencing high dynamic response during the wind-tunnel test and no adverse reactions were encountered. It is difficult to directly assess the effectiveness of the tip ballast as a flutter stopper since other passive flutter suppression devices were always activated simultaneously with the decoupling of the tip ballast. A major accomplishment of the 1989 test was the development and testing of the digital controller. The digital controller hardware and software performed very well during the test. Concerning the control law tests, all three flutter suppression systems were tested and one of these control laws took the model to a dynamic pressure 24 percent above the open-loop flutter dynamic pressure.

In terms of future plans, the 1989 test indicated that improvements in the math model of the AFW would be very beneficial for future control law development. Therefore, an extensive task was undertaken to refine the finite element model. This work is now completed. Also, a free-to-roll math model has been developed to allow analyses appropriate for rolling maneuver load alleviation and for free-to-roll flutter suppression testing. Using these new math models, control laws will be developed for both rolling maneuver load alleviation and flutter suppression system testing during the 1991 wind-tunnel test. A major goal of the 1991 wind-tunnel test is to simultaneously demonstrate rolling maneuver load alleviation and flutter suppression.

CONCLUDING REMARKS

Oct. '89 Test Accomplishments

- Flutter boundary determined
- Tip-ballast store performed extremely well
- Digital controller hardware and software performed extremely well
- Three digital flutter suppression systems (FSS) tested
- 24% increase in flutter dynamic pressure demonstrated for one control law

Feb. '91 Test Plans

- Refine finite element model and develop aeroelastic model for free-to-roll
- Demonstrate RMLA control laws
- Demonstrate FSS control laws for free-to-roll
- Combine and demonstrate FSS during rolling maneuvers

Aeroelastic Modelling of the Active Flexible Wing Wind-Tunnel Model

Walter A. Silva
Lockheed Engineering and Sciences Company
303A Butler Farm Road
Hampton, VA 23666
(804)864-2834

Jennifer Heeg
Mail Stop 243
NASA-Langley Research Center
Hampton, VA 23665-5225
(804)864-28

Robert M. Bennett
Mail Stop 173
NASA-Langley Research Center
Hampton, VA 23665-5225
(804)864-2274

INTRODUCTION

The Active Flexible Wing (AFW) is a full-span, sting-mounted wind-tunnel model that is currently being used by the NASA-Langley Research Center (NASA-LaRC) and the Rockwell International Corporation for evaluation of multifunction, digital control laws[1]. An understanding of the model's open-loop aeroelastic behavior is, therefore, essential for closed-loop analysis and safety during wind-tunnel testing.

Aeroelastic modelling of the AFW includes the structural and aerodynamic definition of the model via the ISAC (Interaction of Structures, Aerodynamics, and Controls) codes[2]. A state-space aeroelastic model that is appropriate for subsequent closed-loop analysis is generated. One of the ISAC codes is the linear doublet lattice unsteady aerodynamic theory for computing linear aeroelastic forces[3]. Aeroelastic analyses of the AFW in the transonic aerodynamic regime, where nonlinear aerodynamic effects are significant, were performed using the CAP-TSD (Computational Aeroelasticity Program-Transonic Small Disturbance) code[4].

This presentation will address the overall modelling process, including assumptions, approximations, modifications, and corrections (using experimental data) that went into obtaining the best "pre-test" aeroelastic model of the AFW. Details of the modelling assumptions required for the CAP-TSD code are also presented. Results for both the linear and nonlinear aerodynamic analyses are presented in the form of flutter boundaries. These predicted results are compared with results from the most recent tunnel entry in the fall of 1989.

LINEAR MATH MODEL DEVELOPMENT
Flowchart and Outline

The first step in developing aeroelastic equations of motion for a flexible vehicle is to define the structural dynamic behavior of the vehicle, that is, the modes of vibration of the vehicle and their associated frequencies and generalized masses. For this purpose, a NASTRAN finite element model (FEM) of the AFW was developed by Rockwell International from which symmetric and antisymmetric sets of modal data were obtained.

Both the symmetric and antisymmetric structural models were used in the ISAC system of codes. The ISAC codes were used to generate state-space equations of motion to predict open- and closed-loop aeroelastic responses (with controller). Details of the ISAC codes and procedures for using test data to improve the accuracy of the equations of motion will be presented. The resultant equations of motion are then passed on to control law designers and simulation engineers.

Due to the large computational requirements of the CAP-TSD code, only symmetric analyses were performed. Details of the CAP-TSD code and its application to the AFW are described following the discussion concerning the linear modelling procedures.

AEROELASTIC MODELLING AND ANALYSIS
Flowchart & Outline

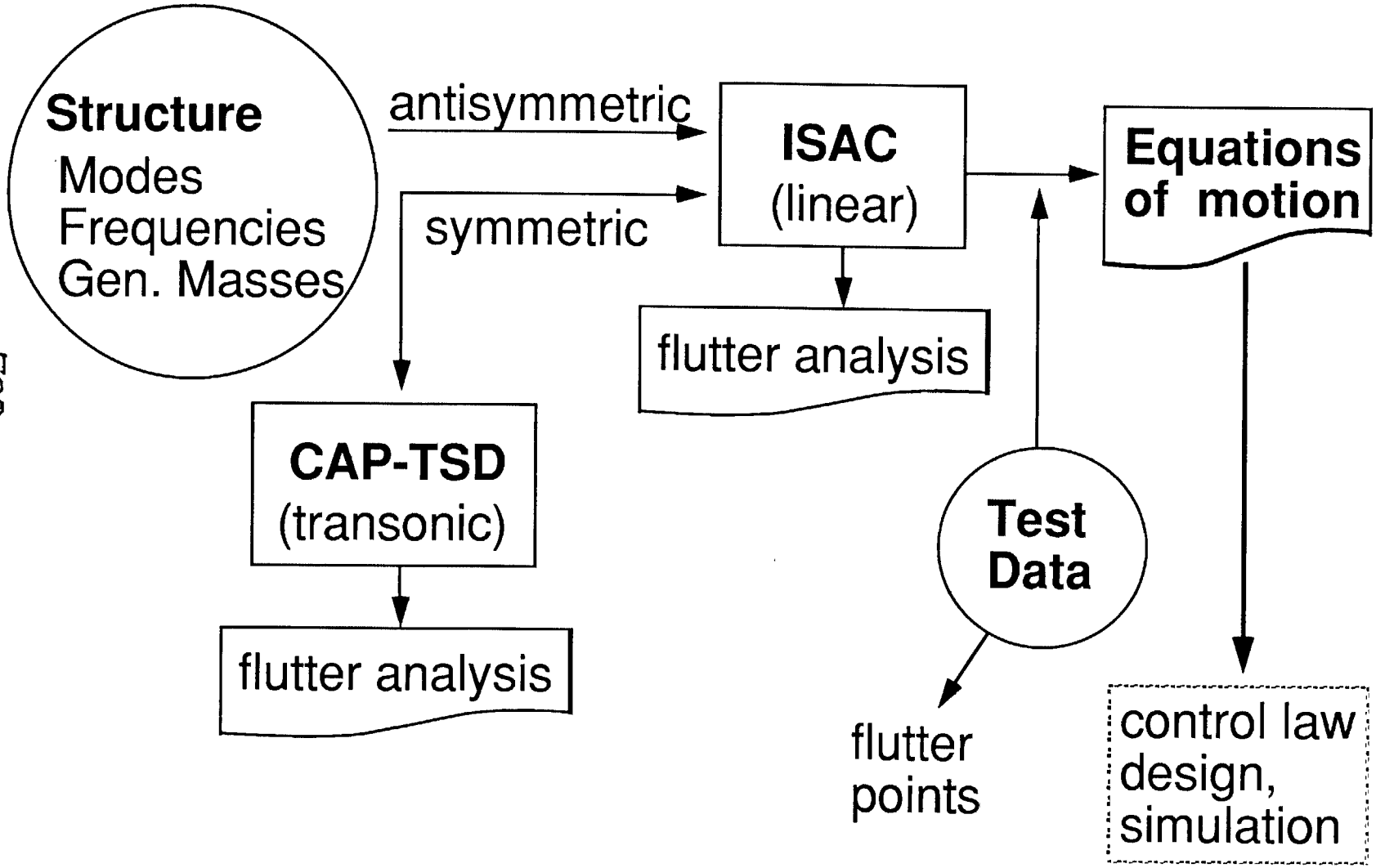

LINEAR MATH MODEL DEVELOPMENT
Configurations Analyzed

Six structural models of the AFW were developed: symmetric and antisymmetric with tip-ballast store coupled and decoupled. In addition, antisymmetric models were also developed with the roll-brake on and the roll-brake off. This presentation, however, will address only the roll-brake-on (no rolling) configurations. The resultant matrix of structural models is shown in the figure.

In the coupled configuration, the wing tip-ballast store is rigidly attached to the wing so that the motion of the ballast is felt by the wing. In the decoupled configuration, the ballast store is decoupled from the wing dynamics by means of a very flexible spring attachment between the store and the wing. The difference between these two configurations can be seen in the figure, which shows the first wing bending mode for both the coupled and decoupled cases. The coupled configuration is the more flutter critical of the two conditions. Experimentally, when flutter is encountered in the coupled configuration, the ballast is mechanically decoupled from the wing so that the vibration characteristics are altered to those of the decoupled configuration, thereby eliminating the flutter condition. Equations of motion (system quadruples) were generated for all of these models for subsequent use in control law design and analysis.

Vibration frequencies were measured during a ground vibration test (GVT) but only those measured for the coupled configuration were considered to be accurate. These GVT measured frequencies, and a subset of the original analytical modeshapes, were then used in the analysis of the coupled configurations.

LINEAR MATH MODEL DEVELOPMENT
Configurations Analyzed

tip ballast store

	coupled	decoupled
sym	x o	x
a/s	x	x

x - linear aerodynamic analysis (doublet lattice)

o - nonlinear aerodynamic analysis (CAP-TSD)

First Wing Bending

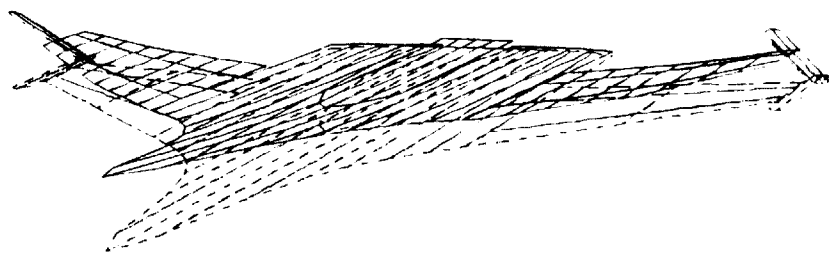

Decoupled

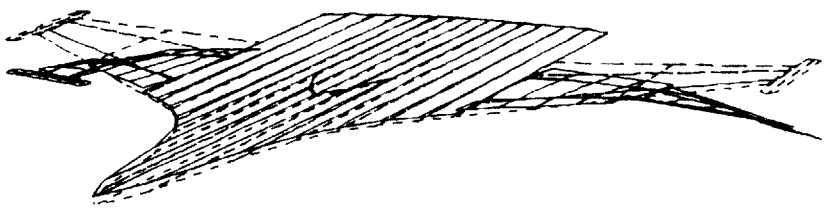

Coupled

LINEAR MATH MODEL DEVELOPMENT
The ISAC Modules

The ISAC compendium of codes consists of four primary modules. DLIN (Doublet Lattice INput) is a preprocessor to the doublet lattice unsteady aerodynamic code. DLIN takes modeshape and planform input and computes deflections and slopes of each modeshape at the quarter- and three-quarter-chord locations of the aerodynamic boxes (shown in a later figure). This information is then used by DLAT (Doublet LATtice), which uses the doublet lattice unsteady aerodynamic theory, to compute generalized aerodynamic forces (GAF's). The GAF's, along with generalized masses, frequencies, and dampings, are input to DYNARES (DYNamic RESponse) where several different analyses can be performed. These include the aerodynamic approximation to be addressed later, flutter analysis, frequency responses, time-history responses, and generation of the state-space system matrices. The fourth module, DCM (Data Complex Manager), handles the processing of data arrays from one module to the other.

LINEAR MATH MODEL DEVELOPMENT
The ISAC Modules

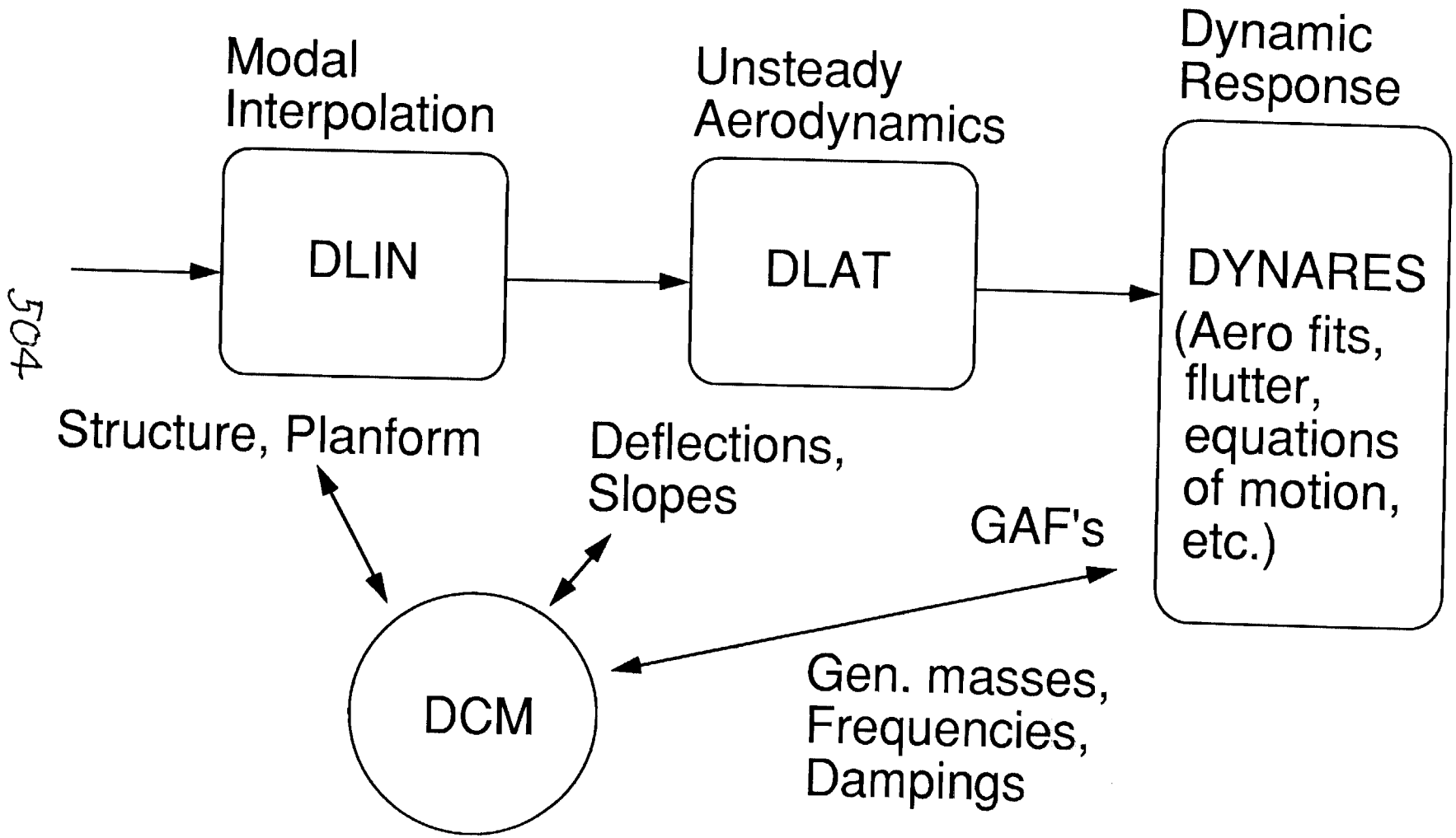

LINEAR MATH MODEL DEVELOPMENT
Linear Aerodynamics

The unsteady aerodynamics induced by the flexible motion of the AFW were computed using the doublet lattice unsteady aerodynamic theory. Doublet lattice theory is a linear, frequency-domain theory limited to subsonic flows. The AFW was modelled aerodynamically as a half model with a plane of symmetry (or antisymmetry) at the fuselage centerline. In doublet lattice theory, lifting surfaces are modelled as flat plates with aerodynamic boxes as shown on the figure. Aircraft components such as fuselage or stores can be modelled as slender bodies. For this analysis, however, the fuselage and tip-ballast store were modelled as flat plates. Modelling of the tip-ballast store as a flat plate was done by varying the width of the paneling arrangement until the flutter dynamic pressure matched the flutter dynamic pressure of an analysis in which a slender body representation of the tip-ballast store was used. The reason for modelling with flat plates instead of slender bodies was to minimize the number of aerodynamic boxes, thereby increasing the efficiency of the code for generating equations of motion.

LINEAR MATH MODEL DEVELOPMENT
Linear Aerodynamics

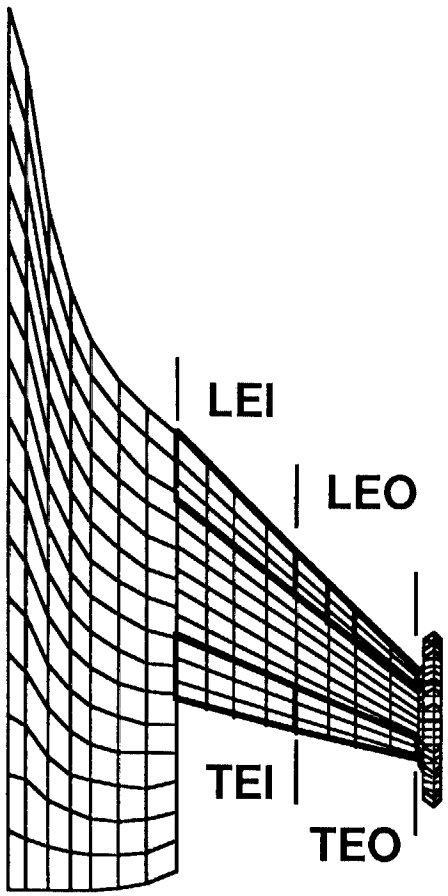

- Applied doublet lattice code (ISAC)
  - linear
  - subsonic
  - frequency domain
  - flat plate lifting surfaces
- Used half model with symmetry
- Fuselage and tip ballast store modelled as flat plates

LINEAR MATH MODEL DEVELOPMENT
Linear Aerodynamics (cont'd)

The output from the doublet lattice code consists of generalized aerodynamic forces (GAF's) which are tabular functions of Mach number and reduced frequency ($\omega b/V$, where ω is the frequency of oscillation, b is the root semi-chord, and V is the freestream velocity). In order to generate time-domain (state-space) equations of motion, however, these aerodynamic forces need to be in the time domain and not the frequency domain. The typical approach to this problem is to approximate the GAF's using rational functions[5] of the nondimensional Laplace variable p. The A coefficients are computed and the b_l terms are the lags arbitrarily specified by the user or obtained using optimization. This then casts the frequency-domain GAF's into the time-domain. This process, however, can significantly increase the size of the state equations of motion. The number of states that the plant structural equations are augmented by due to the inclusion of rational function approximations, developed using a least squares approach, is equal to the number of modes times the number of lags. Ten modes and two lags result in twenty additional aerodynamic states. The larger the number of lags, however, the more accurate the approximation to the aerodynamics. Thus, a tradeoff between accuracy and computational size needs to be defined.

LINEAR MATH MODEL DEVELOPMENT
Linear Aerodynamics (cont'd)

$$Q_{ij} \cong \hat{Q}_{ij}$$

$$\hat{Q}_{ij}(p) = (A_0)_{ij} + (A_1)_{ij}\, p + (A_2)_{ij}\, p^2 + \sum_{\ell=1}^{n} (A_{(\ell+2)})_{ij} \frac{p}{p + b_\ell}$$

$$p = \frac{b\, s}{V}$$

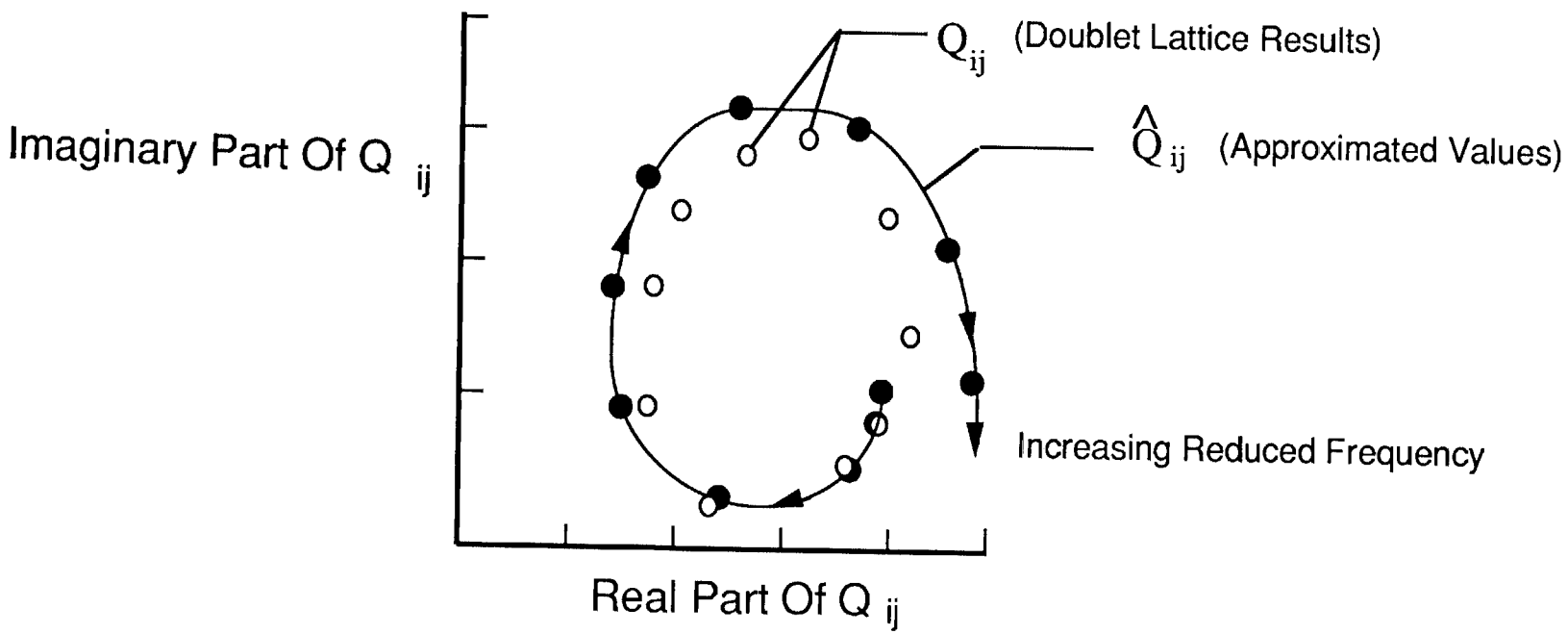

LINEAR FLUTTER PREDICTIONS

Flutter boundaries, computed using the linear doublet lattice unsteady aerodynamic theory, are shown on the figure for the tip-ballast store coupled and decoupled, symmetric and antisymmetric cases along with the Transonic Dynamics Tunnel (TDT) operating envelope. The effect of decoupling the tip-ballast store is evident: flutter boundaries are raised above the tip-ballast-store-coupled boundaries. For a given configuration, the region below the boundary is stable while the region above the boundary is unstable. These flutter boundaries are for a previous set of mode shapes and as such do not represent the latest results. They are being presented only to illustrate the decoupling effect on the flutter boundary. Results using an updated set of modeshapes and frequencies for the coupled tip-ballast store configuration are presented later in this paper; the decoupled flutter boundaries were not recalculated because test results indicated that the boundaries fall outside the tunnel's operating envelope.

LINEAR FLUTTER PREDICTIONS

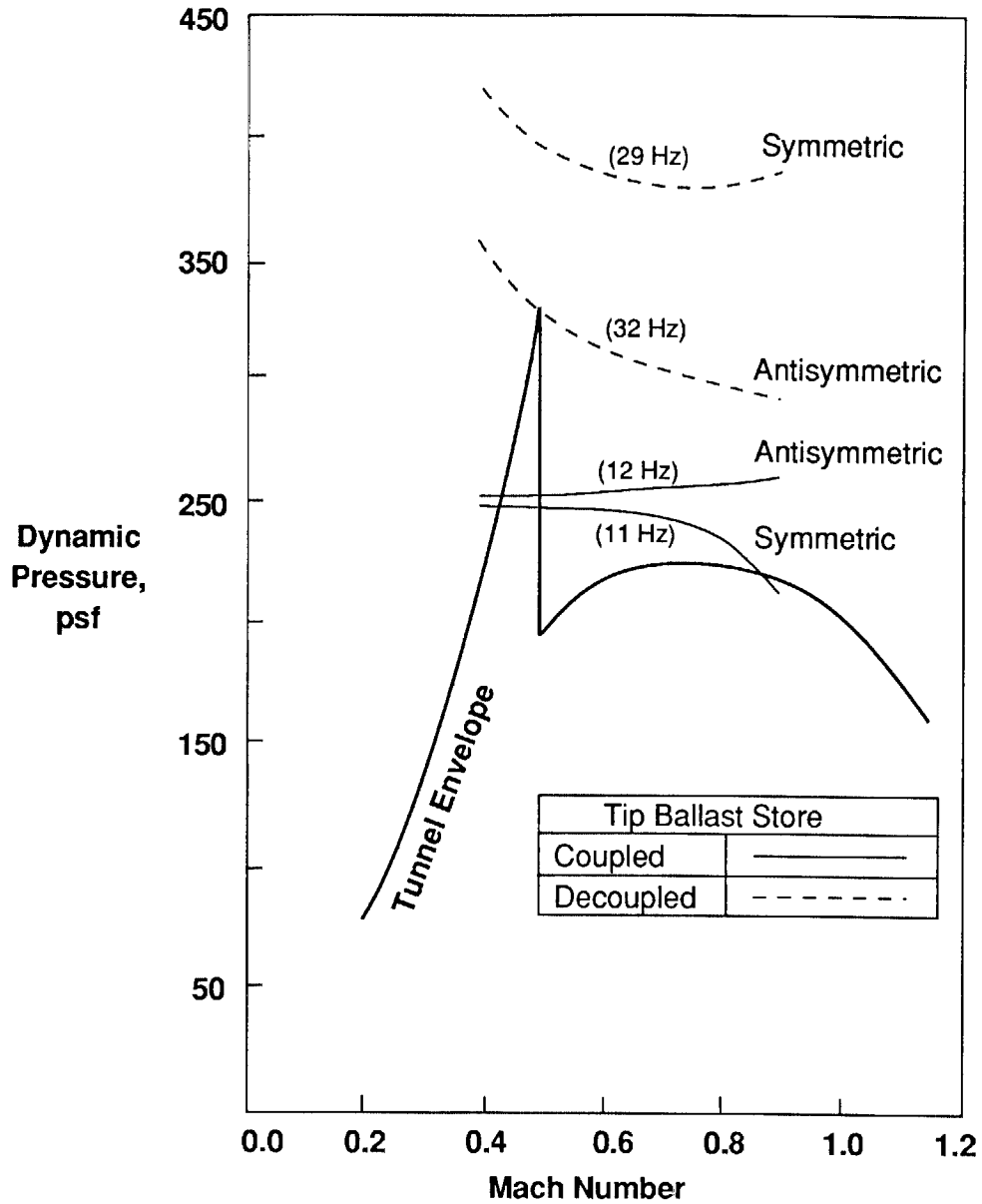

LINEAR MATH MODEL DEVELOPMENT
Control Surface Effectiveness

Accurate prediction of control derivatives (such as lift due to control surface deflection) is essential for accurate control law design. In order to improve the analytical predictions of control derivatives (using the doublet lattice code), a procedure was developed for correcting the analytical derivatives using wind-tunnel data. The wind-tunnel data consists of measured static loads induced by control surface deflections at several dynamic pressures and Mach numbers from which effectiveness parameters (derivatives) can be computed and tabulated. The procedure assumes that each effectiveness parameter (function of dynamic pressure) can be separated into a rigid component (at zero dynamic pressure) and an elastic increment which can be added to the rigid component as dynamic pressure (or flexibility) is increased. This assumption is applied to both the analytical and experimental effectiveness parameters from which two sets of correction factors are computed: a ratio of experimental to analytical rigid values, f_1, and a ratio of experimental to analytical elastic increments, f_2. Note that f_1 is a constant and f_2 is a function of dynamic pressure. Although these corrections are for static conditions only, they were applied at all dynamic conditions as well.

LINEAR MATH MODEL DEVELOPMENT
Control Surface Effectiveness

- Analytical control surface derivatives corrected to match experiment

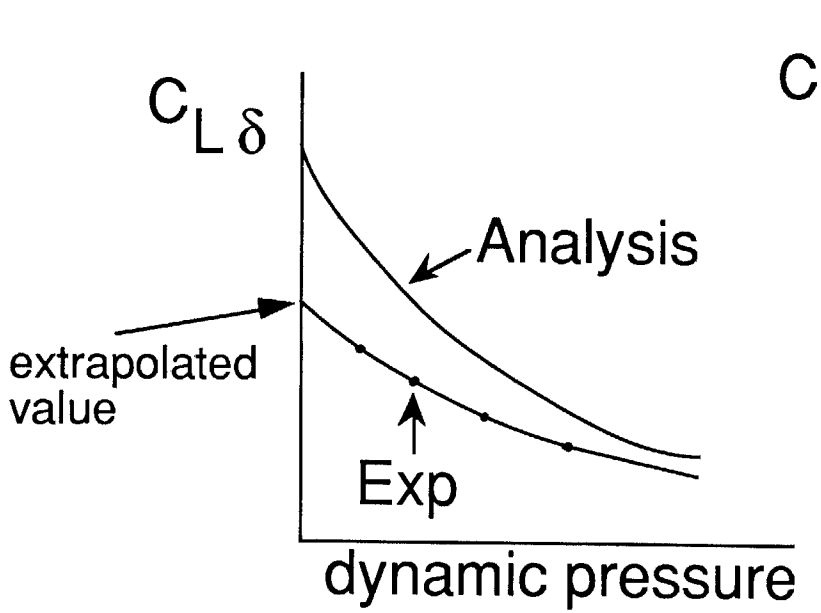

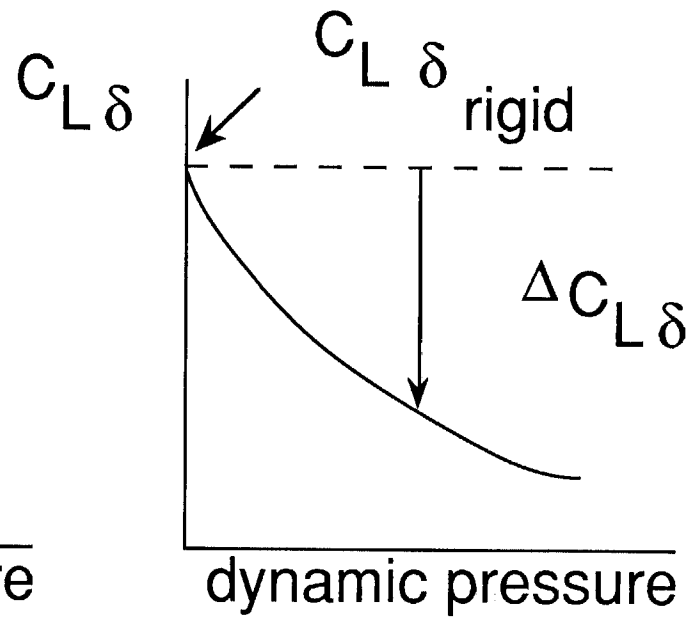

$$C_{L\delta}{}_{corrected} = f_1 \left(C_{L\delta}{}_{rigid}\right)_{analytical} + f_2(q) \left(\Delta C_{L\delta}\right)_{analytical}$$

LINEAR MATH MODEL DEVELOPMENT
Actuator Model

Another important ingredient in the development of an accurate state-space model of the AFW is the modelling of the actuator dynamics. Actuator transfer functions were measured during the GVT for all control surfaces for the aerodynamically unloaded (zero airspeed) case. Analytical transfer functions were generated using a least-squares method to fit the discrete experimental values. A comparison between experimental data and a least-squares fitted model is shown in the figure. The resultant transfer functions are of zeroth order in the numerator and third order in the denominator.

LINEAR MATH MODEL DEVELOPMENT
Actuator Model

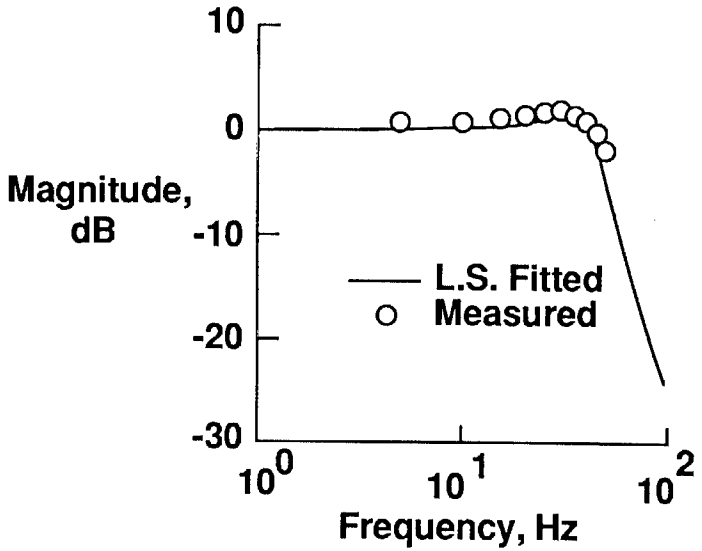

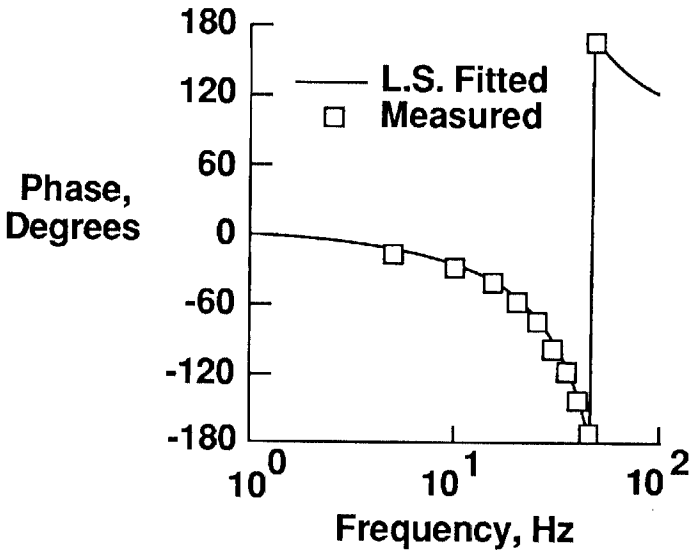

Fitted TF's are $\dfrac{K}{(s - p_1)(s^2 + 2\zeta\omega_n s + \omega_n^2)}$

LINEAR MATH MODEL DEVELOPMENT
State-Space Model

Finally, once all of the previously mentioned modelling steps have been taken, a state-space sytem can be created. This is the plant model which is used by the control system designers for their design and analysis work. A Dryden gust mode is included in the equations of motion to model wind-tunnel turbulence (results in two additional states). The loads, consisting of shear, bending moment, and torsion moment at 14 different locations, were computed using the mode displacement method.

LINEAR MATH MODEL DEVELOPMENT
State-Space Model

$$\dot{x} = Ax + Bu$$
$$y = Cx + Du$$

States (x):

10 elastic modes	= 20
1 aero lag	= 10
4 3rd order act.	= 12
gust modes	= 2
	44

Outputs (y):

sensors	= 8
pilot inputs	= 4
actuators	= 12
loads	= 42
gust	= 1
	67

Inputs (u):

4 control surfs	= 4
gust	= 1
	5

NONLINEAR AERODYNAMIC ANALYSIS
CAP-TSD Code

Before open-loop flutter testing of the AFW was to begin, it was desirable to have analytical predictions of the model's flutter boundary for use as guidance during flutter testing. The range over which testing was to occur included the transonic Mach numbers. Although linear aerodynamics are applicable at subsonic and supersonic Mach numbers, unsteady transonic aerodynamics requires the solution of nonlinear equations. One of these equations is the transonic small disturbance (TSD) equation. A time-accurate, approximate factorization algorithm that solves this equation is the CAP-TSD (Computational Aeroelasticity Program - Transonic Small Disturbance) code developed at the NASA - Langley Research Center. The code can handle realistic configurations that include multiple lifting surfaces with control surfaces, vertical surfaces, bodies (pylons, nacelles, and stores), and a fuselage. The structural equations of motion and the nonlinear aerodynamic equations are coupled and integrated in time. The result of this time stepping is a time history of the generalized displacements of the vehicle.

NONLINEAR AERODYNAMIC ANALYSIS
CAP-TSD Code

- Computational Aeroelasticity Program-Transonic Small Disturbance
- Uses time-accurate, approximate factorization finite-difference algorithm
- Applied to realistic configurations
- Structural equations of motion and aerodynamic solutions are coupled and integrated in time
- Result is the time history of the generalized displacements of the aeroelastic system

NONLINEAR AERODYNAMIC ANALYSIS
Assumptions and Limitations

A full and accurate understanding of the flutter results that are to be subsequently presented requires a knowledge of the assumptions and limitations of transonic small disturbance (TSD) theory and of the CAP-TSD code. TSD theory assumes inviscid, irrotational flow so that the effects of vortices, boundary layer, and separated flow on the aeroelastic behavior of the AFW will not be accounted for. Vorticity and entropy corrections were incorporated into the CAP-TSD code for improved shock modelling but difficulties with this part of the code prevented their use in the AFW analysis.

Bodies, such as the tip-ballast store and the fuselage, are not given any modal definition in the current version of CAP-TSD. That is, bodies serve only as aerodynamic influences on the lifting surfaces. This limitation can and should be corrected in future versions of the code. Another limitation is that only symmetric modes can be analyzed with a half-model of the AFW so that analysis of the antisymmetric modes requires both left and right sides. This is not a limitation of the code but is due to the uncertainty of the loads generated at the centerline of the vehicle due to anti- or asymmetric motions of the vehicle.

NONLINEAR AERODYNAMIC ANALYSIS
Modelling Assumptions and Limitations

- Bodies do not have modal definition; serve only as influence on lifting surfaces
- Vorticity and entropy corrections were not used
- Symmetric, half-model of the AFW analyzed

NONLINEAR AERODYNAMIC ANALYSIS
Model Definition

The computational CAP-TSD model of the AFW consisted of eight symmetric modeshapes (for the coupled case) and the GVT frequencies for those modes. The grid was dimensioned 134 by 51 by 62 grid points in the x-, y-, and z-directions respectively. The grid density was increased in regions where large changes in the flow were expected such as at the leading edge, trailing edge, wing tip, and control surface boundaries. The grid extended ten (10) root chords in the upstream, downstream, positive z- and negative z-directions, and two (2) root chords in the y-direction.

A computer-generated picture of the CAP-TSD model of the AFW is shown on the facing page. The picture shows both left and right sides although only the right side is defined. The modelling of the fuselage and tip ballast store as bodies is clearly seen. In order to model the effects of the wind-tunnel sting mount, the computational fuselage was extended to the downstream boundary of the grid.

NONLINEAR AERODYNAMIC ANALYSIS
Model Definition

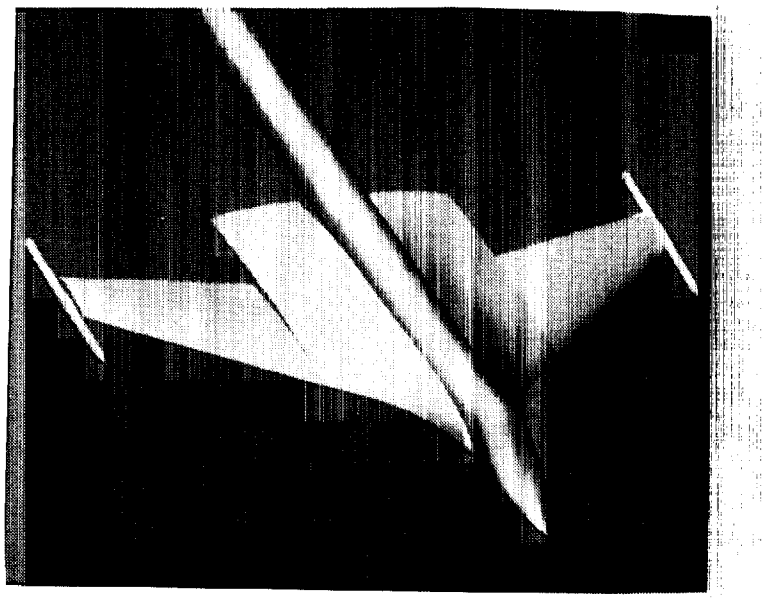

NONLINEAR AERODYNAMIC ANALYSIS
Static Aeroelastic Analysis

In linear aeroelastic analyses, the dynamic behavior is independent of static parameters such as airfoil shape and vehicle angle of attack. At transonic Mach numbers, however, this is no longer true as airfoil shape and angle of attack can significantly affect the dynamic response of the vehicle. The AFW has an unsymmetric airfoil shape which induces static aeroelastic deformations. The magnitude of these deformations needs to be known before any transonic dynamic analysis can be performed since the static results are the initial conditions for the dynamic analyses. A procedure was therefore developed to directly compute static aeroelastic deformations using CAP-TSD. This was done by setting the inital values of the generalized displacements to zero and executing the coupled aerodynamic and structural equations, including some viscous damping, for about two thousand time steps. This resulted in convergence of the generalized displacements, which implies static aeroelastic convergence. Static aeroelastic analyses were performed at each Mach number and dynamic pressure of interest.

NONLINEAR AERODYNAMIC ANALYSIS
Static Aeroelastic Analysis

- AFW has unsymmetric airfoil shape
- Static aeroelastic deformations are induced
- CAP-TSD used to compute static aeroelastic deformations
- Initial values of generalized displacements set to zero
- Effect of viscous damping variation on static aeroelastic convergence studied

NONLINEAR AERODYNAMIC ANALYSIS
Static Aeroelastic Analysis (Cont'd)

Static aeroelastic deformations should, however, be independent of viscous damping. A study was carried out to investigate the effects of different values of viscous damping on the static aeroelastic convergence of the model. The figure shows a representative result of generalized displacement versus computational time steps for three different values of viscous damping. As can be seen, the converged value is indeed independent of viscous damping. However, the larger the damping, the faster the convergence. As a result, all static aeroelastic analyses were performed using a maximum viscous damping value of 0.99. The converged result then becomes the initial condition for the dynamic analysis. In order to dynamically excite the system, generalized velocity excitations are also included.

NONLINEAR AERODYNAMIC ANALYSIS
Static Aeroelastic Analysis (cont'd)

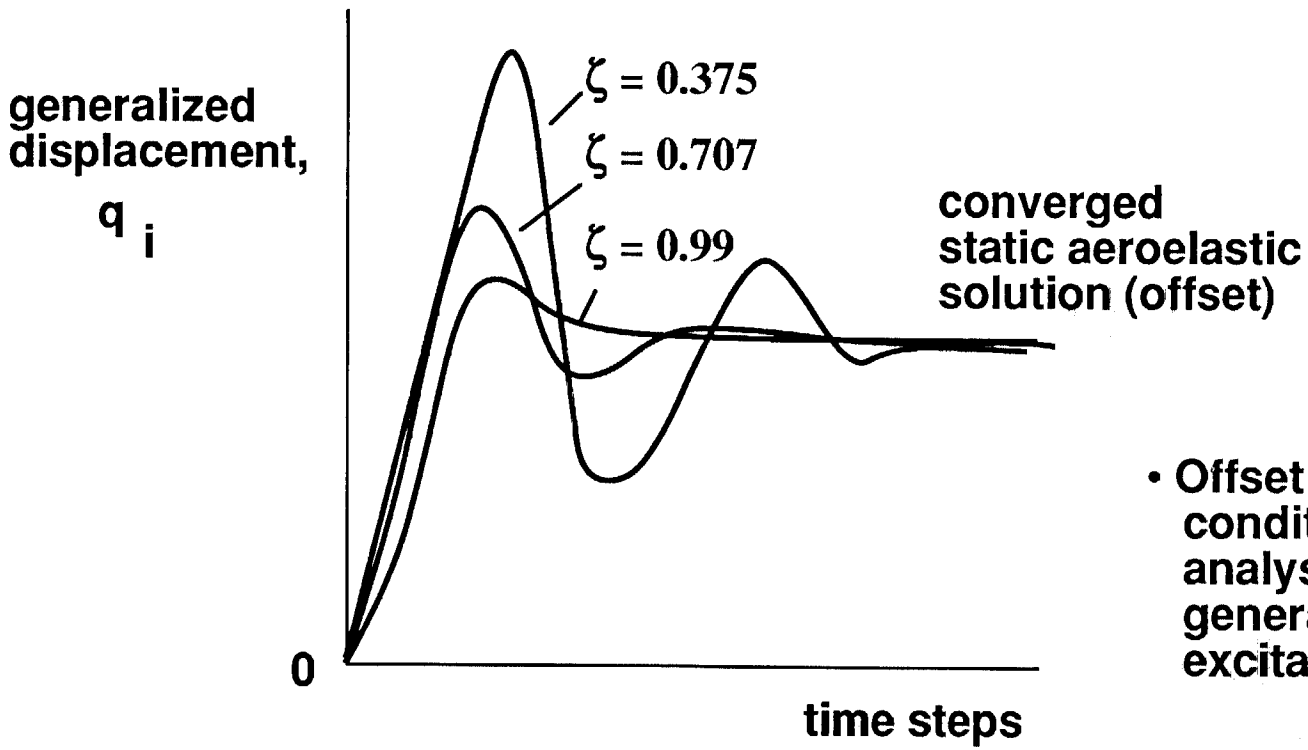

- Offset value is initial condition for dynamic analysis in addition to generalized velocity excitations

$q_i , \dot{q}_i = 0$ at $t = 0$

NONLINEAR AERODYNAMIC ANALYSIS
Dynamic Analysis (Modal Identification)

Once the dynamic analysis is executed, the resultant time history that is output from CAP-TSD is processed through a modal identification technique. This technique identifies the modal components of the response in terms of damping and frequency from which stability information can be obtained. If the system is stable, the dynamic pressure is increased. At each dynamic pressure, a static aeroelastic solution is computed followed by the dynamic response and modal identification. This procedure continues until an unstable root (flutter) is encountered. The flutter boundaries are defined at each Mach number by the dynamic pressure for which flutter occurs.

NONLINEAR AERODYNAMIC ANALYSIS
Dynamic Analysis (Modal Identification)

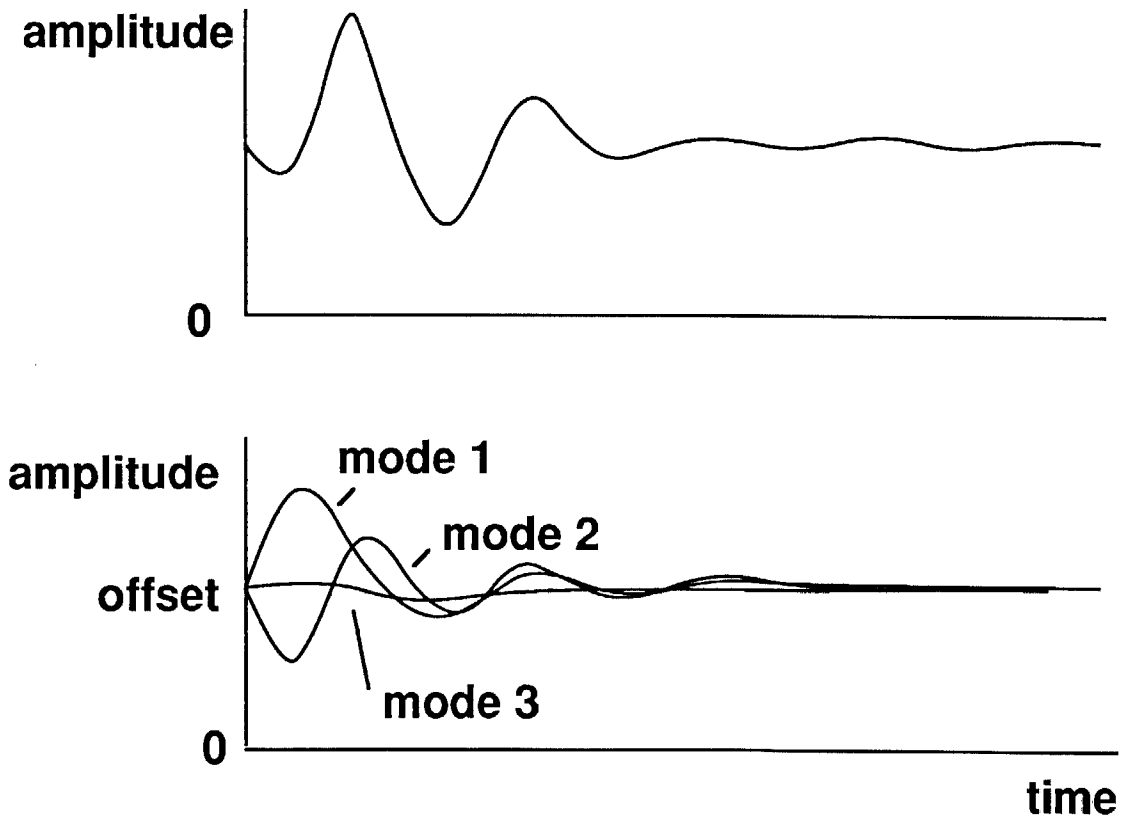

- Time history output from CAP-TSD
- Identified components and static aeroelastic offset

OPEN-LOOP FLUTTER RESULTS
Comparison with Experiment

The open-loop flutter results for the doublet lattice (linear aerodynamics) symmetric and antisymmetric models (tip-ballast store coupled configuration), the CAP-TSD symmetric model, and comparisons with experimental results are shown on this figure. At M=0.4, the experimental flutter instability was antisymmetric and as a result cannot be compared with the subsonic CAP-TSD result. Comparison with the doublet lattice antisymmetric prediction, however, is within 14% of the experimental value in terms of dynamic pressure. At M=0.9, M=0.92, and M=0.93, the experimental flutter instabilities were symmetric flutter instabilities, which compare very well with the CAP-TSD predictions for those Mach numbers. Both the symmetric and antisymmetric doublet lattice predictions seem to have missed the overall trend at these higher Mach numbers, as would be expected for linear theories. The crossing of the doublet lattice symmetric and antisymmetric flutter boundaries, however, appears to be an accurate behavior as experimental data defines the antisymmetric, transonic flutter boundary to be above the symmetric one shown on the figure. The no-flutter track on the figure is the path, in terms of Mach number and dynamic pressure, along which the wind tunnel proceeds for which no experimental flutter was encountered. This then implies that the bottom of the experimental transonic flutter dip occurs at M=0.93 and a dynamic pressure of 140 psf. The CAP-TSD predicted bottom of the transonic flutter dip is at 50 psf and M=0.93. This discrepancy may be due to viscous and/or separated flows not accounted for in TSD theory. It is also possible that the lack of modal definition of the bodies in CAP-TSD (specifically the tip-ballast store) has a significant effect on this result. The CAP-TSD flutter boundary was nonetheless very valuable since it was available during the test and warned test engineers of a potentially dangerous and sudden drop in stability at transonic Mach numbers.

OPEN-LOOP FLUTTER RESULTS
Comparison with Experiment

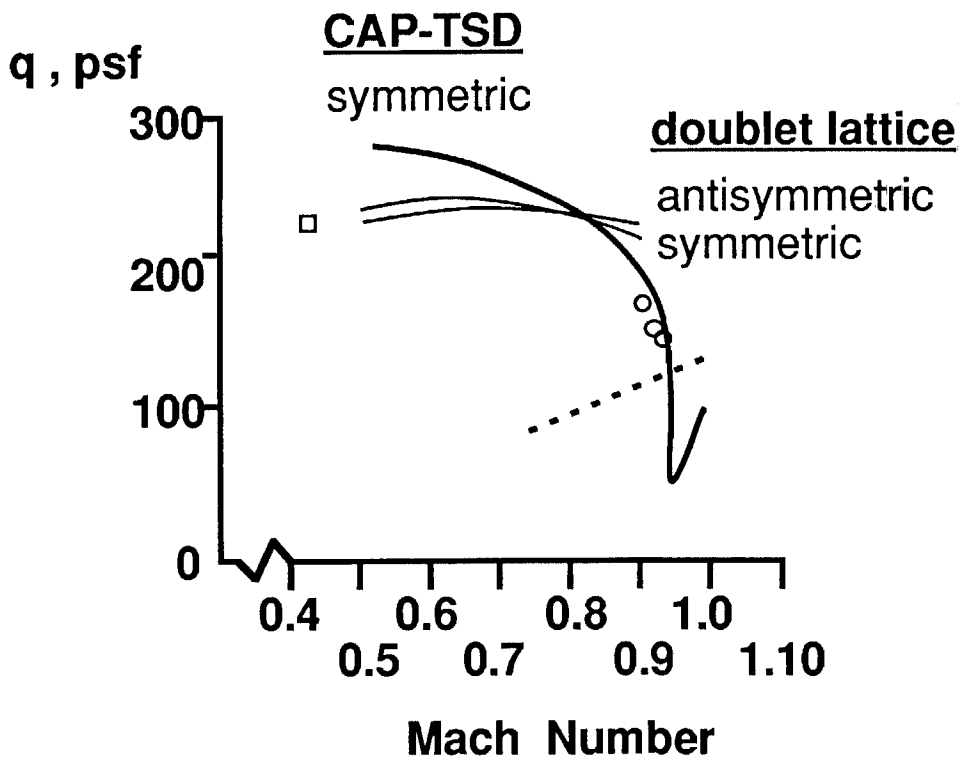

experiment

o symmetric

□ antisymmetric

– – – - no-flutter track

CONCLUDING REMARKS

This presentation addressed the primary issues involved in the generation of linear, state-space equations of motion of a flexible wind-tunnel model, the Active Flexible Wing (AFW). The codes that were used and their inherent assumptions and limitations were also presented and briefly discussed. The application of the CAP-TSD code to the AFW for determination of the model's transonic flutter boundary is included as well.

CONCLUDING REMARKS

- Main ingredients necessary for open-loop aeroelastic equations of motion presented
- ISAC and CAP-TSD codes & applications briefly described
- Experimental data used to improve math model
- Open-loop flutter results for linear, nonlinear, and experimental data presented

REFERENCES

[1]Perry, B. III ; Mukhopadhyay, V.; Hoadley, S. T.; Cole, S. R.; Buttrill, C. S.; and Houck, J. A. : Digital-Flutter-Suppression-System Investigations for the Active Flexible Wing Wind-Tunnel Model, AIAA Paper Number 90-1074, Presented at the 31st Structures, Structural Dynamics, and Materials Conference, Long Beach, CA, April 2-4, 1990.

[2]Peele, Elwood L.; and Adams, W. M. Jr.: A Digital Program for Calculating the Interaction Between Flexible Structures, Unsteady Aerodynamics, and Active Controls. NASA TM-80040, January, 1979.

[3]Geising, J. P.; Kalman, T. P.; and Rodden, W. P.: Subsonic Unsteady Aerodynamics for General Configurations, Part I. Direct Application of the Nonplanar Doublet Lattice Method. AFFDL-TR-71-5, Volume I, November 1971.

[4]Silva, Walter A. ; and Bennett, R. M.: Using Transonic Small Disturbance Theory for Predicting the Aeroelastic Stability of a Flexible Wind-Tunnel Model, AIAA Paper Number 90-1033, Presented at the 31st Structures, Structural Dynamics, and Materials Conference, Long Beach, CA, April 2-4, 1990.

[5]Tiffany, S. H.; and Adams, W. M. Jr.: Nonlinear Programming Extensions to Rational Approximation Methods for Unsteady Aerodynamic Forces. NASA TP-2776, May 1988.

Design and Test of Three Active Flutter Suppression Controllers

David M. Christhilf
Lockheed Engr. and Sc. Co.
144 Research Drive
Hampton, VA 23666
(804) 864-4029

William M. Adams
Mail Stop 489
NASA Langley Research Center
Hampton, VA 23665
(804) 864-4013

Martin R. Waszak
Mail Stop 489
NASA Langley Research Center
Hampton, VA 23665
(804) 864-4015

Dr. S. Srinathkumar
National Research Council Associate
Bangalore 560 017
India

Dr. Vivek Mukhopadhyay
Mail Stop 243
NASA Langley Research Center
Hampton, VA 23665
(804) 864-2835

Presented at the
Fourth Workshop on Computational Control
of Flexible Aerospace Systems
Williamsburg, Virginia
July 11-13, 1990

ABSTRACT

Three flutter suppression control law design techniques are presented. Each uses multiple control surfaces and/or sensors. The first uses linear combinations of several accelerometer signals together with dynamic compensation to synthesize the modal rate of the critical mode for feedback to distributed control surfaces. The second uses traditional tools (pole/zero loci and Nyquist diagrams) to develop a good understanding of the flutter mechanism and produce a controller with minimal complexity and good robustness to plant uncertainty. The third starts with a minimum energy Linear Quadratic Gaussian controller, applies controller order reduction, and then modifies weight and noise covariance matrices to improve multi-variable robustness. The resulting designs were implemented digitally and tested subsonically on the Active Flexible Wing wind-tunnel model. Test results presented here include plant characteristics, maximum attained closed-loop dynamic pressure, and Root Mean Square control surface activity. A key result is that simultaneous symmetric and antisymmetric flutter suppression was achieved by the second control law, with a 24 percent increase in attainable dynamic pressure.

Outline

- Background
- Three Active Controller Designs
  - Modal Rate Feedback
  - Traditional Pole/Zero
  - Modified LQG
- Wind-Tunnel Test Results
- Concluding Remarks

Presented here is an overview of three flutter suppression control law designs. The designs are part of a joint effort by NASA Langley Research Center and Rockwell International Corporation to validate analysis and synthesis methodologies through the development of digital multi-input/multi-output control laws for a sophisticated aeroelastic wind tunnel model.[1,2] The test vehicle used in this effort is the Rockwell Active Flexible Wing wind-tunnel model, modified from its initial configuration through the use of destabilizing wing tip ballasts. The test results refer to testing in the Langley Transonic Dynamics Tunnel conducted in October and November of 1989.

Nature of Wing Flutter

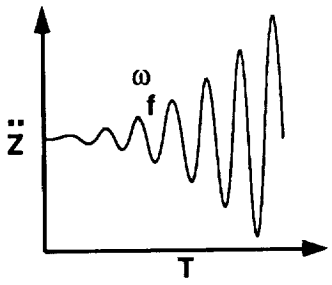

Unstable Time History

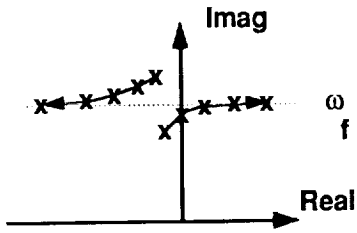

Open-Loop Poles as Function of Dynamic Pressure

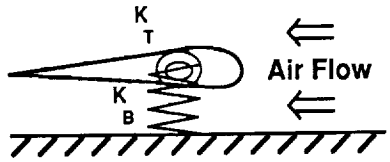

Simple Flutter Model

Wing flutter is a dynamic aeroelastic instability which can be of concern for modern lightweight, flexible, agile fighter aircraft, especially when carrying wing stores. In its classical form, wing flutter is a condition in which bending and torsion vibrations interact with a surrounding air flow in such a way that energy is extracted from the air and drives one of the two modes unstable. The sketch in the upper left depicts an oscillation with a characteristic frequency and divergent growth, as measured by an accelerometer on a wing during flutter. The sketch in the upper right shows that as dynamic pressure increases, characteristic roots of the bending and torsion modes migrate to a common frequency, with one root developing a positive real character indicating exponential growth rather than decay. The schematic of a simple flutter model [3] suggests how an increase in the angle of attack due to the torsion mode would drive the wing tip upward while a decrease in angle of attack due to torsion mode would drive the wing tip downward, in the presence of an air flow, leading to possible instability. The analysis is complicated by the need to model the distribution of mass, inertia, stiffness and damping throughout the wing, as well as quasi-steady and unsteady aerodynamic effects.

ACTIVE FLEXIBLE WING WIND-TUNNEL MODEL

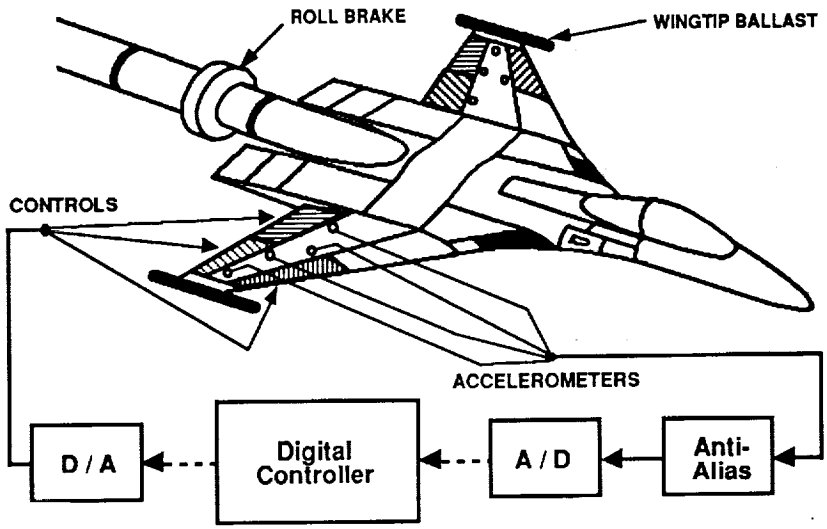

The Active Flexible Wing (AFW) is a full-span, sting-mounted wind-tunnel model with the ability to roll about the sting axis. For the flutter suppression testing in November 1989, the AFW was restricted in roll. The model has a six-degrees-of-freedom force and moment balance on the load path to the sting and has an actuator which can adjust the angle of attack of the model. There are four pairs of control surfaces, as shown in the above figure, with hinge lines near the quarter chord and three-quarter chord locations. The actuators for the control surfaces and for the angle-of-attack adjustment are powered by an onboard hydraulic system. The fuselage of the model is fairly rigid compared with the wings. However, the sting allows some motion up and down and side to side, as well as in torsion.

The three control law designs each used a subset of four pairs of accelerometers and three pairs of control surfaces. Strain gages on the wing are also available but were not used for flutter suppression during the 1989 tests. A digital controller was used to process the signals from the accelerometers to generate commands for the control surface actuators to actively suppress flutter. The accelerometers and actuators are analog devices so that analog-to-digital and digital-to-analog conversions were required.

The original configuration of the AFW was used to study rapid rolling maneuvers for a model with a soft, flexible wing using multiple control surfaces. That configuration did not flutter within the operating range of the Transonic Dynamics Tunnel. Wingtip ballasts were added to the AFW to lower the frequency of the first torsion mode to bring it closer to the frequency of the first bending mode and thereby reduce the dynamic pressure at which flutter occurs to within the range of the wind tunnel.

The tip ballast store, normally coupled in torsion with the wing tip via a hydraulic brake, can be decoupled by releasing the brake and leaving the store restrained in torsion only by a soft spring. Upon brake release the decoupled configuration is flutter free to a much higher dynamic pressure.[4] Thus, the tip ballast store also provides a flutter-stopper capability.

Wind-Tunnel Conditions

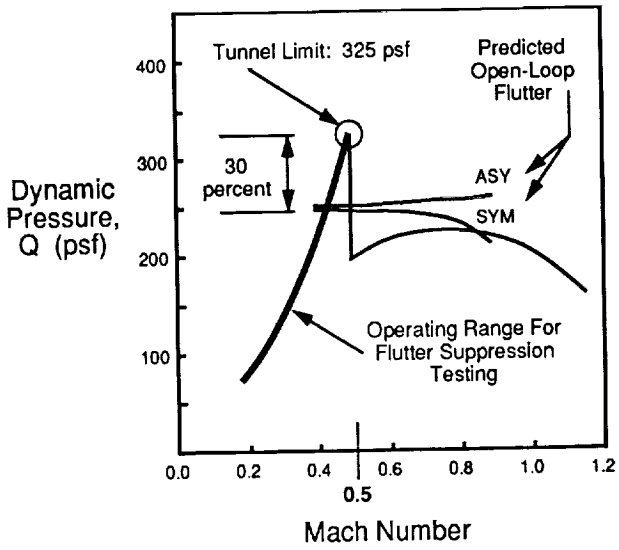

The Transonic Dynamics Tunnel (TDT) is specially configured for testing aeroelastic models.[5] It is a sealed wind tunnel in which Mach number and dynamic pressure can be varied independently by changing motor rpm while simultaneously changing stagnation pressure in the tunnel through the use of pumps. With air as the test medium, as it was for the 1989 test, a maximum dynamic pressure of 325 psf is generated at Mach 0.5 with a stagnation pressure equal to atmospheric pressure. Higher Mach numbers require air to be pumped from the tunnel to reduce the stagnation pressure.

According to analysis prior to the 1989 wind-tunnel entry, when the AFW roll degree of freedom is restrained, the boundaries for symmetric and for antisymmetric flutter occur near the same dynamic pressure, as shown in the above figure. Therefore, a designer must design a control law for each symmetry and plan on having both control laws operate simultaneously.

In order to show the greatest penetration of the AFW flutter boundary within the wind tunnel limits, each control law was designed with the objective of demonstrating closed-loop stability up to the 325 psf condition at Mach 0.5. Although the wind tunnel is capable of changing Mach and dynamic pressure independently, the process of pumping air out of the wind tunnel or bleeding it back in is slower than the process of changing the motor rpm. Also, Mach number effects which are critical in the transonic flight regime are much less significant for Mach numbers at or below 0.5. In the interest of gathering as much data as possible, all flutter suppression control law testing was conducted at a stagnation pressure equal to atmospheric pressure, with Mach number changing as a function of dynamic pressure.

Wind-tunnel turbulence has a direct impact on the expected closed-loop control surface activity for active control flutter suppression, due to control law response to the continual turbulence excitation of the airframe. The magnitude of feedback gains were restricted based upon the control surface rate capability of the AFW and the expected turbulence level in the wind tunnel.

Character of AFW Flutter

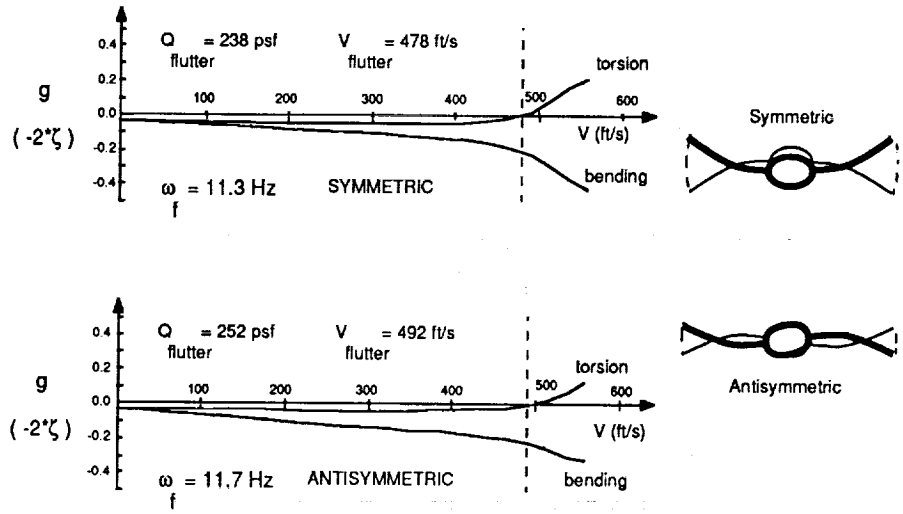

For the AFW, with the roll brake on, the characteristics of the symmetric and the antisymmetric flutter are very similar to each other. This is related to the nearly rigid fuselage and to the mounting conditions. With the roll-brake released (or for a similar vehicle in free flight), the symmetric and antisymmetric flutter would differ significantly from each other. Because of the similarities, a control law designed for one symmetry should require only slight modification in order to be effective for suppression flutter in the opposite symmetry.

The above figure shows a plot of predicted damping as a function of velocity. The damping ratios (ζs) were computed from the eigenvalues of the primary bending and torsion modes for each symmetry, based upon 41st order state-space models for the AFW incorporating 10 second-order structural modes with 1 aerodynamic lag state per mode, 3 third-order actuators, and 1 second-order gust. The plot is shown in a traditional V- g format, where V is velocity and g is the amount of structural hysteresis damping that would be required for neutral stability.[6] The factor of -2 conversion from damping ratio to required hysteresis damping is valid to within 1 percent for the range of values shown here.

Because Mach number effects in the subsonic region were judged to be small, the state space models used to perform the analysis on this page were generated as though a Mach number of 0.5 characterized the air flow regardless of velocity. This approximation is most nearly true as the wind-tunnel operating limit is approached. The symmetric and antisymmetric torsion modes were predicted to go unstable at dynamic pressures of 238 and 252 psf, respectively. The flutter frequency in each case was predicted to be about 11.5 Hz.

At the predicted velocity for onset of symmetric flutter, analysis indicated that the required hysteresis damping increased by 1.7E-3 for an increase in velocity of 1 ft/sec. For the corresponding anti-symmetric case the required hysteresis damping increased by 8.3E-4 for an increase in velocity of 1 ft/sec, indicating the relative predicted onset rates for the two symmetries.

Actuator rate saturation can effectively induce lag and reduce the amplitude of control surface deflections. At the wind-tunnel limit of 325 psf, the open-loop time-to-double for the symmetric flutter mode was predicted to be 1/10 of a second. For this level of instability, actuator rate saturation for even a brief period of time in response to wind-tunnel turbulence could cause unacceptably large growth of the flutter mode. This reinforces the restriction on the magnitude of feedback gains.

Implementation of FSS Control Laws

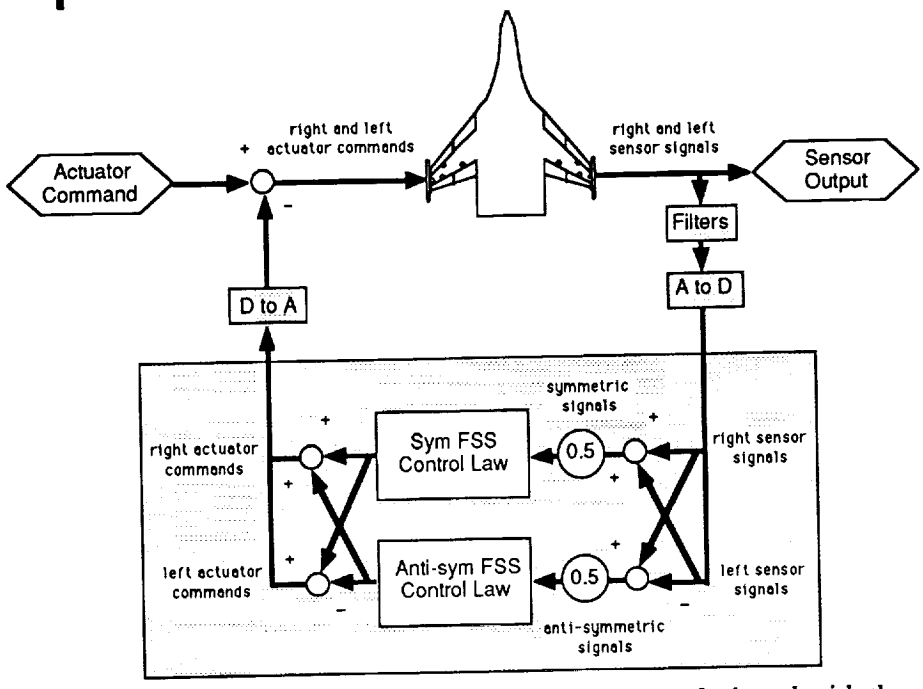

Each of the three Flutter Suppression System (FSS) control laws was designed with the assumption that there was no coupling between symmetric and antisymmetric response for the AFW. The above figure illustrates how the symmetric and antisymmetric forms of the control laws were implemented simultaneously by the digital controller.[7] For each pair of accelerometers, the symmetric signal was determined as the average of the right and left signals and the antisymmetric signal was determined as one half of the difference between right and left signals. Similarly, the right and left control surface commands were determined as the sum and difference of symmetric and antisymmetric commands for each pair of control surfaces.

The digital implementation of the control laws has certain implications for the control law designer. The signal amplitude is quantized in the analog-to-digital and digital-to-analog converters due to finite word length. The sample rate was 200 Hz. An effective 1/2 time step delay on average is introduced by the sampling because after a signal is passed at the beginning of a time step, no additional information is passed until the beginning of the next time step. Computation time required by the digital computer introduces additional delay. The digital-to-analog conversion introduces high frequency transients to the actuators. Finally, an analog anti-aliasing filter is required to attenuate signal strength above 1/2 the sampling rate so that higher frequency harmonic signals are not mistaken for lower frequency signals due to the periodic sampling. A first-order lag at 25 Hz was used for anti-aliasing in preference to a fourth order Butterworth filter at 100 Hz in order to also reduce response to structural modes in the 30 to 40 Hz range.

The trailing edge outboard (TEO) control surfaces tend to be the most effective in controlling flutter, although the actuator hinge moment available for these surfaces is limited compared to the others because of hardware constraints due to the limited space available in the outboard portion of the wing. The leading edge outboard (LEO) surfaces have unfavorable aerodynamic loading which does not tend to restore the surfaces to a neutral position if the actuators become overloaded. The trailing edge inboard (TEI) surfaces have favorable aerodynamic loading, but are not as effective as the TEO surfaces. Each of the wing accelerometer pairs is located near the hinge line of one of the control surface pairs, with the exception of the tip accelerometers (TIP) which are located approximately mid-chord near the wing tip. The tip accelerometers tend to respond most strongly to the flutter mode, while at the same time being relatively insensitive to the higher frequency modes when compared with the inboard accelerometers.

Flutter Suppression System . . .

Design Objective

- Increase in Flutter Q: 30 percent

Design Requirements

- Gain Margin: +/- 6 dB
- Phase Margin: +/- 30°
- $\dot{\delta}$ RMS: < 75°/sec (= 1/3 of max)
- δ RMS: < 1.0° (= 75°/sec at 11.5 Hz)

The design objective for all three flutter suppression control laws was to demonstrate closed-loop stability up to the wind tunnel limit of 325 psf dynamic pressure. This would constitute a 30 percent increase in the flutter dynamic pressure relative to the lowest predicted open-loop flutter boundary in the subsonic region. Because of the similarity between the symmetric and antisymmetric flutter, the control law designs in the following sections are presented as though only one symmetry were involved.

For those control laws which could be represented by single-input/single-output (SISO) gain and phase margins, a predicted gain margin of +/- 6 decibels and a predicted phase margin of +/- 30° was to be maintained throughout the test envelope, according to pretest analysis. The control law which required multi-input/multi-output (MIMO) analysis was judged by potentially conservative multi-variable margins and the stated requirements were slightly relaxed for that case.

The trailing edge outboard control surfaces were predicted to have a peak no-load rate capability of 225°/sec. It is desired that no rate saturation occur. If one accepts no rate saturation for a 3 standard deviation turbulence intensity as adequate for assuring no rate saturation,[8] this constrains the Root Mean Square (RMS) rate for a 1 standard deviation turbulence intensity to be less than 75°/sec. At a predicted flutter frequency of about 11.5 Hz, this translates to a maximum RMS control deflection of 1.0°.

A fifth requirement for evaluating candidate control laws prior to the wind tunnel entry was to be able to demonstrate closed-loop stability throughout the test envelope using a batch simulation. The simulation replicated quantization effects due to finite word length in the signal converters and imposed rate and displacement limits on the control surface actuators. The simulation also allowed both symmetries to be run simultaneously in the presence of simulated turbulence excitation with a separate dynamic actuator model for each of the control surfaces. The actuator models were based upon measured actuator frequency response data. Variations in the actuators introduce a possible source of nonsymmetry or coupling between the symmetric and the antisymmetric cases for the closed-loop system. While this nonsymmetry was generally neglected during design, these effects were addressed during control law evaluation by means of the simulation.

Modal Rate Feedback

Adams/Christhilf

- Design Philosophy:
  - Synthesized flutter mode rate
  - Fixed controller dynamics
  - Optimized sensor & control coefficients

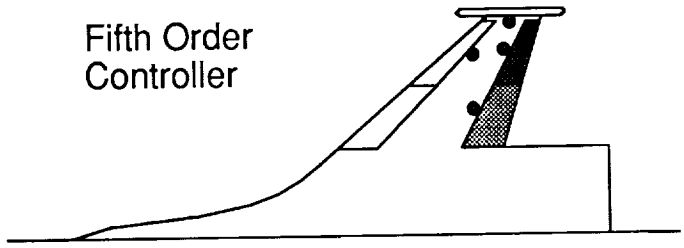

The control law designed and tested by Adams and Christhilf can be described as using modal rate feedback. The design philosophy for the Modal Rate Feedback control law is to use linear combinations of multiple accelerometer signals together with dynamic compensation to synthesize the flutter mode rate for feedback to multiple control surfaces.[9] Multiple sensors are used to identify the activity of the flutter mode not only by frequency, but also by the geometry of its characteristic mode shape. Multiple control surfaces are used in an effort to control the flutter mode exclusively. The coefficients used for the accelerometer pairs, the control surface pairs, and the overall system gain are generated using an optimization procedure. The four pairs of sensors used were the TIP, TEO, LEO, and TEI and the two pairs of control surfaces used were the TEO and TEI, as shown in the above figure.

The controller dynamics were set by the control law designer. Two first-order lags with break frequencies lower than the frequency of the flutter mode were used to act as stable integrators in order to transform modal acceleration into modal rate and position. A first-order "washout" filter with a zero at the origin and a pole at a frequency below the flutter frequency was used to reduce response to steady state bias errors. Finally, a second-order notch filter was used to adjust the phasing of the control action at the flutter frequency and to reduce the response to a nonflutter mode. (The notch for the symmetric case was for a 5.7 Hz sting mode and the notch for the antisymmetric case was for an 18.3 Hz structural mode.)

The method for generating the comparison between predicted and desired response for use in the optimization required individual frequency responses for each accelerometer pair due to excitation by each actuator pair. These can be obtained either through pretest modeling or through experiment.[10] Experimentally derived frequency responses were in fact used during the 1989 wind-tunnel entry to improve the control law.

Flow Chart

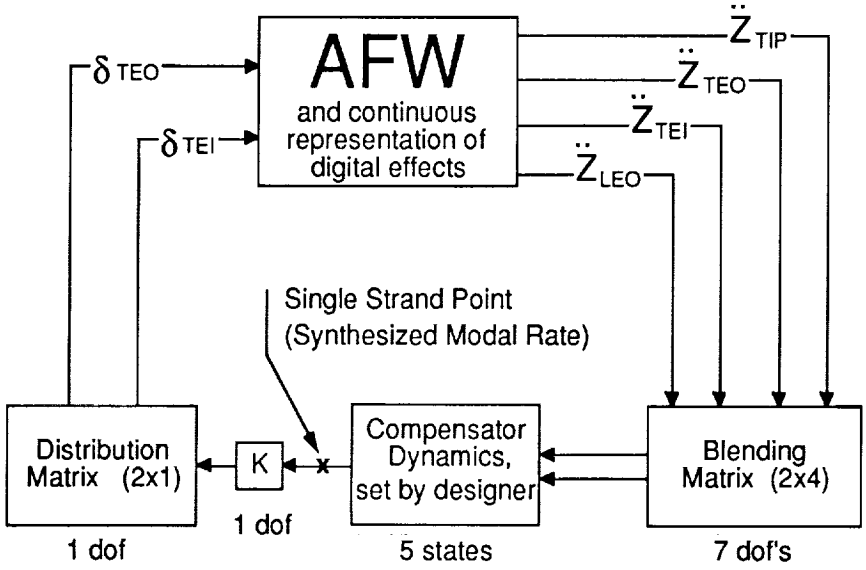

The signals designated in the above figure as δs and $\ddot{z}$'s represent commanded control surface deflections and measured local accelerations for a given symmetry. The frequency response for each acceleration signal due to each control surface command (symmetric or antisymmetric) for continuous models of the AFW at several dynamic pressures were precomputed for the frequency range from 2 to 64 Hz and were retained for further analysis. For the purpose of control law design, frequency responses representing the effects of the time delays and of a candidate set of analog filters and compensator dynamics were also computed and combined with the frequency responses that represented the AFW.

The coefficients of the blending and distribution matrices were used to generate linear combinations of the frequency responses. The blending matrix was actually used to form two dynamically distinct linear combinations. The difference between these two is that one was formed as a linear combination of frequency responses that contained the effect of only one integrator, and the other was formed as a linear combination of frequency responses that contained the effect of two integrators. When implemented in the wind-tunnel test, the discrete state-space equation used to specify the compensator dynamics was set up in such a way that one of the two inputs to the compensator bypassed the second integrator, with the output of the compensator being the sum of the two signals.

The purpose of the blending matrix was to take four local acceleration signals and synthesize two signals, each roughly corresponding to the acceleration of the flutter mode. The purpose of the distribution matrix was to take a single command signal, intended to control the flutter mode, and distribute that command to multiple control surfaces. Isolation of the flutter mode was determined in part by the analog filtering and compensator dynamics, and in part by the extent to which the blending and distributing rejected feedback interaction with other modes.

Although there are 8 and 2 coefficients in the blending and distribution matrices, the magnitude of the largest coefficient of each matrix was factored into a system gain, so that the normalized blending and distribution matrices had 7 and 1 degrees of freedom, respectively, which together with the system gain constituted the 9 degrees of freedom in the formulation of an objective function for an optimization procedure. The output from the dynamic compensator is a single strand point for the feedback path, and the optimizer was used to drive the composite frequency response at that point to match a simple, desired frequency response. The frequency responses representing the compensator dynamics were computed prior to the optimization and the parameters of the compensator dynamics were not optimized.

Optimization Strategy

Antisymmetric, Q = 325 psf

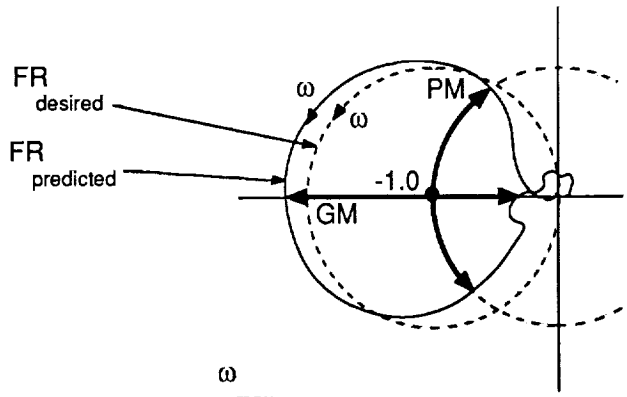

$$\text{Cost Function} = \sum_{\omega=\omega_{min}}^{\omega_{max}} \left(W_\omega * \left(FR_{predicted} - FR_{desired} \right)_\omega^2 \right)$$

The above figure shows a Nyquist plot, or a polar plot of the open-loop frequency response, for the sensor output due to commanded control deflections as defined at the single-strand point. The frequencies used in the AFW analysis span from 2 to 64 Hz. A full Nyquist plot would span frequencies from minus infinity to plus infinity, but the portion of the plot for negative frequencies is symmetric about the real axis to the portion of the plot for positive frequencies so that the information is redundant. The Nyquist stability criterion requires that for each unstable pole of the open-loop system, the Nyquist plot must form one counterclockwise encirclement of the -1 point in order for the closed-loop system to be stable. For oscillatory instabilities, the unstable poles occur in complex conjugate pairs, requiring two encirclements per pair. However, one of the encirclements would occur for the frequency range from minus infinity to zero, which is not shown.

In the case of actively stabilized flutter, the encirclements will occur in the vicinity of the flutter frequency. Gain and phase margins can be read directly from a Nyquist plot as the amount of shift which can be tolerated while still encircling the -1 point. Excess lag at the flutter frequency will shift the positive frequency plot clockwise (and the negative frequency plot counterclockwise) until closed-loop instability is encountered at a frequency slightly above the flutter frequency. Similarly, excess lead results in closed-loop instability at a frequency slightly below the flutter frequency.

The response of modes other than the flutter mode will be evident as additional "lobes" on the Nyquist plot. To the extent that the sensor and control surface blending can isolate the flutter mode, these extra lobes will be small. If these lobes are not small, they can result in clockwise encirclements of the -1 point, indicating that a previously stable mode has gone unstable at a frequency other than the flutter frequency.

The desired frequency response is the response that would result from using rate feedback to stabilize an unstable sinusoidal oscillator. The cost function for the optimization is the sum of the squares of the difference between the predicted and the desired response, weighted with frequency. The weights were chosen to emphasize the flutter frequency. Since the frequency response is complex, the "squaring" is done using complex conjugates, resulting in a real number for the value of the cost function. A Davidon-Fletcher-Powell optimization routine[11] was used to find the system gain and blending and distribution matrix coefficients for which the cost function was minimized at a particular dynamic pressure. Each resulting design was evaluated at other dynamic pressures to see that predicted performance was satisfactory throughout the wind-tunnel test envelope.

Control Surface Rates

Closed-Loop, Symmetric, Q = 300 psf

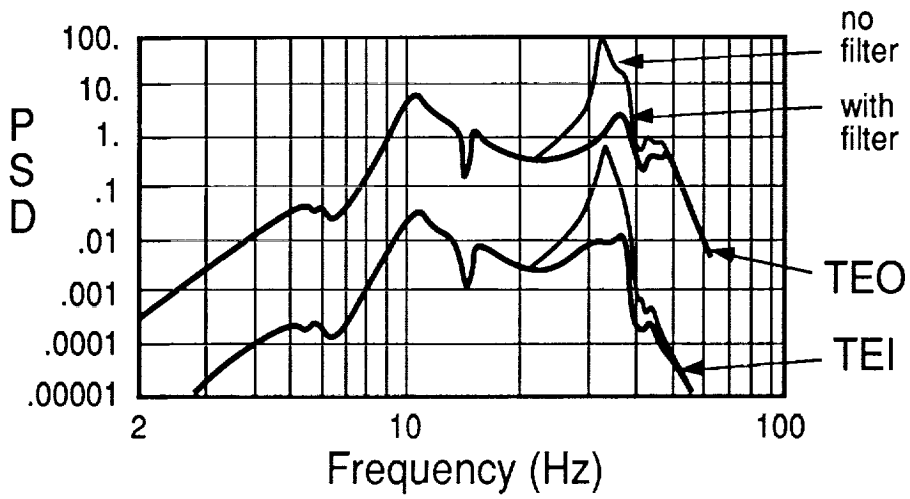

RMS Rates (°/sec) ⟹

	No Filter	With Filter
TEO	138	52
TEI	11	4

To model turbulence, a Dryden gust spectrum was used which has a nonzero value at zero frequency, rises 12 percent to a peak at a frequency of 10 Hz, and decreases monotonically to zero at higher frequencies. An overall RMS turbulence intensity of 1 ft/sec was judged to be a reasonable estimate of the turbulence in the wind tunnel, and this was apportioned as 85 percent symmetric and 15 percent antisymmetric. This gust spectrum was applied to assumed symmetric and antisymmetric gust mode shapes in order to model the effect of the turbulence on the wind-tunnel model.

The above figure shows a power spectral density (PSD) plot for closed-loop rates for the TEO and TEI control surfaces due to the modeled turbulence at a dynamic pressure above the open-loop flutter point. (This is shown as a representative example and does not depict the PSD for the control law actually tested.) The control surface RMS rates in °/sec can be calculated as the square roots of the areas under the curves when plotted on linear scales.

If the symmetric and the antisymmetric responses to turbulence were completely uncorrelated, the total control surface activity would be the square root of the sum of the squares of the symmetric and antisymmetric control surface activity. For design purposes the components were assumed to be constructively correlated so that straight addition was used to estimate the total activity. The figure shows response predicted for 1 ft/sec symmetric turbulence, which would be scaled 85 percent before combining with the antisymmetric turbulence response. The design limit for total control surface activity was chosen to be 75 °/sec, consistent with predicted actuator rate limits.

The figure shows a local peak in the control surface activity at a frequency of about 11.5 Hz. This represents the activity required to suppress the unstable flutter mode as it is excited by turbulence. The figure also shows significant control surface activity in the frequency range from 25 to 40 Hz which results from nonproductive response to excitation of higher frequency structural modes. In order to reduce control surface activity, an analog band-reject filter was used. This filter consists of three fairly broad second-order notches with center frequencies at 32, 40, and 49 Hz. The band-reject filter was used instead of a low-pass filter in order to keep the resulting lag at the flutter frequency to a minimum, while still achieving the desired attenuation. The lag at 11.5 Hz due to the filter is about 28°.

Predicted Performance
Modal Rate Feedback

		At 300 psf		Control Activity (percent of max allowed RMS)	
	Max Q	+/- GM	+/- PM	TEO	TEI
SYM	>325	9 dB	34 °	67 percent	25 percent
ASY	>325	12 dB	49 °		

The above figure shows predicted performance for the modal rate feedback controller resulting from linear analysis and substantially confirmed by nonlinear batch simulation. "Max Q" refers to the maximum dynamic pressure, measured in psf, for which the closed-loop system was predicted to be stable for both linear analysis and simulation. Gain margins and phase margins are shown at a dynamic pressure of 300 psf, which was chosen as a common evaluation point for the three control laws tested. Margins were predicted by linear analysis to meet the stated requirements throughout the wind-tunnel test envelope. Gain margins were verified in simulation at selected dynamic pressures by varying symmetric and antisymmetric system gains individually until simulation time histories showed divergence. The gain margins obtained from simulation were comparable to those obtained through linear analysis. Phase margins were not verified through simulation.

The percentage of maximum allowed control surface activity is relative to the designated maximum RMS control surface rate of 75 °/sec. The predicted RMS control surface rate was determined by using the batch simulation with simultaneous symmetric and antisymmetric turbulence excitation. The simulation indicated that the specified control surface rate limit was not exceeded for either pair of control surfaces. It also shows significant activity on the TEO and TEI surfaces, although the TEO surfaces dominate.

Traditional Pole/Zero Design

Srinathkumar/Waszak

- Design Philosophy:
  - Simplify problem
  - Develop understanding
  - Design controller as simple as possible

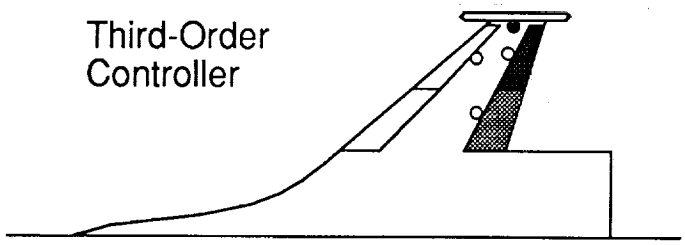

The control law designed and tested by Srinathkumar and Waszak is generated using traditional complex plane mappings of poles and zeros. A driving philosophy behind this design effort is to avoid getting lost in complexities which are of secondary importance with respect to the flutter control problem and to reduce the problem to its bare essentials. One step toward accomplishing this is to concentrate primarily on the two structural modes that participate directly in the flutter and on the SISO zeros in the same frequency range which result from the choice of a particular sensor pair and control surface pair. Sting modes and their associated zeros are ignored, as are higher frequency modes. This is possible due to fortuitous effective pole/zero cancellations associated with chosen control surfaces and sensors, and also due to frequency separation between the flutter dynamics and higher order modes.

Selection of sensors and control surfaces was a necessary first step in the controller design. The accelerometer pair at the TIP location was chosen because it is the pair most responsive to the flutter and also least responsive to higher frequency modes. The TEO control surface pair was chosen as being the most effective in controlling flutter without the danger of going "hard over" if the actuator hinge moment capability is exceeded. The TEI control surface pair was added later to reduce the TEO control surface activity. The commands sent to the TEO and TEI surfaces were dynamically equivalent in that they differed only by a constant gain factor so that SISO design and analysis techniques could still be used.

Straight feedback with no dynamic compensation was investigated first to see whether this would be sufficient to stabilize the system, and if not, what problems would be encountered when attempting to employ a simple solution. Consideration of the high gain required and the desire to ensure a favorable root locus path led to the use of a second-order "dipole" filter to be described later in this section. A final consideration was that the response of the system to steady state bias errors must be acceptably small, leading to the addition of a first-order washout filter and bringing the controller order up to three.

Critical Zero

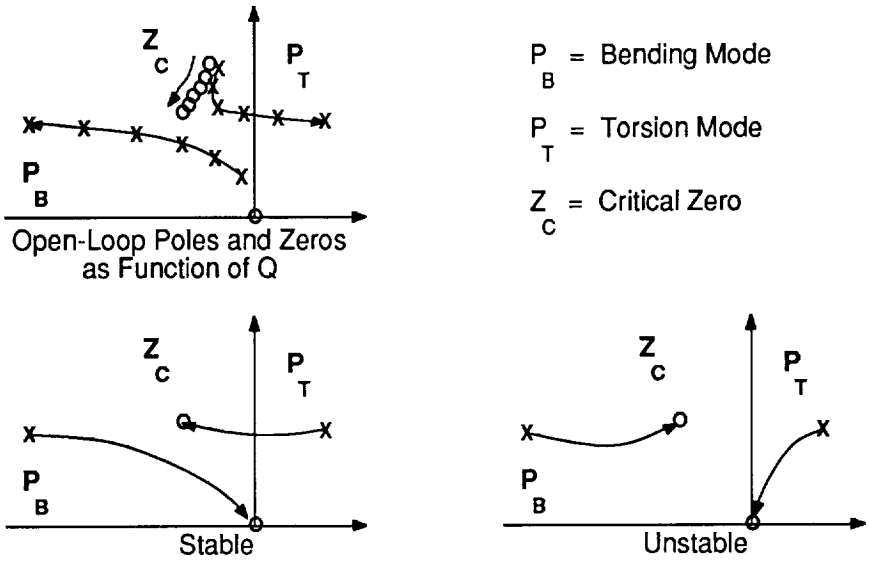

Closed-Loop Gain Root Loci at Post Flutter Q

For the sketches of poles and zeros presented above for this design, the horizontal axis is greatly exaggerated relative to the vertical axis in order to show more detail. All poles and zeros not associated with the compensator should be considered to lie near the imaginary axis. The sketch in the upper left shows a locus of poles and zeros as a function of dynamic pressure. The poles represent the bending and torsion modes for the AFW with no active compensation, and the zeros arise from a particular choice of sensors and actuators. The pair of zeros at the origin results from the fact that accelerometers were used for feedback. It was found that for the TEO control surface and the TIP sensor, there is a critical zero which is closely associated with the torsion mode. Note that as dynamic pressure increases the critical zero and the pole associated with the torsion mode tend to stay near each other until just below the flutter dynamic pressure at which point the pole breaks away to the right, crossing into the right half of the complex plane and indicating instability.

The use of simple feedback will drive the closed-loop roots from the open-loop poles to the transfer function zeros, as a function of feedback gain. However, given uncertainties in the model of the plant it is not always clear what path the roots will take.[12] For the lower two figures, the one on the left shows how the system might be stabilized by simple feedback whereas the one on the right shows a case where there is no value of gain for which the closed-loop system will be stable.

Even when the desired path is followed, the location of the isolated critical zero near the imaginary axis indicates that a high gain would be required to drive the unstable root close enough to the zero to stabilize the system with sufficient damping. One difficulty associated with high-gain controllers is that the control surface rates required to control the flutter while subject to continual turbulence excitation would be large and threaten to saturate the capability of the actuators, causing loss of control of the flutter. Another difficulty associated with high-gain controllers is that higher frequency modes or actuator roots can be driven unstable.[13]

Dipole Filter

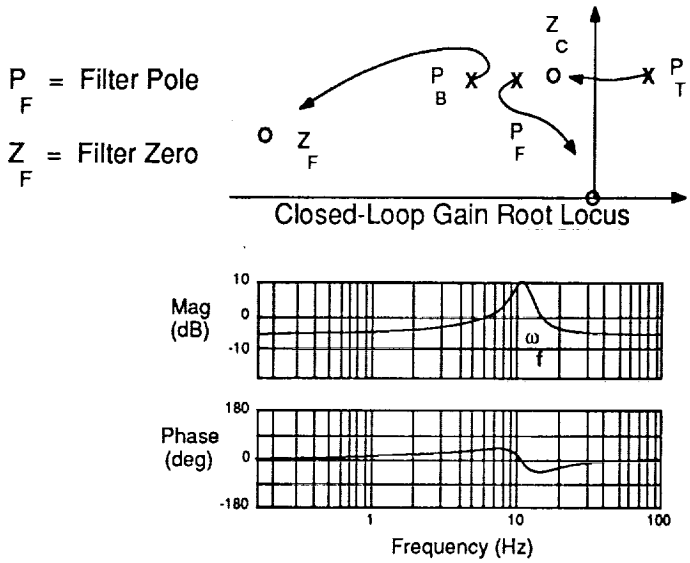

Dipole Filter Dynamics

In order to reduce the feedback gain required for stabilization due to the location of the critical zero near the imaginary axis, dynamic filtering is required. The intent for this control law is to "soften" the effect of the critical zero by placing a filter pole near the critical zero and placing a filter zero further to the left. The result is similar to an inverted notch and will be referred to as a dipole filter.

The location of the critical zero changes as a function of dynamic pressure, whereas the location of the open-loop filter pole is independent of dynamic pressure unless scheduling of dynamic parameters is used. Also, the locations of system zeros are difficult to predict analytically and can be difficult to measure experimentally. In the interest of avoiding scheduling and due to the uncertainty about the exact location of the critical zero, the filter pole is placed somewhat to the left of the predicted critical zero, with a damping ratio of about 10 percent. Using frequency domain Nyquist criteria for stability margin analysis, a 50 percent damping ratio at a natural frequency 20 percent higher than that for the compensator pole can be shown to be a good choice for the compensator zero location.

The lower portion of the figure shows magnitude and phase plots of the frequency response of the dipole filter by itself. It can be seen that the dipole filter amplifies the control surface activity in the frequency range predicted for flutter, which in this case is about 11.5 Hz. Because the control surface activity is concentrated at this frequency, the controller makes efficient use of the available control power and is fairly insensitive to modeling errors outside the frequency range of interest.

Note that although pole/zero cancellation is generally thought to be sensitive to having accurate knowledge of the plant, the dipole filter was evaluated using variations in the model of the AFW and it was judged to be tolerant to changes in the frequency of the flutter mode. This is due in part to the "robust" placement of the filter pole with respect to the critical zero, with the result that the stabilizing character of the root locus did not change despite the frequency shifts.

Predicted Performance
Traditional Pole/Zero Design

		At 300 psf		Control Activity (percent of max allowed RMS)	
	Max Q	+/- GM	+/- PM	TEO	TEI
SYM	>350	7 dB	33°	73 percent	3 percent
ASY	>350	7 dB	38°		

As with the previous control law, the traditional pole/zero design was predicted through analysis and simulation to provide closed-loop stability up to the limit of the operating range of the wind tunnel. The gain and phase margins at the common evaluation point compare favorably with the requirements, and the required margins were predicted through linear analysis to be maintained throughout the test envelope. Positive and negative gain margins were verified through simulation. Phase margins were more difficult to determine from simulation, and only tolerance to phase lag was estimated. This was done by reducing the break frequency on a simulated 100 Hz fourth-order Butterworth anti-aliasing filter until simulation time histories showed oscillatory divergence, and determining the resulting lag at the predicted flutter frequency. The 100 Hz fourth-order Butterworth filter was used instead of the first-order 25 Hz anti-aliasing filter for this analysis.

The rate limit constraints of the actuators were not violated. It can be seen from the percent of maximum allowed control surface activity as shown in the above figure that although the TEO and TEI surfaces were both used, clearly the dominant activity is on the TEO surfaces.

In order to test the robustness of this control law design to parametric uncertainties, the control law was analyzed for closed-loop stability for a variety of wind-tunnel conditions which were not part of the planned wind-tunnel test envelope. Specifically, an early version of the control law was designed for a Mach number of 0.9 in Freon and was evaluated at a Mach number of 0.8 in Freon, and 0.5 in air. This early control law was designed to suppress symmetric flutter, but was used with only minor modifications to evaluate its effectiveness for suppression of antisymmetric flutter for each of the listed wind-tunnel conditions. In each case the closed-loop system was predicted stable up to at least 325 psf.

Modified LQG

Mukhopadhyay

- Design Philosophy:
  - Start with optimal minimum energy design
  - Simplify controller
  - Improve MIMO robustness

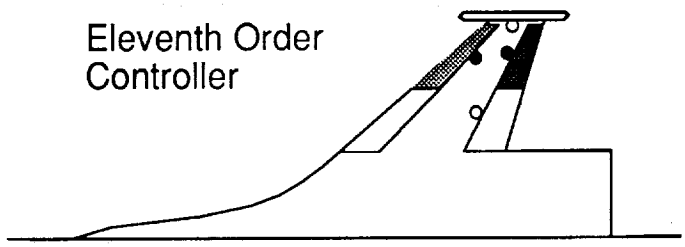

The control law designed and tested by Mukhopadhyay is designed using a modified Linear Quadratic Regulator procedure with a state estimation for output feedback. The philosophy behind this control law design is to exploit MIMO degrees-of-freedom through a systematic procedure which allows the designer to perform trade-offs between desired closed-loop performance and considerations of control surface activity.[14] This method is truly multi-input/multi-output and requires the use of singular values for stability margin analysis rather than SISO gain and phase margins. The inputs to the procedure were modified by the designer to improve the robustness to uncertainty in the modeling of the plant. These modifications were based upon singular values or on equivalent MIMO measures of gain and phase margins which can be derived from singular values.[15]

The Linear-Quadratic-Gaussian (LQG) method used here results in a controller with a large number of states so that controller order reduction is required for implementation. After order reduction the Modified LQG design had 11 states per symmetry. The trailing-edge-outboard and leading-edge-outboard control surfaces were used, as well as their co-located accelerometers.

Design Steps

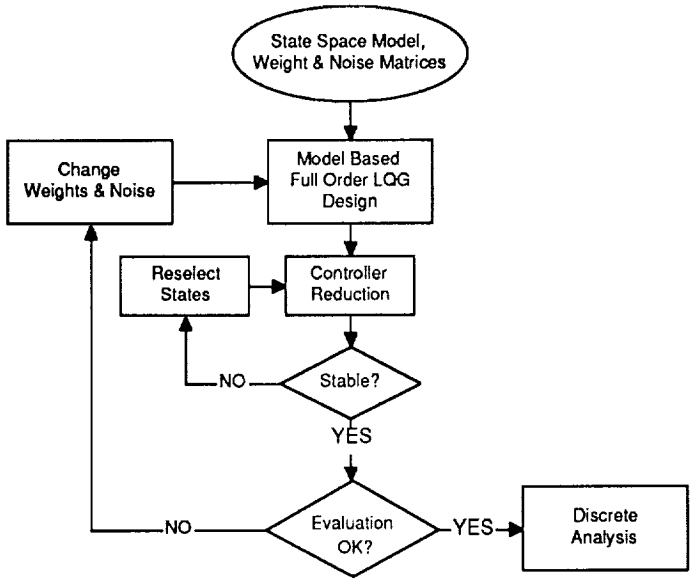

The LQG procedure uses a plant state-space model and weight and noise covariance matrices to generate a model-based, full-order compensator. For a design point at a wind-tunnel condition for which the open-loop plant is unstable, a full-state-feedback optimal regulator was designed with a zero weighting matrix for the states and an identity weighting matrix for the controls. This regulator has the property that for the closed-loop system the unstable characteristic roots are reflected into the left half plane while all other roots remain unchanged, and represents the minimum control energy solution for stabilizing the plant.[16] A model-based minimum variance state estimator was also designed with 0.000001 radian plant input noise, 1/12 foot-per-second gust input noise and 0.32 ft/sec^2 (0.01 g) measurement noise.

The full-state-feedback regulator was combined with the state estimator to generate a full-order compensator which uses only sensor feedback with no direct knowledge of the states of the plant. Based on nonminimum phase transmission zeros contained in the state-space model and many poorly controllable and observable states for the control surfaces and sensors used, the noise intensities were chosen after a few trials so as to produce a low-gain LQG control law which stabilized the plant and itself had stable characteristic roots.

The next step was to reduce the order of the control law. The full-order LQG control law was reduced through a process of balanced realization and modal truncation, based in part upon evaluation of modal residues.[17] Although a lower-order stabilizing control law could be found, a tenth-order control law was chosen since its performance was close to the performance of the full-order LQG control law. An 11th state was added as part of a washout filter used to attenuate the response to bias errors.

When a stable reduced-order control law was found, the full-order and the reduced-order control laws were analyzed and the singular values, frequency responses, and RMS control surface activity were compared. Based upon this overall evaluation, modifications were made to the LQG weight and noise covariance matrices to improve robustness to modeling errors and to meet constraints. The final step was to discretize the continuous control law at a sample rate of 200 samples per second using Tustin transformations and perform further analysis.

Poles as Function of Q

Symmetric

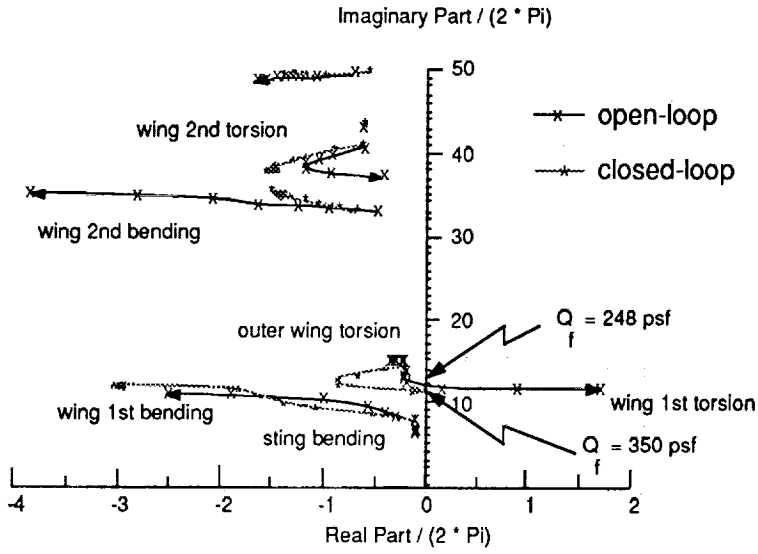

The above figure shows the plant open-loop poles and fixed-gain, closed-loop roots as functions of dynamic pressure. To simplify the figure, compensator poles and roots are not shown. Although the open-loop compensator poles do not change as a function of dynamic pressure, the compensator roots interact with the roots of the plant in the presence of feedback and therefore change with dynamic pressure. However, for this design the compensator poles are stable open-loop and the compensator roots are stable closed-loop for the dynamic pressure range shown.

Typically the poles for the full-order compensator will be located in the same frequency ranges as the poles for the open-loop plant. During compensator order reduction, compensator poles above about 25 Hz were removed since they tended to have little effect on the control of flutter at 11.5 Hz. However, it was found through singular value analysis that the stability margins in the frequency range around 32 Hz needed improvement. Since the open-loop plant poles in this region are stable, an analog notch filter with a center frequency of 32 Hz was used to prevent the compensator from driving the modes in this region unstable.

The solid lines indicate the paths of the open-loop poles and the shaded lines indicate the paths of the closed-loop roots. The crossing point where the 11.5 Hz flutter mode goes unstable is identified in the figure as 248 psf for the design model of the symmetric plant with no compensation and 350 psf for the symmetric plant with compensation.

Predicted Performance
Modified LQG

		At 300 psf *		Control Activity (percent of max allowed RMS)	
	Max Q	+/- GM	+/- PM	TEO	LEO
SYM	350	3 dB	18°	62 percent	26 percent
ASY	325	4 dB	20°		

* Equivalent multi-variable margins for simultaneous changes on all channels

The Modified LQG control law was predicted through analysis and simulation to provide closed-loop stability up to the limit of the operating range of the wind tunnel. The gain and phase margins shown here represent guaranteed minimum margins for simultaneous variations on multiple channels. These margins can be conservative if they represent an unlikely combination of variations. The margins shown here do not meet the requirements for SISO gain and phase margins. However, because of their potential conservative nature, these margins were judged to be sufficient for testing the control law.

The closed-loop RMS control surface rates in the presence of random gust excitation are within the specified limits. The percent of maximum allowed control surface activity for each pair of surfaces indicates that both the TEO and LEO control surface pairs are used to a significant extent, with the TEO surfaces being the dominant surfaces.

Measured vs Predicted Behavior

Symmetric, Q = 175, Open-Loop, Plant Only

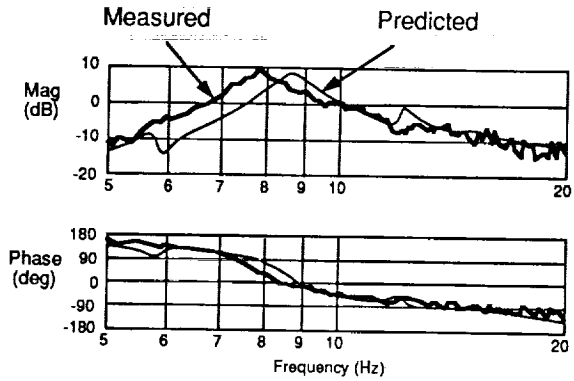

	Q_f (psf)	ω_f (Hz)
Measured	220	9
Predicted	248	11

Frequency Response for $\ddot{Z}_{TIP}$ due to δ_{TEO}

One thing found during the wind-tunnel test was that the wind-tunnel model did not behave quite as predicted. One difference which became evident early in the testing was that the frequencies at which dominant frequency response peaks occurred were somewhat lower than predicted. For a dynamic pressure of 175 psf, the above figure shows a frequency shift of about 1 Hz for the bending mode for the symmetric case. Prior to the wind-tunnel test, the analytical model had been adjusted so that the frequencies at zero dynamic pressure matched the frequencies measured during a ground vibration test (GVT). The differences between predicted and measured frequencies must, therefore, be related to aerodynamic effects.

The dynamic pressure for zero damping of the flutter mode was also found to be lower than predicted by about 30 psf or 13 percent. Large open-loop structural response was encountered in the wind tunnel at a dynamic pressure of about 220 psf and has been judged to be primarily antisymmetric. Analysis indicated that symmetric flutter would occur first at about 248 psf, with antisymmetric flutter occurring at about 252 psf.

Since none of the control laws were scheduled with dynamic pressure, it is more significant to compare the difference between measured and predicted flutter frequencies at corresponding flutter dynamic pressures than it is to compare the difference between measured and predicted frequencies at a given dynamic pressure. This means that the relevant frequency shift for the control law designers was about 2 Hz, as shown in the chart.

The phase characteristics of the response shown in the figure indicate a frequency shift consistent with the frequency shift for the peak magnitude. In fact, a Nyquist plot for the measured and predicted open-loop responses shown here would be almost identical because the phase angle for the peak response is nearly the same for the two and the frequency shift would not be apparent. However, if a control law has dynamics in the flutter frequency range, the shifted plant dynamics can interact with the controller dynamics to introduce potentially large phase shifts. Therefore a control law designer should be aware of the effects of changes in frequency for critical modes, and not rely strictly on phase margins.

Maximum Q Obtained

Closed-Loop Testing

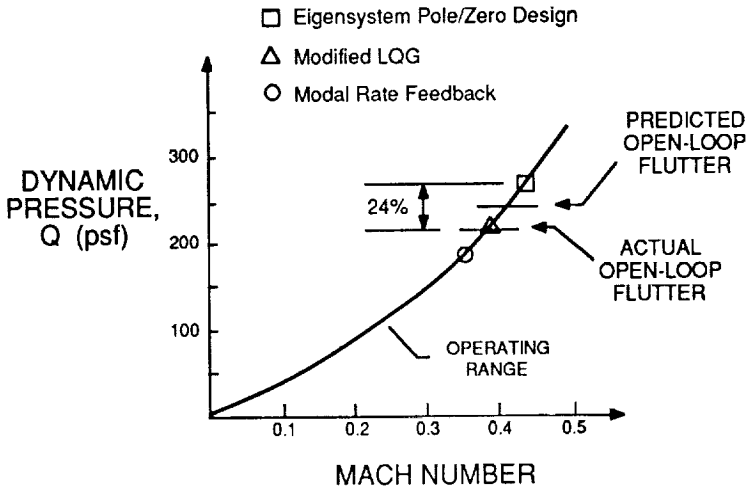

The above figure shows the highest closed-loop stable dynamic pressure achieved by each control law. Notice that the open-loop plant goes unstable at a dynamic pressure lower than expected, at about 220 psf rather than 248 psf.

The Traditional Pole/Zero design demonstrated closed-loop stability up to a dynamic pressure of about 272 psf. This represents an increase of about 24 percent relative to the observed open-loop flutter boundary. The controller stabilized the model at the 272 psf condition for several minutes while time histories for loads and for commanded control deflections due to tunnel turbulence were being recorded for RMS analysis. The wind-tunnel safety system was activated automatically after the model responded to a burst of turbulence and the structural loads exceeded preset limits. Since the control law was able to limit the amplitude of the flutter mode for lower turbulence levels, it is quite possible that increasing the feedback gain would keep the structural loads due to turbulence within the prescribed limits, at least in the flutter frequency range.

The Modified LQG controller did not significantly change the observed flutter dynamic pressure relative to the open-loop case. The closed-loop control surface activity due to turbulence for this controller was lower than anticipated, suggesting that a higher gain solution might achieve flutter suppression with an acceptable increase in control surface activity.

The Modal Rate Feedback caused a large structural response at a dynamic pressure below the open-loop flutter boundary. At the start of the flutter suppression testing for this control law, experimentally derived open-loop controller performance evaluation (CPE) at 125 psf and 175 psf indicated that closing the loop would drive the system unstable. The primary cause for this was undue sensitivity to frequency shifts of the critical structural modes due to the design of the controller dynamics. However, since the method is able to use experimentally derived frequency responses as inputs to the optimization, the frequencies of the controller dynamics were shifted to match the observed shift and the blending and distribution matrices were reoptimized using data collected at 125 and 175 psf. Subsequent open-loop CPE and closed-loop testing with the redesigned controller showed that the system performed as expected at 125 and 175 psf. The large response occurred at 185 psf at a frequency of about 7 Hz. The cause for the large response has not been determined, but it may have been related to differences between the left and right actuators for the TEI control surfaces.

RMS Control Rates

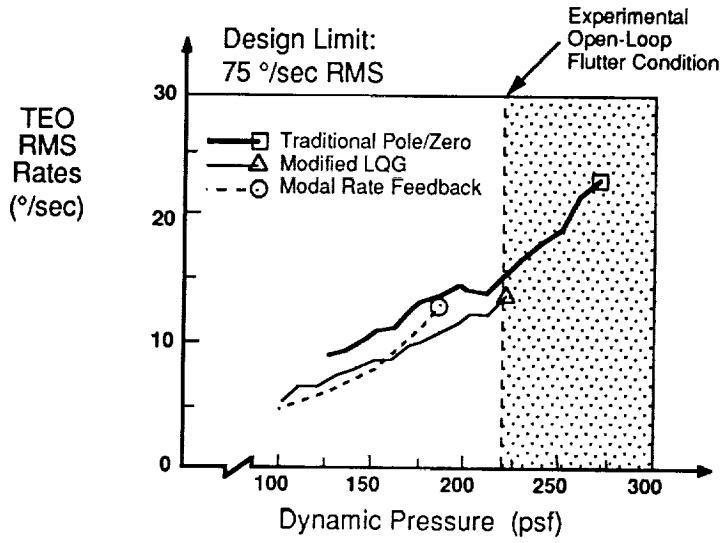

The above figure depicts closed-loop control surface RMS rates as functions of dynamic pressure. The RMS rates were synthesized from commanded deflections since rates were not commanded directly. The three curves represent the measured response for the three control laws during testing. Since the TEO control surfaces were dominant for each control law, rates are shown for the TEO surfaces. If there was a difference between the RMS value for the left surface and the RMS value for the right surface, the maximum of the two is shown.

Note that all three control laws command about the same level of control surface activity for the dynamic pressures tested. This reflects the fact that all three were designed with the same turbulence model and the same design limits. Note also that none of the control laws had difficulty staying within the design limit of 75°/sec RMS. In fact, the peak measured rate is only about 1/3 of the limit for the Traditional Pole/Zero design at 272 psf. This suggests that the turbulence levels used for design should be reduced prior to the next wind tunnel entry to allow more use of the available control power.

Concluding Remarks

- Three FSS control laws designed and tested
- Analysis predicted that all three would meet objective
- Wind-tunnel model behaved differently than expected
- One FSS control law demonstrated flutter suppression to 24 percent above open-loop flutter dynamic pressure

Three flutter suppression control laws were designed for the Rockwell Active Flexible Wing. The control laws were implemented digitally and tested subsonically in the Transonic Dynamics Tunnel at NASA Langley Research Center. All three control laws were predicted to meet the objective of significantly raising the flutter onset dynamic pressure, while maintaining stability margins and not violating control surface rate and displacement limits. Wind-tunnel testing generally confirmed the analytical predictions for the open-loop character of the AFW, although differences were observed. Of the control laws tested, only one was sufficiently robust to the observed differences to raise the flutter dynamic pressure. The Traditional Pole/Zero Design was able to demonstrate simultaneous symmetric and antisymmetric flutter suppression for several minutes at a dynamic pressure 24 percent above the observed open-loop flutter boundary, in the presence of turbulence.

The 1989 wind-tunnel test has provided data for assessing the fidelity of the analytical models of the AFW and for evaluating the robustness of the control laws to "real world" implementation considerations. Data is available for upgrading the mathematical models of the AFW for possible distribution to other control law designers. Further, the AFW project team has had an opportunity to work together in a multidisciplinary effort involving aeroelastic modeling and simulation, control law design and analysis, digital controller implementation, and near-real-time controller performance evaluation.

References

1 Noll, T., Perry, B. III, et al.: "Aeroservoelastic Wind-Tunnel Investigations Using the Active Flexible Wing Model - Status and Recent Accomplishments," NASA TM-89-101570, April 1989.

2 Perry, B. III, Mukhopadhyay, V., et al.: "Design, Implementation, Simulation, and Testing of Digital Flutter Suppression Systems for the Active Flexible Wing Wind-Tunnel Model," ICAS Paper No. 90-1.3.2, September 1990.

3 Horikawa, H. and Dowell, E. H.: "An Elementary Explanation of the Flutter Mechanism with Active Feedback Controls," Journal of Aircraft, Vol. 16, April 1979, pp. 225-232, AIAA 79-4049.

4 Reed, W. H. III, Cazier, F. W. Jr., and Foughner, J. T. Jr.: "Passive Control of Wing/Store Flutter," NASA TM-81865, December 1980.

5 Staff, NASA LaRC: "The Langley Transonic Dynamics Tunnel," Langley Working Paper, September 1969.

6 Garrick, I. E. and Reed, W. H. III: "Historical Development of Aircraft Flutter," Journal of Aircraft, Vol. 18, November 1981, pp. 897-912, AIAA 81-0491R.

7 Hoadley, S. T., Buttrill, C. S., McGraw, S. M., and Houck, J. A.: "Development, Simulation Validation, and Wind-Tunnel Testing of a Digital Controller System for Flutter Suppression," 4th NASA Workshop on Computational Control of Flexible Aerospace Systems, Williamsburg, VA, July 1990.

8 Newsom, J. R., Abel, I., and Dunn, H. J.: "Application of Two Design Methods for Active Flutter Suppression and Wind-Tunnel Test Results," NASA TP-1653, May 1980.

9 Harvey, C. A., Johnson, T. L., and Stein, G.: "Adaptive Control of Wing/Store Flutter", AFFDL-TR-79-3081, April 1979.

10 Adams, W. M. Jr., Tiffany, S. H., and Bardusch, R. E.: "Active Suppression of an 'Apparent Shock Induced Instability'," AIAA/ASME 28th Structures, Structural Dynamics and Materials Conference, Monterey, CA, April 1987.

11 Fletcher, R. and Powell, M. J. D.: "A Rapidly Convergent Descent Method for Minimization," Computer Journal, Vol. 6, 1963/64.

12 Schmidt, D. K. and Chen, T. K.: "Frequency Domain Synthesis of a Robust Flutter Control Law," Journal of Guidance and Control, Vol. 9, May-June 1986, pp. 346-351.

13 Srinathkumar, S. and Adams, W. M. Jr.: "Active Flutter Suppression Using Invariant Zeros / Eigensystem Assignment," Guidance, Navigation, and Control Conference, August 1989, AIAA 89-3610.

14 Mukhopadhyay, V.: "Digital Robust Control Law Synthesis Using Constrained Optimization," Journal of Guidance, Control, and Dynamics, Vol. 12, March-April 1989, pp. 175-181.

15 Mukhopadhyay, V. and Newsom, J. R.: "A Multiloop System Stability Margin Study Using Matrix Singular Values," Journal of Guidance, Control, and Dynamics, Vol. 7, September-October 1984, pp. 582-587.

16 Kwakernaak, H. and Sivan, R.: Linear Optimal Control Systems, Wiley Interscience, New York, 1972.

17 Moore, B. C.: "Principal Component Analysis in Linear Systems: Controllability, Observability, and Model Reduction," IEEE Transaction on Automatic Control, Vol. AC-26, February 1981.

ROLL PLUS MANEUVER LOAD ALLEVIATION CONTROL SYSTEM DESIGNS FOR THE ACTIVE FLEXIBLE WING WIND TUNNEL MODEL

D.B. Moore, G.D. Miller, and M.J. Klepl

North American Aircraft
ROCKWELL INTERNATIONAL CORPORATION
Los Angeles, California

FOURTH WORKSHOP ON COMPUTATIONAL CONTROL OF FLEXIBLE AEROSPACE SYSTEMS

July 11-13 1990
Williamsburg, Virginia

Rockwell International
North American Aircraft

Abstract

Three designs are discussed for controlling loads while rolling for the Active Flexible Wing (AFW). The goal is to provide good roll control while simultaneously limiting the torsion and bending loads experienced by the wing. Successful development will allow for lighter wing structures to be used, with the control system insuring loads remain within allowable limits. Each controller has been designed for testing in the NASA Langley Transonic Dynamics tunnel on the Rockwell AFW wind tunnel model

The first design uses LQG/LTR techniques to develop a MIMO controller structure between the control surfaces and roll rate and four separate torsion loads. The control system consisted of two parts: The loop controller for stability and a pre-filter which generates load commands as a function of roll command input to the loop controller for performance. Conversion of the physical requirements to LQG/LTR design parameters is shown.

The second design uses a nonlinear gearing function imbedding implicit load control information as an element of a modified SISO controller. While only roll rate has an explicit feedback mechanism, torsion, bending, and hinge load are controlled through the a priory knowledge of the model's control surface to roll and load transfer functions. System stability and robustness are shown by analysis and simulation.

The third design integrates the above RMLA controllers with a high frequency structural mode controller. Using the same surfaces as the RMLA control, its object is to reduce high frequency responses caused by the RMLA and to act as a flutter suppression system. The goal is to operate the integrated controller beyond the model's natural flutter boundary. Design issues of integrating the RMLA and structural mode controllers are discussed.

Introduction

The Advanced Flexible Wing (AFW) is an aeroservoelastically scaled model of a Rockwell fighter design. By allowing the wings to be flexible, they may be lighter and the flexibility exploited for such things as twist and camber control. Additional flexibility, however, reduces the flutter envelope of the wing and active control schemes may be required to stabilize the wing modal dynamics. Control systems discussed in this paper cover maneuver, load, and flutter control systems. An integrated maneuver, load, and flutter controller is a goal of this test program.

Two roll plus maneuver load control designs are discussed. The first design is based on LQG/LTR modern control methods to control roll rate and torsion loads at four different wing locations. The controller is a five input, five output system with 11 internal states. The controller acts a command tracker, generating surface commands to drive the AFW to the state requested by the command generator. The command generator works as a prefilter to provide input signals to the controller corresponding to the desired roll rate and loads profile. With these two things, the prefilter and the controller, a roll maneuver may be performed with a 40% reduction in torsion loads on the wing.

The second design uses a nonlinear surface command function to produce surface position commands as a function of current roll rate and commanded roll rate. It is designed to keep specified wing loads below some specified value while permitting the greatest possible roll axis performance. (A conventional control system design would attempt to control the wing loads continuosly, even when they were well below structural limits. This method degrades roll performance as some control power is used by the load controller.) This controller, in contrast, only controls the loads when they reach some threshold, say 80% of structural limits, to permit the control power to be used for aircraft maneuvers until it is necessary to perform load control. The trade off for this design method is the controller becomes a nonlinear controller instead of a linear one with the accompanying increase in design and analysis complexity.

The final design is a flutter suppression control system. This system stabilizes both symmetric and antisymmetric flutter modes of the AFW. Due to the fact that accelerometers have an output which is a function of the frequency, load sensors are used to provide the feedback signal. The control system design is done using classical techniques. An integrated flutter and roll/loads design is also being developed.

Slide 1 Description of Control Systems

For a top level design goal, Reducing wing loads while maintaining roll performance is the objective of the roll controllers. There are two designs to meet this objective: 1) Linear Feedback (RMLA) using roll rate and load feedback in the controller. This design uses LQG/LTR modern control techniques as the synthesis method. 2) Feedforward Nonlinear Optimal using only roll rate feedback for control and having surface command functions providing load control.

Slide 2 Design Objectives

For both Roll Maneuver designs, similar design goals were used. The stability and time response goals correspond to the MIL-STD parameters for fighter aircraft. The load control criteria were chosen to represent a first step to prove the validity of the concept. Higher levels of load control are achievable at a cost of reduced maneuverability. The robustness criteria is derived from known measurement uncertainty; plant variations from the analytical models may well be higher.

Slide 3 Block Diagram of RMLA

This diagram describes the basic structure used in the RMLA controller. Roll and load commands go through a pre-filter to provide tracking signals to the RMLA controller. The controller is a 5 input (roll rate and wing torsion at four locations) 5 output (trailing edge inboard surfaces together, trailing edge outboard left, trailing edge outboard right, leading edge outboard left and leading edge outboard right) MIMO design with 11 internal dynamic states (the states do not necessarily correspond to physical quantities).

Slide 4 Prefilter Design

An integral part of the RMLA controller is the prefilter. The pre-filter's function is to output 5 tracking commands derived from a roll rate input command. The pre-filter output is based on the open loop dynamics of the AFW. For this design, the roll rate signal was fed directly and the torsion commands were gain scheduled to the roll rate command.

Slide 5 Linear Performance

A step response to a 1 rad/sec roll rate command shows the good roll rate tracking and load control of the LQG/LTR RMLA. A command for torsion only shows the decoupling performance of the controller.

Slide 6 Nonlinear Performance

The response of the AFW+ LQG/LTR RMLA in a complete nonlinear simulation shows the roll tracking of the LQG/LTR RMLA. A simulation of a 40% load reduction with no change in roll performance from the nominal case.

Slide 7 LQG/LTR RMLA Summary

The LQG/LTR RMLA controller has achieved the basic design goals. The LQG/LTR RMLA shows good tracking, channel decoupling, and stability properties.

Slide 8 LQG/LTR RMLA Future Directions

The RMLA controller can be refined in its design by expanding the design to handle non-square cases. This would allow for inputs to be any combination of control commands and outputs to be the desired surfaces. The pre-filter may also be improved by designing it as a dynamic model follower or command generator.

Slide 9 Feedforward Block Diagram

The RMLA Feedforward Nonlinear Optimal Controller block diagram shows how the roll rate command is input to the control surface functions. The surface functions contain the load information which provides the load control. The only inputs to this control system are the commanded roll rate and the actual roll rate. From this information, the surface functions output surface commands which will produce the desired acceleration about the current roll rate.

Slide 10 Design Method for Feedforward

The design method for the feedforward controller can be stated as 'Control loads only when they are near limits'. This is accomplished by developing surface control functions by optimization methods. Using loads as constraints, surface deflections are found which will provide the desired roll rate and roll acceleration without violating the constraints. The surface functions will have a linear range where no load constraints have been encountered and a nonlinear range where constraints are active.

Slide 11 Example of Surface Function

This plot are two views of the control surface functions. Notice the linear region around zero and the nonlinearities as constraints are encountered. In the 2-d plot, the trailing edge outboard

surface becomes the primary load control surface with the trailing edge inboard increasing in gain to maintain roll performance. This follows our intuitive expectations as the trailing edge outboard surfaces have high load authority but low roll power and the trailing edge inboard surfaces have the highest roll power. Given we are trying to keep total surface deflections to a minimum, this pattern makes sense.

Slide 12 Summary of Feedforward Optimal Design

The feedforward optimal controller is capable of maintaining roll performance while controlling wing loads. An important consideration is the controller is a linear design in term of roll rate and roll acceleration. A simulation of this controller is currently underway for test this winter.

Slide 13 Flutter Control Block Diagram

Flutter control is used on the AFW to expand the flight envelope while keeping the low weight, flexible wings. The flutter control block diagram show how the flutter suppression system is an integral part of the aircraft dynamics.

Slide 14 Flutter Suppression Control Law

The Rockwell method for flutter design is similar to that employed by NASA except load sensors were used for feedback instead of accelerometers. This is because load sensors are also used for the roll control laws and to eliminate the frequency gain of accelerometers.

Slide 15 Combined Maneuver, Flutter, and Load Control

A proposed design for integrated maneuver, flutter, and load control would exploit the frequency separation between the maneuver dynamics and the flutter dynamics. The controllers will be designed separately and combined to produce the total controller.

Slide 16 Combined Maneuver, Flutter, and Load Control Block Diagram

The block diagram indicates how each surface command signals would be combined into the total controller design. Any combination of flutter controller and maneuver/loads controller could be used in this scheme.

Slide 17 Future of AFW Controls

A goal of this design/testing program is to demonstrate a snap-roll maneuver beyond the flutter boundary with load reduction. This would open up new areas of performance for aircraft in such things as weight reduction and improved agility. Additional work is also being done with new nonlinear controllers to improve the aircraft performance while coping with conflicting control requirements.

ROLL PLUS LOAD ALLEVIATION CONTROL SYSTEMS

Objective: To maintain maximum roll capability while reducing wing loads.

- Torsion
- Bending
- Hinge Moments

Approach: 1) Linear Feedback Design (Roll Maneuver Load Alleviation, RMLA)

- Roll and Load Feedback
- Command Following
- LQG/LTR Synthesis

2) Feedforward Nonlinear Optimal Design

- Use constrained optimization to develop surface command functions producing the desired roll performance without exceeding wing loads.
- Roll feedback only

Rockwell International
North American Aircraft

DESIGN OBJECTIVES

Stability: 6dB of gain margin and 45 degrees of phase margin. These apply to every loop for multivariable designs.

Time Response: Achieve time-to-90 degrees in 0.4 seconds (scaled MIL-SPEC) with minimal overshoot and good command tracking

Load Control: For design 1, reduce torsion moments by >20% throughout the roll maneuver. For design 2, limit Torsion, Bending, and Hinge moments to <80% of the test trip limits.

Robustness: Controllers must handle the known uncertainty of the model parameters.

Rockwell International
North American Aircraft

RMLA CONTROL BLOCK DIAGRAM

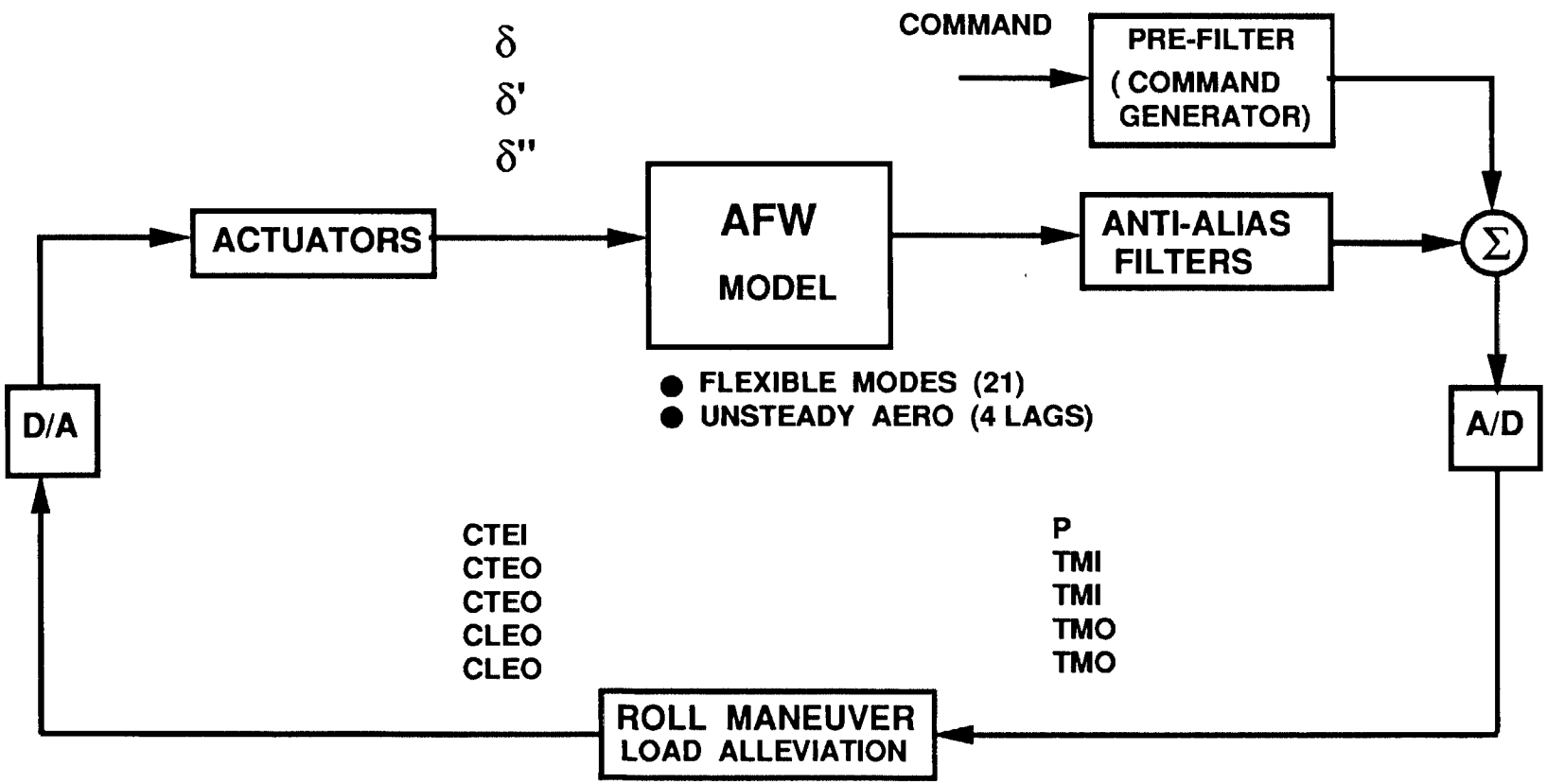

PRE-FILTER DESIGN AND IMPLEMENTATION

The pre-filter takes a roll rate command and generates the 5 commands required by the RMLA controller.

Roll Rate is used directly.

The torsion commands are generated using the knowledge of the open loop (for load control) response. Load commands are given as some percentage of the open loop response.

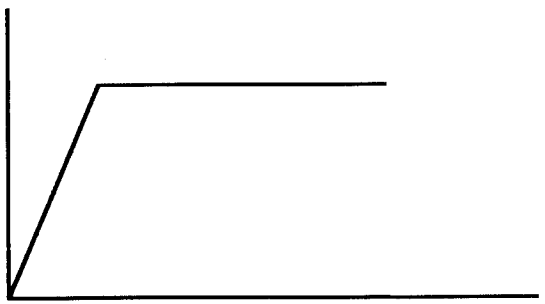

Roll Rate Command

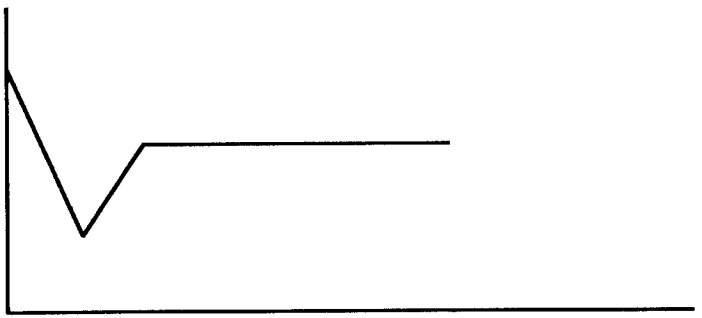

Typical Torsion Command

LINEAR PERFORMANCE ANALYSIS INDICATES CONTROL OF ROLL RATE AND LOADS

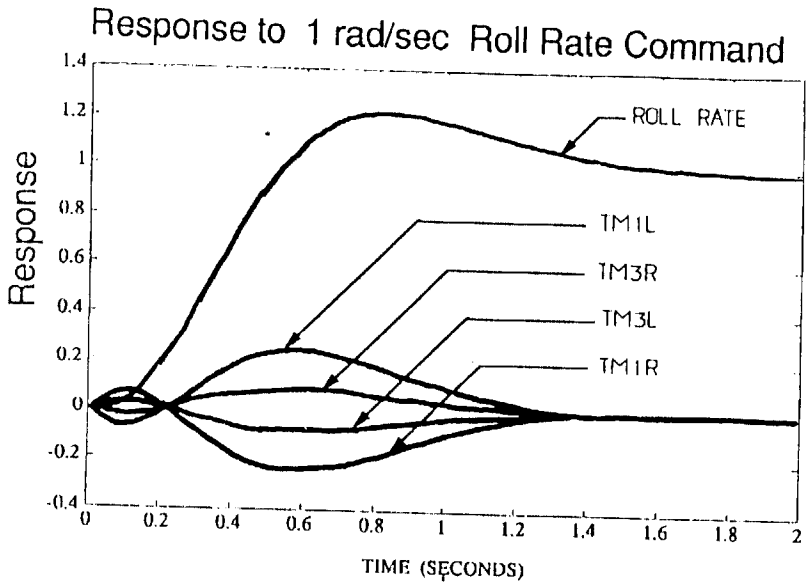

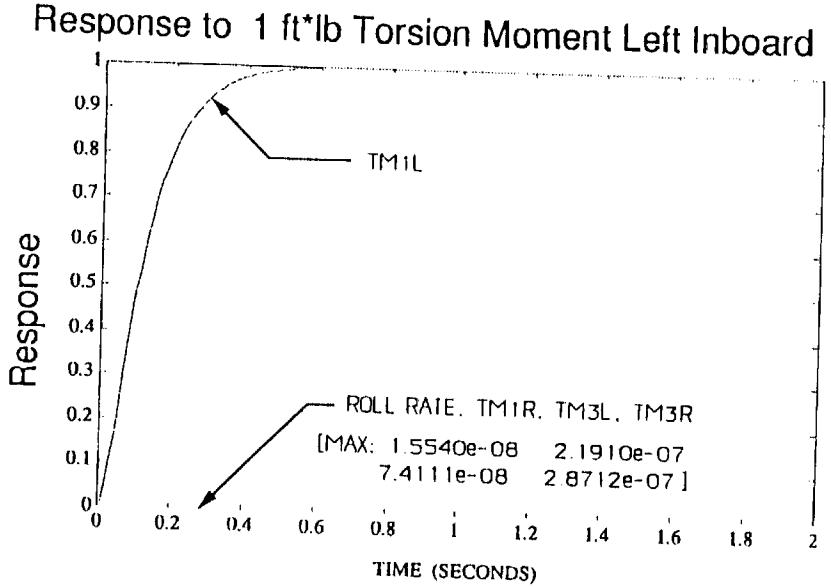

Rockwell International
North American Aircraft

FULL ATW SIMULATION OF ROLL MANEUVER WITH LOAD REDUCTION

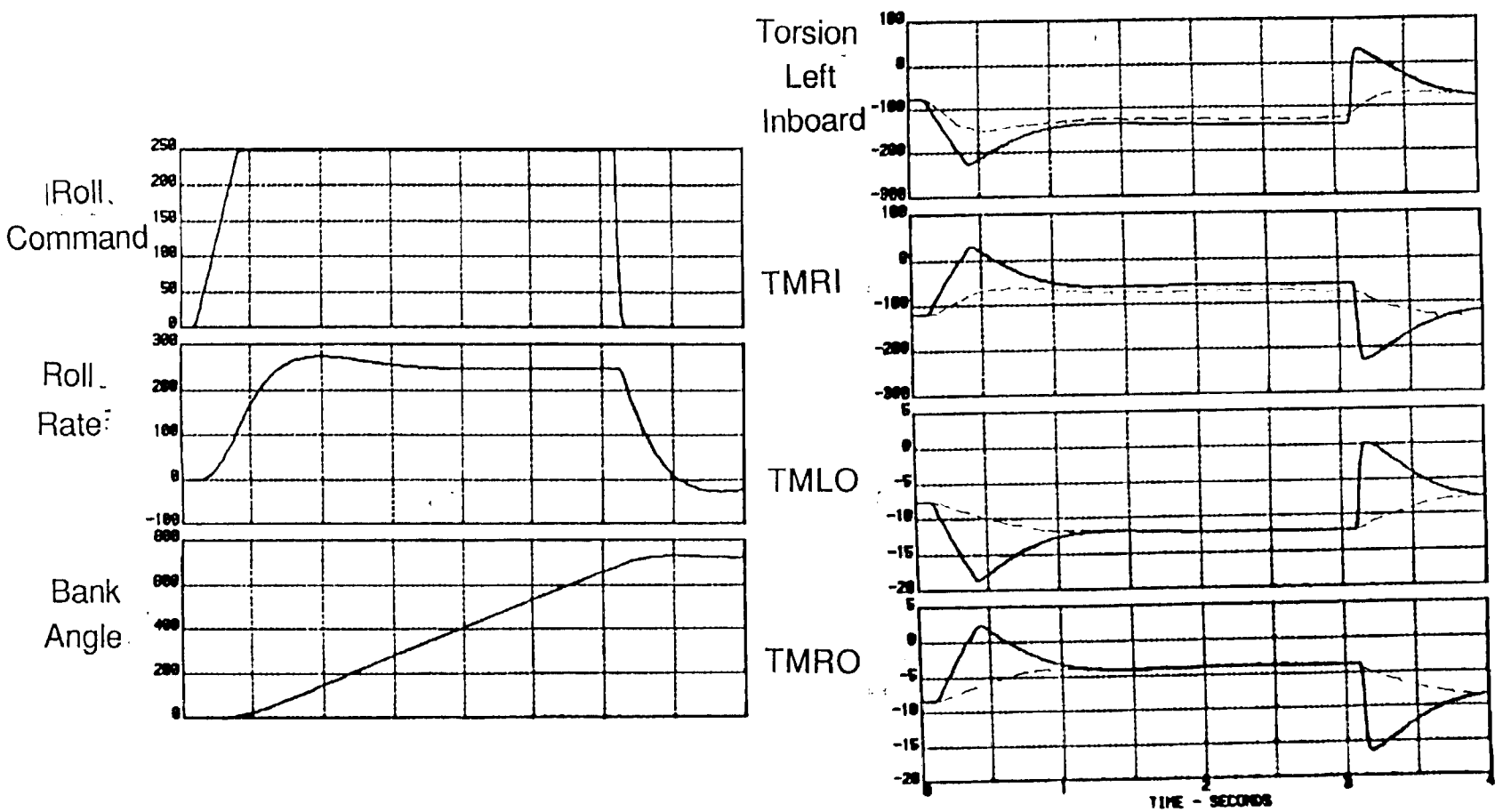

Rockwell International
North American Aircraft

572

RMLA SUMMARY OBSERVATIONS

- **DECOUPLING**
  - ACHIEVE ROLL RATE WITHOUT TORSION MOMENT
  - ACHIEVE TORSION MOMENT WITHOUT ROLL RATE
- **GOOD TRACKING**
  - ALL OUTPUTS EQUAL ALL COMMANDS
  - ZERO ERROR
  - SMALL CROSS-COUPLING TRANSIENT
- **GAIN MARGIN AND PHASE MARGIN**

RMLA FUTURE DIRECTIONS

1. **Non-square input-output**
   - (e.g. more load control feedback locations than control surfaces)

2. **Expand pre-filter designs**
   - Implicit model following
   - Command Generator Tracker

3. **Extend the method**
   - all-axis Maneuver Load Control for aircraft to reduce / limit loads on all aircraft surfaces.

FEEDFORWARD NONLINEAR OPTIMAL CONTROL BLOCK DIAGRAM

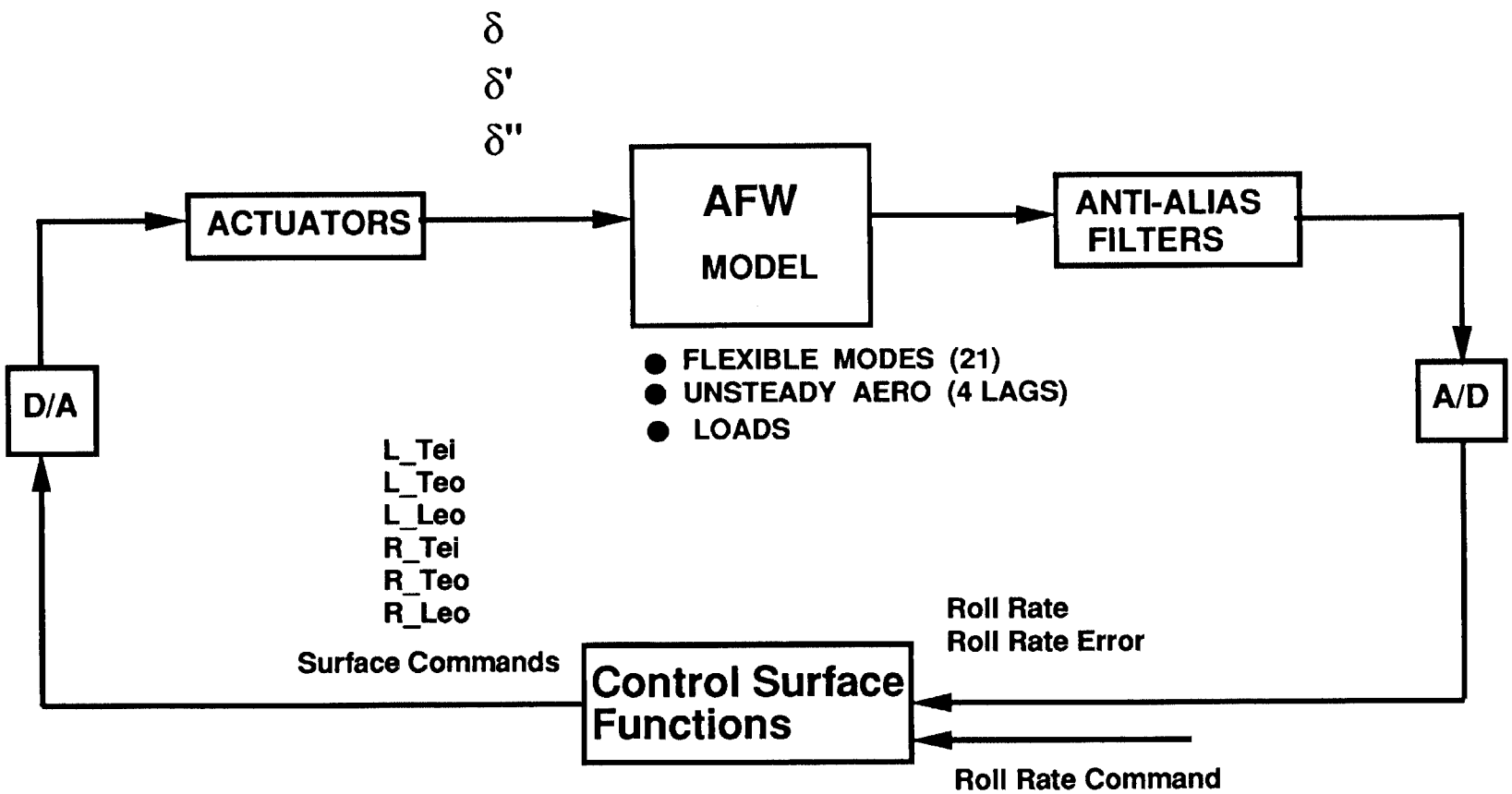

DESIGN METHOD FOR FEEDFORWARD NONLINEAR OPTIMAL FUNCTIONS

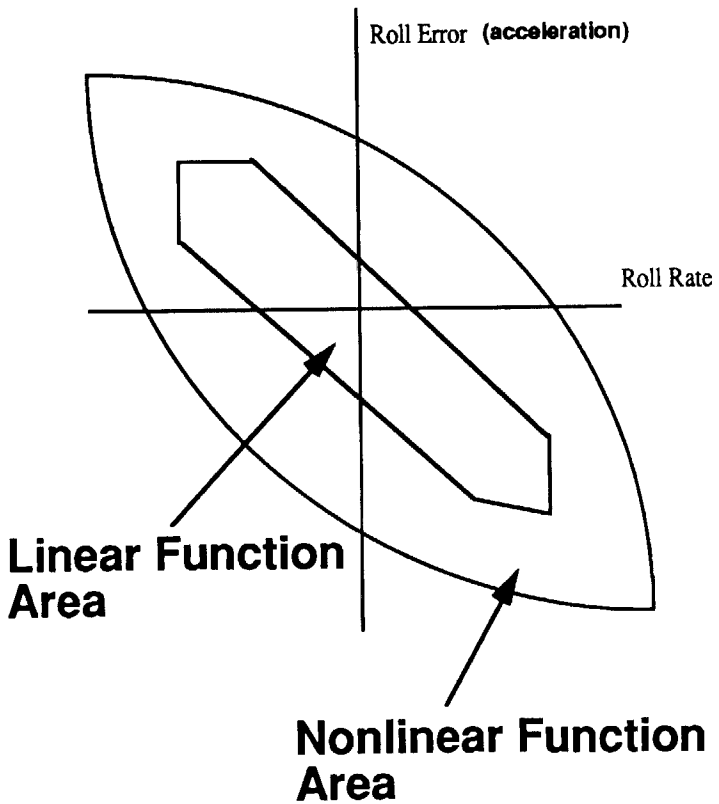

Loads < Design Limits

Roll Rate and Roll Acceleration are inputs.

Min(f) = $\Sigma\ \delta_i$

The limit of the achievable envelope occurs when multiple conflicting load limit constraints are encountered.

575

EXAMPLE OF SURFACE CONTROL FUNCTION

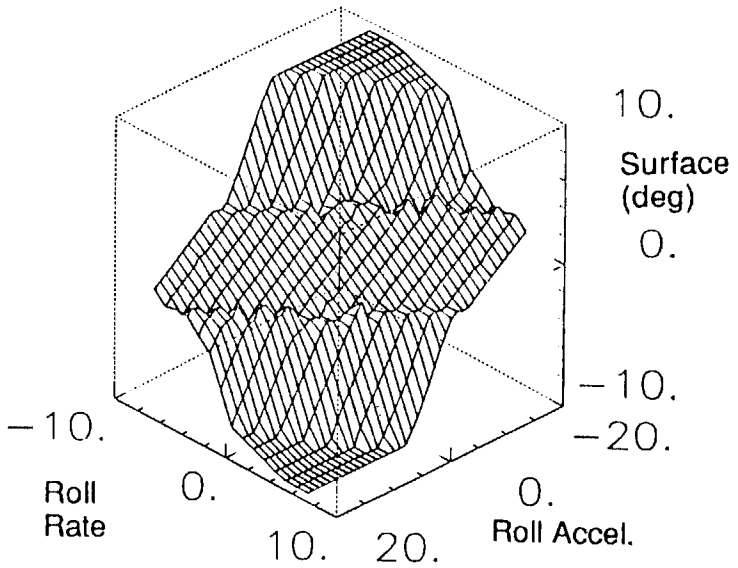

Left Trailing Edge Inboard Deflection vs Roll Rate and Acceleration

Surface Deflections @ zero Roll Acceleration

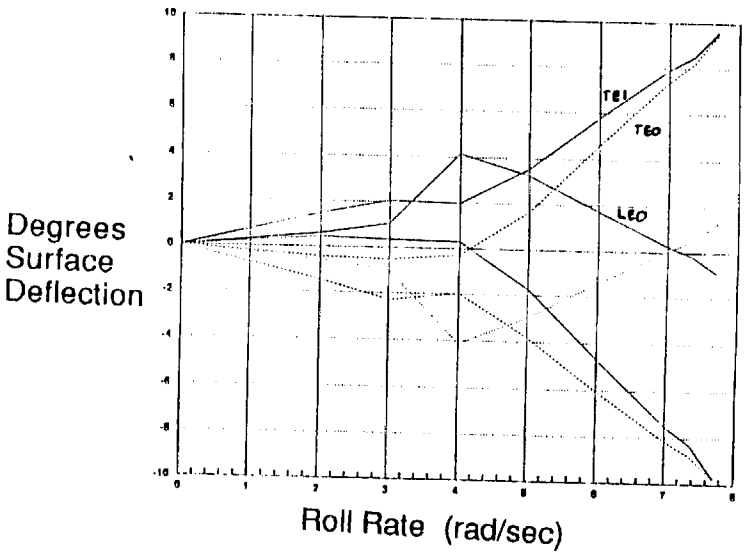

Rockwell International
North American Aircraft

SUMMARY OF FEEDFORWARD OPTIMAL DESIGN

The Feedforward Nonlinear Optimal Controller can maintain roll performance while achieving loads <80% of non load control algorithms.

The design is linear in terms of roll rate and roll acceleration control; control power is a linear function of rate and acceleration.

Has applications to agility control as the system delivers maximum control force available.

FLUTTER CONTROL BLOCK DIAGRAM

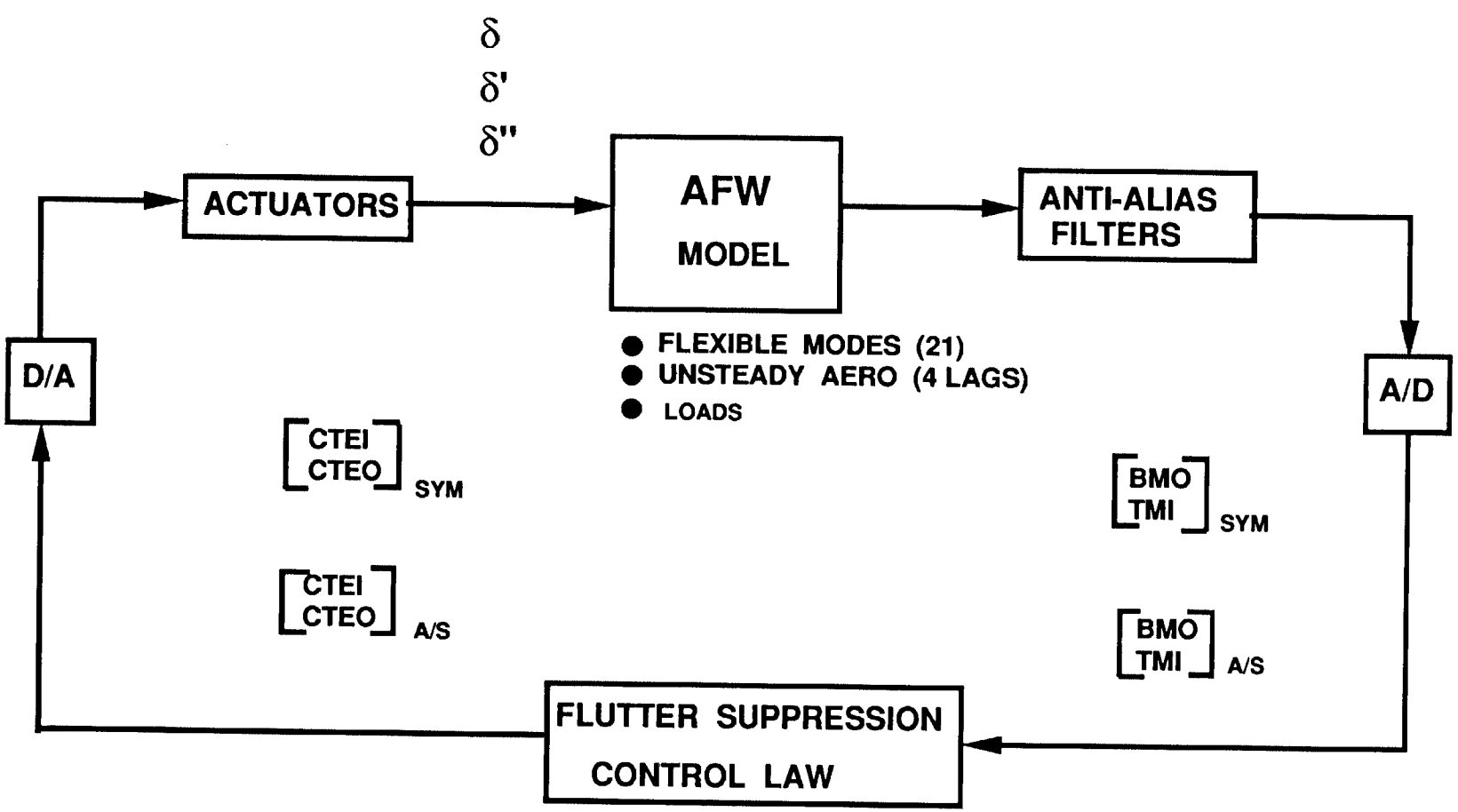

FLUTTER SUPPRESSION CONTROL LAW

Classical design method to stabilize flutter dynamics

Uses load sensors for feedback control. Load sensors are used to avoid the nonlinear frequency effects of accelerometers.

Both SISO and MIMO control designs. SISO designs use one sensor input and give one control surface output. MIMO designs use two sensors for input and generate two distinct surface output commands.

580

DESIGN PHILOSOPHY OF COMBINED MANEUVER, FLUTTER SUPPRESSION AND LOAD CONTROL

Flutter controllers and Maneuver + Loads controllers can be designed separately and combined in a linear manner.

Frequency separation of the flutter and maneuver + loads phenomenon allows for this design method.

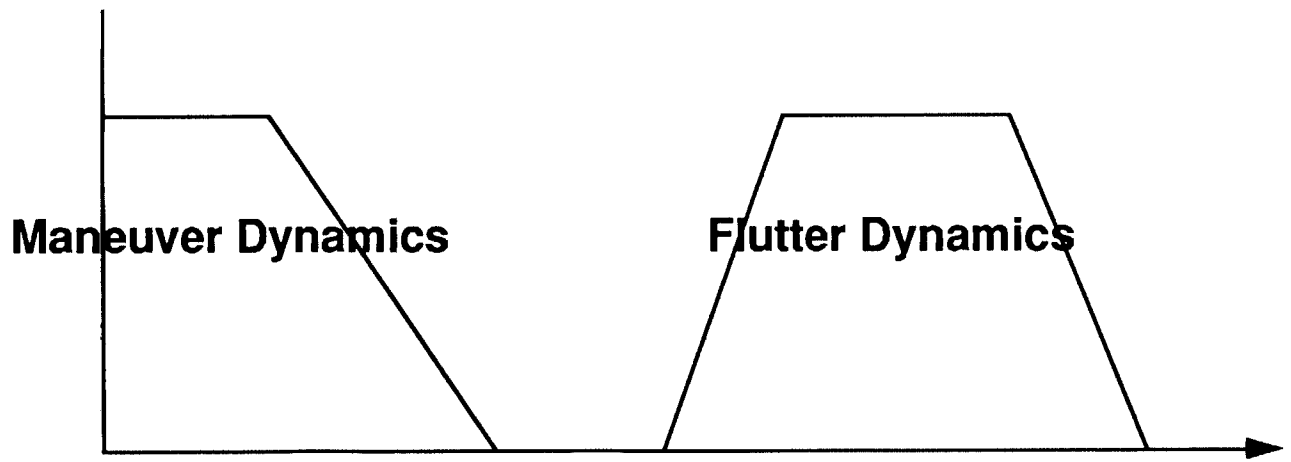

COMBINED RMLA AND FLUTTER CONTROL BLOCK DIAGRAM

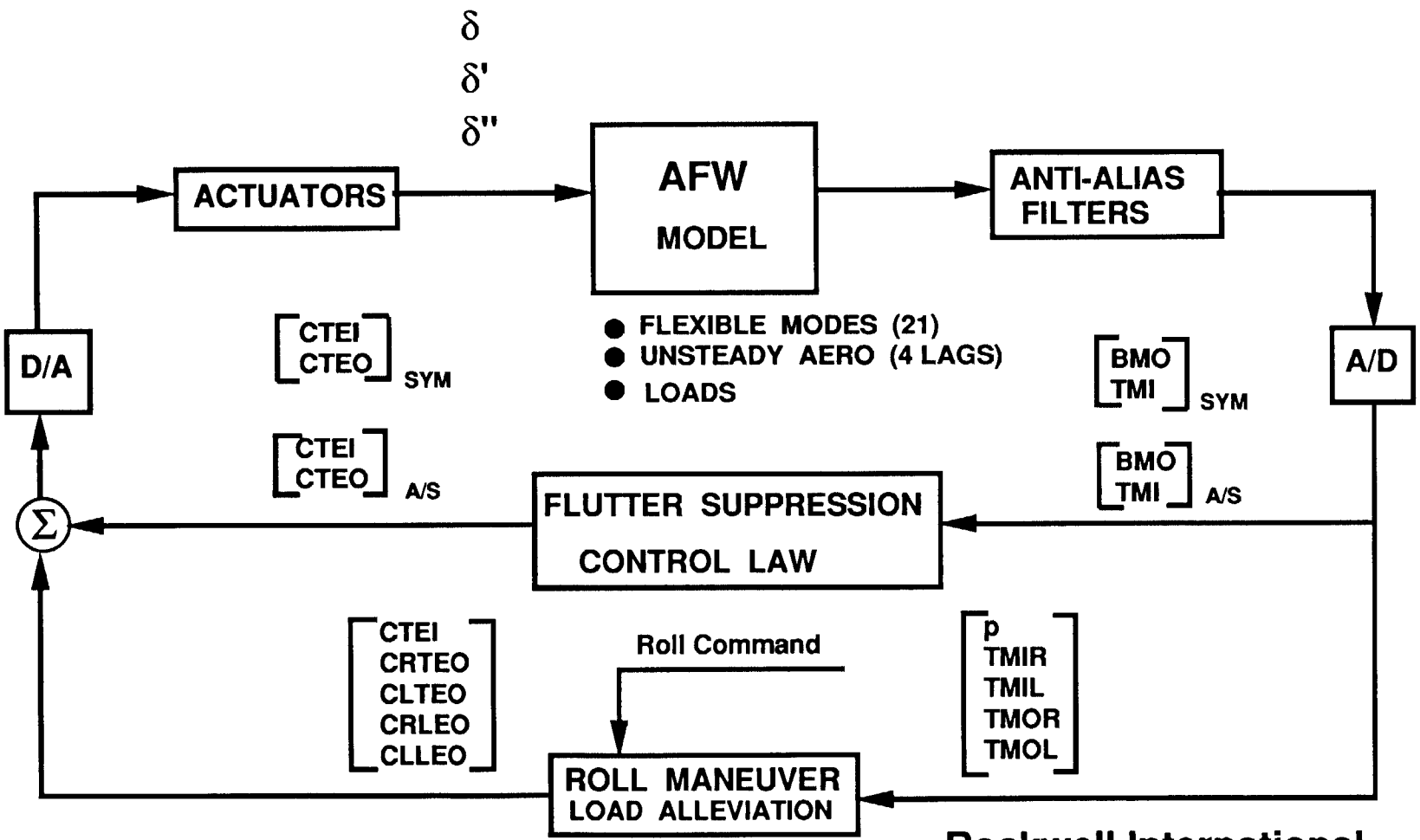

Rockwell International
North American Aircraft

FUTURE OF ATW CONTROL EFFORT

- Final objective is to demonstrate a snap-roll maneuver (time to 90 < 0.4 sec.) with load reduction beyond the flutter boundary.

- Possibility to integrate all axis maneuver + load + flutter control. Additional control schemes show promise for resolving conflicting design constraints while maintaining an intuitive design method for the flight control system.

- With all aircraft designs seeking ways to reduce weight, active control schemes can allow lighter and more flexible aircraft a larger flight envelope and greater safety margins.

Development, Simulation Validation, and Wind-Tunnel Testing of a Digital Controller System for Flutter Suppression

by

Sherwood T. Hoadley
Aeroservoelasticity Branch
NASA Langley Research Center

Carey S. Buttrill
Aircraft Guidance and Control Branch
NASA Langley Research Center

Sandra M. McGraw
Lockheed Engineering and Sciences Co.

and Jacob A. Houck
Analysis and Simulation Branch
NASA Langley Research Center

presented at

The Fourth NASA Workshop on Computational Control of Flexible Aerospace Systems
Williamsburg, VA
July 11-13, 1990

Introduction

The Active Flexible Wing (AFW) Program (refs.1 and 2) is a cooperative effort between the NASA Langley Research Center and Rockwell International Corporation. The program objective is the validation of analysis and synthesis methodologies through the development of real-time digital multi-input multi-output (MIMO) control laws for a sophisticated aeroelastic wind-tunnel model. This model was tested in the Langley Transonic Dynamics Tunnel during the Fall of 1989.

Flutter suppression (FS) is one of the active control concepts being investigated in the AFW Program. The design goal for FS control laws was to increase the passive flutter dynamic pressure 30 percent. In order to meet this goal, the FS control laws had to be capable of suppressing both symmetric and antisymmetric flutter instabilities simultaneously. In addition, the FS control laws had to be practical and of low-order, robust, and capable of real-time execution within a 200 hz. sampling rate.

The purpose of this paper is to present an overview of the development, simulation validation, and wind-tunnel testing of a digital controller system for flutter suppression.

AFW DIGITAL CONTROLLER DESIGNED, ASSEMBLED, CODED, VALIDATED, AND TESTED

Designed

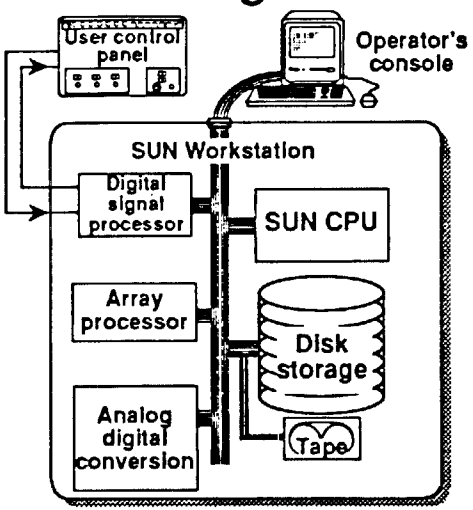

Assembled/Coded

Validated

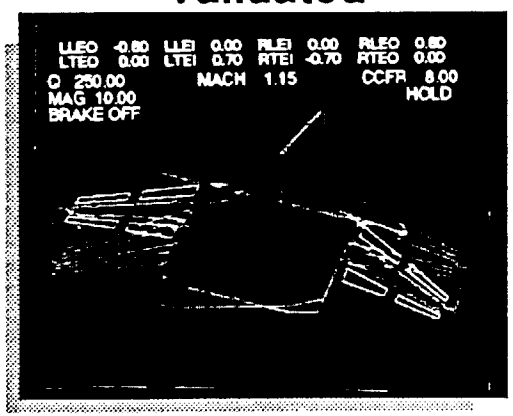

Tested

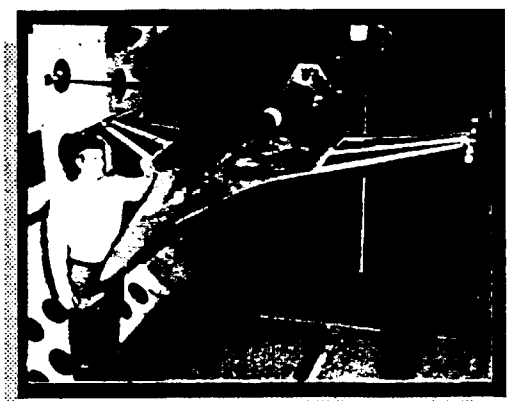

AFW Digital Controller Designed, Assembled,Coded, Validated, and Tested

The AFW digital controller was designed, assembled, coded, validated, and tested completely in-house. This represents a "first" for the agency. The accompanying figure illustrates each of these accomplishments.

DESIGNED shows schematically a digital controller, comprised of various computers, tape drive, disks, array processor, analog-to-digital conversion boards all residing within the same chassis as a SUN host central processing unit. Design specifications required that the controller have the capability of receiving and providing analog and discrete signals from/to the model and user control panel. The Digital Controller controls the wind-tunnel model by digitizing the incoming sensor signals, processing the currently-implemented control law, and then providing the appropriate control-surface actuator commands to effect these laws.

ASSEMBLED/CODED shows an operator sitting at the SUN 3/160 Workstation. Over 22,000 lines of code in C-language were written during 1989 for the 1989 Wind-Tunnel test . The implementation of control laws into the control computer is a time-critical path leading up to the hot-bench simulation and wind-tunnel tests. This means that the control laws need to be generic in form. The digital controller software can be modified easily and quickly as required, and the generic form of the control systems allows for changes in a design to be implemented easily and reliably.

VALIDATED shows a color-coded three-dimensional wireframe outline of the AFW model generated by the NASA/LaRC Advanced Real-Time Simulation (ARTS) facility. The ARTS facility was used to verify and validate the functionality of the digital controller.

TESTED shows the AFW wind-tunnel model in the NASA/LaRC Transonic Dynamics Tunnel during its October/November 1989 entry. The digital controller operating an FS control law took the AFW wind-tunnel model 24% (in dynamic pressure) above its open-loop boundary.

CONTROL SYSTEM HARDWARE SCHEMATIC

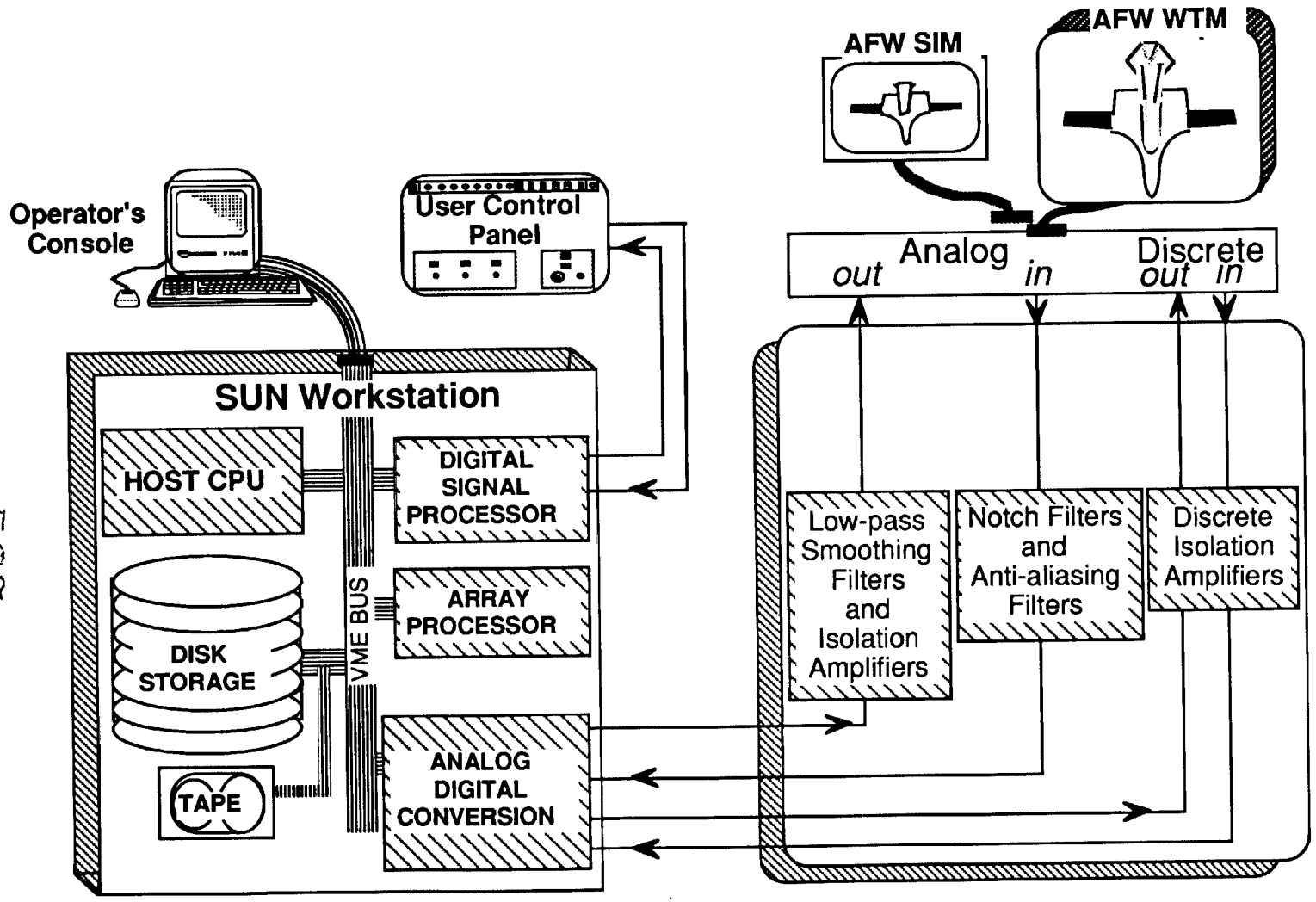

Control System Hardware Schematic

Digital Controller

One of the primary objectives of the AFW Program is to gain practical experience in designing, fabricating, and implementing a real-time MIMO digital controller and in developing the hardware interface between the controller and the actual wind-tunnel model and simulator. The hardware components of the digital controller, on the left side of the figure, show schematically how the host central processing unit (CPU), the disk and tape drives, and the added boards communicate across the VME BUS. During closed-loop operation, the ADC boards convert analog sensor signals to digital data; the DAC boards convert digital actuator commands to analog signals; the host CPU and the user control panel provide user interface to the signal processing board; the signal processing board ("the controller") controls the real-time processing; and the array processing board performs floating-point calculations of the flutter suppression control laws. The entire operation is repeated 200 times a second for real-time operation. To meet these requirements with reasonable resources, a SUN 3/160 workstation driven by a Unix Operating system was selected as the "shell" of the Digital Controller.

NASA/Rockwell Interface

The hardware components of the interface box are shown schematically on the right side of the figure. The interface box contains the analog circuitry for processing the analog signals coming from or going to either the wind-tunnel model or the simulator. The circuitry includes low-pass filters (break frequencies of 1000 hz) to reduce the high-frequency noise and limit voltage spikes, antialiasing filters, and electrical isolation networks. The antialiasing filters are configured to provide either first-order roll-off or fourth-order roll-off with either a 25 hz break frequency or a 100 hz break frequency. The sensor signals coming to the controller can also be filtered through notch filters, specified with each control law to prevent signals with undesired frequencies from being input to the control law. The isolation amplifiers provide optical isolation between two electronic systems.

COMPONENTS OF DIGITAL CONTROLLER

Host Computer
SUN 3/160

Provides user interface to controller
- Initializes options, arrays, control parameters
- Controls saving of data to external files and tapes

Digital Signal Processor
SKY Challenger

Controls real-time processing
- Analog input/output
- Control law execution
- Interface through User Control Panel
- Sending of signals for Controller evaluation

Array Processor
SKY Warrior I

Performs floating-point processing
- Unit conversions and scaling
- Control-law matrix computations

ADC's and DAC's
Data Translation
(2-DT 1401's and 2-DT 1406's)

Performs analog and digital conversions
- Converts analog (sensor) signals to digital data
- Converts digital (actuator) commands to analog signals

User Control Panel
Designed and built in-house

Provides real-time interface to controller
- Allows option selection
- Displays current status of selectable options
- Provides warning for critical conditions

Components of Digital Controller

Besides the host computer, the Digital Controller consists of several special purpose processors linked to the workstation via a data bus. These processors include a digital signal processor, a high speed array processor, and four data translation boards.

The host computer is a SUN 3/160 workstation. It provides the user interface to the digital signal processor board, which is the heart of the real-time digital controller. All user options, control law arrays, control parameters, and excitation definitions are specified through the host user interface. The host downloads signal-processor software and determines and downloads the array-processor command code to implement a currently-selected control law. It allows real-time changes in selection of mode of operation, selection of gains, excitation amplitudes and the control surfaces to be used. The host controls the saving of the digitized data to external files and tapes and provides the display of important parameters such as control-surface deflections, errors between commanded and actual deflections, overall control-law gain, and switch selections.

The digital signal processor (DSP) is a Challenger-I board manufactured by SKY Computers, Inc. and is composed primarily of two TMS 32020 microcomputers and 64K integer words (one word equals 2 bytes) of memory. The DSP is the "real-time digital controller" because it provides the management of all signal processing and scheduling of control laws. As bus master, the DSP controls, directs, and sequences the real-time activities and tasks. It controls all the real-time processing of analog input and output signals. It controls control-law execution by sending commands to the array processor to implement a desired control law and adds digitized model excitations or bias commands to statically position control surfaces. It provides the interface to the user control panel lights and switches and checks for faults; and it sets switches (software flags) for the host computer which specify when blocks of data can be stored and transferred.

The array processor (AP) is a SKY Warrior I board with 16Mbytes of memory which provides the high-speed floating-point arithmetic computations required in executing a particular control law. Included in these computations are unit conversions, scaling, and all matrix computations.

The data translation boards consist of two DT-1401 analog-to-digital converter (ADC) boards and two DT-1406 digital-to-analog converter (DAC) boards manufactured by Data Translation, Inc. They provide all the analog data conversions required between the model and the controller. The ADC's are used to convert the incoming analog sensor signals to digital integer values which can be processed by the DSP. The DAC's are used to convert integer actuator command signals sent by the DSP into analog voltages which are then sent to the control surface actuators.

The user control panel, designed and built in-house by NASA, provides the real-time interface to "the controller". It allows real-time selection of certain options via lighted switches and provides real-time status of various control parameters through status display lights. These switches are simulated in the host interface software for use with the simulator and as a backup.

NASA

90-01865

Langley Research Center
Hampton, Virginia 23665-5225

591

ORIGINAL PAGE IS
OF POOR QUALITY

Digital Controller Simulation Lab

The accompanying figure is a photograph of the Digital Controller Simulation Lab. The components in Lab include:

- Two SUN 3/160's (housed in rolling cabinets under the table)
- NASA/Rockwell Interface Box with User Control Panel and Patch Box (shown on the extreme left). The User Control Panel and Patch Box are located in the top of the box. The power supply is in the bottom, the anti-aliasing, notch filters, etc. are in the box above the power supply.
- Oscilloscope and Simulation Video Monitor with wireframe image displayed (on table)
- Operator's console (to the right of the monitor)
- Printer

The Patch Box is used to bypass the hardware in the NASA/Rockwell Interface Box when hooked to the simulator when software-implemented anti-aliasing filters are used and when trouble-shooting problems with the hardware.

The oscilloscope is used to monitor specific analog signals for checkout, debugging, and trouble-shooting. The Simulation Video Monitor provides the controller operator with a visual wireframe image of the model which includes the dynamics of the model and the motion of the control surfaces.

DIGITAL CONTROLLER SOFTWARE

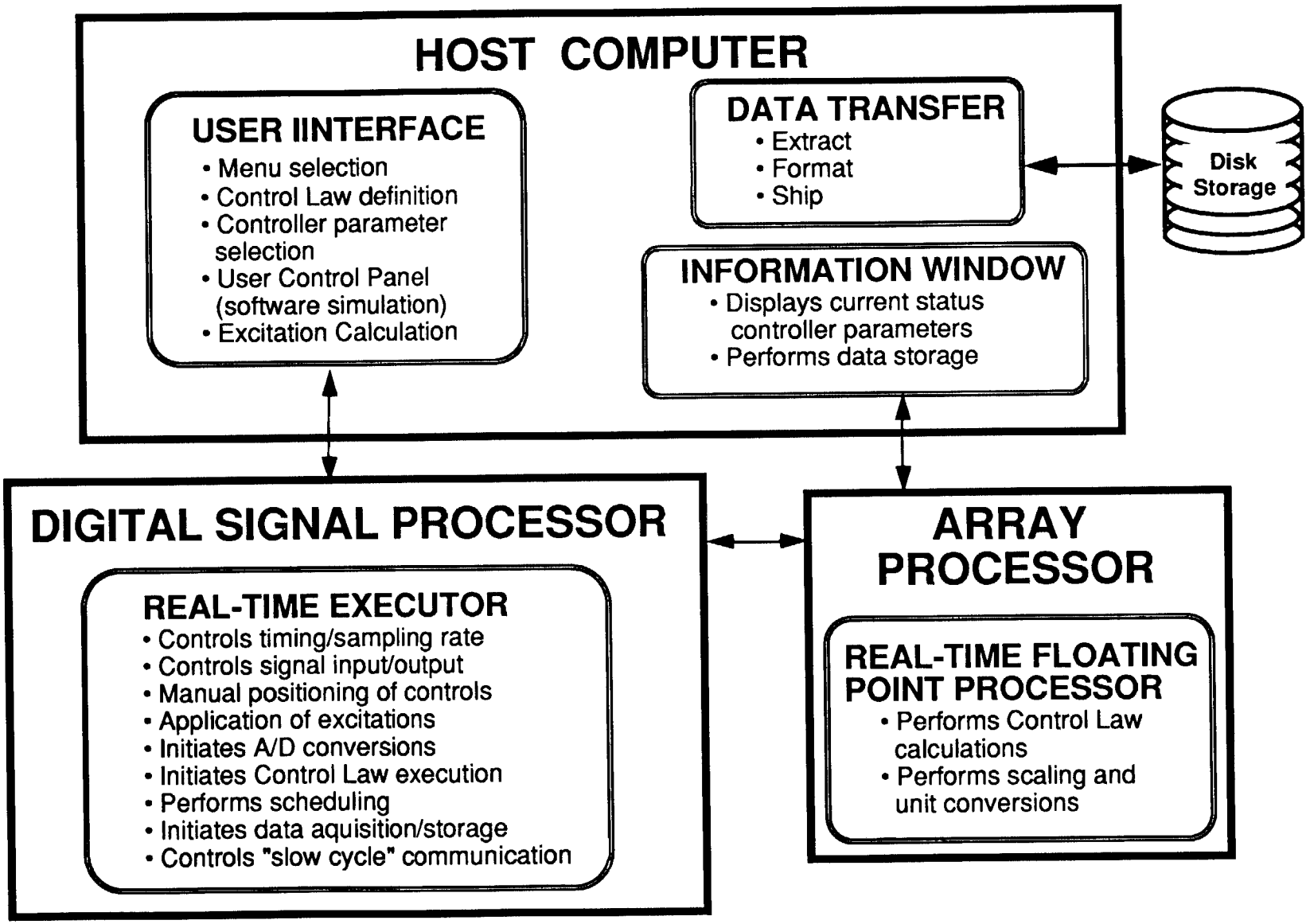

Digital Controller Software

A generic form of the control law function was identified such that one set of software would accommodate a given control law while imposing minimal constraints on the designers. The generic structure allows the designers to choose sensors with options to blend them, freedom of controller order with upper limits, scheduling of controller parameters with respect to dynamic pressure, and selection of various control surfaces with or without distribution of controller outputs to different actuators. Components of the Digital Control System were identified and separate program modules were developed. Their various functions are outlined below. All the Digital Controller software is written in the high level C programming language except for the commands required to perform the actual calculations on the array processor. Operation code command blocks were generated for these.

HOST computer:

There are three primary HOST programs, all of which run simultaneously:

1. HOST INTERFACE providing menus for
   - Control Law Definition
   - Controller parameter selection
   - Calculation of excitation signals for Controller Performance Evaluation
   - User Control Panel software simulation
   - Calculation of the excitations for Control Law verification
2. DATA TRANSFER providing capability to
   - Extract sampled experimental data which is in main memory and/or stored on disk
   - Format data for external use
   - Ship data to disk, tape, or external computer
3. INFORMATION WINDOW displays current status of controller parameters:
   - Actual Control Surface Deflections and percent errors
   - Mach and q
   - Roll angle, roll-rate, pitch
   - Current Sampling Speed
   - Current switch selections
   - Type, size, amplitude, and frequency of excitation
   - Status of data storage
   - Control Law inputs and outputs

Digital Signal Processor (DSP):

There is one program residing on the Digital Signal Processing board written in C which controls the real-time execution for

- Specifying timing and sampling rate
- Controlling sampling of specified input signals
- Initiating A\D and D\A conversions of signals
- Manually positioning the control surfaces
- Sending excitation signals to various control surfaces
- Initiating Control Law execution by sending command codes to array processor
- Performing scheduling of control laws based on dynamic pressure
- Initiating data acquisition and storage
- Controlling all the "slow cycle communications between the host INTERFACE program, the Array Processor and the host INFORMATION WINDOW program.

Array Processor (AP):

Control law execution code written using the array processor command language which is stored by the HOST computor in the Digital Signal Processor memory. When control laws are executed, the DSP sends these commands to the array processors. This code performs:

- Control Law calculations
- Scaling and unit conversions

FLUTTER SUPPRESSION SYSTEM

with ROLL TRIM CONTROL as coded for 1989 Wind-Tunnel test

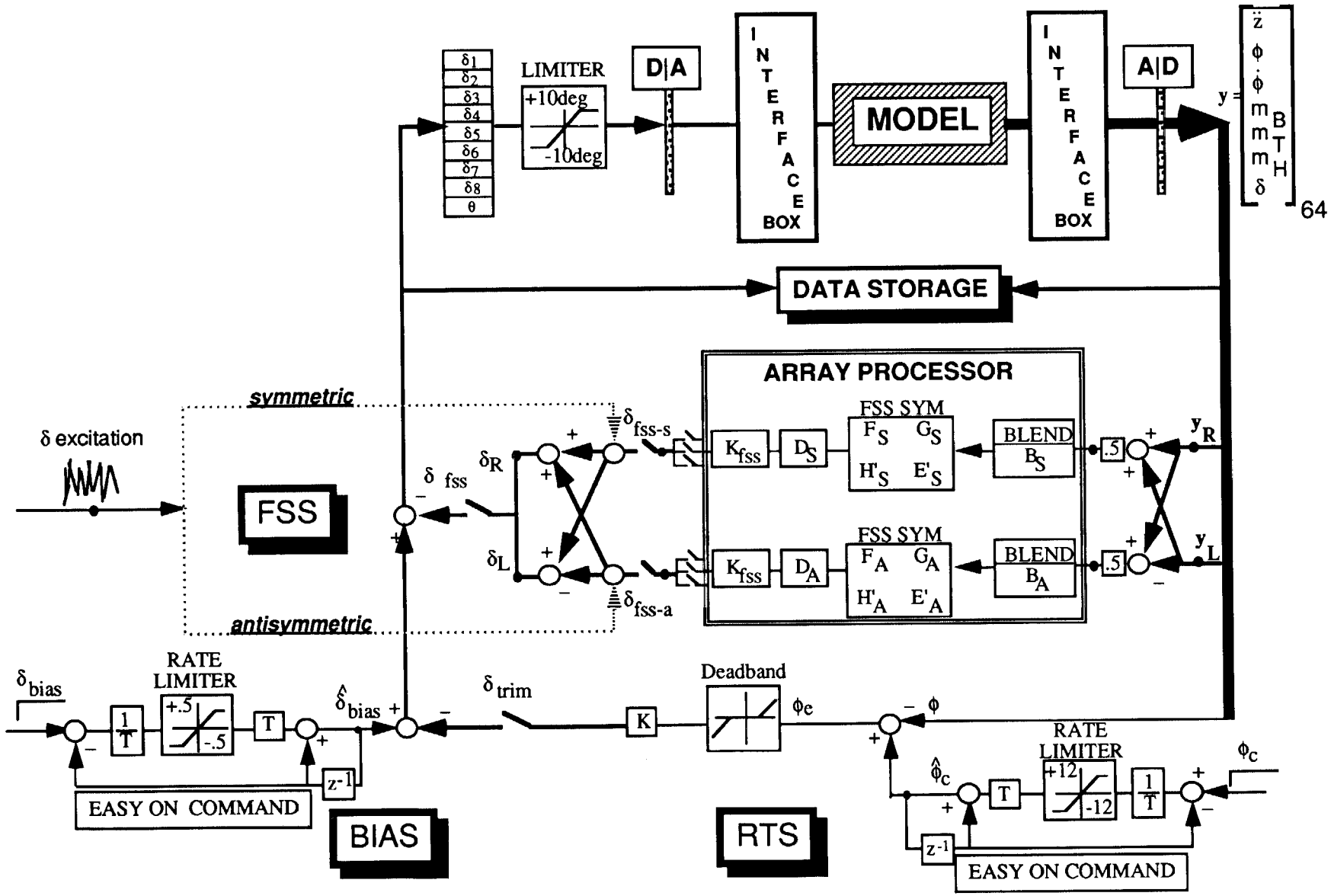

595

Flutter Suppression System Flow Diagram

This figure is a detailed schematic of the various blocks of code involved in the actual FSS control execution. All blocks of code reside on the Digital Signal Processor (DSP). Commands to operate the Array Processor (AP) are sent from the DSP to the AP during execution each time cycle. Commands for adding bias to a control surface or for performing roll trim are added to the flutter suppression commands. The Roll Trim System feedback is switch selectable. Both the bias commands and the roll trim command are implemented using an "easy on" procedure. The AP performs the actual floating-point calculations of the Control Law matrix operations, indicated by the "boxed-in" area in the figure. The conversion to 16 bit integers and the averaging of the signals for the FSS control law are performed on the DSP using fast masking and binary shifts operations. A subset of the sampled incoming signals and outgoing signals are sent to memory located on the array processor by the DSP.

TIMING SCHEDULE

(200 samples / sec = 5 milliseconds)

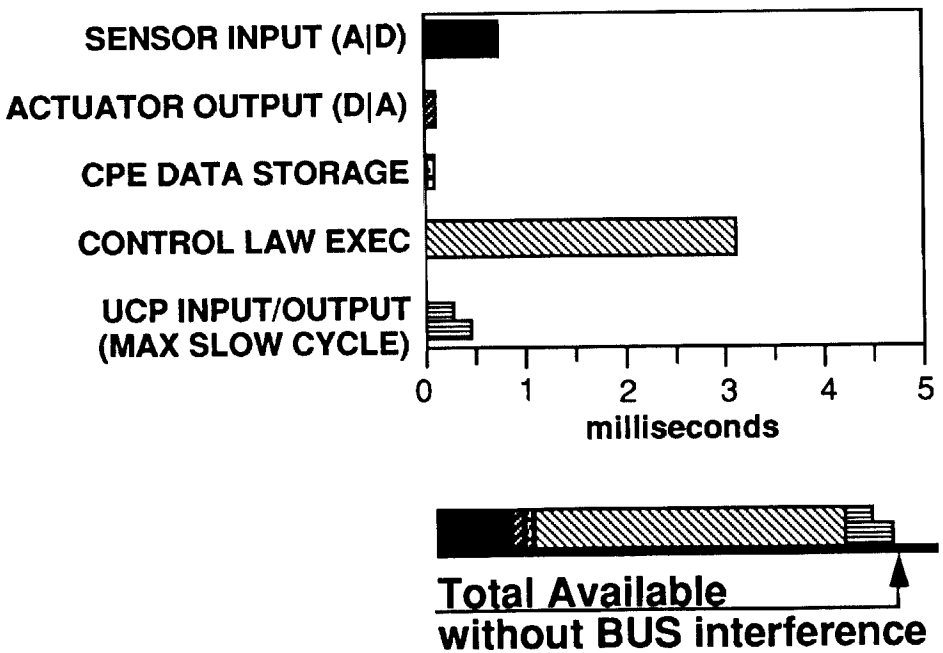

Execution Times for FSS controller components as implemented Nov. 1989

Timing Schedule

The different amounts of time involved in performing the FSS control law functions as delineated in the block diagram in the previous figure are shown in this figure. The first operation is the sampling of the required sensors and shipping them to the array processor memory. This block of code requires approximately 0.68 ms. The actuator commands are then summed and sent to the D\A converters. This requires approximately 0.06 ms. Data storage for Controller Performance Evaluation is then performed. This takes approximately .03 ms. Sending the command blocks of code to the Array Processor to execute the control law requires the most time and is dependent on the number of inputs and outputs, or on the number of states and blended signals. The maximum time required is approximately 3.2ms. There are 10 different "slow-cycle" blocks of code, each executed every 10 iterations (if operating at 200 hz, this translates to 20 times a second). Code for performing communication between different programs or devices is executed during each of these "slow" cycles. Included in this is code to read switch settings from the HOST Interface program and to send parameters to the HOST Information Window program which do not need to be updated every iteration. Types of communications parameters passed are:

mode of operation selected,
excitation and symmetry selected,
desired sampling frequency,
whether or not to perform scheduling of the control law,
whether to open or close the feedback loop,
sampling time left at end of cycle,
whether or not add excitation to actuator commands,
whether or not to save data,
type of excitation selected,
Mach number and dynamic pressure.

The sum of each of these blocks of code must be less than approximately 4.5ms in order to operate without BUS interference. One of the controls laws could not quite meet this goal and had to be slowed by 5% in order to operate without BUS interference.

SUMMARY OF PROBLEMS RESOLVED

- **Real-Time controller operation 3.3 times HOST *required***
  - ~ code development to give system control to DSP
  - ~ supplied software modification so controller operations could be initiated by DSP

- **DSP and AP multiple memory access lock-out to HOST *required***
  - ~ program code specialization on HOST
  - ~ passing of parameters between various HOST programs via the DSP

- **16-bit integer arithmetic on DSP *required***
  - ~ performance of necessary floating-point calculations on AP
  - ~ slow integer division algorithms to be implemented on DSP
  - ~ 'approximate' fast divisions using binary shifts
  - ~ solution of overflow and underflow problems

- **12-bit data translation boards *caused***
  - ~ undesirable overhead for data conversion
  - ~ sign extension problems
  - ~ limiting signals using special code 'compare' operations
  - ~ consideration quantization errors

- **Time budget/BUS interference *resulted in***
  - ~ reduced number of signals saved
  - ~ reduced sampling rate of one control law by 5%
  - ~ removal of some deflection limiting safety features

Summary of Problems Resolved

The primary difficulties involved in designing, coding, and assembling this one-of-a-kind digital controller revolved around four basic problems. The first was that the real-time controller had to operate at 200 hz within a Unix-based operating system which runs at 60 hz. This necessitated obtaining code from SKY Computers, Inc. which gave control of the data bus to the Challenger (DSP) computer which was able to run as fast as calculations would permit. Furthermore, modifications to software library routines supplied by the SKY Computers, Inc. had to be modified so that controller operations could be initiated by the DSP.

The second major problem incurred was that no two host software codes could communicate with the array processor memory or the Challenger memory simultaneously. Since the primary functions of the host computer fell into three categories:

1) selection of control options, definitions of control laws and excitations, and setting of various parameters for the controller;
2) display of current sensor, actuator command, and control law parameters employed by the controller; and
3) controller performance data storage and transfer (refs. 3 and 4),

different software packages were developed for each. The interfacing of these various packages with the controller provided an interesting challenge which was met by using the Challenger to pass information between the various host programs.

The third problem resulted from the fact that the DSP was only capable of performing integer arithmetic. It had no floating point registers. This was solved by performing most floating point arithmatic on the AP; however, this entailed transferring data and command codes to the AP. Some processes only required a crude integer division capability which was implemented within the DSP. It would have been preferable to have a DSP which was capable of some floating point arithmetic. The 16-bit address registers along with 32K-byte memory map also caused problems in storing data.

The fourth problem revolved around the fact that the data translation boards which were used only generated 12 bits of resolution. This not only caused some voltage resolution loss, but also necessitated careful handling of sign extensions and truncations from and to 16-bit integer data by the DSP and used a significant portion of the 5ms time budget allowed by the 200 hz sampling rate. It also forced special code to implement voltage limiters on signals which required comparisons of 12-bit 'signed' data with 16-bit compare registers. It would have been highly desirable to have had 16-bit data translation boards.

As a result of time budget and BUS interference problems, some problems were resolved in a fashion which was less than desired. The number of signals to be save had to be reduced, the sampling rate of one control law was reduced by 5 percent, and some deflection-limiting safety features had to be removed.

SIMULATION OVERVIEW

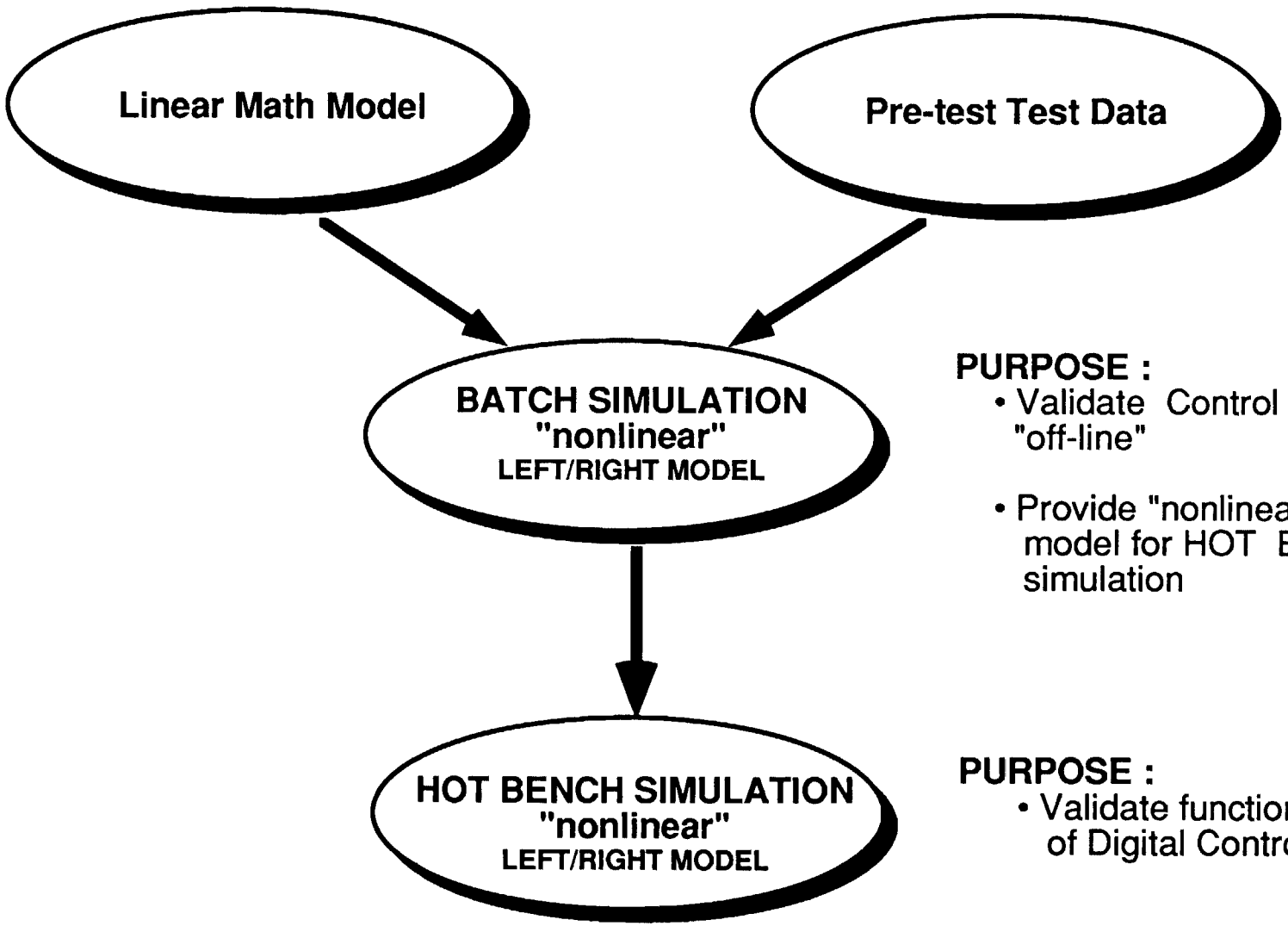

PURPOSE :

- Validate Control Laws "off-line"
- Provide "nonlinear" model for HOT BENCH simulation

PURPOSE :

- Validate functionality of Digital Controller

Simulation Overview

Pre-test analytical open-loop flutter results for the model indicated that the onset of flutter would be very rapid. At test conditions of 0.5 Mach number and 300 psf, the predicted flutter frequency was 7.2 hz. This means that the time-to-double amplitude for flutter was about 0.12 seconds. For closed-loop testing above the open-loop flutter boundary, any digital control system failure might result in very rapid loss of the model before "flutter stopper" mechanisms: releasing the tip-ballast store brake and/or effectively reducing tunnel conditions by opening the tunnel bypass valves - could be effected. Also, the effectiveness of the use of the tip-ballast store as a "flutter stopper" was unknown prior to the test. Because there was a lot of concern for the safety of the wind-tunnel model, it was felt that it was essential to do pre-test verification of the digital controller to gain confidence that the systems functioned properly. This verification is performed by coupling the digital controller to a computer simulation of the model being tested in the tunnel. Because the computer simulation sends signals to and receives signals from the hardware setup, it is referred to as a hot bench simulation (HBS).

The data used to build up the batch and hot bench simulations come from both linear system theory analysis from which a linear math model is developed and from pre-test test data such as experimentally generated actuator transfer functions, aerodynamic correction factors, etc.

These are combined to make up a "nonlinear" BATCH Simulation model which includes the linear model of the plant along with nonlinear rate limiting of the actuators, and represents the whole aircraft, both left and right. There are two primary purposes for the BATCH simulation. First is to provide a mechanism for control law designers to validate their control laws "off-line" from the actual hardware of the HOT BENCH simulator. Computational time delays and sampling effects are included in the model for this purpose. The second purpose is to provide a "nonlinear", whole aircraft model for HOT BENCH simulation.

The purpose of the HOT BENCH simulation is to validate the functionality of the Digital Controller.

SIMULATION DETAILS

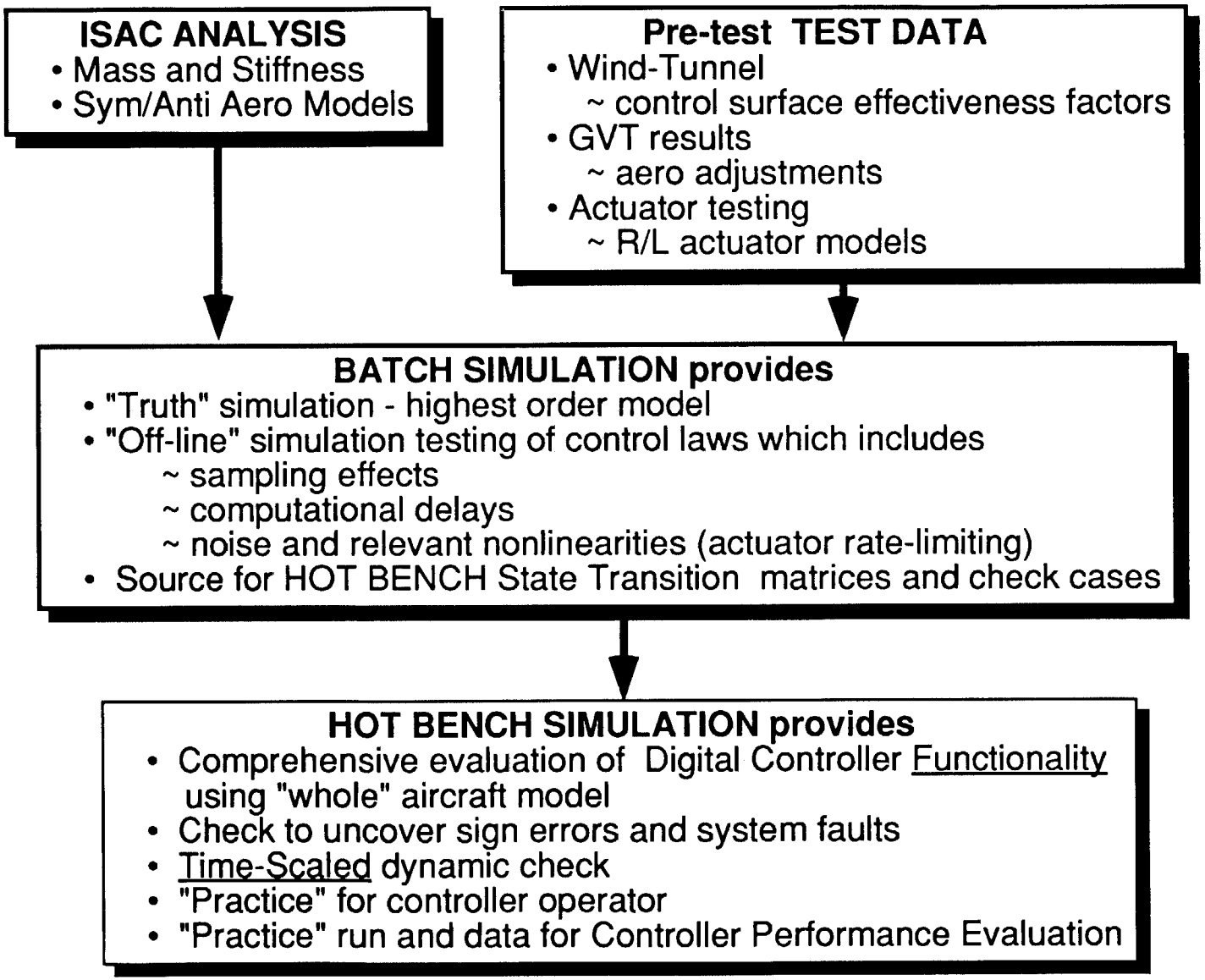

Simulation Details

The data used to build up the batch and hot bench simulations come from three sources, (1) a collection of aeroservoelastic analysis programs known as ISAC , ref. 5, (2) some vibration codes to calculate natural frequencies, and (3), measured data. From ISAC come the generalized mass and stiffness matrices, and the generalized aerodynamic forces (GAF's). The generalized aerodynamic forces are calculated in ISAC by linear lifting surface theory. Complex-valued matrices of GAF's are produced as tabular functions of reduced frequency ($k = b\omega/v$). These tabulated aerodynamic matrices can be approximated in ISAC as rational functions of the parameter "p" where "p"="jk" and j = sqrt(-1). These rational function approximations (RFA's) can be formulated in a variety of ways. A good summary of the various methods of forming RFA's can be found in refs 6 and 7.

The other source of data for the batch simulation is experimental. The elastic mode frequencies resulting from a vibration analysis are replaced with measured GVT frequencies where applicable. The actuator transfer functions are the result of fitting measured frequency response data with third order transfer functions. As a result, the right and left actuator models are not equal for actuator pairs. These actuator models are implemented in the simulations. In addition, the simulated response of the actuators is rate-limited according the published specifications. Extensive static data was taken in the last wind-tunnel entry of the roll moments and lift force produced by control surface deflections. When roll (lift) per unit deflection, both measured and predicted, are plotted as functions of dynamic pressure, they are not the same. The predictions come from lifting surface theory and the lack of agreement is no surprise. By judicious use of "effectiveness factors", the predicted roll(lift) can be brought into agreement with the measured data. Two points of interest where agreement in predicted and measured control effectiveness is sought is (1), the limiting value as dynamic pressure goes to zero and, (2), the dynamic pressure where control surface deflection produces no change in roll(lift) due to elastic deformation of the wing, the reversal point. These effectiveness factors are implemented in the simulations.

Both the batch and hot bench simulations are "whole" aircraft models. The inputs are right and left actuators and the outputs are right and left measurements. The GAF's, mass and stiffness matrices are in terms of symmetric and anti-symmetric modes, which are combined in the simulation models.

The batch simulation is intended to be the "truth" (or most correct) model. The hot bench simulation model will typically be simplified in some fashion to reduce the required computational time. Currently the hot bench simulation is the same order as the batch simulation, but it is anticipated that as the batch simulation is updated, the order will increase from 115 to 196. Various methods of model reduction are being examined to create a reduced order hot bench simulation.

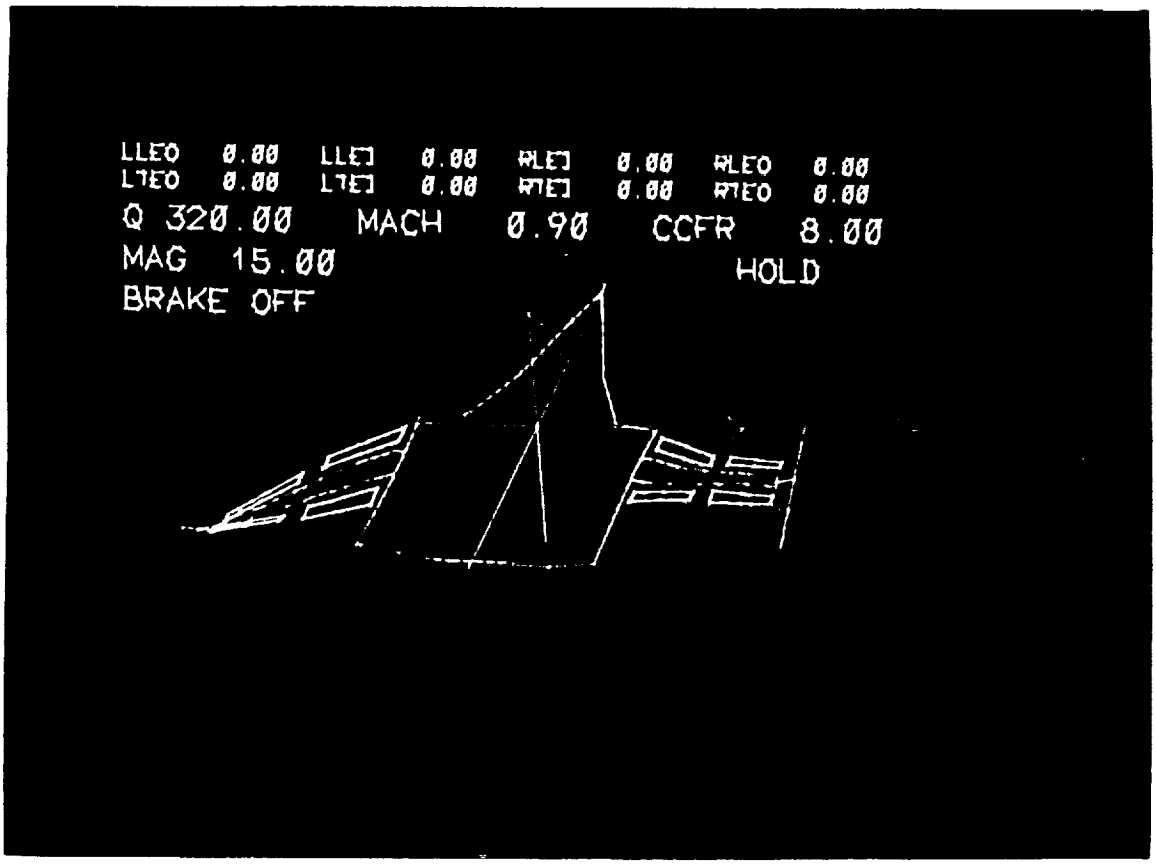

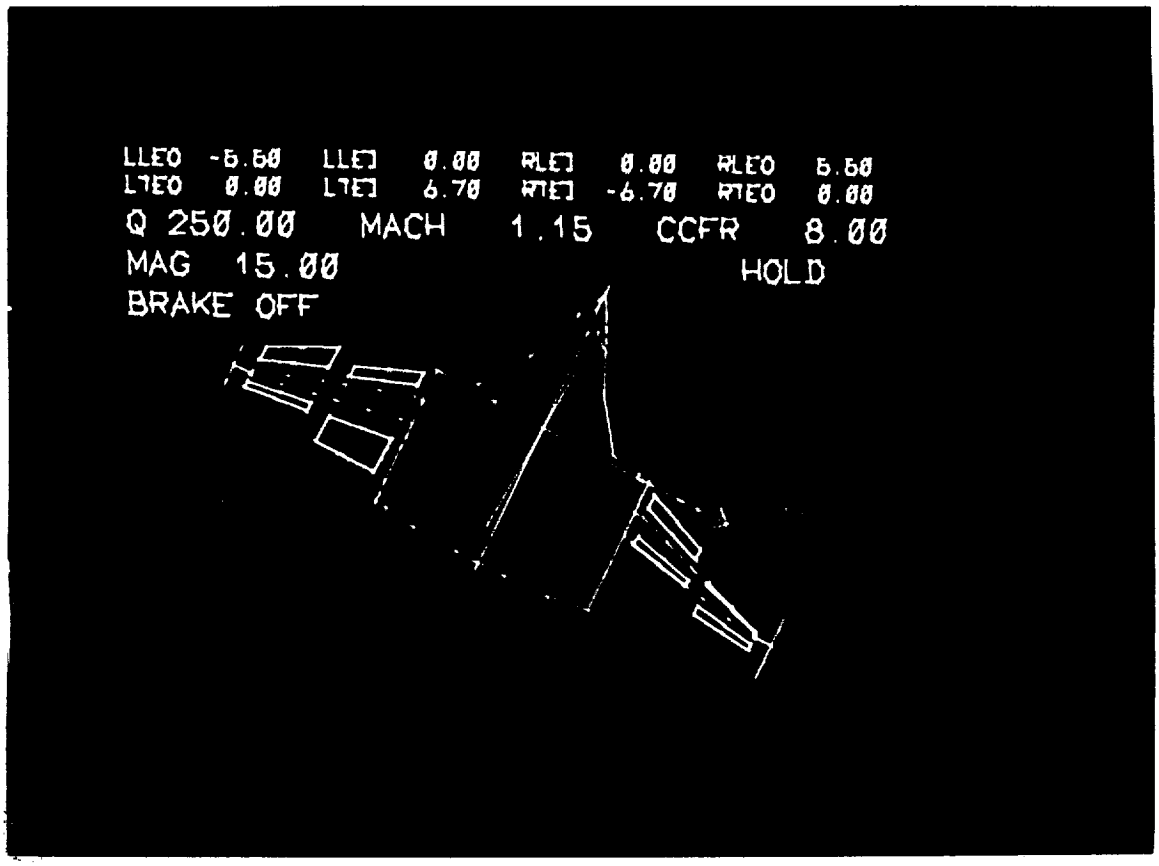

Wireframe Simulation Image

An ADAGE (Eagle1000) graphics computer generates a color-coded, three-dimensional articulating wireframe image of the flexing AFW model. The display presents model pitch, roll and yaw, control surface deflections and total model deformation which can be magnified for visual clarity. A blue shadow wireframe of the undeformed model is drawn so that deformations are more easily seen. Examples of both an aerodynamically deforming model and a flexible/rigid rolling model are displayed in this figure. The undeformed model can be seen as a horizontal, undistorted "shadow" image.

FROM BATCH TO HOT BENCH SIMULATION

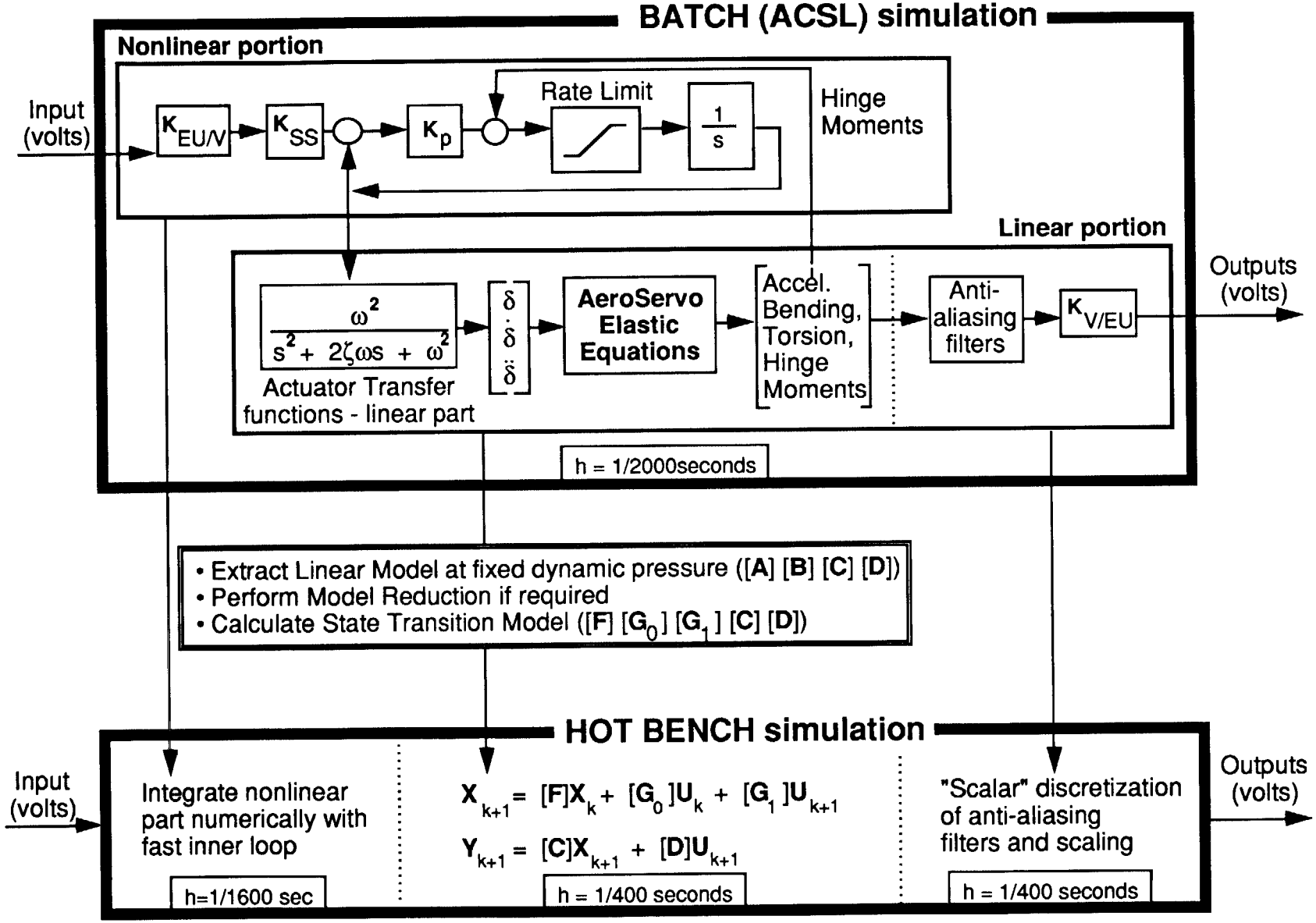

From Batch to Hot Bench Simulation

The batch simulation is implemented as if it were a nonlinear system. Dynamic pressure is a parameter that can be varied during a run. All the states are collected in a large state vector and integrated with a Runge-Kutta second order integration scheme. The integration step used in the batch simulation is 1/2000 seconds. Sensitivity studies indicate a small degradation in accuracy with an integration step of 1/1600 seconds and significant degradation for larger steps.

If dynamic pressure is held fixed, the batch simulation is linear except for the rate limit imposed on the single pole portion of the actuator transfer functions. There are eight actuators modeled with third order transfer functions. The second-order part of the third-order actuator models can be lumped with the remaining linear dynamics. The aeroservoelastic (ASE) equations are highly coupled and currently contain 49 states, broken down as follows:

8	symmetric elastic mode positions
8	symmetric elastic mode velocities
8	symmetric aerodynamic lag states (1 lag formulation)
2	symmetric gust states (modified Dryden)
7	anti-symmetric elastic mode positions
7	anti-symmetric elastic mode velocities
7	anti-symmetric aerodynamic lag states (1 lag formulation)
2	anti-symmetric gust states (modified Dryden)
49	

Together with the 16 states associated with the second-order part of eight actuator models, a coupled linear system of 65 states, 10 inputs (8 actuator and 2 noise), and 40 outputs can be extracted from the "linear" portion of the batch simulation. Order reduction techniques can be applied to this dynamic system followed by conversion to a state transition model based on an integration step of 1/400 seconds.

The anti-aliasing filters are applied to each output signal and result in a diagonal system. The anti-aliasing filters are therefore not lumped with the actuator-ASE coupled system to avoid making full matrix-multiply operations if they can be avoided. The anti-aliasing filter dynamics are digitized in a sequential scalar manner in the hot bench simulation with an integration step of 1/400 seconds.

The nonlinear portion is integrated numerically with an integration step of 1/1600 seconds. Four integration steps are made to predict the value of the input to the coupled linear system at time (k+1)h where h = 1/400 seconds. Since input to the coupled linear system at time (k+1)h is now available, a trapezoidal state transition scheme can be employed. Let $\{u_k\}$ denote the quantity $\{u(t=kh)\}$ where the vector $\{u\}$ is a function of time, t. Given the linear dynamic system

$$\{\dot{x}\} = [A]\{x\} + [B]\{u\}$$

if the ramp input signal ,

$$\{u(t)\} = \{u_k\} + (t-kh)\frac{\{u_{k+1}\} - \{u_k\}}{h}$$

over the interval

$$kh \leq t < (k+1)h$$

then the following exact solution for $\{x\}$ at time t = (k+1)h exists:

$$\{x_{k+1}\} = [F]\{x_k\} + [G_0]\{u_k\} + [G_1]\{u_{k+1}\}$$

where,

$$[F] = e^{[A]h}$$

$$[G_0] = (e^{[A]h} - e^{[A]h}[A]^{-1}/h + [A]^{-1}/h)\,[A]^{-1}[B]$$

$$[G_1] = (e^{[A]h}[A]^{-1}/h - [I] - [A]^{-1}/h) [A]^{-1}[B]$$

The above equations are not valid if [A] is not invertible (i.e. if [A] has eigenvalues equal to 0, such as occurs with rigid-body modes); however, using Taylor series identities, the equations for $[G_0]$ and $[G_1]$ can be put into a form that can be calculated:

$$[G_0] = \left(\sum_{p=2}^{\infty} \frac{1}{p!} (-1)^p ([A]h)^{p-2} \right) h\, e^{[A]h} [B]$$

$$[G_1] = \left(\sum_{p=2}^{\infty} \frac{1}{p!} ([A]h)^{p-2} \right) h [B]$$

The matrices $[G_0]$ and $[G_1]$ are calculated by summing the above series until the next term is under some tolerance. This Taylor series approximation approach may not work in general if [A] is ill conditioned.

It can be shown that integrating the nonlinear portion of the equations with an integration step of 1/1600 and the linear equations in the fashion above with an integration step of 1/400 gives only a small degradation in the accuracy of the solutions to the differential equations of motion.

The issue of time scaling deserves some explanation. The Cyber can only integrate the equations of motion of the plant at 80 frames per second without losing time synchronization. This means that implementation of the hot bench simulation in a similar fashion as the batch simulation creates an unacceptably slow time scale ratio (2000:80 = 25:1) due to the 80 frames/second rate of the Cyber (on which the hot bench simulation runs). Since the linear simulation equations can be integrated with a time step of 1/400 seconds, this means the Cyber simulation is only running 5:1 (400:80) slow. The control laws are digitized for an integration time step of 1/200 seconds. Thus the digital controller must be clocked at 40 frames per second (200/5) to be dynamically equivalent. Since there is no human operator in the loop, a slow time scale can be accommodated.

Currently no model reduction is being performed on the extracted 65 state model. This will change in the near future. The ASE dynamic models being formulated as a result of the Fall 1989 tunnel entry will have the following set of states:

10	symmetric elastic mode positions
10	symmetric elastic mode velocities
40	symmetric aerodynamic lag states (4 lag formulation)
2	symmetric gust states (modified Dryden)
11	anti-symmetric elastic mode positions
11	anti-symmetric elastic mode velocities
44	anti-symmetric aerodynamic lag states (4 lag formulation)
2	anti-symmetric gust states (modified Dryden)
130	

Combined with 16 actuator states, this leads to a 196 state coupled linear system to be integrated with matrix state transition equations. Some model reduction will be necessary to retain the current 5:1 time scale ratio and is being investigated.

SCHEMATIC OF HOT BENCH SIMULATION

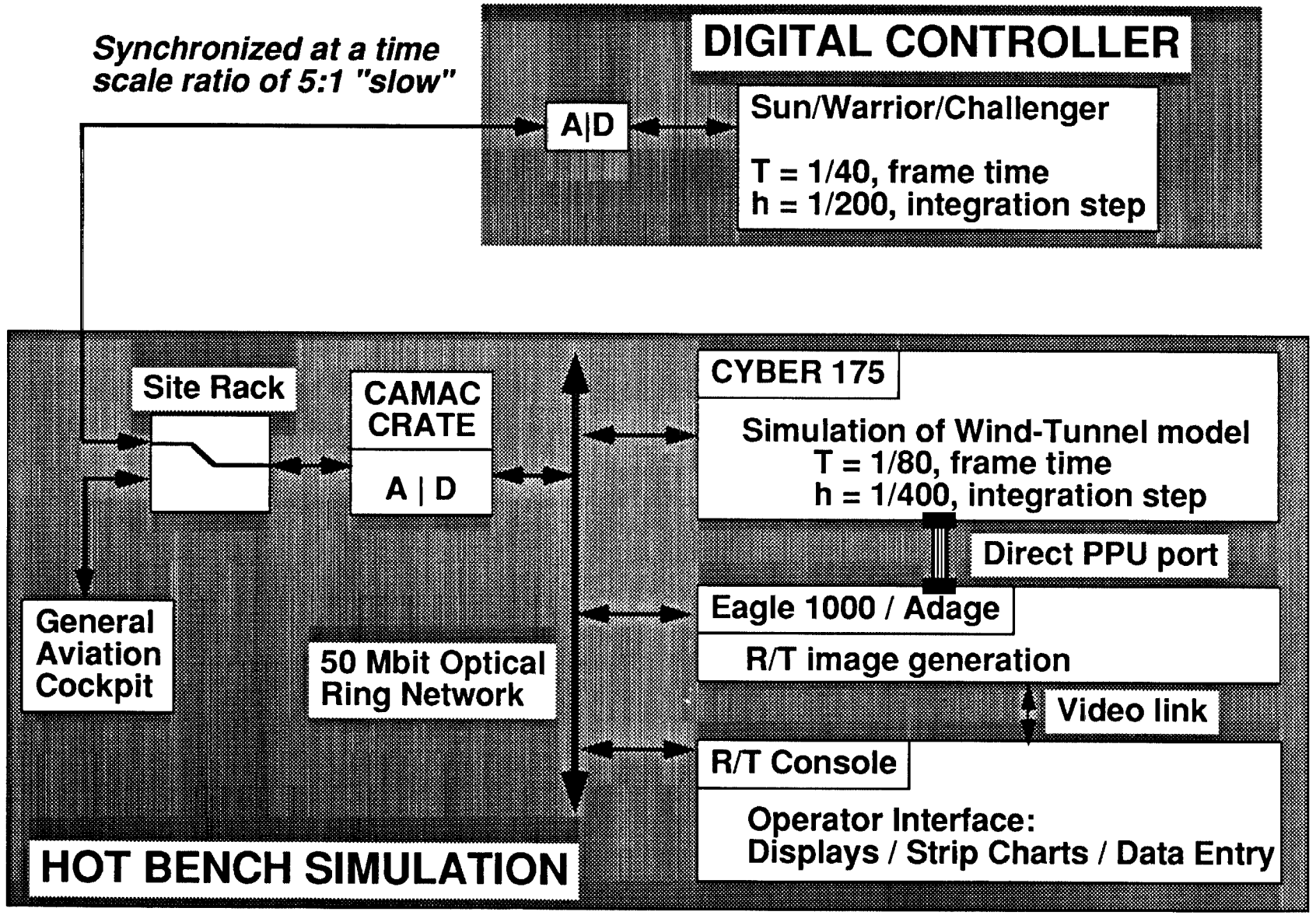

Schematic of Hot Bench Simulation

The digital controller communicates with the central Langley Advanced Real Time Simulation (ARTS) System via analog lines that are connected to a site rack (ref.8). The ARTS consists of two Cyber 175 computers connected to an array of simulation sites by means of a 50-megabit/second fiber optic digital data network called Computed Automated Measurement and Control (CAMAC). The CAMAC interface converts outgoing Cyber 175 digital signals to analog signals and incoming analog signals to digital signals for the Cyber 175. The simulation of the AFW wind-tunnel model consists of: (1), an engineering console that controls the simulation, (2), a Cyber 175 wherein the equations of motion are integrated, and (3), an ADAGE graphics computer that generates a color-coded, three-dimensional articulating wireframe image of the flexing AFW model.

Both the Cyber and the Adage are dated and are in the process of being replaced. The Cyber communicates directly with the ADAGE graphics computer through a PPU port on the Cyber. The ADAGE will soon be replaced with an Eagle 1000. The Eagle will communicate over the the 50 Mbit optical ring just as the Cyber and the real time console do.

SUMMARY OF DIGITAL CONTROLLER ACHIEVEMENTS

DEVELOPED VERSATILE SYSTEM WHICH

- Operates at 200 Hz within a 60 Hz operating system environment
- Allows simultaneous FSS and data aquisition, storage, and transfer
- Allows flexibility in control law implementation
- Coordinates and synchronizes the operation of three different computers

ALLOWED SUCCESSFUL DEMONSTRATION OF

- Active flutter suppression
- Near real-time Controller Performance Evaluation

Digital Controller Achievements

An extremely versatile system has been developed which operates at 200 hz. within a 60 hz operating system environment. It allows simultaneous Flutter suppression and data acquisition, storage, and transfer. Normally, a controller system would not be expected to also provide for data acquisition. It allows not only flexibility in control law implementation both in the number of sensors and actuators employed, but also in the number of states, and the selection of sensors. It coordinates and synchronizes the operation of three different computers: a host SUN 3/160, a Digital Signal Processor, and an Array Processor.

Most importantly, it allowed the successful demonstration of active flutter suppression, and provided the data for near real-time controller performance evaluation.

References

1. Noll, Thomas E.; Perry, Boyd III; Tiffany, Sherwood Hoadley; et al: *Aeroservoelastic Wind-Tunnel Investigations Using the Active Flexible Wing Model - Status and Recent Accomplishments*, AIAA Paper No. 89-1168-CP, April 1989. Also published as NASA TM-101570, April 1989.

2. Perry, Boyd III; Mukhopadhyay, Vivek; Hoadley, Sherwood T.; et al: *Digital-Flutter-Suppression-System Investigations for the Active Flexible Wing Wind-Tunnel Model*, AIAA Paper No.90-1074-CP March 1990. Also published as NASA TM-102618, March 1990.

3. Pototzky,A.S.; Wieseman*,C.D.; Hoadley, S.T.; Mukhopadhyay, V.: *Development and Testing of Controller Performance Evasluation Methodogy for Multi-Input/Multi-Output Digital Control Systems.* Fourth Workshop on Computational Control of Flexible Aerospace Systems, July 11-13, 1990.

4. Pototzky*,A.S.; Wieseman,C.D.; Hoadley, S.T.; Mukhopadhyay, V.: *Development and Testing of Methodology for Evaluating the Performance of Multi-Input/Multi-Output Digital Control Systems.* Paper presented at AIAA Guidance, Navigation, and Control Conference, AIAA Paper No. 90-3501, August 20-22, 1990, Portland, Oregon.

5. Peele, E.L. and Adams, W.M., Jr.: *A Digital Program for Calculating the Interaction Between Flexible Structures, Unsteady Aerodynamics, and Active Controls*, NASA TM-80040, January 1979.

6. Tiffany*, S. H.; and Adams, W. M., Jr.: *Nonlinear Programming Extensions to Rational Function Approximations of Unsteady Aerodynamics*, AIAA Paper 87-0854-CP, April 1987.

7. Tiffany, Sherwood.H. and Adams, William.M.Jr.: *Nonlinear Programming Extensions to Rational Function Approximation Methods for Unsteady Aerodynamic Forces Which Allow Variable Selection of Constraints,* NASA TP 2776, May 1988.

8. Crawford, Daniel J.; Cleveland, Jeff I. II; and Staib, Richard O.: *The Langley Advanced Real-Time Simulation (ARTS) System Status Report*, AIAA-88-4595-CP, September 1988.

*Presenter of paper

DEVELOPMENT AND TESTING OF CONTROLLER PERFORMANCE EVALUATION METHODOLOGY FOR MULTI-INPUT/MULTI-OUTPUT DIGITAL CONTROL SYSTEMS

Anthony Pototzky*, Carol Wieseman†§, Sherwood Tiffany Hoadley† and Vivek Mukhopadhyay†

Fourth Workshop on the Computational Control of Flexible Aerospace Systems

Williamsburg, Virginia

July 11-13, 1990

*Lockheed Engineering and Sciences Company †NASA Langley Research Center §Presenter

OUTLINE

- Motivation
- Objectives of CPE
- CPE Computations
- CPE Implementation
- Wind-Tunnel Test Results
- Concluding Remarks

MOTIVATION

Active controls are becoming an increasingly important means to enhance the performance of aircraft. But, because the process of designing some of the multi-input/multi-output (MIMO) digital control laws uses relatively untested theoretical methods, it has become crucial to validate the design methodology through experimentation. For classical single-input/single-output (SISO) control systems, analysis tools such as Nyquist diagrams were developed and used to determine the stability and robustness of the closed-loop system. For MIMO systems, Nyquist techniques are inadequate. However, analytical methods based on the use of singular values of return-difference matrices at various points in the control loop have been developed recently (references 1 - 3) to examine the stability and robustness of the MIMO closed-loop system.

Flutter testing of aeroelastic wind-tunnel models is, in general, a risky endeavor because the onset of flutter cannot be predicted precisely using even the most sophisticated analysis tools available. Closed-loop flutter suppression testing adds an extra risk because the controller itself can potentially destabilize the model. To reduce these risks, on-line near real-time controller-performance-evaluation (CPE) methods were developed to assess the stability and the robustness of MIMO flutter suppression systems.

This presentation describes the development and implementation of this CPE capability and briefly discusses the structure of the data flow, the signal processing methods used to process the data, and the software developed to generate the transfer functions. This methodology is generic in nature and can be used in any type of MIMO digital controller application including digital flight control systems, digitally-controlled spacecraft structures, and actively controlled wind-tunnel models. Results of applying the CPE methodology to evaluate (in near real-time) MIMO digital flutter suppression systems being tested on the Rockwell Active Flexible Wing (AFW) wind-tunnel model (reference 4) are presented to demonstrate the CPE capability. The AFW wind-tunnel test program is described in references 5 and 6.

MOTIVATION

- Active controls becoming increasingly important means to enhance aircraft performance
- Validation of control law design methodology
- CPE method to evaluate performance of MIMO digital controllers
  - Stability
  - Robustness
- Reduce risk of flutter suppression testing
- Demonstrate CPE method during FSS tests on AFW

OBJECTIVES OF CPE

Simplified block diagrams of the basic control problems are presented in the figure. The plant to be controlled is represented mathematically by a frequency domain transfer matrix, **G**, with outputs, y, and inputs, e. The controller is represented mathematically by a transfer matrix, **H**, with inputs, y, and outputs, x. An external excitation, u, is used to excite the system in a specified fashion. This excitation is used to compute transfer functions between outputs and inputs in either open- or closed-loop systems. The open-loop system is one in which the control law outputs (commands required for controlling plant response) are not fed back into the system; i.e., the switch depicted in the figure on the left is open.

Controller performance is evaluated both open and closed loop. The process is outlined conceptually for the flutter suppression system application as follows:

Open-loop

Step 1: Verify the controller, **H**, by comparing the computed transfer functions with transfer functions supplied by control law designers.

Step 2: Predict closed-loop stability based on open-loop information to determine whether the control law will stabilize or destabilize the system when the loop is closed.

Closed-loop

Step 1: Determine the stability margins of the closed-loop system during the closed-loop testing.

Step 2: Determine open-loop plant stability during the closed-loop testing to determine the open-loop flutter boundary.

OBJECTIVES OF CPE

Open Loop

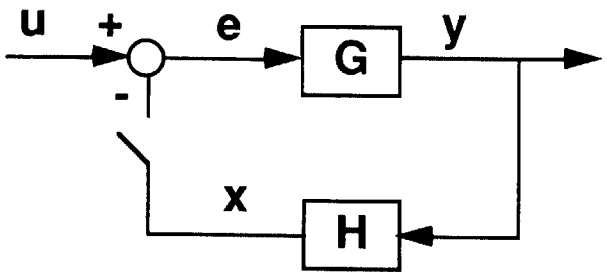

1) Verify controller
2) Predict closed-loop system stability

Closed Loop

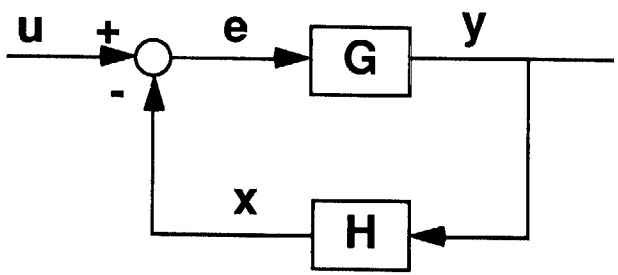

1) Calculate closed-loop stability margins
2) Determine open-loop plant stability

FLOWCHART OF CPE PROCEDURES

This figure shows a flowchart which outlines the CPE procedures and identifies the calculations involved. This figure will serve as an outline for a description of the CPE methodology.

Two basic tasks are involved. The first involves converting the time history data to the frequency domain and computing transfer functions of each plant response and controller output to the excitation and then combining them to form the transfer matrices. The second task involves using the transfer matrices to determine the plant and controller transfer matrices, to obtain the return difference matrices and their singular values, and to calculate determinants and eigenvalues to meet the objectives that were stated previously.

The calculation of the transfer functions is described in more detail in the next figure.

FLOWCHART OF CPE PROCEDURES

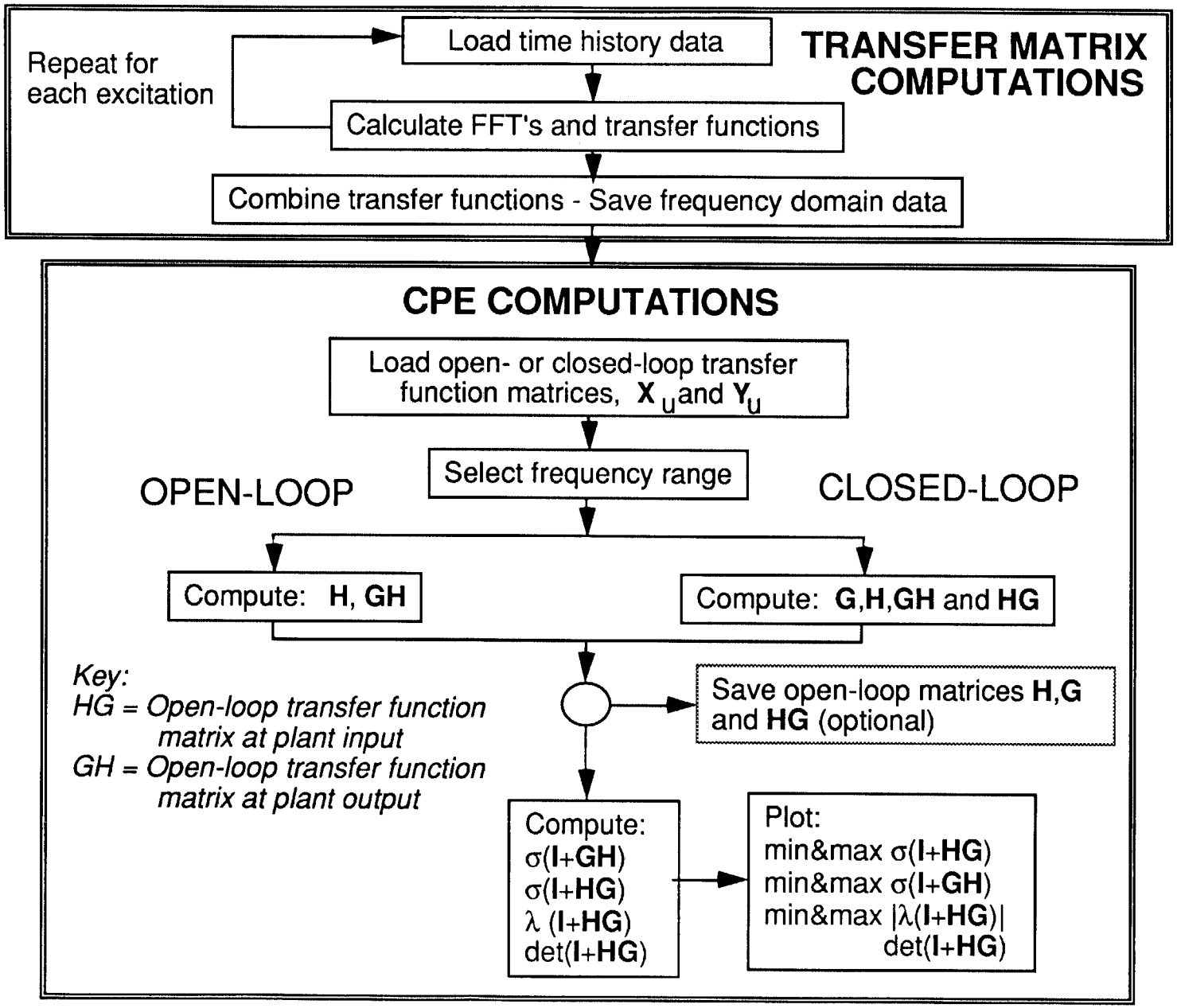

TRANSFER FUNCTION CALCULATION

The first step in computing transfer functions **G** and **H** is to acquire time histories of excitations, u, and responses, x and y. The first and last five seconds of an example time history of an excitation and a typical response are shown in the figure. The input excitation to perform CPE was a constant amplitude logarithmic sine sweep with a ramp-in and ramp-out. The initial frequency was 5 Hz and the final frequency was typically 35 Hz. The duration of the excitation is approximately 150 seconds. The data was saved at a 200 Hz sampling rate. The sample rate and low quantization levels explains the jaggedness in the time history plots.

Because of the long time history and large number of data points, overlap averaging was performed. The overlap-averaging capability allows long time histories to be partitioned into shorter time spans, taking advantage of long periods of time history data to average out noise. In addition, a zero-fill capability was available to zero-fill time history data to an exact increment of a power of two needed for FFT computations. The overlap-averaging capability with zero-fill provided optimum use of the time history data which were obtained. The size of the time-history partition as well as the amount of overlap were options which could be chosen.

The next step in computing transfer functions is to employ Fast Fourier Transform (FFT) techniques and overlap averaging. The FFT's of the excitation and each response are computed and from the FFT's the appropriate power spectra and cross spectra are constructed. The transfer functions are then calculated from the ratio of the averaged cross spectrum at some output resulting from the excitation to the averaged power spectrum of the excitation. The equations used in the computation of the transfer function at the controller output, X_u, and at the plant output, Y_u, are shown in the bottom of the figure. N is the number of overlap components making up the averaged spectrum.

The method was extended in the present study to include additional data-windowing capabilities. Windowing capabilities include ramp-in/ramp-out, Hanning, cosine taper, and cosine bell. Hanning windows were used during the flutter suppression testing.

TRANSFER FUNCTION CALCULATION

Time Domain

Excitation, u

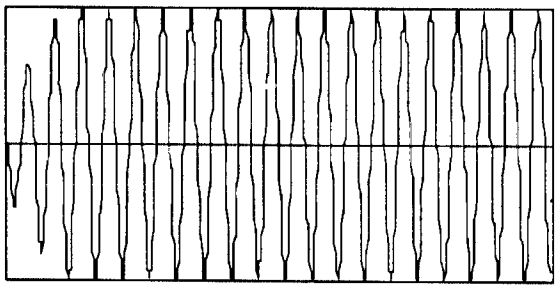

. . .

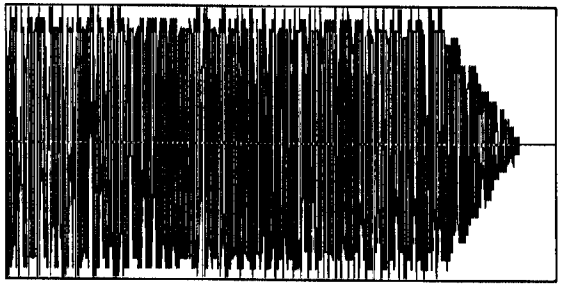

Response, y or x

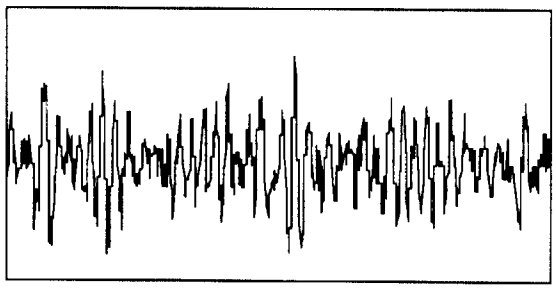

. . .

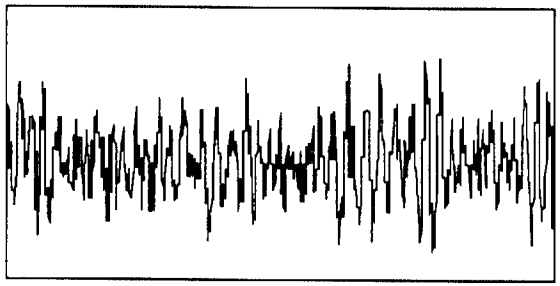

Frequency Domain

$$(X_u)_{ij} = \frac{\sum_{m=1}^{N} \left(S_{u_i x_j}\right)_m}{\sum_{m=1}^{N} \left(S_{u_i u_i}\right)_m}$$

$$(Y_u)_{ij} = \frac{\sum_{m=1}^{N} \left(S_{u_i y_j}\right)_m}{\sum_{m=1}^{N} \left(S_{u_i u_i}\right)_m}$$

TRANSFER MATRIX FORMATION

This figure shows how the transfer matrices are constructed from the transfer functions for a two by two controller. Each input to **G** represents a pair of control surfaces; each output from **G** represents a pair of accelerometers.

The first pair of control surfaces is excited with a sine-sweep excitation, u_1, and the transfer functions of each plant response, y_1 and y_2, and each controller output, x_1 and x_2, with respect to the excitation, u_1, are calculated. The transfer functions of the plant outputs to the first excitation make up the first column of the plant-output transfer matrix, $\mathbf{Y}_u$, shown in the upper right of the figure. The transfer functions of the controller outputs to the first excitation make up the first column of the controller-output transfer matrix, $\mathbf{X}_u$, shown in the bottom right of the figure.

The second pair of control surfaces is excited with a sine-sweep excitation, u_2, and the transfer functions of each plant response, y_1 and y_2, and each controller output, x_1 and x_2, with respect to the excitation, u_2, are calculated. The second column contains the transfer functions of the outputs with respect to the second excitation.

The two matrices, $\mathbf{X}_u$ and $\mathbf{Y}_u$, form the basis of all the remaining CPE calculations.

TRANSFER MATRIX FORMATION

FOR 2X2 CONTROLLER

Time Domain

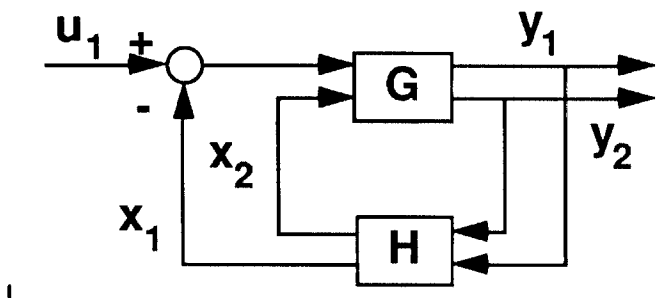

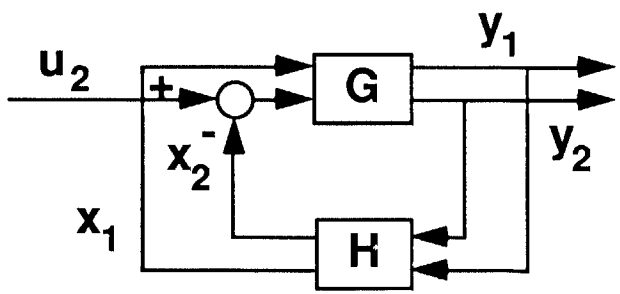

Frequency Domain

$$Y_u(\omega) = \begin{bmatrix} \frac{Y_1}{U_1} & \frac{Y_1}{U_2} \\ \frac{Y_2}{U_1} & \frac{Y_2}{U_2} \end{bmatrix}$$

$$X_u(\omega) = \begin{bmatrix} \frac{X_1}{U_1} & \frac{X_1}{U_2} \\ \frac{X_2}{U_1} & \frac{X_2}{U_2} \end{bmatrix}$$

COMPUTATION OF PLANT, CONTROLLER AND RETURN DIFFERENCE MATRICES

In order to accomplish the objectives of open- and closed-loop CPE, the plant transfer matrix, controller transfer matrix, and return difference matrices must be determined. This chart outlines how this is accomplished.

Open loop. In the open-loop case, both transfer matrices, $\mathbf{X}_u$ and $\mathbf{Y}_u$, are obtained from a control system in which the loop is open at the controller output. In this case, the plant transfer matrix, **G**, (dimensioned number of sensors by number of actuators, i.e. n_s by n_a) has been directly obtained from the experimental data and is $\mathbf{Y}_u$. The open-loop controller-plant transfer matrix, **HG**, (dimensioned n_a by n_a) is also directly obtained from the experimental data and is $\mathbf{X}_u$.

The controller transfer matrix, **H**, (dimensioned n_a by n_s) is given by the equation shown below the arrow. If n_a is greater than n_s, then this is actually a least square solution.

To perform the first step of the open-loop CPE, the resulting controller transfer matrix, **H**, is compared with the designed control law transfer matrix to verify the implementation of the controller. Specifically, the transfer functions are compared for each output/input pair.

Closed Loop. The difference between closed-loop and open-loop computations is that the transfer matrices, $\mathbf{X}_u$ and $\mathbf{Y}_u$, are obtained from the closed-loop system. During closed-loop testing, the plant transfer matrix is determined from the first equation on the top right side of the figure and the open-loop controller-plant transfer matrix is determined from the second equation. Noting that the quantity,

$$\left[\mathbf{I} - \mathbf{X}_u(\omega)\right]^{-1}$$

is common in both equations, transfer matrices **G** and **HG** are obtained simultaneously using matrix partitioning. The controller transfer matrix, **H**, is calculated the same whether the system is open or closed loop.

The matrix product **GH** is determined by multiplying the two matrices **G** and **H**. The return difference matrices at the plant input (**I+HG**) and at the plant output (**I+GH**) can then be calculated. The significance of these matrices and their singular values, determinants, and eigenvalues will be described next.

COMPUTATION OF PLANT, CONTROLLER AND RETURN DIFFERENCE MATRICES

	OPEN LOOP	CLOSED LOOP
Plant	$G(\omega) = Y_u(\omega)$	$G^T(\omega) = [I - X_u(\omega)]^{-1} Y_u^T(\omega)$
	$HG(\omega) = X_u(\omega)$	$[HG]^T(\omega) = [I - X_u(\omega)]^{-1} X_u^T(\omega)$

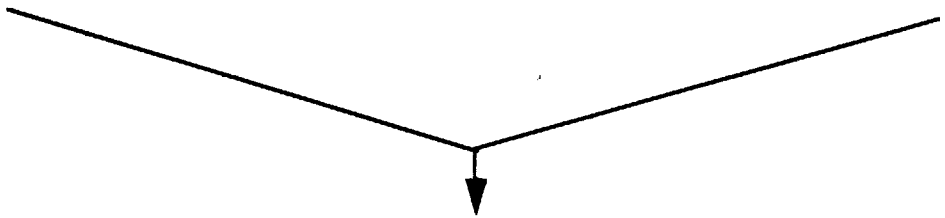

Controller $$H^T = \left[Y_u Y_u^T\right]^{-1} Y_u X_u^T$$

Return difference matrices:

at Plant input	I+HG
at Plant output	I+GH

MEASURE OF STABILITY

DETERMINANT

For MIMO control systems the determinants of the return difference matrices can be used as a direct measure of system stability. Since determinants of the return difference matrix at the plant input and the plant output are identical, only the determinant of one needs to be calculated (the plant input was chosen). The locus of the determinant of the return-difference matrix as a function of frequency has properties similar to those of a Nyquist diagram for SISO control systems. If the open-loop system is stable, an encirclement of the critical point (the origin) for $\det(\mathbf{I}+\mathbf{HG}(\omega))$ indicates that the controller is destabilizing. Furthermore, the proximity of the determinant locus to the critical point is a direct indication of how near to an instability the closed-loop system is. Although Nyquist diagrams for a SISO system can also be used to obtain gain and phase margins, determinant plots cannot provide similar information for MIMO systems. Robustness information for MIMO systems can be obtained from minimum singular values, and how this is obtained is described next.

MEASURE OF STABILITY

DETERMINANT

$$\det (\mathbf{I} + \mathbf{HG})$$

- **Applicable to MIMO control systems**
- **Properties similar to Nyquist diagrams**

MEASURE OF ROBUSTNESS

MINIMUM SINGULAR VALUES

To perform the second step in the open-loop CPE (predicting closed-loop performance based on open-loop information), it is convenient with a MIMO system to evaluate robustness by examining the minimum singular values of the return-difference matrices at the plant input, σ_{min} **(I+HG)** and the plant output , σ_{min} **(I+GH)**.

System instabilities occur when the minimum singular value of the return difference matrix becomes zero. Therefore, the proximity to zero indicates the frequency at which the system is prone to go unstable and provides a quantitative measure of robustness. Reference 3 contains a derivation which relates guaranteed gain and phase margins to minimum singular values. This relationship is shown in the figure, which is a reproduction of figure 2 from reference 3, and will be referred to later when discussing results.

The plot in the lower part of the figure contains information for determining equivalent guaranteed gain and phase stability margins from the minimum singular values of return difference matrices at either the plant input or the plant output. In the figure, the quantity on the ordinate is the minimum singular value; the quantity on the abscissa is gain perturbation, in decibels; the curves are parametric variations in phase perturbation, in degrees. The heavy curve (ϕ=zero degrees) and the heavy vertical line at zero dB have special significance. By using the heavy curve and heavy vertical line, minimum singular values may be "translated" into equivalent guaranteed gain and phase margins (with the conventional SISO interpretations of these margins); by using the parametric curves, minimum singular values may be "translated" into equivalent guaranteed gain and phase margins (with unconventional interpretations of these margins).

The horizontal dashed line in the figure corresponds to a minimum singular value of 0.37. The conventional SISO interpretation of margins is as follows: the intersections of the horizontal dashed line with the heavy curve determines gain margins; the intersection of the horizontal dashed line and the heavy vertical line determines phase margins. Based on these intersections (the right-most, left-most, and center circles), the closed-loop system has guaranteed gain margins of -2.6 dB and +4.0 dB in each loop simultaneously and guaranteed phase margins of +/-22 degrees in each loop simultaneously. The gain margins are understood to be the margins resulting when there is no perturbation in phase introduced into the closed-loop system; the phase margins are understood to be the margins resulting when there is no perturbation in gain introduced into the closed-loop system.

There are an infinite number of unconventional interpretations of these margins. One will be offered and corresponds to the intersections of the horizontal dashed line with the +/-20 degree phase perturbation curve. Based on these intersections (the second and fourth circles), the closed-loop system has guaranteed gain margins of -0.8 dB and +2.1 dB and guaranteed phase margins of +/-20 degrees in each loop simultaneously. That is, within each loop, gain may be varied within these limits (with each loop experiencing a different perturbation in phase), and the closed-loop system is guaranteed to remain stable.

The singular values are a conservative measure of robustness in that a set of gain and phase margins could be constructed that violates the guaranteed margins but fails to destabilize the system. A less conservative measure are the minimum eigenvalues which are described next.

MEASURE OF ROBUSTNESS

MINIMUM SINGULAR VALUES

At the Plant Input:

$\sigma_{min}(I + HG)$

At the Plant Output:

$\sigma_{min}(I + GH)$

Guaranteed Gain and Phase Stability Margins from Minimum Singular Values

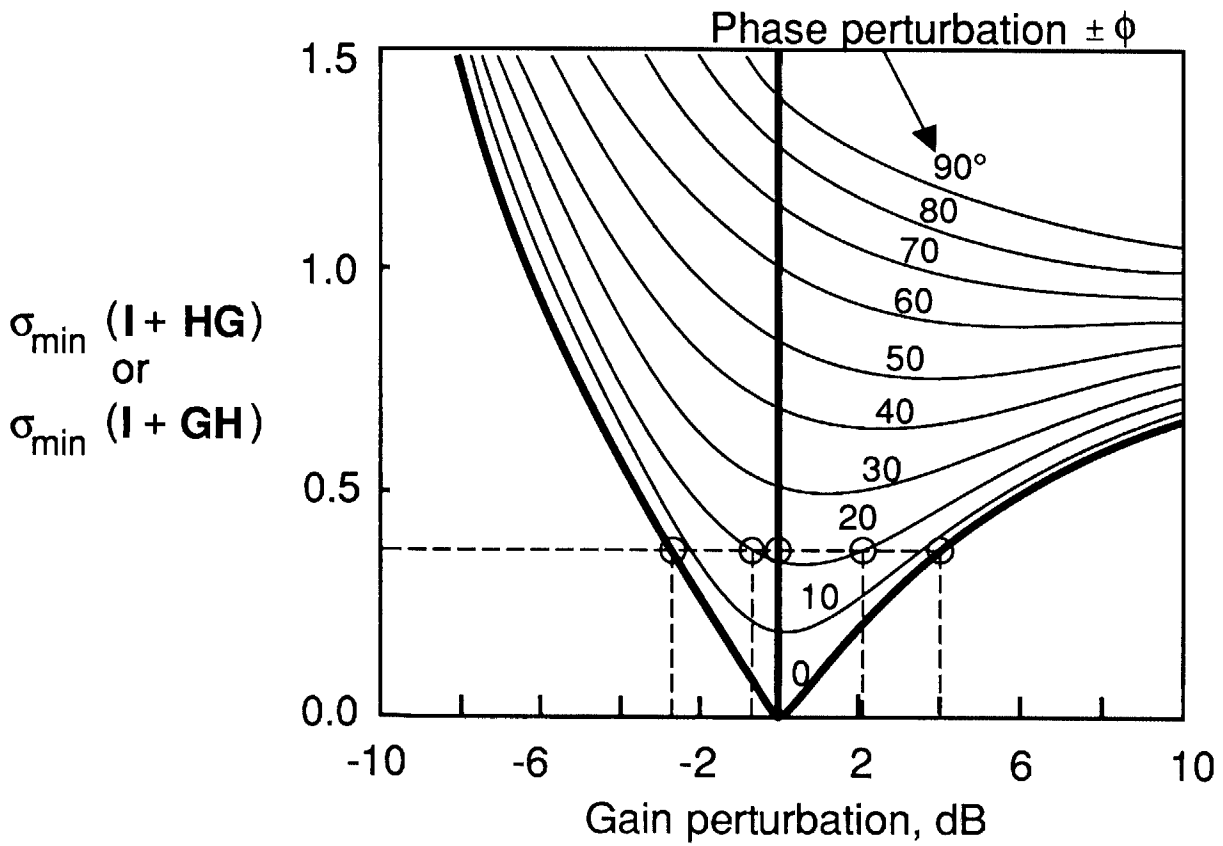

ALTERNATE MEASURE OF ROBUSTNESS

EIGENVALUES

An alternate, and generally less conservative, measure of robustness may be obtained by examining the minimum eigenvalues of the return difference matrices. The minimum eigenvalue at the plant input and the plant output are identical. Therefore, the eigenvalues are only calculated of the return difference matrix at the plant input. In general, the properties of the magnitude of the minimum eigenvalues are similar to the properties of the minimum singular values; both are measures of how close the return-difference matrices are to a singularity.

With minimum eigenvalues now substituted for minimum singular values, the chart from the previous page may be used in an identical manner to obtain gain and phase margins. The interpretation of the margins, however, is different. For a given minimum eigenvalue, in the case of changing the gains by the same amount in all the loops simultaneously without changing phase, the values for the gain margin can be determined from the universal gain and phase margin diagram using the value of the magnitude of the minimum eigenvalue. The same holds true for identical phase changes in all the loops simultaneously with no gain perturbation. These phase and gain changes gives a more realistic indication of the margins than those obtained from minimum singular values.

ALTERNATE MEASURE OF ROBUSTNESS

EIGENVALUES

$$| \lambda_{min}(I + HG) |$$

- **Applicable to MIMO control systems**
- **Less conservative measure of robustness than minimum singular values**

IMPLEMENTATION OF CPE METHODOLOGY

This figure shows schematically the hardware used to perform the CPE for the AFW Flutter Suppression System (FSS). Two SUN 3/160 computers were used to conduct Controller Performance Evaluation. The computer identified as SUN-1, not only provided basic control and flutter suppression of the model, but was the source for the excitations needed for CPE. The excitation was generated digitally and added to the control law actuator commands. The digital excitation, actuator commands, and sensor measurements used by the control law were stored and then transferred to SUN-2, equipped with an array processor board. The FFT computations, transfer function calculations and detailed CPE computations were performed on SUN-2.

The FFT's of the time histories of the excitations and the responses, and the transfer functions, were computed by a Fortran-77 program, optimized to take advantage of the vector-processing capabilities on the array processor. The detailed CPE analysis capability was implemented using MATLAB software operations (reference 8). Functions and procedure files were written to perform the matrix computations, eigenvalue analysis, and plot the results.

IMPLEMENTATION OF CPE METHODOLOGY

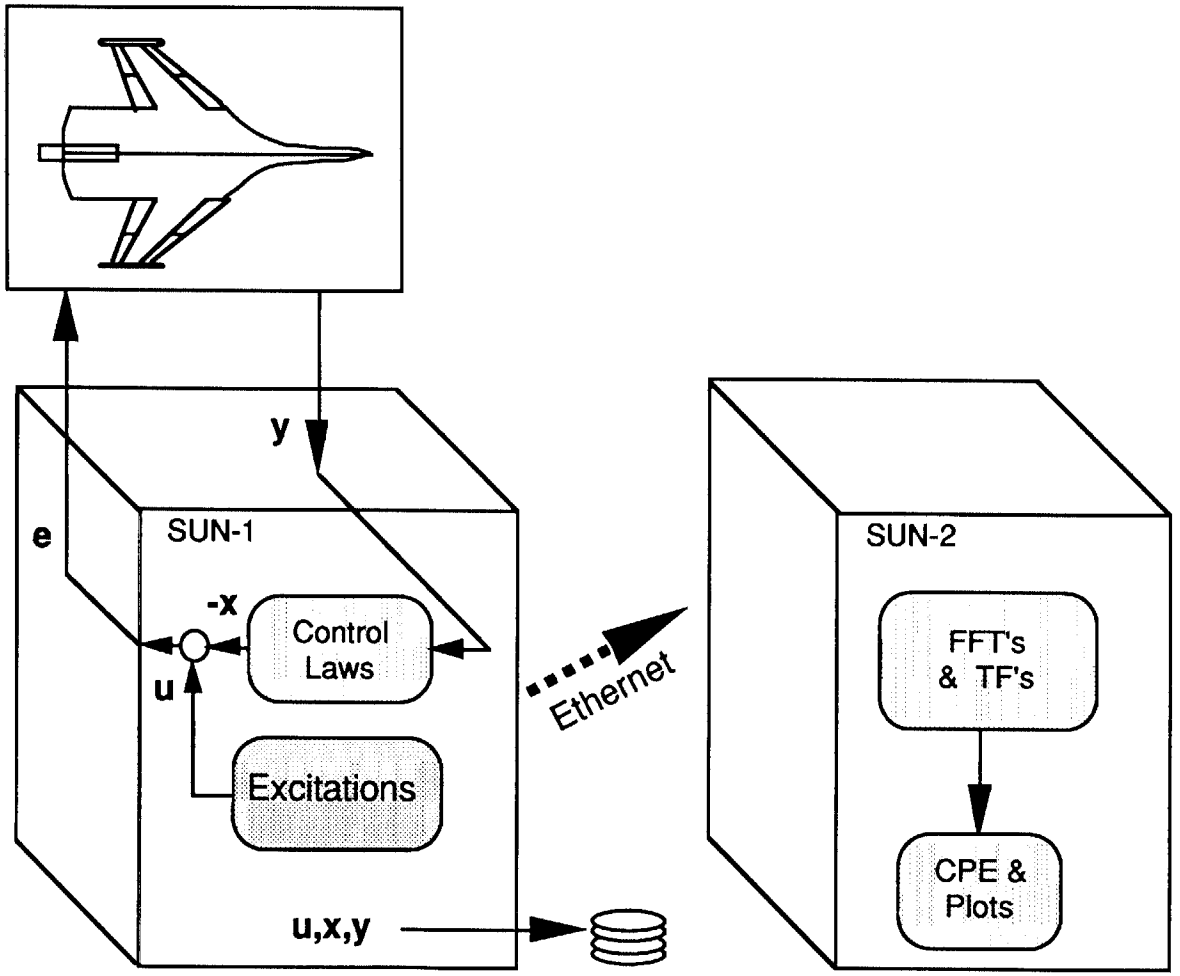

- **Fortran 77 optimized for array processor**
- **Commercially available software package**

OPEN-LOOP CPE RESULTS

EVALUATION POINTS

Wind-tunnel test results will be provided for both open- and closed-loop CPE to demonstrate the objectives which were specified earlier. Both SISO and MIMO flutter suppression control laws were designed for the AFW wind-tunnel model. During the wind-tunnel test the FSS control laws were successfully tested and their closed-loop performance was evaluated using the CPE capability presented in this paper.

Open-loop CPE results are presented first. Shown in the figure is the atmospheric H line along which wind-tunnel testing was conducted. This curve gives the dynamic pressure and Mach number variation as the tunnel fan blade speed is increased when the wind-tunnel total pressure is initially one atmosphere. The two solid circles represent conditions at which open-loop CPE was performed: the first, at a dynamic pressure of 100 psf, corresponds to a stable plant and a stable closed-loop system. The closed-loop system was predicted to be stable and therefore the loop was closed. Closed-loop flutter suppression testing commenced. At a dynamic pressure of approximately 175 psf, below the flutter boundary of 221 psf, the closed-loop system became unstable. The safety mechanisms installed in the model and in the wind tunnel tripped and the dynamic pressure was decreased. The system was then tested open loop and the dynamic pressure was again increased. Open-loop CPE was performed at a dynamic pressure of 175 psf. The results for a dynamic pressure of 100 psf will be presented first followed by the results at 175 psf.

OPEN-LOOP CPE RESULTS

Evaluation Points

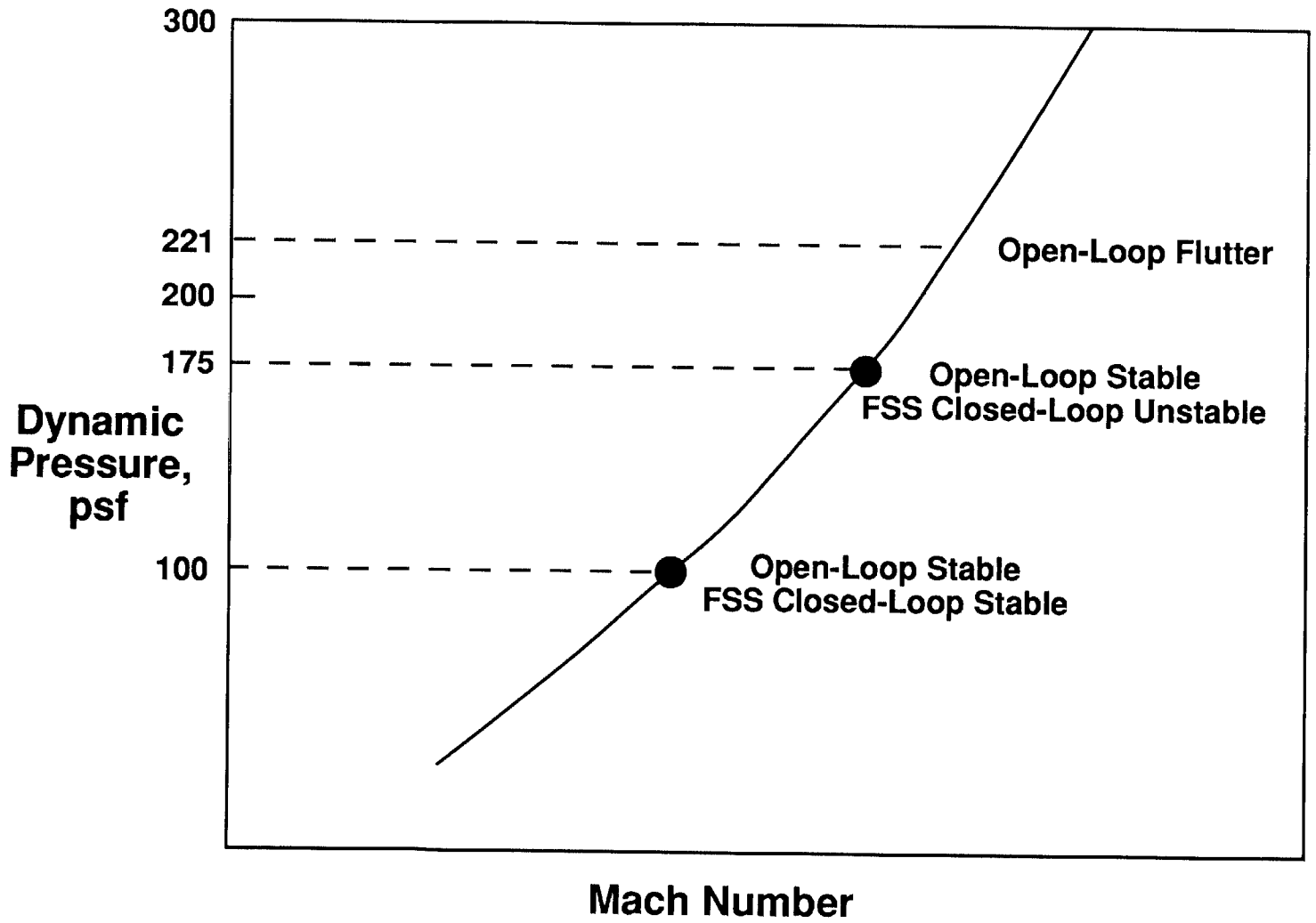

OPEN-LOOP CPE RESULTS

Stable Plant/Stabilizing Controller

This figure contains CPE information exactly the way it comes off the laser printer in the control room during the wind-tunnel test. The CPE results consist of four plots, which together give a complete picture of the performance of the controller. In the upper left hand side are the maximum and the minimum singular values of the return difference matrix at the plant input. On the upper right are the maximum and minimum singular values of the return-difference matrix at the plant output. The lower left shows the magnitudes of the minimum eigenvalue of the return difference matrix. The lower right is the locus of the determinants of the return difference matrix.

This figure corresponds to the first solid circle from the previous figure. During FSS testing, this CPE information is used in the following way: First, the determinant plot in the lower right is examined. Since there are no encirclements about the critical point, the prediction is that the closed-loop system would be stable if the loop were closed. Next the guaranteed gain and phase margins are determined from the minimum of the minimum singular values (which for this case is 0.17) and the universal gain and phase margin diagram. If the loop is closed, the stability margins will consist of simultaneous gain margins of -1.5, 1.5 dB for 0 phase perturbation and 8 degrees of phase margin with 0 dB gain perturbation. A low minimum singular value is observed near a frequency of 20 Hz which is attributed to a control mode. This is a frequency range where one needs to be alert for instability when the loop is closed.

During wind-tunnel testing the loop was closed on the control law and the closed-loop CPE looked very similar. The control surface activity was quite large at a frequency of 20 Hz which was expected.

The dynamic pressure was then increased. An instability was reached at approximately 175 psf which was below the previously measured open-loop flutter boundary at 221 psf. The loop was then opened and open-loop CPE was performed at a dynamic pressure of 175 psf. These results are presented on the next slide.

OPEN-LOOP CPE RESULTS

Stable Plant / Stabilizing Controller

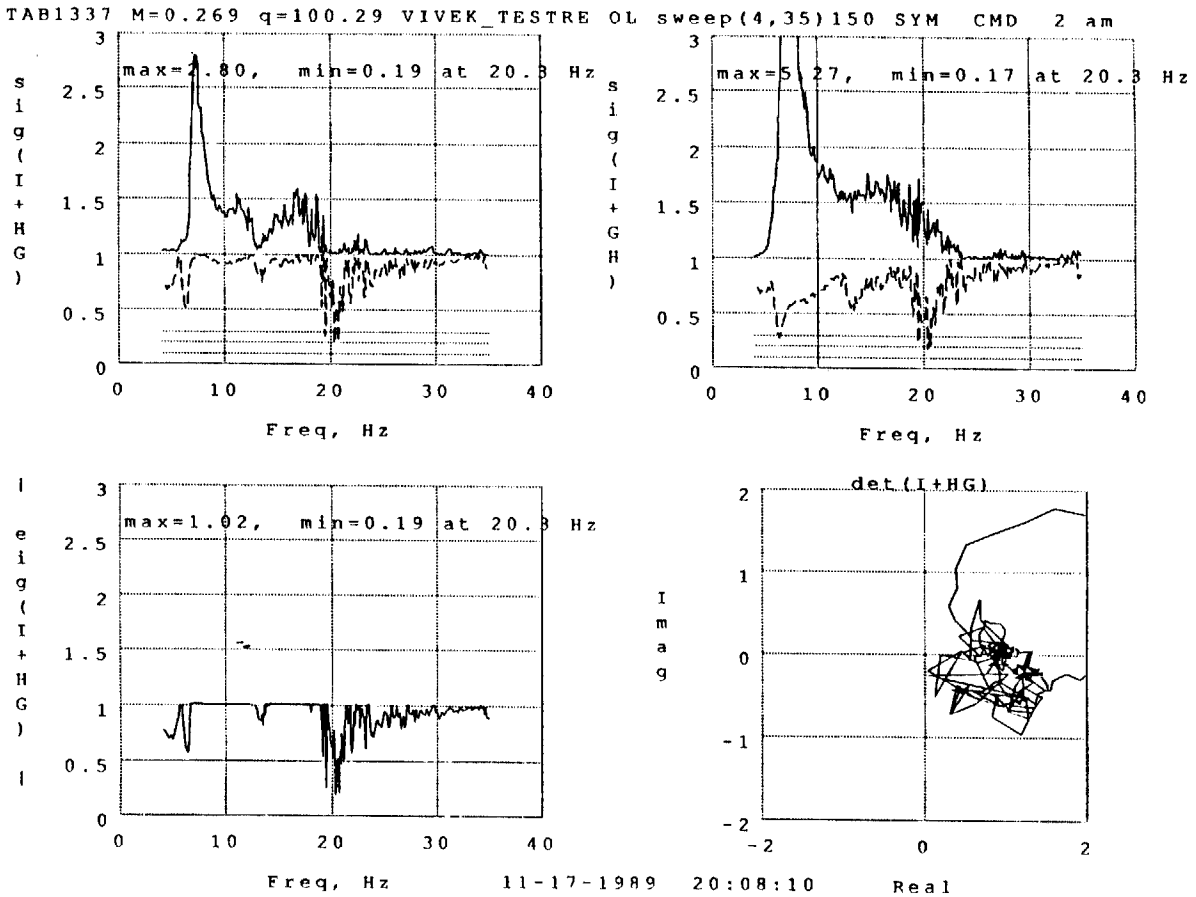

Interpretation: **Closed-loop system stable**

GM= -1.5, 1.5 dB (Phase= 0 deg)

PM= 8 deg (Gain= 0dB)

OPEN-LOOP CPE RESULTS

Stable Plant/Destabilizing Controller

This figure contains open-loop CPE results at a condition corresponding to a stable plant and a destabilizing controller. For such a situation, theory predicts that the determinant plot should contain a clockwise encirclement of the origin. The determinant plot (lower right) shows just such an encirclement. This result provided confidence that in the future determinant plots can be used to predict destabilizing control laws.

OPEN-LOOP CPE RESULTS

Stable Plant / Destabilizing Controller

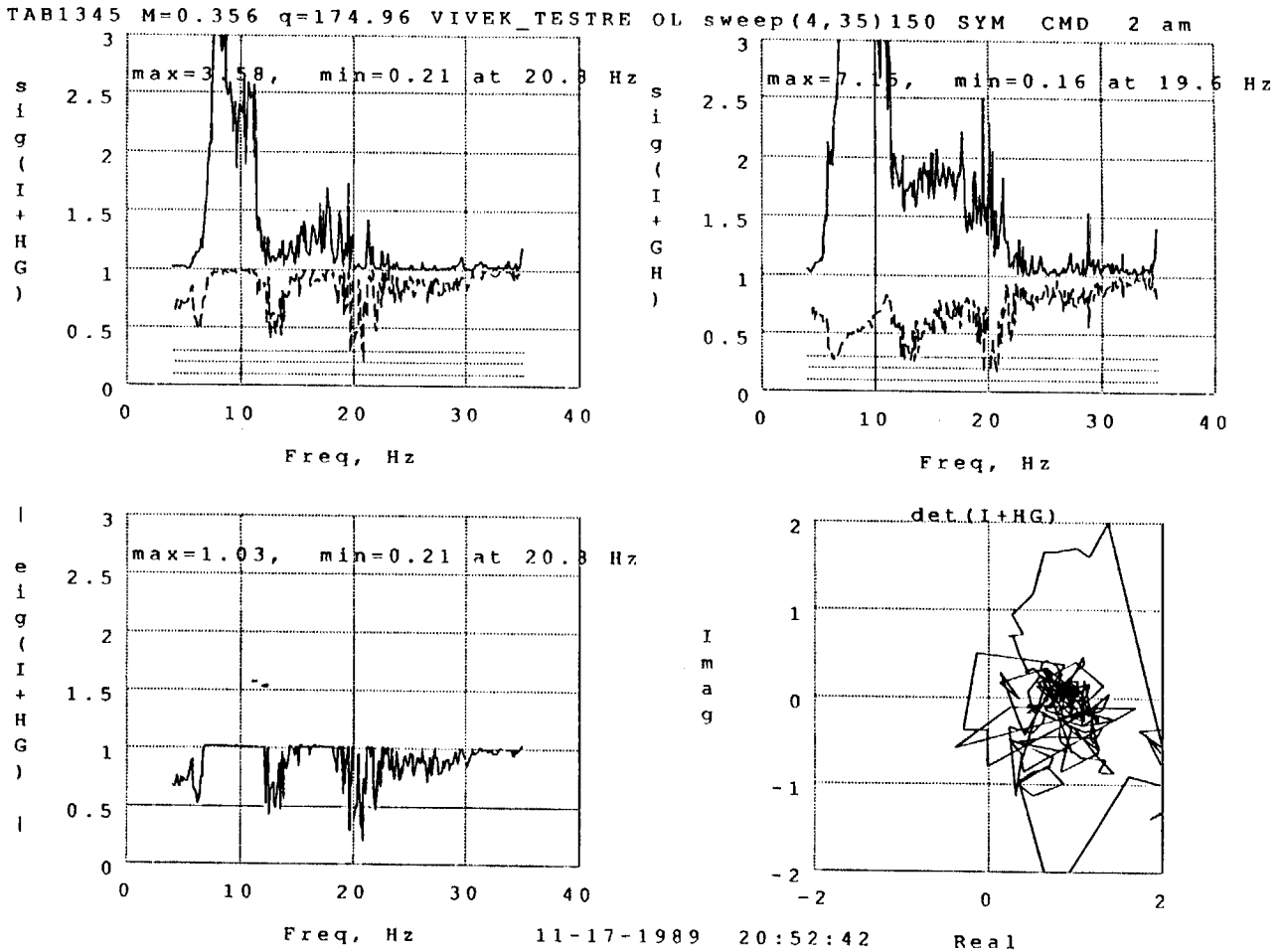

Interpretation: **Closed-loop system unstable**

CLOSED-LOOP CPE RESULTS

Evaluation Points

Typical CPE results obtained during the closed-loop wind-tunnel tests are described next. This figure shows the atmospheric H line along which the wind-tunnel testing was conducted. Two results will be presented. The first is at a point where it is known that the open loop plant was stable and the second where the plant was known to be unstable. The controller was stabilizing for both cases.

CLOSED-LOOP CPE RESULTS

Evaluation Points

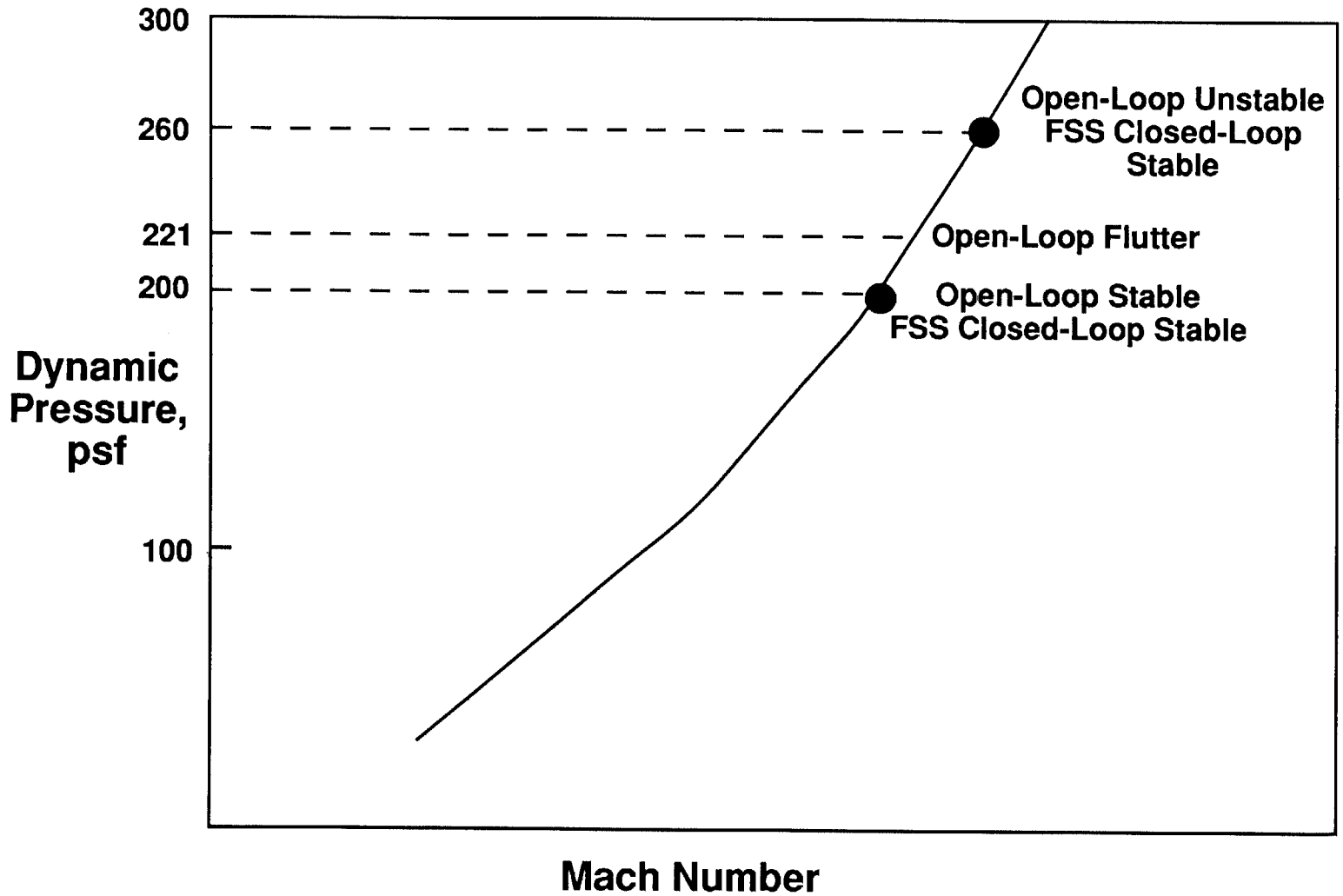

CLOSED-LOOP CPE RESULTS

Stable Plant/Stabilizing Controller

This figure shows the closed-loop CPE results at a dynamic pressure where the plant is known to be stable and the controller is stabilizing. The first objective of closed-loop CPE was to evaluate the stability margins. The guaranteed simultaneous gain and phase margins obtained for a minimum singular value of 0.34 were determined to be -2.6, 3.8 dB gain margin with 0 phase perturbation and 27-degree phase margin with 0 dB gain perturbation. The determinant plot on the bottom right shows no encirclement about the origin (the critical point) which is expected since the plant is stable and the closed-loop system is stable.

The dynamic pressure was then increased to a point above the open-loop flutter boundary, and these results are shown on the next slide.

CLOSED-LOOP CPE RESULTS

Stable Plant / Stabilizing Controller

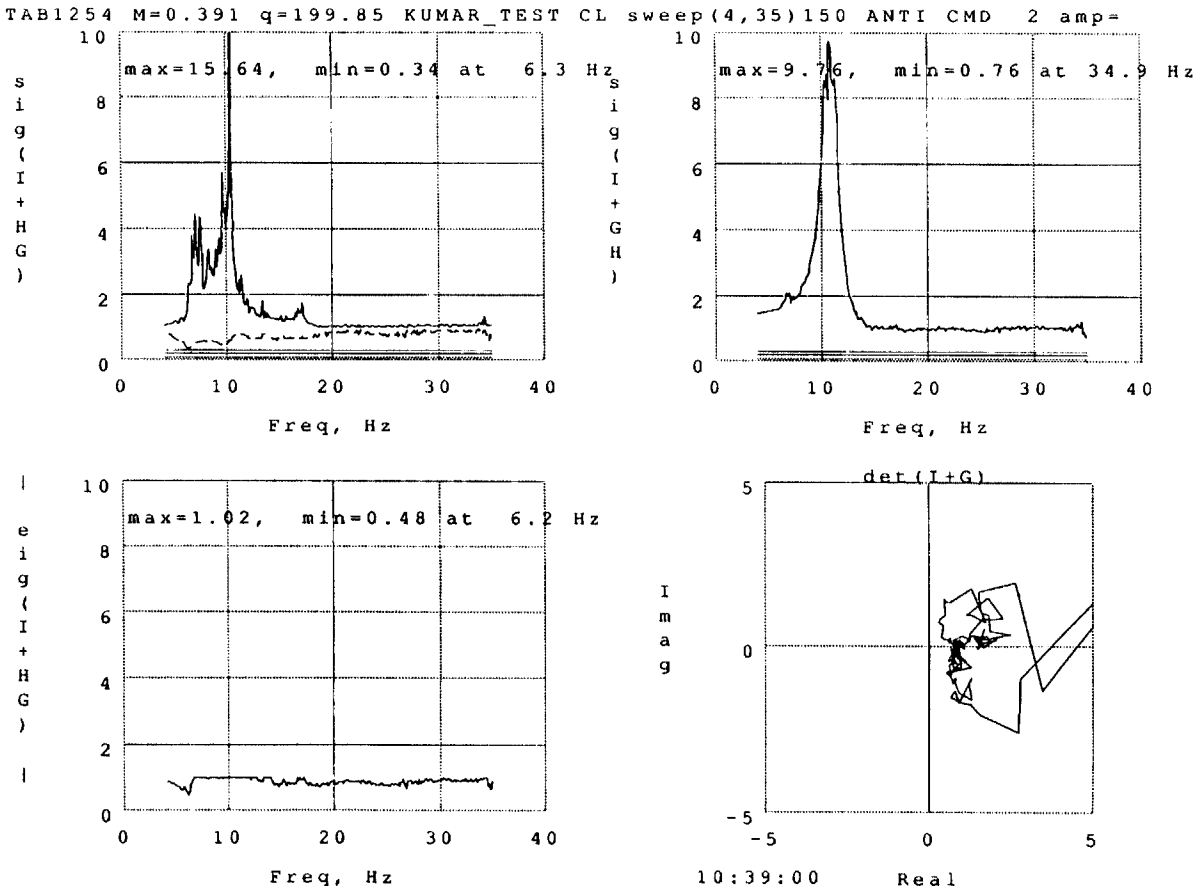

Interpretation { GM= -2.6, 3.8 dB (Phase= 0 deg)
PM= 27 deg (Gain= 0dB)

646

CLOSED-LOOP CPE RESULTS

Unstable Plant

The CPE results of a closed-loop system where the plant is known to be unstable and the controller is stabilizing are presented in this figure. Observation of the model in the wind tunnel indicates that the controller is stabilizing the plant so a counterclockwise encirclement about the critical point is expected. The determinant plot shows no clear encirclement. This could be attributed to poor frequency resolution in the region of the encirclement.

Using the minimum singular value of 0.22, the gain margin for 0 phase perturbation are approximately -1.7,+2.1 dB and the phase margin for 0 gain perturbation is ±12.5 degrees.

CLOSED-LOOP CPE RESULTS

Unstable Plant / Stabilizing Controller

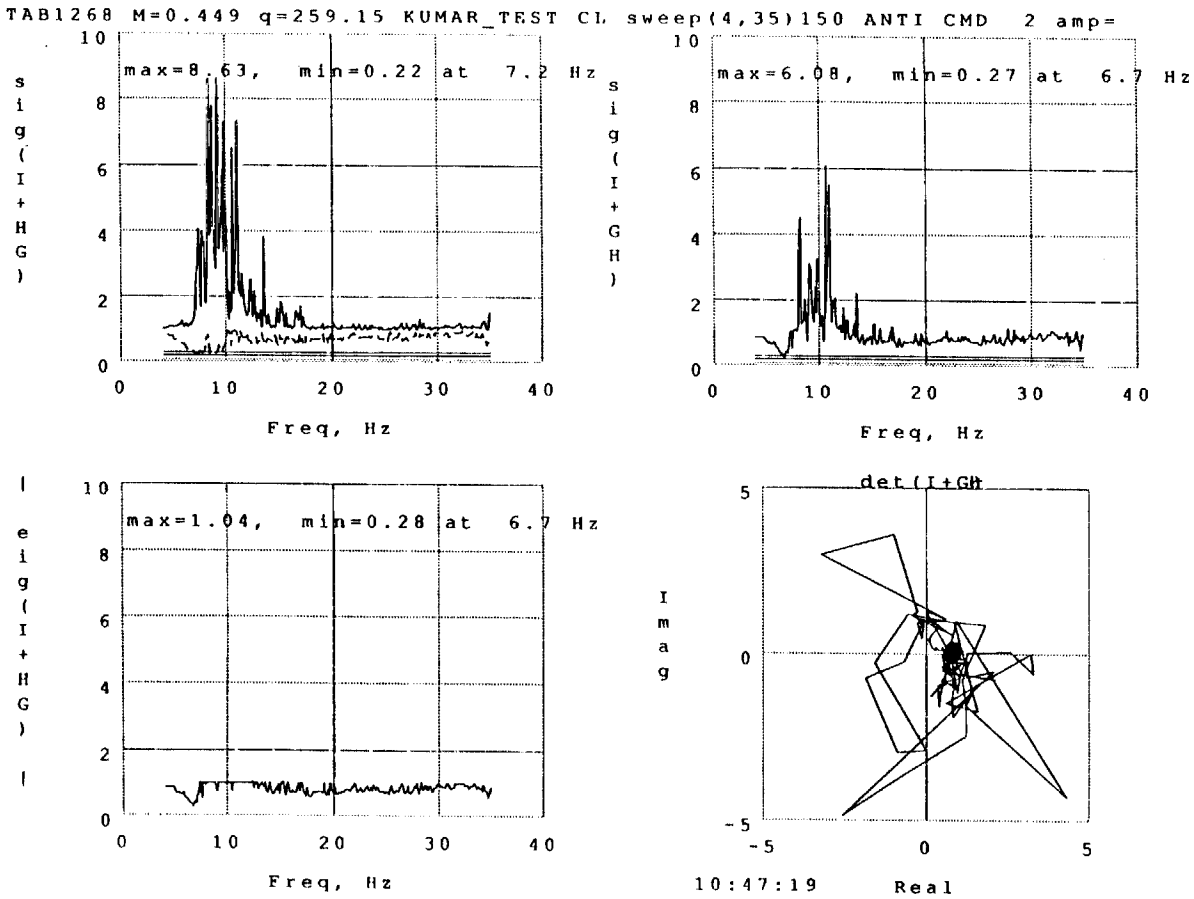

Interpretation { GM= -1.7, 2.1 dB (Phase= 0 deg)
PM= 12.5 deg (Gain= 0dB)

FLUTTER PREDICTION PROCEDURE USING CLOSED-LOOP CPE RESULTS

The second objective of the closed-loop CPE was to determine the open-loop stability of the plant during closed-loop testing. The method chosen was based on the observation that poles near the neutral stability axis produce large magnitudes in (SISO) transfer functions. Since maximum singular values of MIMO systems in this respect have similar properties to the SISO transfer functions, then the minimums of the reciprocal of the maximum singular values could be used to indicate how close the the poles of a MIMO system are to being neutrally stable and also the frequencies at which the minimums occur.

During wind-tunnel testing, the plant transfer matrices were obtained during the process of performing closed-loop CPE. A plot of typical inverse maximum singular values of the plant transfer matrix computed from closed-loop tests for a dynamic pressure of 200 psf is shown in the plot on the left. The frequencies (approximately 8.5 and 11 Hz) at which the two local minima of the inverse maximum singular value curve occur are indicated by the arrows. These frequencies correspond to the frequencies of the modes which coalesce to create flutter. These frequencies were determined for many dynamic pressures and the figure on the right shows a plot of the two frequencies as a function of dynamic pressure. The dynamic pressure at which the two curves appear to coalesce indicates a potential point for open-loop flutter.

FLUTTER PREDICTION PROCEDURE USING CLOSED-LOOP CPE RESULTS

650

$$\frac{1}{\sigma_{max}(G)}$$

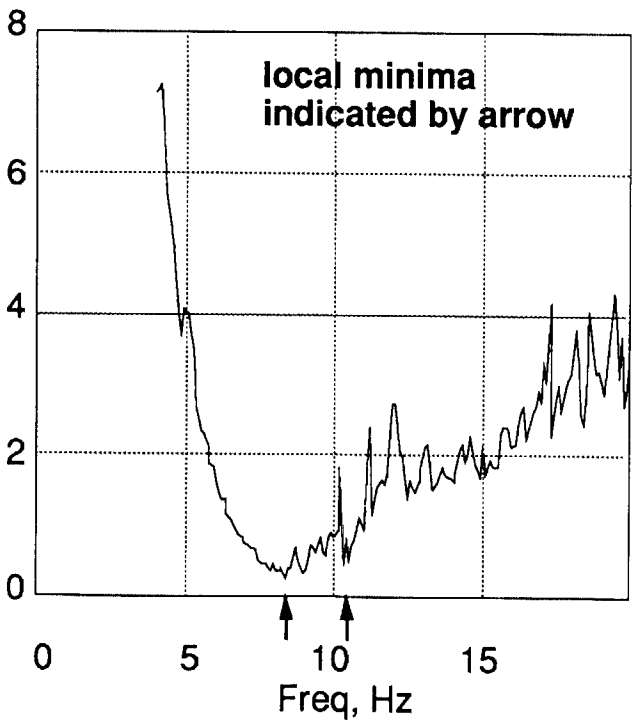

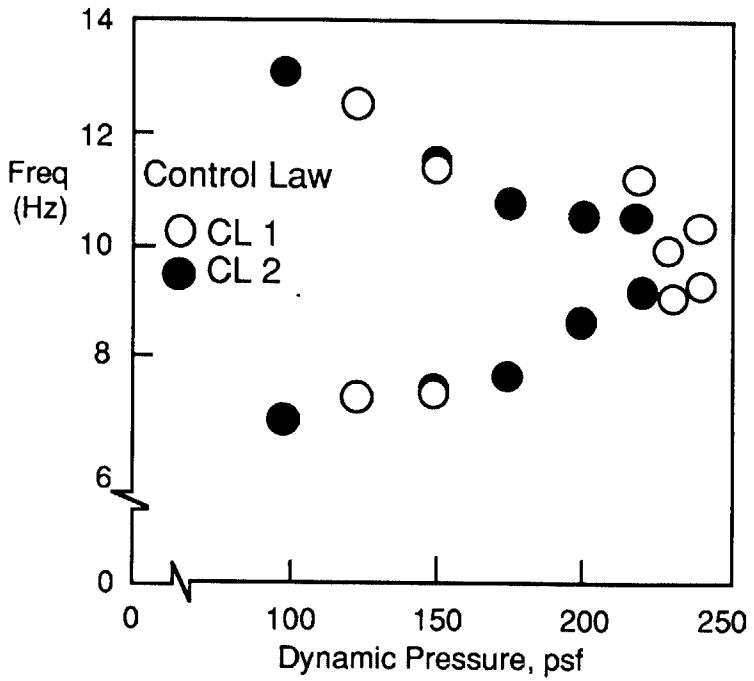

CONCLUDING REMARKS

A Controller Performance Evaluation methodology was developed to evaluate the performance of multivariable, digital control systems. The method was used and subsequently validated during the wind-tunnel testing of an aeroelastic model equipped with a digital flutter suppression controller. Through the CPE effort a wide range of sophisticated near real-time analysis tools were developed. These tools proved extremely useful and worked very well during wind-tunnel testing. Moreover, results from open-loop CPE were the sole criteria for beginning closed-loop testing. In this way, CPE identified potentially destabilizing controllers before actually closing the loop on the control system, thereby avoiding catastrophic damage to either the wind-tunnel model or the wind tunnel. Open-loop plant transfer functions derived from CPE computations were used to redesign and improve control laws. CPE results also proved useful in determining open-loop plant stability during closed-loop test conditions.

CONCLUDING REMARKS

- Developed CPE methodology and tools
- Improved wind-tunnel and model safety
- Sole criteria for closed-loop testing
- Objectives of CPE met
  - Closed-loop system stability predicted from open-loop information
  - Closed-loop stability margins calculated
  - Open-loop plant stability investigated from closed-loop information

REFERENCES

1. Mukhopadhyay, V.; and Newsom, J. R.: A Multiloop System Stability Margin Study Using Matrix Singular Values. *Journal of Guidance, Control, and Dynamics*, Vol. 7 No. 5, September - October 1984, pp. 582-587.

2. Mukhopadhyay, V.; and Newsom, J. R.: Application of Matrix Singular Value Properties for Evaluating Gain and Phase Margins of Multiloop Systems. AIAA Paper 82-1574, AIAA Guidance, Control, and Dynamics Conference, August 9-11, 1982, San Diego, California.

3. Mukhopadhyay, V.; Pototzky, A. S.; and Fox, M. E.: A Scheme for Theoretical and Experimental Evaluation of Multivariable System Stability Robustness. Paper presented at the 1990 American Control Conference, May 23-25, 1990, San Diego, California.

4. Miller, G. D.: Active Flexible Wing (AFW) Technology. AFWAL TR-87-3096, February 1988.

5. Noll, T. E.; et al.: Aeroservoelastic Wind-Tunnel Investigations Using the Active Flexible Wing Model - Status and Recent Accomplishments, NASA TM-101570. AIAA Paper 89-1168, AIAA 30th Structures, Structural Dynamics and Materials Conference, Mobile, Alabama, April 1989.

6. Christhilf, D.; Adams, W. M.; Srinathkumar, S.; Waszak, M.; and Mukhopadhyay, V.: Design and Test of Three Active Flutter Suppression Controllers. 4th Workshop on Computational Control of Flexible Aerospace Systems.

7. Adams, W. M., Jr.; Tiffany, S. H.; and Bardusch, R. E.: Active Suppression of an Apparent Shock Induced Instability, AIAA Paper 87-0881-CP, AIAA 28th Structures, Structural Dynamics, and Materials Conference, April 6-8, 1987, Monterey, California.

8. PRO-MATLAB User's Guide, The MathWorks Inc., 21 Eliot Street, South Natick, MA 01760.

57-18
7550
87

N91-22338

ACTIVE VERSUS PASSIVE DAMPING IN LARGE FLEXIBLE STRUCTURES [1]

Gary L. Slater
University of Cincinnati
Cincinnati, OH 45221

Mark D. McLaren
Ford Aerospace Corporation
Palo Alto, CA 94303

Abstract

Optimal passive and active damping control can be considered in the context of a general control/structure optimization problem. Using a mean square output response approach, it is shown that the weight sensitivity of the active and passive controllers can be used to determine an optimal mix of active and passive elements in a flexible structure.

1 Introduction

Because of the low inherent damping of the typical large flexible structure, some form of vibration control methodology is necessary to reduce the vibration response to an acceptable level. The control community has traditionally addressed this problem from an active control viewpoint, and has proposed a multitude of mathematical techniques for solving this difficult feedback control problem. While elegant in their mathematics, these analyses often show little consideration for the mass, cost, and reliability of the hardware required for these control strategies.

An alternate approach to active vibration control is to implement vibration suppression through some type of passive means. Passive schemes have a long history of use in the satellite business, having been used for suppression of rigid body motions for many years. The most typical of these are probably the viscous damper (e.g. a ball in a fluid filled tube), or the magnetic damper. For flexible structures the natural damping inherent in real materials will cause vibratory motions to damp out, although the time scale may be quite large. There is currently an effort to identify materials which can significantly increase the material damping with no other adverse effects.

A question which has seldom been addressed is whether there is a combination of active and passive techniques which is optimum for a structure to use? The entire question of optimization is one which must be considered carefully in the spacecraft design area. For the current study we define "optimal" to mean the minimum mass structure, while keeping all other constraints within specified limits. Optimal simultaneous structure/control design is an area of much recent interest in both the structures and the control communities. The answers obtained to any optimization problem are very much dependent on the initial assumptions, the mathematical framework, and the decision as to the definition of optimality. In previous works, the authors have proposed a stochastic approach to optimal control/structure design whereby the optimization problem is to find a minimum weight structure subject to fixed output constraints and to fixed control energy constraints (Refs. 1-3). The controller can be arbitrary, or the controller structure can be set in a specified way. For

[1]This work was supported in part by the Air Force Office of Sponsored Research at the Flight Dynamics Laboratory, Wright Aeronautical Laboratories, and also by a grant from CRAY Research Inc. provided through the Ohio Supercomputer Center in Columbus, Ohio.

example, in a perfect information environment, a full state controller yields the best performance, and hence the minimum weight structure. If feedback is restricted to outputs, either with or without additional measurement noise, then the control structure can be modified to a direct output feedback, or filter feedback form. Using this approach one can, for example, determine the mass reduction possible through additional sensors.

Our approach to include passive control means is to consider the passive damper as a special type of output controller. For example, a linear dashpot is an element which generates a force opposing relative motion between two connected locations. This can be considered as an output controller, where the controller gain is the damping coefficient associated with that element. The task required to complete the optimization is a difficult one. If we are attempting to minimize the total mass of the structure, what is the mass penalty associated with the controller (either active or passive) and how does that mass penalty vary with control energy? In fact we are in no position to answer that question completely in this paper. Rather our approach will be to consider the problem parametrically, so that sensitivities of the optimal solution to component masses can be ascertained. The actual optimum can be obtained when appropriate information is available to the designer.

The outline of this paper is as follows. In Section 2 we give a short outline of the control/structure optimization approach required for this study. A short section on hardware implementations is included as Section 3 for general information only, as the authors' quantitative information is this area is incomplete. Finally, two simple examples are given which show of the benefits and possibilities for this type of analysis, followed by our conclusions.

2 Mathematical Framework for Control/Structure Optimization

The approach taken in this analysis is to consider the structure from a dynamic response point of view. We assume that the fundamental structural constraint is to support a load, or to hold various sub-system components (experiments, etc.) together to a required degree of accuracy in the presence of some form of excitation. The excitation specification may be either static or dynamic, deterministic or random, but to quantify the structure design we generally need to know the applied loads to ensure that stress or displacement constraints are met. The effect of the control system on this design problem is to effect a trade-off to reduce the effect of flexibility. As the structure is made lighter and more flexible, the control system can be used to reduce deflections and stresses to acceptable levels.

Structure/Control Optimization

The mathematical approach taken to quantify the control-structure relationship is to initially regard the controller structure as fixed and satisfying certain control magnitude constraints, which for this analysis will be assumed to be a mean square control energy bound. Similarly the external force environment on the structure is known and is assumed to be stochastic with known mean square energy and spectrum. Within this framework the optimal structure-control design problem is to find the structural parameters and the control law to minimize a performance index while satisfying control energy and displacement constraints. This may be posed as a mathematical programming problem.

Assume the system is given as

$$\begin{aligned} \dot{\boldsymbol{x}} &= A\boldsymbol{x} + B\boldsymbol{u} + G\boldsymbol{d} \\ \boldsymbol{y} &= C\boldsymbol{x} \\ \boldsymbol{z} &= H\boldsymbol{x} + \boldsymbol{v} \end{aligned} \tag{1}$$

where we have the conventional definitions of the state($\boldsymbol{x}$), control($\boldsymbol{u}$), performance output($\boldsymbol{y}$), measured output($\boldsymbol{z}$), and input and output disturbances ($\boldsymbol{d}, \boldsymbol{v}$, respectively).

The disturbance $\boldsymbol{d}$ is taken as the specified load. Generally we have assumed that $\boldsymbol{d}$ is Gaussian white noise, $\boldsymbol{d} \sim N(0, D)$, although other forms (e.g. harmonic disturbance) could be used. For this system we pose the following optimization problem:

Optimization Problem

Minimize the function $J(p_1, p_2, \ldots)$, where the p_i are structural parameters such as mass, stiffness, area, etc., and find the feedback law

$$\boldsymbol{u} = f(\boldsymbol{z}) \tag{2}$$

where $f(\cdot)$ is a specified functional form based on the controller type desired. For example, if $\boldsymbol{z} \equiv \boldsymbol{x}$, then the problem is full state feedback and $f(\cdot)$ becomes naturally a gain matrix. The resulting optimization becomes a special form of the linear quadratic regulator. The functional $f(\cdot)$ can specify an (unknown) dynamical system in the general output feedback problem. For the problem considered in this paper we consider the controller to consist of two parts: The first is the passive controller which consists of unknown damping coefficients of the specified form. The second part is a "conventional" full state active controller. The active controls must satisfy the control energy constraints

$$\mathrm{E}[\boldsymbol{u}^T R \boldsymbol{u}] = \beta^2 \tag{3}$$

while the outputs satisfy

$$\mathrm{E}[\boldsymbol{y}^T W_i \boldsymbol{y}] \leq w_i \qquad \text{(Output disturbance Inequalities, } i = 1, \ldots, n) \tag{4}$$

The rationale for a fixed control energy constraint is that for an active control implementation, the desired control should utilize the full control capability to reduce the structural loading. The output inequalities may be several, in which case one or more constraints may be equality constraints, but others will be strict inequalities.

Using the Gaussian disturbance case, the expectations can be converted to simple operations on the covariance matrix, which is determined by a Lyapunov equation (assuming here linear controls). For details on this see the references. Using this approach the optimization framework is quite flexible and can be adjusted to a variety of special types of constraints and controllers. Numerically the resulting optimization problem can be solved by a variety of general non-linear optimization software. For the full state feedback case, linear regulator software can be incorporated also.

3 Active and Passive Control Implementation

There are a number of technologies possible for the active and passive control of the damping of flexible space structures. The simplest in concept are the linear and rotational momentum exchange devices. Linear momentum devices (LMED's) are extremely simple in concept, yet have proven remarkably difficult to construct

(for a real space environment). For the LMED there is a trade-off between the magnitude of the proof mass and the total track length. For the low frequencies contemplated in most large space structures, the LMED's will probably have a mass which is a large fraction of the structure mass, a generally undesirable feature! For a fixed geometry track, the force obtained from the LMED is directly proportional to the proof mass itself, hence we may expect the mass contributed by this controller to be roughly proportional to the square root of the control energy β^2.

Torque wheel actuators or momentum wheels, are similar in concept to the LMED, absorbing angular momentum, rather than linear momentum. Track length here however is not a problem; the primary limitation is wheel speed. Maximum wheel speed is rarely encountered, although some means of dumping stored angular momentum must also be considered. Note that for a free-free structure every non-zero frequency vibration mode has zero linear and angular momentum. Hence both these devices need only worry about the saturation due to vibration transients, not in the steady state. It seems very likely that momentum wheels used for rigid body control, could easily be accomodated for control of flexible motions also.

Linear thrusters are generally used on satellites for attitude control, and could easily be adapted to the vibration suppression role. Note that for the rocket, thrust is proportional to mass flow, so that again average energy consumption would make thrustor mass proportional to β^2. In reality for the common reaction jet, specific impulse is relatively low, and fuel required for a long duration mission could be a significant problem. This may be no worse than the the LMED mass problem, and seems to be considerably more reliable.

Passive control elements could be one of a variety of viscoelastic materials used as coatings, or internal strut material. For such materials, the damping coefficient is proportional to the amount, hence the mass, of the damping material added. Other devices are "passively active" (or is it "actively passive"?) such as piezoelectric materials (coating or embedded). For most materials considered then the mass added by damping elements can be considered to be proportional to the mean square energy (β^2), or more directly for the passive damping elements to the damping element "c". The exact proportionality constant is extremely important in establishing an optimum, as is any fixed mass components not considered here.

4 Two Simple Examples

(a) Longitudinal vibration of a rod

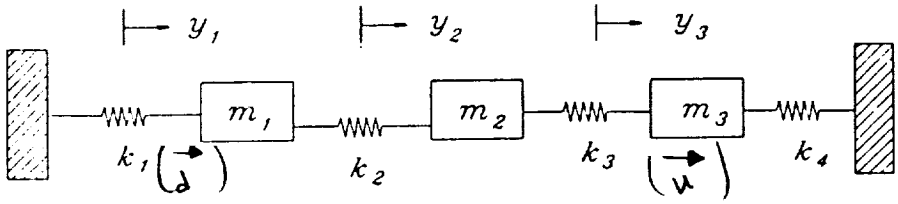

Figure 1: Discretized model for Example (a)

To demonstrate the approach to evaluate the effectiveness of active or passive control, consider the longitudinal vibrations of a rod, where the rod is discretized to the simple mass-spring-damper system shown in Figure 1. For this case we will consider only the trade-off between the active control element, assumed to be acting at mass 3, and the damping element, which is assumed to be inserted between masses 2 and 3. For this problem,

we assume the rod structural elements are themselves fixed, although in the general optimization problem, the segment areas (hence spring constants) would be design variables also. For this problem Figure 2 shows the amount of active control energy required to meet the displacement constraint $E[x_2^2] = \alpha^2$ for variable passive damping. Note that this curve has a minimum at a fairly low value of damping, meaning that as passive damping goes up, the active controller must work harder to meet the output displacement constraint. This curve is typical, although for different constraint levels the minimum will shift and may, in fact, disappear. For this example the system mass is considered to be fixed but we may propose a cost function then to be

$$J = \gamma_1 c_3 + \gamma_2 \beta^2$$

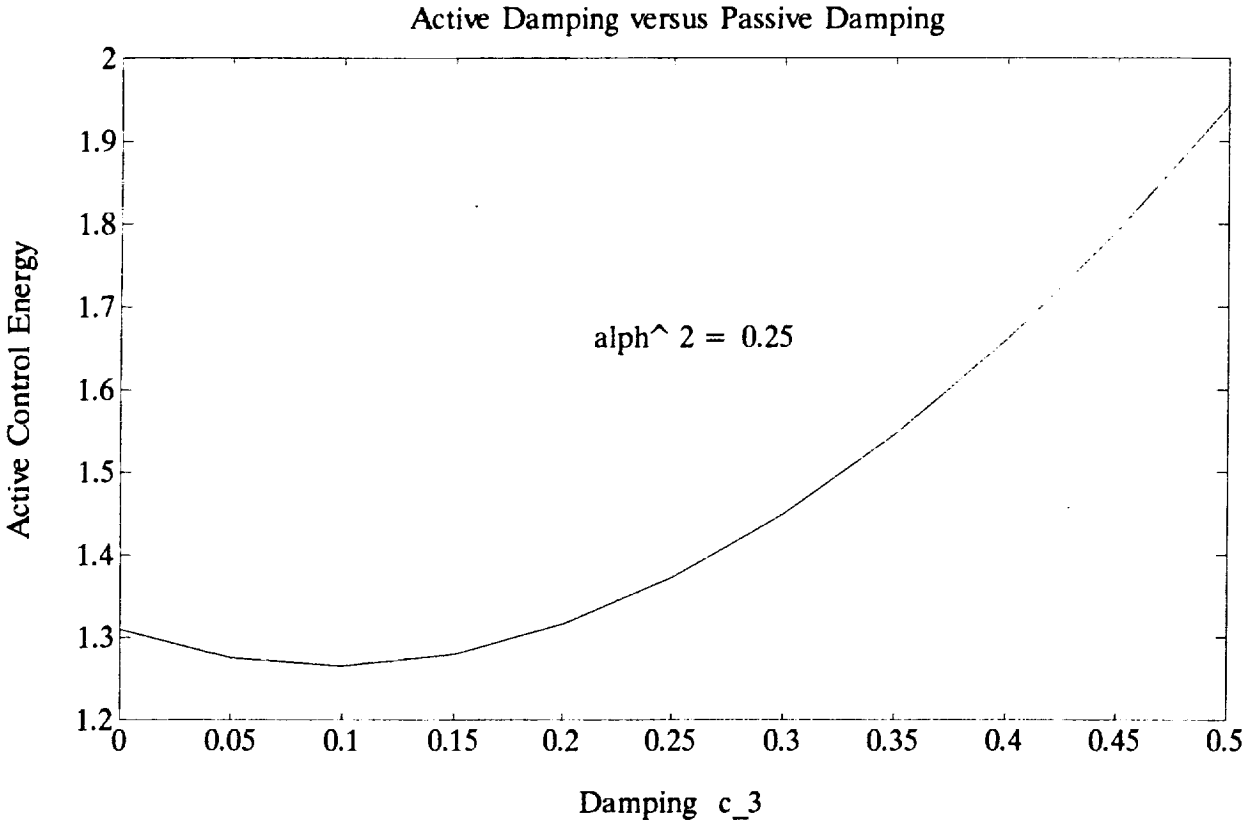

Figure 2: Active control energy required to achieve mean square response constraint

Constants γ_1 and γ_2 reflect the relative cost (either mass or dollars) of the active and passive control components. A line of constant cost then is a straight line on Figure 2 with a slope $m = -(\gamma_1/\gamma_2)$ meaning that the optimal mix of active and passive damping is somewhere to the left of the absolute minimum shown on Figure 2, and is found from meeting a tangency condition between the curve and the straight line. If the passive damping cost is much less than the active damping cost (a common assumption in most discussions), then the optimal passive damping is that value at the minimum of Figure 2.

(b) DRAPER I optimal truss

In solving an optimal structure/controller problem McLaren and Slater [Ref. 3] determined the optimal mass of the tetrahedral truss model model known as "Draper I" (see Figure 3), for various types of controller

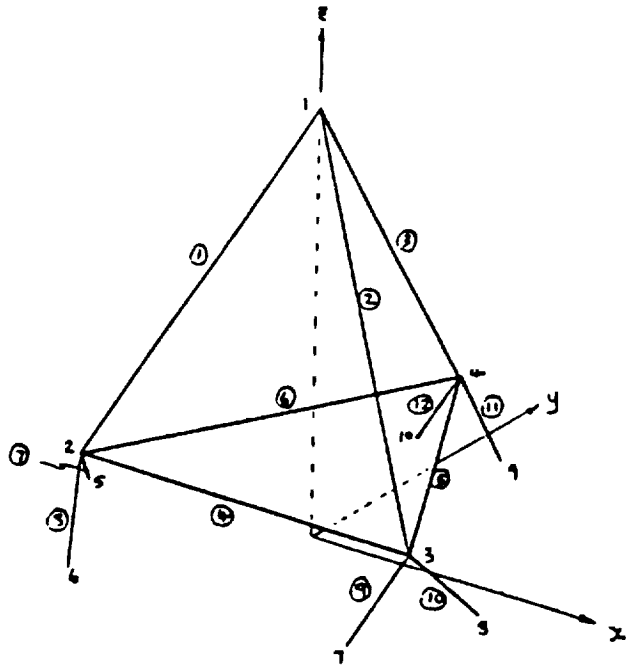

Figure 3: The DRAPER I truss model

implementations. For this structure there are six control actuators, situated in each of the base legs of the truss, and six collocated velocity sensors, giving the longitudinal velocity of each truss leg. The comparison between full state feedback and direct output feedback then is almost a direct comparison of the active versus passive control analysis done for the previous simple model. (The comparison is not exact as the results in Ref. 3 determined the optimal general feedback matrix. For a passive damping study we need to go back and additionally restrict the gain matrix to be diagonal. This is straight-forward and hopefully will be done soon.)

For this case the problem was to design the optimal structural elements to minimize the mass and to simultaneously design the controller. The controller mass was not considered part of the performance index, nor was a fixed controller mass part of the system. The output constraint is to keep the vertex of the truss within specified limits. For these two cases the final masses are shown in Figure 4. The results indicate that generally full state designs may achieve almost 50% less mass than the optimum velocity feedback designs. Ideally we should go back and re-run with these two controllers in parallel, and with relative weights associated with each. The resultant family of controllers, combined with mass information on the controller implementation, could then be used to determine an optimal control implementation. Based on the large mass reduction from full state feedback, its seems reasonable that for this, and probably for most structures, the advantage of an active feedback scheme can be quantified explicitly.

5 Conclusions

The results shown indicate that there is an easy way to explicitly characterize the relative merits of an active versus a passive control scheme. No attempt here is made to quantify the exact trade-off due to the uncertainty in mass figures associated with the controller types. This, and further exploration of controller trade-offs, are subjects of continuing research.

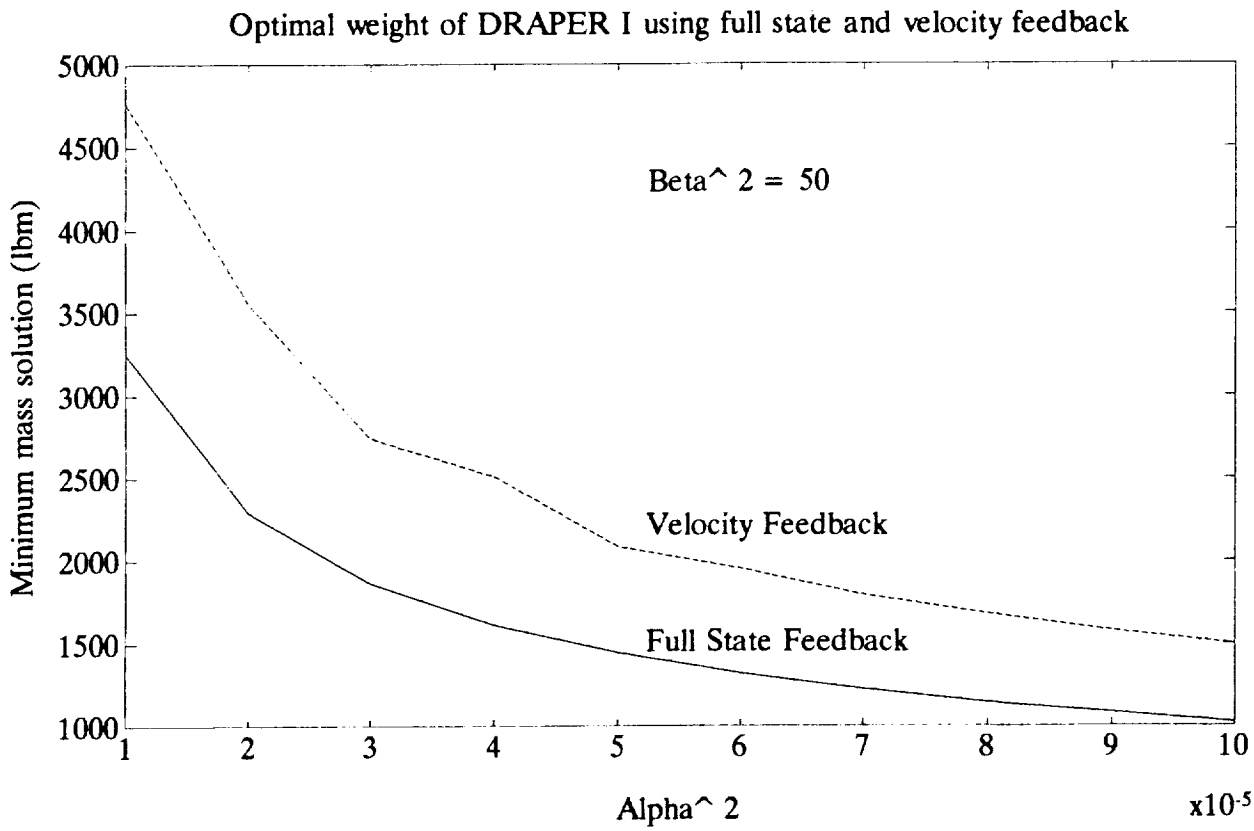

Figure 4: Comparison of optimal DRAPER I mass for full state vs. velocity feedback

Pouts mes excuses

Due to time constraints, it was not possible to include a reference list for the many pertinent documents that are available in the literature. Only earlier material of the authors which fills in many of the missing details in this paper is listed below.

References

[1] Slater, G.L., "A Disturbance Model for the Optimization of Control/Structure Interactions for Flexible Dynamic Systems", Paper 88-4058, AIAA Guidance & Control Meeting, Minneapolis, MN, August, 1988.

[2] McLaren, M.D., Slater, G.L., "A Disturbance Based Control/Structure Design Algorithm", Proceedings of the 3^{rd} Annual Conference on Aerospace Computational Control, August, 1989, Pasadena, CA.

[3] McLaren, M.D., Slater, G.L., "A Covariance approach to Integrated Control/Structure Optimization", Paper 90-1211, AIAA Dynamics Specialist's Conference, April, 1990.

Vibration Suppression and Slewing Control of a Flexible Structure

Daniel J. Inman†
Ephrahim Garcia††
Brett Pokines†††
Department of Mechanical & Aerospace Engineering
University at Buffalo
Buffalo, NY 14260

Abstract

This work examines the effects of motor dynamics and secondary piezoceramic actuators on vibration suppression during the slewing of flexible structures. The approach focuses on the interaction between the structure, the actuators and the choice of control law. The results presented here are all simulated but are based on experimentally determined parameters for the motor, structure, piezoceramics actuators and piezofilm sensors. The simulation results clearly illustrate that the choice of motor inertia relative to beam inertia make a critical difference in the performance of the system. In addition the use of secondary piezoelectric actuators reduces the load requirements on the motor and also reduces the overshoot of the tip deflection.

The structures considered here are a beam and a frame. The majority of the results are based on an Euler Bernoulli beam model. The slewing frame introduces substantial torsional modes and a more realistic model. The slewing frame results are incomplete and represent work in progress.

1. Introduction

A slewing motion consists of the rotation of a structure about a point. In the case considered here, a DC electric motor is used to move a beam and/or a frame about the axis of the motor in order to orient the length of the structure in a new direction (see figure 1). In the past, slewing maneuvers have been carried out on passive structures, i.e., structures which have no internal control or sensing mechanisms. Here, the effects of slewing an active structure are considered. An active or smart structure is defined as a structure with sensors and actuators integrated within the structure (Wada, 1989). A passive structure does not contain any integrated control hardware. The slewing of a passive beam has been considered by several researchers. Garcia (1989) and Garcia and Inman (1990) examine the dynamic interaction between the structure and actuator in slewing a passive beam. Juang et al (1986), Yurkovich and Tzes (1990), Cannon and Schmitz (1984) and Hastings and Book (1987) have all consider the effects of slewing passive beams. Park et al (1989) considered slewing a passive beam with a secondary voice coil actuator attached to improve vibration suppression. Their results motivated the work presented here which considers the effects of slewing an active beam. This presents a multiple input control problem. The active beam consists of a flexible aluminum beam with embedded piezoelectric actuators and sensors. The results for the active beam have been presented in preliminary form at the Army Research

† Professor and Chair
†† Visiting Assistant Professor
††† Graduate Student

Office Workshop (see Inman et al 1990). The slewing frame example is experimental and represents work in progress.

The analysis proceeds by forming a Hamiltonian consisting of the elastic and kinetic energy in the Euler-Bernoulli beam, plus the nonconservative work done on the beam by the DC motor and piezoceramic actuator. Garcia (1989) illustrated that the dynamic interaction between the slewing actuator, the DC motor, and the flexible structure can lead to improved vibration suppression. Traditionally, the slewing control of a flexible single link structure has been a single actuator problem. Park et al (1989) proposed the use of a "voice-coil" actuator in addition to the slewing motor; this actuator was rigidly attached to the slewing hub and actuated the beam near the clamped end. This approach achieved improved structural dynamic performance and reduced peak motor voltages. However, these performance gains were at the cost of adding the mass of the coil actuator and its supporting mechanical fixture to the slewing payload.

We propose that direct structural actuation be achieved in the slewing maneuver by use of a piezoceramic actuator. This active structure will contain a layered piece-wise distributed, or segmented, piezoceramic crystal in the case of the beam and an active longeron element consisting of bending piezoceramics for the frame. The active beam being considered here is similar to those considered earlier in a damped configuration by Fanson and Caughey (1987) and Burke and Hubbard (1987). Fanson and Caughey considered a cantilevered flexible beam controlled by a collocated pair of piezoelectric actuators and strain sensors coupled with a positive position feedback control law. In the case presented here a piezofilm will be used instead of a piezoceramic for the strain measurement and piezoceramics are used for actuators.

A theoretical optimal control study is performed using a linear quadratic regulator (LQR) control formulation. This is presented only for the beam. A comparison of control laws is made where the penalty function is varied to change the degree of control effort afforded by the active beam. The goal here is to illustrate that increased vibration suppression may occur in slewing maneuvers by taking advantage of control structure interaction and to investigate the vibration suppression effects of slewing an active structure.

2. System Dynamics

The dynamics of the slewing beam system are developed from Hamilton's principle. First, the dynamics of a slewing piezo-actuated structure are considered with the effects of a piece-wise distributed piezo actuator. The actuator dynamics, that is, the interaction of motor and beam are also modeled. The moment generated by the piece-wise distributed, piezo actuator is calculated. Finally, the equations of motion for this active slewing structure are assembled in a lumped mass model representation. The details can be found in Inman et al (1990) and follws directly from Garcia (1989).

Figure 1 illustrates the coordinates used in defining the equations of motion of a flexible structure undergoing a slewing motion through an angle $\theta(t)$. The deflection of the beam $y(x,t)$ is defined relative to the rigid motions θ. The torque causing the motion is denoted by τ. The beam, of length L, deforms and rotates in the X-Y plane. Figure 2 illustrates the model of the motor. Figure 3 illustrates the use of piezoceramics in the slewing beam.

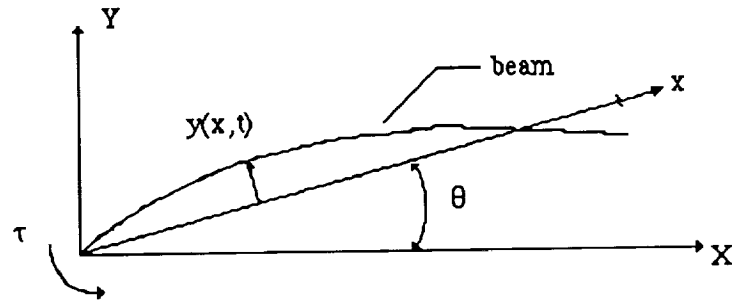

Fig. 1. Slewing flexible beam schematic.

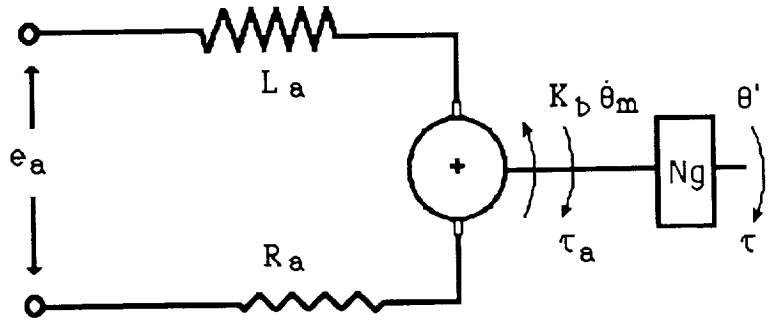

Fig. 2. Motor armature circuit and gear box schematic.

EDGE VIEW

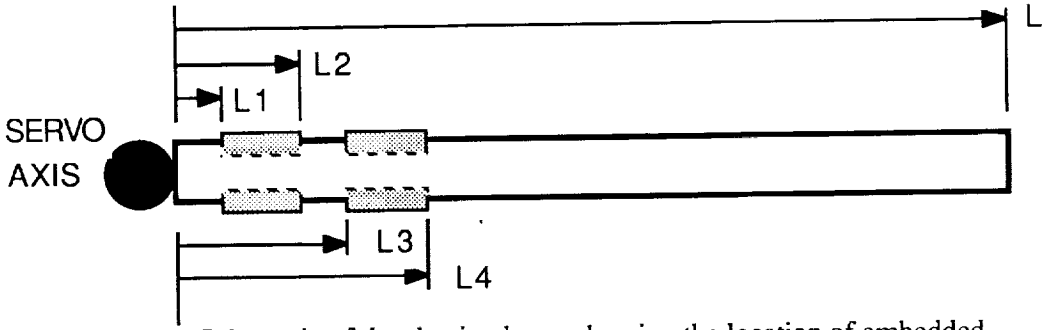

Fig. 3. Schematic of the slewing beam showing the location of embedded piezoceramic actuators.

3. Control Design

A linear quadratic regulator control law was designed to illustrate the effects of slewing an active structure versus slewing a passive structure. The results are based on a beam/motor system designed to take maximum advantage of the interaction between the structural modes and the motor torque. Both the voltages to the electric motor and to the embedded piezoceramic were used as control inputs.

To perform the control analysis, the mathematical model presented in Inman et al (1990) is discretized in space and manipulated into state space form. Combining the governing equations and assuming that only n terms are used in a modal approximation (5), the equations of motion of the slewing active structure can be written in matrix form as the vector differential equation

$$M\ddot{\mathbf{q}} + D\,\dot{\mathbf{q}} + K\,\mathbf{q} = B_f\,\mathbf{u} \tag{1}$$

where the vector $\mathbf{q}$ is defined by $\mathbf{q}^T = [\theta(t)\ q_1(t)\ q_2(t)\ \ldots\ q_n(t)]$. The mass, damping and stiffness coefficient matrices are:

$$M = \begin{bmatrix} I_b+I_s & I_1+I_s\Gamma_1(0) & \ldots & I_n+I_s\Gamma_n(0) \\ I_1+I_s\Gamma_1(0) & M_1 & & \vdots \\ \vdots & & & \vdots \\ I_n+I_s\Gamma_n(0) & \ldots & & M_n \end{bmatrix} \tag{2}$$

$$D = \begin{bmatrix} b_v & b_v\Gamma_1(0) & \ldots & b_v\Gamma_n(0) \\ b_v\Gamma_1(0) & b_v\Gamma_1(0)^2 & \ldots & b_v\Gamma_1(0)\Gamma_n(0) \\ \vdots & & & \vdots \\ b_v\Gamma_n(0) & b_v\Gamma_n(0)\Gamma_1(0) & \ldots & b_v\Gamma_n(0)^2 \end{bmatrix} \tag{3}$$

$$K = \begin{bmatrix} 0 & \mathbf{0}_{1\times n} \\ & M_1\omega_1^2 \quad\quad \vdots \\ \mathbf{0}_{n\times 1} & \vdots \\ & \ldots \quad\quad M_n\omega_n^2 \end{bmatrix} \tag{4}$$

where $\Gamma_i = \phi_i'(0)$, the ith modal participation factor. In addition, M_i is the ith modal mass, ω_i denotes the structures natural frequencies and the ith inertia term is given by

$$I_i = \int_0^L \rho x \phi_i(x) dx$$

The control input vector $\mathbf{u}$ is the 2 x 1 vector $\mathbf{u}^T = [e_a, V_p]$ and the control coefficient matrix is

$$B_f^T = \begin{bmatrix} \frac{N_g K_t}{R_a} & \frac{N_g K_t}{R_a}\Gamma_1 & \ldots & \frac{N_g K_t}{R_a}\Gamma_n \\ 0 & \mu[\phi_1'(L_1)-\phi_1'(L_2)] & \ldots & \mu[\phi_n'(L_1)-\phi_n'(L_2)] \end{bmatrix} \tag{5}$$

for a single segment piezoceramic actuator.

Active control is performed by using state feedback and solving a standard linear quadratic regulator (LQR) control law design. The system of Eq. (1) is first put into state space form by defining the state vector **x** as

$$\mathbf{x} = \begin{bmatrix} \mathbf{q} \\ \dot{\mathbf{q}} \end{bmatrix} \tag{6}$$

and the corresponding state matrix

$$A = \begin{bmatrix} 0 & I \\ -M^{-1}K & -M^{-1}C \end{bmatrix} \tag{7}$$

where 0 denotes the matrix of zeros and I denotes the identity matrix of appropriate dimension. With this change of coordinates, Eq. (1) becomes

$$\dot{\mathbf{x}} = A\mathbf{x} + B\mathbf{u} \tag{8}$$

with output measurements defined by

$$\mathbf{y} = C\mathbf{x} \tag{9}$$

Here the matrix of constants C specifies which coordinates of the vector **x** are measured. State feedback control is implemented by specifying the relation

$$\mathbf{u} = -K_f\mathbf{x} \tag{10}$$

The LQR control algorithm then calculates the value of the gain matrix K_f such the cost functional

$$J = \int_0^\infty (\mathbf{x}^T Q\mathbf{x} + \mathbf{u}^T R\mathbf{u})dt \tag{11}$$

is minimized. The matrices Q and R are symmetric positive definite weighting matrices which are chosen to produce acceptable responses. In the case presented here the matrix Q was chosen to be

$$Q = \text{diag}\,[\,8\ \ 3\ \ 1\ 1\ \ 8\ \ 3\ \ 1\ 1\,] \tag{12}$$

which places emphasis on minimizing the angular displacement (and velocity) and the first modal displacement (and velocity). The control law determined from this weighting attempts to drive the angular position and structure displacement to zero. The weighting matrix R is chosen to have two different values to generate a control law with vibration suppression both with and without the use of the piezoceramic actuator. For the case with the added piezo actuator, the matrix R is chosen to be

$$R_1 = \text{diag}\,[\,1.0\ \ 1 \times 10^{-4}\,] \tag{13}$$

This choice penalizes the use of the motor voltage in factor of the piezoelectric actuator voltage. For the case without piezo actuator control, the weighting matrix R is chosen to be

$$R_2 = \text{diag}\,[\,1.0 \quad 1 \times 10^8\,] \tag{14}$$

A comparison of the results of using the piezoceramic actuator versus using only the motor torque for vibration suppression of the beam is illustrated in figures 5-8. In each case the control or response without the advantage of the piezoceramic is given by the dashed line and those with the use of the active beam are given by the solid lines. Figure 5 illustrates that the voltage supplied to the armature of the motor is reduced by 33% (from - 3 volts to -2 volts) when slewing is performed on an active beam versus a passive beam. Figure 7 clearly illustrates that the maximum tip deflection (overshoot) is reduced by almost 50% by using the piezoceramic actuator.

4. Closing Remarks

This paper examines slewing control by introducing the concept of using an active structure to improve performance. Slewing an active structure, as opposed to slewing a passive structure, offers the advantage of reducing the peak voltage demands on the slewing motor hence increasing reliability and potentially saving weight (a smaller motor could be used). In addition the active structure approach promises to substantially reduce maximum tip deflection of the structure. Simulation results were presented for a beam. These results, although simulated, use experimentally measured parameters from laboratory tests of the beam, motor and piezoceramics. The passive slewing beam model has been experimentally verified using a PID control (Garcia, 1989).

The frame experiment of figure 4 is in progress. The finite element model is developed and experimentally tested. The active strut has been designed and constructed and is being installed in the frame. The key experimental results of interest are the strong coupling between the bending vibration of the frame and the torsional vibration of the frame. While this is to be expected, the flexibility of the frame (ω_1 = 1.6 Hz) enhances the problem of suppressing tip vibration. Preliminary controllability calculations indicate that, unlike the beam, the secondary piezoelectric actuator is needed to produce large enough control effort to suppress the torsional modes.

In conclusion, the slewing of flexible structures requires a detailed examination of control structure interaction and can benefit from the use of "smart" structures. The result is best illustrated by examining the control input matrix B_f of equation (5). Without modeling the interaction and flexibility of the structure the matrix, B_f is a scalar (i.e., $\Gamma = 0$). When the interaction is modeled ($\Gamma \neq 0$) the matrix B_f becomes a row vector. When the secondary piezoceramic actuators are added, the matrix B_f becomes 2xn and the system is approaching full state feedback which is known to yield the best performance.

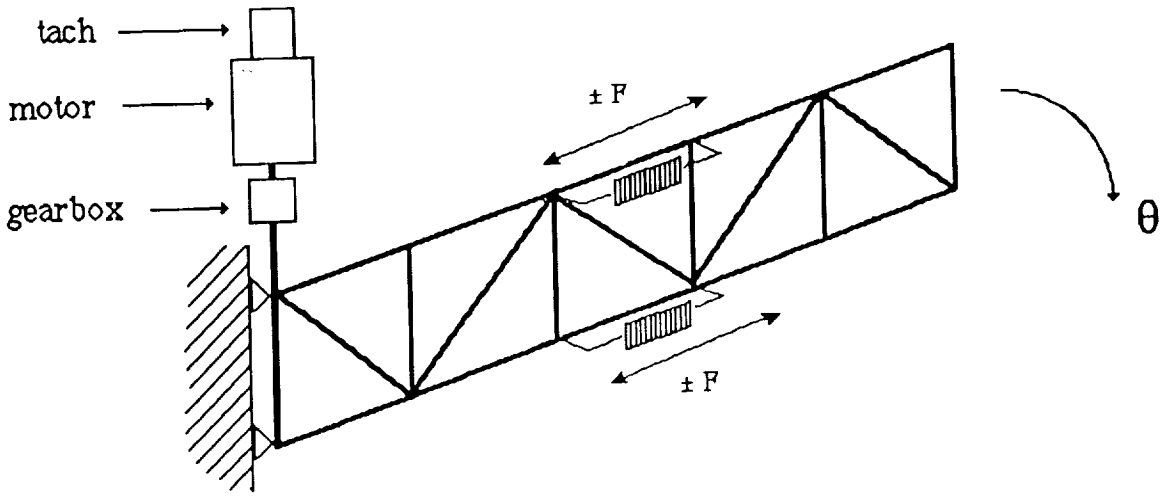

Fig. 4. The experimental slewing frame with active, piezoceramic struts in bending.

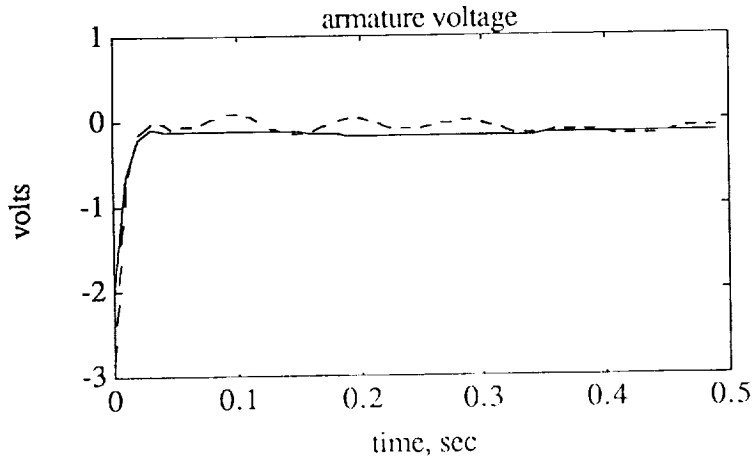

Fig. 5. Voltage applied to the armature of the motor for each of the two control laws.

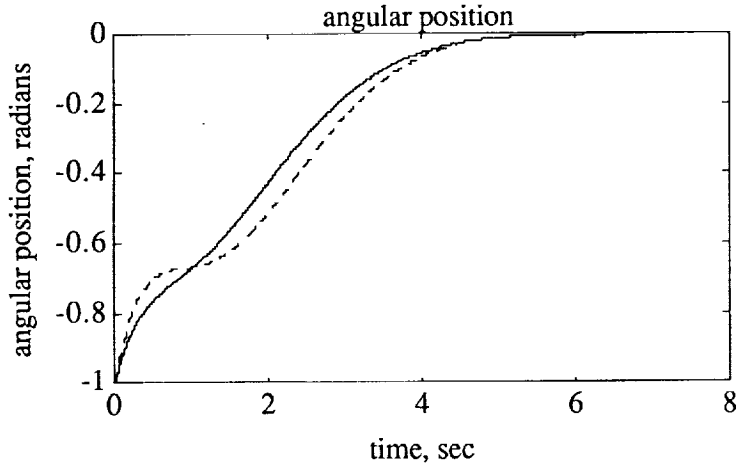

Fig. 6. Angular position versus time for each of the two control laws.

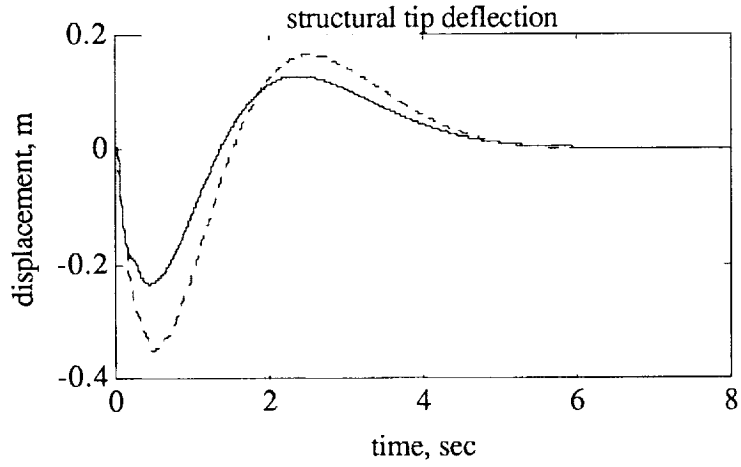

Fig. 7. The deflection of the tip of the beam versus time for each of the two control laws.

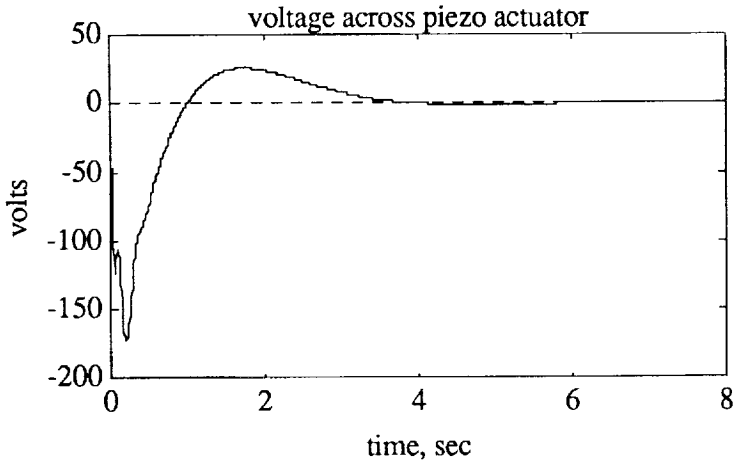

Fig. 8. The voltage applied to the piezoceramic versus time for each of the two control laws.

References

Burke S. B., and Hubbard J. E., 1987, "Active Vibration control of a Simply Supported Beam Using a Spatially Distributed Actuator" *IEEE Control Systems Magazine*, Vol . 7 No. 4.

Cannon, H.C. Jr. and Schmitz, E., 1984, "Initial Experiments on the End-Point Control of a Flexible One-Link Robot," *International Journal of Robotics Research*, Vol. 3, No. 3, pp. 62-75.

Crawley, E.F. and Anderson, E.H.,1990, "Detailed Models of Piezoceramic Actuation of Beams, "*Journal of Intelligent Material Systems and Structures*, Vol. 1, pp. 4-25. Also AIAA paper number 89-1388 CP in the *Proceedings of 1989 AIAA Structure Dynamic and Materials Conference*, pp. 2000-2010.

Fanson J. L. and Caughey T.K., 1987, "Positive Position Feedback Control for Large Space Structures," AIAA Paper No. 87-0902.

Garcia, E.,1989, "On the Modeling and Control of Slewing Flexible Structures," Ph. D. Thesis, Department of Mechanical and Aerospace Engineering, State University of New York at Buffalo.

Garcia, E., Inman, D.J., 1990, "Modeling Actuator-Structure Interaction in the Slewing of Flexible Structures," *Proceedings of the American Controls Conference*, San Diego, California, May 23-25, to appear.

Hastings, G.G. and Book, W.J., 1987, "A Linear Dynamic Model for Flexible Robotic Manipulators," *IEEE Control Systems Magazine*, pp. 61-64.

Inman, D.J., Garcia, E. and Pokines, B., 1990, "Issues in Slewing an Active Structure," Proceedings U.S.-Japan Workshop on Smart/Intelligent Materials and Structures, May 1990.

Juang, J.N., Horta, L.G. and Robertshaw, H.,1986, "A Slewing Control Experiment for Flexible Structures," *AIAA Journal of Guidance, Control and Dynamics*, Vol. 9, No. 5, pp. 599-607.

Park, Y.-P., Kim, S.-H., Ha, Y.-K., Park, H.-S., 1989, "Analysis and Test on the Digital Optimal Control of a Flexible Rotor Arm Vibration," *Proceeding of the 7th International Modal Analysis Conference*, pp. 1489-1495.

Randall, D. S., and O'Neill, C. G., 1981, "Axial-mode Piezoelectrically-Driven Beam Deflectors" SPIE Vol. 299 Advances In Laser Scanning Technology.

Wada, B.K., 1989 (ed), *Adaptive Structures*, Book No. AD-Vol. 5, ASME, New York, NY.

Yurkovich, S. and Tzes, A., 1990, "Experiments in Identification and Control of Flexible-Link Manipulators," *IEEE Control Systems Magazine*, Vol. 10, No. 2.

Candidate Proof Mass Actuator Control Laws for the Vibration Suppression of a Frame

Jeffrey W. Umland†

Daniel J. Inman††

Dept. of Mechanical and Aerospace Engineering
University at Buffalo
Buffalo, NY 14260

Abstract

The vibration of an experimental flexible space truss is controlled with internal control forces produced by several proof mass actuators. Four candidate control law strategies are evaluated in terms of performance and robustness. These control laws are experimentally implemented on a quasi free-free planar truss. Sensor and actuator dynamics are included in the model such that the final closed loop system is self-equilibrated. The first two control laws considered are based on direct output feedback and consist of tuning the actuator feedback gains to the lowest mode intended to receive damping. The first method feeds back only the proof mass's position and velocity relative to the structure, this results in a traditional vibration absorber. The second method includes the same feedback paths as the first plus feedback of the local structural velocity. The third control law is designed with robust H_∞ control theory. The fourth control strategy is an active implementation of a viscous damper, where the actuator is configured to provide a bending moment at two points on the structure.

The vibration control system is then evaluated in terms of how it would benefit the space structure's position control system. This assessment is necessary since the additional actuator dynamics in the model effectively adds two state variables to the system which could lead to instabilities in the position control system.

1 Introduction

Proof mass actuators (PMA's) have been considered for use in large space structure vibration control systems[1]. These control systems are usually configured such that the PMA's provide a closed loop control force based on the output from a combination of both colocated and noncolocated sensors[2,3]. The colocated sensor provides measurements of the position of the proof mass relative to the structure. A benefit of colocated control is that stable control laws can be designed that provide vibration attenuation at the point of actuator attachment. Several experimental implementations of colocated PMA control have resulted in control laws that are based on the traditional vibration absorber[4,5]. In an effort to gain increased vibration attenuation, noncolocated sensors provide actual structural vibration measurements at the point where performance is desired. The problem of designing a noncolocated control is constrained by the requirement that the control law must provide stable vibration suppression at sensor locations on a flexible structure that is not necessarily well modeled.

This paper addresses the issue of the effective use of the proof mass actuator's control effort towards the robust vibration suppression of a flexible unconstrained planar frame. An

† Graduate Research Assistant
†† Professor

unconstrained or free-free structure is used, rather than a constrained or cantilevered structure. It is observed that in some cases an entire vehicle will vibrate indicating that a constrained analysis is not appropriate[7,8]. The approach taken is to compare several control law and actuator-sensor combinations when the actuator provides a point force on the structure. As a counterpoint, the actuator is also mounted to the structure such that the actuator's control effort provides both an axial force and a bending moment applied at two points on the structure. A control structure interaction approach is undertaken in the sense that the actuator, sensor, and controller dynamics are included or accounted for in the structural control design.

The paper outline is as follows: Section 1 gives an introduction to the control structure interaction problem undertaken here. The flexible structure control testbed is described in Section 2. The PMA control law designs to be compared are detailed in Section 3. The results of experimental implementation of these control laws are provided in Section 4. The research is summarized in the final section.

2 Hardware Description

The experimental flexible structure is constructed such that it exhibits the characteristics commonly associated with large flexible space structures. The structure is light weight, with most of its mass concentrated at the joints. There are both colocated and noncolocated sensors and actuators. The structure displays numerous modes of vibration that have a low natural frequency, are lightly damped, and are closely spaced relative to each other. A soft cable suspension system is used to simulate the free boundary conditions of space, and to minimize the effects of attaching the structure to ground.

2.1 Flexible Structure

Figure 1 illustrates the 6-bay, 3 m long plane frame. The width of the structure is 0.5 m, and the diagonal dimension is 0.707 m. The frame is constructed from aluminum truss links and joints manufactured by the Mero Corporation. A truss link consists of an aluminum tube, with nominal cross section dimensions of 22 mm O. D. and 20 mm I. D., terminated in bolt assemblies which attach to the truss nodes. The truss node is Mero's standard M12 aluminum node. The links are attached to the nodes and tightened with a torque wrench to 25 in-lb. The total weight of the structure is 61 N.

The frame is suspended from the ceiling by two soft bungee cables 2 m in length. It was found necessary to double up the cables to support the total weight of the structure and actuators. The cables are attached at nodes 2 and 6. These joints were chosen for the suspension points since they were nearly coincident with the nodes of the first structural mode of vibration, therefore minimizing the interaction of the structure and its suspension. The electrical cables are suspended from the ceiling such that they do not carry the weight of the structure, and the mass loading of the structure by these cables is minimized.

The dynamic characteristics of this structure are evident in figure 2, which shows an experimental transfer function of node 1's linear acceleration in the x direction given an impact at node 1 in the x direction. The modal properties of the first 8 structural modes of vibration are given in table 1. The vibration of the frame is characterized by flexural deflection rather than axial deflection that would occur in a true truss structure. The structure is sufficiently long such that the low structural vibration modes are not coupled to local member bending modes.

Not all of the dynamic characteristics displayed in figure 2 can be attributed to the structure, rather the suspension provides a significant portion of the response shown in this test. Three pendulous modes at approximately 1/3 Hz replaced the three rigid body modes in the x-y plane. A double pendulum mode at 1.2 Hz replaced the rigid body rotation about the y -axis. Translation in the z direction and rotation about the x axis are replaced by two translational vibration modes at 1/2 Hz which are due to stretching of the suspension cables. The cables also have transverse vibration modes that occur at 12 Hz, 37 Hz, and 55 Hz.

2.1.1 Structural Model

A finite element model of the structure was constructed for use in control design. The frame links were modeled as uniform aluminum tubes whose dimensions are the same as the manufacturer's nominal specifications. The frame joints were modeled as rigid. The combined mass of the joints and the link bolt assemblies were modeled as a point mass, with zero rotational inertia, located at each finite element node. Table 2 gives the structural parameters used in the finite element analysis. In order to simplify the model, Guyan reduction was used to eliminate translation in both the z and y directions, and rotations about the x axis. Only motion out of the y-z plane is modeled.

The transverse vibration of the suspension cables was also modeled, since these vibration modes appear in the control bandwidth. Modeling the suspension gave better agreement between the pole-zero pairs as shown in figure 2.

2.2 Proof Mass Actuators

The proof mass actuators used are illustrated in figure 3. These actuators were originally developed at the NASA Langley Research Center[1]. The intent of this design is that a magnetic field is produced by the permanent magnets and the iron in the proof mass that is normal to the current flowing through conductors in the coil. This electromagnetic coupling is then described by Eq. 1.

$$\mathbf{F} = nl\mathbf{I} \times \mathbf{B} \tag{1}$$

I represents the current carried in the conductor, n the number of conductors in the gap, **B** the magnetic field across the gap, l the length of the conductor. An average conductor length is found from the average circumference around the coil. A useful control force oriented along the axis of the coil results from this coupling. This force is then applied to the conductors in the coil, and subsequently the structure. The reaction of this force is applied to the proof mass and causes it to translate upon a linear bearing. Hence, the PMA can be modeled as providing an ideal point force at the place of attachment on the structure and a reaction force on the proof mass. This force is taken to be proportional to the current supplied to the coil. The power amplifier for the actuator is configured as a current amplifier, which provides a means by which the actuator can be controlled by a voltage signal. The proof mass actuator characteristics are given in table 3.

A complete model of the PMA should also include the dead mass and rotational inertia associated with the actuator. The motivation behind this is that for lightweight structures the actuator's dead mass will constitute a significant percentage of the total mass of the structure. The addition of a relatively large discrete mass to a structure has the tendency to attract the nodes of the higher modes of vibration of the structure to the point of attachment. This effect minimizes the ability of a point force to provide a useful control force to higher modes of vibration. The rotational inertia of the actuator used here cannot be considered negligible compared to the structure. The high actuator inertia is in part due to the overall length of actuator measured from the base.

2.2.1 Actuator Nonlinearities

There are several nonlinearities associated with the actuator, several of these are better described as saturation limits. The total stroke length of the proof mass is ±0.0127 m. The actuator produces a useful control force only when the proof mass is free to translate. Therefore, feedback of the proof mass position relative to the structure is used to maintain the proof mass in

the center of its stroke. The finite stroke length is the limiting factor for low frequency, large amplitude motions.

The power amplifier used is operated as a voltage controlled current amplifier On the amplifier there is a current limiter that provides for a saturation limit on the output. The maximum output current of the amplifier determines the maximum force output of the actuator. An important design tradeoff here is to determine how much control effort should be used towards the proof mass centering force and how much should be available for a control force based on a noncolocated sensor.

The damping in the actuator is primarily due to friction in the linear bearing and steel shaft interface. This friction has been described by a typical Coulomb friction relation. The normal load that generates the friction force is a combination of the weight of the proof mass and a magnetic force between the permanent magnets and the steel shaft and ball bearings. These frictional effects further limit the effectiveness of the actuator at low frequencies. Secondly, the source of the damping is important in the sense that previously implemented PMA control laws have relied upon available actuator damping to obtain closed loop stability. The problem is that a large portion of this damping would not be available in a zero-g environment.

The electromagnetic coupling between the coil and the proof mass is described by Eq. 1 for only a portion of the total stroke. This is illustrated in figure 4. This plot shows the static force produced by the actuator for a constant input current. Ideally the actuator should output a constant force for a constant input current independent of the stroke position. During bench testing of the actuator, this led to closed loop instability.

2.2.2 Attachment to Structure

The structural equations of motion must be modified to include the actuator dynamics. The structure is originally described by m degrees of freedom $\mathbf{x}$, and if n actuators are used then n degrees of freedom represented by the relative displacements η are appended to the equations of motion. Note that the coupling appears in the mass matrix rather than the stiffness matrix.

$$M_{ol}\,\ddot{\mathbf{x}} + K_{ol}\,\mathbf{x} = B\,\mathbf{f_g} \tag{2a}$$

$$\mathbf{x} = \left\{ x_{fem} \quad \eta_{act} \right\}^T \tag{2b}$$

$$K_{ol} = \begin{bmatrix} K_{fem} & 0_{mxn} \\ 0_{nxm} & 0_{nxn} \end{bmatrix} \tag{2c}$$

$$M_{ol} = \begin{bmatrix} M_{fem} & 0_{mxn} \\ 0_{nxm} & 0_{nxn} \end{bmatrix} + \begin{bmatrix} M_d + J_d + M_{p1} & M_{p2} \\ M_{p2}^T & m_p I_{nxn} \end{bmatrix} \tag{2d}$$

$$M_d = m_d\ \mathrm{diag}(0,\ldots,\ 0,1,0,0,\ldots.,0) \tag{2e}$$

$$J_d = j_d\ \mathrm{diag}(0,\ldots,\ 0,0,1,0,\ldots.,0) \tag{2f}$$

$$M_{p1} = m_p\ \mathrm{diag}(0,\ldots,\ 0,1,0,0,\ldots.,0) \tag{2g}$$

$$M_{p2j} = m_p(0,\ldots,\ 0,1,0,0,\ldots.,0)^T,\ j = 1{:}n \tag{2h}$$

$$B = \begin{bmatrix} 0_{mxn} \\ g_{act} I_{nxn} \end{bmatrix} \tag{2i}$$

2.3 Linear Variable Differential Transformer

A linear variable differential transformer (LVDT) is mounted on each PMA to provide a measurement of the proof mass position relative to the structure. The LVDT used is a Schaevitz Eng. No. 500. The input voltage is selected such that a displacement of ±0.375 inch produces ±5 Volts. The sensor bandwidth is 0 - 500 Hz. These sensors produce a measurement that is colocated with the control force.

2.4 Accelerometers

The structural sensors are Kistler Piezobeam accelerometers. The calibration is 10 mv/g, and have a frequency range of 0.5 to 5000 Hz. An approximate integrator is then used to integrate the acceleration signal to provide a measurement of the structural velocity[2]. The approximate integrator is given by the following input/output description

$$\frac{O}{I}(s) = \frac{\omega_c^2 s}{s^2 + \omega_c s + \omega_c^2} \tag{3}$$

This approximate integrator is the combination of a critically damped unity gain second order low pass filter, and a pure differentiator. The low pass filter provides the integrating action, while the differentiator removes the DC portion of the input signal. The transfer function is strictly proper, giving a state space realization for either analog or digital implementation. This type of integrator is used in order to avoid the integration of any DC bias produced by the accelerometer and associated signal conditioning.

2.5 Digital Controller

The digital controller used is a Systolic Systems Optima 3. The input and output voltage range is ±5 Volts The input channels are anti-alias filtered and the output channels are smooth filtered. The digital to analog converters on this system present a practical design issue, since they do not saturate. Rather, when the control law produces an output that exceeds the output range of the converter the conversion process wraps the desired signal value around the available output range. In other words, if the control law produces a desired signal of 6 Volt, the D/A converters will produce a -4 Volt signal. The solution to this problem used is to place the static controller gain on the power amplifiers. This is fine for static compensators or direct output feedback of sensor signals of known and bounded signal strength, such as the LVDT output. For dynamic compensators this is not necessarily a robust solution. A second solution would be to place logic statements in the control software that would provide saturation levels. Such logic statements would lower the achievable sampling rate.

3 Control Design

The application of a proof mass actuator to the control of a simple flexible structure is considered in this section. The structure consists of one rigid body mode, and one flexible mode of vibration. This problem is illustrated in figure 5. This problem has been proposed as a benchmark robust control problem[14]. The difference here is that the control force is produced by an actuator whose dynamics cannot be ignored. The open loop equations for this system are given by

$$\begin{bmatrix} M_S & 0 & 0 \\ 0 & M_S+m_p+m_d & m_p \\ 0 & m_p & m_p \end{bmatrix}\begin{Bmatrix} \ddot{x}1 \\ \ddot{x}2 \\ \ddot{\eta} \end{Bmatrix} + \begin{bmatrix} K_S & -K_S & 0 \\ -K_S & K_S & 0 \\ 0 & 0 & 0 \end{bmatrix}\begin{Bmatrix} x1 \\ x2 \\ \eta \end{Bmatrix} = g_{act}\begin{Bmatrix} 0 \\ 0 \\ 1 \end{Bmatrix} f_g(t) + \begin{Bmatrix} -1 \\ 1 \\ 0 \end{Bmatrix} d(t) \qquad (4)$$

The measurement equations are for the relative position, η,

$$y_p = K_{LVDT}\eta = [0\ 0\ K_{LVDT}]\ \mathbf{x} \qquad (5)$$

The following values are used for all calculations in this section.

$M_s = 1$
$0.5 < K_s < 2$, nominally $K_s = 1$
$m_p = 0.2$
$m_d = 0$
$g_{act} = 1$
$K_{LVDT} = 1$

In the following subsections several vibration control strategies are considered. The effectiveness of each system is then evaluated by giving the system an impact disturbance across masses 1 and 2, and the response of x_2 is measured. This type of disturbance does not excite the system's rigid body mode.

3.1 Controllability

The controllability of this system is then computed with standard techniques[9]

$$\text{rank}\left[B\ AB\ A^2B\ \ldots\ A^5B\right] = 4 \neq 6 \qquad (6)$$

Indicating that the system is not completely controllable. The control force produced by the actuator should be considered as a force internal to the system, and as such cannot change the location and motion of the system's center of mass. The lack of complete controllability is because the actuator cannot control the rigid body mode of the system. A further explanation of this is the actuator configured as a point force cannot produce a force at zero frequency. Therefore, a statement of the obvious is that the actuator should be only used for vibration control. In other words the actuator should be used to give the structure damping. It is also evident that a rigid body control system must be designed for this system. A design goal for the vibration control system is that it should enhance the rigid body controller.

3.2 Observability

The observability of the system is computed from

$$\text{rank}\left[C\ CA\ CA^2\ \ldots\ CA^5\right]^T = 4 \neq 6 \qquad (7)$$

Indicating that the system is also not completely observable. Similar to the previous section the rigid body modes of the system are not observable.

3.3 Vibration Absorber

The first control law considered is direct feedback of the relative proof mass position, η, and velocity, $\dot{\eta}$. This is considered a colocated design, since the resulting closed loop stiffness and damping matrices are symmetric. Although the LVDT measures the position η only, it is assumed that $\dot{\eta}$ is available from a lead network or digital derivative. This type of feedback compensation is a proportional plus derivative control. Equivalently, this type of control may also be thought of as designing an actuator spring stiffness, k_a, and viscous damper, c_a. One criterion for the choice of the feedback gains, k_a and c_a, is that used to design a passive vibration absorber[10,11,4]. The actuator spring stiffness is found from

$$\omega_a^2 = \frac{k_a}{m_p} = \frac{\omega_i^2}{(1+\mu_a)^2} \tag{8}$$

$$c_a^2 = m_p \mu_a \omega_i^2 \frac{1}{(1+\mu_a)^3} \tag{9}$$

$\mu_a = m_p(\phi_{ij})^2$
$k_a = g_{act} K_{pos} K_{LVDT}$
$c_a = g_{act} K_{vel} K_{LVDT}$
ω_i - frequency of interest, ith mode
ϕ_{ij} - jth degree of freedom, eigenvector of the ith mode, normalized with respect to the mass matrix

The resulting closed loop equations of motion are then

$$\begin{bmatrix} M_S & 0 & 0 \\ 0 & M_S+m_p+m_d & m_p \\ 0 & m_p & m_p \end{bmatrix} \begin{Bmatrix} \ddot{x}1 \\ \ddot{x}2 \\ \ddot{\eta} \end{Bmatrix} + \begin{bmatrix} 0 & 0 & 0 \\ 0 & 0 & 0 \\ 0 & 0 & c_a \end{bmatrix} \begin{Bmatrix} \dot{x}1 \\ \dot{x}2 \\ \dot{\eta} \end{Bmatrix} + \begin{bmatrix} K_S & -K_S & 0 \\ -K_S & K_S & 0 \\ 0 & 0 & k_a \end{bmatrix} \begin{Bmatrix} x1 \\ x2 \\ \eta \end{Bmatrix} = \begin{Bmatrix} -1 \\ 1 \\ 0 \end{Bmatrix} d(t) \tag{10}$$

Alternatively, the feedback gains can be calculated from the following quadratic cost function[11]

$$J = E\left[\int_0^\infty q_{ei}^2 \, dt\right] = E\left[\int_0^\infty \mathbf{z}^T \mathbf{Q} \mathbf{z} \, dt\right] \tag{11}$$

This system is stable provided that the feedback gains, k_a and c_a, are positive. The constant gain feedback of sensor signals that are colocated with an actuator does not destabilize the system. The colocation of sensors and actuators is evidenced by the symmetric closed loop stiffness and damping matrices.

The spring stiffness and damping coefficient for this example are calculated to be

$k_a = 0.331$
$c_a = 0.173$

The response of x_2 for the given disturbance is shown in figure 7. The responses shown are calculated for the minimum, maximum and nominal value for the structural spring stiffness, K_s. The vibration control system's performance when K_s is increased to its maximum value is comparable to its performance for the nominal value of K_s. On the other hand, when K_s is allowed to decrease to its minimum the performance of the system is diminished.

The performance of this type of control is explained in a control system sense as a pole-zero cancellation. The second order dynamics of the PMA add a pole and a zero to the system, which will be less that the structure's pole and zero. The zero associated with the structure will appear in between the actuator pole and the structural pole. These poles are closely spaced, since the mass ratio, μ_a, is usually small. Hence, the structural zero will tend to cancel either the actuator or the structural pole, depending on sensor and actuator placement. Because this type of control relies upon pole zero cancellation its effectiveness for more than one mode of vibration is limited.

3.4 Direct Velocity Feedback

The second control strategy considered consists of direct structural velocity feedback[13]. The idea being that the actuator will provide a force at a given point on the structure that is directly proportional and opposite in direction to the structure's velocity at that point. It is pointed that the control force is determined on the basis of both a colocated and a noncolocated sensor. Therefore, the stability of the closed loop system must be considered. The difficulty here is the design of the feedback compensator to provide the proof mass centering force. The control force is given as

$$f_g(t)= c\,\dot{x}_2 - f(\eta) \tag{12}$$

where $f(\eta)$ represents the output of the feedback compensator.

In the following subsections the velocity feedback gain, c, is held constant and two feedback compensators for η are designed. The value used for the feedback gain c is

$$c = 0.5$$

3.4.1 Direct Output Feedback

In this section a proportional plus derivative compensator is designed for the feedback of the proof mass relative position, η. Again, this type of control may be thought of as determining an equivalent actuator spring stiffness, k_a, and viscous damper, c_a. The control force is

$$f_g(t)= c\,\dot{x}_2 - k_a\eta - c_a\dot{\eta} \tag{13}$$

The closed loop equations of motion for this system are then

$$\begin{bmatrix} M_S & 0 & 0 \\ 0 & M_S+m_p & m_p \\ 0 & m_p & m_p \end{bmatrix}\begin{Bmatrix} \ddot{x}1 \\ \ddot{x}2 \\ \ddot{\eta} \end{Bmatrix} + \begin{bmatrix} 0 & 0 & 0 \\ 0 & 0 & 0 \\ 0 & -c & c_a \end{bmatrix}\begin{Bmatrix} \dot{x}1 \\ \dot{x}2 \\ \dot{\eta} \end{Bmatrix} + \begin{bmatrix} K_S & -K_S & 0 \\ -K_S & K_S & 0 \\ 0 & 0 & k_a \end{bmatrix}\begin{Bmatrix} x1 \\ x2 \\ \eta \end{Bmatrix} = \begin{Bmatrix} -1 \\ 1 \\ 0 \end{Bmatrix} d(t) \tag{14}$$

This is a noncolocated control system, and as such its stability is in question. The characteristic equation for this system is evaluated to be

$$s^2\left[s^4 + \left(\frac{c_a+c}{M_s} + \frac{c_a}{m_p}\right)s^3 + \left(\frac{2K_s+k_p}{M_s} + \frac{k_p}{m_p}\right)s^2 + \left(\frac{(c_a+c)K_s}{M_s^2} + \frac{2c_aK_s}{M_sm_p}\right)s + \left(\frac{K_sk_p}{M_s^2m_p}(2M_s + m_p)\right)\right] = 0 \qquad (15)$$

Applying the Routh-Hurwitz test to portion of the characteristic equation inside the brackets the following stability relation is obtained, assuming that each individual parameter is positive

$$\left(c_a^2 + 2c_ac + c^2\right)K_s^2m_p^2 + \left[2\left(c_a^2 + c_ac\right)K_s^2 + \left(-c_ac - c^2\right)K_sk_a\right]M_sm_p - c_acK_sk_aM_s^2 > 0 \qquad (16)$$

When the actuator damping is held at zero, i. e. $c_a = 0$, Eq.13 reduces to

$$\frac{K_s}{M_s} > \frac{k_a}{m_p} \qquad (17)$$

In other words, the actuator natural frequency should be less than the structure's natural frequency of vibration. Also, note that the velocity feedback gain, c, is not present in Eq. 14. Figure 6 illustrates the stability boundary of k_a for a range of both c_a and c, for the nominal spring stiffness K_s. Actuator spring stiffnesses below this boundary result in a stable system. The smallest stable k_a in figure 6 occurs for $c_a = 0$, independent of c. Also, the surface is relatively flat over most of the range of c_a and c, indicating that in this case stability is insensitive to actuator damping. In order to ensure stability robustness against the permissible variations in the structural spring stiffness, K_s, the minimum permitted value should be used as the nominal of design value.

The feedback gains, k_a and c_a, are determined by following the same optimization strategy that was outlined in the previous section[12]. For this example k_a and c_a are found to be

$k_a = 0.105$
$c_a = -0.0027$

The performance of this system is illustrated in figure 8. The system's settling time for both the nominal and maximum spring stiffnesses is less than that of the vibration absorber design. Although it is not apparent in this figure, when K_s is varied to its minimum value the system becomes unstable.

Following this strategy the actuator spring stiffness is found to be less than the vibration absorber spring stiffness. Performance is improved with an increased feedback gain c. In comparison to the vibration absorber system the proof mass here exhibits more relative motion and does more work on the structure.

3.4.2 Robust Control Design

An attempt to design a compensator for the feedback of the relative position, η, using an H_∞ robust control design technique was unsuccessful. The system rigid body modes were first removed from the state space equations of motion by model reduction. The rigid body mode associated with the proof mass was retained in the system equations, since it is this output that the compensator is being designed to control. The H_∞ design procedure failed because there was a plant pole on the $j\omega$-axis which then produces a closed loop pole also on the $j\omega$-axis.

3.5 Passive Damper

As a counterpoint to the above control designs the actuator is also configured to act as a passive linear damper which applies a bending moment at two locations on the structure, as shown in figure 10. Only feedback of the proof mass relative velocity, $\dot{\eta}$ is used here. In other words this is direct velocity feedback. A proof mass centering force is not required since this is provided for by the structure and fixturing. The actuator can be attached at nonadjacent joint locations to better distribute the control effort to low frequency modes.

4 Experimental Implementation

The experimental implementation of the control laws considered above is addressed in this section. An impact is given to the structure at node 1 in the x direction and the structure's acceleration is measured at node 4 also in the x direction. Each response is filtered with a 25 Hz low pass filter to give a cleaner picture of the actuator's effect. The resulting settling time for each test is used as a measure of control law performance. The actuator location is chosen in order to provide the greatest effect on the first vibration mode. The control laws are implemented digitally, with the sampling rate for each set at 4000Hz. As a basis for comparison the response of the uncontrolled structure is shown in figure 10. The settling time for this test is greater than 3.5 seconds. It is also evident that the structure must be considered more complicated than a single degree of freedom.

The vibration absorber was designed to provide damping to the first mode whose frequency is shifted to 5.8 Hz when the actuator dead mass and inertia are added. The actuator is placed at node 4. The result of this implementation is illustrated in figure 11. It is seen here that the settling time is reduced in comparison to the uncontrolled structure, but is greater than 2.5 seconds. When the actuator was tuned to the second mode at approximately 12 Hz the actuator was made unstable. This is a result of the nonlinear electromagnetic coupling of the coil and permanent magnets.

The effect of adding structural velocity feedback is shown in figure 12. The acceleration of node 4 is integrated by the approximate integrator given in Eq. 3. The cutoff frequency for the integrator is 1 Hz. Following the stability guideline for this case the actuator spring stiffness is kept low such that the actuator frequency is below that of the first mode of vibration. The settling time for this case is an improvement from the vibration absorber. Figure 12 displays a signal of approximately 1 Hz, which is the double pendulum mode of the structure suspension system. Closed loop instability for this set of feedback paths resulted when the magnitude of the disturbance impact caused the proof mass to hit the end of its stroke. These resulting impacts caused the accelerometer to overload which subsequently made the control computer overflow which induced the more proof mass impacts.

Figure 13 illustrates that the viscous damper implementation has an effect comparable to that of using structural velocity feedback. Although, there is more second mode behavior for this case. The actuator was attached at nodes 3 and 5. In comparison to the point force application of the actuator where the proof mass uses the entire stroke length, the travel of the proof mass here is at most 0.25 in.

5 Conclusions

Several structural vibration control laws have been considered analytically and implemented experimentally. Two of these control strategies are essentially active implementations of passive control concepts, namely the viscous damper and the vibration absorber. The feedback of the local structural velocity is an active control idea. A control structure interaction approach was taken in the sense that the actuator dynamics were included in the control design, and that there are several nonlinearities in the closed loop system that can lead to instability.

6 References

[1]Zimmerman, D. C., G. C. Horner, and D. J. Inman, 1988. "Microprocessor Controlled Force Actuator," *AIAA J. of Guidance, Control, and Dynamics*, Vol. 11, No. 3, pp. 230-236.

[2]Hallauer, W. and S. Lamberson, 1989. "Experimental Active Vibration Damping of a Plane Truss Using Hybrid Actuation," AIAA Paper No. 89-1169, *Proc. of the 30th AIAA/ASME/ASME/ASCE/AHS/ASC Structures, Structural Dynamics, and Materials Conference*, Mobile, AL, pp. 80-90.

[3]Balas, G. J., and J. C. Doyle, 1990. "Collocated versus Non-collocated Multivariable Control for Flexible Structure," *Proc. of the 1990 American Control Conference*, San Diego, CA, pp. 1923-1928.

[4]Minas, C., E. G. Garcia, D. J. Inman, 1989. "Control of a Flexible Planar Truss Using Proof Mass Actuators," *Proc. of the 3rd Annual Conference on Aerospace Computational Control*, Oxnard, CA, pp. 434-445.

[5]Miller, D. W. and E. F. Crawley, 1988. "Theoretical and Experimental Investigation of Space-Realizable Inertial Actuation for Passive and Active Structural Control," *AIAA J. of Guidance, Control, and Dynamics*, Vol. 11, No. 5, pp. 449-458.

[6]Balas, M. J., 1982, "Trends in Large Space Structure Control Theory: Fondest Hopes, Wildest Dreams," *IEEE Trans. on Automatic Control*, Vol. AC-27, No. 3, pp. 522-535.

[7]Hablani, H. B., 1982. "Constrained and Unconstrained Modes: Some Modeling Aspects of Flexible Spacecraft," *AIAA J. of Guidance, Control, and Dynamics*, Vol. 5, No. 2, pp. 164-173.

[8]Hughes, P. C., 1974. "Dynamics of Flexible Space Vehicles with Active Attitude Control," *Celestial Mechanics*, Vol. 9, pp 21-39.

[9]Inman, D. J., 1989. *Vibration with Control, Measurement, and Stability*, Prentice Hall, Englewood Cliffs, NJ.

[10]Den Hartog, J. P., 1956. *Mechanical Vibrations*, 4th ed., McGraw-Hill Book Co., New York, NY.

[11]Juang, J., 1984. "Optimal Design of a Passive Vibration Absorber for a Truss Beam," *AIAA J. of Guidance, Control, and Dynamics*, Vol. 7, No. 6, pp. 733-739.

12 Umland, J. W., 1989. "Proof Mass Actuators and Vibration Absorption," Mechanical Systems Laboratory Report No. 89-10, State University of New York at Buffalo, Buffalo, NY.

[13]Balas, M. J., 1979. "Direct Velocity Feedback Control of Large Space Structures," *AIAA J. Of Guidance and Control*, Vol. 2, No. 3, pp. 252-253.

[14]Wie, B., and D. S. Bernstein, 1990. "A Benchmark Problem for Robust Control Design," *Proc. of the 1990 American Control Conference*, San Diego, CA, pp. 961-962.

Mode #	Experimental Natural Frequency (Hz)	Damping Ratio (%)	MSC/PAL Natural Frequency (Hz)	Mode Type
1	6.4	0.021	6.5	1st bending
2	15.1	0.026	15.6	1st torsional
3	17.7	0.010	17.7	2nd bending
4	29.6	0.018	29.9	2nd torsional
5	35.4	0.025	35.2	3rd bending
6	45.6	0.014	45.2	3rd torsional
7	58.0	0.026	55.6	4th bending
8	63.3	0.022	60.8	4th torsional

Table 1: Modal Properties of Flexible Structure

Link O. D.	d_o	22 mm
Link I. D.	d_i	20 mm
Density	ρ	2.45×10^3 kg/m^3
Elastic modulus	E	70 GPa
Shear modulus	G	26 GPa
Joint mass	m_j	0.0759 kg
Bolt mass	m_b	0.0578 kg

Table 2: Structure link and joint characteristics

Proof mass	m_p	0.225 kg
Dead mass	m_d	0.730 kg
Dead inertia	j_d	0.008 kg-m^2
Force constant	g_{act}	2.75 N/A
Friction coefficient	μ	0.01

Table 3: Linear Proof Mass Actuator Properties

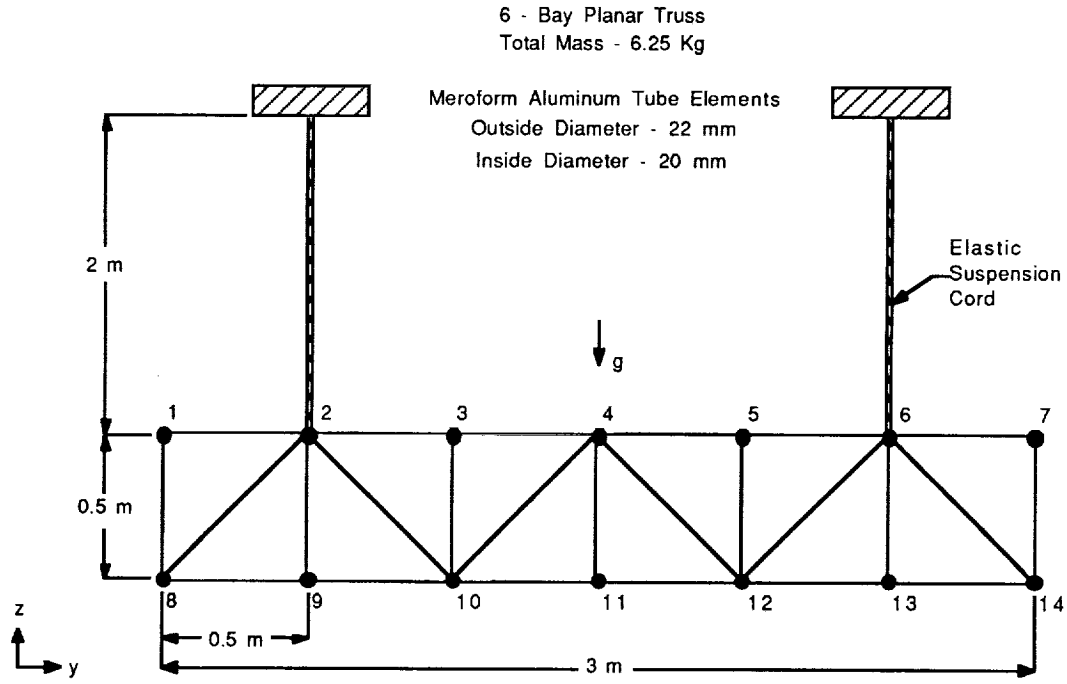

Figure 1: Experimental Flexible Structure

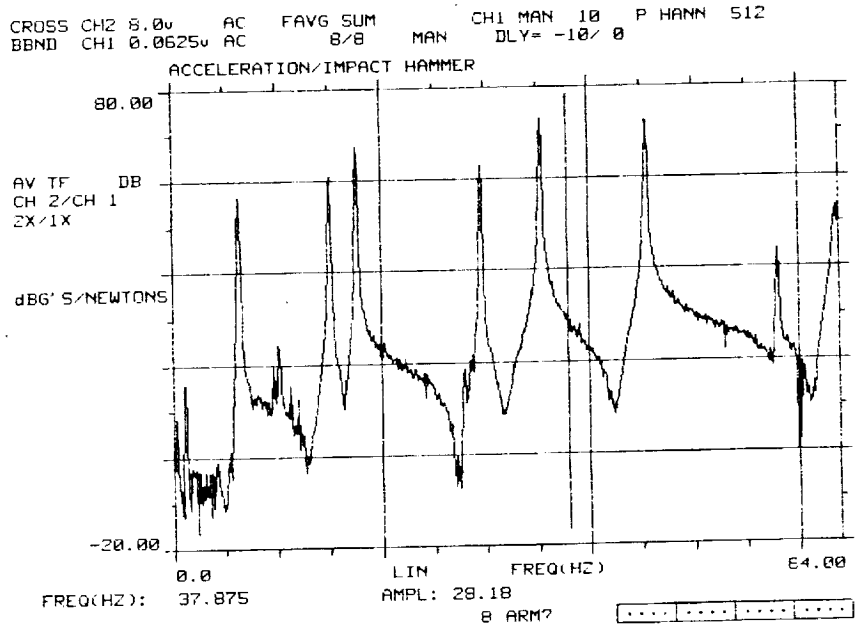

Figure 2a: Experimental Frequency Response

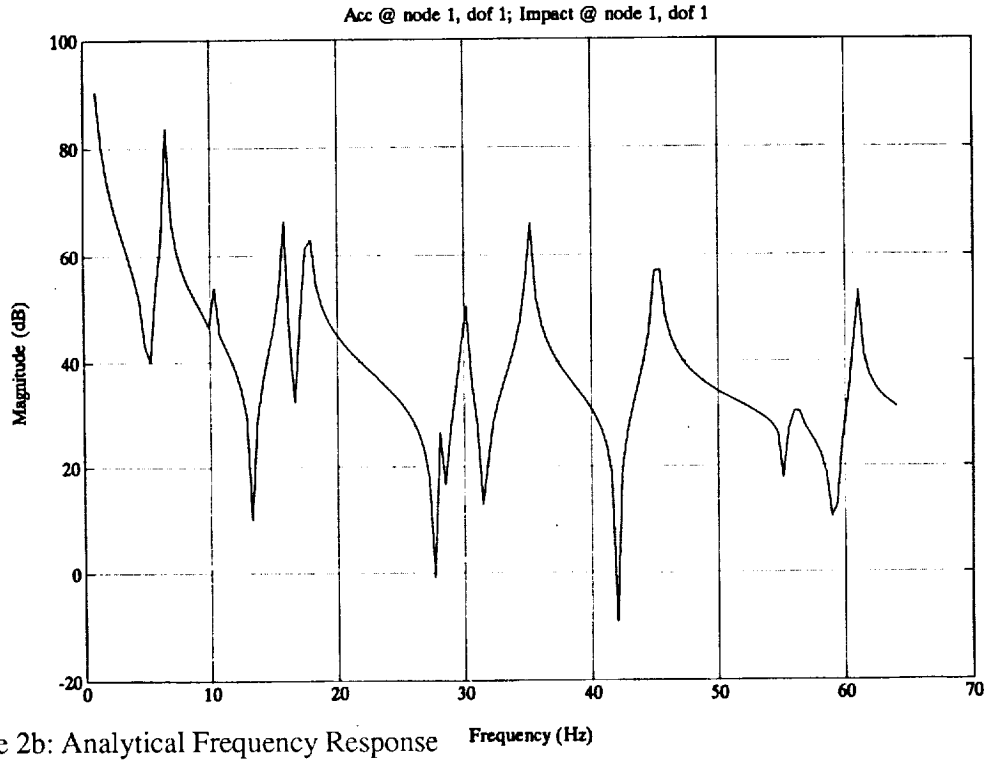

Figure 2b: Analytical Frequency Response

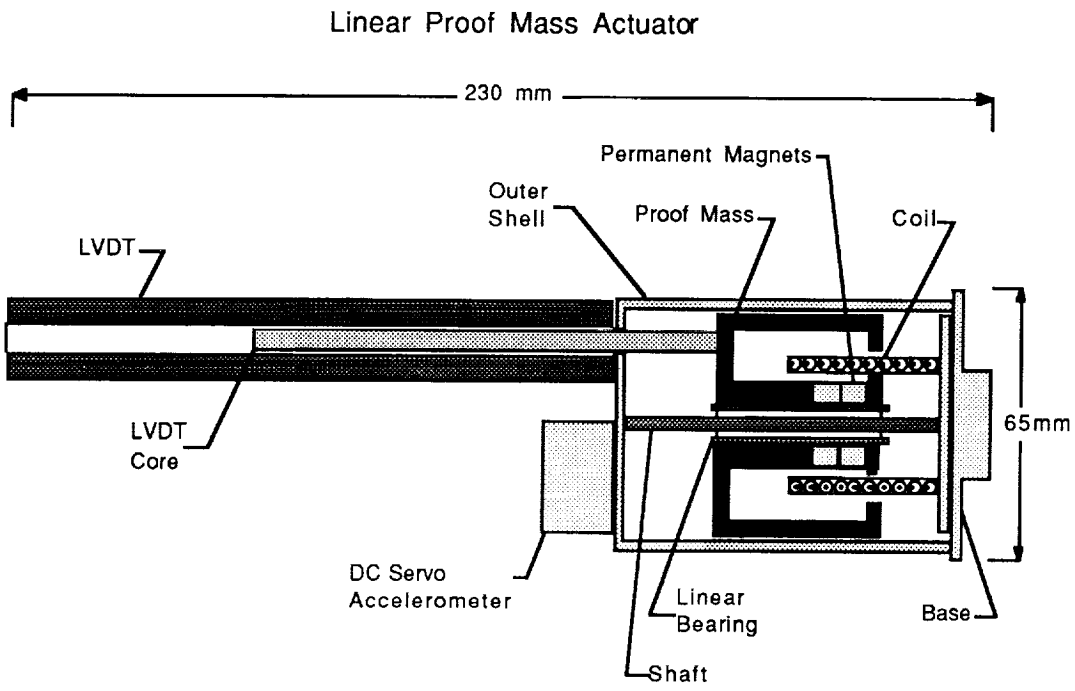

Figure 3: Linear Proof Mass Actuator

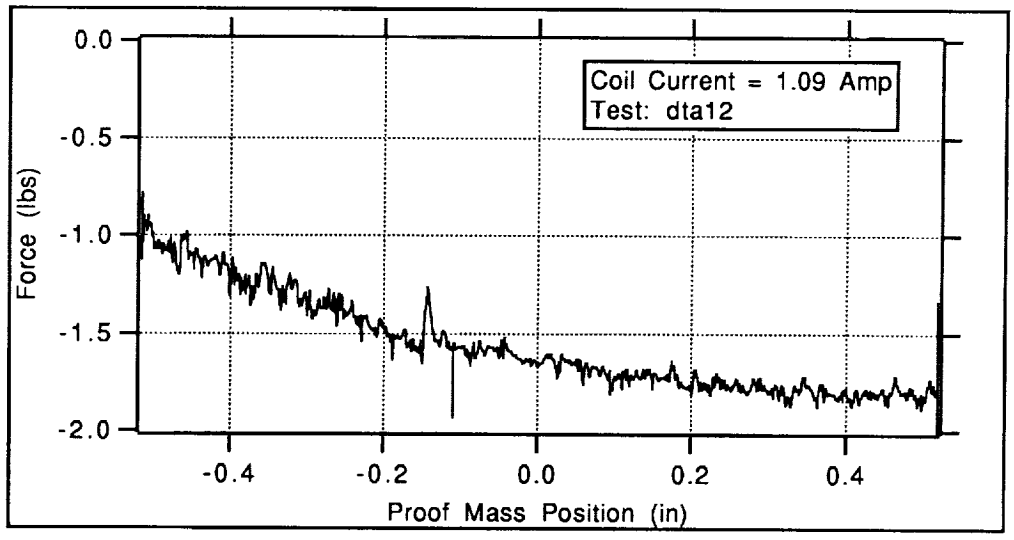

Figure 4: Static force versus proof mass position, coil current constant

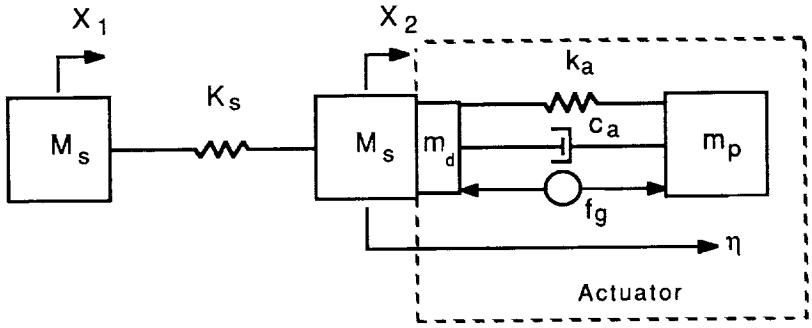

Figure 5: Free single mode structure with proof mass actuator

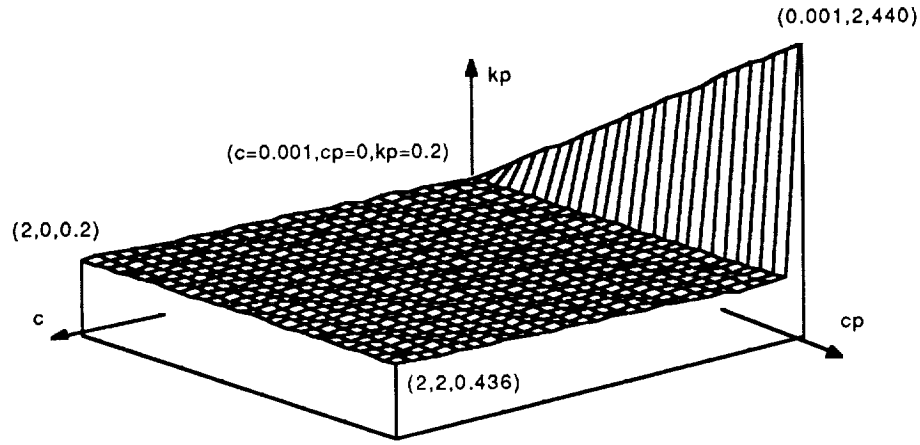

Figure 6: Constant feedback gain stability map

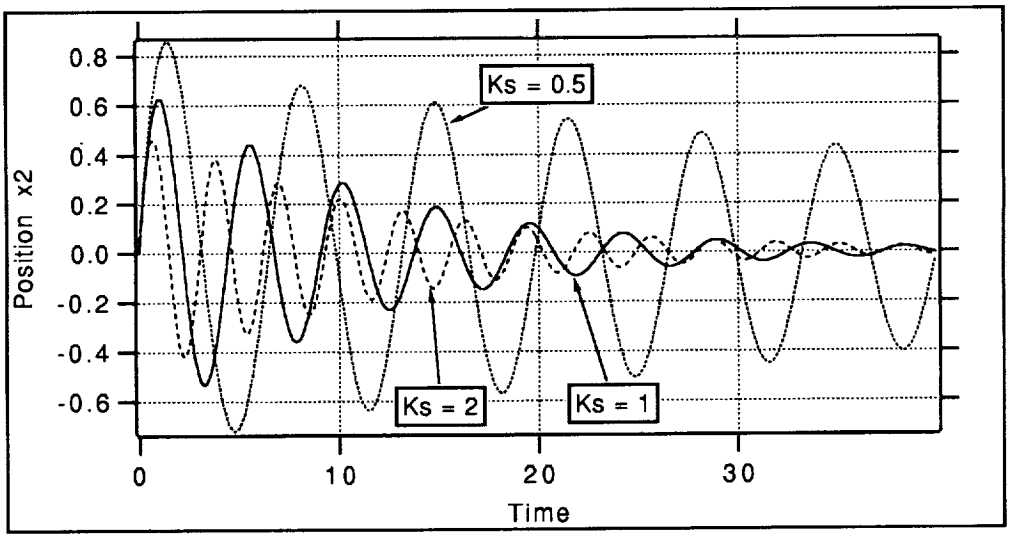

Figure 7: X_2 response to disturbance for minimum, maximum, and nominal K_s, vibration absorber design.

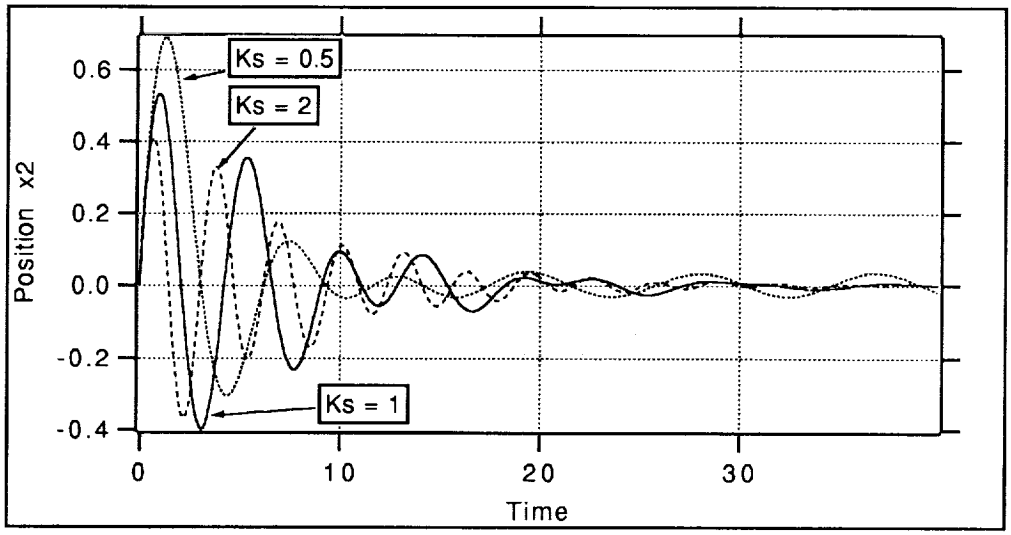

Figure 8:X2 response to disturbance for minimum, maximum, and nominal Ks, with structural velocity feedback.

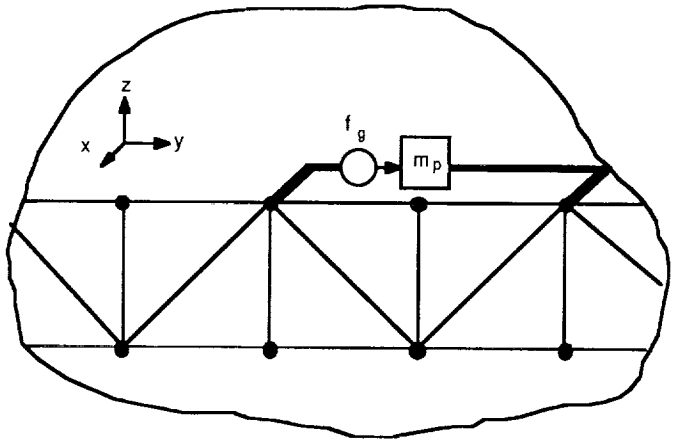

Figure 9: Viscous damper configuration.

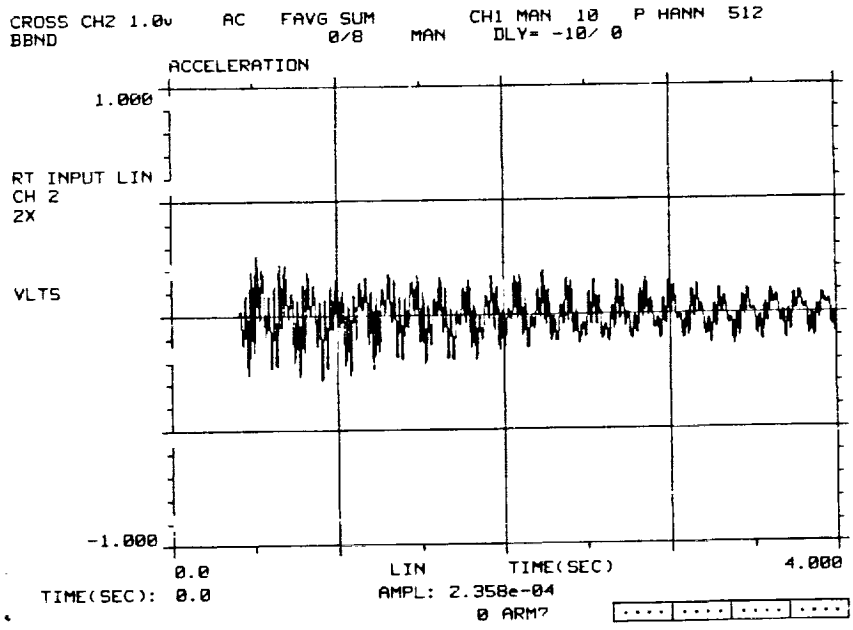

Figure 10: Response of uncontrolled structure.

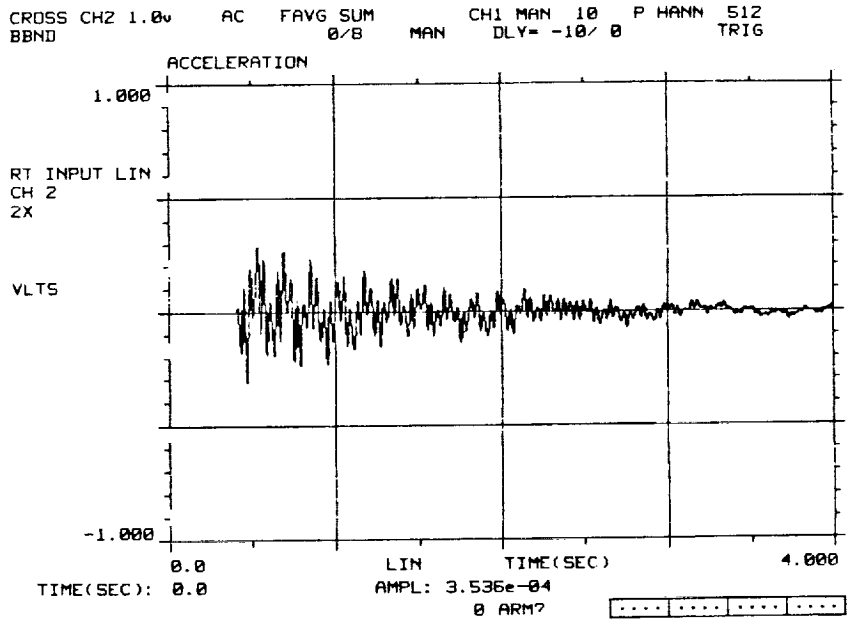

Figure 11: Response of structure, vibration absorber design.

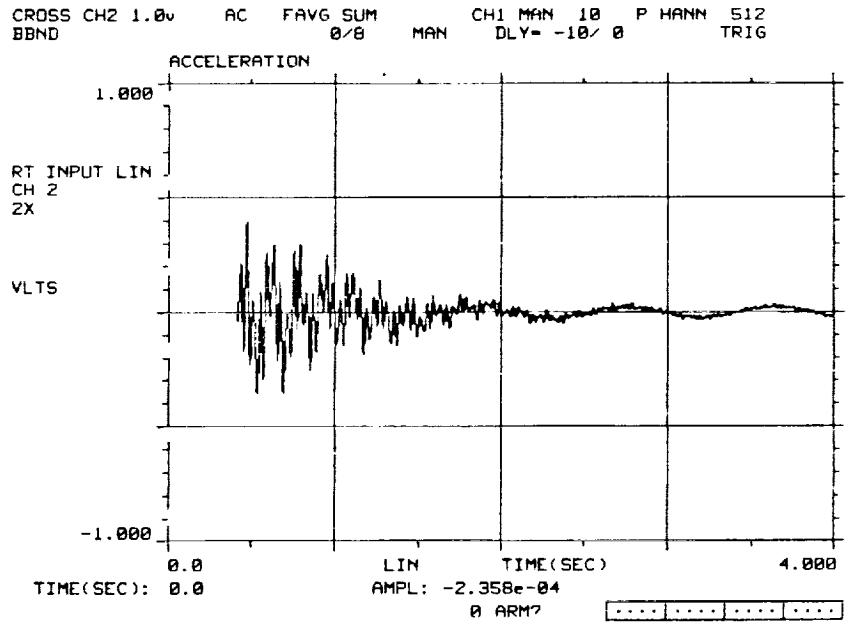

Figure 12: Response of structure, direct velocity feedback.

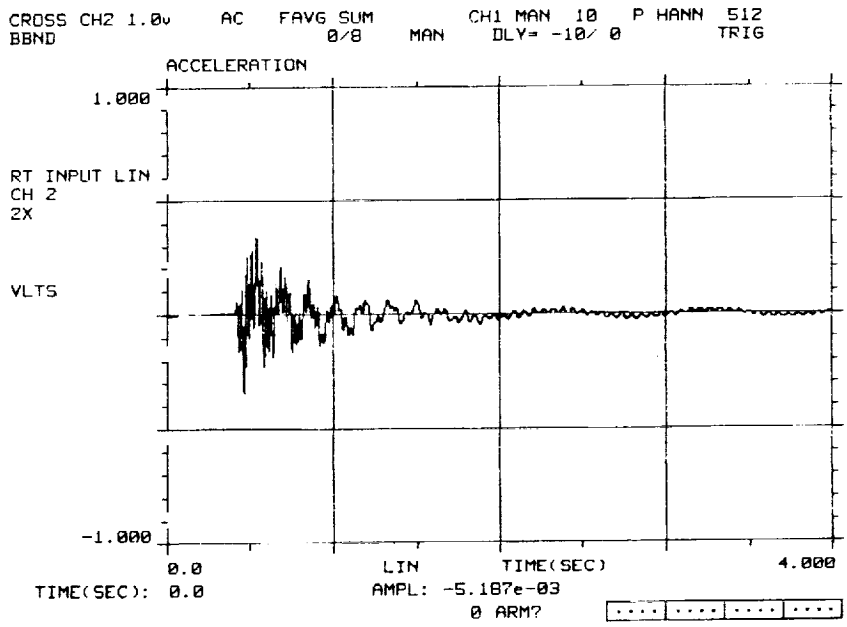

Figure 13: Response of structure, viscous damper.

SIMULATOR EVALUATION OF SYSTEM IDENTIFICATION WITH ON-LINE CONTROL LAW UPDATE FOR THE CONTROLS AND ASTROPHYSICS EXPERIMENT IN SPACE

Raymond C. Montgomery, Dave Ghosh, Michael A. Scott,
Spacecraft Control Branch

and Dirk Warnaar
Spacecraft Dynamics Branch

NASA Langley Research Center
Hampton, VA 23665

4th Workshop on Computational
Control of Flexible Aerospace Systems
Williamsburg, VA

July 11-13, 1990

SIMULATOR EVALUATION OF SYSTEM IDENTIFICATION WITH ON-LINE CONTROL LAW UPDATE FOR THE CONTROLS AND ASTROPHYSICS EXPERIMENT IN SPACE

Raymond C. Montgomery*, Dave Ghosh†
Michael A. Scott*, and Dirk Warnaar‡

ABSTRACT

This paper presents a procedure for optimizing the performance of large flexible spacecraft that require active vibration suppression to achieve required performance. The procedure is to conduct on-orbit testing and system identification followed by a control system design. It is applied via simulation to a spacecraft configuration currently being considered for flight test by NASA -- the Controls, Astrophysics, and Structures Experiment in Space (CASES). The system simulator is based on a NASTRAN finite-element structural model. A finite number of modes is used to represent the structural dynamics. The system simulator also includes models of the electronics, actuators, sensors (including an optical sensor that can sense deflections at locations along the CASES boom), the digital controller and the internal and external disturbances. Nonlinearities caused by quantization are included in the study to examine tolerance of the procedure to modelling errors. Disturbance and sensor noise is modeled as a gaussian process.

For system identification, the structure is excited using sinusoidal inputs at the resonant frequencies of the structure using each actuator. Mode shapes, frequencies, and damping ratios are identified from the unforced response sensor data after each excitation. Then, the excitation data is used to identify the actuator influence coefficients. The results of the individual parameter identification analyses are assembled into an aggregate system model. The control design is accomplished based only on the identified model using multi-input/output linear quadratic gaussian theory. Its performance is evaluated based on time-to-damp as compared with the uncontrolled structure.

---

* Aerospace Technologist, Spacecraft Controls Branch.

† Strucural Dynamics Analyst, Lockheed Engineering and Sciences Co., Hampton, VA.

‡ Principal Engineer, Lockheed Engineering and Sciences Co., Hampton, VA.

CASES - Controls, Astrophysics, and Structures Experiment in Space

This paper presents a procedure for optimizing the performance of large flexible spacecraft that require active vibration suppression to achieve required performance. The procedure is to conduct on-orbit testing and system identification followed by a control system design. Having applied the procedure successfully to the Mini-Mast ground test article (reference 1), this paper considers application in a spacecraft currently being considered for flight test by NASA -- the Controls, Astrophysics, and Structures Experiment in Space (CASES).

CASES is a very long focal-length camera. The "film" of the camera is in the payload bay of the Space Shuttle and the "lens" is at the opposite end of the 105 ft. boom extending from the payload bay. This accommodates the astrophysics role of CASES. Relative to this role, CASES accommodates an Astrophysics/Solar Physics Hard X-Ray Imaging experiment, thereby addressing two primary science goals. The "lens" is actually a pinholed plate and the "film" is an X-ray photon counter. The goals supported by this configuration are identifying energy sources from the galactic center, and the energy release mechanisms during solar flares. Precision pointing and stability of the optical axis is required when high energy photons are counted so that image reconstruction can be made.

CASES also accommodates research in controls and structural dynamics. The structural dynamics research capability is enhanced by a Parameter Modification System which is designed to alter the mode shapes and frequencies while in orbit. Advanced control law research can be accomplished using a variety of sensors and actuators provided by CASES covered in the next chart.

CASES - CONTROLS, ASTROPHYSICS, AND STRUCTURES EXPERIMENT IN SPACE

- X-RAY ASTRONOMY
- CONTROLS AND STRUCTURES EXPERIMENTS

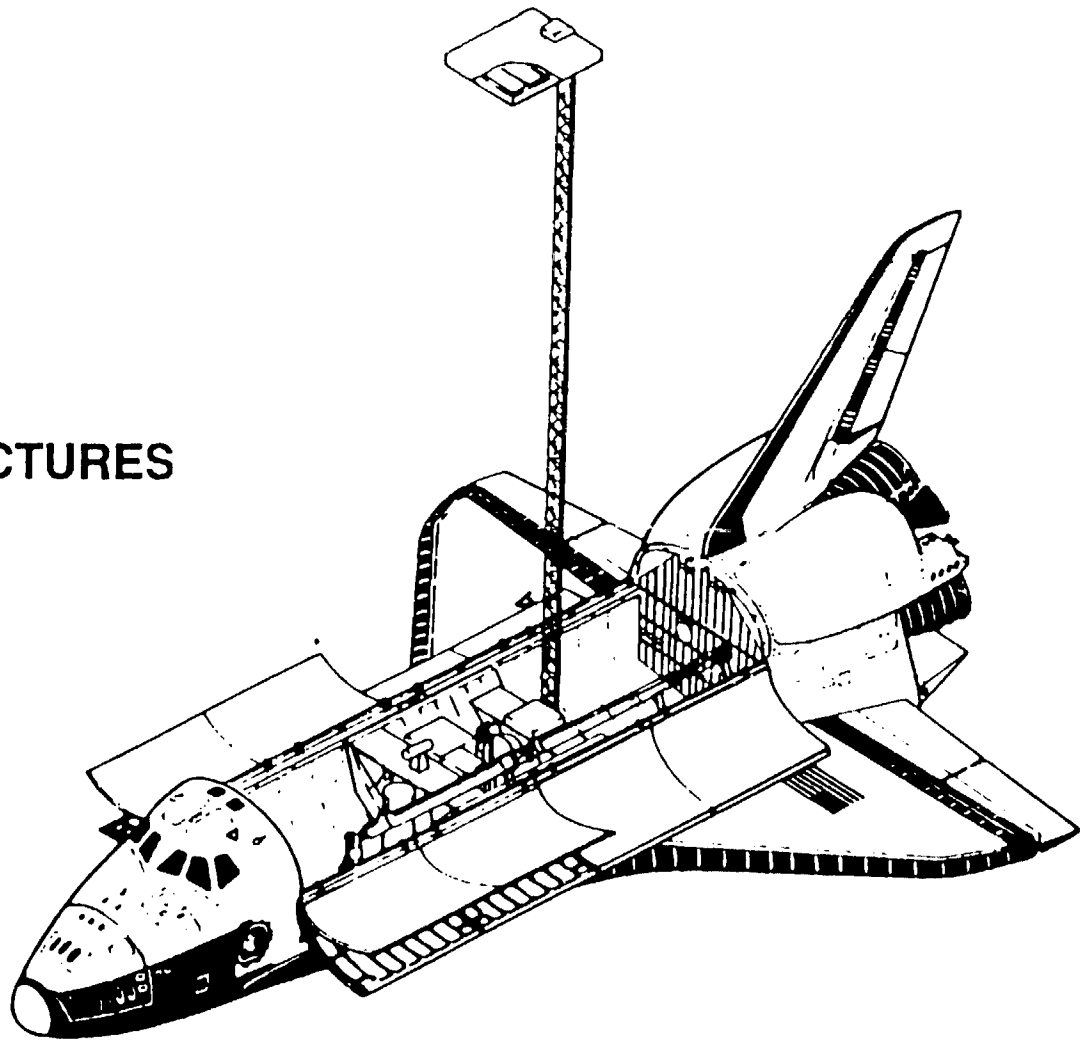

CASES INTEGRATED FINITE-ELEMENT MODEL

A finite-element model of the on-orbit CASES configuration has been assembled from 2050 beam elements. This chart is a sketch of the model which also indicates the location and type of sensors and actuators available on CASES. The actuators include small cold gas thrusters and angular momentum exchange devices (AMEDs). AMEDs are electric motors with flywheels attached to the armatures to affect moment control. The sensors include rate gyros, accelerometers, and a novel optical sensor that detects motion of optical targets distributed along the mast.

CASES INTEGRATED FINITE-ELEMENT MODEL

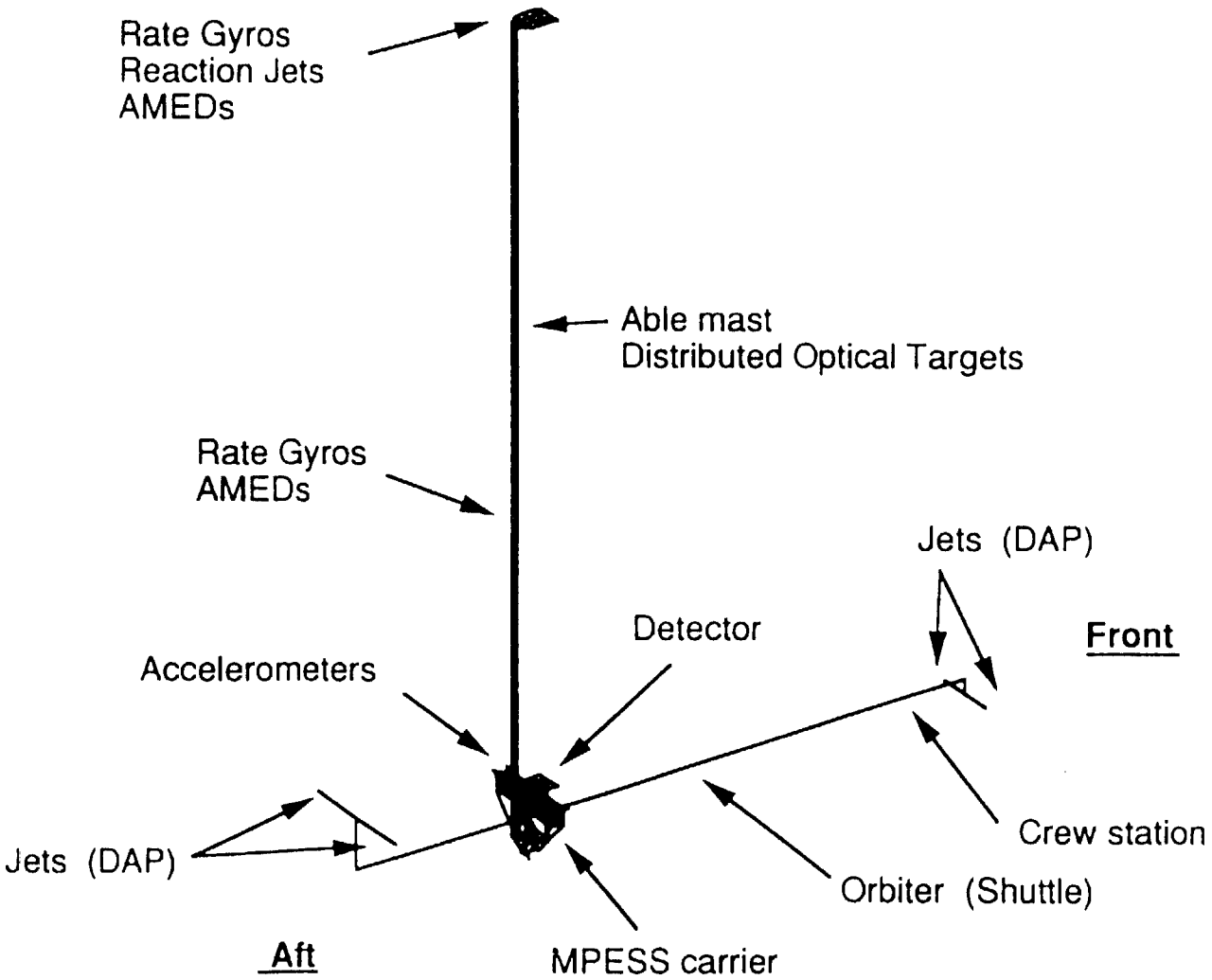

CONFIGURATION FOR BOOM MOTION TRACKER USING RAMS

The remote attitude measurement system (RAMS) employs a laser to illuminate retroreflective targets. The return from the laser targets is focused onto a linear CCD (charge-coupled device) array. The output of the array is processed to indicate the movement of the targets. RAMS is capable of optically sensing the motions of the boom at multiple target locations. Twenty-four targets distributed along the 102-foot boom are optically detected by the RAMS system to monitor boom motion and the tip displacement. Additionally, targets are placed on the tip-plate that allow determining the rigid-body rotation and translation of the plate. Two single-axis sensor heads on orthogonal axes at the base of the experiment platform are used to detect target motion. The discrete projections of the target images as perceived from the sensor heads are used in the control system.

CONFIGURATION FOR BOOM MOTION (Eigenvector) TRACKER USING RAMS

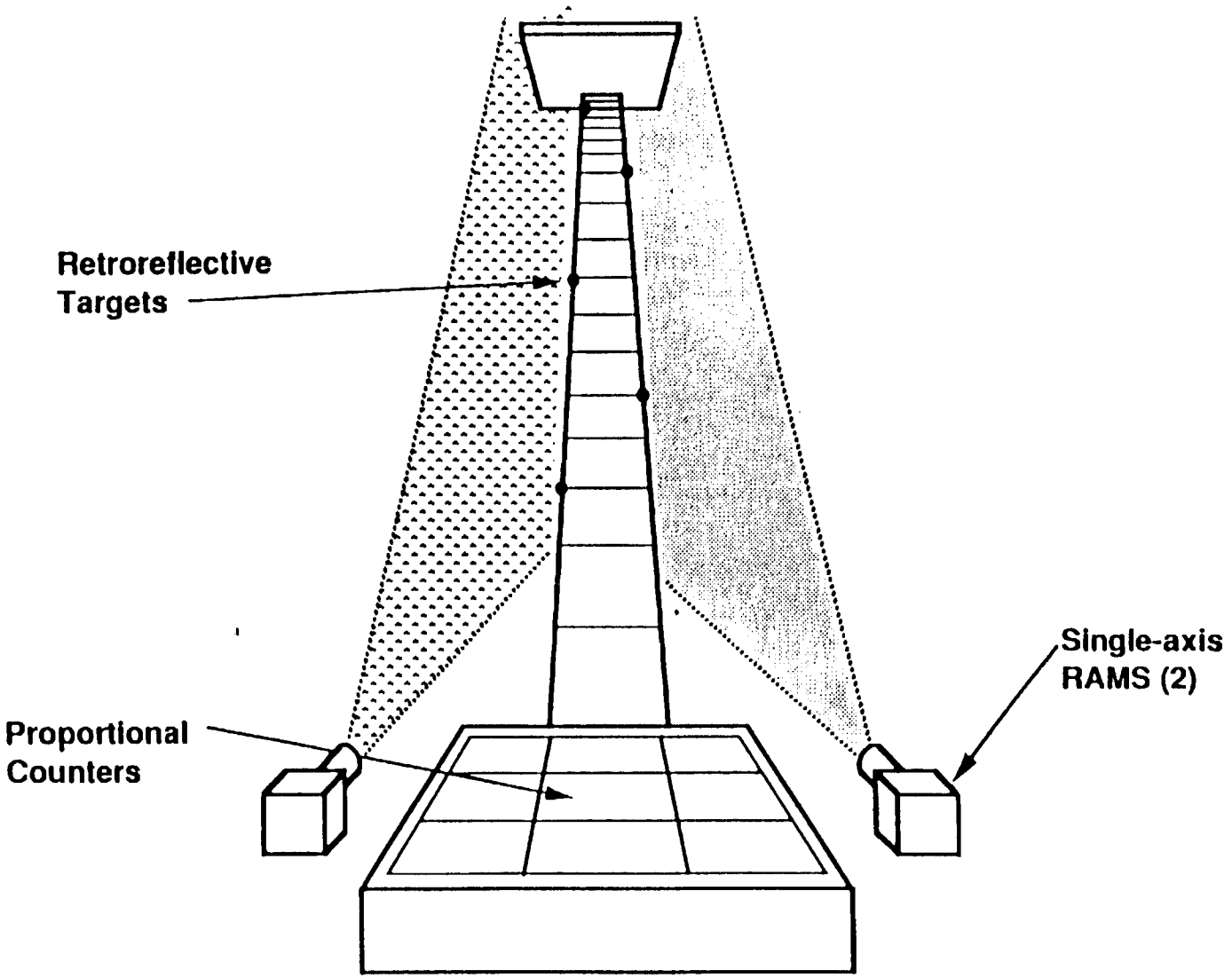

SYSTEM SIMULATION

The design procedure presented in the paper is applied to the CASES configuration. This is done by developing a system simulator capable of accurately representing the on-orbit environment. NASTRAN model data is passed to a preprocessor that generates a discrete-time model of the CASES dynamics suitable for digital control. Actuator and sensor data is also input to this module. This data is also used in the control system design module along with output from the system identification conducted using simulated open-loop, on-orbit data. The discrete-time model as well as the control system design are passed on to the simulator for the closed-loop control system performance evaluation. Thus, the control system design is based only on results of the system identification and prior knowledge of the sensors and actuators (assumed obtained from bench tests and geometrical mounting data for locations of the components).

SYSTEM SIMULATION

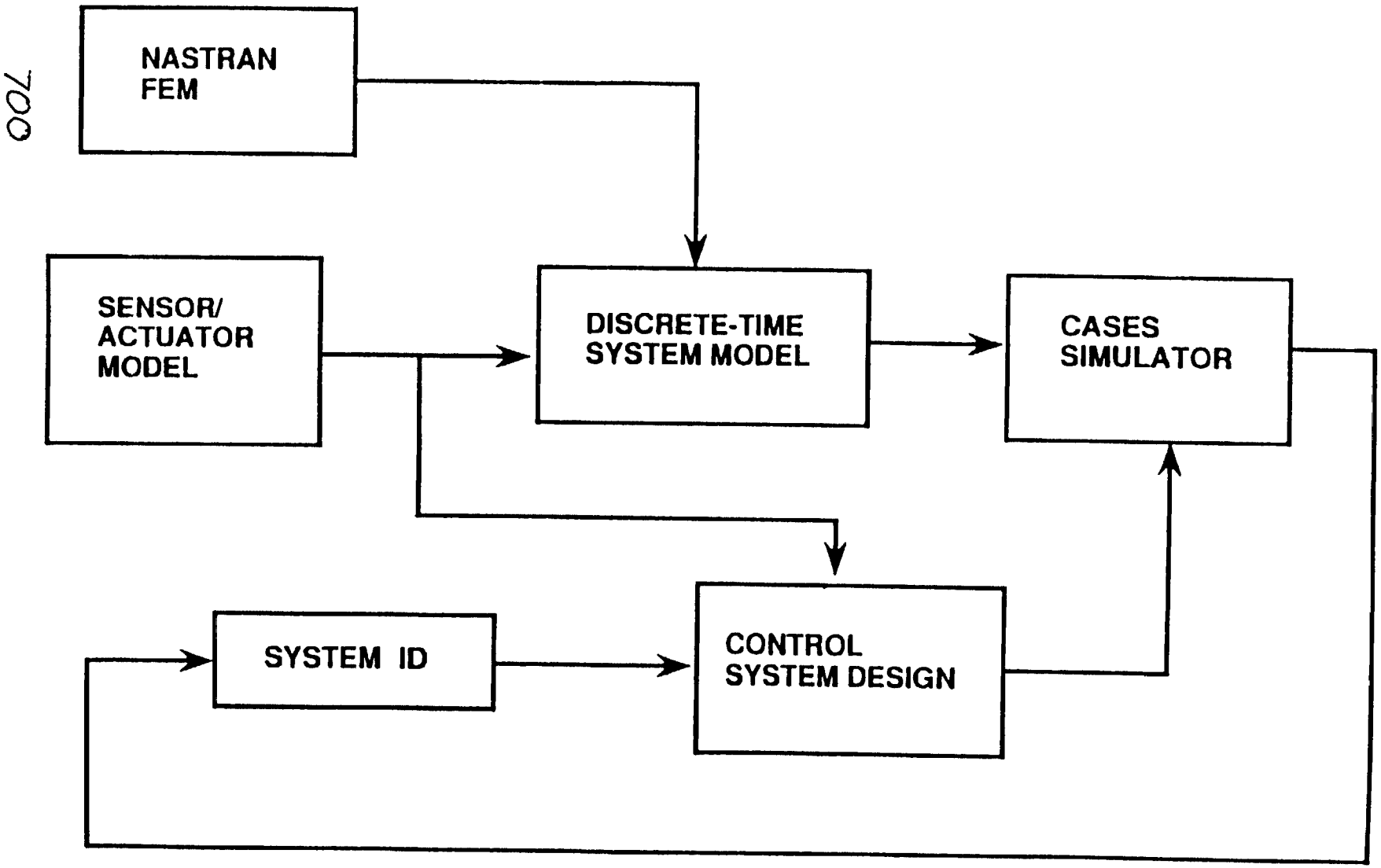

SIMULATOR FEATURES

The finite-element model of the CASES configuration includes 663 grid points, 2050 beam elements, and lumped masses representing the actuator and sensor components at the tip and mid boom assemblies. NASTRAN was asked for the modes with frequencies less that 10 Hz. Open-loop eigensolution analysis provided the necessary mode shapes and frequencies to build the system simulator. Based on the 40 Hz sample frequency fourteen modes were used in the simulator. The table below lists the frequencies and description of these modes (0.5 percent structural damping was assumed for each mode). In addition to the structural model, the system simulator also includes detailed models of the electronics, actuators, sensors (including RAMS) and the digital controller. Sensor noise and disturbances are modelled as Gaussian random noise. The procedure for modelling the in-situ noise characteristics of the sensors caused by uncertainty in modelling, mounting, and quantization is covered later.

TABLE - List of frequencies obtained from the FEM and used in the simulations.

Mode no.	Description	Frequency (Hertz)
1-6	Rigid Body	0
7	1^{st} Bending Y	0.033
8	1^{st} Bending X	0.034
9	1^{st} Torsion Z	0.165
10	2^{nd} Bending Y	0.431
11	2^{nd} Bending X	0.441
12	3^{rd} Bending Y	1.412
13	3^{rd} Bending X	1.543
14	4^{th} Bending Y	2.744

SIMULATOR FEATURES

FINITE ELEMENT MODEL -- 2050 ELEMENTS, MODES < 10 Hz

MODAL SIMULATION -- 6 RIGID BODY, 8 FLEX MODES

DETAILED MODEL OF OPTICAL SENSOR

DIGITAL CONTROL AT 40 HZ SAMPLE RATES

QUANTIZATION FROM DIGITAL CONVERSION

OPEN-LOOP RESPONSE TO AN IMPULSE
1 N-SEC

The response of the system to an impulse of 1 N-sec is shown in the figure. The important characteristic is that the system does not damp to an undetectable motion for 4,000 sec and does not fall below 1 cm for over 1,000 sec.

OPEN-LOOP RESPONSE TO AN IMPULSE
1 N-SEC

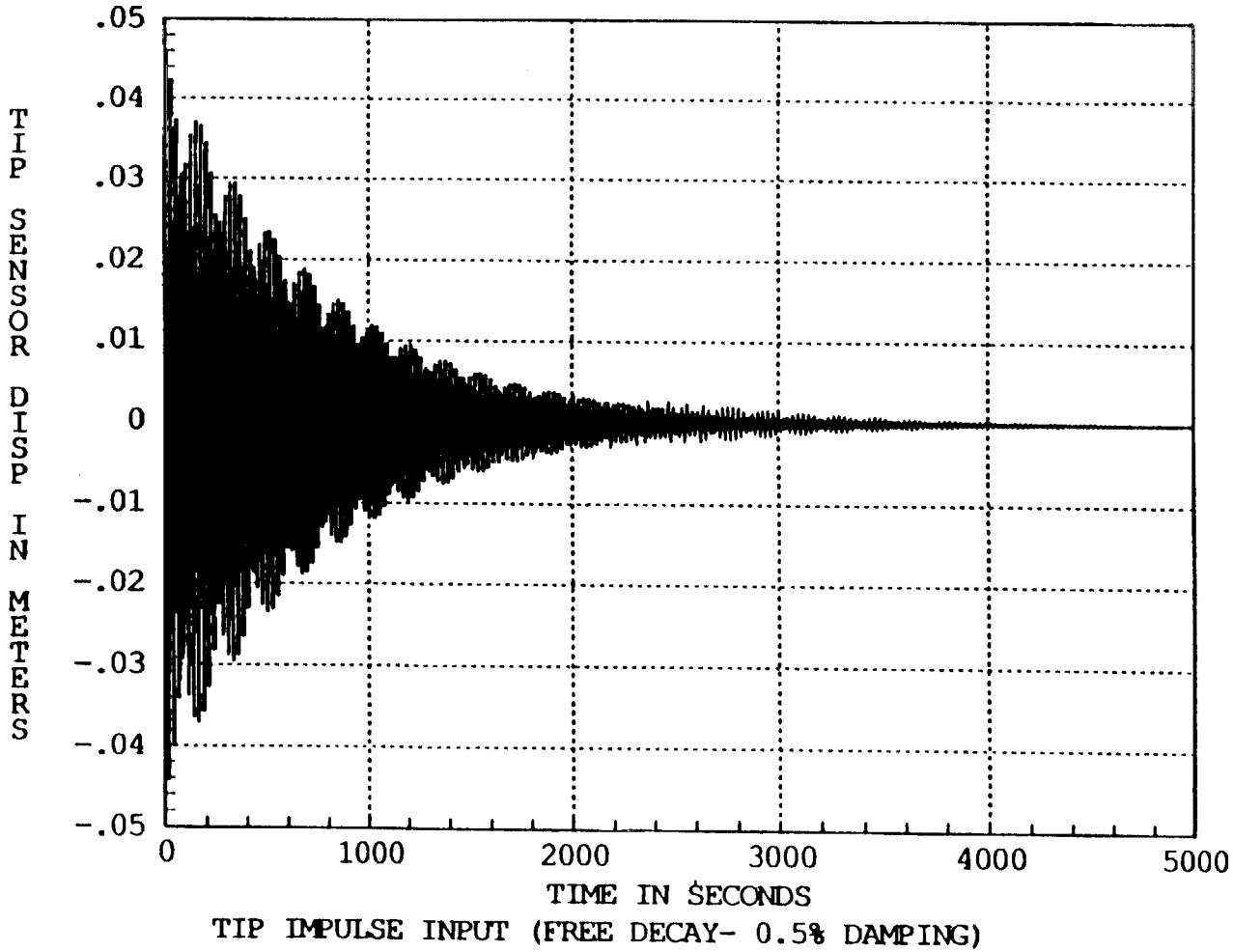

SENSOR RANGES AND NOISE LEVELS AND ACTUATOR LIMITS

The sensor range and noise levels used in the system simulator are shown in the chart. The expected range of the sensors is determined during the excitation period of the system identification tests. Therefore, prior to assigning values for the sensor noise a complete simulation was performed to determine the peak response of the sensors to each of the SID excitation tests. To prevent sensor saturation, the expected range is defined as six times the peak of the actual response of the SID tests. Thus, the data were carefully inspected, peak displacements were identified, noise levels were determined and added to the data prior to performing system identification on the data. The three-sigma noise range levels correspond to one percent of the expected range for the inertial sensors. The optical sensor noise levels correspond to 0.1 of one percent of the expected range. The open loop excitation tests indicated the peak displacements are high near the tip of the boom. Thus, the noise levels added to the optical sensor increase near the tip of the boom.

The actuator limits were determined based on the maximum output of the components in the CASES flight experiment design. In the case of the bilinear thrusters (BLTs), their maximum force is almost equal to the static buckling limit of the boom. Here an industry standart safety factor of 2.5 was applied to the maximum commanded value of the thrust resulting in a .43 lbf limit.

SENSOR RANGES AND NOISE LEVELS

RANGE --

- ACCELEROMETERS - .012 M/S/S
- RATE GYROS - .06 1/S
- OPTICAL - .04 TO 1 M, DEPENDS ON TARGET LOCATION

NOISE LEVELS --

- ACCELEROMETERS - 3 SIGMA = 1% OF RANGE
- RATE GYROS - 3 SIGMA = 1% OF RANGE
- OPTICAL - 3 SIGMA = 0.15% OF RANGE

ACTUATOR LIMITS --

- AMEDS - 141.2 OZ-IN (1 N-M)
- BLTS - 1.5 LBF - SAFETY LIMIT AT .43 LBF (2 N)
  SAFETY FACTOR OF 2.5 OVER STATIC BUCKLING LOAD

EFFECTS OF QUANTIZATION
MID-BOOM DEFLECTION

This chart shows the character of the signals that resulted from application of the actuator command limits of the previous chart. Here the boom is excited with the mid-station torque wheel at the mode 8 resonant frequency. The effect of quantization in the signal is apparent by the step-like nature of the sensor output. The maximum amplitude of the signal is approximately 4 mm peak-to-peak and the quantization is approximately in .2 mm increments.

EFFECTS OF QUANTIZATION
MID-BOOM DEFLECTION

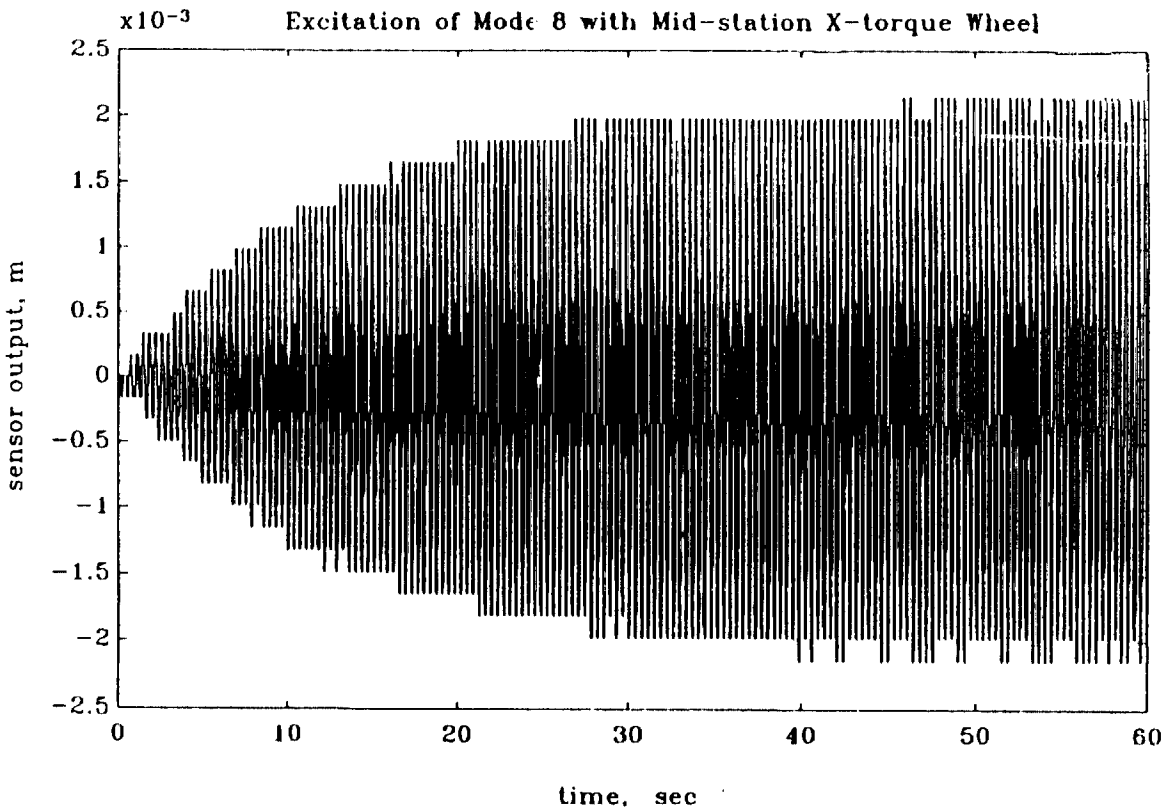

EXCITATION RESPONSE
(8th MODE)

This chart shows the first 4 seconds of the previous chart with the scale of the ordinate expanded.

EXCITATION RESPONSE

(8TH MODE)

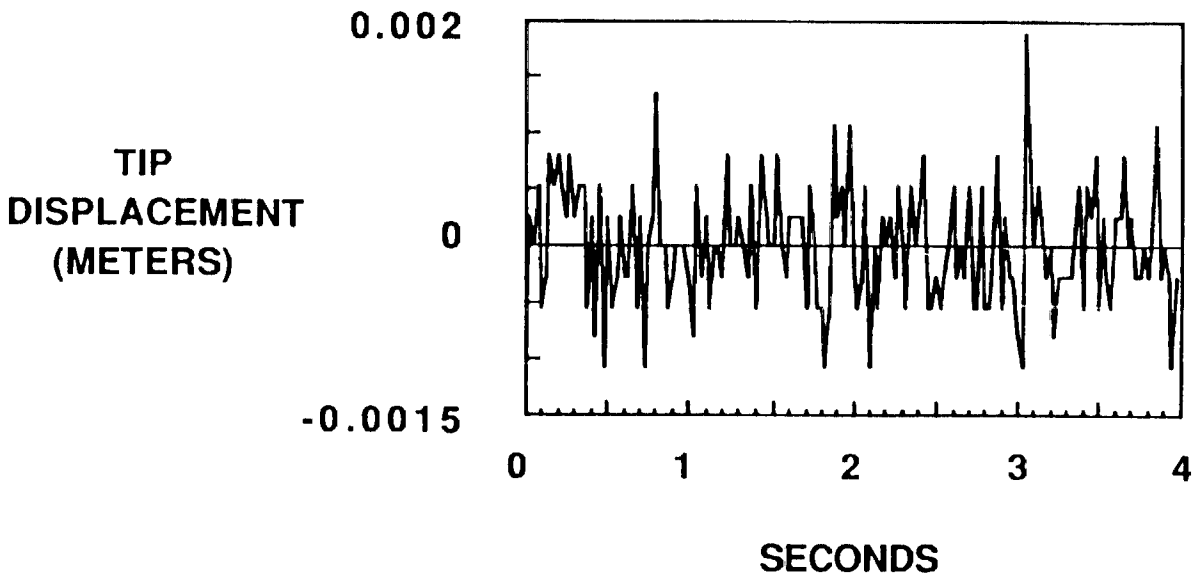

SYSTEM IDENTIFICATION

System identification was carried out using the simulator to generate data sets as they would be generated in a flight experiment. The flight computer generated an excitation signal that is implemented by the actuators on CASES. This generates a response of the structure which gives rise signals from the CASES sensors simulated.

SYSTEM IDENTIFICATION

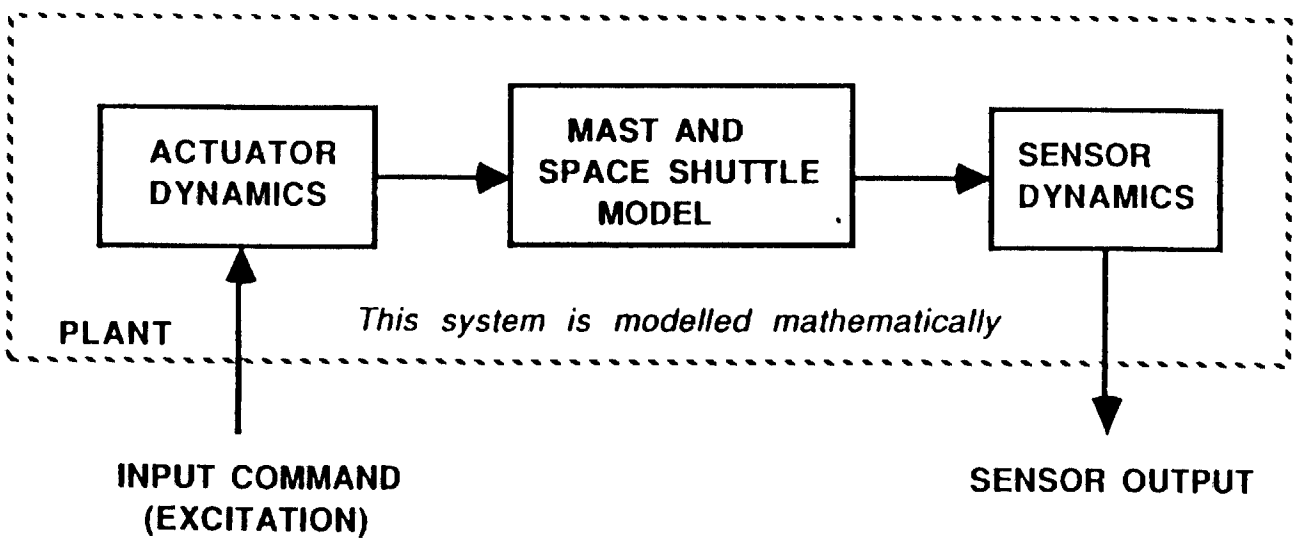

SYSTEM IDENTIFICATION APPROACH

An unsuccessful attempt was made to identify the mode shapes using the sine-sweep and random excitation tests. Because of actuator input limitations dictated by flight safety requirements, sine-sweep and random excitation techniques do not excite the structure sufficiently to identify mode shapes and actuator influence coefficients. However, the modal frequencies can be identified. First, ERA (reference 2) was used to determine the frequencies from a sine-sweep test. It was used again to identify the mode shapes, frequencies, and damping ratios from 28 sine-dwell tests. These tests were determined from the finite-element predictions to eliminate unnecessary data processing. In an actual flight the complete matrix of tests (number of modes by the number of actuators) would be used. The least squares method (reference 3) and a closed form solution method (the b-coefficient method, explained herein) were used on the data to determine the actuator influence coefficients. The results of the individual parameter identification analyses are then assembled into an aggregate system model for use in the control system design phase.

The actuator influence coefficients were identified using least squares estimation and a closed form solution method. Both techniques analyze single-input, single-output data. The sensor with the highest output to noise ratio was selected for determining the actuator influence coefficient for the corresponding mode-actuator combination. For the higher frequency modes, quantization effects and low levels of excitation prohibited least squares estimation from converging. For these modes the b coefficient method was used. This method is based on fitting the the envelope of the forced response curve. The equation governing the envelope for this method is

$$y(t) = \frac{b\,[1 - e^{-\zeta\omega_n t}]}{\omega_n(2\zeta\omega_n)}$$

which assumes zero initial conditions, small damping, and the presence of a single mode. The unknown b coefficient is determined from the knowledge of a sensor output y at time t. The damping coefficient ζ and the natural frequency ω_n were previously determined using ERA.

The closed form method accurately predicts the magnitude of the coefficient. However, it does not predict the sign of the coefficient. The sign is determined by examining the phase relationship of the sensor output to the excitation input. If the output lags the input by 90°, the influence coefficient is positive. If the output leads the input, the coefficient is negative.

SYSTEM IDENTIFICATION APPROACH

ACTUATOR INFLUENCE COEFFICIENTS

- SINUSOIDAL EXCITATION AT PREDICTED RESONANTES
- ALGORITHMS -- LEAST SQUARES, LOG DECREMENT, B COEF

FREQUENCY, DAMPING, AND MODE SHAPES

- FREE-DECAY FOLLOWING SINUSOIDAL EXCITATION
- ALGORITHMS -- ERA

ACTUATOR INFLUENCE COEFFICIENTS

This chart shows the actuator influence coefficients that were generated in the finite-element analysis and which were simulated (BFEM). It also shows the results of the system identification of the same parameters. The elements blocked are the best and worst case system identifcation results.

ACTUATOR INFLUENCE COEFFICIENTS

BFEM =

-0.0002	0.0000	-0.0003	0.0000	0.0000	0.0000	0.0066
0.0000	-0.0002	0.0000	-0.0003	0.0002	-0.0061	0.0000
0.0000	0.0002	0.0000	0.0002	0.0240	0.0065	0.0000
-0.0019	0.0000	0.0032	0.0000	0.0000	0.0000	-0.0022
0.0000	-0.0020	0.0000	0.0033	0.0018	0.0027	0.0000
-0.0046	0.0000	0.0170	0.0000	0.0000	0.0000	-0.0018
0.0000	0.0066	0.0000	-0.0180	-0.0021	-0.0035	0.0000
-0.0063	0.0000	-0.0184	0.0000	0.0000	0.0000	-0.0011

916

BID =

-0.0002	0.0000	-0.0003	0.0000	0.0000	0.0000	0.0072
0.0000	-0.0002	0.0000	-0.0003	0.0002	-0.0060	0.0000
0.0000	0.0002	0.0000	0.0003	0.0250	0.0067	0.0000
-0.0019	0.0000	0.0032	0.0000	0.0000	0.0000	-0.0022
0.0000	-0.0019	0.0000	0.0028	0.0016	0.0025	0.0000
-0.0045	0.0000	0.0170	0.0000	0.0000	0.0000	-0.0019
0.0000	0.0065	0.0000	-0.0174	-0.0020	-0.0034	0.0000
-0.0071	0.0000	-0.0204	0.0000	0.0000	0.0000	-0.0019

SYSTEM IDENTIFICATION RESULTS

Using ERA the mode shapes, frequency, and damping coefficients of the 8 lowest frequency flexible modes were identified. This chart tabulates results of the ERA analysis and shows a line graph of the mode 1 sensor influence coefficients plotted against sensor number. For the line graph, the first 4 sensors are rate gyros. The next 24 are laser retroreflective targets using one of the detectors and the last 24 are the retroreflective targets for the other detector. Also plotted is the finite-element simulated value of the parameter. It cannot be destinguished from the parameter identification value on this chart.

SYSTEM IDENTIFICATION RESULTS

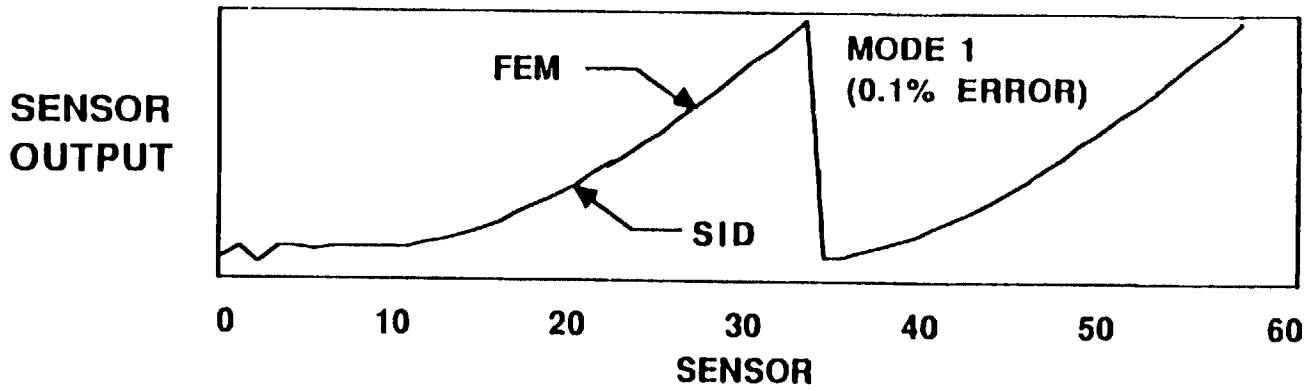

	SYSTEM		SYSTEM IDENTIFICATION	
FLEXIBLE MODE	FREQUENCY (HZ)	DAMPING (%)	FREQUENCY (HZ)	DAMPING (%)
1	0.033	0.5	0.033	1.674
2	0.034	0.5	0.034	1.013
3	0.165	0.5	0.165	0.667
4	0.431	0.5	0.431	0.463
5	0.441	0.5	0.441	0.297
6	1.412	0.5	1.412	0.501
7	1.543	0.5	1.543	0.482
8	2.744	0.5	2.743	0.540

CONTROL DESIGN PROCESS

The vibration suppression control law is developed using the linear quadratic gaussian analytic design method (reference 4). This procedure uses a linear steady-state minimum-variance estimator to obtain the states for use in a linear fixed gain regulator. The control law chosen minimizes the time integral of weighted squared disturbance and applied control signals. The weighting matrix for the disturbance is the identity matrix divided by the frequency squared. The weighting matrix for the control input is the identity matrix.

CONTROL DESIGN PROCESS

SENSORS ⟶ ESTIMATOR ⟶ CONTROL LAW ⟶ ACTUATOR COMMAND

CRITERIA : ESTIMATION - MINIMUM VARIANCE

CONTROL LAW - MINIMIZE THE TIME INTEGRAL OF WEIGHTED SQUARED DISTURBANCE AND APPLIED CONTROL SIGNALS.

DESIGN USES

- 8 LOWEST FREQUENCY VIBRATION MODES
- 2 JETS (1 NEWTON)
  5 TORQUE WHEELS (1 N-M)
- 24 LASER TARGETS
  5 RATE GYROS
  3 ACCELEROMETERS

CLOSED-LOOP PERFORMANCE

The closed loop performance of CASES was evaluated with the results of the system identification information. An updated regulator and state estimator based on the SID results was obtained. This chart shows the tip displacement (in meters) of the CASES mast due to sinusoidal excitation (using the tip thruster) at the first resonant frequency of the structure. The upper graph shows the forced response for the first 60 seconds and free decay response after 60 seconds. The lower graph shows the forced response to the same input disturbance with the controlled response after 60 seconds. The open-loop system (0.5 percent damping) takes approximately 10 times longer to achieve the same level of damped response as the closed-loop system (5 percent damping).

CLOSED LOOP PERFORMANCE

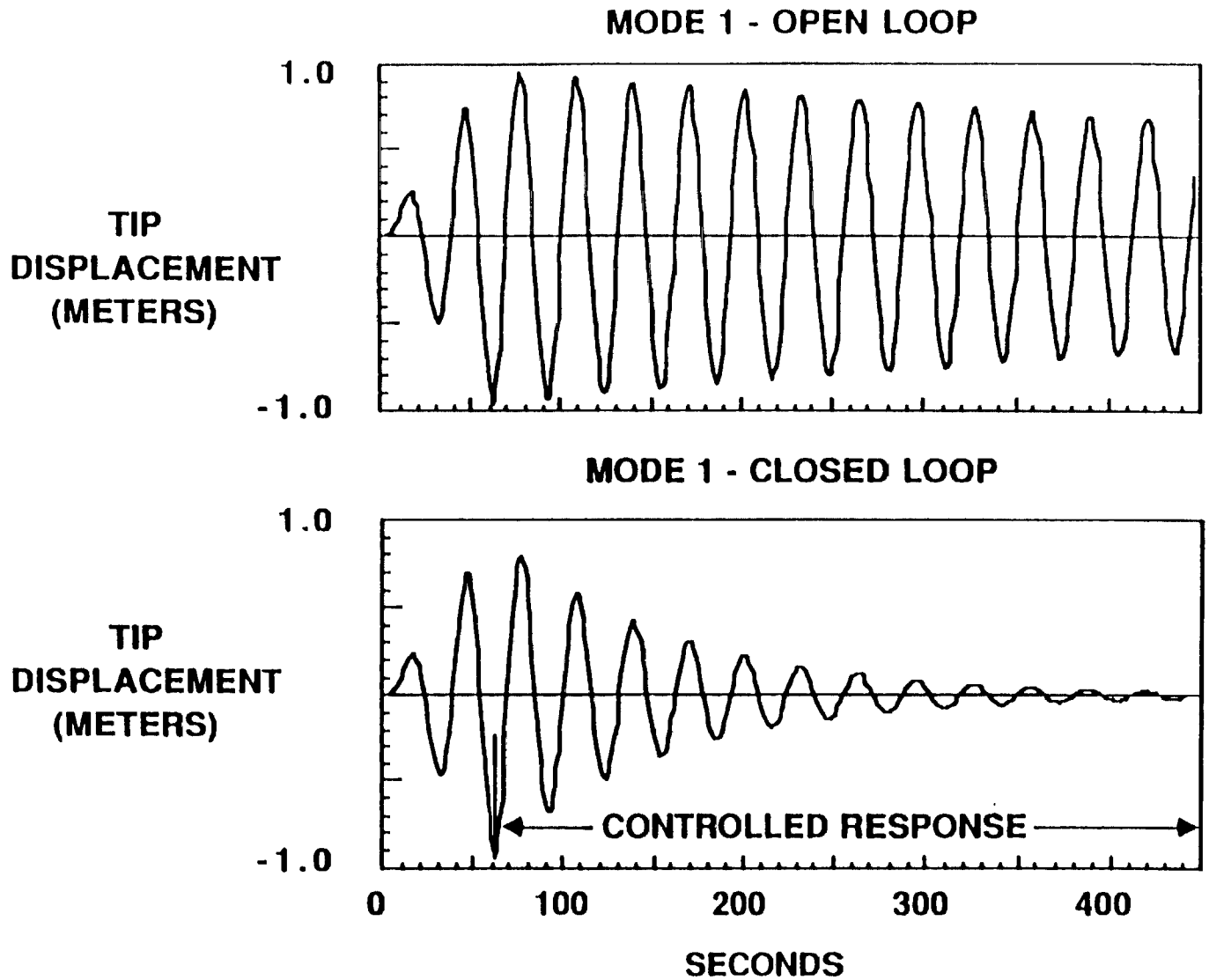

CONCLUDING REMARKS

A procedure has been presented for the on-orbit design of a control system for flexible space structures. This procedure has been successfully implemented in a CASES flight experiment simulation. Results indicate that system identification will be difficult but can be done. The actuator influence coefficients are difficult to obtain with the levels of actuator force allowed. With current actuator force levels, 5 percent damping can be added to the system.

CONCLUDING REMARKS

- SYSTEM IDENTIFICATION WILL BE DIFFICULT BUT CAN BE DONE
- 5% DAMPING CAN BE ACHIEVED WITH CURRENT ACTUATOR FORCE LEVELS

References

1. Montgomery, R. C. and D. Ghosh: LQG Control for the Mini-Mast Experiment. Proceedings of the Sixth VPI&SU/AIAA Symposium on Control of Large Structures. June 29, 1987.

2. Juang, J. and R.S. Pappa: An Eigensystem Realization Algorithm for Modal Parameter Identification and Model Reduction. Journal of Guidance, Control, and Dynamics, vol. 8, no. 5, pp 620-627, 1985.

3. Sparks, D. W., Jr., R.C. Montgomery, R.C. Elder, D.B. Lenox. Parameter Identification for Vibration Control of SCOLE. ASME Paper No. 88-WA/DSC- presented at the 1988 ASME Winter Annual Meeting, Chicago, Ill. Nov-Dec 1988.

4. Kwakernaak, H. and R. Sivan: Linear Optimal Control Systems. Wiley Interscience; New York, N.Y.

DYNAMICS MODELING AND ADAPTIVE CONTROL OF FLEXIBLE MANIPULATORS

J.Z. Sasiadek

Department of Mechanical & Aerospace Engineering

Carleton University

Ottawa, Ontario, Canada

Abstract

This paper presents an application of Model Reference Adaptive Control (MRAC) to the position and force control of flexible manipulators and robots. In this paper a single-link flexible manipulator has been analyzed as an example [1].

1. Introduction

Control of flexible structures is of paramount importance in various applications in aerospace, mechanical and construction industry. The problem itself is not a new one and has been described extensively in literature related to control of distributed parameter systems. Robots with flexible links are interesting examples of mechanical systems with the flexible structure. Flexibility of links poses several difficult problems with position control. One of the most severe problems is vibration of the end-point caused by links structural flexibility. Design of an appropriate control system requires a good knowledge of dynamics. In general there are several methods for dynamics modeling. Two are of special interest: 1. an assumed modes method, 2. finite elements method. Both methods have been described in several books [2] and papers [3]. If, dynamics of a flexible manipulator or robot has been identified and

determined, an appropriate control system can be designed. Robots have strongly nonlinear characteristics. This feature is even more visible for flexible manipulators. Thus, flexible robots require especially efficient control systems. There are numerous control systems based on feedback or feeedforward principle. The link inertias change continuously with position, payload and time, therefore control system has to follow and adapt itself to assure a steady and smooth performance. The adaptive control seems to be well suited for that purpose. One of the most promising of such systems is Model Reference Adaptive Control (MRAC). The main advantage of adaptive control is that the system is payload insensitive and that its performance is steady over broad range of conditions.

2. Problem Formulation

The problem addressed in this paper was to develop a mathematical model of a flexible robot. The model has to be accurate and in some applications a real-time simulation may be required. Dynamics of the manipulator have been used in designing of its controller. Adaptive control schemes require special attention to make sure that stability of the system is maintained. The objective is to show that the adaptive control performs better than "conventional" systems and is suitable for flexible structure control.

3. Mathematical Model

The mathematical model described in this paragraph has been developed and described in detailed in [1]. The single link flexible manipulator has been modelled as a cantilever beam and following assumptions have been made [1]:

- the mass and elastic properties of the link are distributed uniformly along its longitudinal direction;
- Euler's beam theory is applicable, thus the transverse shear stresses and the moment of inertia with respect to elastic deformation are negligible;
- the elastic deformation of the link is small;
- the change in potential energy of gravity due to elastic deformation of the link is negligible.

Single-link flexible manipulator has been shown in fig.1 (all figures from [1]) and its dynamic performance has been shown in subsequent figures [1].

4. Adaptive Control

Figures 7 to 12 present various dynamic responses with control. The comparison between those responses and free responses has been shown. Simulation results show that the adaptive control system performance is satisfactory and is payload insensitive. It is clear that adaptive control can be used with success for flexible robots control.

5. Conclusions

- Modal expansion method is an accurate representation of flexible manipulator dynamics.
- Three flexible modes approximation can be considered as satisfactory.
- The discontinuities in the robot response caused by coupling between the rigid and flexible modes can be eliminated by an efficient control system.
- An adaptive control system reduces the positioning error of the end-effector and shortens the settling time.

Acknowledgement

This work is based on [1].

References

[1] Sasiadek J.Z. and Srinavasan R., Dynamic Modeling and Adaptive Control of a Single-Link Flexible Manipulator, AIAA Journal of Guidance, Control and Dynamics, November 1989, Vol.12, No.6.

[2] Meirovitch L., Elements of Vibration Analysis, McGraw-Hill, New York, 1986.

[3] Cetinkut S. and Book W.J., Performance Limitations of Joint Variable-Feedback Controllers Due to Manipulator Structural Flexibility, IEEE Transaction on Robotics and Automation, April 1990, Vol.6, No.2.

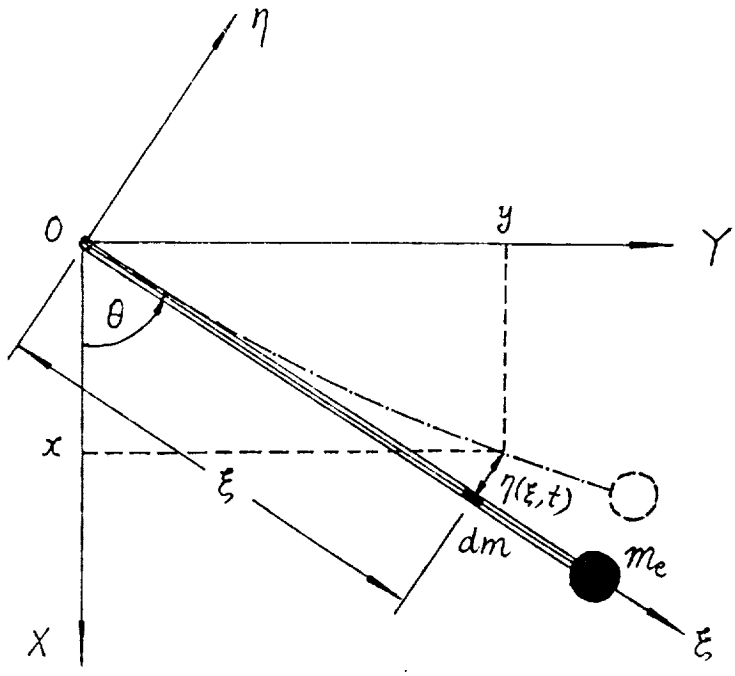

Fig. 1 Single-Link Flexible Manipulator [1]

[Fig. 2] MODAL SHAPE OF MANIPULATOR

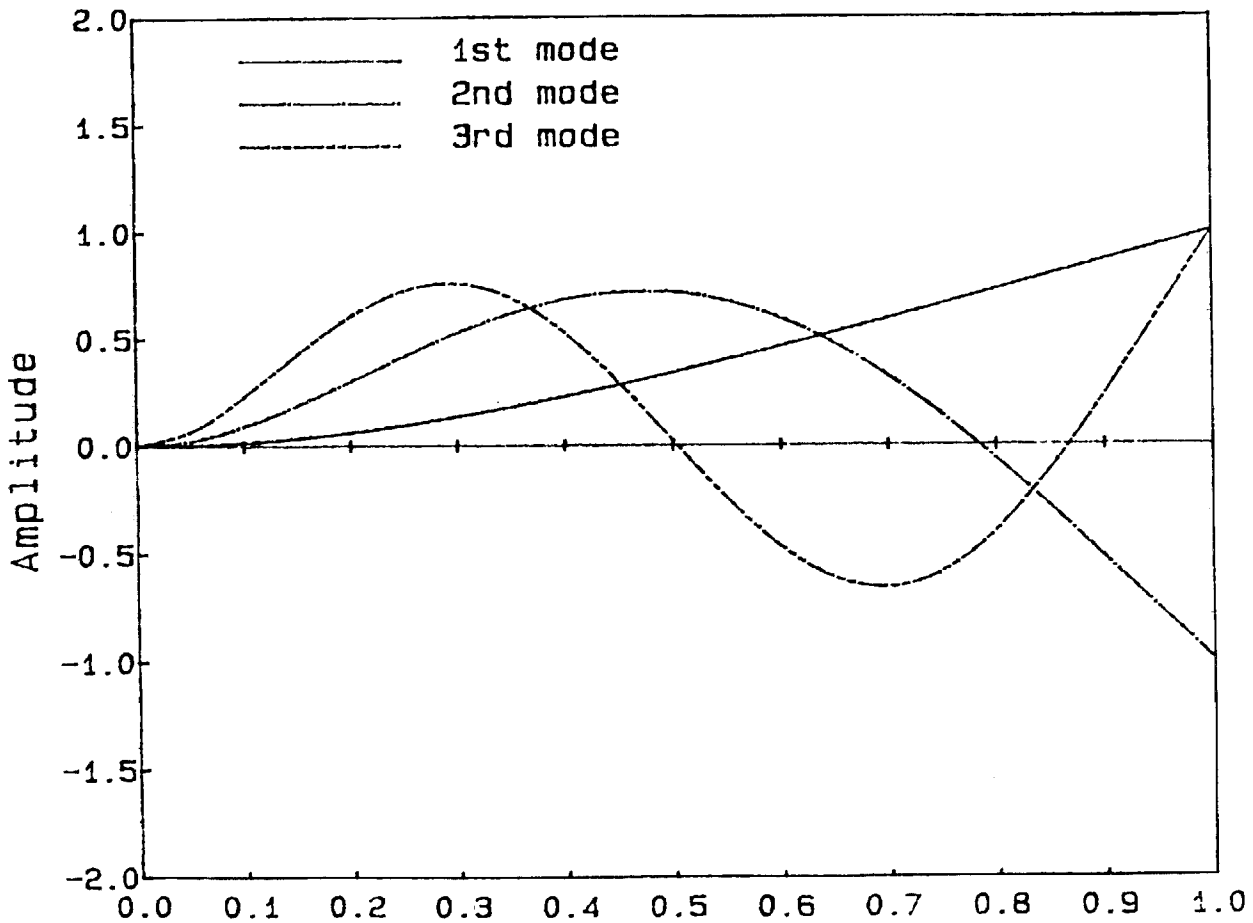

[Fig. 3] TRANSIENT RESPONSE OF MANIPULATOR

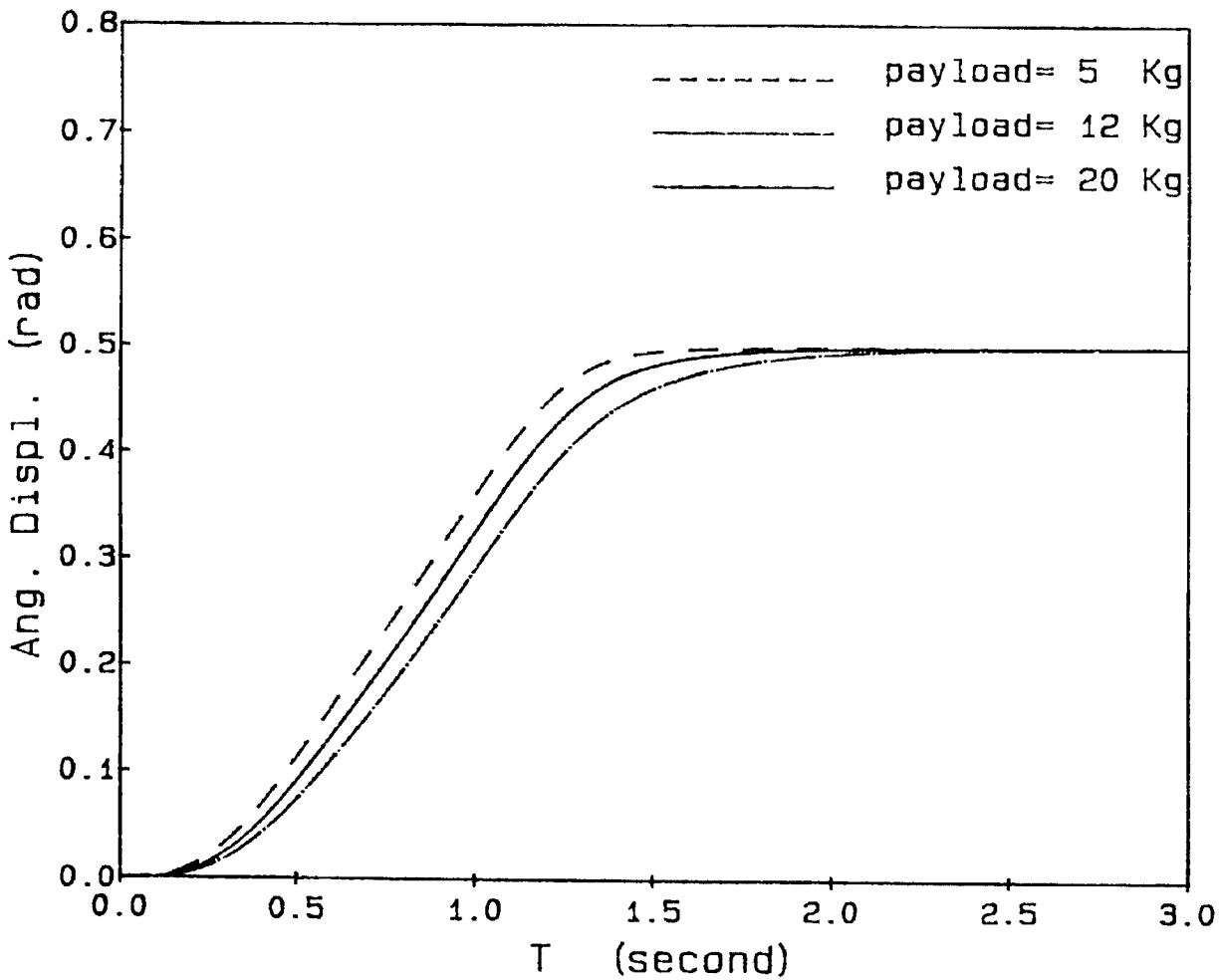

7.32

[Fig. 4] TRANSIENT RESPONSE OF MANIPULATOR

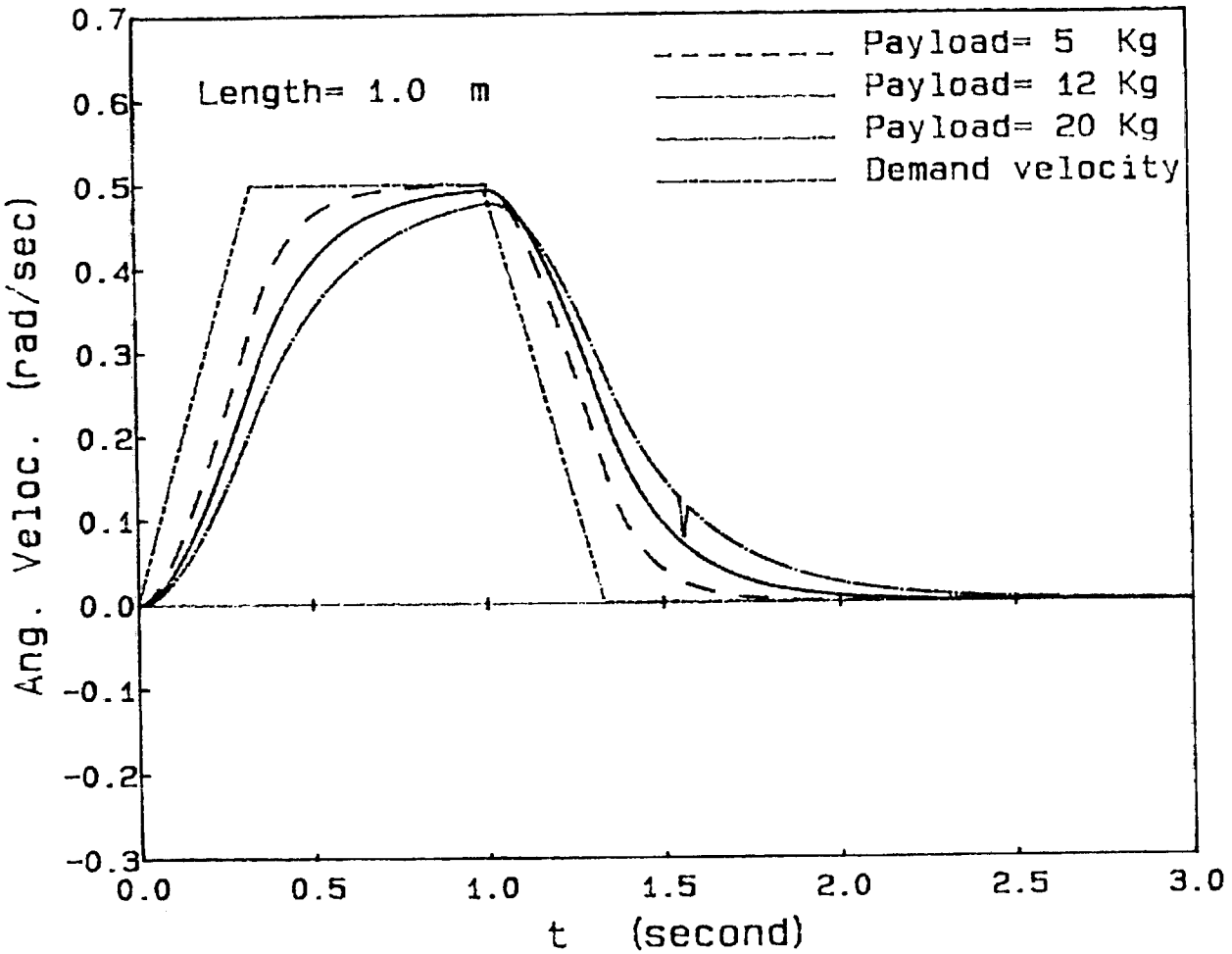

733

[Fig. 5] TRANSIENT RESPONSE OF MANIPULATOR

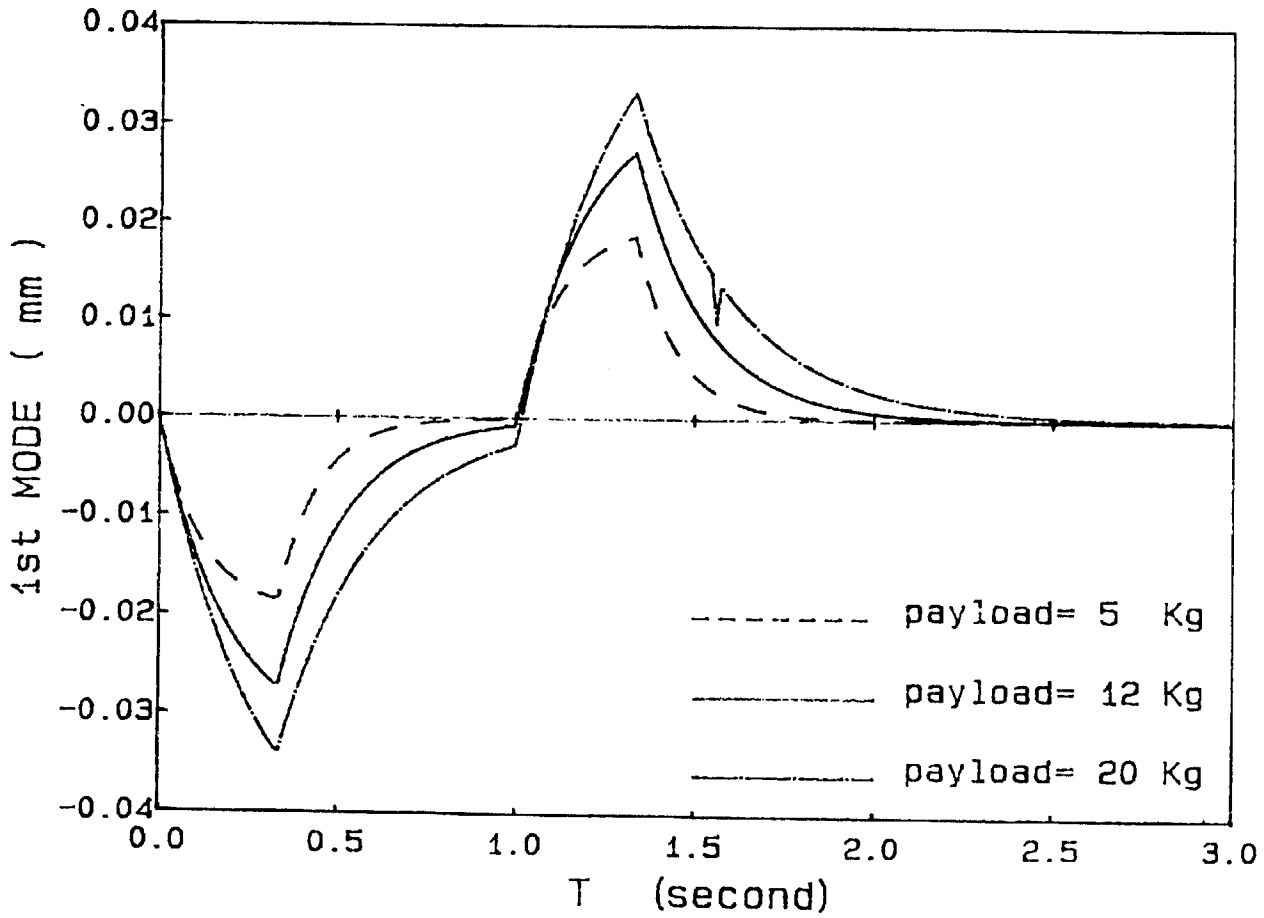

734

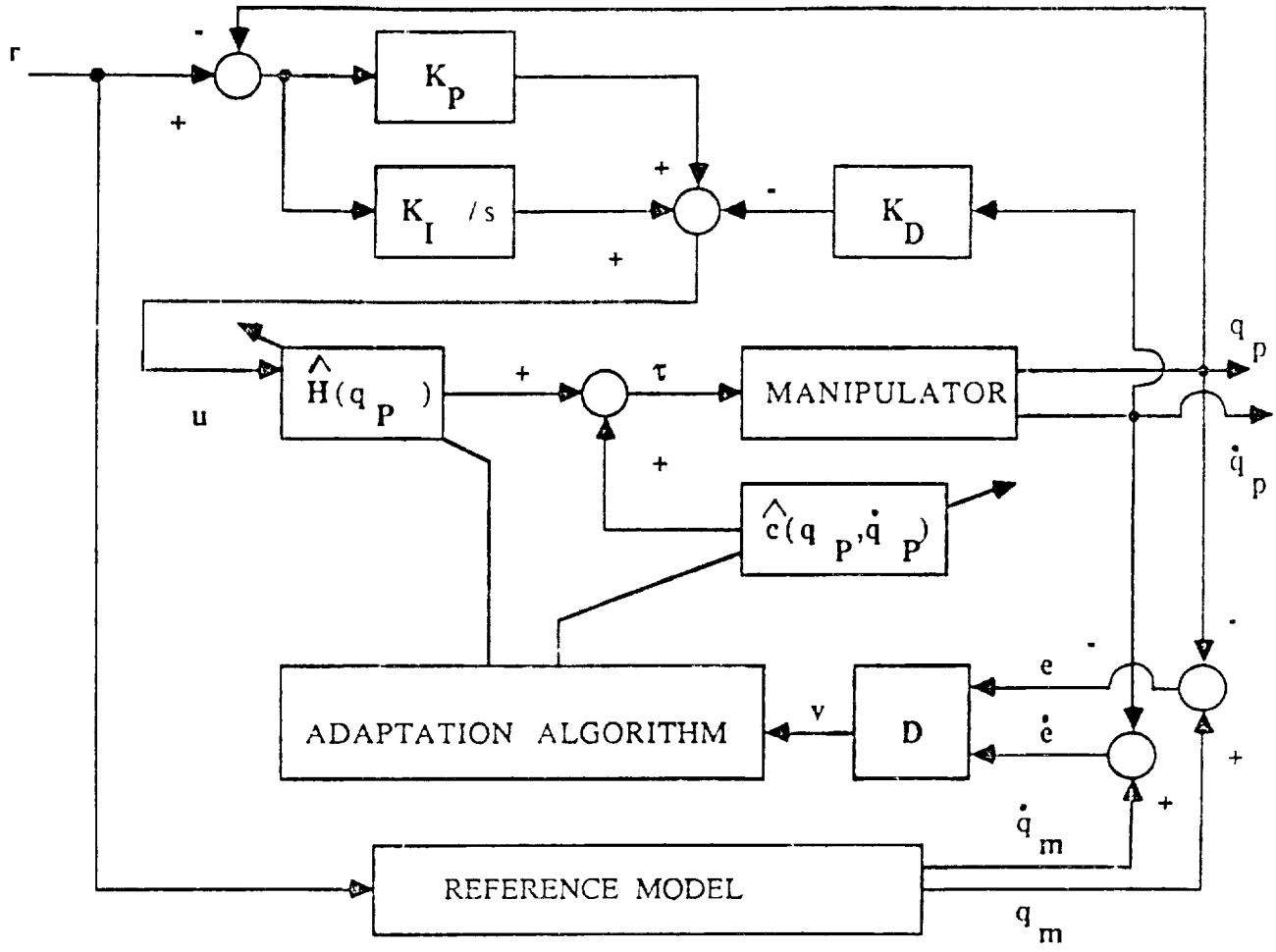

Fig. 6 Block Diagram of MRAC [1, Asada-Nukobon]

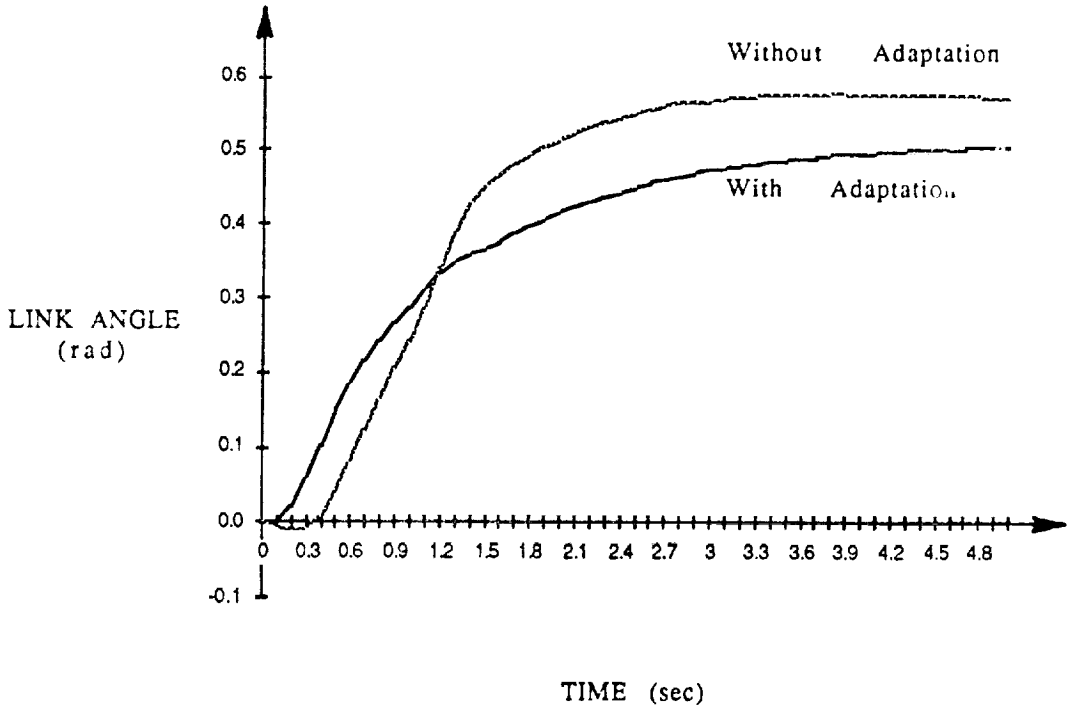

Fig. 7 Step Response of Joint Angle [1]

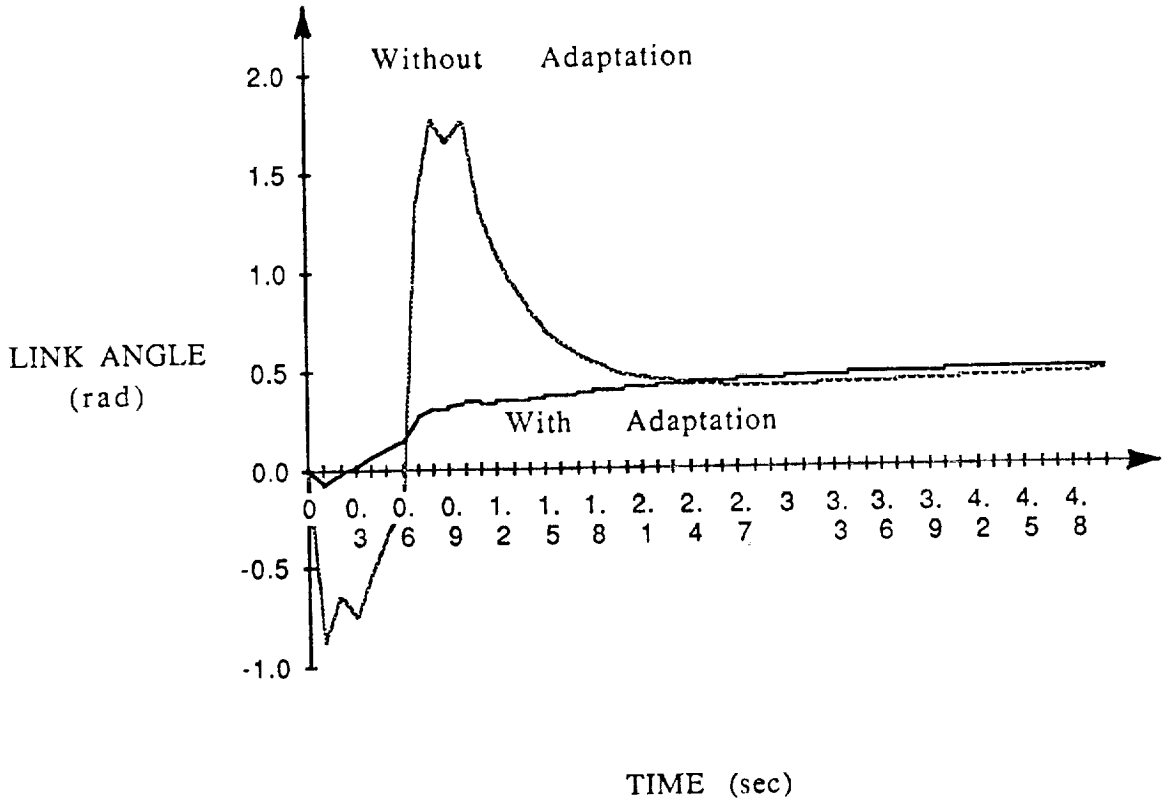

Fig. 8 Impulse Response of Joint Angle [1]

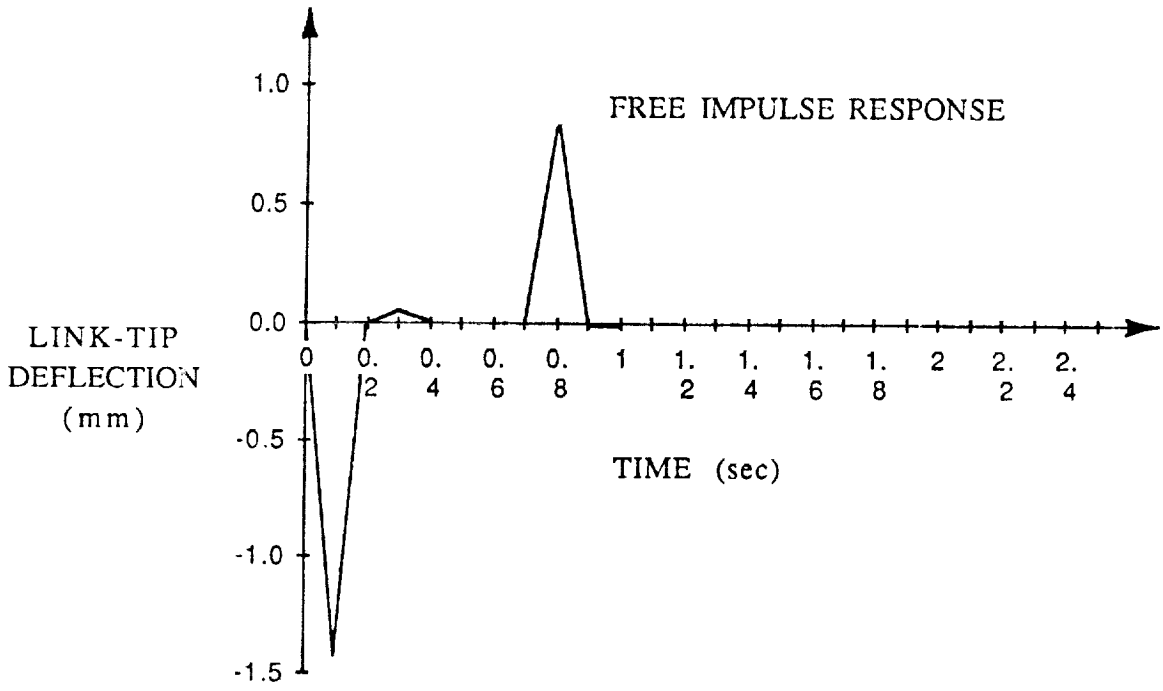

Fig. 9 Free Impulse Response of the Flexible Manipulator [1]

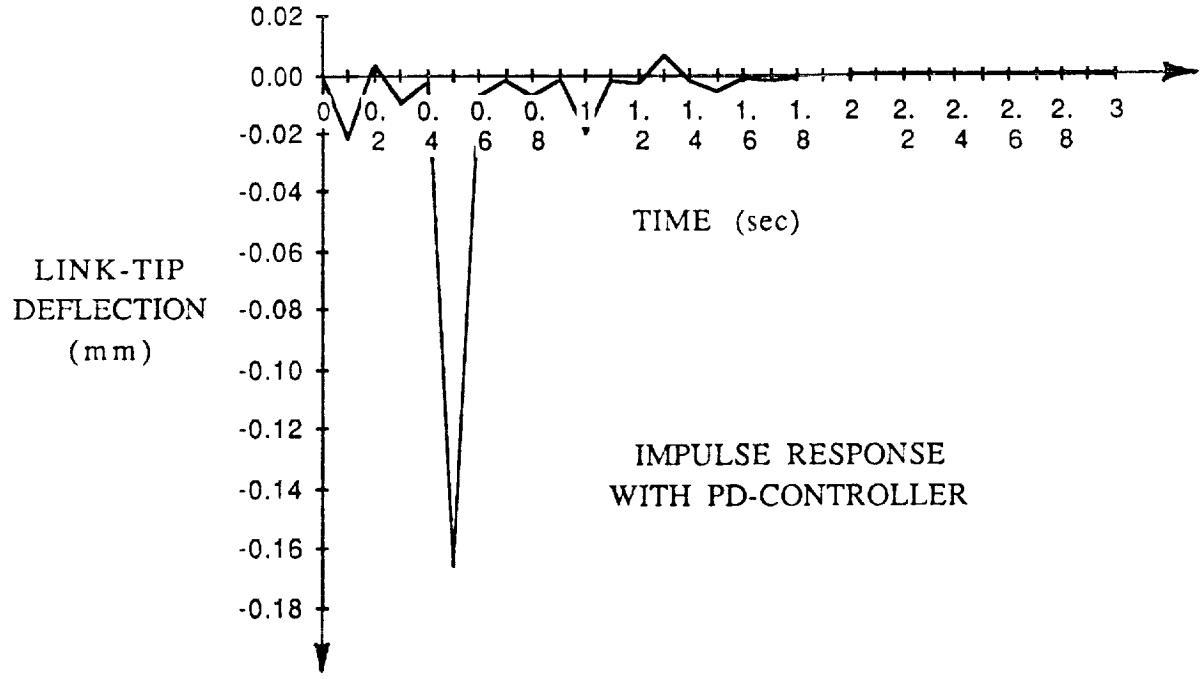

Fig. 10 Impulse Response with PD Controller [1]

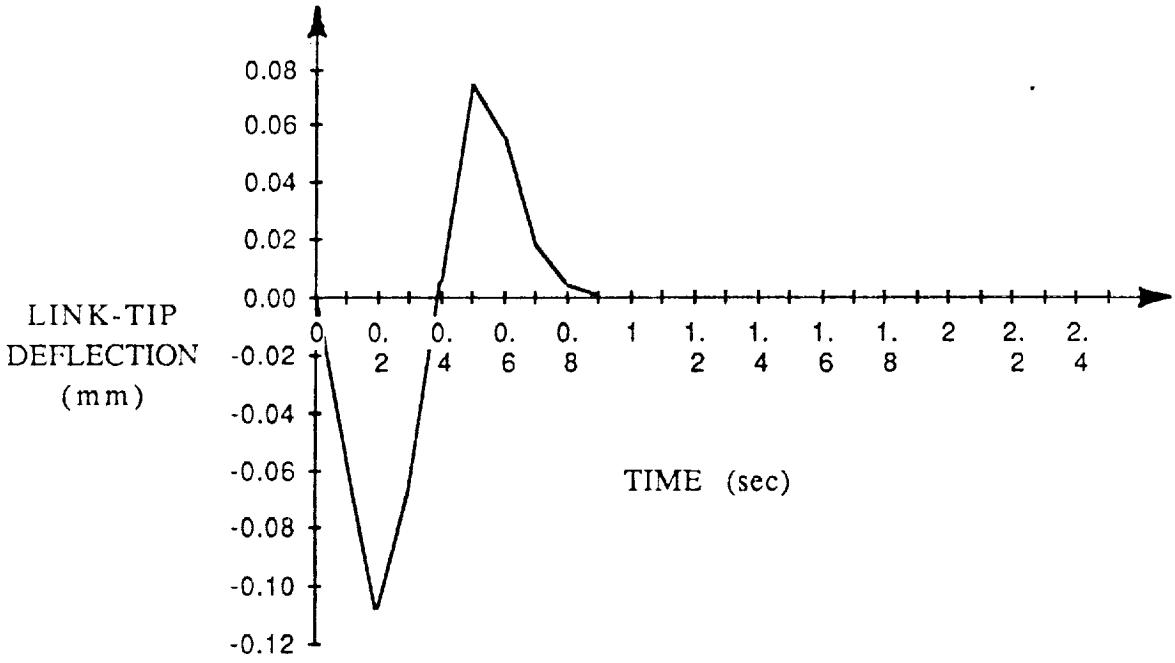

Fig. 11 Flexible Manipulator Response with MRAC [1]

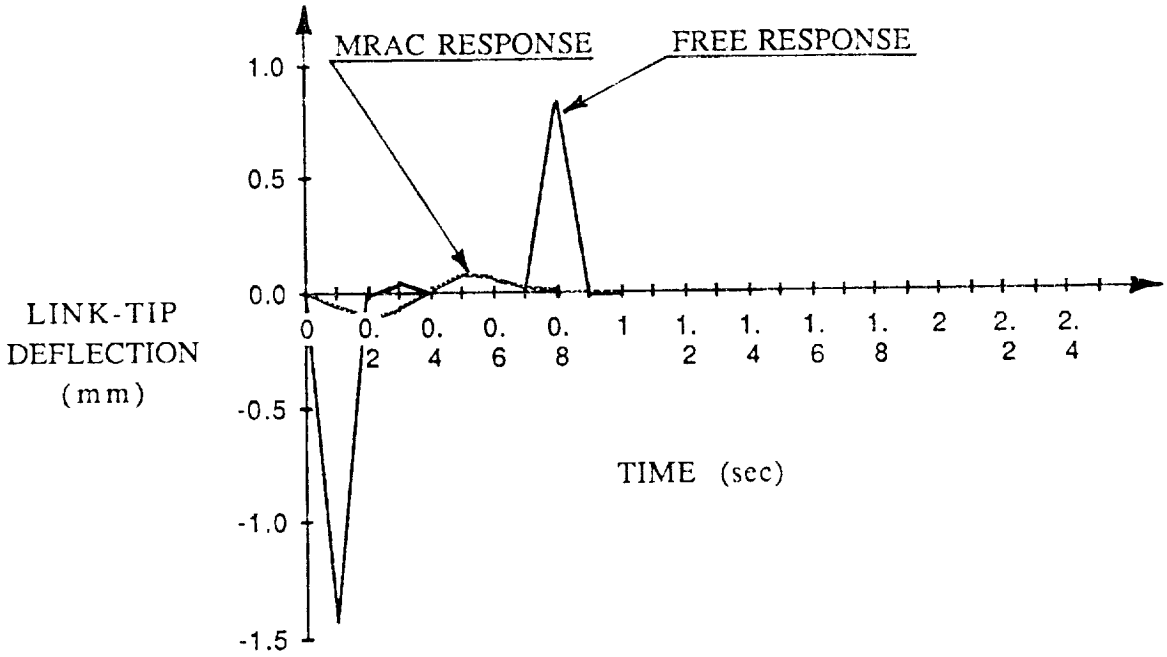

Fig. 12 Comparison between Free and MRAC Responses [1]

N91-22343

Active & Passive Vibration Suppression For Space Structures

D. C. Hyland
Harris Corporation
Government Aerospace Systems Division

Applicable Passive Treatments for LSS

Several test proven damping treatments apply

* Viscoelastic shear damper
* Rotational damper
* Tube constrained layer damping
* Plate constrained layer damping
* Strut viscous damper

Fig. 1

In this presentation, we contemplate the relative benefits of passive and active vibration suppression for Large Space Structures (LSS). The intent is to sketch the true ranges of applicability of these approaches using previously published technical results for this review. In part also, it is our hope to counter past incidences of overzealous advocacy of exclusive use of passive damping or exclusive use of active control and argue, instead, for the proper combination of both approaches.

First, let us consider the various methods of intrastructural damping treatment in use or being considered for use in LSS. Most of the listed damping techniques work by constraining a layer or annulus of viscoelastic material so that it is placed in a state of shear strain. Some devices use the resulting energy dissipation from shear-strain-rate to damp translational motions, whereas others, such as the rotational damper concept, employ an annulus of viscoelastic material to damp rotational motion. In addition there are essentially "add-on" damping treatments using a thin layer of viscoelastic material covered by a stiff "constraining layer" for the purpose of damping flexural vibrations in beams or plates. Finally, strut viscous damper concepts are well adapted to the damping of axial deformations of strut elements within built-up truss structures. These are all intrastructural damping concepts. There are also inertial damping concepts -e.g. the tuned-mass damper which we'll discuss in a moment.

Passive Damping for Vibration Suppression in LSS

\+

* inherently stable
* simpler to implement - no on-line processor necessary
* reasonably weight efficient

−

* inherent performance limitations
* Viscoelastics are
  - are temperature sensitive
  - outgass
  - have low specific stiffness and strength
  - creep (dimensional stability issue)
* tuned-mass dampers are effective only when the target mode frequency is well predicted
* effective design requires good modelling information on performance - significant modes and modal strain energy maps.

Fig. 2

Passive damping approaches offer many inherent advantages for LSS vibration suppression, i.e., these approaches are inherently stable, usually require no on-line processing or electronics and are reasonably weight-efficient. These advantages are presently well recognized and demonstrated. However, a sober assessment must recognize a number of engineering design and implementation issues that arise in LSS applications. First, there are inherent performance limitations to passive damping that we review presently. There are detailed design issues connected with the properties of viscoelastic materials -e.g. temperature dependence of the damping loss factor, outgassing, low specific stiffness and strength and viscoelastic creep which has a direct impact on dimensional stability performance of LSS. These negative factors are not necessarily irremediable - but the successful resolution of these issues in detailed design does contribute to the cost and complexity of final implementation.

Also, the "bottom-line" performance (e.g. line-of-sight jitter, etc.) achieved by a given passive suppression system *does* often depend critically upon the accuracy of *a priori* structural dynamic modelling. For example, tuned-mass dampers are particularly effective only when the target mode frequency is well predicted. With regard to constrained-layer or truss member damping, effective design requires good-quality modelling information on the performance - significant modes and their strain energy maps. If in-mission changes or parameter errors cause significant departures from design-model dynamics, actual damping can be far less than that predicted or specified. Thus, while there is no issue with *stability robustness*, the issue of *performance robustness* remains.

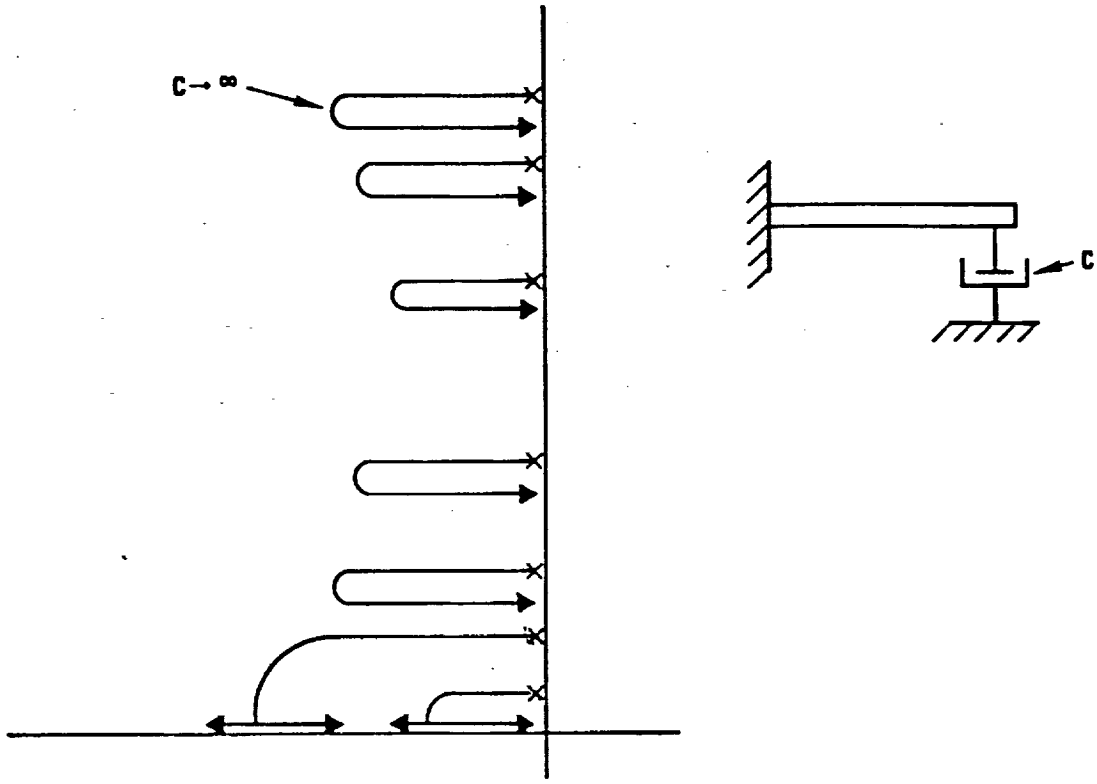

- There is a maximum damping coefficient beyond which there is no further improvement
- For complex structures, sufficiently large damping coefficients decrease energy dissipation

Figure 3. Inherent Limitation to Passive (Semi-Passive) Damping

We illustrate the well-known performance limitations of intrastructural passive damping with the simple cantilevered beam example shown. The point is that the structural damping does not always increase with further increase in the end-mounted damper viscoelastic constant, C. In fact, there is a maximum value of C beyond which there is no further improvement in system damping. In the limit as C increases without bound, the system poles coalesce with zeros on the imaginary axes and there is no damping since the damper acts as a rigid constraint. This effect is due to the fact that spatially discrete dampers modify both the structural mode damping *and* the mode shapes. In consequence, it can sometimes happen that sufficiently large damping coefficients in discrete damper devices can actually decrease energy dissipation in critical regions of a complex multi-component structure.

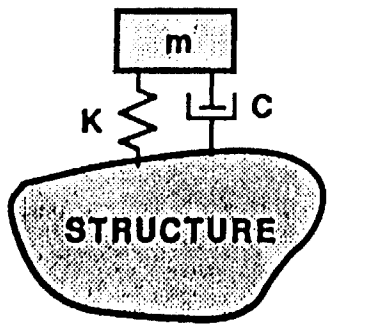

$\omega_d = \sqrt{\frac{K}{m}}$ $\eta_d = \frac{C}{2\sqrt{mK}}$

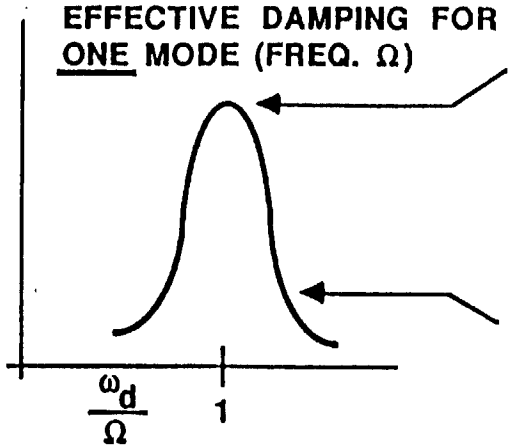

- BEST CASE: LOCATED AT MAX DEFL. POINT, PERFECTLY TUNED, I.E. $\omega_d = \Omega$
  EFFECTIVE DAMPING ≅ $\eta_d \sqrt{\frac{m}{M_{mode}}}$, FOR $\frac{m}{M_{mode}} < 1$
- IF $\Omega \neq \omega_d$, THEN EFFECTIVE DAMPING ≅ $\eta_d \left(\frac{m}{M_{mode}}\right)$

750

- M_{mode} TYPICALLY > 380 LBS., THEREFORE VERY LARGE m NEEDED TO GET 20% STRUCTURAL DAMPING.
- A DIFFERENT SET OF DAMPERS IS REQUIRED FOR EACH SIGNIFICANT MODE (MORE THAN 30).

Fig. 4

Having taken a brief (but perhaps sobering) look at the pros and cons of passive vibration suppression, we pose the question of crucial interest here: With respect to robust performance and simplicity of implementation are active vibration control and passive damping really so distinct after all? (Or has the debate occurring over the recent past been largely a war of words?)

Let us explore this question by contrasting a passive approach with a corresponding active approach to inertial damping.

First, the passive approach considered here is the "tuned-mass" device illustrated in the Figure. Basically, this consists of a small mass (m) connected to the structure with an elastic element (with stiffness k) with viscoelastic material (the dashpot) in the load path to provide a large viscoelastic damping. This is a very simple and inherently stable damping augmentation device. On the other hand, although modal damping augmentation for the "targeted" structural mode can be substantial when the damper resonance (ω_d) is near the targeted mode frequency, damping augmentation is slight when there is frequency mismatch. Overall effectiveness depends on the ratio of the damper mass to the generalized mass of (M_{mode}) of the targeted mode (and in the system context of this particular diagram M_{mode} was typically several hundred pounds so that a large m would have been required to obtain the desired 20% damping). Thus, if there's modelling error resulting in significant "detuning", damping will be far less than predicted and one is stuck with the resulting performance loss. (Of course, a possible way around this problem is to build in an active electromechanical device capable of changing the damper stiffness, k, so as to "re-tune" the damper on-line, during the mission - but this refinement would negate most of the distinction between "passive" versus "active"!).

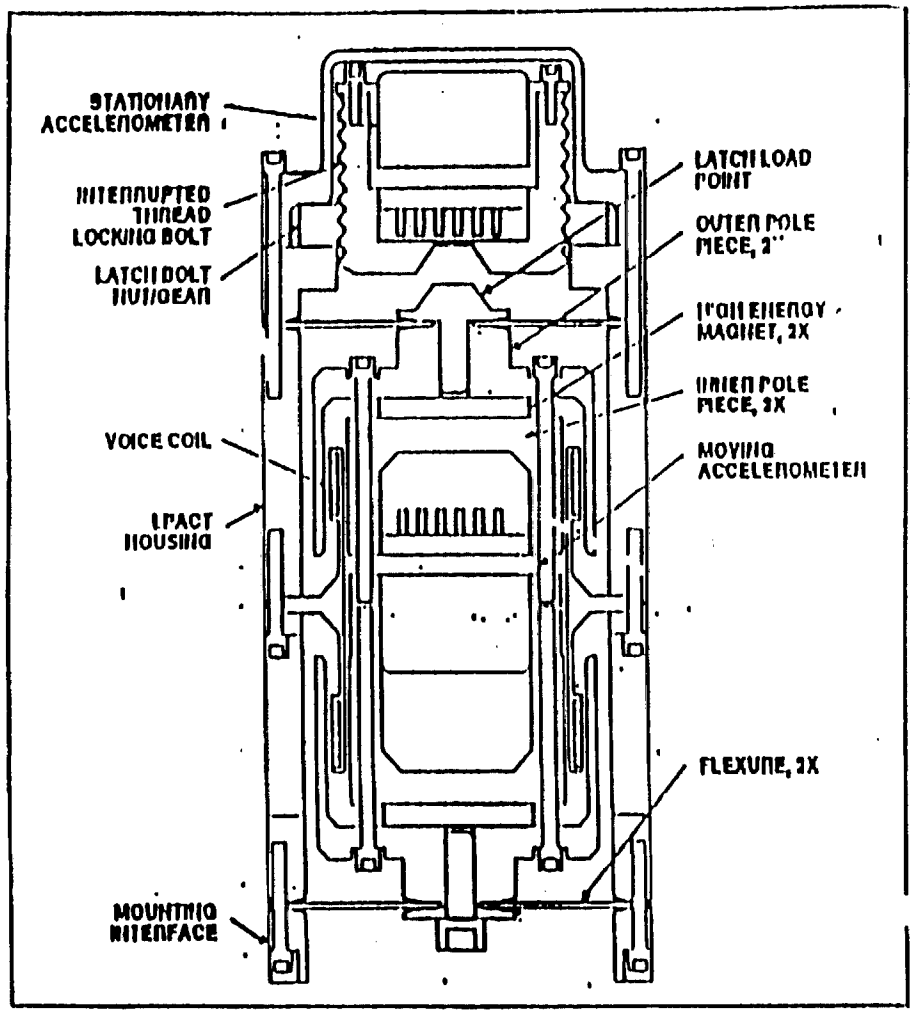

- PROOF MASS / VOICE COIL DESIGN
- GRAPHITE-EPOXY FLEXURES OBVIATE BEARING STICTION PROBLEMS
- ULTRA-HIGH-BANDWIDTH CASING-MOUNTED ACCELEROMETER MEASURES STRUCTURAL MOTION
- PROOF-MASS MOUNTED ACCELEROMETER CLOSES INTERNAL CONTROL LOOP RESULTING IN RELIABLY SHAPED FREQUENCY RESPONSE

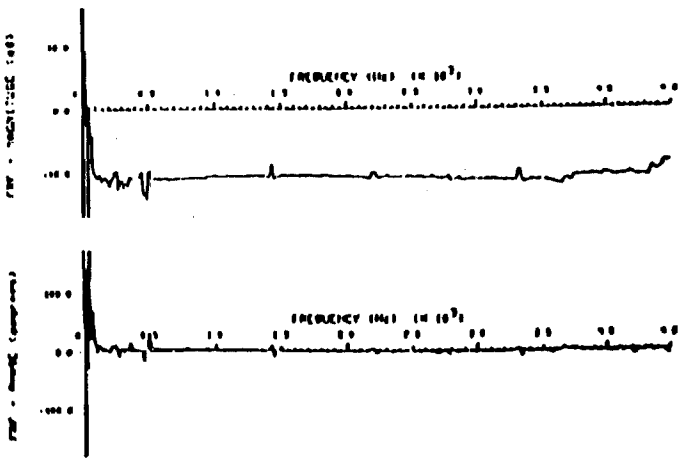

Fig. 5

LPACT Damping Unit Provides Reliable, High-Bandwidth Sensor/Actuator in a Single Package.

Now, consider an analogous *active* approach to vibration suppression using the Linear Precision Actuator (LPACT). The patented LPACT device (see Reference 1) is a bearingless voice coil proof-mass actuator which uses a proof-mass-mounted accelerometer to close a force control loop which serves to override nonlinearities and temperature-dependent effects. With this internal force compensation loop, the LPACT has flat frequency response from 3–10 Hz to at least 5 KHz. The LPACT design currently used in Harris test beds provides a maximum force of 5 pounds with 20 micropound resolution. Each LPACT has a casing-mounted accelerometer for implementation of vibration control feedback.

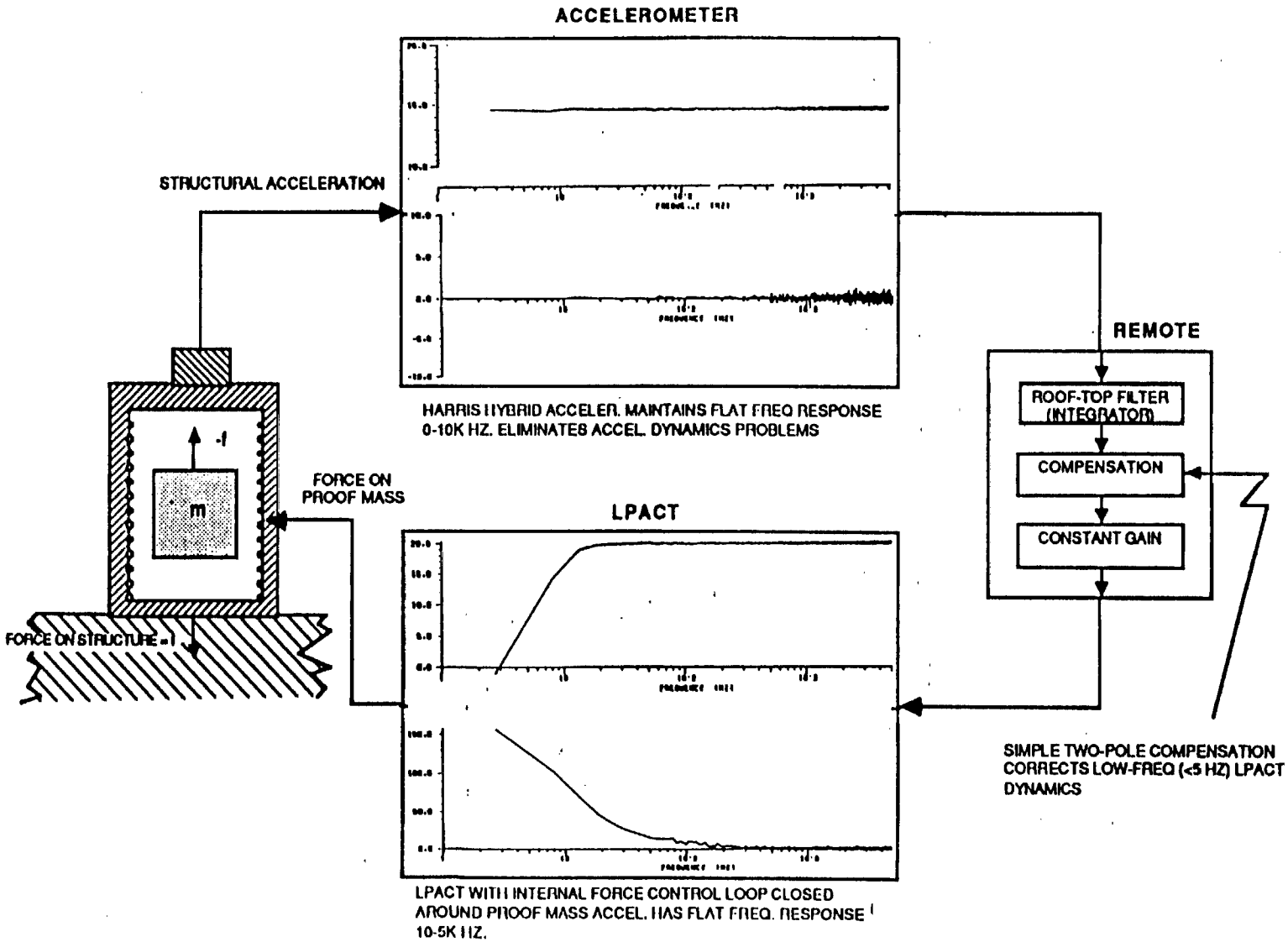
ACCELEROMETER
STRUCTURAL ACCELERATION
HARRIS HYBRID ACCELER. MAINTAINS FLAT FREQ RESPONSE 0-10K HZ. ELIMINATES ACCEL. DYNAMICS PROBLEMS
REMOTE
ROOF-TOP FILTER (INTEGRATOR)
COMPENSATION
CONSTANT GAIN
-f
m
FORCE ON PROOF MASS
FORCE ON STRUCTURE = f
LPACT
SIMPLE TWO-POLE COMPENSATION CORRECTS LOW-FREQ (<5 HZ) LPACT DYNAMICS
LPACT WITH INTERNAL FORCE CONTROL LOOP CLOSED AROUND PROOF MASS ACCEL. HAS FLAT FREQ. RESPONSE 10-5K HZ.

Fig. 6

The casing-mounted accelerometer is the new "Hybrid Accelerometer", an advanced acceleration sensor design providing flat frequency response from DC to at least 10 KHz.

The diagram illustrates that with the exceedingly high bandwidth and flat frequency response of the LPACT actuator and colocated Hybrid Accelerometer, it is now possible to implement a simple collocated rate feedback controller to provide broadband damping. Note that the LPACT with its Hybrid Accelerometer form one single compact "active damping unit."

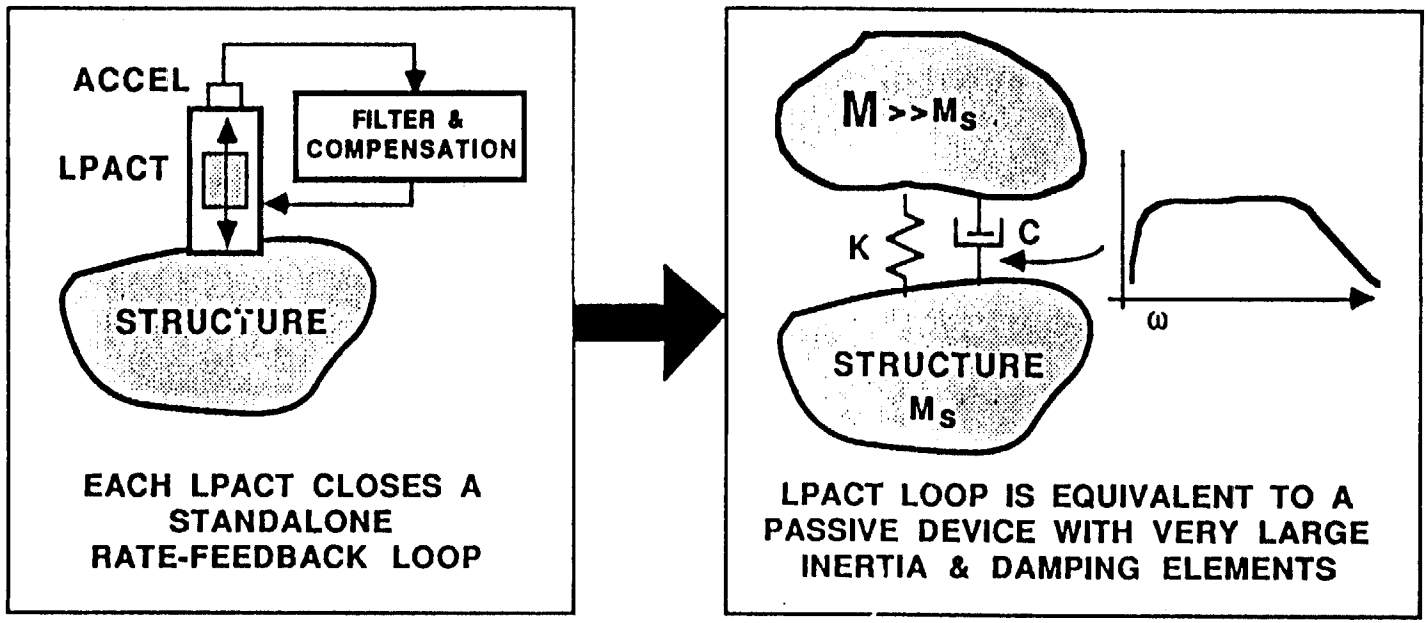

- CONTROL IS EQUIVALENT TO A NETWORK OF PASSIVE DEVICES, BUT WE USE THE ELECTRICAL ENERGY OF THE LPACT TO EMULATE MUCH LARGER INERTIA & DAMPING THAN IS MECHANICALLY POSSIBLE.
- LARGE BROADBAND DAMPING IS REALIZED DESPITE THE SMALL ACTUAL MASS OF THE LPACT.

Fig. 7

If as indicated on the left of the illustration, we use the LPACT to close a standalone feedback loop, then due to the high band width of the sensor/actuator hardware, the LPACT loop closely approximates a passive device – similar to the tuned mass damper – but with very large inertia and damping elements. As illustrated, the LPACT is equivalent to an inertially anchored damper with large viscoelastic damping and is thus able to provide very broadband damping (not just frequency-tuned damping) despite the small actual mass of the LPACT.

Thus, there presently does exist *active* control hardware that can emulate the inherently stable operation of passive vibration suppression but with the added flexibility to provide much larger effective inertia and damping than would be mechanically possible with passive devices.

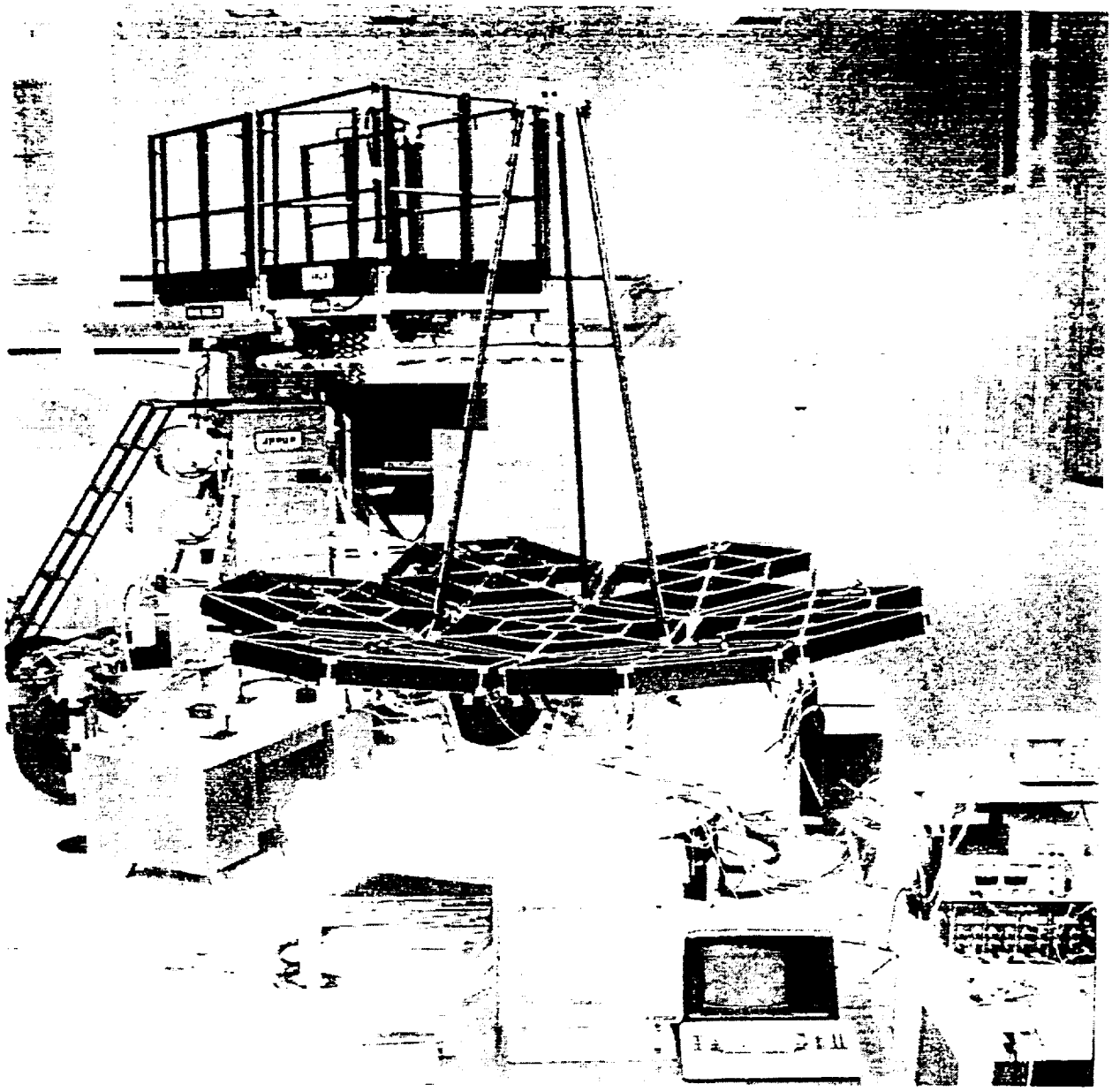

Figure 8. The Mult-Hex Prototype Experiment is the third in a series of 3 experiments designed and implemented at Harris.

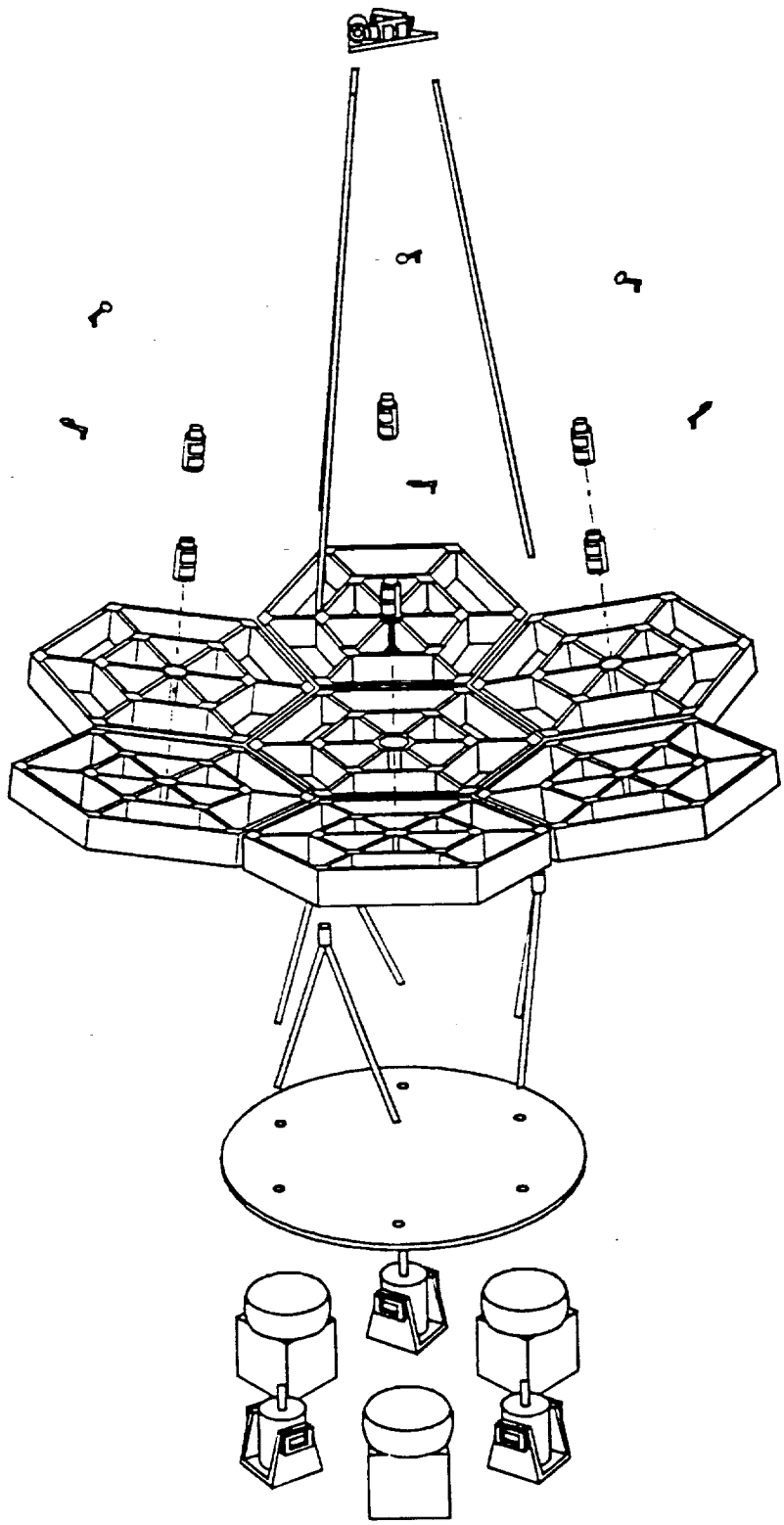

SC-7 (XPro)

Fig. 8.a

759

The above performance benefits of LPACT sensor/actuator units have been experimentally demonstrated using the Multi-Hex Prototype Experiment (MHPE). The MHPE (Reference 2,3) is a vibration control testbed developed on Harris IR&D to study the vibration issues associated with generic Cassagrain configurations with large multi-segment primaries.

As illustrated in the photograph, the MHPE consists of a secondary mirror and support platform supported by a Gr/Ep tripod tower connected to the center segment of the primary reaction structure. The primary reaction structure is an array of seven Gr/Ep hexagonal box trusses. The array is approximately 4M across. A six member truss connects the seven-panel array to a circular baseplate (emulating a spacecraft bulkhead). The total static weight is supported by air-bag isolators and electrodynamic shakers are interfaced to the baseplate to provide disturbances emulating broadband spacecraft-generated disturbances. Line-of-Sight (LOS) jitter and panel-to-panel misalignments due to vibration are monitored by three complementary subsystems: (1) a pseudo-dephase-measurement system using a large number of accelerometers and on-line processing, (2) the Optical Performance Measurement Subsystem using laser interferometry to measure panel-to-panel misalignments and (3) an optical LOS scoring subsystem using a faceted secondary and optical flats distributed over the primary reaction structure.

IF ONLY THE PRIMARY MIRROR WERE RIGID, OUR PROBLEMS WOULD BE SOLVED! BUT...

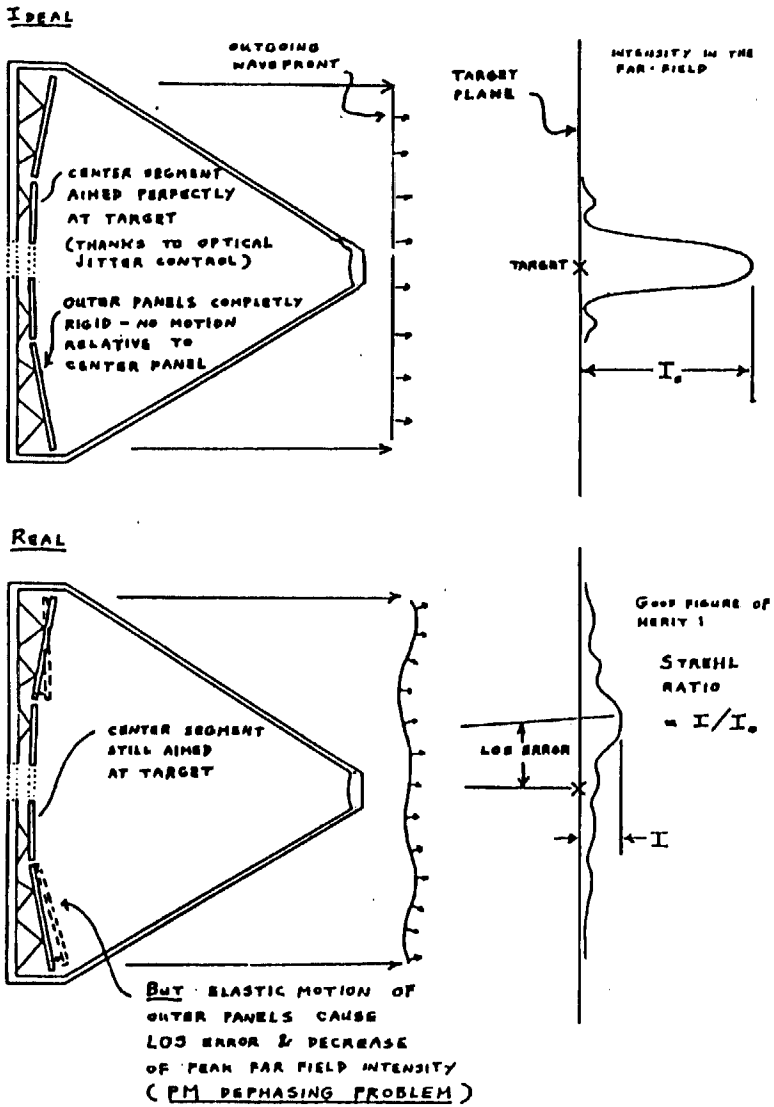

- POINTING AND ALIGNMENT LOOPS ALIGN SECONDARY + PRIMARY CENTER SEGMENT WITH TARGET

- POINTING AND ALIGNMENT LOOPS DO NOT COMPENSATE FOR OUTER SEGMENT MOTION RELATIVE TO CENTER SEGMENT ("PM DEPHASING")

- PM DEPHASING DEGRADES BOTH LOS ACCURACY AND MAXIMUM FAR-FIELD INTENSITY

Fig. 9

The MHPE was designed to study a number of vibration control issues in large RF or optical systems, including both LOS jitter and "Primary Mirror (PM) dephasing". The PM dephasing issue illustrated here, arises because vibrational disturbances cause misalignments of the individual PM segments relative to one another. According to the laws of diffraction such "dephasing" of the PM segments can cause considerable reduction of the peak radiation intensity in the far field. Often, PM dephasing cannot be readily compensated by alignment elements in the system optical train and structural control of the PM assembly may be desired.

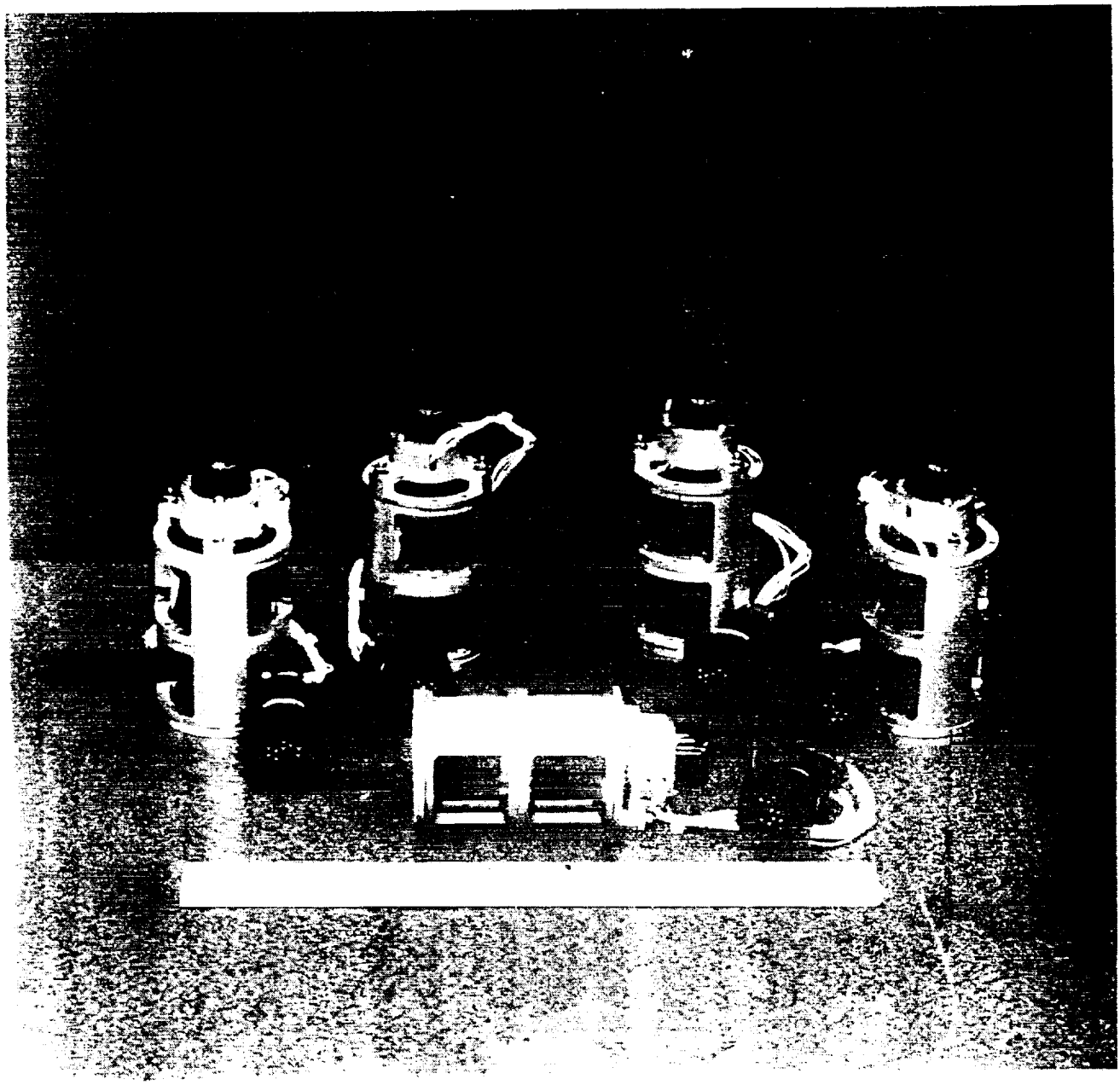

Figure 10. The Harris Linear Precision Actuator (LPACT) is a proof mass actuator developed for vibration suppression of flexible structures. The internal control loops of the LPACT yield a device transfer function which has high bandwidth and flat response over a large frequency range.

For active vibration control, the MHPE is instrumented with nine LPACT sensor/actuator units: three LPACTs on the secondary mirror platform to control the tower bending modes contributing to LOS jitter and six LPACTs mounted within the outer hex panels to control primary reaction structure panel dephasing. Both data acquisition and on-line control algorithm implementation are executed via the MCX-5 computer.

The system can implement both centralized, MIMO, control algorithms and/or decentralized control designs and a variety of designs have been tested and included in live demonstrations of active vibration control provided to Harris visitors over the last two years. Here we show data (References 4,5) on the decentralized rate-feedback control design discussed above.

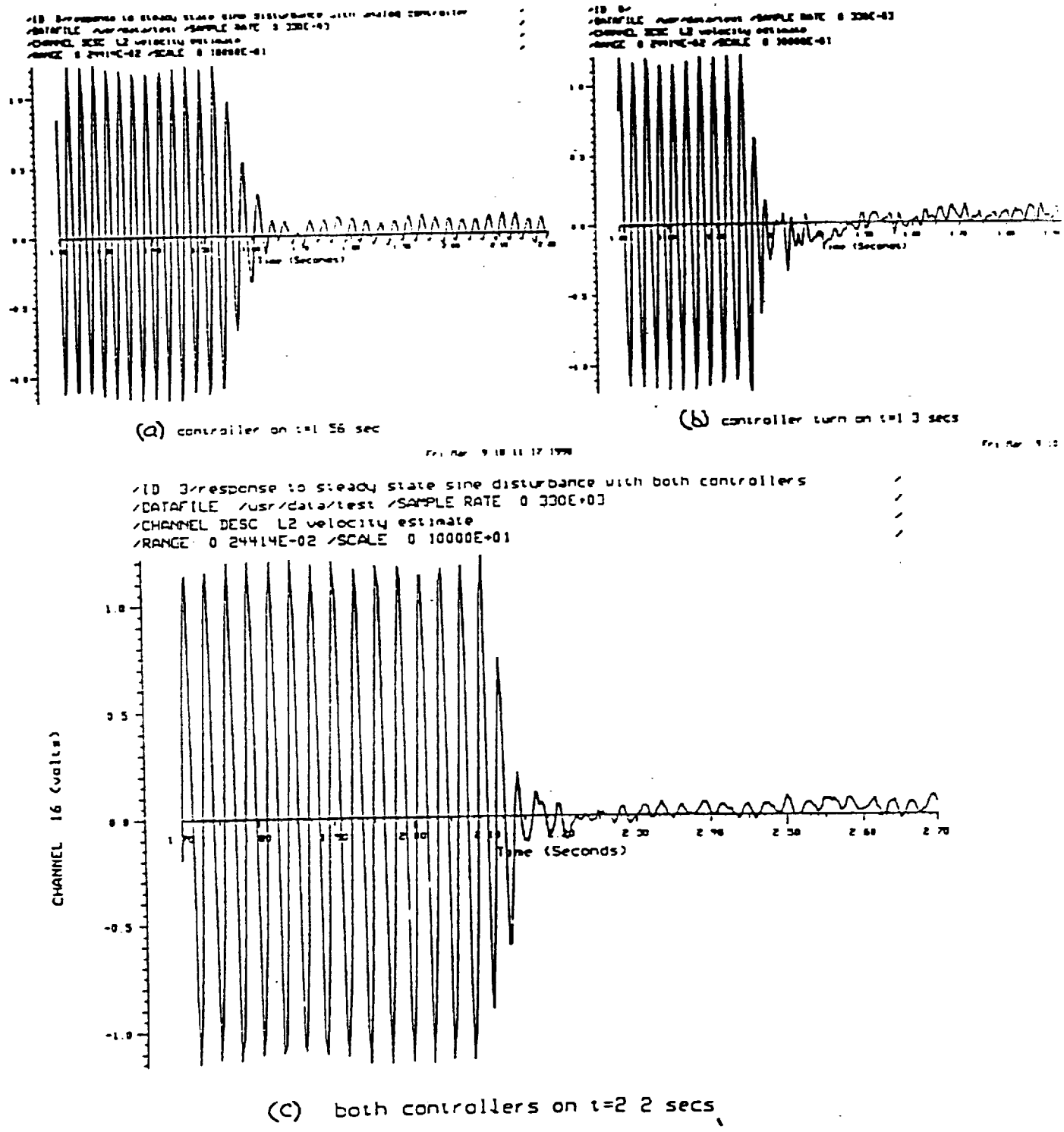

Figure 11. The MHPE hybrid control heirarchy features both performance and fault tolerance.

The decentralized design is a hybrid design consisting of a high bandwidth (1000 Hz) analog control for damping of very high frequency modes and a lower bandwidth high gain digital control for enhanced suppression of the lower frequency modes. Overall, an order of magnitude suppression of LOS jitter and rms dephasing is obtained for broadband disturbances. To illustrate this capability for visitors in our live demonstrations we show open and closed-loop performance for a medley of modes -using sinusoidal disturbances at modal frequencies in order to make the vibrations palpable to the human senses. The demonstration sequence starts with lower frequency modes, which can be felt by touching the MHPE panels and concludes with high frequency modes which can be clearly heard.

Here, for example, we show via one of the accelerometer measurements, the open and closed-loop vibration for a 35 Hz mode involving large panel-to-panel misalignment. The bottom plot shows the complete hybrid controller. Here the mode is excited sinusoidally with the disturbance maintained throughout the test period. Up to $t = 2.2$ sec., the control is turned off and open-loop vibration is observed. When, at $t = 2.2$ sec., the controller is turned on, the vibration level quickly drops by approximately an order of magnitude.

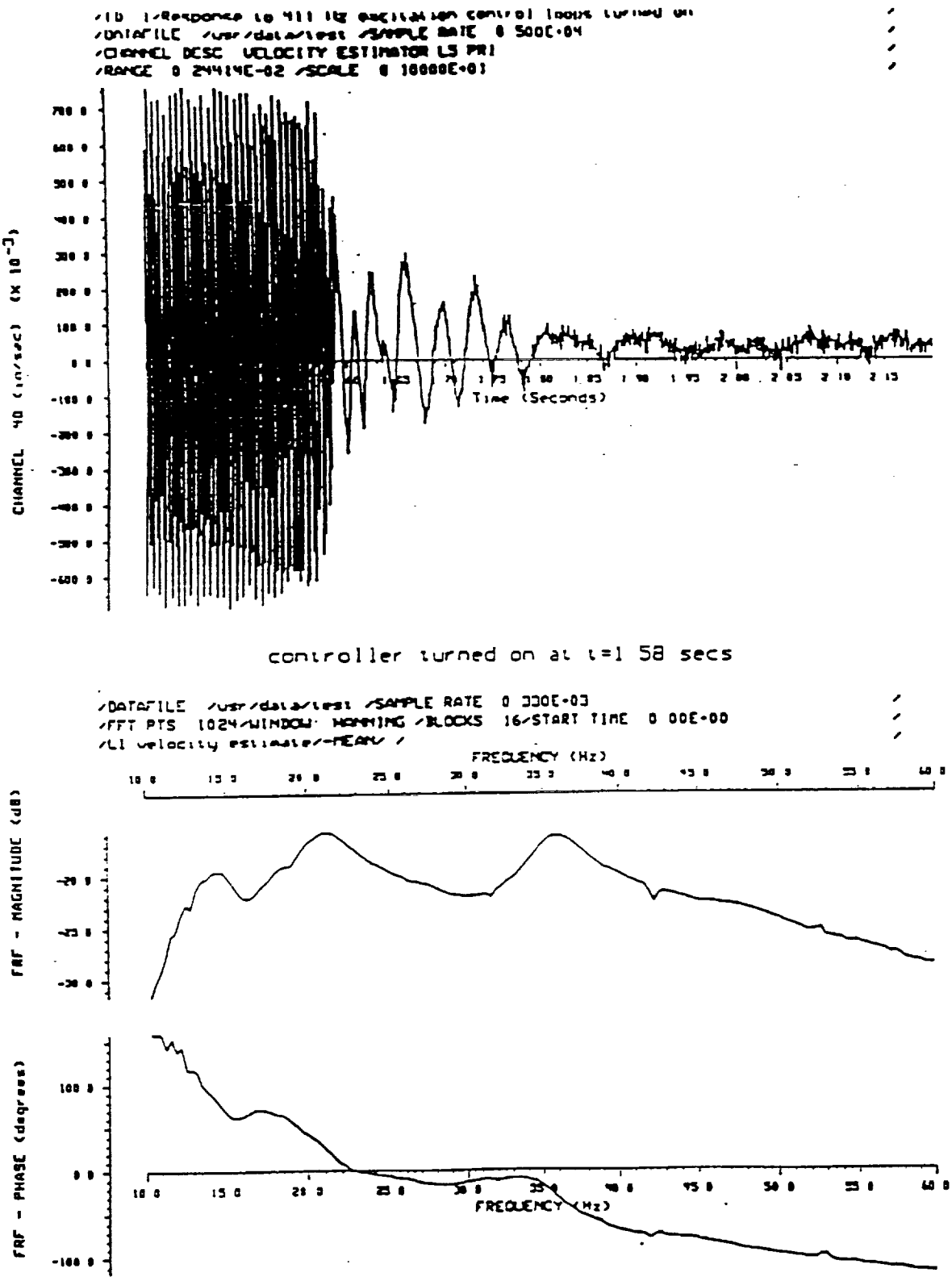

Figure 12. Colocated analog control loops performance illustrated in both time and frequency domain.

Similar results are obtained for the other performance-significant modes. In addition, we demonstrate high levels of active damping even for very high frequency modes (up to approximately 900 Hz). For example, the top plot shows open- versus closed-loop results when a 411 Hz mode is excited (vibration in this mode is clearly audible). When the control is turned on at $t = 1.58$ sec., the vibration amplitude again drops to a substantially lower level. Similar attenuation is observed for the other high frequency modes - up to approximately 900 Hz where the control feedback gain begins to toll-off.

Such results demonstrate simple decentralized control that implements "semi-active" damping, and show an order of magnitude improvement in dephasing with rugged bolt-on hardware. Again, an important point is that active control has matured to produce active hardware permitting control that is at least as effective and as reliable as passive damping over frequencies below 1 KHz. Added benefits include the scope to achieve even better performance with more sophisticated control strategies and the capability to revise these strategies as needed.

Further MHPE experiments have combined active control with passive constrained-layer damping. Although these activities are the subject of a separate report, we should note that the active and passive components are clearly complementary, the active control providing large attenuation from 10 to 900 Hz and the passive damping providing suppression of the multitude of very closely spaced modes near 1 KHz and above.

Passive Damping and Active Control

With active control, passive/active system requires

- less power
- fewer actuators
- increased robustness
- simpler control algorithms

Passive Damping must be designed in early in design process

Fig. 13

Now that active control technology has matured to the point that its risk and complexity have been greatly reduced, it's time to consider an overall approach combining active control and passive damping. Individually, these technologies are not panaceas but the most cost-effective route is the proper *orchestration* of both. As indicated in the chart, the combination of active and passive technologies offers many synergistic advantages. In particular a combined active/passive vibration suppression system may require less power, less instrumentation, less complicated control algorithms while offering more robust performance.

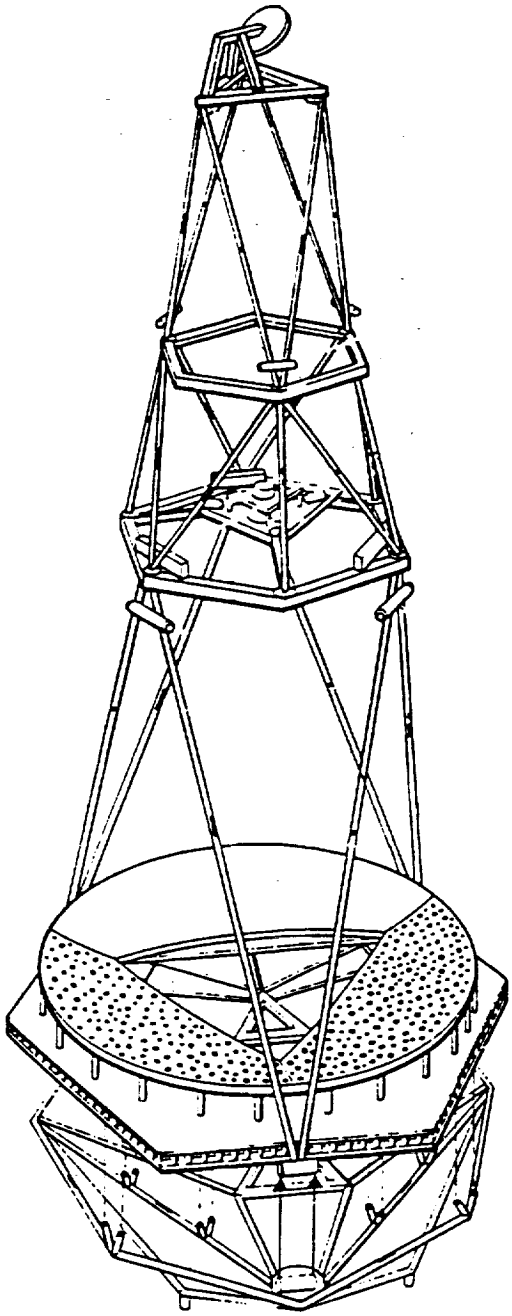

- Base disturbances broadband over 5–1000 Hz
- Control objective: reduce vibration 40–60 dB relative to open loop response over frequency band from 5 to 500 Hz

Figure 14. HALO Optical Structure

The mutually reinforcing benefits of passive stiffness augmentation, passive or "semi-passive" damping augmentation and active control are illustrated by some results obtained approximately five years ago (see Ref. 6). This example involves an experimental configuration for the HALO (High Altitude Large Optics) structure, which is a graphite/epoxy truss with ellipsoidal optics, and we postulate the use of HALO as a test-bed for various vibration control methodologies. To this end, the basic scheme features the use of electrodynamic shakers to provide broadband force excitations to the base of the bottom truss structure and to the secondary mirror platform. In particular three independent base disturbances are postulated having flat power spectral density over 5–1000 Hz. The overall vibration suppression objective is to reduce rms line-of-sight (LOS) and wave front (WF) errors by approximately 60 dB relative to the open loop. An iterative design process led to the selection of vibration control hardware consisting of a number of colocated accelerometer/voice coil actuator units and noncolocated linear DC motor actuators and internal alignment optical sensors.

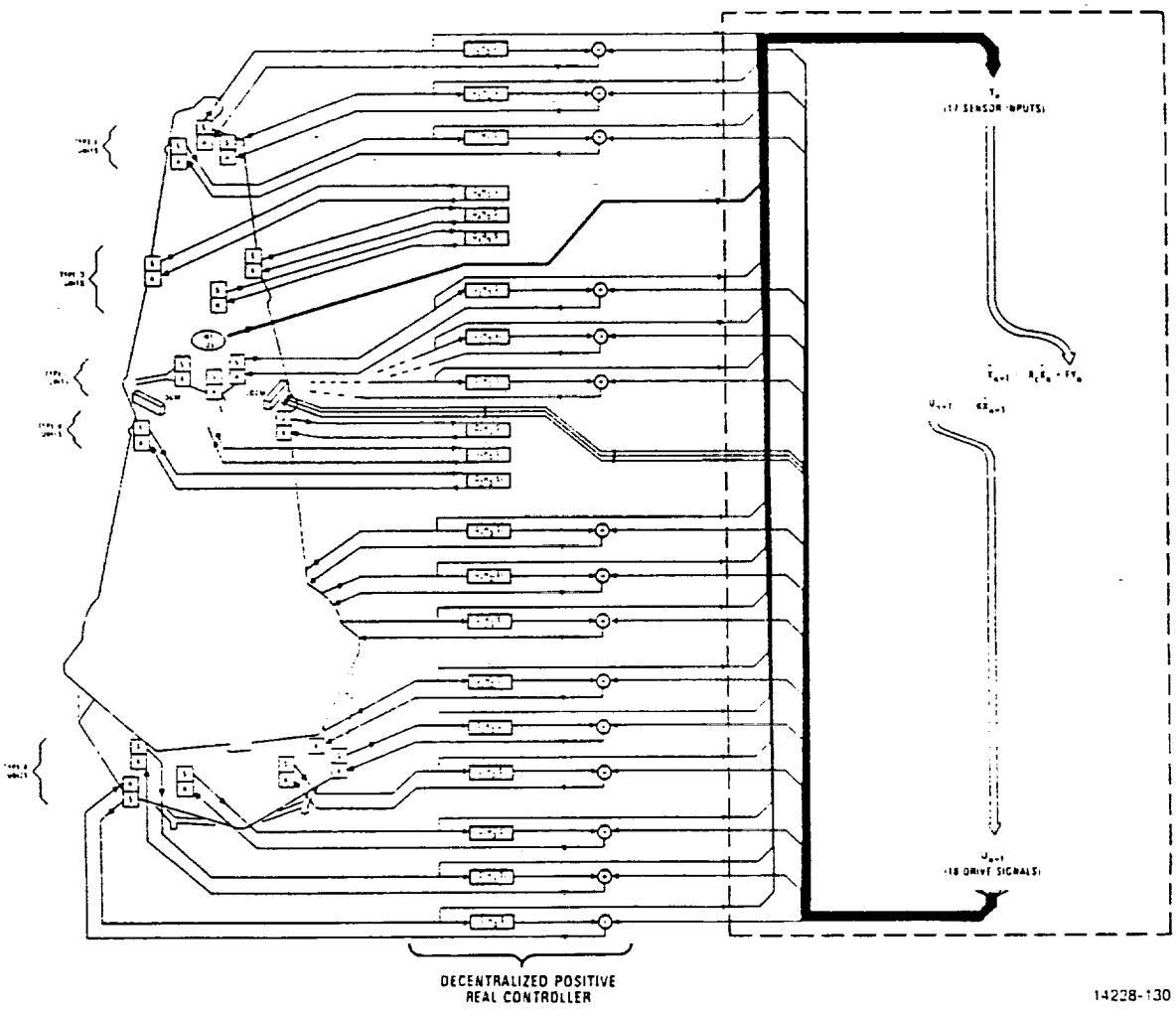

Fig. 15

In the design studies for the HALO modal, we traded off various levels of advanced materials usage, semi-passive damping and active control. As indicated in the diagram, the control system has a two-level architecture consisting of:

1. 21 independent decentralized positive-real controllers (DPRC's) imposing local feedback between voice-coils and colocated accelerometers.
2. A Centralized Coordinating Dynamic Compensator (CCDC) which provides simultaneous coordination of many noncolocated sensors and actuators.

The DPRC's represent a semi-passive damping approach similar to the LPACT rate feedback loops discussed above for the MHPE. The CCDC is the centralized "active" control component.

With this two-level control architecture, we compared cases involving the original Gr/Ep structure with a structure wherein the main components are composed of a Metal Matrix Composite (MMC) offering a four-fold increase in the stiffness of Gr/Ep.

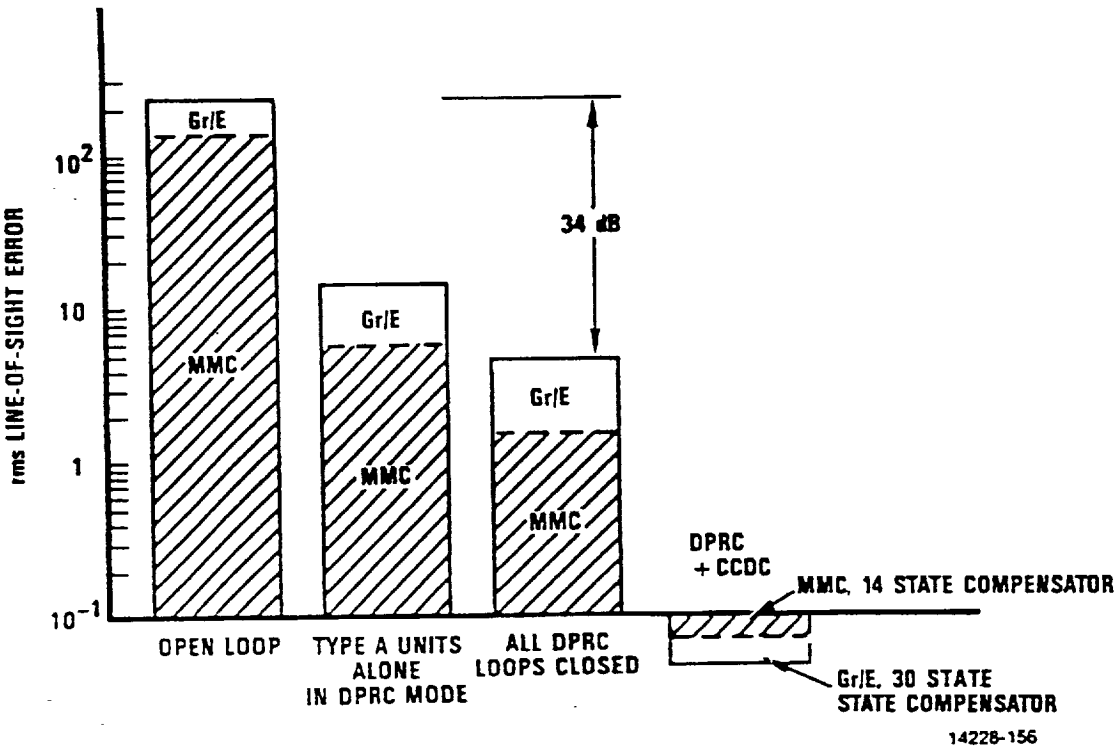

Figure 16. Summary of HALO Controller Performance Results: Line-of-Sight Error

This Figure summarizes LOS jitter performance results for both Gr/Ep and MMC structures. Specifically, for both material selections we show rms LOS errors for the open-loop, for the semi-passive controllers alone and finally, for the complete control including the centralized active control design. The increased stiffness of the MMC structure gives only modest performance improvement in the open-loop. However, it is evident that increased stiffness combined with semi-passive vibration suppression and centralized active control gives performance improvement well beyond what might be expected of each design measure individually. The final performance, being more than the sum of its parts, indicates the synergistic benefits of combining passive and active suppression techniques.

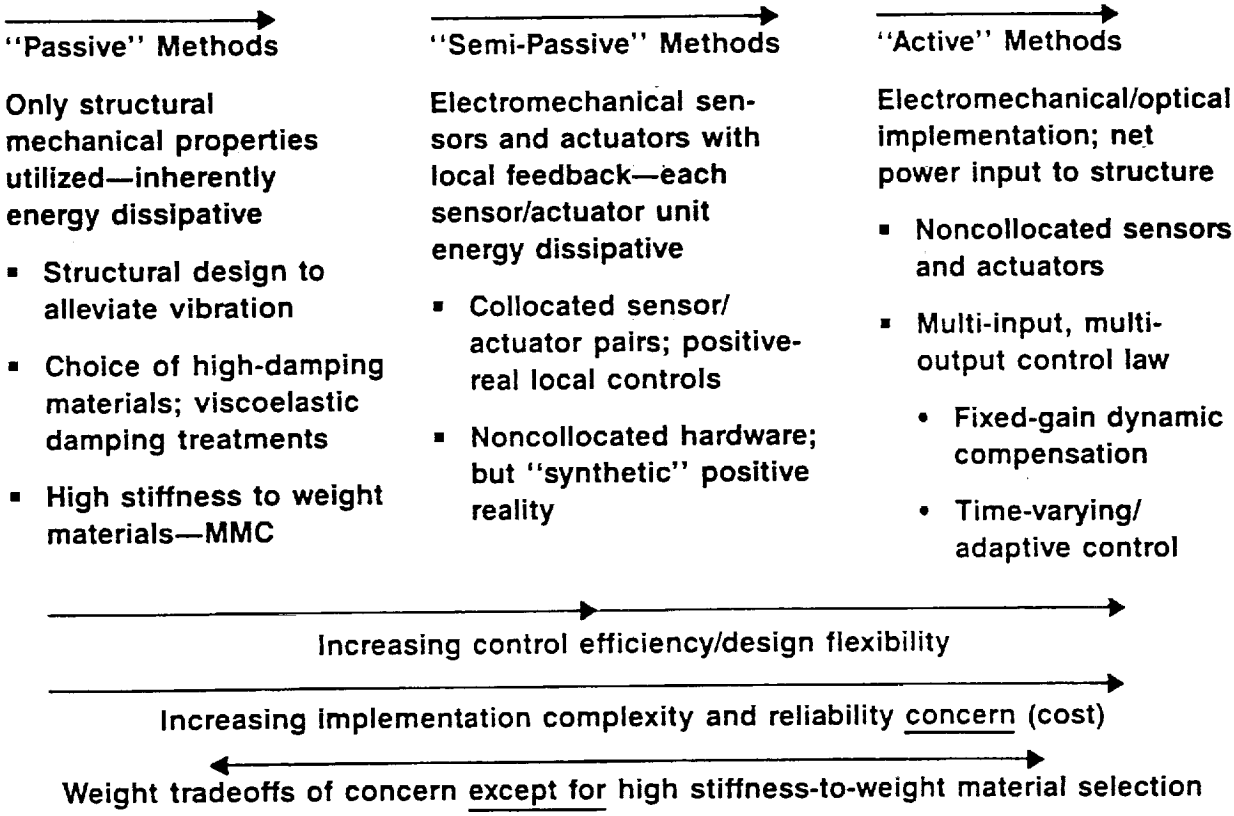
"Passive" Methods
Only structural mechanical properties utilized—inherently energy dissipative
▪ Structural design to alleviate vibration
▪ Choice of high-damping materials; viscoelastic damping treatments
▪ High stiffness to weight materials—MMC
"Semi-Passive" Methods
Electromechanical sensors and actuators with local feedback—each sensor/actuator unit energy dissipative
▪ Collocated sensor/actuator pairs; positive-real local controls
▪ Noncollocated hardware; but "synthetic" positive reality
"Active" Methods
Electromechanical/optical implementation; net power input to structure
▪ Noncollocated sensors and actuators
▪ Multi-input, multi-output control law
• Fixed-gain dynamic compensation
• Time-varying/adaptive control
Increasing control efficiency/design flexibility
Increasing implementation complexity and reliability concern (cost)
Weight tradeoffs of concern except for high stiffness-to-weight material selection

Fig. 17

In summary, we have examined the distinction between "passive" and "active" approaches to vibration suppression for LSS and have found that the distinction is not as sharp as might be thought at first. The relative simplicity, reliability, and cost-effectiveness touted for passive measures are vitiated by "hidden costs" bound up with detailed engineering implementation issues and inherent performance limitations. At the same time, reliability and robustness issues often cited against active control as risk factors are greatly mitigated by recent advances in active vibration control hardware. Accordingly, we see not a sharp "passive versus active" dichotomy, but as illustrated in this chart, a *continuum* of vibration suppression measures offering mutually supporting capabilities. The challenge for LSS vibration suppression is the proper *orchestration* of this spectrum of methods, (via system-level design) to reap the *synergistic* benefits of combined advanced materials, passive damping and active control.

References

1. D. C. Hyland and D. J. Phillips, "Development of the Linear Precision Actuator," 11th Annual AAS Guid. Contr. Conf., Keystone, CO, January 1988.
2. D. C. Hyland, "Experimental Investigations in Active Vibration Control for Application to Large Space Systems," in *Space Structures, Power, and Power Conditioning*, R. F. Askew, Ed., Proc. SPIE, Vol. 871, pp. 242–253, 1988.
3. D. C. Hyland, "An Experimental Testbed for Validation of Control Methodologies in Large Space Optical Structures," in *Structural Mechanics of Optical Systems II*, pp. 146–155, A. E. Hatheway, Ed., Proceedings of SPIE, Vol. 748, Optoelectronics and Laser Applications Conference, Los Angeles, CA, January 1987.
4. D. J. Phillips and E. G. Collins, Jr., "Four Experimental Demonstrations of Active Vibration Control for Flexible Structures," *Proc. AIAA Guid. Nav. Contr. Conf.*, pp. 1625–1633, Portland, OR, August 1990.
5. A. W. Daubendiek, D. C. Hyland , and D. J. Phillips , "System Identification and Control Experiments on the Multi-Hex Prototype Test Bed," *2nd USAF/NASA Workshop on System Identification and Health Monitoring of Precision Space Structures*, Pasadena, CA, March 1990.
6. B. J. Boan and D. C. Hyland, "The Role of Metal Matrix Composites for Vibration Suppression in Large Space Structures," *Proc. MMC Spacecraft Survivability Tech. Conf.*, MMCIAC Kaman Tempo Publ., Stanford Research Institute, Palo Alto, CA, October 1986.

Real Time Digital Control and Controlled Structures Experiments

Michael J. Rossi and Gareth J. Knowles

Grumman Corporate Research Center

Frank Rauch
Vibrations and Flutter Laboratory

Controlled Structures Technology at Grumman

Grumman has a very active group in CST drawn from the Applied Mechanics Lab, Controls and Dynamics Lab and the Materials Lab of the Corporate Research Center with experimental support from the Thermal Lab, the Vibrations and Flutter Lab and the Structures and Materials Division of the Aircraft Systems Division.

Active and Passive Technology: Experiment and Modeling

- Coupon experiments of viscoelastic materials
- Modeling of viscoelastic and piezoceramic treatments
- Controlled laboratory experiments with piezoceramic and piezopolymer actuators and sensors
- Complex models of actuator and sensor dynamic effects on closed loop control

Active and Passive Synthesis

- Develop models of partial treatments using constrained viscoelastic layers
- Incorporate ANSYS models of piezo-ceramics
- Utilize the MCR code with extended FEM's of complex structures
- Refine our combined control/structure optimization to minimize added mass of passive treatment and control energy while meeting performance goals

Controlled Structures Technology Laboratory Objectives

- Validate analytical and finite-element models
- Demonstrate practical advantages and limitations of proposed schemes on real hardware
- Stimulate innovative control schemes based on experience in the laboratory
- Offer a testbed for downloading control algorithms developed on workstations using Protoblock

Issues to be Addressed in CSTL Research

- Materials issues
  - --Constrained layer viscoelastic dampers
  - --Piezoceramic actuators and sensors
  - --Bonding methods: crazy glue/epoxy
  - --Wiring scheme: overlap/grounding
  - --Constitutive relations: finite element modeling
- Passive or passive/active controls
- Time delays and filters in digital control
- Data acquisition and system identification

Applications of CSTL Findings

- Passive/active vibration control
- Precision pointing of instruments
- Optical element shape control
- Active suppression of structure borne noise
- Aircraft wing camber and twist control

Plans for the Incipient CSTL Experiment

- Cantilevered aluminum beam
  --15" x 1.25" x 0.125"

- Piezoceramic sensors and actuators
  --2.5" x 1.5" x 0.010" each

- Power voltage ampliers for each actuator
  --gain of 20, up to 200V-1A output up to 4kHz

- IBM PC/AT host computer
  --33MHz, 32bit floating point coprocessor with:
  internal bus to 34 analog inputs and 18 outputs
  and 17 Megabytes of local RAM
  --software to provide dual trace real time scope
  and spectral analyzer
  --cross c and assembler development system

Vacuum Chamber Test Experiment: Objectives

- Simulate space environment for simple CSI experiments
- Validate ground effects to enable extrapolation into more complex CSI experiments
- Estimate inherent viscoelastic damping component of piezoelectric devices

Vacuum Chamber Test Experiment: Setup

- Evacuation system & gauges
- Exciter & sensor
- 52 lb Heavy Fixture
- HP digital storage spectral analyzer
- Optional piezoceramic sensor and passive viscous damping

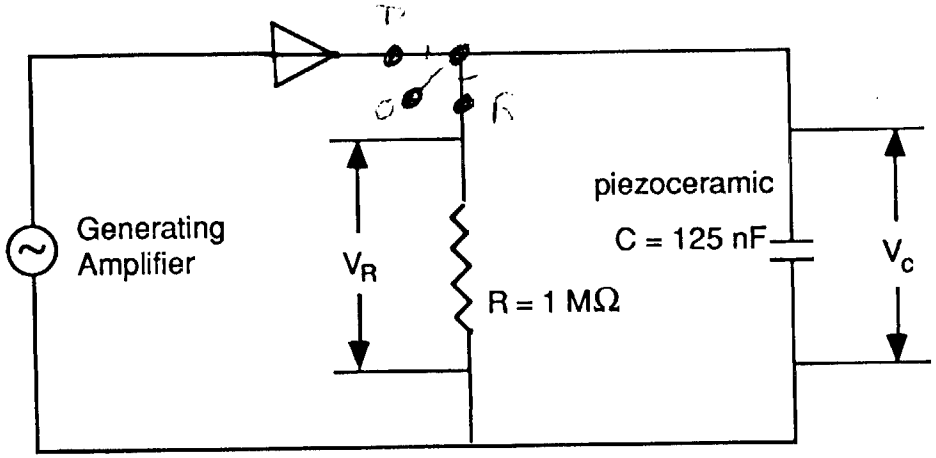

- Choose RC by setting $RC = \frac{1}{w_o}$ = relaxation time constant
- Fundamental frequency at 7.8 Hz, so period = 128.5 ~~MHz~~
- Measured no of cycles to ensure $\frac{x_o}{x_f} = 4$
- Open circuit (64 cycles), $\frac{x_o}{x_f} = 4$, hence $\zeta = \frac{\ln 4}{128\pi} = 0.35\%$
- Shunted circuit (53 cycles), $\frac{x_o}{x_f} = 4$, hence $\zeta = \frac{\ln 4}{106\pi} = 0.42\%$

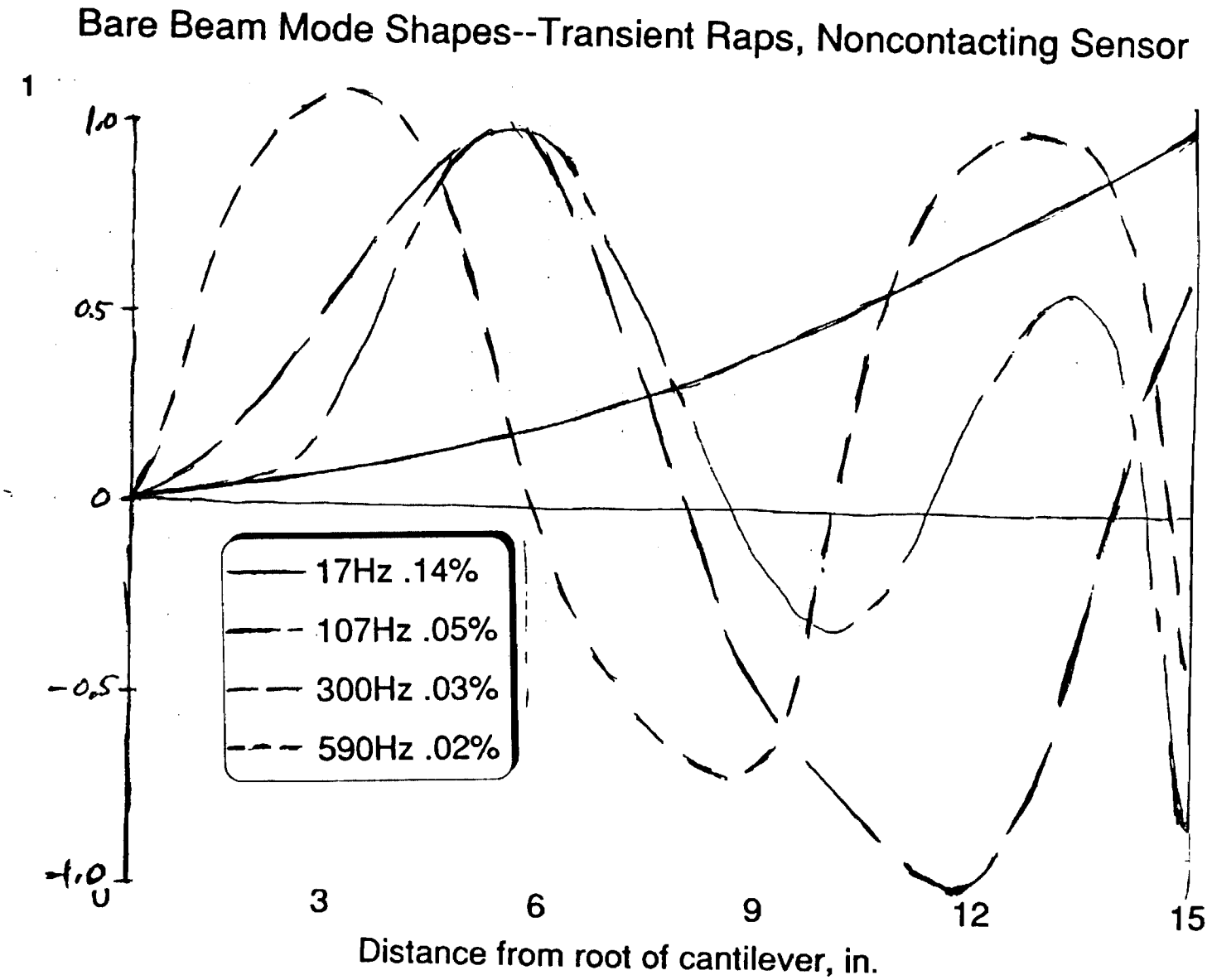
Bare Beam Mode Shapes--Transient Raps, Noncontacting Sensor
1
1.0
0.5
0
-0.5
-1.0
17Hz .14%
107Hz .05%
300Hz .03%
590Hz .02%
0
3
6
9
12
15
Distance from root of cantilever, in.

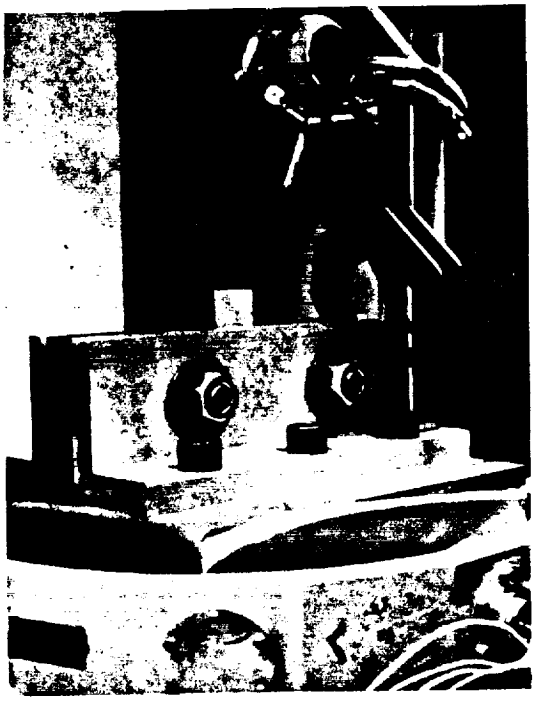

1

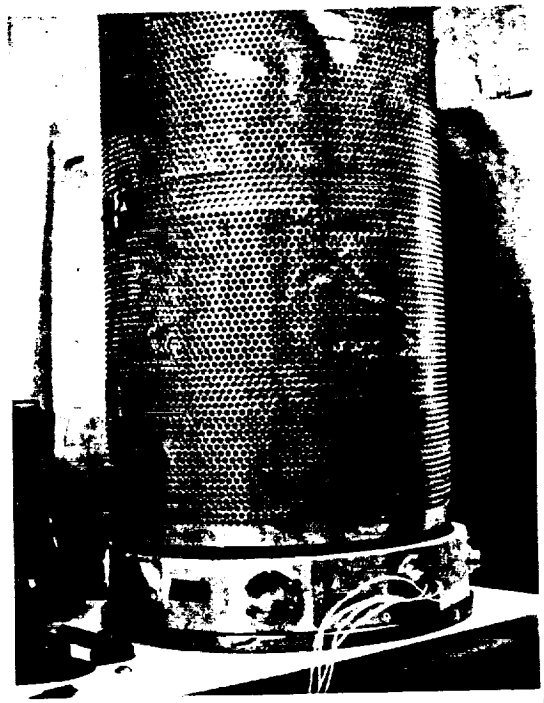

7

10

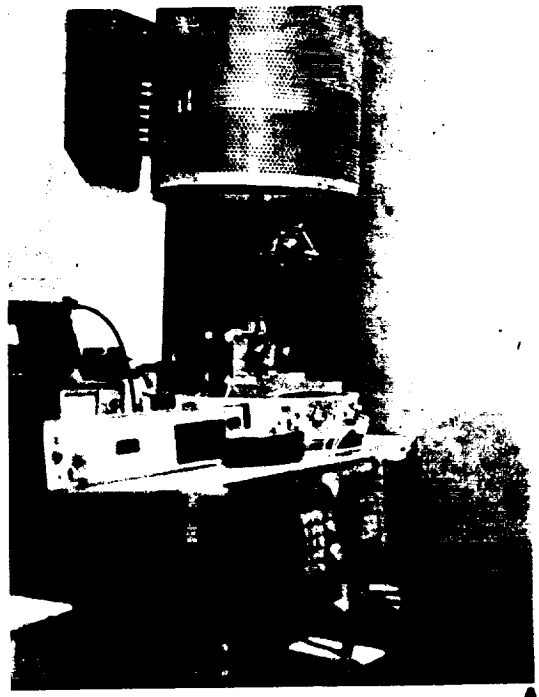

14

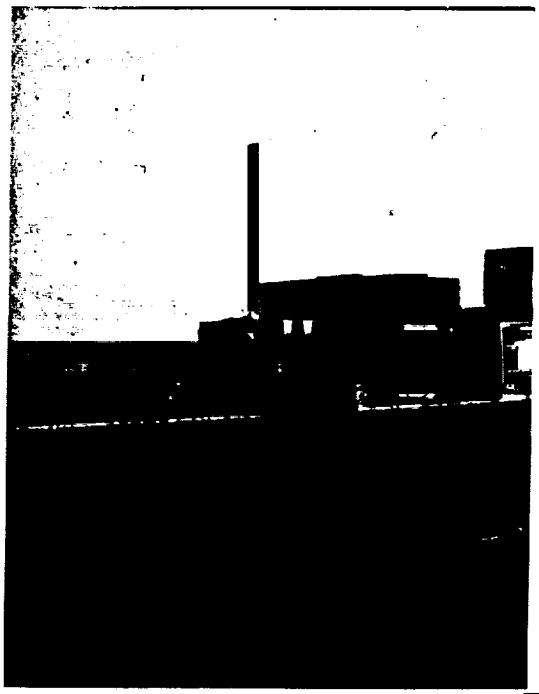

15

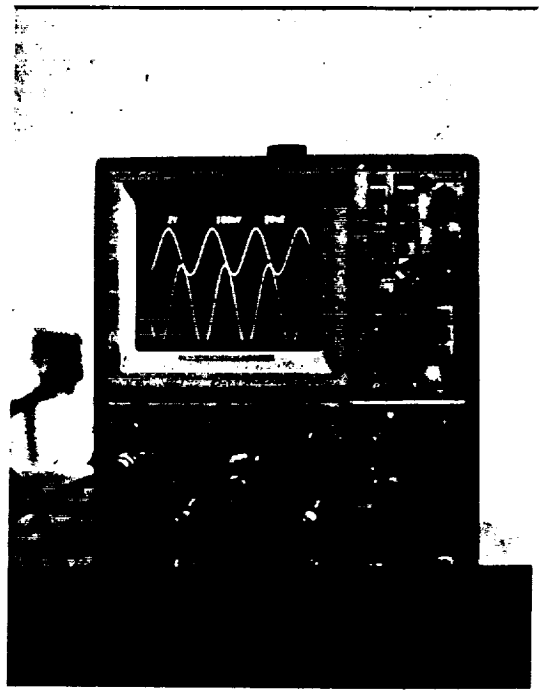

17

19

FINITE ELEMENT MODELING OF TRUSS STRUCTURES WITH FREQUENCY-DEPENDENT MATERIAL DAMPING

GEORGE A. LESIEUTRE

Aerospace Engineering
The Pennsylvania State University

4th WORKSHOP ON COMPUTATIONAL CONTROL
OF FLEXIBLE AEROSPACE SYSTEMS

Williamsburg, Virginia
July 13, 1990

FINITE ELEMENT MODELING OF TRUSS STRUCTURES WITH FREQUENCY-DEPENDENT MATERIAL DAMPING

ABSTRACT

In advanced engineering systems such as large space structures (LSS) or robots, the combination of severe disturbances, stringent requirements, and structural design constraints can result in structures which exhibit significant flexibility. The design of stable, fast-responding structural control systems benefits from accurate knowledge of structural dynamic behavior, including the magnitudes and mechanisms of inherent damping.

Material damping is likely to be an important, perhaps dominant, contributor to damping in "monolithic" structures and to on-orbit damping in precision spacecraft. The damping of most engineering materials exhibits a strong dependence on frequency.

A physically-motivated modelling technique for structural dynamic analysis that accomodates frequency-dependent material damping has been developed. Key features of the technique are the introduction of augmenting thermodynamic fields (ATF) to interact with the usual mechanical displacement field, and the treatment of the resulting coupled governing equations using finite element analysis methods. The ATF method is fully compatible with current structural finite element analysis techniques.

The method is demonstrated in the dynamic analysis of a 10-bay planar truss structure, a structure representative of those contemplated for use in future space systems. Analytical results from modal analyses of an ATF-damped and an undamped truss structure agree well in terms of modal frequencies, but the ATF analysis also yields modal damping and complex mode shapes. The undamped frequencies are lower by as much as five percent in higher modes because the relaxed (static) modulus value is used, as is usual practice. In addition to preserving the characteristic frequency dependence of material *damping*, the ATF method reflects the frequency dependence of material *modulus* as well.

With the continued development of better analytical tools such as this ATF method, damping will be modelled more accurately in the design of engineering systems and may ultimately become more accessible to design specification.

SOURCES OF DAMPING

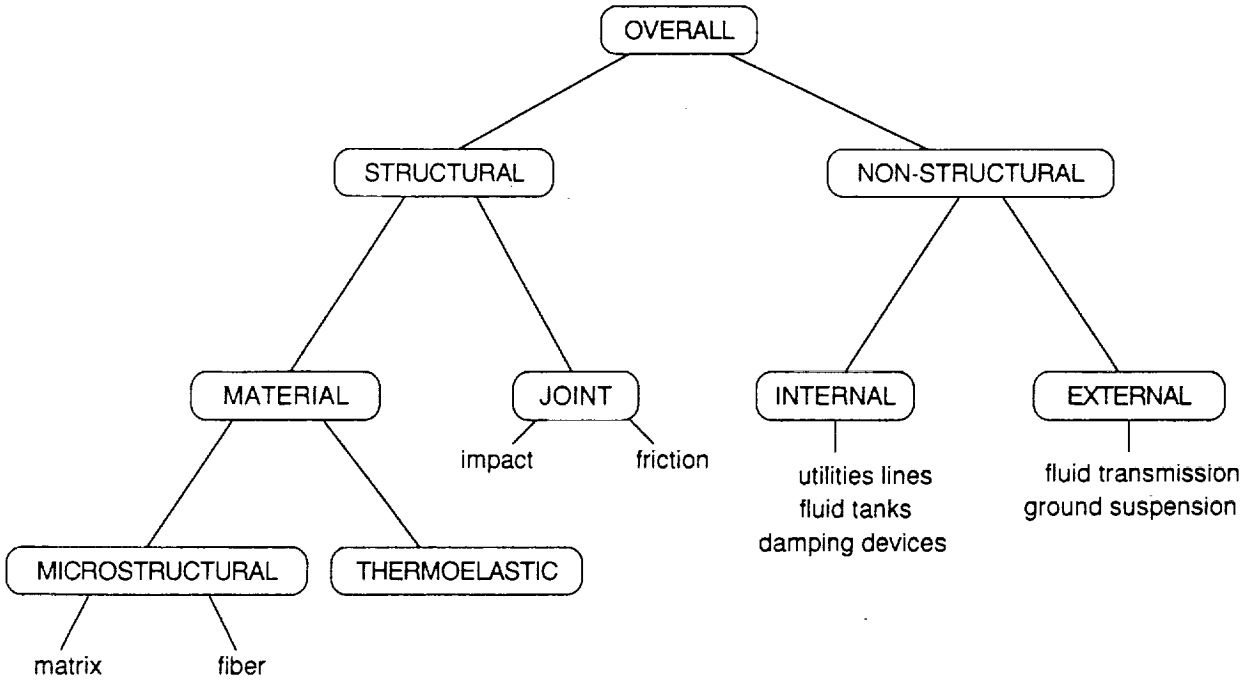

MATERIAL DAMPING WILL BE IMPORTANT IN PRECISION SPACE SYSTEMS

In advanced engineering systems such as large space structures (LSS) or robots, the combination of severe disturbances, stringent requirements, and structural design constraints can result in structures which exhibit significant flexibility. Passive and active damping of these structures is important for several reasons. In terms of performance, higher damping can reduce steady-state vibration levels and can reduce the time needed for transient vibrations to settle. Inherent passive damping can reduce the magnitude of control needed, and can reduce control system complexity. Passive damping can also strongly couple vibration modes which are closely-spaced in frequency and computed assuming no damping. Most importantly, however, the design of stable, fast-responding control systems benefits from accurate knowledge of structural dynamic behavior, which depends on the magnitudes and mechanisms of inherent damping.

Many sources of inherent damping exist for a given aerospace vehicle. A potential classification scheme for such sources is shown above. In general, damping is not well-quantified in the design process, which results in significant design decisions being made on the basis of qualititative information. There is considerable room for improvement in the analysis of damping in aerospace systems. For example, a damping design budget might allocate contributions to total damping required from individual damping sources.

A case can be made for the importance of material damping in at least some precision space vehicles. In common built-up structures which operate in the atmosphere, air damping and joint damping typically dominate system damping. However, air damping is clearly eliminated in space, and the effects of joint damping will be reduced because of requirements for precision ("tight" joints) and typically low vibration levels (friction "lockup"). Material damping is thus likely to be an important, perhaps dominant, contributor to damping in "monolithic" structures and to on-orbit damping in precision spacecraft.

MATERIAL DAMPING IS COMPLEX

- **DEPENDS ON FREQUENCY, TEMPERATURE, DEFORMATION, AMPLITUDE, GEOMETRY**

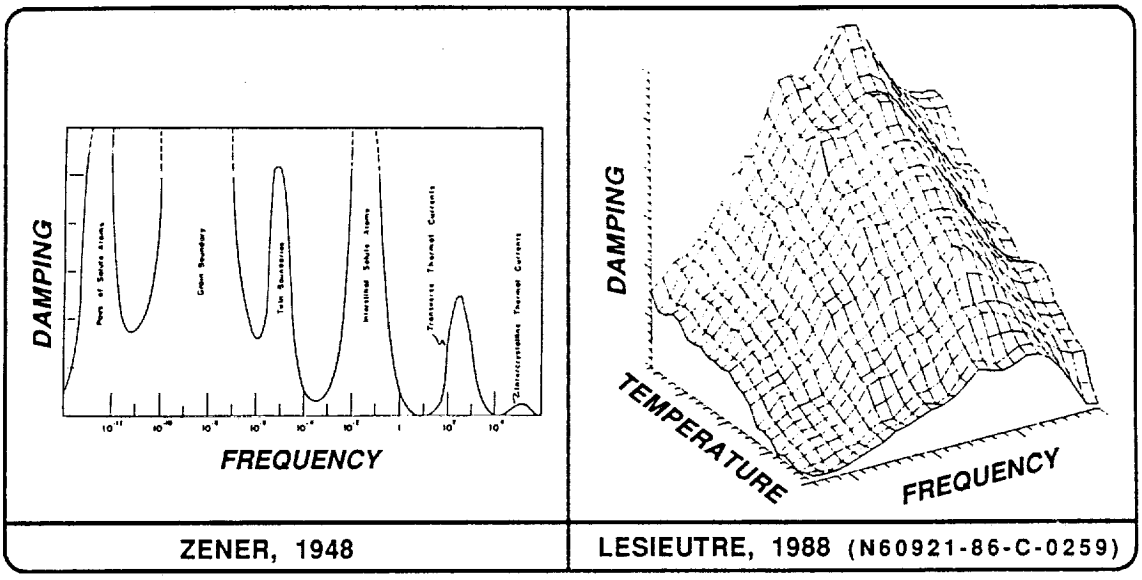

ZENER, 1948 | LESIEUTRE, 1988 (N60921-86-C-0259)

- **ATF METHOD ADDRESSES FREQUENCY-DEPENDENCE**

Material damping is generally a complex function of frequency, temperature, type of deformation, amplitude, and structural geometry.

The figure on the left is adapted from the frontispiece of the pioneering text, Elasticity and Anelasticity of Metals and illustrates the typical frequency-dependence of material damping. Note that there are a number of discrete damping peaks, and that a physical (possibly atomic) process is associated with each peak (*e.g.*, "transverse thermal currents").

The figure on the right shows some data recently obtained for aluminum in a flexural vibration test. The frequency dependence of damping is apparent. Similar data were obtained for graphite/aluminum composite materials, although weaker frequency dependence was observed.

Current popular treatments of damping in structural dynamics are generally not physically-motivated and do not preserve the fundamental frequency-dependence of material damping. This observation provided the motivation for the subject work.

DAMPING MODELS AND RELATED WORK

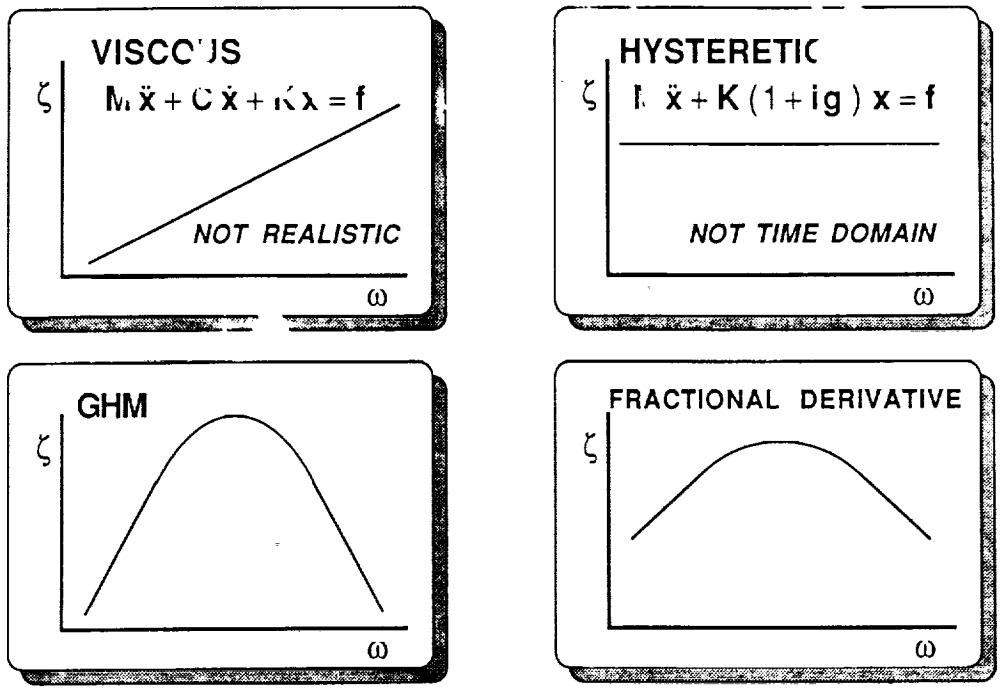

Several methods are currently used to incorporate the effects of material damping into structural models. These methods include viscous damping, frequency-dependent viscous damping, complex modulus, hysteretic damping, structural damping, viscoelasticity, hereditary integrals, and modal damping. Modal damping is probably the most widely used in structural control design applications. Each has some utility, but each suffers from one flaw or another. For example, a one-dimensional structure made from a single material with viscous damping would exhibit damping that increases monotonically with frequency—such behavior is not observed in practice. Although some damping models, such as viscoelasticity, have the potential for better accuracy than more widely-used methods, they are not commonly used in the engineering community—perhaps because of the lack of physical motivation, difficulty of use, or lack of data.

Other researchers have noted the inadeqacy of current damping modeling techniques and have addressed the development of improved methods.

Golla, Hughes, and McTavish (GHM) of the University of Toronto have developed a time-domain finite element formulation of viscoelastic material damping. Their work was guided by the observation that experimental results, often recorded in the frequency domain, are of little direct use in time-domain models. Their results resemble those reported here in an important way—in the introduction of additional "dissipation coordinates." It might not be surprising that additional degrees of freedom would be required to model material behavior with increased accuracy. However, the GHM approach is fundamentally a mathematical one, developing time-domain realizations from frequency-domain models—no attempt is made to provide a physical interpretation of the dissipation coordinates as thermodynamic field variables with a direct relationship to microstructural features of real materials. The GHM technique has been successfully used to fit a portion of an experimentally-determined curve of damping versus frequency, and standard analysis tools can be used to solve the resulting equations.

Bagley and Torvik of the Air Force Institute of Technology have also developed a relevant model of material damping. The core of their concept is the use of fractional time derivatives in material constitutive equations. Their development was motivated by the observation that the frequency dependence observed in real materials is often weaker than the dependence predicted by first-order viscoelastic models. With four and five parameter models, they have been able to accurately represent the elastic and dissipative behavior of over 100 materials over frequency ranges as broad as 8 decades. The application of the general fractional derivative approach to time-domain analysis is an area of continuing research.

BASIS FOR ATF

- "INTERNAL STATE VARIABLES" OF MATERIALS SCIENCE MOTIVATE INTRODUCTION OF "AUGMENTING THERMODYNAMIC FIELDS" (ATF)

CONSTITUTIVE EQUATION $\sigma = E_u u' - \delta \xi$

ATF DYNAMICS $\dot{\xi} + B\xi = \left(\frac{B\delta}{\alpha}\right) u'$

- FREQUENCY-DEPENDENT DAMPING AND MODULUS

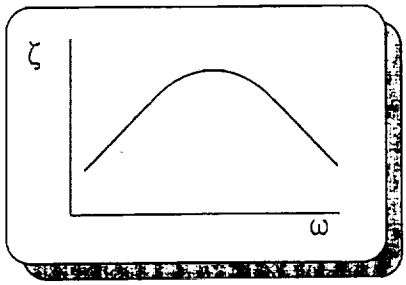

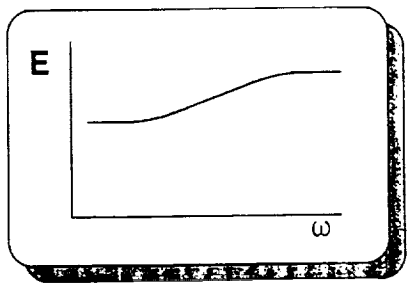

$$\zeta = \frac{\delta^2}{4E\alpha}\left(\frac{2(\omega/B)}{1+(\omega/B)^2}\right)$$

$$E = E_u\left(1 - \frac{\delta^2}{E_u\alpha}\left(\frac{1}{1+(\omega/B)^2}\right)\right)$$

(SMALL DAMPING)

Structural dynamicists are the unintended beneficiaries of a sizable literature on material damping. For many years, crystallographers and metallurgists have used "internal friction" as a probe into the underlying structure of materials. By measuring damping as a function of frequency, temperature, load type, and amplitude, they can determine the mobility and activation energies of various microstructural features of materials. These researchers have identified a multitude of internal variables and relaxation mechanisms which range in geometrical scale from crystal lattice dimensions on up to structural dimensions and, in temporal scale, over a similarly broad range.

The "internal variables" of materials science suggest the introduction of augmenting thermodynamic fields (ATF) to interact with the usual displacement field of continuum structural dynamics. In the one-dimensional case where stress is coupled to a single augmenting thermodynamic field (ATF), and where the ATF dynamics are governed by a first-order relaxation equation, the effective material modulus increases with frequency to an asymptotic value of E_u, and a damping peak is observed. This is in accord with the observed behavior of many engineering materials.

The ATF modeling approach essentially implements a continuum version of the "standard anelastic solid." Weaker frequency dependence, such as that observed in high damping viscoelastic polymers, can be addressed through the introduction of multiple ATFs.

STRAWMAN PROBLEM

- MODAL ANALYSIS OF ATF-DAMPED TRUSS
- ELEMENTS WITH DIFFERENT ELASTIC AND DISSIPATIVE PROP'S

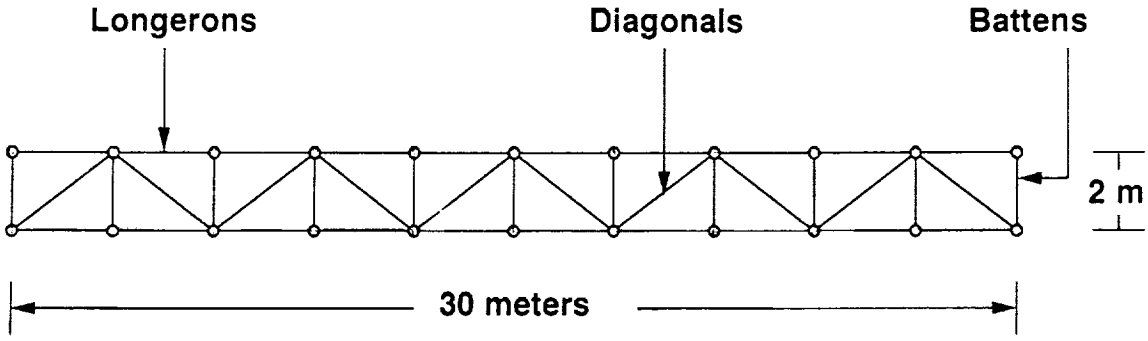

- COMPARE TO RESULTS OF CONVENTIONAL UNDAMPED ANALYSIS

The ATF modeling approach is illustrated through application to the dynamic analysis of a large planar space truss, shown above. Such a structure resembles those proposed for many future space missions. It is an efficient beam-type structure built from 3 basic structural elements: longerons, which are parallel to the beam axis; diagonals, which bisect each rectangular bay; and battens, which are oriented transverse to the beam axis. The total length of the structure is 30 meters and the truss depth is 2 meters.

Members of the truss of interest are connected through frictionless pins so that no bending moments are transmitted through the joints, and so that no damping is introduced by the joints. Joint mass and other non-structural masses are ignored. Finally, each kind of structural element is assumed to be made of a different material having different elastic, inertial, and dissipative properties. For this problem, it is assumed that a single augmenting thermodynamic field is sufficient to characterize the dissipative properties of each material in the frequency range of interest.

Conventional damping analysis, if damping were considered at all, would likely employ the modal strain energy (MSE) method to estimate "modal damping." This is an iterative process, requiring analysis of the undamped structure to determine the frequencies and mode shapes of the undamped modes. The mode shapes are used to determine the distribution of strain energy over the structure, while the frequencies are used to determine frequency-dependent elastic and dissipative properties. Modal damping is then estimated for each mode and, roughly speaking, is numerically equal to the sum of material damping ratios weighted by the fraction of the strain energy stored in each material. The MSE method can lead to serious errors when modes are closely spaced in frequency and when the damped mode shapes are much different than the undamped mode shapes.

The vibration modes and frequencies of this ATF-damped truss are sought for comparison to those of the undamped case. A one-dimensional ATF-damped finite element appropriate for modeling the dynamic behavior of a single truss strut is developed first, then used in the analysis of the overall structure.

FINITE-LENGTH ROD EXECUTING LONGITUDINAL VIBRATION

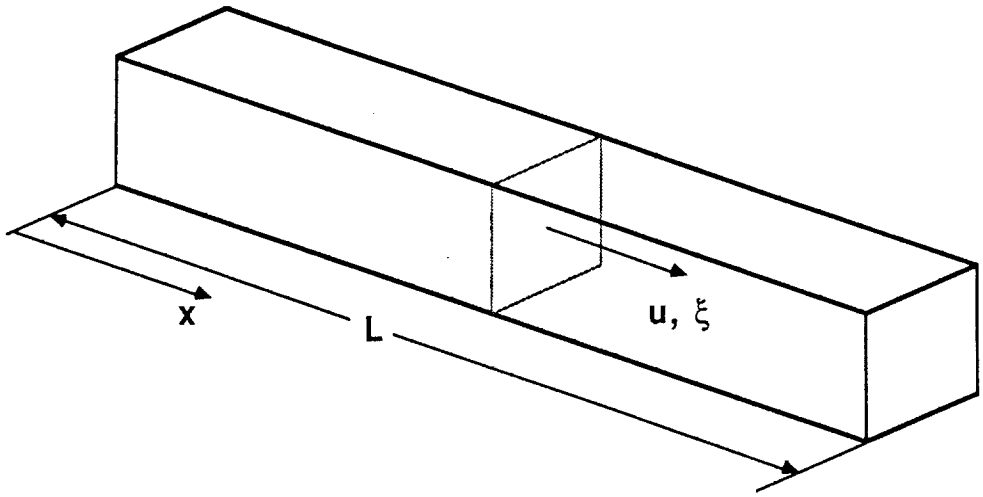

COUPLED FIELDS: MECHANICAL DISPLACEMENT, u(x)

AUGMENTING THERMODYNAMIC, ξ (x)

ENDS MECHANICALLY UNCONSTRAINED

Consider the case of one-dimensional motion, corresponding to longitudinal vibration of a thin rod of length L. The mechanical displacement along the rod is denoted by u(x) (strain $\varepsilon(x)=u'(x)$), and the rod has uniform mass density ρ and *unrelaxed* or *dynamic* modulus of elasticity E. A single augmenting thermodynamic field, $\xi(x)$, is introduced.

The material property δ describes the strength of the coupling of the two dependent fields, u and ξ. In the absence of coupling of the two fields, increments of stress and strain are proportional, with E the relating factor. Analogously, α is the material property that relates changes in A, the thermodynamic conjugate of ξ, to those in ξ. B is the inverse of the time constant for uncoupled relaxation of the augmenting field.

GOVERNING EQUATIONS

PDEs

PRIMARY FORM

$$\rho\ddot{u} - Eu'' = -\delta\xi'$$

$$\dot{\xi} + B\xi = \left(\frac{B\delta}{\alpha}\right)u'$$

ALTERNATE FORM

$$\rho\ddot{u} - Eu'' = -\delta\gamma$$

$$\dot{\gamma} + B\gamma = \left(\frac{B\delta}{\alpha}\right)u''$$

BCs

At ends ($x=0$ and $x=L$)

$$u(x)=u_0 \quad \text{or} \quad \sigma(x)=\sigma_0$$

ATF are internal variables (no BC)

The equation of evolution for the mechanical displacement field, u(x), is developed from consideration of momentum balance (zero body forces are assumed). The equation of evolution for the augmenting thermodynamic field, ξ, is found through the use of a basic assumption of irreversible thermodynamics, namely that the rate of change of ξ is proportional to its deviation from an equilibrium value. This results in a first-order differential equation, a "relaxation" equation. The result is a set of two coupled partial differential equations in u and ξ.

The augmenting thermodynamic field is essentially an *internal* field, *i.e.*, there are no explicit boundary conditions that it alone must satisfy. However, the mechanical displacement field must satisfy either displacement ("geometric") or stress ("natural") boundary conditions at each end of the rod, as is the case in undamped structural dynamics. Note that the stress boundary condition involves the augmenting field, ξ.

An alternative formulation of this one-dimensional case may be considered. For example, the preceding primary equations can be expressed in terms of γ, the gradient of the ξ-field. Such a formulation contains only even spatial derivatives, and leads to some benefits in numerical solution, such as symmetric element submatrices and better convergence in terms of damping versus frequency.

FINITE ELEMENT TREATMENT

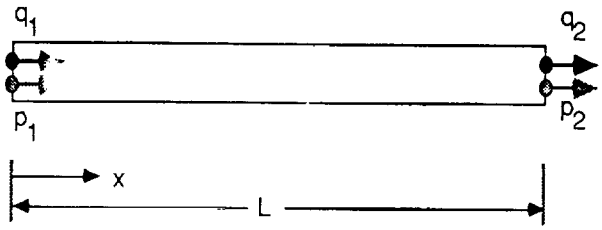

$$u(x,t) = \xi^T(x)\, D \begin{Bmatrix} u_1(t) \\ u_2(t) \end{Bmatrix}$$

$$\gamma(x,t) = \Omega^T(x)\, T \begin{Bmatrix} \gamma_1(t) \\ \gamma_2(t) \end{Bmatrix}$$

METHOD OF WEIGHTED RESIDUALS

$$\rho\ddot{u} - Eu'' = -\delta\gamma$$

$$\dot{\gamma} + B\gamma = \left(\frac{B\delta}{\alpha}\right)u''$$

SINGLE ELEMENT

$$\int_0^L \left[\rho D^T \theta\theta^T D\{\ddot{u}\} + ED^T\theta'\theta'^T D\{u\} + \delta D^T\theta\Omega^T T\{\gamma\}\right] dx = 0$$

ALTERNATE FORMS POSSIBLE

MATRIX NOTATION

$$M\{\ddot{u}\} + K\{u\} + F\{\gamma\} = 0$$

The method of weighted residuals (MWR) is used to develop element matrices. The u-γ formulation of the equations has been found to be superior to the u-ξ formulation, and is shown above. Integration by parts is employed, changing the continuity required of the approximating and weighting functions.

The same functions used to approximate the behavior of the dependent fields in the spatial region bounded by the element are used as weighting functions—when there is only one dependent field, this is known as Galerkin's method.

The resulting sets of equations may be written compactly in matrix form, as shown.

In this treatment, both dependent fields are approximated with linear interpolation functions. The corresponding element and the nodal values for the two dependent fields, u and γ are shown in the figure. Anticipating solution of a first-order matrix eigenvalue problem, and to facilitate global matrix assembly, the elemental degrees of freedom are ordered as follows.

$$x = [\dot{q}_1, q_1, p_1, \dot{q}_2, q_2, p_2]^T$$

MATRIX EQUATIONS

UNDAMPED

$$[\mathbf{M}]\{\ddot{\mathbf{u}}\} + [\mathbf{K}]\{\mathbf{u}\} = \{\mathbf{0}\}$$

$$\begin{bmatrix} \mathbf{M} & 0 \\ 0 & \mathbf{I} \end{bmatrix} \begin{Bmatrix} \ddot{\mathbf{u}} \\ \dot{\mathbf{u}} \end{Bmatrix} + \begin{bmatrix} 0 & \mathbf{K} \\ -\mathbf{I} & 0 \end{bmatrix} \begin{Bmatrix} \dot{\mathbf{u}} \\ \mathbf{u} \end{Bmatrix} = \begin{Bmatrix} 0 \\ 0 \end{Bmatrix}$$ FIRST-ORDER FORM

ATF

$$\begin{bmatrix} \mathbf{M} & 0 & 0 \\ 0 & \mathbf{I} & 0 \\ 0 & 0 & \mathbf{C} \end{bmatrix} \begin{Bmatrix} \ddot{\mathbf{u}} \\ \dot{\mathbf{u}} \\ \dot{\gamma} \end{Bmatrix} + \begin{bmatrix} 0 & \mathbf{K} & \mathbf{F} \\ -\mathbf{I} & 0 & 0 \\ 0 & \mathbf{B} & \mathbf{H} \end{bmatrix} \begin{Bmatrix} \dot{\mathbf{u}} \\ \mathbf{u} \\ \gamma \end{Bmatrix} = \begin{Bmatrix} 0 \\ 0 \\ 0 \end{Bmatrix}$$

The structure of the undamped matrix equations of motion are shown in both second-order and first-order form. The structure of the ATF-damped matrix equations is shown for comparision. The ATF equations are more complex, describing the dynamics of the augmenting field as well as the coupling of the two fields.

The "augmented mass matrix" is generally symmetric and positive definite, while the "augmented stiffness matrix" is neither. Certain submatrices, **K** and **H** in particular, are generally symmetric and positive semidefinite, while the properties of the coupling submatrices, **B** anf **F**, depend on the specifics of the numerical approximation scheme employed.

ELEMENT MATRICES

UNDAMPED

$$\begin{bmatrix} \left(\frac{\rho AL}{3}\right) & \left(\frac{\rho AL}{6}\right) \\ \left(\frac{\rho AL}{6}\right) & \left(\frac{\rho AL}{3}\right) \end{bmatrix} \qquad \begin{bmatrix} \left(\frac{EA}{L}\right) & -\left(\frac{EA}{L}\right) \\ -\left(\frac{EA}{L}\right) & \left(\frac{EA}{L}\right) \end{bmatrix}$$

ATF (FIRST ORDER)

$$\begin{bmatrix} \left(\frac{\rho AL}{3}\right) & 0 & 0 & \left(\frac{\rho AL}{6}\right) & 0 & 0 \\ 0 & 1 & 0 & 0 & 0 & 0 \\ 0 & 0 & \left(\frac{AL}{3}\right) & 0 & 0 & \left(\frac{AL}{6}\right) \\ \left(\frac{\rho AL}{6}\right) & 0 & 0 & \left(\frac{\rho AL}{3}\right) & 0 & 0 \\ 0 & 0 & 0 & 0 & 1 & 0 \\ 0 & 0 & \left(\frac{AL}{6}\right) & 0 & 0 & \left(\frac{AL}{3}\right) \end{bmatrix} \qquad \begin{bmatrix} 0 & \left(\frac{EA}{L}\right) & \left(\frac{\delta AL}{3}\right) & 0 & -\left(\frac{EA}{L}\right) & \left(\frac{\delta AL}{6}\right) \\ -1 & 0 & 0 & 0 & 0 & 0 \\ 0 & \left(\frac{B\delta A}{\alpha L}\right) & \left(\frac{BAL}{3}\right) & 0 & -\left(\frac{B\delta A}{\alpha L}\right) & \left(\frac{BAL}{3}\right) \\ 0 & -\left(\frac{EA}{L}\right) & \left(\frac{\delta AL}{6}\right) & 0 & \left(\frac{EA}{L}\right) & \left(\frac{\delta AL}{3}\right) \\ 0 & 0 & 0 & -1 & 0 & 0 \\ 0 & -\left(\frac{B\delta A}{\alpha L}\right) & \left(\frac{BAL}{3}\right) & 0 & \left(\frac{B\delta A}{\alpha L}\right) & \left(\frac{BAL}{3}\right) \end{bmatrix}$$

For future reference and comparison, details of the elemental mass and stiffness matrices for the undamped and ATF-damped cases are shown. The matrices for the undamped case are shown in second-order form, while the ATF-damped matrices are shown in first-order form. Note that the elements of the undamped matrices also appear in the damped element matrices.

Note that the material modulus, E, is different in the two cases shown. In the undamped case, it is the static or "relaxed" modulus normally used in structural analysis. In the damped case, it is the "unrelaxed" or high-frequency asymptotic modulus. The unrelaxed modulus is always greater than the relaxed value.

FREE VIBRATION PROBLEM

- FREE LONGITUDINAL VIBRATION OF ROD

$$\begin{bmatrix} 0 & K & F \\ -I & 0 & 0 \\ 0 & B & H \end{bmatrix} \begin{Bmatrix} \dot{u} \\ u \\ \gamma \end{Bmatrix} = \lambda \begin{bmatrix} M & 0 & 0 \\ 0 & I & 0 \\ 0 & 0 & C \end{bmatrix} \begin{Bmatrix} \dot{u} \\ u \\ \gamma \end{Bmatrix}$$

$$Ax = \lambda Bx$$

- GENERAL, UNSYMMETRIC EIGENVALUE PROBLEM

- COMPLEX MODES

In order to evaluate the performance of this formulation of an ATF-damped rod element, a specific problem was addressed, namely the determination of the natural modes of vibration of a free-free rod. Accordingly, no geometric boundary conditions were enforced.

The elastic properties used correspond roughly to those of aluminum in SI units. The ATF and coupling properties were chosen to yield a peak damping ratio of 0.01 at the frequency of the 5^{th} mode. Note that numerical values for α and δ cannot be uniquely specified in this approach.

The matrix equations of motion were formulated and a general unsymmetric eigenvalue problem solved to yield complex eigenvalues, λ, and mode shapes, x. Global system matrices are assembled from element matrices and geometric boundary conditions are enforced in the usual manner of structural finite element analysis. The damping ratio, ζ, for each mode was determined as the ratio of the negative of the real part of the eigenvalue to the total magnitude and plotted against the magnitude.

Note that the spectrum of eigenvalues contains "vibration modes," "relaxation modes," and "rigid-body modes." In the complex plane, the damped vibration modes lay near the imaginary axis, slightly in the LHP with negative real parts; the relaxation modes lie on the negative real axis. These relaxation modes are characteristic of the response of the γ field.

RESULTS OF TRUSS ELEMENT MODAL ANALYSIS

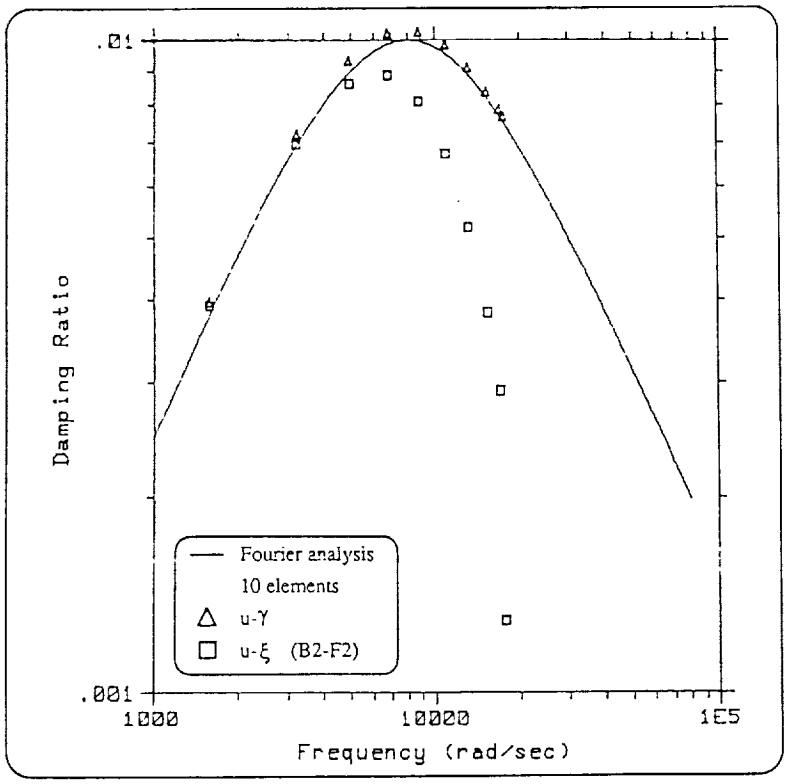

u- γ EQ'NS PROVIDE BETTER DAMPING CONVERGENCE

Typical numerical results for modal damping versus frequency obtained using this approach are shown above. The solid line shows the results expected on the basis of approximate Fourier analysis of the governing equations, while the symbols show the results of ATF-damped modal analysis using 10 elements. The square symbols indicate results obtained using the primary form of the governing equations, while the triangular symbols show the results of using the preferred, alternate form of the equations.

Preservation of the characteristic variation of material damping with frequency is apparent in the results. As previously noted, conventional damping modeling techniques are incapable of producing such results. The frequencies predicted using this method appear to converge from above, as is the case with undamped elements. The finite element implemention based on the alternate form of the governing equations exhibits the proper variation of damping with frequency at all frequencies, while the implementation based on the primary equations "rolls off" too rapidly at high frequencies. Predicted frequencies and damping from both implementations improve with increasing numbers of elements.

LARGE SPACE TRUSS MODAL ANALYSIS

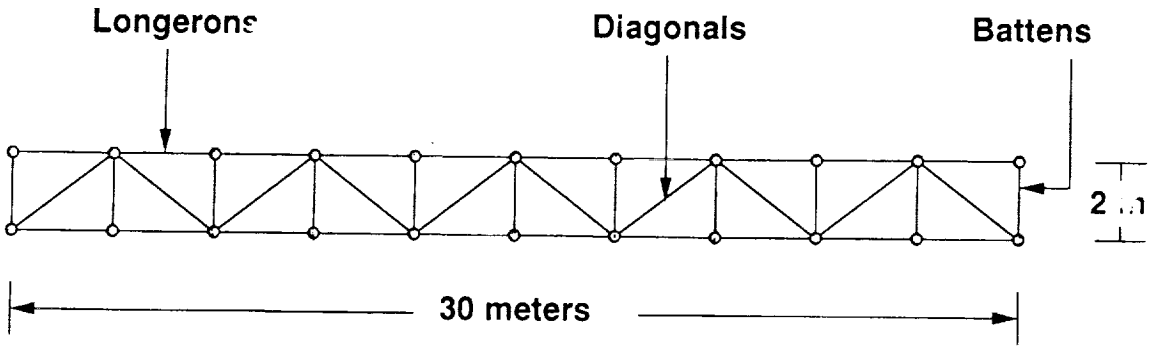

	LONGERON	DIAGONAL	BATTEN
CS area (m2)	31 e-5	19 e-5	6.3 e-5
Modulus (unrelaxed) (Pa)	36.72 e10	18.72 e10	8.4 e10
Density (kg/m3)	2200	1600	2700
Peak damping ratio	0.005	0.01	0.05
Frequency of peak (r/s)	200	2000	8000

The utility of this ATF modeling method is demonstrated in a modal analysis of the previously-described strawman 10-bay, 30-meter planar truss structure. The damped rod elements just described are modified to include the kinetic energy of transverse motion, and to address requirements for interelement continuity of the augmenting fields.

The table above summarizes the key properties of the truss member materials. In particular, the peak damping ratios for each material are different, and are found at different frequencies.

RESULTS OF TRUSS MODAL ANALYSIS

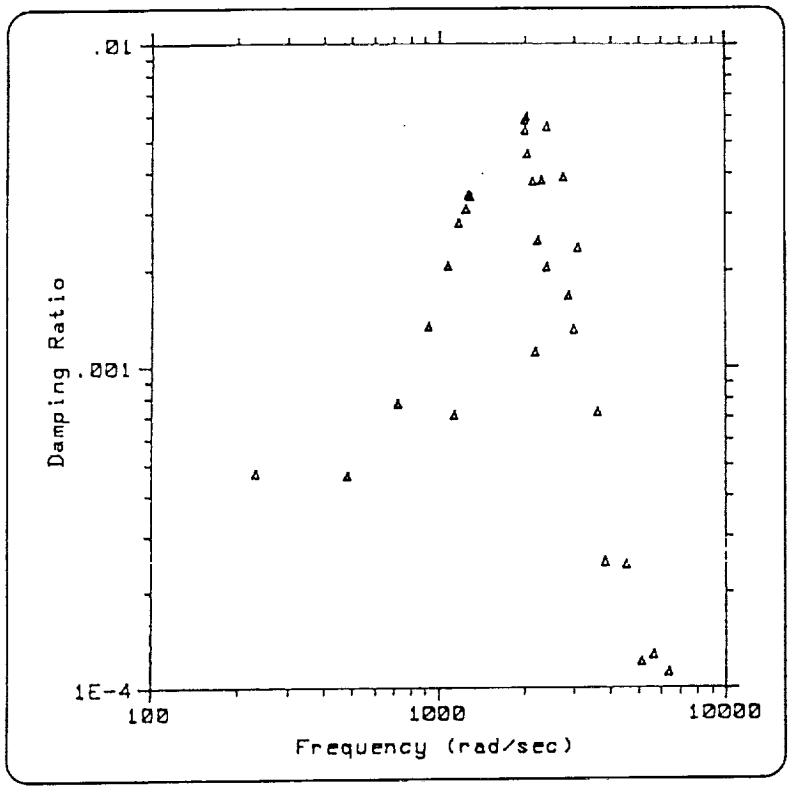

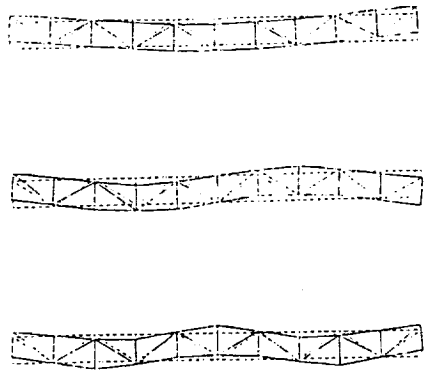

SOME UNDAMPED MODE SHAPES

The figure above shows the results of the truss modal analysis in terms of damping versus frequency. Where conventional analysis using the MSE method would have required considerable effort to generate multiple modal damping values, the ATF method delivers them in a single, standard modal analysis. In addition, it delivers more accurate complex modes.

Note that the damping in the lowest bending modes increases quite rapidly with frequency. This is due to two unrelated factors: First, in this kind of truss structure, the fraction of strain energy stored in the diagonal members increases with mode number—this is analagous to the effects of transverse shear in an isotropic beam. Second, in this case, the damping of the material from which the diagonal members are made is increasing at frequencies below 2000 rad/sec. Also note that the 6th flexible mode is an extensional mode, and has considerably lower damping than neighboring bending modes.

RESULTS — TRUSS MODAL ANALYSIS

MODE NO.	UNDAMPED FREQUENCY (R/S)	DAMPED FREQUENCY (R/S)	DAMPING RATIO (10e-3)
4	228.6	231.4	0.47
5	472.2	480.8	0.46
6	701.6	719.3	0.77
7	887.2	917.5	1.32
8	1024.	1069.	2.04
9	1102.	1127.	0.70
10	1109.	1168.	2.77

For comparison, an undamped analysis was performed. The table summarizes the frequency and damping results. The ATF and undamped results agree well in terms of frequency, differing by about one percent for the first mode. The undamped frequencies are lower by as much as five percent in the tenth mode because the relaxed (static) modulus value was used for that analysis, as is usual practice.

SUMMARY

ATF METHOD *AUGMENTING THERMODYNAMIC FIELDS*

- PHYSICALLY-MOTIVATED, PRESERVES CHARACTERISTIC VARIATION OF MATERIAL DAMPING WITH FREQUENCY
- FULLY COMPATIBLE WITH CURRENT FE TECHNIQUES
- MIX DAMPED, UNDAMPED ELEMENTS
- MULTIPLE FIELDS TO FIT DATA

FUTURE WORK

- DAMPING BUDGET
- CONTROLS
- MSE COMPARISON
- OTHER ELEMENTS
- OPTIMIZATION
- IDENTIFICATION
- MATH ASPECTS

A physically-motivated material damping model fully compatible with current computational structural analysis methods has been developed. Termed the Augmenting Thermodynamic Fields (ATF) method, its key feature is the introduction of additional fields to interact with the usual displacement field of continuum structural dynamics. ATF-damped rod elements were developed and provided the basis for a modal analysis of a large space truss structure.

This method preserves the characteristic frequency-dependence of material damping. The results for a single augmenting field per material are readily extended to multiple fields. In addition, the method readily accommodates a combination of damped and undamped elements. Also note that an increase in the accuracy of a structural dynamic model comes with a cost of dimensionality—additional coordinates are required to represent additional aspects of material behavior, *viz*, damping.

With the continued development of analytical tools such as this ATF method, damping will be better treated in the design of engineering systems and may ultimately become more accessible to design specification.

BIBLIOGRAPHY

Ashley, H., "On Passive Damping Mechanisms in Large Space Structures," AIAA Paper 82-0639, 1982.

Bert, C.W., "Material Damping: An Introductory Review of Mathematical Models, Measures, and Experimental Techniques," *Journal of Sound and Vibration*, Vol. 29, No. 2, 1973, pp. 129-153.

Golla, D.F., and Hughes, P.C., "Dynamics of Viscoelastic Structures - A Time-Domain, Finite Element Formulation," *Journal of Applied Mechanics*, Vol. 52, December, 1985, pp. 897-906.

Lesieutre, G.A., and Mingori, D.L., "Finite Element Modeling of Frequency-Dependent Material Damping using Augmenting Thermodynamic Fields," to appear in *Journal of Guidance, Control and Dynamics*, 1990.

Nowick, A.S., and Berry, B.S., *Anelastic Relaxation in Crystalline Solids*, Academic Press, 1972.

Torvik, P.J., and Bagley, D.L., "Fractional Derivatives in the Description of Damping Materials and Phenomena," at the *11th ASME Biennial Conference on Mechanical Vibration and Noise*, Boston, Sept., 1987.

Zener, C.M., *Elasticity and Anelasticity of Metals*, University of Chicago Press, 1948.

An Experimental Study of Nonlinear Dynamic System Identification

Greselda I. Stry[1] and D. Joseph Mook[2]

Department of Mechanical and Aerospace Engineering
State University of New York at Buffalo
Buffalo, New York 14260
716–636–3058

Abstract

A technique based on the Minimum Model Error optimal estimation approach is employed for robust identification of a nonlinear dynamic system. A simple harmonic oscillator with quadratic position feedback was simulated on an analog computer. With the aid of analog measurements and an assumed linear model, the Minimum Model Error Algorithm accurately identifies the quadratic nonlinearity. The tests demonstrate that the method is robust with respect to prior ignorance of the nonlinear system model, and with respect to measurement record length and regardless of initial conditions.

Introduction

The widespread existence of nonlinear behavior in many dynamic systems is well-documented, e.g, Thompson and Stewart [1]; Nayfeh and Mook [2]. In particular, virtually every problem associated with orbit estimation, flight trajectory estimation, spacecraft dynamics, etc., is known to exhibit nonlinear behavior. Many excellent methods for analyzing nonlinear system models have been developed. However, a key practical link is often overlooked, namely: How does one obtain an accurate mathematical model for the dynamics of a particular complicated nonlinear system? Identification, the process of developing an accurate system model from system output measurements, may provide the answer.

Nonlinear systems are commonly described using linear models. Many efficient algorithms for the identification of linear systems exist and their accuracy and ease of application encourages their use. However, linearization does not work in every application, and even when it does provide a reasonable approximation, the approximation is normally limited to a small region about the operating point of linearization. In the case

[1] Graduate Resarch Assistant; NASA Graduate Researcher
[2] Assistant Professor

of systems with severe nonlinear behavior using a linear model to describe such a system leads to inconsistencies ranging from inaccurate numerical results to misrepresentation of the system's qualitative behavior. Since nonlinearities are seldomly easily characterized, nonlinear identification techniques may prove beneficial in developing accurate mathematical representations of nonlinear systems.

Numerous methods for the identification of nonlinear systems have been developed in the past two decades (Natke, Juang and Gawronski [3]). Among the most widely used nonlinear identification methods are describing the nonlinear system using a linear model, or representing the nonlinear system in a series expansion and obtaining the respective coefficients either by using a regression estimation technique, by minimizing a cost functional, by using correlation techniques, or by some other approach. Some algorithms use the direct equation approach, while others obtain a graphical representation of the nonlinear term(s) and then find an analytical model for the nonlinearity. The interested reader can find more information on these nonlinear identification techniques in Stry and Mook [4].

The diversity of nonlinear identification techniques prompts the choice of an algorithm based on the needs of the particular application. Typical criteria to look for are: iterations required, robustness in the presence of measurement noise, number of measurements needed, robustness with respect to knowledge of the inital conditions, and robustness with respect to initial assumptions regarding the form of the nonlinearity. The results presented in this paper confirm that the Minimum Model Error algorithm excels in the above mentioned requirements.

In previous papers, the Minimum Model Error algorithm (MME) was explained in detail (Mook and Junkins [5]), modified for nonlinear identification (Mook [6]), and shown to accurately identify exotic nonlinearities in higher order systems (Stry and Mook [4]). In this paper, it is shown how the MME algorithm successfully identifies nonlinearities using experimental data. An analytical model representing a harmonic oscillator with quadratic position feedback is studied. Output data is obtained from an analog computer simulation of the nonlinear system and the quadratic term is accurately identified. It is shown that the Minimum Model Error algorithm is capable of identifying a nonlinear model which accurately reproduces the analog output regardless of knowledge an initially assumed model, initial conditions or record length.

MME Algorithm

In this section, we briefly review the MME algorithm and how it is used to identify nonlinear dynamic systems. A more detailed explanation may be found in Mook and Junkins [5], Mook [6], and Stry and Mook [4].

The MME may be summarized as follows. Suppose there is a nonlinear system whose exact analytical representation is unknown, but for which output measurements

are available. Using "normal" means (analysis, finite elements, etc.), a system model, denoted assumed model, is constructed. The MME combines the assumed model with the measurements to determine the correct form of the nonlinear system. The approach consists of adding the to-be-determined correction term to the assumed model. A cost functional composed of the weighted sum of the correction term plus measurements minus estimate residuals is minimized. The minimization yields optimal state trajectories in addition to the correction term. A least squares fit of the correction term is performed to find the form of the dynamic model error.

Consider a forced nonlinear dynamic system which may be modeled in state-space form by the equation

$$\dot{\underline{x}}(t) = A\underline{x}(t) + \underline{F}(t) + \underline{f}(\underline{x}(t), \dot{\underline{x}}(t)) \tag{1}$$

where $\underline{x}(t)$ is the $n \times 1$ state vector consisting of the system states, A is the $n \times n$ state matrix, $\underline{F}(t)$ is an $n \times 1$ vector of known external excitation, and $\underline{f}(\underline{x}(t), \dot{\underline{x}}(t))$ is an $n \times 1$ vector which includes all of the system nonlinearities. State-observable discrete time domain measurements are available for this system in the form

$$\tilde{\underline{y}}(t_k) = \underline{g}_k(\underline{x}(t_k), t_k) + \underline{v}_k, \qquad t_0 \leq t_k \leq t_f \tag{2}$$

where $\tilde{\underline{y}}(t_k)$ is an $m \times 1$ measurement vector at time t_k, $\underline{g}_k$ is the accurate model of the measurement process, and $\underline{v}_k$ represents measurement noise. $\underline{v}_k$ is assumed to be a zero-mean, gaussian distributed process of known covariance R_k. The measurement vector $\tilde{\underline{y}}(t_k)$ may contain one or more of the system states. To implement MME, assume that a model, which is generally not the true system model because of the difficulties inherent in obtaining the true system model, is constructed in state-vector form as

$$\dot{\underline{x}}(t) = A\underline{x}(t) + \underline{F}(t) \tag{3}$$

Here, we show a linear model because in practice, linearization is the most common approach to modeling nonlinear systems. MME uses the assumed linear model in (3) and the noisy measurements in (2) to find the model error.

The model error, which might include linear terms as well as unknown nonlinear term(s), is represented by the addition of a correction term to the assumed linear model as

$$\dot{\underline{x}}(t) = A\underline{x}(t) + \underline{F}(t) + \underline{d}(t) \tag{4}$$

where $\underline{d}(t)$ is the $n \times 1$ correction term (dynamic model error) to be estimated later.

A cost functional, J, that consists of the weighted integral square of the correction term plus the weighted sum square of the measurement-minus-estimated measurement residuals, is formed:

$$J = \sum_{k=1}^{M} \left\{ [\tilde{\underline{y}}(t_k) - \underline{g}_k(\hat{\underline{x}}(t_k), t_k)]^T R_k^{-1} [\tilde{\underline{y}}(t_k) - \underline{g}_k(\hat{\underline{x}}(t_k), t_k)] \right\}$$

$$+\int_{t_o}^{t_f} \underline{d}(\tau)^T W \underline{d}(\tau) d\tau \tag{5}$$

where M is the number of measurement times, $\underline{\hat{x}}(t_k)$ is the estimated state vector and W is a weight matrix to be determined.

J is minimized with respect to the correction term, $\underline{d}(t)$. The necessary conditions for the minimization lead to the following two point boundary value problem (TPBVP), (see Geering [7]),

$$\dot{\underline{x}}(t) = A\underline{x}(t) + \underline{F}(t) + \underline{d}(t) \tag{5a}$$

$$\dot{\underline{\lambda}}(t) = -A^T \underline{\lambda}(t) \tag{5b}$$

$$\underline{d}(t) = -\frac{1}{2} W \underline{\lambda}(t) \tag{5c}$$

$$\underline{\lambda}(t_k^+) = \underline{\lambda}(t_k^-) + 2H_k R_k^{-1} [\underline{\tilde{y}}(t_k) - \underline{g}_k(\underline{\hat{x}}(t_k), t_k)] \tag{5d}$$

$$H_k = \frac{\delta g}{\delta \underline{x}} \Big|_{\underline{\hat{x}}(t_k), t_k}$$

$$\underline{x}(t_o) = \underline{x}_o \quad or \quad \underline{\lambda}(t_o) = 0 \tag{5e}$$

$$\underline{x}(t_f) = \underline{x}_f \quad or \quad \underline{\lambda}(t_f) = 0 \tag{5f}$$

where $\underline{\lambda}(t)$ is a vector of costates (Lagrange multipliers). Estimates of the states and of the dynamic model error are produced by the solution of this two-point boundary value problem. The estimates depend on the particular value of W. The solution is repeated until a value of W is obtained which produces state estimates which satisfy the "covariance constraint", explained next.

According to the covariance constraint, the measurement-minus-estimated measurement residual covariance matrix must match the measurement-minus-truth error covariance matrix. This may be written as

$$[\underline{\tilde{y}}(t_k) - \underline{g}_k(\underline{\hat{x}}(t_k), t_k)]^T [\underline{\tilde{y}}(t_k) - \underline{g}_k(\underline{\hat{x}}(t_k), t_k)] \approx R_k \tag{6}$$

During the minimization, the weight W is varied until the state estimates satisfy the covariance constraint, i.e., the left hand side of Eq. (6) is approximately equal to the right hand side. The correction term or model error is, therefore, the minimum adjustment to the model required for the estimated states to predict the measurements with approximately the same covariance as the measurement error.

After W has been determined such that the state estimates satisfy the covariance constraint, the final step in the identification procedure is to use a least squares algorithm to fit the model error $d(t)$ to the unknown dynamic term(s). The error is expanded into some combination of linear and nonlinear terms, for example,

$$d(t) = \alpha x(t) + \beta x^2(t) + \gamma x^3(t) + \ldots \tag{7}$$

where α, β, γ, ... are unknown coefficients to be determined by least squares. The least squares approach is explained in detail in Mook[6]

The TPBVP represented by Eqs. (5a) to (5f) contains jumps in the costates and, consequently, in the correction term. As evident from Eq. (5d), the size of the jump is directly proportional to the measurement residual at each measurement time. The noisier the measurements, the larger the jump size. A multiple shooting algorithm, developed by Mook and Lew [8], converts this jump-discontinuous TPBVP into a set of linear algebraic equations which may be solved using any linear equation solver. Multiple shooting also facilitates the analysis of a large number of measurements, by processing the solution at the end of every set of jumps.

The multiple shooting algorithm presented by Mook and Lew [8] was used to obtain the MME solutions used in the tests presented in this paper. It was assumed in the examples that MME obtained the dynamic error term without knowledge of the boundary conditions on $\underline{x}$, so some distortion of the correction term at the initial and final times was expected due to the constraints of Eqs. (5e-5f), i.e., by assuming no state knowledge is available at t_0 or t_f, we constrain $\lambda(t_0) = 0$ and $\lambda(t_f) = 0$. Therefore, in all test cases, the initial and final ten percent of the correction term data was ignored in the least squares fit.

Application Examples

Two nonlinear equations of motion were studied, which represent the motion of an undamped harmonic oscillator with different amounts of quadratic position feedback (identical equations may arise in other physical systems as well). The equations in state space form are

$$\begin{pmatrix} \dot{x} \\ \ddot{x} \end{pmatrix} = \begin{pmatrix} 0 & 1 \\ -1 & 0 \end{pmatrix} \begin{pmatrix} x \\ \dot{x} \end{pmatrix} + \begin{pmatrix} 0 \\ -0.526x^2 \end{pmatrix} \tag{8}$$

$$\begin{pmatrix} \dot{x} \\ \ddot{x} \end{pmatrix} = \begin{pmatrix} 0 & 1 \\ -1 & 0 \end{pmatrix} \begin{pmatrix} x \\ \dot{x} \end{pmatrix} + \begin{pmatrix} 0 \\ -1.137x^2 \end{pmatrix} \tag{9}$$

where x is position, and the dot indicates differentiation with respect to time. No forcing was applied.

In the following discussion, Eq. (8) is denoted Model A and Eq. (9) is denoted Model B. Different initial conditions were used for each system, for a total of four different tests. These are shown in Table 1.

Table 1. List of conditions used for each test

Test #	x(0)	v(0)	x*x
A1	0.000	0.261	-0.526
A2	0.000	0.523	-0.526
B1	0.000	0.087	-1.137
B2	0.000	0.261	-1.137

To utilize MME, the linear part of Eqs. (8) and (9) was chosen as the assumed model, rendering the model error equivalent to the nonlinear term, $c * x^2$. Measurements for the MME nonlinear identification were generated by simulating test A1 to B2 on an analog computer. Position measurements for all four tests were recorded and nonlinear models identified. The results were compared with the analytical position and analytical error term data, $c * x^2$, which were generated for Models A and B using a digital computer. MME proved capable of accurately identifying the nonlinear quadratic term in spite of ignorance of the assumed model, true initial conditions and record length.

Analog computer results

One hundred position measurements were generated on an EAI–2000 analog computer for all four test cases. All measurements with a sampling rate of 4 Hertz were used in the analysis. Position, velocity, and position squared were chosen as the basis functions for the least squares fit. It was uncertain if the analog computer would add some damping to the system or if it was able to correctly reproduce the stiffness term. By including position and velocity in the least squares fit, stiffness and damping could be identified if they existed. The identification procedure yielded the numerical values shown in Table 2.

Table 2. Least Square estimates of the nonlinear terms using measurements generated by the analog computer.

Test #	True x	MME x	True v	MME v	True x*x	MME x*x
A1	0.000	0.003	0.000	0.000	-0.526	-0.528
A2	0.000	0.003	0.000	0.000	-0.526	-0.526
B1	0.000	0.008	0.000	0.005	-1.137	-1.141
B2	0.000	0.003	0.000	0.000	-1,.137	-1.135

The numerical results for the least squares fit of the error term matched the analytically predicted coefficients with great accuracy. Figures (1a-4a) show the analytical position, analog measurements and position predicted by the MME analysis for all analog tests. Figures (1b-4b) show the analytical correction term and the error term estimated by MME. In all cases the MME identification produced good state estimates.

The MME algorithm could accurately identify a nonlinear model regardless of the initial conditions. As seen from Figures (1a) and (4a) (test A1 and B2), the measured position and the analytical position differ significantly. The analytical position was digitally recalculated for test A1 and B2 using the initial analog measurements as initial conditions instead of the initial conditions presented in Table 1. The results are shown in Figures (5a) and (6a). In this set of plots the analytical position and the measurements are almost identical. Also, as shown in Figures (5b) and (6b), the analytic correction term is much more similar to the estimated correction term, confirming that MME does not need any knowledge of the initial or final state vector value.[3]

MME could identify the nonlinear term accurately idenpendent of the record length. In test B1 only 40 measurements were employed in the analysis because subsequent measurements were saturated. The nonlinear term is identified very well.

Note that the data appears to be noiseless, as shown in Figures (1a-4a). Successfull analysis of noisy data using the MME algorithm can be found in Mook[6] and Stry and Mook[4].

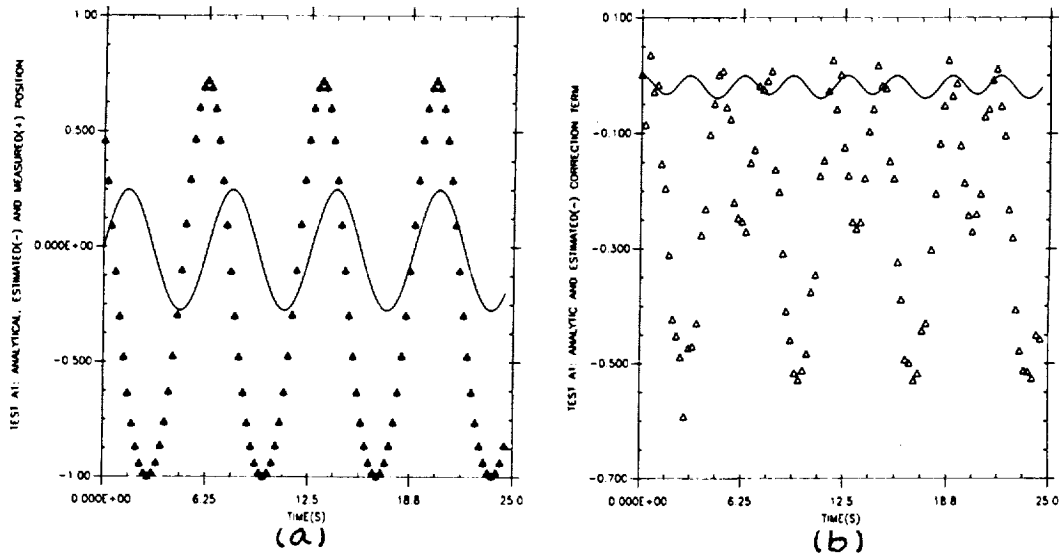

Figure 1. Test A1 a) Analytical, measured (+), and MME estimated (^) position. b) Analytical and MME estimated (^) correction term. The MME estimates are essentially identical to the measurements.

[3] It was shown in Eqs. (5e) and (5f), that by setting the initial and final costate values to zero, MME does not need any knowledge of the initial or end conditions.

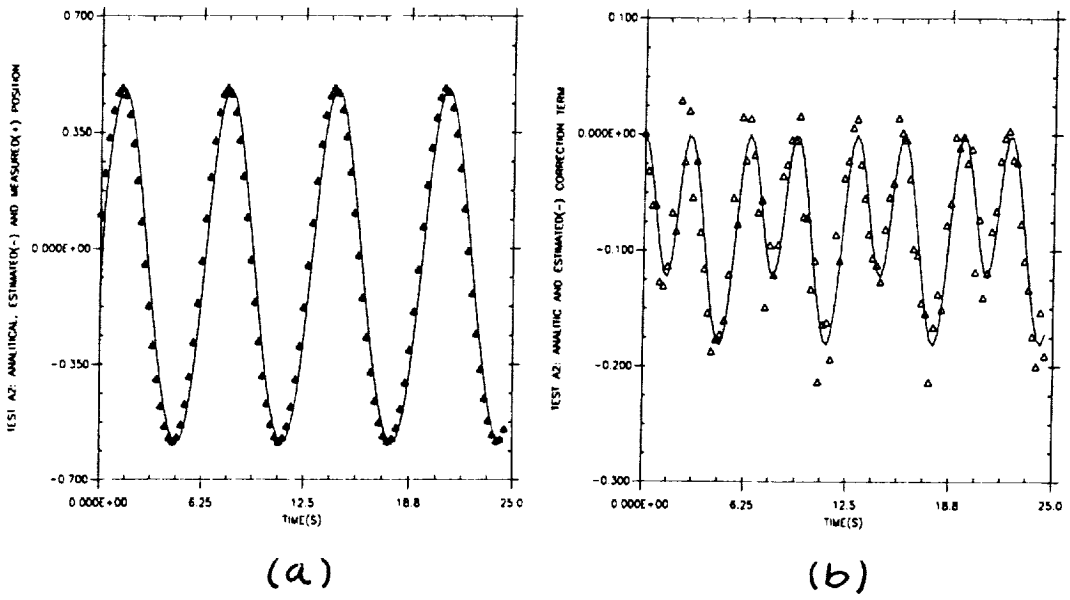

Figure 2. Test A2 a) Analytical, measured (+), and MME estimated (^) position. b) Analytical and MME estimated (^) correction term. The MME estimates are essentially identical to the measurements.

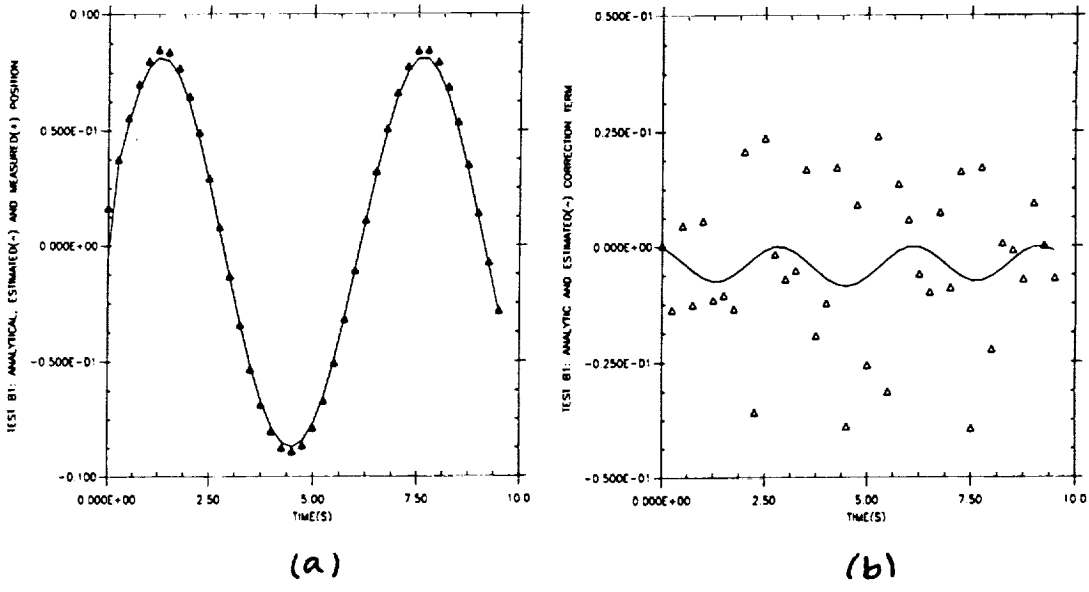

Figure 3. Test B1 a) Analytical, measured (+), and MME estimated (^) position. b) Analytical and MME estimated (^) correction term. The MME estimates are essentially identical to the measurements.

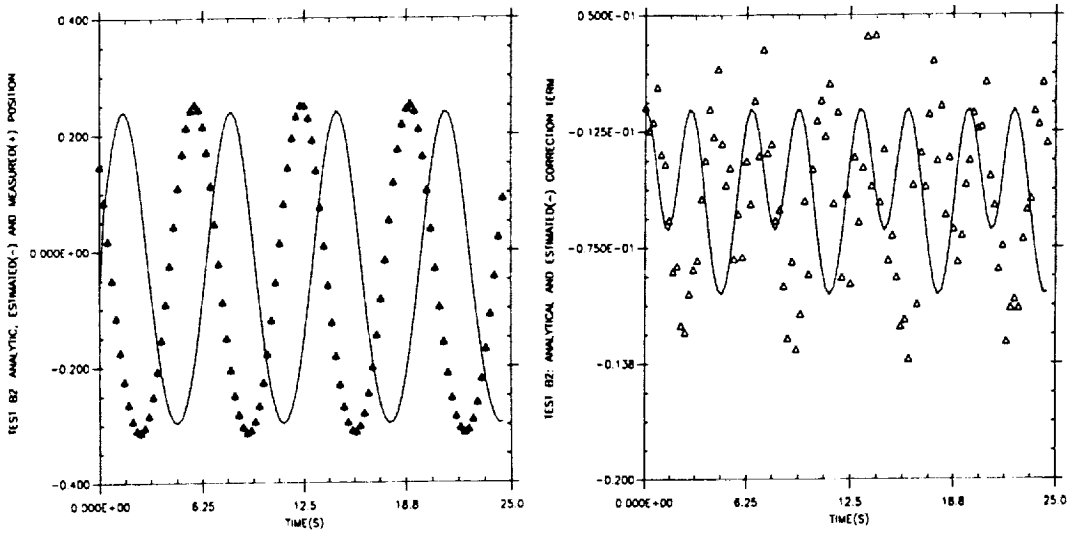

(a) (b)

Figure 4. Test B2 a) Analytical, measured (+), and MME estimated (^) position. b) Analytical and MME estimated (^) correction term. The MME estimates are essentially identical to the measurements.

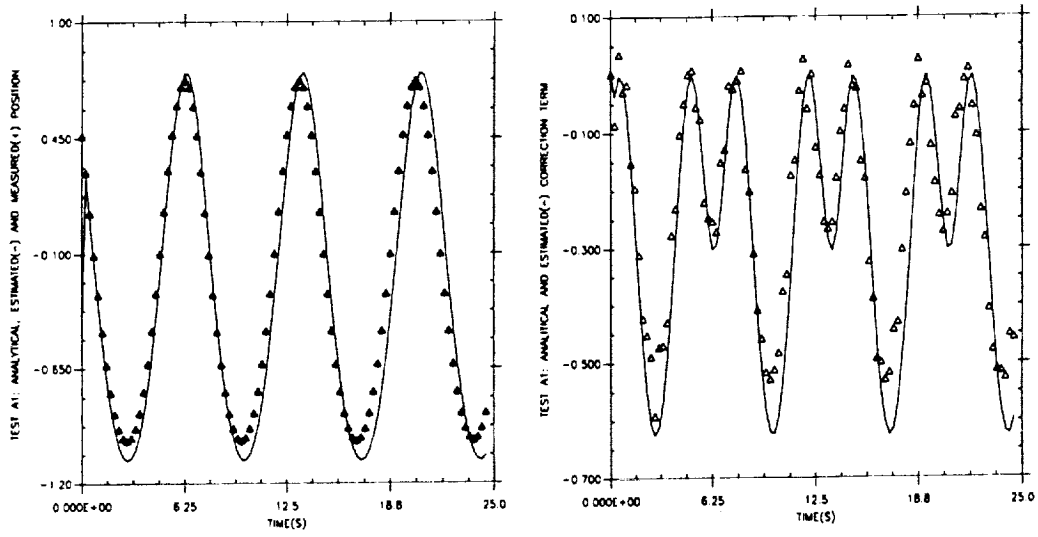

(a) (b)

Figure 5. Test A1 a) Analytical, measured (+), and MME estimated (^) position. b) Analytical and MME estimated (^) correction term. The analytical position was calculated using as initial conditions the initial position and velocity measurements from the analog computer.

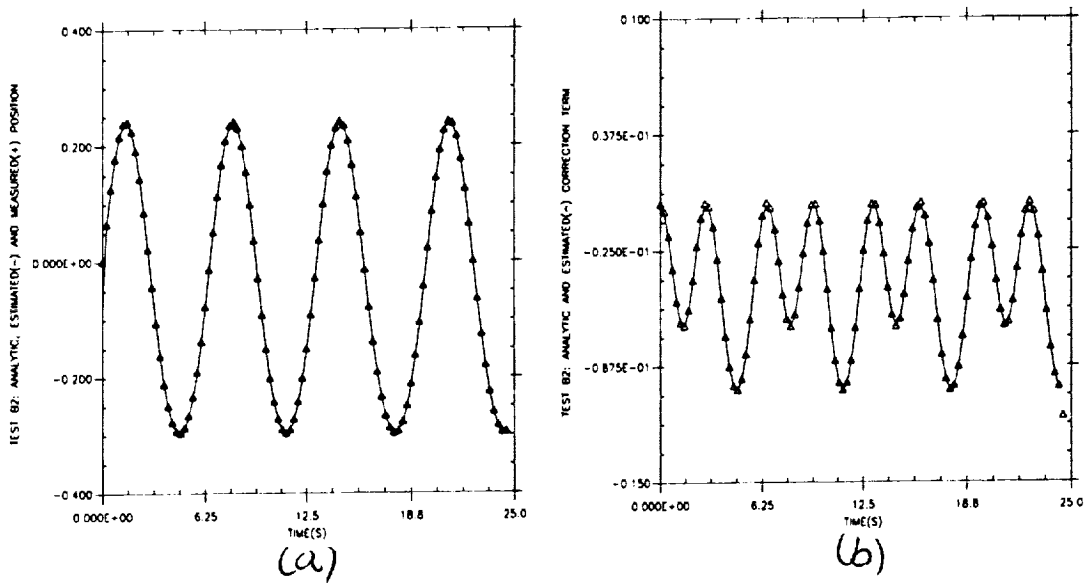

Figure 6. Test B2 a) Analytical, measured (+), and MME estimated (^) position. b) Analytical and MME estimated (^) correction term. The analytical position was calculated using as initial conditions the initial position and velocity measurements from the analog computer.

Conclusion

In this paper, an MME based algorithm was used to accurately identify the quadratic term of a nonlinear harmonic oscillator. Data was obtained from an analog computer simulation of the nonlinear system. It is demonstrated that the method is robust with respect to (lack of) a priori knowledge of the system dynamics. The identification was accurate regardless of initial conditions or data record length.

References

1. Thompson, J.M.T., and Stewart, H.B., *"Nonlinear Dynamics and Chaos"*, Wiley, New York, 1986.
2. Nayfeh, A.H., and Mook, D.T., *"Nonlinear Oscillations"*, Wiley, New York, 1979.
3. Natke, H.G., Juang, J.-N., and Gawronski, W., "Identification of Nonlinear Mechanical Systems: A Brief Review," NASA Langley Research Center, Hampton, VA, U.S.A. .
4. Mook, D.J., and Junkins, "Minimum Model Error Estimation for Poorly Modeled Dynamic Systems", *AIAA J.*, Vol. 11, No. 3, 1988, pp. 256–261.
5. Mook, D.J., "Estimation and Identification of Nonlinear Dynamic Systems," *AIAA J.*, Vol. 27, No. 7, 1988, pp. 968–974.

6. Stry, G.I., and Mook, D.J., "Identification of Higher-Order Systems with Exotic Nonlinearities," in review.
7. Geering, H.P., "Continuous Time Optimal Control Theory for Cost Functionals Including Discrete State Penalty Terms," *IEEE Trans. A.C.*, Vol. AC-21, 1976, pp. 866–869.
8. Mook, D.J., and Lew, J-H., "Multiple Shooting Algorithm for Jump Discontinuous Problems in Optimal Control and Estimation ," to appear in the *IEEE Trans. A. C.* .

Time Domain Modal Identification/Estimation of the Mini-Mast Testbed

Michael J. Roemer† *and* **D. Joseph Mook***

Department of Mechanical and Aerospace Engineering
State University of New York at Buffalo
Buffalo, New York 14260

Abstract

The Mini-Mast is a 20 meter long, 3-dimensional, deployable/retractable truss structure designed to imitate future trusses in space. This structure has undergone various static and dynamic experiments at NASA Langley Research Center to identify its modal properties so that control laws can be developed and tested. This paper presents results from a robust (with respect to measurement noise sensitivity), time domain, modal identification technique for identifying the modal properties of the Mini-Mast structure even in the face of noisy measurements. Three testing/analysis procedures are considered: (1) sinusoidal excitation near the resonant frequencies of the Mini-Mast, (2) frequency response function averaging of several modal tests, and (3) random input excitation with a free response period. The results indicate that the robust technique of the paper is more accurate using the actual experimental data than existing techniques.

Introduction

Recently, many experimental modal analysis (EMA) techniques have been developed to improve current modal testing and analysis procedures. Modal analysis techniques can usually be classified as either frequency or time domain procedures. Some experimental difficulties arise in the frequency domain when the natural frequencies of a system are closely distributed and/or the system contains a high

† Graduate Research Assistant
* Assistant Professor

degree of damping. In the time domain, noisy output measurements are the most troublesome for accurate modal identification. However, both time and frequency domain methods encounter the most difficulty when particular modes are poorly excited during a testing procedure. For this case, the amplitudes of the poorly excited modes can be less than the RMS amplitude of the noise. In this paper, a time-domain identification algorithm which is robust with respect to measurement noise is used to identify some of the primary modes of the Mini-Mast Testbed at NASA's Langley Research Center.

The modal identification algorithm used in this paper combines the ERA identification/realization technique [1] with an optimal state estimation algorithm called MME [2] to successfully identify modal properties of a structure even in the face of noisy measurements. The ERA technique is based on the singular value decomposition of a generalized Hankel matrix composed of discrete, time-domain measurements. This time-domain technique is capable of accurately identifying modal parameters for cases involving perfect or low-noise measurements. However, difficulties may arise when high noise levels are present in the output measurements. Thus, by combining the MME optimal state estimation algorithm with the ERA identification algorithm, improved modal identification is achieved through lowering the algorithm's sensitivity to noise. This ability has been demonstrated in numerous simulations of different test systems [3-6].

The Minimum Model Error (MME) estimation algorithm is well suited for the modal identification problem because it does not assume that the model error is a white noise of known covariance as do other estimation filters (e.g., Kalman filter). Instead, the model error is assumed to be an unknown quantity and is estimated as part of the solution. The theoretical advantages of this assumption are obvious for the present problem, since the model is unknown *apriori*. Since the model is comprised of deterministic modes, the identification problem is one of finding (eliminating) deterministic model error. In several previous studies, the MME has been shown to produce state estimates of high accuracy for problems involving both significant model error and significant measurement error [7].

Reducing the noise sensitivity of the Eigensystem Realization Algorithm has been investigated in several computer simulations. The results were based on 3 and 4 mode simulated truths to which gaussian distributed white noise was added to simulate noisy measurements. The ERA was found to be extremely accurate at low noise levels. However, the accuracy is diminished if the measurement noise is increased enough to effect the lower amplitude modes. This result was also reported by Juang and Pappa [8]. However, compared with ERA by itself, the

combined ERA/MME algorithm produced more accurate results with respect to identifying the number of modes, frequencies, damping ratios, and mode shapes. For example, in a 4 mode simulation example using noisy measurements with a variance of 0.004, the ERA algorithm could only identify 3 of the 4 modes. The combined ERA/MME algorithm, on the other hand, identified all 4 modes and their respective mode shapes accurately [4]. The purpose of this paper is to extend this theoretical/simulation background to the Mini-Mast CSI testbed, in order to examine its identification ability on actual experimental data taken from a large space structure.

Mini-Mast Testing Procedure

The Mini-Mast is a deployable/retractable test truss structure designed to imitate future trusses to be used in space. A representative illustration supplied by NASA is shown in Figure 1. The Mini-Mast is approximately 20 meters in length (18 bays, 1.12 meters each), and has a three-longeron construction forming a triangular cross-section with points inscribed by a circle of 1.4 meters in diameter [10]. The truss is cantilevered vertically to the ground by bolting the lowest three joints. The joints are made of machined titanium (6Al-4V) to hinge the longeron and diagonal members securely. The tubing members are constructed of a graphite/epoxy composite. The Mini-Mast has undergone various static and dynamic experiments. The work of this paper is concentrated on the data taken from selected dynamic tests.

Several types of response sensors are available on the Mini-Mast testbed. The sensors chosen for the dynamic tests discussed here are Kaman KD-2300 displacement probes. The probes are positioned to measure deflections orthogonal to the face of the probe, and are mounted in parallel to the Mini-Mast's corner joints. All of the bays except bay 1 are instrumented with three of these displacement sensors. The operating principle of the sensors is based on the impedance variations caused by eddy currents induced in a conductive metal target. The displacement is sensed from the coupling between a coil in the sensor and a particular target. Resolution of the Kaman KD-2300-10CU at mid range is 0.0025 mm, with a static frequency response up to 50 kHz

Three testing/analysis procedures are examined. First, frequency response functions (FRF) were constructed from (1) a finite element model, and (2) experimental data supplied by NASA's Spacecraft Dynamics Branch. A plot illustrating the type of data used in this analysis is shown in Figure 2.

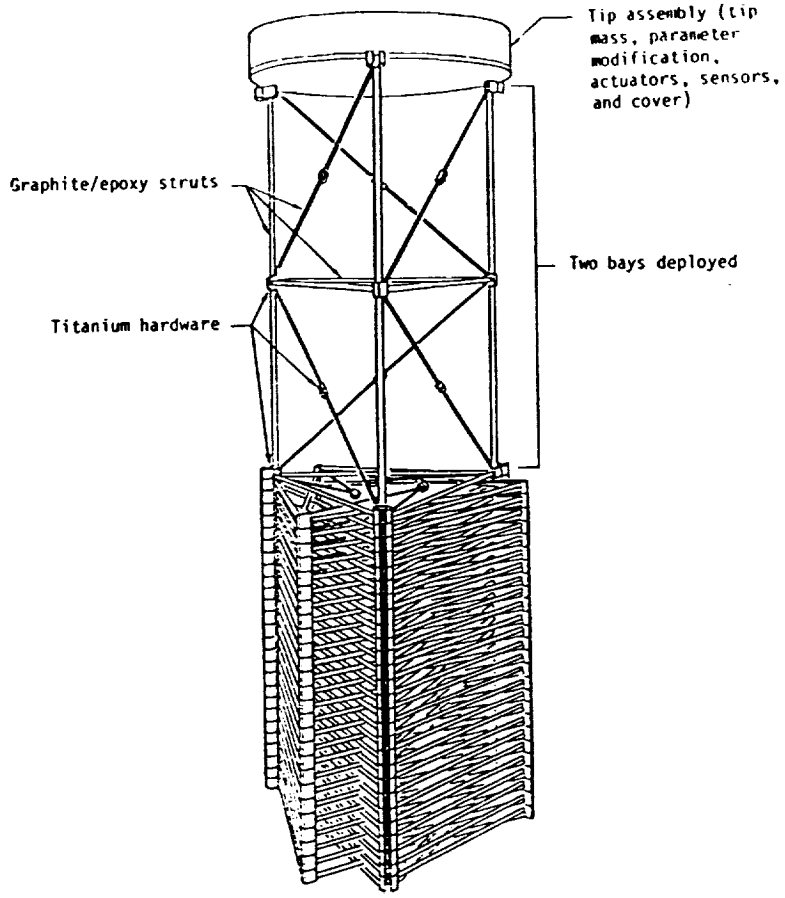

Figure 1 NASA's Mini-Mast Testbed

Referring to Figure 2, the frequency response function distinguished by the crosses represents the finite element or analytical model. The remaining frequency response function is derived from many sets of experimental data and generated using SDRC's I-DEAS test analysis package. The first analysis procedure discussed in this paper identifies the modal properties of the Mini-Mast structure by taking inverse fourier transforms of the averaged FRF's and using them as input to the identification algorithm. The identified natural frequencies establish a "truth" for comparing the other identification and testing procedures. The second testing procedure consisted of exciting the Mini-Mast test structure at frequencies close to its predicted natural frequencies. The time domain responses are then transformed into the frequency domain where a transfer function is formulated using auto and cross correlations. Finally, the impulse response (to be analyzed) is found by transforming back to the time domain. The third testing/analysis procedure consisted of randomly exciting the Mini-Mast structure and then allowing it to free decay until it comes to rest. Three response points were monitored at bay 10 at a sampling

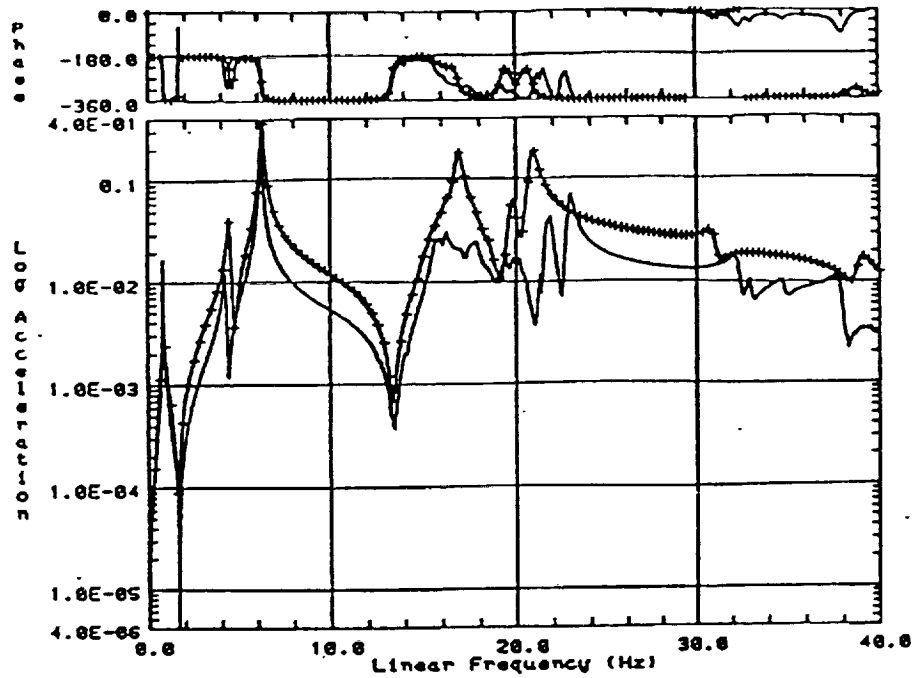

Figure 2 Example Frequency Response Function

rate of 128 Hz The response portion used in the identification/estimation algorithm included 100 data points from the free response of the structure. The combined ERA/MME algorithm was compared against the ERA by itself. The results were compared with respect to the following criteria: (1) the "truth" established by the frequency response function averaging, (2) damping ratio identification, and (3) modal amplitude coherence factors. Improvements were noted with respect to all three performance measures.

Frequency Response Function Analysis

The inverse fourier transforms of select frequency response functions were obtained to get a representative impulse time history. This impulse response data was then filtered so that a small frequency bandwidth could be investigated closely. The first frequency bandwidth considered was 0 Hz to 10 Hz. In this region, the first and second bending modes were observed as well as the first torsion mode. Included in the frequency range of 10Hz to 20 Hz are a cluster of 108 "local" modes. These modes are primarily due to the bending of the 54 diagonal truss members. The final frequency range considered was 20 Hz to 30 Hz. In this range, the second torsion mode was identified. The transformed time-domain data was used as input to the combined ERA/MME algorithm. A summary of the steps associated with

this experimental analysis is provided below.

Modal Identification Algorithm

1. Obtain time-domain measurements from either the inverse transforms of the frequency response functions or raw data from the Mini-Mast.

2. Apply the Eigensystem Realization Algorithm (ERA) to the measurements obtained from the Mini-Mast test structure.

3. Input a realized model and the measurements into the Minimum Model Error (MME) algorithm to produce optimal state estimates.

4. Sample the MME produced state estimates at discrete-time intervals to create simulated measurements of higher accuracy than the original measurements.

5. Apply ERA to the simulated measurements in order to realize/identify the new modal parameters.

6. Examine the identified modal parameters for some convergence criteria, and repeat the procedure if necessary.

The first two bending and torsion modes of the Mini-Mast were isolated as modes of particular interest in this paper. Utilizing a 10^{th}-order, Butterworth, low-pass filter, the first two bending modes and the first torsion mode were clearly identified using the FRF data. Because the exact frequencies of the Mini-Mast are unknown, a small range is given for each identified frequency to serve as the "truth". Using the fourier inverse of several averaged data sets, the first bending mode was identified in the range of 0.87 - 0.88 Hz, the first torsion mode between 4.20 - 4.35 Hz, and the second bending mode was in the range of 6.25 - 6.35 Hz The second torsion mode was identified with the help of a 10^{th}-order, Butterworth, band-stop filter. A band-stop filter was chosen in order to filter out the effects of the 108 "local" modes in the frequency range of 10 to 20 Hz The identified natural frequency of this mode was between 22.1 - 22.7 Hz. An illustration of the frequency and time domain equivalents used in this analysis are shown in Figures 3 and 4.

The identification results presented above are produced from the combined ERA/MME algorithm. However, the ERA algorithm alone produced the same results. This result is expected because the frequency response functions were formed from an average of several tests. Also, the averaged FRF's were filtered to iso-

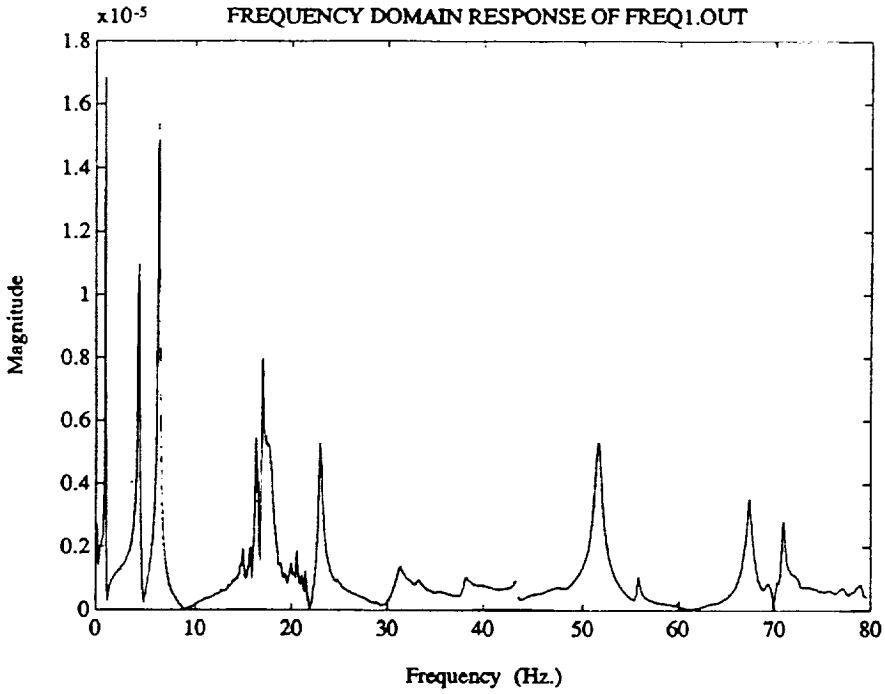

Figure 3 Frequency Response

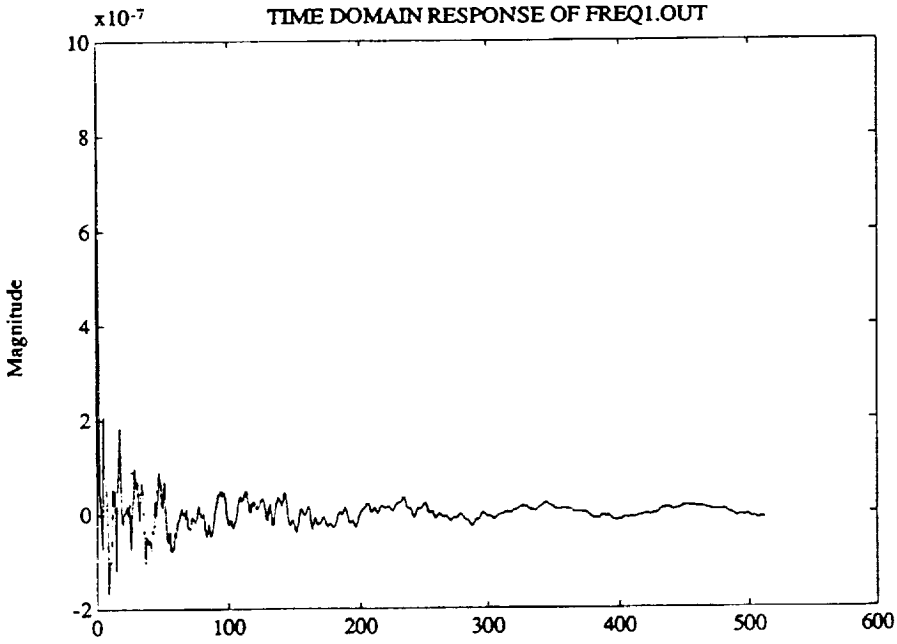

Figure 4 Impulse Response

late the particular modes to be identified. The ranges of the Mini-Mast's first four

natural frequencies of interest are given below.

$$\omega_{b1} \approx 0.87 - 0.88 \ \ Hz$$
$$\omega_{t1} \approx 4.20 - 4.35 \ \ Hz$$
$$\omega_{b2} \approx 6.25 - 6.35 \ \ Hz$$
$$\omega_{t2} \approx 22.1 - 22.7 \ \ Hz$$

Sinusoidal Excitation Analysis

In this section, sinusoidal excitations are applied to the Mini-Mast test structure. The frequencies of the sinusoidal forces are set near the assumed natural frequencies of the structure in an attempt to produce a more accurate identification. A torque wheel located at the top of the mast was used to excite the structure, while the Kaman displacement probes sensed the structure's motion. Once the measurements from the input and output sensors are collected, a transfer function of the Mini-Mast can be constructed. The transfer function equation is composed of cross and auto correlations as:

$$G(j\omega) = \frac{S_{xx}(\omega)}{S_{fx}(\omega)}$$

where

$$S_{xx} = auto - spectral\ density$$
$$S_{fx} = cross - spectral\ density$$
$$G(j\omega) = frequency\ response\ or\ transfer\ function$$

This equation is based on the fast fourier transform of the input/output time histories. Excluding the initial transient response of the structure due to the torque wheel force, the frequency response is dominated by the frequency of excitation. Because of this, a mathematical problem exists when computing the system's transfer function. More specifically, at frequencies other than the excitation frequency, the fourier transform of the input produces numbers very close to zero. Therefore, a problem of dividing by numbers that are very close to zero is unavoidable. To overcome this difficulty, a small amount of gaussian distributed white noise with variance of $4x10^{-6}$ was added to the measurements. As expected, the addition of white noise produced larger numbers in the frequency response of the structure at frequencies other than the excitation frequency. After the transfer function is

formulated, the impulse response can be generated for input to the identification algorithm. The impulse response is calculated by taking the inverse fourier transform of the structure's transfer function or FRF.

The modal identification procedure started by using the ERA by itself. Individual input/output time histories were used to construct a 100x100 Hankel matrix, from which a 12^{th}-order model was realized. An average of 5 tests were used to arrive at the identified frequencies for both the ERA and ERA/MME algorithms. Most of the individual time histories only revealed information about a couple of the modes at one time. Therefore, several different time histories were used to formulate each identified natural frequency.

The ERA/MME identification algorithm takes advantage of the realized model ERA produces in order to robustly identify a structure's modal properties. More specifically, the realized model is used in the MME estimation scheme to smooth the measurements. However, a concern of particular importance is how much error is present in the realized model. The realized model was produced from undoubted noisy measurements and truncated modes. The fact that model error is often composed of truncated modes makes the common estimation assumption of using white noise for model error particularly poor. Minimum Model Error (MME) estimation addresses this concern by estimating the model error as part of the solution. The model error is assumed as part of the solution, so no assumptions (such as white noise) are required. Instead of the need to assume both measurement and model error covariances, as in the case of the Kalman filter, only the measurement error covariance is needed. In addition, a study performed in reference [11] concluded the following important result. When predicting the measurement error covariances (the *only* input covariance needed for the ERA/MME algorithm), it is important to predict a low covariance in the beginning and slowly increase the prediction until the best modal amplitude coherence factors are found. The reason for this is that if the predicted measurement error covariance is lower than the unknown actual measurement error covariance, then the estimate can never be worse than the measurements are already. This result allows the user to have faith when implementing the ERA/MME algorithm. However, if the predicted measurement error covariance is higher than the unknown actual measurement error covariance, then the simulated measurements from the estimates could become worse (more noisy) than the original measurements. Because of this, it is important to assume measurement error covariances low when satisfying the covariance constraint of the MME estimation technique

Following the six step procedure of the ERA/MME algorithm, only two

iterations were used for identifying the first four natural frequencies. Simple one- and two-mode models were used in the estimation/identification scheme. The use of these truncated models highlights the importance of not modeling the truncated modes as white noise. A table illustrating all of the results is given below.

Table 1 Sinusoidal Analysis Result Comparison

	"Truth"	ERA	ERA/MME
	frequency (Hz)	frequency (Hz)	frequency (Hz)
1 bending	0.87 - 0.88	0.8470	0.8668
1 torsion	4.20 - 4.35	4.1175	4.4027
2 bending	6.25 - 6.35	7.0457	6.8943
2 torsion	22.1 - 22.7	22.150	22.091

Comparing the ERA and combined ERA/MME algorithms with the FRF analysis results indicates an overall improvement when using the combined procedure. More specifically, identification accuracy of the first three frequencies identified by the ERA/MME algorithm were improved by up to 5% over ERA by itself. The fourth frequency remained basically the same.

Using available NASA data, inverse and regular fourier transformations were performed in order to get the impulse time histories needed for time domain modal identification. Transformed and filtered data is not the type of data the ERA/MME identification/estimation procedure was intended for use on. This is because the noise that might have been present in the original test data would have been altered significantly by these transformations etc. Therefore, the improved results (using MME estimation) were not as significant as might be expected if raw impulse response data or data generated from random input excitations were available. Using raw data is the next step for testing the ERA/MME algorithm.

Random Excitation/Free Response Analysis

In this section, the Mini-Mast test structure was excited using a random

input with a bandwidth ranging from 0 to 40 Hz. The random excitation was applied for 26 seconds and then the structure was allowed to free respond until the response went to zero. Three response points were monitored at bay 10 of vortices A, B, and C, and the shaker was located at bay 9. The data sampling rate was 128 Hz and the free response portion of the time history began at the 33 second mark. The response portion that was used in the identification/estimation algorithm included 100 data points ranging in time from 34.0 to 34.8 seconds. The combined ERA/MME identification algorithm was compared against ERA by itself to examine the advantages of the combined technique. A predicted noise variance of 1×10^{-12} was used in the MME estimation scheme to satisfy the covariance constraint.

To examine if the results of the combined ERA/MME algorithm are better than the ERA identification results, the modal amplitude coherence (MAC) factors were calculated for each mode. MAC's estimate the degree of modal excitation or controllability for each mode. A MAC factor close to 1 means that the mode was identified well during the testing procedure. As shown in Tables 2 through 5, the MAC factors are indeed improved for all four primary modes. The damping ratios also seem to be improved, assuming that the damping ratios of the Mini-Mast are less than 5% (a reasonable assumption for such a structure). For example, the damping ratio of the first torsional mode identified by ERA was 0.101 and the ERA/MME identified it to be 0.0044. Note, the most improved damping ratios and MAC factors were found to be associated with the torsional modes of the Mini-Mast. This can be explained by the fact that the shaker was used in only one direction. Therefore, the linear or bending modes were excited more rigorously than the torsional modes. This result highlights a major advantage of using the combined ERA/MME algorithm, namely to help identify modes not excited very well in a testing procedure.

First, let's examine the identification results of the responses at bay 10, vortex A as shown in Tables 2 and 3. Improvements were made with respect to the MAC factors for all four primary modes. However, a more distinct improvement was observed when identifying the 2 torsional modes. Specifically, the first torsional mode's MAC factor as identified by ERA was 0.8974, while the ERA/MME identified MAC factor was increased to 0.9842. The MAC factor of the second torsional mode was identified by ERA as 0.8633, and the ERA/MME algorithm improved it to 0.9457. The improved MAC's are also supported by the identified frequencies and damping ratios. The "true" torsional frequencies were identified by the averaged FRF's in the range of 4.20 - 4.35 Hz and 22.1 - 22.7 Hz. The torsional modes identified by ERA were 4.77 Hz and 22.61 Hz respectively, and those identified by

the combined algorithm were 4.37 Hz and 22.4 Hz respectively, a supportive conclusion. The damping ratio of the first torsional mode identified by ERA was over 10% and the ERA/MME technique reduced it to 0.4%. Hence, when examining the MAC factors, natural frequencies, and damping ratios, the combined algorithm produced improvements with respect to each one.

The identification results from the responses at bay 10, vortex B are given in Tables 4 and 5. The MAC factors for each identified mode are again improved, but not as significant as in the previous case. The most improved mode was the first torsional mode. The MAC factor identified by ERA was 0.9546, while the ERA/MME algorithm improved it to 0.9719. The natural frequency associated with this mode was identified by ERA to be 4.56 Hz and the ERA/MME procedure identified it to be 4.39 Hz. Recall, the "true" natural frequency identified by the averaged FRF's was in the range of 4.20 - 4.35 Hz. The damping ratio was also reduced from 2.87% (using ERA) to 0.72% (using ERA/MME).

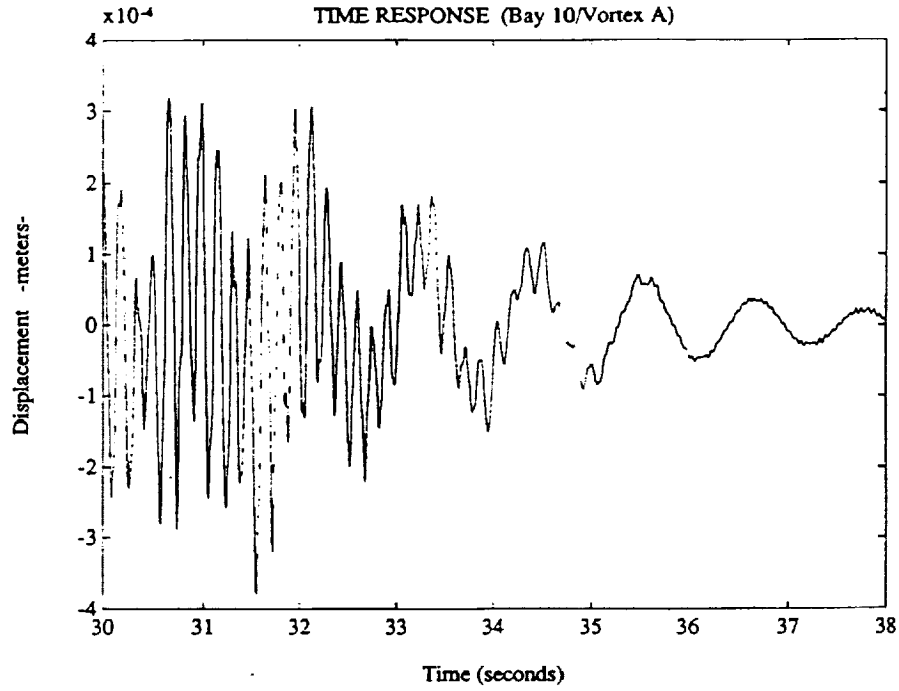

Figure 5 Output Vortex A

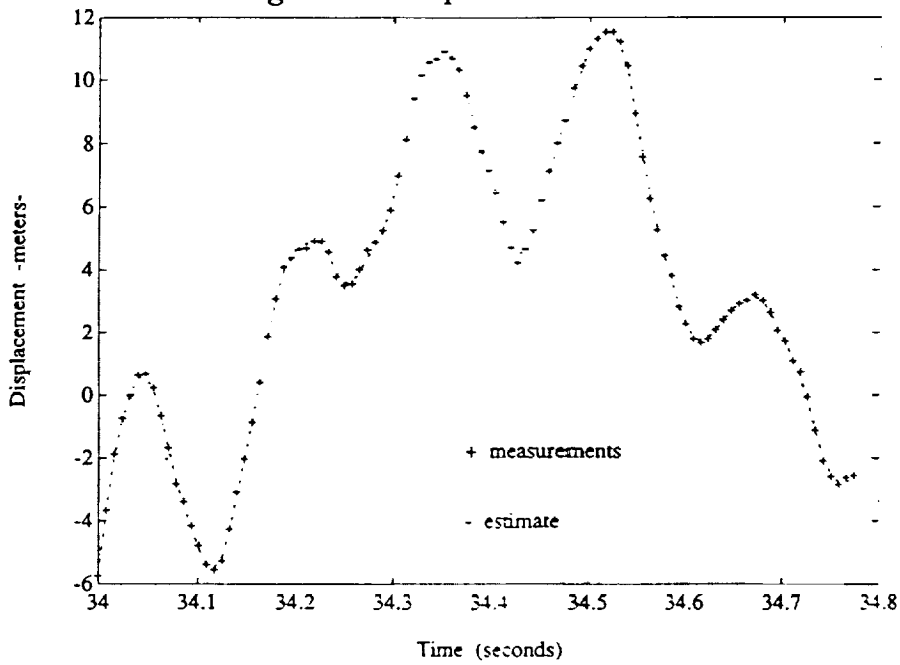

Figure 6 Estimate and Measurements Vortex A

Table 2 ERA Vortex A Results

	"Truth"	ERA		
	frequency (Hz)	frequency (Hz)	damping ratio	MACF (0-1)
1 bending	0.87 - 0.88	0.8821	0.0377	0.9981
1 torsion	4.20 - 4.35	4.7713	0.1019	0.8974
2 bending	6.25 - 6.35	6.1479	0.0287	0.9901
2 torsion	22.1 - 22.7	22.607	0.0322	0.8633

Table 3 ERA/MME Vortex A Results

	"Truth"	ERA/MME		
	frequency (Hz)	frequency (Hz)	damping ratio	MACF (0-1)
1 bending	0.87 - 0.88	0.8814	0.0240	0.9993
1 torsion	4.20 - 4.35	4.3719	0.0044	0.9842
2 bending	6.25 - 6.35	6.2156	0.0299	0.9962
2 torsion	22.1 - 22.7	22.443	0.0164	0.9457

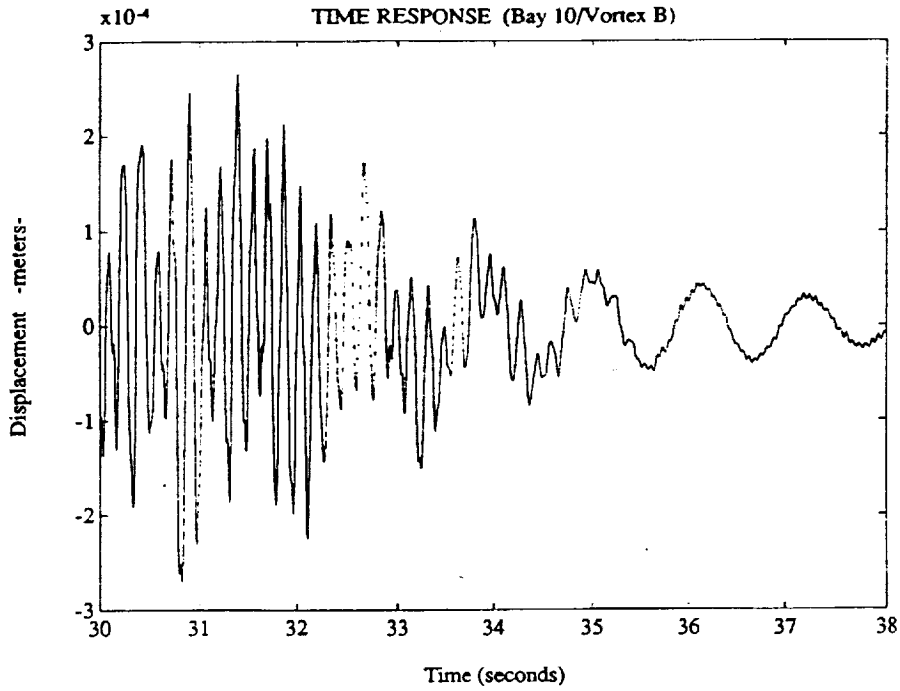

Figure 7 Output Vortex B

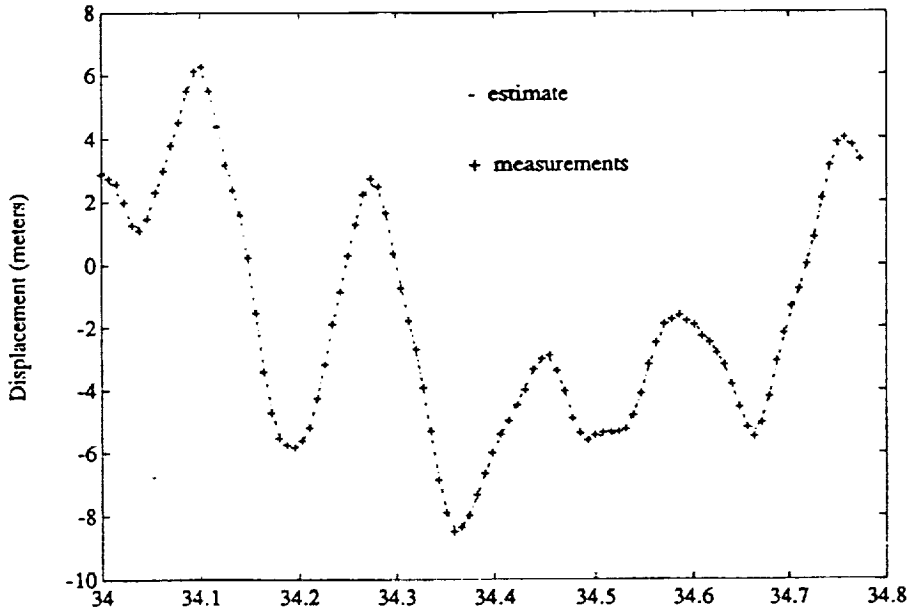

Figure 8 Estimate and Measurements Vortex B

Table 4 ERA Vortex B Results

	"Truth"	ERA (b)		
	frequency (Hz)	frequency (Hz)	damping ratio	MACF (0-1)
1 bending	0.87 - 0.88	0.8585	0.1206	0.9914
1 torsion	4.20 - 4.35	4.5576	0.0287	0.9546
2 bending	6.25 - 6.35	6.2174	0.0209	0.9925
2 torsion	22.1 - 22.7	22.324	0.0283	0.9472

Table 5 ERA/MME Vortex B Results

	"Truth"	ERA/MME (b)		
	frequency (Hz)	frequency (Hz)	damping ratio	MACF (0-1)
1 bending	0.87 - 0.88	0.8590	0.1217	0.9930
1 torsion	4.20 - 4.35	4.3978	0.0072	0.9719
2 bending	6.25 - 6.35	6.2004	0.0211	0.9955
2 torsion	22.1 - 22.7	22.227	0.0272	0.9488

Mini-Mast Identification Summary

Three different modal testing techniques for identifying some of the primary modes of NASA's Mini-Mast testbed were examined. The frequency response function analysis served to create a "truth" which the sinusoidal excitation and impulse response tests could be compared against. The authors believe the "truth" is accurate because of the many tests that produced the averaged results. The sinusoidal testing procedure included adding white noise to the original measurements so that a transfer function could be approximated. The transfer functions were then transformed into the time domain for input to the identification algorithms. Results from the identification algorithms revealed improvements (up to 5%) in identifying the first three natural frequencies of the Mini-Mast. The third test included shaking the Mini-Mast structure with a random input for 26 seconds and then allowing the structure to come to rest. The results of this test gave the best improvements when compared with the other tests because the developed algorithms were intended for use on raw impulse response or free response data. The other tests employed FFT's and inverse FFT's to construct the impulse responses. The identification of the torsional modes were especially improved using the combined identification/estimation algorithm. The identification improvements were based on; (1) the damped natural frequncies identified by ERA and ERA/MME being closer to the FRF averaged identified frequencies, (2) The damping ratio identification, specifically having damping ratios approximately 2% or less, and (3) the modal amplitude coherence (MAC) factors being close to 1. The most improved case was found in the identification of the first torsion mode. The ERA identified MAC factor was 0.8984 and the combined ERA/MME improved the MAC factor to 0.9842. Also, the damping of this mode was identified by ERA to be 0.1019 and the ERA/MME identified it to be 0.0044, a noticeable improvement if the damping is indeed close to 0.

The fact that the MAC factors of the torsional modes were lower than the bending modes (for both the ERA and ERA/MME identification techniques) allows us to conclude that the torsional modes were not excited very well during the modal test. This concern, along with improvements in the identification of the damping ratios and natural frequencies, was addressed by the ERA/MME identification scheme (specifically by the results of the free decay tests given in Tables 2 through 5). The combined identification/estimation algorithm can therefore improve time domain identification methods in the case of noisy output measurements or poorly excited modes.

References

1. Juang, J.-N., and Pappa, R.S., "An Eigensystem Realization Algorithm (ERA) for Modal Parameter Identification and Model Reduction", **AIAA Journal of Guidance, Control, and Dynamics**, Vol. 8, No. 5, pp. 620-627, Sept.-Oct. 1985.

2. Mook, D.J., and Junkins, J.L., "Minimum Model Error Estimation for Poorly Modeled Dynamic Systems", **AIAA Journal of Guidance, Control, and Dynamics**, Vol. 11, No. 4, pp. 367-375, May-June. 1988.

3. Mook, D.J., and Lew, J.S., "A Combined ERA/MME Algorithm for Robust System Realization/Identification", **Journal of the Astronautical Sciences** to appear.

4. Roemer, M. J., and Mook, D. J., "Enhanced Realization/Identification of Physical Modes", **A.S.C.E. Journal of Aerospace Engineering.**, Vol. 3, No. 2, pp. 122-136, April 1990.

5. Roemer, M. J., and Mook, D. J., "An Enhanced Mode Shape Identification Algorithm", 30^{th} Structures, Structural Dynamics, and Materials Conference (S.D.M.), Mobile, Alabama, April 1989.

6. Roemer, M. J., and Mook, D. J., "Robust Realization/Identification of Damped Structures", Damping 89 Conference, West Palm Beach, FL, February 1989.

7. Mook, D.J., and Lin, J.-C., "Minimum Model Error Estimation of Modal Truncation Errors", Proceedings of the 1987 Spring Meeting of the Society for Experimental Mechanics, Houston, TX, June 1987.

8. Juang, J.-N., and Pappa, R.S., "Effects of Noise on Modal Parameters Identified by the Eigensystem Realization Algorithm", **AIAA Journal of Guidance, Control, and Dynamics**, Vol. 9, No. 3, pp. 294-303, May-June, 1986.

9. Lew, J.S., and Mook, D.J., "Two-Point Boundary Problems Containing Jump Discontinuities", in Review.

10. Pappa, R., Miserentino, B., Bailey, J., Elliot, K., Perez, S., Cooper, P., Williams, B., Suul, J., Ghosh, D., Montegomery, R., "**Mini-Mast CSI Testbed Users Guide**", NASA Langley Research Center, Hampton, VA.

11. Roemer, M. J., "Robust System Realization/Identification via Optimal State Estimation", Ph.D. Dissertation, S.U.N.Y at Buffalo, 1990.

12. Vold, H., Kundrat, J., Rocklin, G. T., and Russell, R., "A Multiple Input Modal Estimation Algorithm for Minicomputers", SAE paper number 820194, 1981.

13. Inman, D. J., **Vibration with Control, Measurement, and Stability**, Prentice-Hall Inc., New Jersey, 1989.

14. Kalman, R.E., "A New Approach to Linear Filter and Prediction Problem", **Trans. ASME, J. Basic Engr.**, Vol. 82, pp 34-45, 1960.

	"Truth"	Low-Pass Filtered ERA (f = 40 Hz) @Vortex A		
	frequency (Hz)	frequency (Hz)	damping ratio	MACF (0-1)
1 bending	0.87 - 0.88	0.8731	0.0622	0.9942
1 torsion	4.20 - 4.35	4.3591	0.0311	0.9266
2 bending	6.25 - 6.35	6.3199	0.0268	0.9855
2 torsion	22.1 - 22.7	22.343	0.0443	0.7489

	"Truth"	Low-Pass Filtered ERA (f = 40 Hz) @Vortex B		
	frequency (Hz)	frequency (Hz)	damping ratio	MACF (0-1)
1 bending	0.87 - 0.88	0.8396	0.0211	0.9489
1 torsion	4.20 - 4.35	4.5066	0.2984	0.8797
2 bending	6.25 - 6.35	6.2918	0.0573	0.9853
2 torsion	22.1 - 22.7	21.240	0.0825	0.7792

AN OVERVIEW OF THE ESSENTIAL DIFFERENCES AND SIMILARITIES OF SYSTEM IDENTIFICATION TECHNIQUES

Raman K. Mehra
Scientific System
500 W. Cummings Pk
Suite 3950
Woburn, MA 01801

4th NASA Workshop on Computational Control of
Flexible Aerospace Systems, Williamsburg, VA
July 11 - 13, 1990

Outline

1. System Identification - Four Basic Steps
2. Bayesian Statistical Decision Theory Framework
3. Maximum Likelihood Estimation and E-M algorithm
4. Similarities and Differences between Indentification Methods
5. Minimal Realizations - Deterministic & Stochastic
6. Structural Mode Identification using Stochastic Realization Algorithm
7. Identification Results
   - o Membrane Simulations
   - o AL Grid
   - o X-29 Flutter Flight Test Data
8. Conclusions

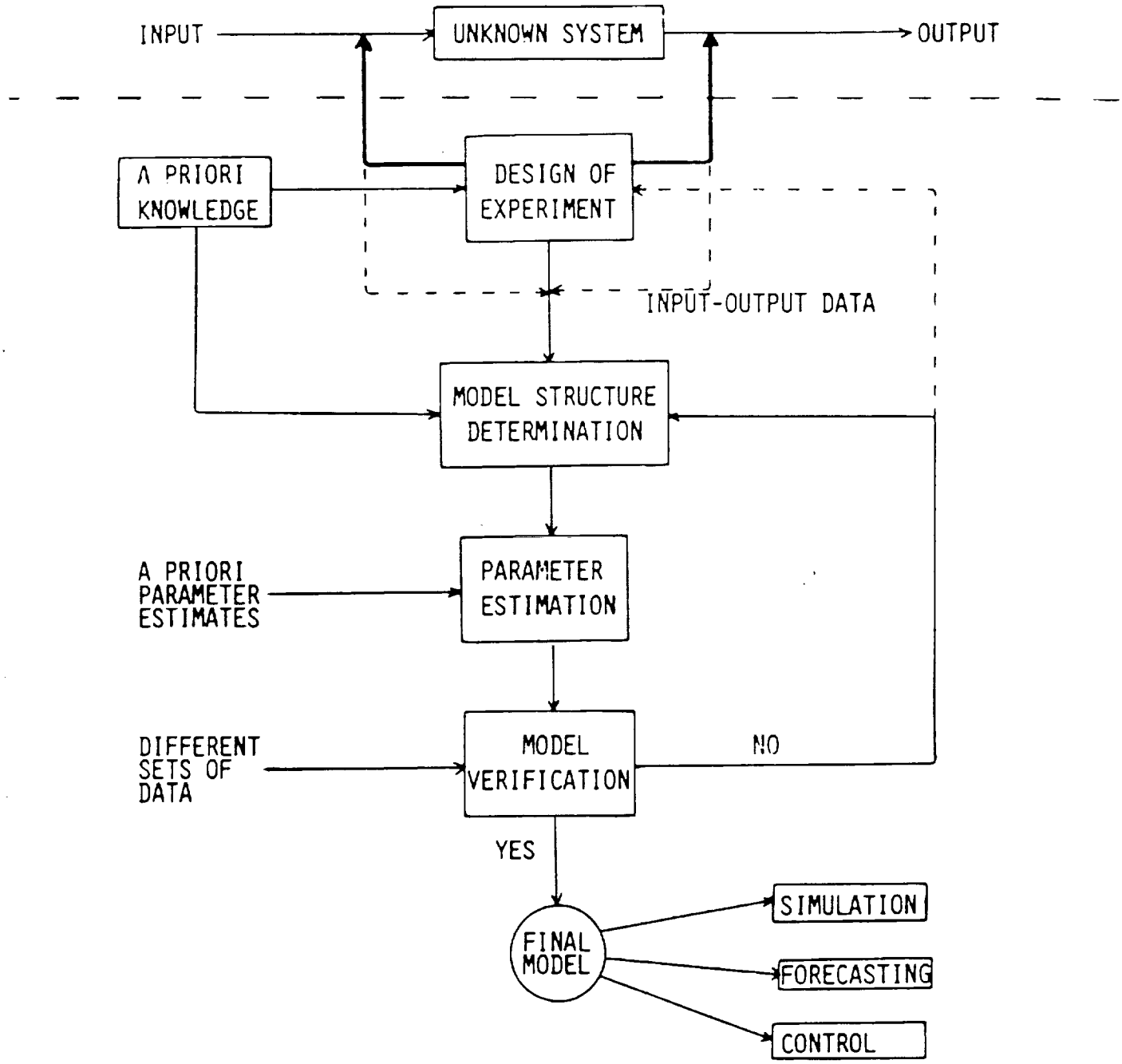

STEPS IN SYSTEM MODELING AND IDENTIFICATION

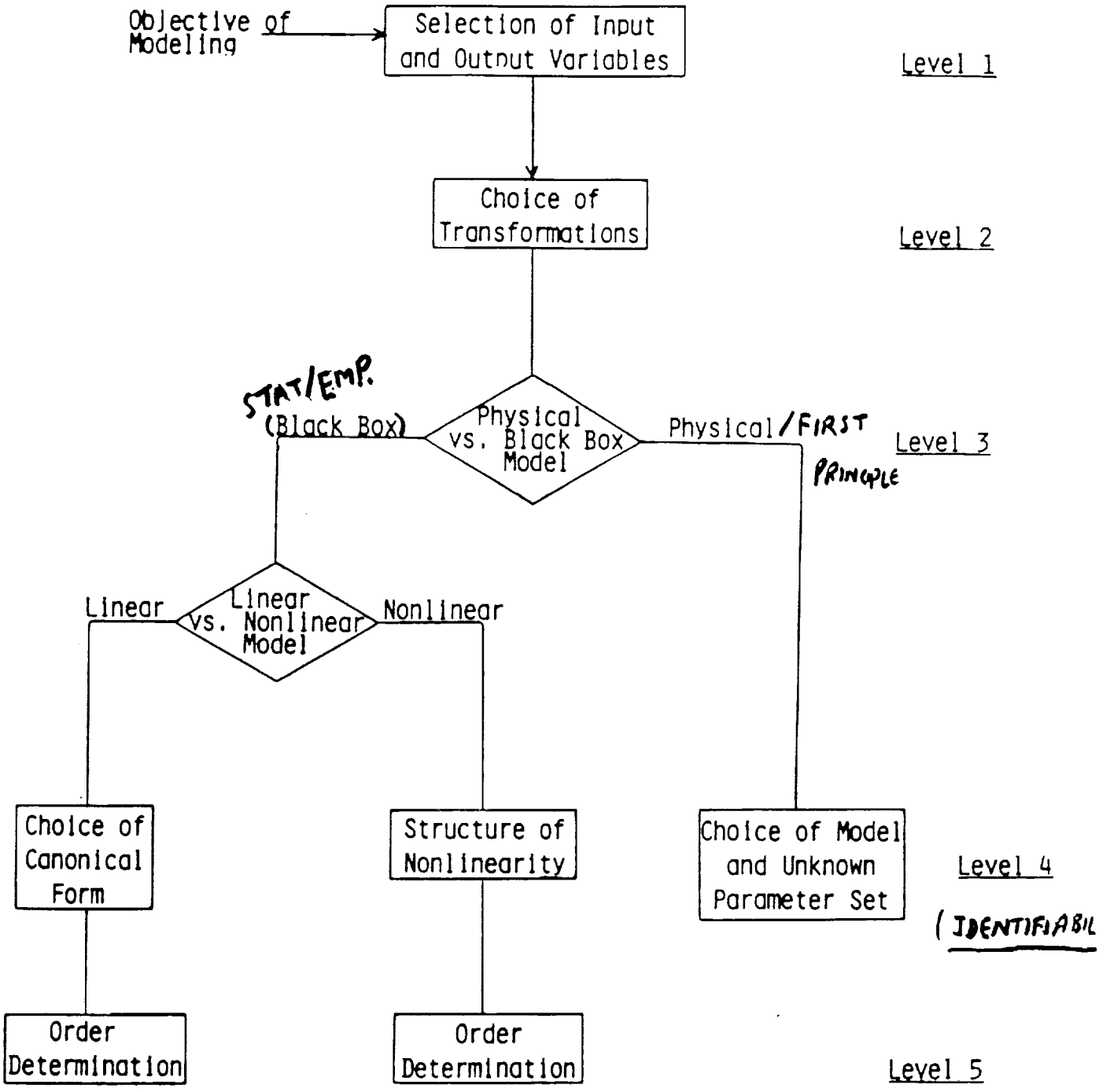

Hierarchical Levels in Model Structure Determination

2. Bayesian Statistical Decision Theory Framework for System Identification

1. Unknown state of the world denoted by state vector $\{x(t)\}$.

2. A set of models $M_1, M_2, \ldots M_\ell$ with a priori probabilities $p(M_i)$, which describe the evolution of the state $x(t)$.

3. Unknown parameters θ_i associated with Model M_i and prior probibilities $p(\theta_i | M_i)$

4. Vector of observations $\{y(t)\}$ related to the state of the system $\{x(t)\}$, according to probability distributions. $p(\{y(t)\} | \{x(t\}, M_i)$

5. Loss function $\mathcal{L}(M, \hat{M})$ which expresses the loss to the decision maker of choosing model $\hat{M}$ when M is the true model.

Bayesian Solution:

Obtain posterior distributions $p(M_i | \{y(t)\})$ and select M_i which minimizes the expected value of the loss function.

Bayes Rule:

$$p(M_i | \{y(t)\}) = \frac{p(\{y(t)\} | M_i)\ p(M_i)}{p(\{y(t)\})}$$

$$p(\{y(t)\} | M_i\}) = \int_{\otimes} p(\{y(t)\} | M_i, \theta_i)\ p(\theta_i) d\theta_i$$

Likelihood Function:

$$L(M_i, \theta_i) = p(\{y(t)\} | M_i, \theta_i)$$

Maximum Likelihood Estimation

- $\hat{\theta}_{ML}$ maximizes $p(\{y(t)\}|\theta)$ or its logarithm, $LL(\theta) = \log p(\{y(t)\}|\theta)$

- Cramer-Rao Lower Bound:

$$\text{cov}(\hat{\theta}) \geq \left[E \frac{\partial LL(\theta)}{\partial \theta} \left(\frac{\partial LL(\theta)}{\partial \theta} \right)^T \right]^{-1}$$

  The quantity in brackets is the **Fisher Information Matrix** which is very useful for determining Identifiability and for Input Design.

- when $p(\{y(t)\}|\theta)$ is Gaussian and θ effects the conditional mean linearly, $LL(\theta)$ is quadratic in θ and MLE is same as Weighted Least Squares.

- $\hat{\theta}_{ML}$ can be obtained by a sequence of Expectation & Maximization steps (E-M Algorithm), each one of which is simpler than direct maximization of the Likelihood Function.

  E-step: Estimate state given parameters
  E-step: Estimate parameters given state statistics.

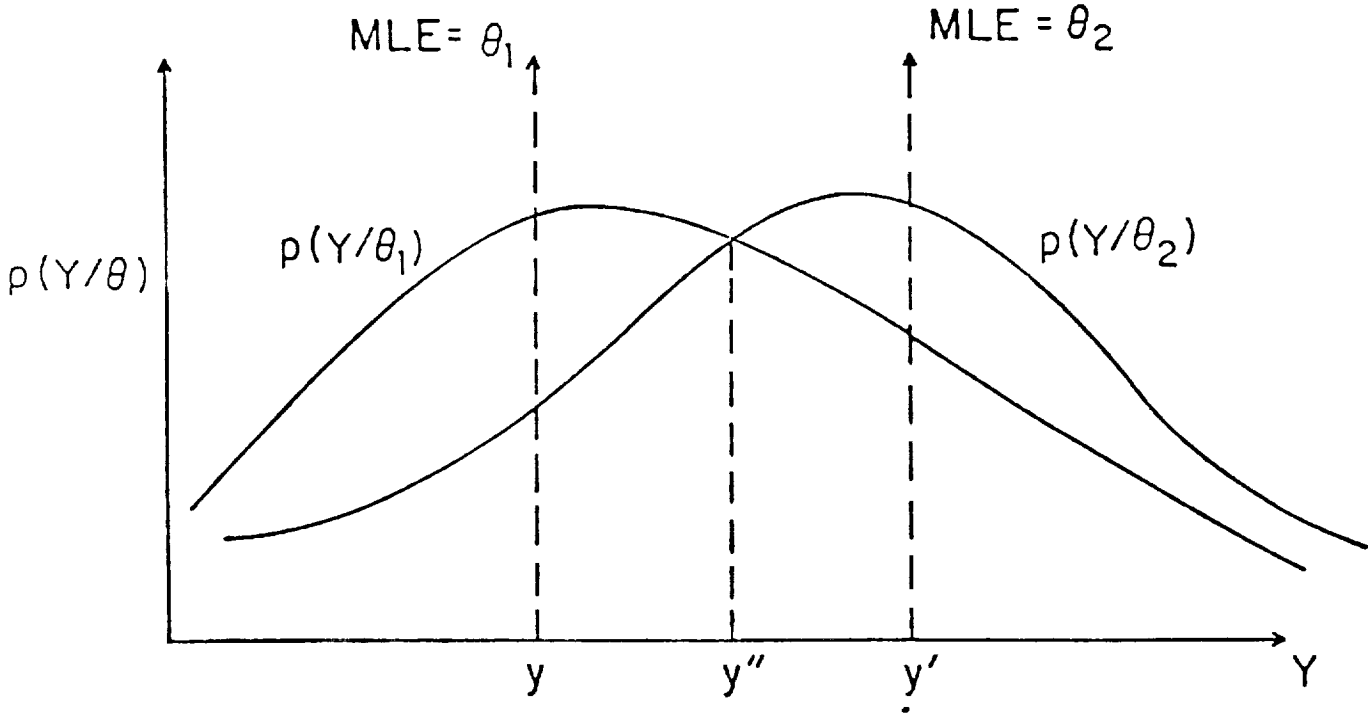

MAXIMUM LIKELIHOOD ESTIMATION

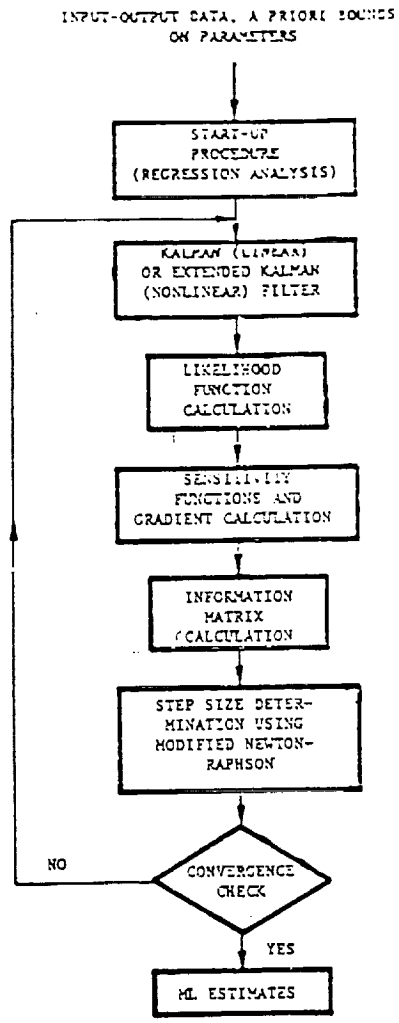

Steps in Maximum Likelihood Estimation

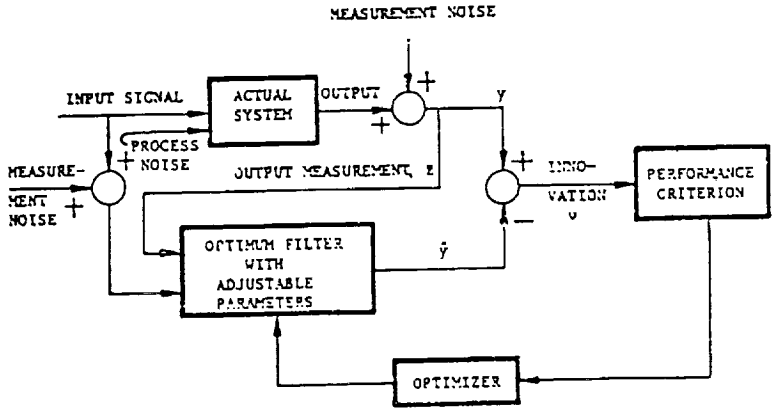

Block Diagram for Maximum Likelihood

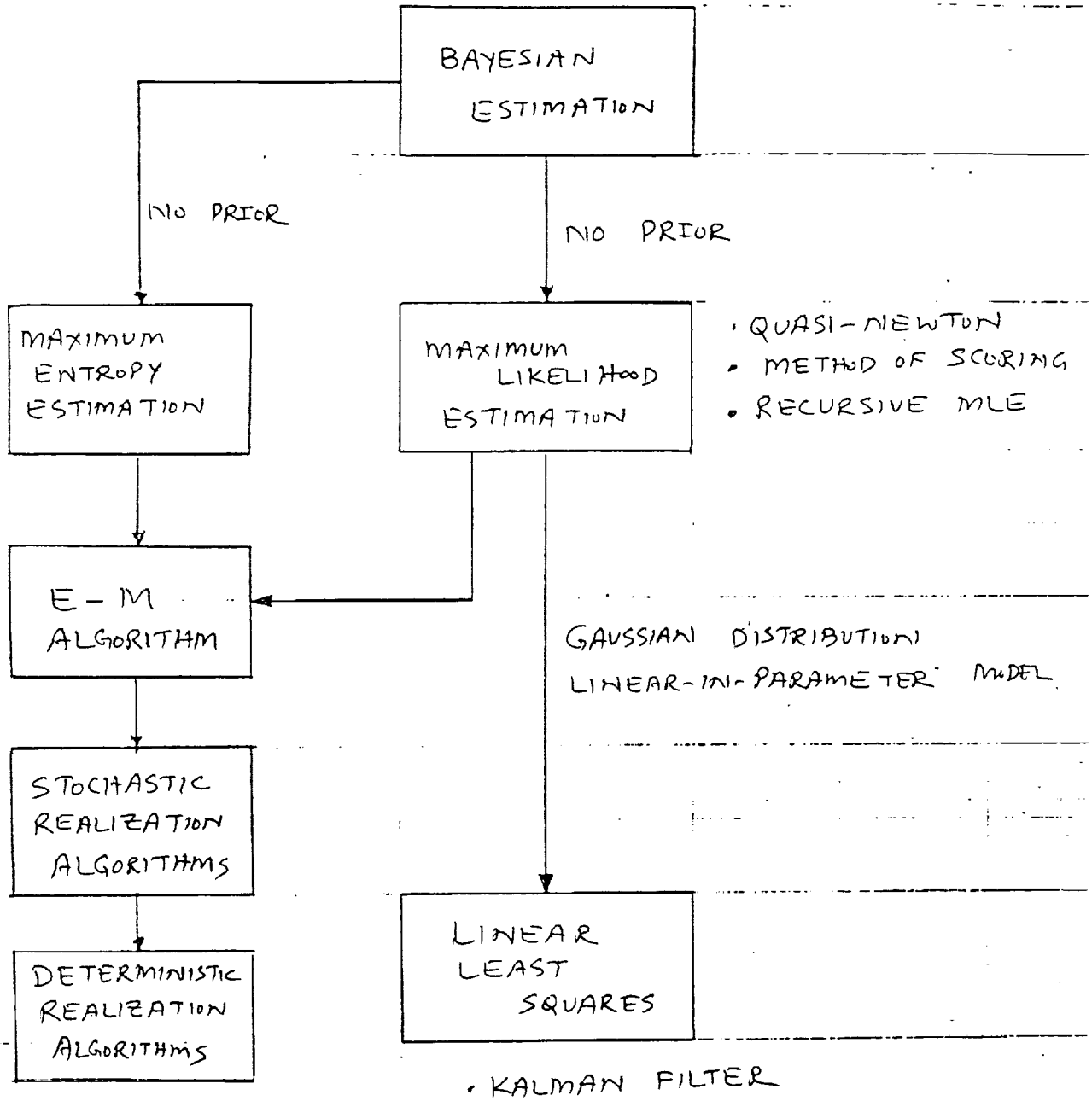

FIG: RELATIONSHIP OF DIFFERENT TECHNIQUES FOR PARAMETER ESTIMATION

Combined Model Structure Determination
and Parameter Estimation for
Linear Systems

$$x_{t+1} = A\,x_t + B\,u_t + K\,e_t$$

$$y_t = Cx_t + D\,u_t + e_t$$

$$t = 1, \ldots N$$

Stochastic Realization:

Given $\{y_t, u_t\}$, identify system order n and matrices A, B, C, D, K and Cov (e_t).

Deterministic Realization:

Given impulse response parameters $CA^{k-1}B$, identify A, B, C and n

Solutions:

- o Deterministic (Ho-Kalman, Balanced Realization, ERA)
- o Stochastic (Akaike, Mehra, Aoki, QMARKOV, CVA, SRA)

Stochastic Realization Algorithm

DEFINE:

$$p_t = \text{column}\left[y_{t-1}\, u_t, y_{t-2}, u_{t-1}, \ldots \right], \qquad \text{Past}$$

$$f_t = \text{column}\left[y_t, y_{t+1}, y_{t+2}, \ldots \right], \qquad \text{Future}$$

Correlation of Past & Future:

$H = E\,(f_t\, p_t{}')$, Hankel Matrix

Singular Value Decomposition:

$H = U \Sigma V'$

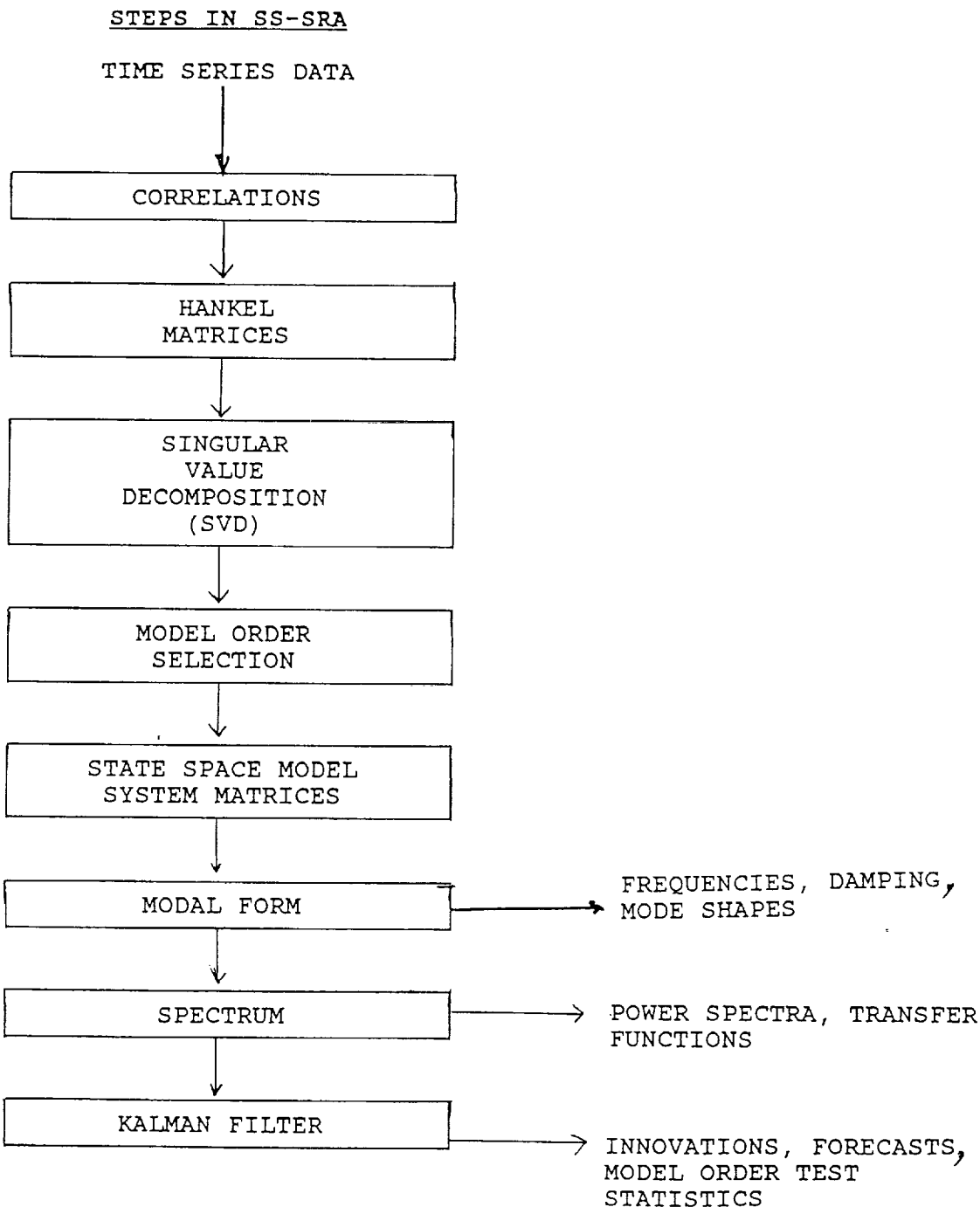
STEPS IN SS-SRA
TIME SERIES DATA
CORRELATIONS
HANKEL MATRICES
SINGULAR VALUE DECOMPOSITION (SVD)
MODEL ORDER SELECTION
STATE SPACE MODEL SYSTEM MATRICES
MODAL FORM
FREQUENCIES, DAMPING, MODE SHAPES
SPECTRUM
POWER SPECTRA, TRANSFER FUNCTIONS
KALMAN FILTER
INNOVATIONS, FORECASTS, MODEL ORDER TEST STATISTICS

Identification Results

1. Membrane Simulation:

   - Data provided by Mark Norris, AFAL
   - Two lightly damped modes at 0.5Hz
   - 5 velocity measurements contaminated with different levels of multiplicative noise (1% to 1,000%).
   - SRA results are satisfactory for 300% noise!

FREE-FREE MEMBRANE SIMULATION

- DATA GENERATED BY MARK NORRIS (AFAL) WITH NOISE RANGING FROM 0% TO 1000% AND 2 DIFFERENT INITIAL CONDITIONS (VEL 1 AND VEL 2).

- TRUE MODEL:

NATURAL FREQUENCIES	DAMPING
0 Hz	0
0.5 Hz	0.01
0.5 Hz	0.01

(REPEATED EIGENVALUE)

MODE SHAPES:

$$\phi_1(X, Y) = 1$$
$$\phi_2(X, Y) = \cos(\pi X)$$
$$\phi_3(X, Y) = \cos(\pi Y)$$

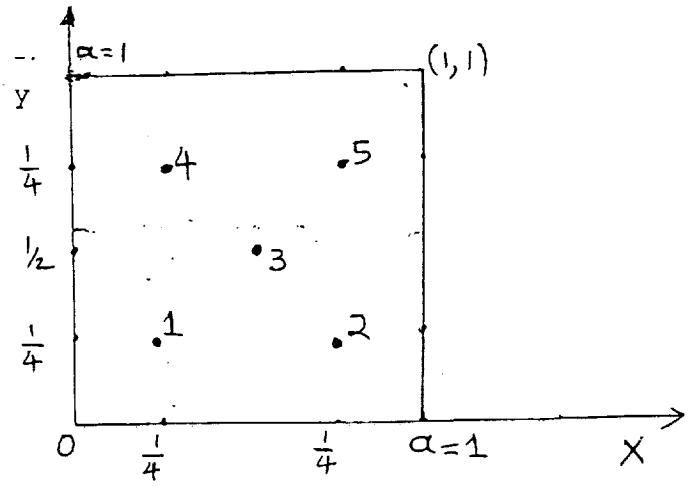

TENSION T=1 N/

DENSITY ρ=1kg/

a=1m

MEMBRANE SENSOR LOCATIONS

IDENTIFICATION RUNS BY SCIENTIFIC SYSTEMS ON

MEMBRANE SIMULATION DATA USING SS-SRA

1. IDENTIFICATION DONE USING BOTH FREE AND FORCED RESPONSE DATA WITH 200 POINTS FOR 5 AND 10 OUTPUTS AT 0.1 HZ.

2. FREE RESPONSE RESULTS ARE BETTER DUE TO POOR INPUT EXCITATION FOR THE FORCED RESPONSE DATA

3. FREE RESPONSE RESULTS WITH VEL2 INITIAL CONDITION (IC) ARE BETTER THAN VEL1 IC RESULTS DUE TO BETTER OUTPUT EXCITATION

4. BEST RESULTS ARE OBTAINED BY AVERAGING THE CORRELATIONS FROM VEL1 AND VEL2 OUTPUTS, PARTICULARLY IN THE IDENTIFICATION OF MODE SHAPES. THESE RESULTS ARE SUPERIOR TO RESULTS USING 10 OUTPUTS AND CONCATENATED DATA (400 POINTS).

5. SATISFACTORY RESULTS ARE OBTAINED BY SS-SRA FOR ALL NOISE CASES INCLUDING 300% NOISE, AS OPPOSED TO ERA RESULTS WHICH DEGRADE GREATLY AFTER 50% NOISE. THE ACCURACY OF THE RESULTS IS SURPRISING CONSIDERING THE NOISE IS MULTIPLICATIVE.

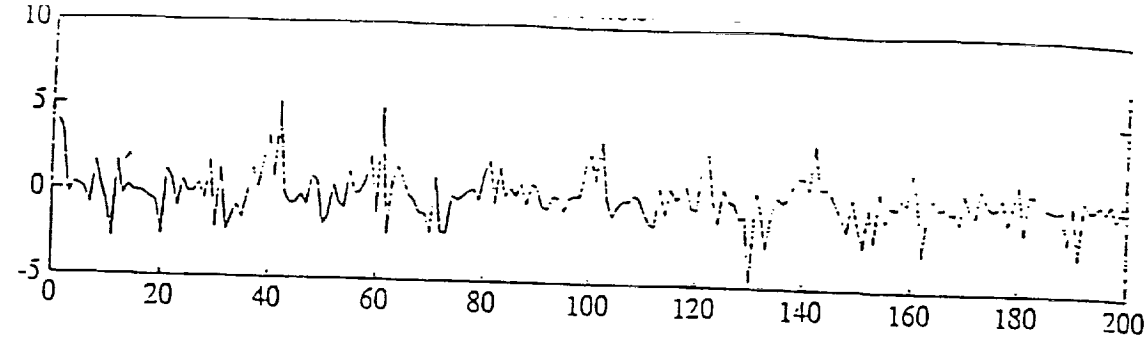

Series 1

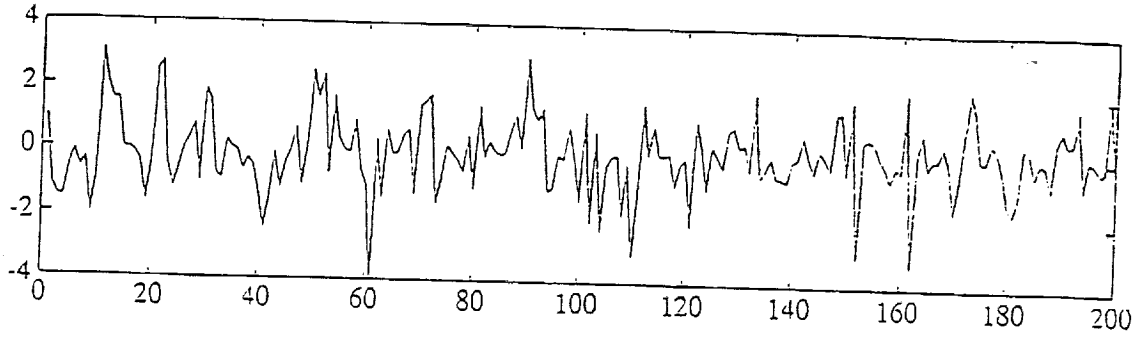

Series 2

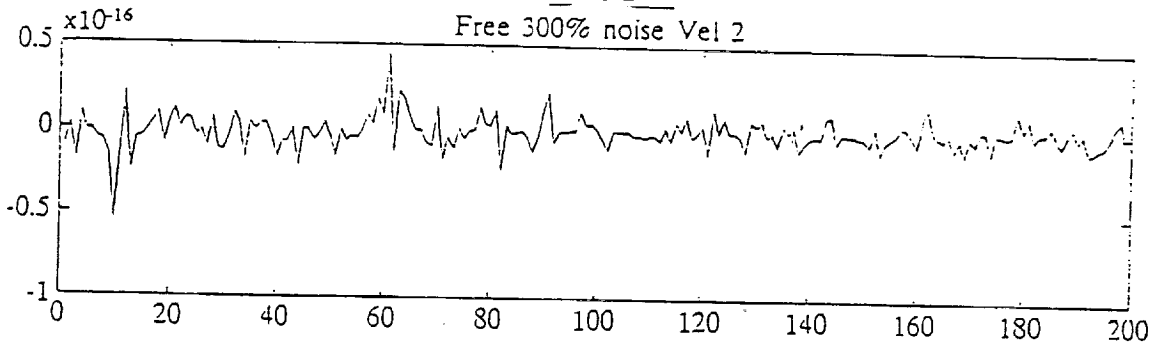

Series 3

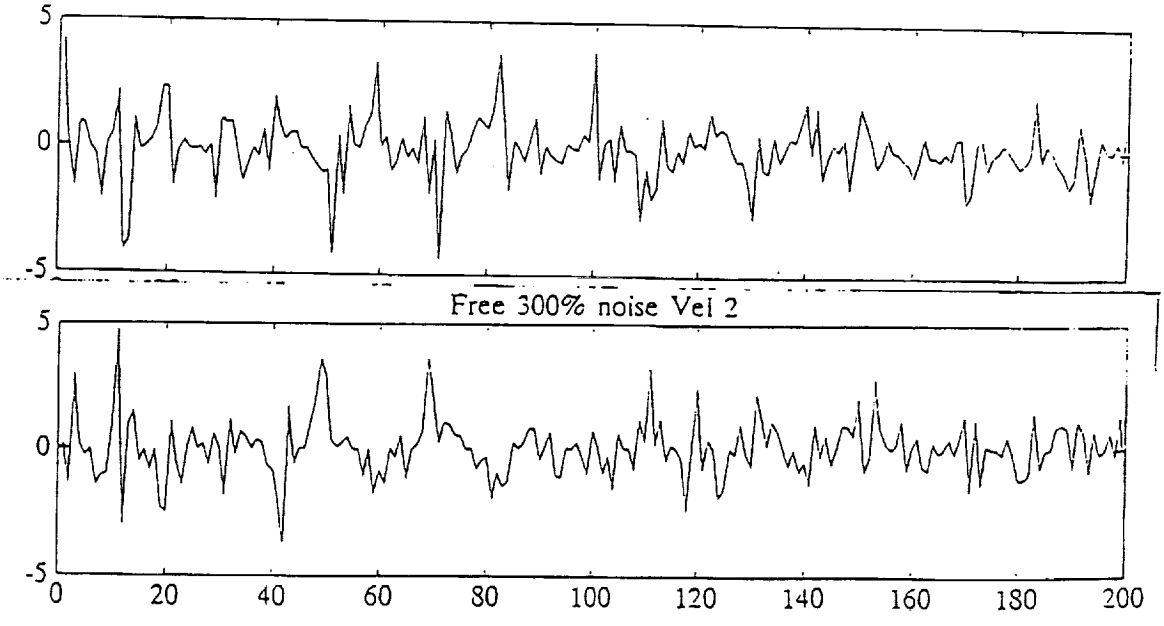

Series 5

862

PRECEDING PAGE BLANK NOT FILMED

ORIGINAL PAGE IS
OF POOR QUALITY

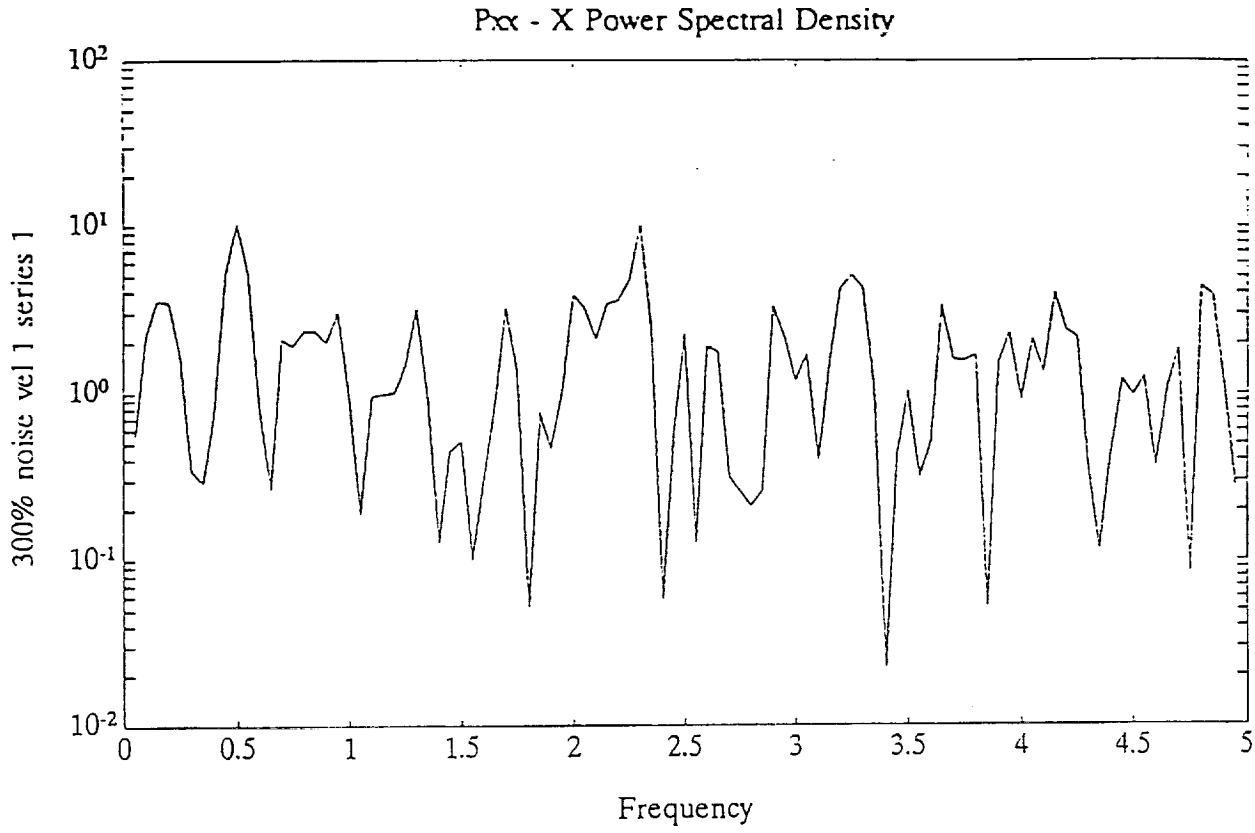
Pxx - X Power Spectral Density
300% noise vel 1 series 1
10^2
10^1
10^0
10^{-1}
10^{-2}
0
0.5
1
1.5
2
2.5
3
3.5
4
4.5
5
Frequency

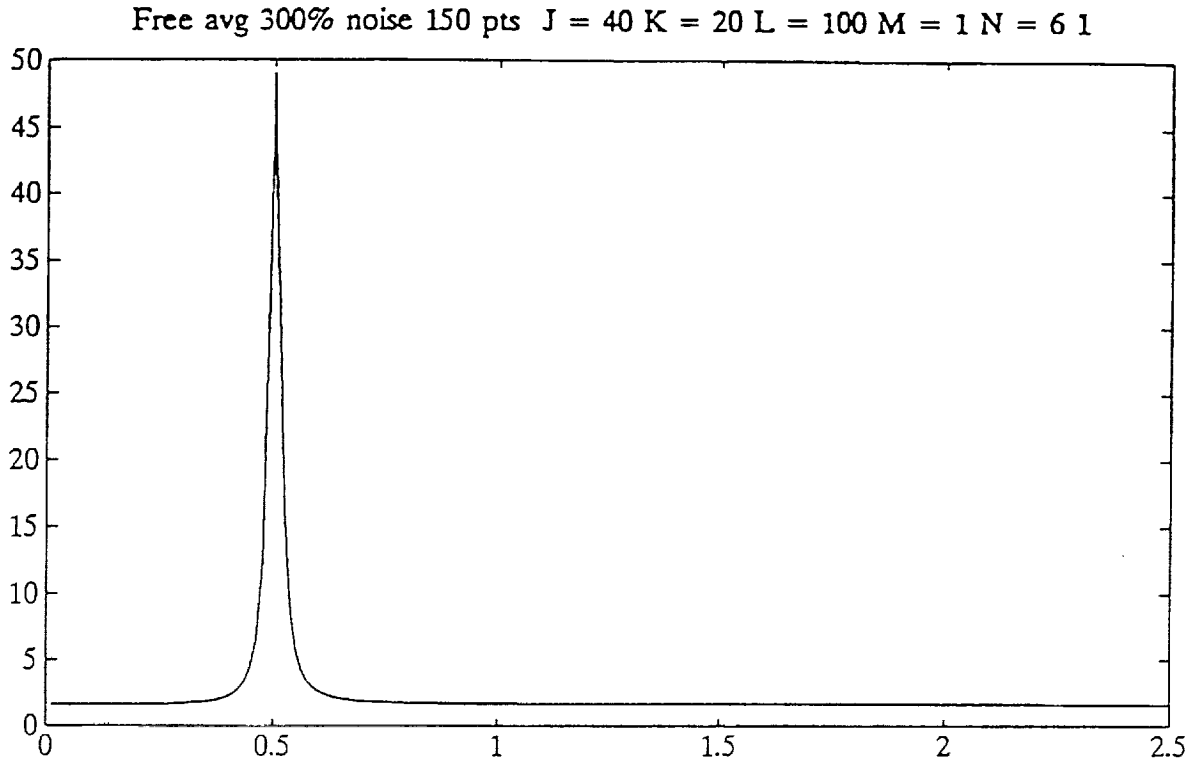

New spectrum calculation

```
ans =

Free avg 300% noise 150 pts  J = 40 K = 20 L = 100 M = 1 N = 6


ans =

Magnitude    Phase     Freq     Damping      Air Force Values


ans =

    0.9808    2.3658    3.7655    0.0082         0         0
    0.9808   -2.3658    3.7655    0.0082    0.5000    0.0100
    0.9920    0.3120    0.4968    0.0256    0.5000    0.0100
    0.9920   -0.3120    0.4968    0.0256         0         0
    0.9899    0.3206    0.5105    0.0318         0         0
    0.9899   -0.3206    0.5105    0.0318         0         0


ans =

        Singular Values


ans =

    1.0000    7.4279
    2.0000    7.4144
    3.0000    2.8451
    4.0000    2.8444
    5.0000    2.2254
    6.0000    2.2090
    7.0000    1.6678
    8.0000    1.6350
    9.0000    1.6062
   10.0000    1.5315
   11.0000    1.5038
   12.0000    1.4938
   13.0000    1.4624
   14.0000    1.4458
   15.0000    1.4098
   16.0000    1.3894


cyy0 =

  Columns 1 through 3

    1.954367688700000e+00   -9.804237999999993e-03    1.222204885150001e-03
   -9.804237999999993e-03    1.533202479950000e+00   -1.735176744450000e-03
    1.222204885150001e-03   -1.735176744450000e-03    4.806341140050000e-04
    1.715561279090000e-01   -1.606591878000000e-01    1.414021973600000e-03
   -4.222937015000000e-01    2.431914045500003e-02    3.260060618799988e-04

  Columns 4 through 5

    1.715561279090000e-01   -4.222937015000000e-01
   -1.606591878000000e-01    2.431914045500003e-02
```

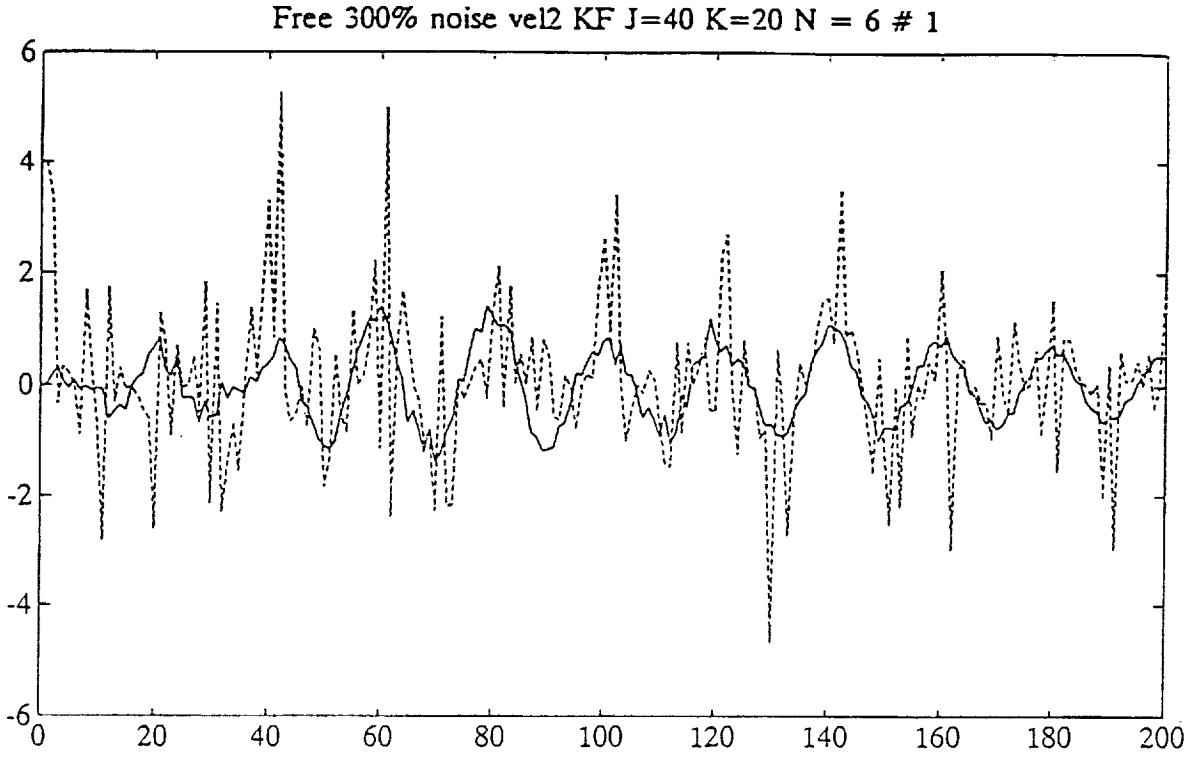
Free 300% noise vel2 KF J=40 K=20 N = 6 # 1
6
4
2
0
-2
-4
-6
0
20
40
60
80
100
120
140
160
180
200

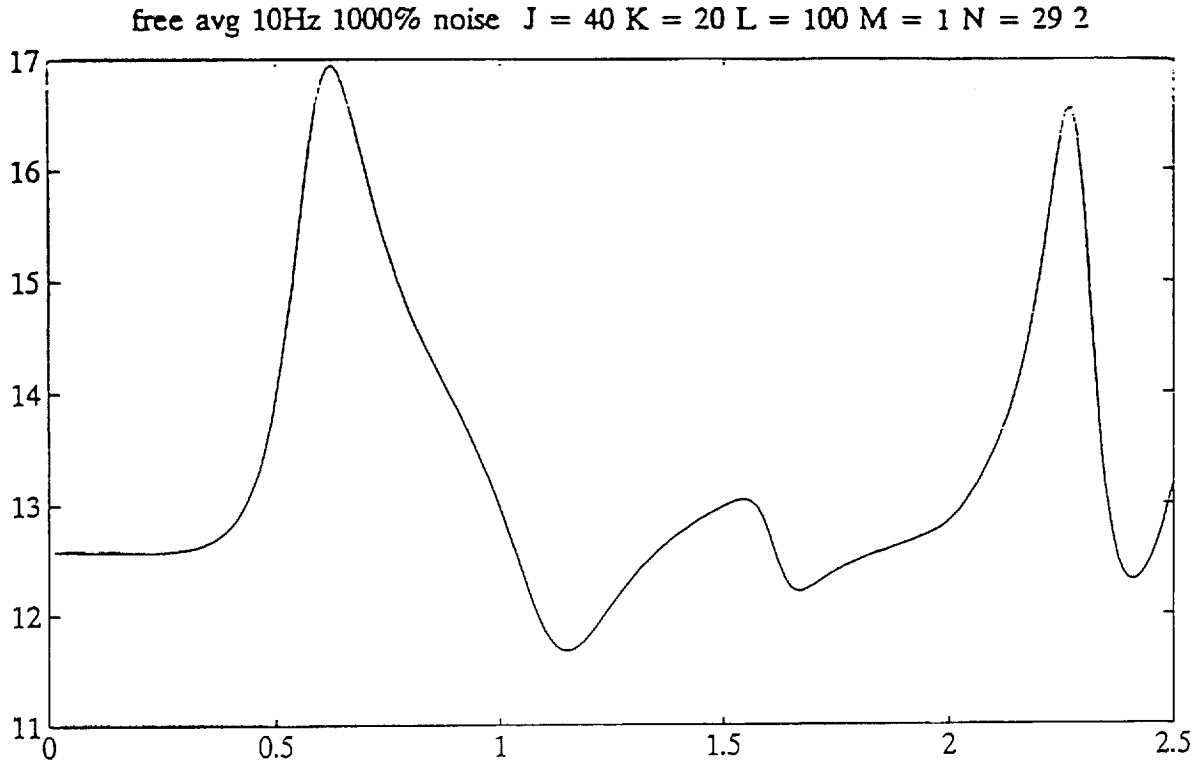

New spectrum calculation

AFAL Grid Data

- Data provided by Mark Norris, AF Astronautics Lab
- Three sets of data at 100hz.

  (i) PMASS Input (2000 pts)
  (ii) X-TORQUE Input (24,000 pts)
  (iii) Y-TORQUE Input (24,000 pts)

- SRA identifies all 11 modes in all cases and proivides good estimates of freq., dampings and mode shapes.

- ERA identifies all 11 modes only for combined X and Y Torque inputs

- Damping estimates from SRA are satisfactory with 2000 pts of P-MASS Input.

- SRA gives satisfactory identification results with single output.

AFAL GRID

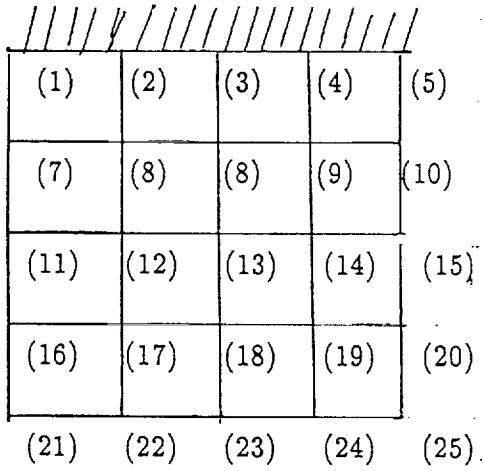

↑

→ X Z - OUT OF PAPER (NORMAL TO GRID)

NODES (1) ➡ (5) HAVE NO DISPLACEMENT AND NO ROTATION.

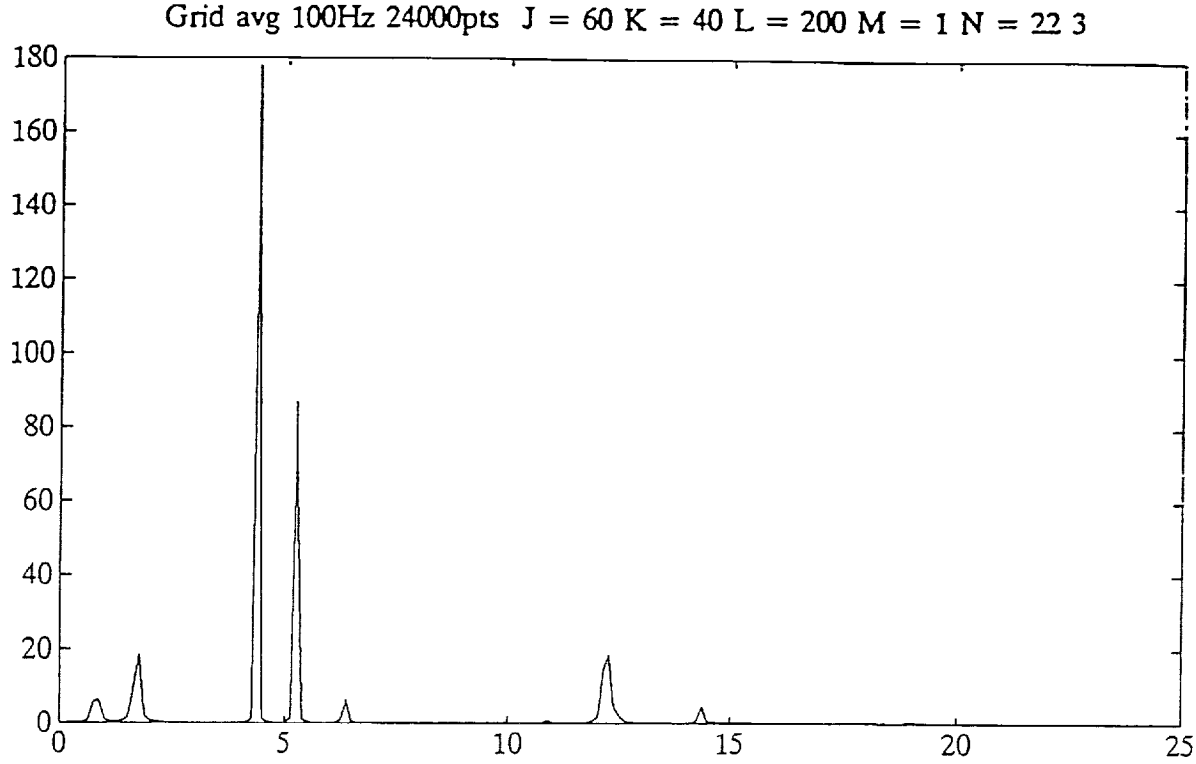
Grid avg 100Hz 24000pts J = 60 K = 40 L = 200 M = 1 N = 22 3
180
160
140
120
100
80
60
40
20
0
0
5
10
15
20
25
New spectrum calculation

ans =

Grid avg 100Hz 24000pts J = 60 K = 40 L = 200 M = 1 N = 22

ans =

Magnitude	Phase	Freq	Damping	Air Force Values	
0.9978	1.1919	18.9699	0.0019	0.8100	0.0023
0.9978	-1.1919	18.9699	0.0019	1.6610	0.0016
0.9987	1.1350	18.0648	0.0011	4.3550	0.0013
0.9987	-1.1350	18.0648	0.0011	5.2120	0.0017
0.9980	0.9013	14.3439	0.0023	6.2910	0.0013
0.9980	-0.9013	14.3439	0.0023	10.7550	0.0011
0.9986	0.7822	12.4486	0.0018	12.1530	0.0016
0.9986	-0.7822	12.4486	0.0018	12.3840	0.0016
0.9986	0.7659	12.1900	0.0018	14.2540	0.0019
0.9986	-0.7659	12.1900	0.0018	17.9550	0.0015
0.9991	0.6813	10.8428	0.0013	18.7720	0.0010
0.9991	-0.6813	10.8428	0.0013	0	0
0.9994	0.1066	1.6967	0.0053	0	0
0.9994	-0.1066	1.6967	0.0053	0	0
0.9993	0.0512	0.8142	0.0132	0	0
0.9993	-0.0512	0.8142	0.0132	0	0
0.9991	0.3986	6.3441	0.0022	0	0
0.9991	-0.3986	6.3441	0.0022	0	0
0.9994	0.3292	5.2401	0.0019	0	0
0.9994	-0.3292	5.2401	0.0019	0	0
0.9994	0.2750	4.3775	0.0021	0	0
0.9994	-0.2750	4.3775	0.0021	0	0

ans =

Singular Values

ans =

1.0000	7.4654
2.0000	6.0473
3.0000	4.9555
4.0000	3.1561
5.0000	2.9364
6.0000	2.8078
7.0000	2.4539
8.0000	2.3086
9.0000	1.0343
10.0000	0.9902
11.0000	0.7768
12.0000	0.7767
13.0000	0.7255
14.0000	0.7051
15.0000	0.1895
16.0000	0.1849

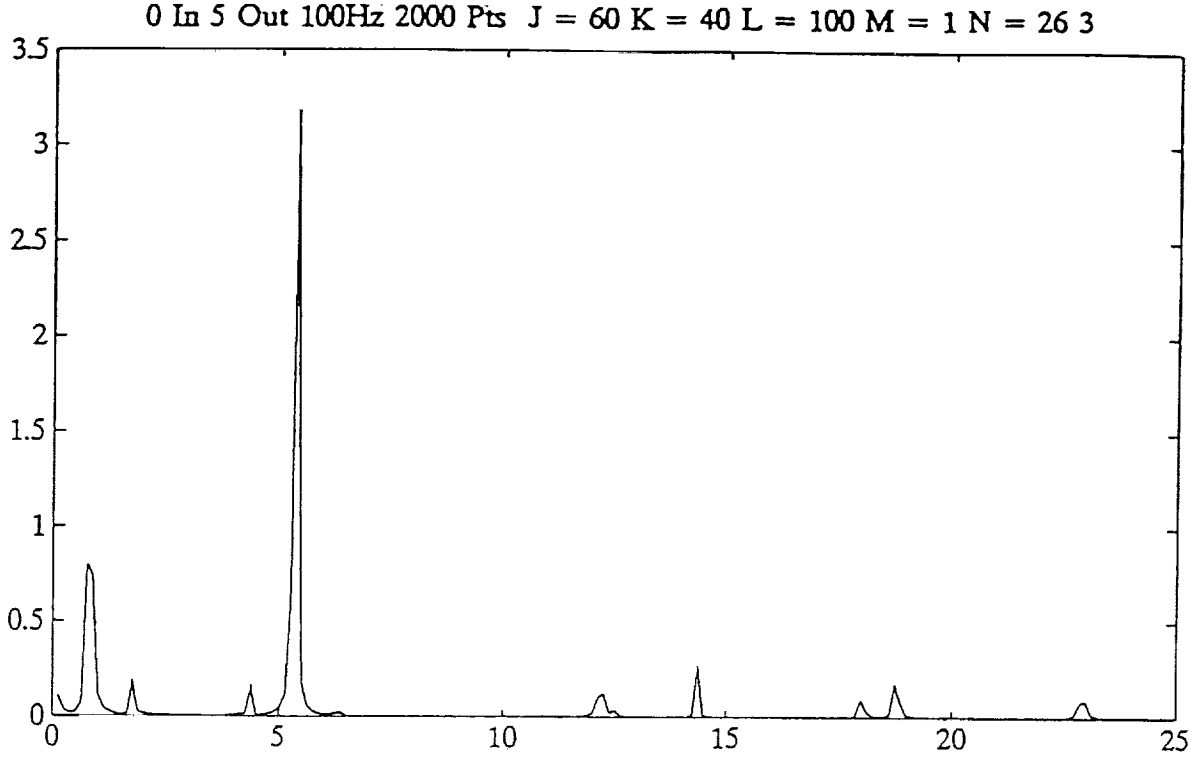
0 In 5 Out 100Hz 2000 Pts J = 60 K = 40 L = 100 M = 1 N = 26 3
3.5
3
2.5
2
1.5
1
0.5
0
0
5
10
15
20
25

ans =

0 In 5 Out 100Hz 2000 Pts J = 40 K = 20 L = 100 M = 1 N = 26

ans =

Magnitude	Phase	Freq	Damping	Air Force Values		Computed Values
0.9853	1.4770	23.5089	0.0100	0.8100	0.0023	.0019
0.9853	-1.4770	23.5089	0.0100	1.6610	0.0016	.0078
0.0163	3.1416	82.3967	0.7948	4.3550	0.0013	.0024
0.9984	1.1810	18.7954	0.0013	5.2120	0.0017	.0023
0.9984	-1.1810	18.7954	0.0013	6.2910	0.0013	.0044
0.9985	1.1336	18.0411	0.0014	10.7550	0.0011	.0022
0.9985	-1.1336	18.0411	0.0014	12.1530	0.0016	.0036
0.9989	0.9029	14.3699	0.0013	12.3840	0.0016	.0017
0.9989	-0.9029	14.3699	0.0013	14.2540	0.0019	.0013
0.9986	0.7821	12.4471	0.0017	17.9550	0.0015	.0014
0.9986	-0.7821	12.4471	0.0017	18.7720	0.0010	.0013
0.9972	0.7675	12.2151	0.0036	0	0	
0.9972	-0.7675	12.2151	0.0036	0	0	
0.9985	0.6840	10.8855	0.0022	0	0	
0.9985	-0.6840	10.8855	0.0022	0	0	
0.9982	0.3981	6.3367	0.0044	0	0	
0.9982	-0.3981	6.3367	0.0044	0	0	
0.9992	0.3355	5.3394	0.0023	0	0	
0.9992	-0.3355	5.3394	0.0023	0	0	
0.9993	0.2752	4.3797	0.0024	0	0	
0.9993	-0.2752	4.3797	0.0024	0	0	
0.9992	0.1078	1.7151	0.0078	0	0	
0.9992	-0.1078	1.7151	0.0078	0	0	
0.9994	0	0.0099	1.0000	0	0	
0.9990	0.0508	0.8082	0.0190	0	0	
0.9990	-0.0508	0.8082	0.0190	0	0	

ans =

Singular Values

ans =

1.0000	2.5860
2.0000	2.3951
3.0000	2.3470
4.0000	2.0355
5.0000	1.9648
6.0000	0.2399
7.0000	0.2144
8.0000	0.2021
9.0000	0.1929
10.0000	0.1778
11.0000	0.0959
12.0000	0.0919

X-29 Flutter Flight Test Data

- Data provided by Mike Kehoe, NASA Dryden (33,000 points, 400hz).
- X-29 Flutter modes are excited by natural turbulence
- SRA identifies all the modes from each data channel.
- Damping and frequency estimates in good agreement with NASA values.
- SRA parameter estimates based on 2,000 points are satisfactory.

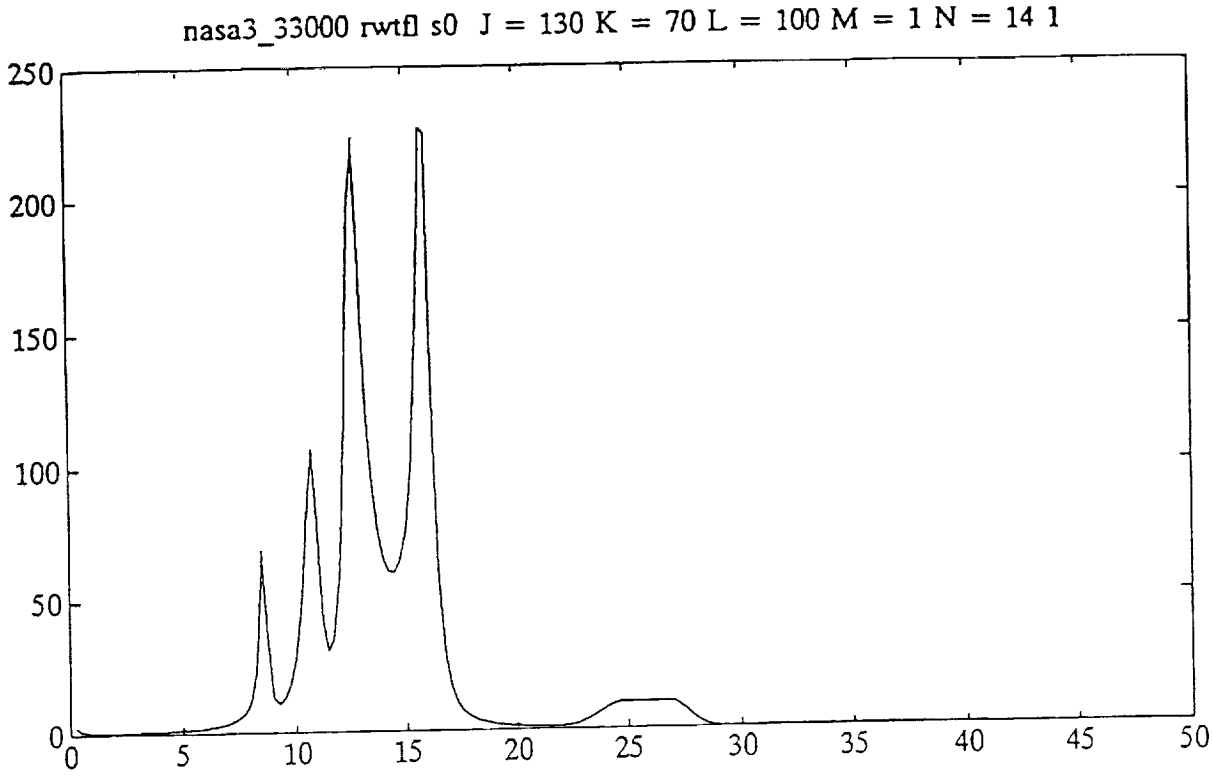

New spectrum calculation

ans =

nasa3_33000 rwtfl s0 J = 130 K = 70 L = 100 M = 1 N = 14

ans =

Magnitude	Phase	Freq	Damping	Nasa Values	
ans =					
0.6474	0	27.6811	1.0000	8.5900	.0182
0.9845	0.4328	27.5681	0.0361	10.6400	.0370
0.9845	-0.4328	27.5681	0.0361	12.7900	.0224
0.9774	0.3760	23.9821	0.0606	15.7200	.0286
0.9774	-0.3760	23.9821	0.0606	0	0
1.0000	0	0.0023	1.0000	0	0
0.9941	0.2502	15.9314	0.0236	0	0
0.9941	-0.2502	15.9314	0.0236	0	0
0.9924	0.1979	12.6095	0.0387	0	0
0.9924	-0.1979	12.6095	0.0387	0	0
0.9973	0.1348	8.5838	0.0197	0	0
0.9973	-0.1348	8.5838	0.0197	0	0
0.9936	0.1694	10.7909	0.0377	0	0
0.9936	-0.1694	10.7909	0.0377	0	0

ans =

Singular Values

ans =

1.0000	60.7314
2.0000	41.1338
3.0000	38.8540
4.0000	23.9111
5.0000	23.5237
6.0000	5.4193
7.0000	5.0483
8.0000	4.6103
9.0000	4.4074
10.0000	3.6840
11.0000	3.4194
12.0000	1.2080
13.0000	1.0580
14.0000	0.6707
15.0000	0.6336
16.0000	0.4258
17.0000	0.3790
18.0000	0.3534
19.0000	0.3174
20.0000	0.1659
21.0000	0.1548
22.0000	0.1426
23.0000	0.1332
24.0000	0.1189

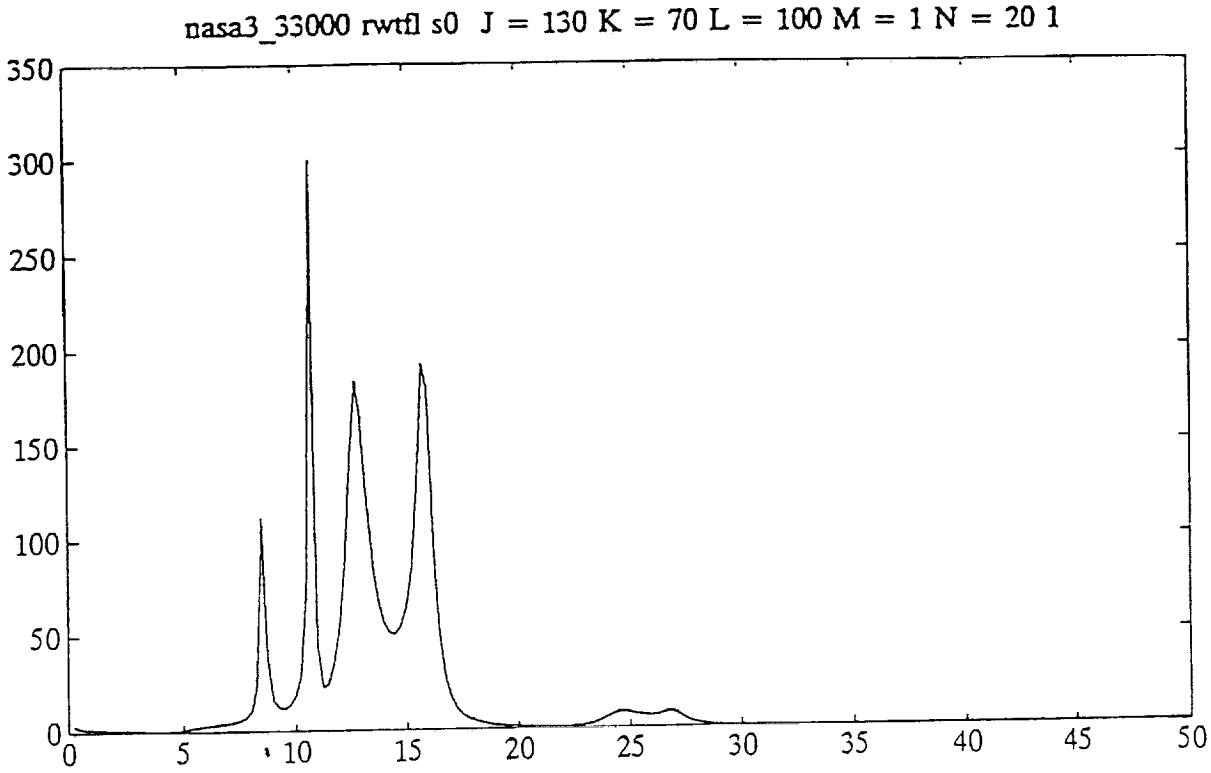

New spectrum calculation

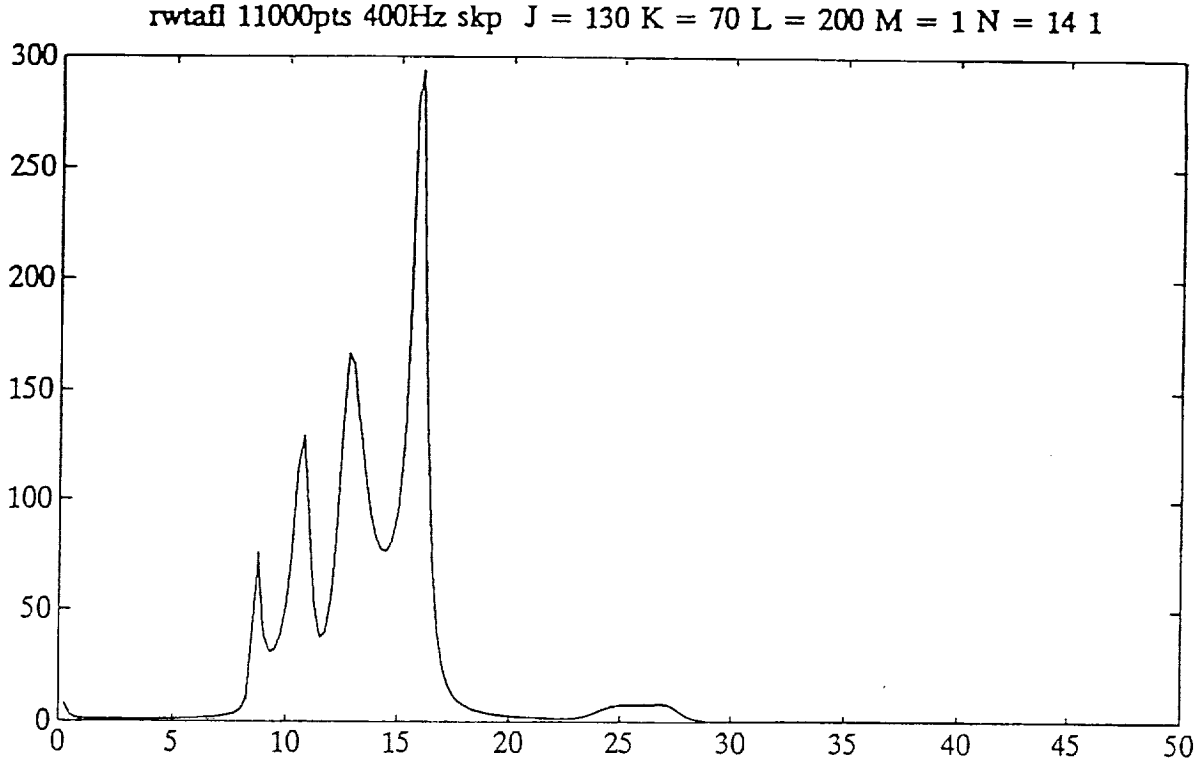

New spectrum calculation

CONCLUSIONS

1. BAYESIAN STATISTICAL DECISION TEHORY PROVIDES A UNIFYING FRAMEWORK FOR SYSTEM IDENTIFICAION TECHNIQUES. FUNDAMENTAL SIMILARITIES ALSO EXIST BETWEEN STRUCTURAL MODE IDENTIFICATION AND EXTRACTION OF SINUSOIDS FROM NOISE. (APPLICATION IN RADAR AND SONAR SIGNAL PROCESSING

2. STOCHASTIC REALIZATION ALGORITHM (SRA) IS HIGHLY ROBUST AGAINST NOISE. IT PROVIDES COMPLETE IDENTIFICATION OF MULTI-INPUT MULTI-OUTPUT SYSTEMS IN A FULLY STOCHASTIC SETTING.

3, SRA OUTPERFORMS ERA UNDER CONDITIONS OF
   - o LOW SIGNAL TO NOISE RATIO
   - o SHORT DATA LENGHTS
   - o POOR INPUT EXCITATION
   - o SINGLE OUTPUT MODELING

4. SRA CAN INDENTIFY SYSTEMS WITHOUT INPUT MEASUREMENTS. NO PRIOR KNOWLEDGE OF SYSTEM MODEL STRUCTURE AND ORDER REQUIRED.

5. SRA STATE SPACE MODELS ARE IN NESTED KALMAN FILTER FORM. LOWER ORDER MODELS ARE OBTAINED FROM HIGHER ORDER MODELS BY SIMPLE DELETION OF ROWS AND COLUMNS. NOISE CONVARIANCES ARE IDENTIFIED ALONG WITH SYSTEM MATRICES.

6. MODEL ORDER DETERMINATION IS DONE EASILY USING BREAKS IN SINGULAR VALUES AND AIC (AKAIKE INFORMATION CRITERION).

7. AS SYSTEM ORDER IN INCREASED, FREQUENCIES WITH LARGE SPECTRAL POWER ARE IDENTIFIED FIRST.

8. SEPARATION OF CLOSELY SPACED FREQUENCIES REQUIRES INCREASE IN THE DIMENSION OF THE HANKEL MATRIX, BUT NOT THE SYSTEM DIMENSION.

9. <u>SURPRISING RESULTS:</u>
   - o SATISFACTORY FREQUENCY AND DAMPING IDENTIFICATION CAN BE DONE FROM SINGLE OUTPUT DATA SERIES.
   - o FREQUENCY AND DAMPING PARAMETERS IDENTIFIED FOR THE 300% NOISE CASE (MEMBRANE SIMULATION). THE NOISE CAN BE MULTIPLICATIVE!
   - o THE IMPROVEMENT IN IDENTIFICATION RESULTS USING INPUT DATA IS MINOR.

10. <u>IMPORTANCE FOR CONTROL DESIGN:</u>

    ADAPTIVE CONTROL IS FEASIBLE SINCE MODES WITH DISCERNIBLE SPECTRAL POWER CAN BE IDENTIFIED USING SRA. SINCE IT IS NOT POSSIBLE TO DESIGN CONTROLLERS, WHICH ARE ROBUST AGAINST ALL POSSIBLE UNCERTAINTIES, ADAPTIVE CONTROL OF STRUCTURAL MODES USING ON-LINE IDENTIFICATION IS A MORE PRACTICAL APPROACH.

Likelihood Estimation For Distributed Parameter Models For The NASA MINI-MAST Truss

Ji Yao, Shen and Jen Kuang, Huang

Old Dominion University, Norfolk, Virginia

Lawrence W.Taylor, Jr.

NASA Langley Research Center, Hampton, Virginia

Likelihood Estimation For Distributed Parameter Models For NASA MINI-MAST Truss

Ji-Yao Shen*, Jen-Kuang Huang†
Old Dominion University, Norfolk, Virginia

Lawrence W. Taylor, Jr.‡
NASA Langley Research Center, Hampton, Virginia

SUMMARY

In this paper, maximum likelihood estimation for distributed parameter models of large flexible structures has been formulated. Distributed parameter models involve far fewer unknown parameters than independent modal characteristics or finite element models. The closed-form solutions for the partial differential equations with corresponding boundary conditions have been derived. The closed-form expressions of the sensitivity functions lead to highly efficient algorithms for analyzing ground or on-orbit test results. For illustration of this approach, experimental data of the NASA Mini-MAST trust have been used. The estimations of modal properties involve its lateral bending modes and torsional modes. The results show that distributed parameter models are promising in the parameter estimation of large flexible structures.

* Ph.D. Candidate, Dept. of Mechanical Engineering and Mechanics
† Associate Professor, Dept. of Mechanical Engineering and Mechanics
‡ Chief Scientist, Guidance and Control Division

INTRODUCTION

Large spacecraft structures, such as, Solar Array Flight Experiment, Mini-MAST (CSI) employ large complex trusses in their constructions. Because of their large size and because of gravitational loads, it is not possible to determine with suitable accuracy their structural dynamic characteristics from ground-based testing of a full-scale prototype. Analysis of on-orbit response data will be necessary. In recent years, numerous variations of system identification methods have been developed. Unfortunately, current approaches to parameter estimation cannot handle the complex models foreseen to be necessary. As the number of modes increases, the accuracy will be decreased and the complexity significantly increases.

Two distinct approaches to the solution of large space structural parameter identification problems have emerged. One is the lumped parameter approach, the other is the distributed parameter approach [1–5]. The obvious fact is that by far the most effort put into the study of the identification problem has been based on the lumped parameter model. With the increase of the number of modes, the number of parameters increases rapidly for the lumped parameter approach. However, for the distributed parameter approach, the total number of parameters needed to be identified almost keeps the same.

Distributed parameter model is based on the partial differential equation (PDE). In this approach, instead of identifying the modal frequency, damping and mode shape deflection of each mode, only the coefficients of the partial differential equation and initial conditions need to be estimated.

This paper intends to create a very simple distributed parameter model, combining the use of maximum likelihood estimation technique (MLE), to identify the modal characteristics of NASA Mini-MAST truss which is treated as a cantilevered beam with two concentrated masses. Wave equation and Bernoulli-Euler beam equation are introduced to describe the torsional and bending behavior of the Mini-MAST truss. Proportional damping will be taken into account simply by adding a damping term in the PDE's, which is proportional to velocity [6].

A series of closed-form solutions of the PDE's will be used to match the measurements of the vibrations. Based on the optimal fitness between the measurement response and the theoretical response in the sense of maximization of likelihood function, the coefficients in the PDE's and the parameters dependent on the initial conditions are estimated. The closed-form expressions of the sensitivity functions are derived, which carry out the innovations of the unknown parameters in the iteration process. The comparison of the results with other methods shows that the proposed approach is promising in the parameter estimation of large flexible structures.

NASA MINI-MAST (CSI) TESTBED

NASA Mini-MAST (see Fig. 1) is a generic space truss built primarily for research in the areas of structural analysis and vibrational control [7]. Mini-MAST is deployed vertically inside a high-bay tower, cantilevered from its base on a rigid foundation. The total height of the truss is 20.16 meters, containing 18 bays (1.12 meters each) in a single-laced configuration with every other bay repeating. The deployable/retractable truss beam has a three-longeron construction forming a triangular cross-section with points inscribed by a circle of diameter 1.4 meters. The beam has three member types: longerons, battens, and diagonals. Longerons are parallel to the beam axis and provide beam stiffness and strength in bending. Battens are in the beam face planes and provide beam stability. Finally, diagonals, also in the beam face planes, provide beam stiffness and strength in torsion and shear. Two instrumentation platforms, holding actuators and sensors for CSI control experiment, have been installed at Bay 10 and Bay 18 (beam tip). These additional components have a significant effect on the structural dynamic characteristics.

In this paper, the real Mini-MAST truss is treated as a cantilevered beam with two concentrated masses at Bay 10 and Bay 18 respectively (Fig. 2). The continuum model is equivalent to the real truss in the sense that both have the same dynamic properties, say, natural frequency, damping ratio and mode shape. To keep the equivalency, the structural parameters of the equivalent must be set up properly. All these parameters will be divided into two types. Some physical quantities of the real structure, such as length, weight, etc., are called unadjustable

parameters which are assumed to be known a priori. Another type of parameters, such as the composed parameters appearing in the PDE's, will be adjusted in the estimation process. This type of parameters is called adjustable parameters, which will be the elements of the unknown parameter vector in the maximum likelihood estimator. The parameters of the equivalent of the Mini-MAST truss is listed in Table 1.

The control inputs of the system are three orthogonal torque wheel actuators located at the top platform (Bay 18). Output pulse responses were obtained by applying single pulse signals at each input channel. Twenty seconds of output pulse response were collected for each input channel. A sampling frequency of 50 Hz is used. Two sets of data [8] are selected for our analysis here. The acquisitions of the selected data are recounted as follows. The first set of data was obtained from the measurement of the rotation rate about the x-axis, which was measured by one rate gyro mounted at the tip platform. The second one was obtained from the measurement of y-direction displacement, which was measured by one displacement sensor installed at Bay 18, mounted parallel to the flat face on the corner joints of the structure and positioned to measure deflections normal to the face. The locations of the actuators and sensors concerned are shown in Fig. 3.

MODELLING

In this paper, the analysis of modal characteristics of NASA Mini-MAST truss involves torsional and bending motions. The damped torsional vibration is described by the wave equation

$$J_b \frac{\partial^2 \theta}{\partial t^2} + c \frac{\partial \theta}{\partial t} - k \frac{\partial^2 \theta}{\partial x^2} = 0 \tag{1}$$

where $\theta(x,t)$ angle of twist, $J_b = \rho I_b$ moment of inertia of the beam, $k = GI_b$ torsional rigidity, and C damping constant of proportionality. Two parameters a and b, which relate the coefficients of the PDE, are defined by

$$a^2 = \frac{k}{J_b}, \quad 2b = \frac{c}{J_b} \tag{2}$$

The lateral bending vibration is described by the Bernoulli-Euler beam equation with proportional damping term

$$m\frac{\partial^2 y}{\partial t^2} + c\frac{\partial y}{\partial t} + k\frac{\partial^4 y}{\partial x^4} = 0 \tag{3}$$

where $y(x,t)$ lateral displacement, $m = \rho A$ mass per length of the beam, and $k = EI$ lateral bending rigidity. Two parameters a and b are also defined by

$$a^2 = \frac{k}{m}, \quad 2b = \frac{c}{m} \tag{4}$$

The solutions of Eqs. (1) and (3) can be written in a generic form (see Appendix)

$$y(x,t) = \sum_i Y_i(x)\, e^{-\xi_i \omega_{n_i} t} \left(A_i \cos \omega_{d_i} t + B_i \sin \omega_{d_i} t\right) \tag{5}$$

where, $y(x,t)$ represents either angle of twist (θ) or lateral displacement y, A_i and B_i the coefficients dependent on the initial conditions, ω_{n_i} and $\omega_{d_i} = \omega_{n_i}\sqrt{1-\xi_i^2}$ the natural frequency and damped natural frequency, respectively, and ξ_i is the damping ratio. All these modal properties are related to the parameters a and b by

$$\omega_{n_i} = a k_i^q, \quad \omega_{d_i} = \sqrt{\left(a k_i^q\right)^2 - b^2}\ , \quad \xi_i = \frac{b}{a k_i^q} \tag{6}$$

where, q represents the order of power, with $q = 1$ for torsion and $q = 2$ for bending. From Eq. (6), the solution Eq. (5) can be expressed in terms of the parameters a and b,

$$y(x,t) = \sum_i Y_i(x)\, e^{-bt} \left[A_i \cos t\sqrt{\left(a k_i^q\right)^2 - b^2} + B_i \sin t\sqrt{\left(a k_i^q\right)^2 - b^2}\right] \tag{7}$$

$Y_i(x)$ in the solutions (5) or (7) are the eigenfunctions given as follows. For torsional equation:

$$Y_i(x) = \begin{cases} \left[\frac{\cot k_i x_{10}}{g(k_i l)} + 1\right] \sin k_i x & 0 \le x \le x_{10} \\ \frac{\cos k_i x}{g(k_i l)} + \sin k_i x & x_{10} \le x \le l \end{cases} \tag{8}$$

where,

$$g(k_i l) = \frac{\sin k_i l + \frac{J_t}{J_b} k_i l \cos k_i l}{\cos k_i l - \frac{J_t}{J_b} k_i l \sin k_i l}$$

For Bernoulli-Euler equation

$$Y_i(x) = \begin{cases} r_i(\mathrm{sh} k_i x - \sin k_i x) + (\mathrm{ch} k_i x - \cos\ k_i x) & \\ & 0 \le x \le x_{10} \\ \alpha_i [h_1(k_i l)\sin k_i x + h_4(k_i l)\cos k_i x + sh k_i x] + & \\ \beta_i [h_3(k_i l)\sin k_i x + h_2(k_i l)\cos k_i x + ch k_i x] & \\ & x_{10} \le x \le l \end{cases} \tag{9}$$

where,

$$h_1(k_i l) = g_1(k_i l) + 2\frac{W_t}{W_b} k_i l \cos k_i l\ sh k_i l; \quad h_2(k_i l) = g_2(k_i l) - 2\frac{W_t}{W_b} k_i l \sin k_i l\ ch k_i l$$

$$h_3(\mathrm{k_i} l) = g_3(k_i l) + 2\frac{W_t}{W_b} k_i l \cos \mathrm{k_i} l\ ch k_i l; \quad h_4(k_i l) = g_4(k_i l) - 2\frac{W_t}{W_b} k_i l \sin k_i l\ sh k_i l$$

and

$$g_1(k_i l) = \cos k_i l\ ch k_i l + \sin k_i l\ sh k_i l, \quad g_2(k_i l) = \cos k_i l\ ch k_i l - \sin k_i l\ sh k_i l$$

$$g_3(k_i l) = \cos k_i l\ sh k_i l + \sin k_i l\ ch k_i l, \quad g_4(k_i l) = \cos k_i l\ sh k_i l - \sin k_i l\ ch k_i l$$

and α_i, β_i and $\mathrm{r_i}$ are the modal participant coefficients.

Finally, the most important quantities are the eigenvalues K_i's of the system. They are the roots of the corresponding characteristic equations given as follows,

For torsional equation:

$$\frac{J_{10}}{2J_b} kl \sin 2kx_{10} + \frac{J_{10}}{J_b} kl\ g(kl) \sin^2 kx_{10} = 1 \tag{10}$$

For Bernoulli-Euler equation:

$$\mathrm{DET} \begin{vmatrix} SHX & CHX & -SHX & -CHX \\ h_1 SNX + h_4 CSX & h_3 SNX + h_2 CSX & SNX & CSX \\ h_1 CSX - h_4 SNX + CHX & h_3 CSX - h_2 SNX + SHX & CSX - CHX & -SNX - SHX \\ 2CHX & 2SHX & -2CHX + \frac{W_{10}}{W_b} kl(SNX - SHX) & -2SHX + \frac{W_{10}}{W_b} kl(CSX - CHX) \end{vmatrix} = 0 \tag{11}$$

where,

$$SNX = \sin kx_{10}, CSX = \cos kx_{10}, SHX = \mathrm{sh}\ kx_{10}, \text{ and } CHX = \mathrm{ch}\ kx_{10}$$

Maximum Likelihood Estimator

Assume that the outcome Y of an experiment depends on an unknown parameter vector θ. We want to estimate the best value of θ according to the observation Y. One of the advanced technique is based on the Maximum Likelihood Estimate (MLE) principle. The essence of the MLE method is to maximize the conditional probability density function, i.e., so-called likelihood function, $P(Y|\theta)$.

Suppose we have the measurement response sequences $y(1)$, $y(2),...,y(m)$. The matrix Y_m consisting of all measured outputs is introduced, $Y_m = [y(1), y(2),..., y(m)]$. If the probability distribution of Y_m has a density $P[Y_m|\theta]$, it then follows from the definition of conditional probability that

$$P[Y_m|\theta] = P[y(1), y(2),..., y(m)|\theta] = \prod_{i=1}^{m} P[y(i)|Y_{i-1}, \theta] \tag{12}$$

If the assumption of Gaussian distribution is taken, the likelihood function has the form of

$$L(\theta) = P[Y_m|\theta] = \prod_{i=1}^{m} \frac{1}{(2\pi)^{mp/2} R^{1/2}} \exp\left\{-\frac{1}{2}[y(i|i-1,\theta) - \bar{y}(i|i-1,\theta)]^T \cdot R^{-1}[y(i|i-1,\theta) - \bar{y}(i|i-1,\theta)]\right\} \tag{13}$$

where $\bar{y}_o(i|i-1,\theta)$ is the norminal response calculated by using θ_o. If the constants are ignored, we have the log-likelihood function

$$\begin{aligned} J(\theta) &= -\ln L(\theta) \\ &= \frac{1}{2}\sum_{i=1}^{m}\left\{[y(i|i-1,\theta) - \bar{y}(i|i-1,\theta)]^T R^{-1}[y(i|i-1,\theta) - \bar{y}(i|i-1,\theta)] + \ln R\right\} \end{aligned} \tag{14}$$

Linearizing $\bar{y}(i|i-1,\theta)$ with respect to the unknown parameter vector θ, we have

$$\bar{y}(i|i-1,\theta) = \bar{y}_o(i|i-1,\theta) + (\nabla_\theta y_i)(\theta - \theta_o) \tag{15}$$

where $\nabla_\theta y_i$ gradient of y with respect to θ, and θ_o is norminal θ vector. Substituting Eq. (15) into Eq. (14) for $J(\theta)$ and setting $\frac{\partial J}{\partial \theta}|_{\theta=\hat{\theta}} = 0$, we may obtain.

$$\hat{\theta} = \theta_o + \left[\sum_{i=1}^{m} (\nabla_\theta y_i)^T R^{-1} (\nabla_\theta y_i)\right]^{-1} \left[\sum_{i=1}^{m} (\nabla_\theta y_i)^T R^{-1} (y_i - \bar{y}_{io})\right] \tag{16}$$

In this paper, the unknown parameter vector will be

$$\theta = [a, b, A_1, A_2, ..., A_n, B_1, B_2, ..., B_n]^T$$

The relationship between the modal properties and the unknowns is given in Eq. (6). Thus we can obtain the modal properties through the solution of the PDE as long as these unknown parameters are determined. The gradients of $y(x,t)$ with respect to the unknowns in Eq. (16) can be derived from Eq. (7) simply by taking derivatives.

$$\frac{\partial y}{\partial a}(x,t) = \sum_i Y_i(x)\, e^{-bt} \frac{k_i^{2q} at}{\sqrt{(ak_i^q)^2 - b^2}} \left[-A_i \sin t\sqrt{(ak_i^q)^2 - b^2} \;\; + B_i \cos t\sqrt{(ak_i^q)^2 - b^2}\right] \tag{17}$$

$$\frac{\partial y}{\partial b}(x,t) = \sum_i Y_i(x)\, te^{-bt} \left\{-A_i \cos t\sqrt{(ak_i^q)^2 - b^2} \;\; - B_i \sin t\sqrt{(ak_i^q)^2 - b^2} \right.$$
$$\left. + \frac{b}{\sqrt{(ak_i^q)^2 - b^2}} \left[A_i \sin t\sqrt{(ak_i^q)^2 - b^2} \;\; - B_i \cos t\sqrt{(ak_i^q)^2 - b^2}\right]\right\} \tag{18}$$

$$\frac{\partial y}{\partial A_i}(x,t) = Y_i(x)\, e^{-bt} \cos t\sqrt{(ak_i^q)^2 - b^2} \tag{19}$$

$$\frac{\partial y}{\partial B_i}(x,t) = Y_i(x)\, e^{-bt} \sin t\sqrt{(ak_i^q)^2 - b^2} \tag{20}$$

Analysis of Modal Properties

As mentioned before, the procedure by using distributed parameter approach to analyze the modal properties is quite different from that of the lumped parameter approach. First, based on the unadjustable structural parameters, the eigenvalues k_i and the eigenfunctions $Y_i(x)$ (mode shapes) of the system can be determined through the solutions of the corresponding characteristic equations before the estimation iteration starts. Second, only the coefficients of the PDE's and the parameters relevant to the initial conditions need to be estimated rather than the modal frequency, damping and mode shape deflection of each mode. These two characteristics greatly decrease the number of unknown parameters and speed up the iterative process.

Solution of the PDE is in the form of infinite series mathematically, so no modal truncation problem is involved theoretically. However the contributions to the response are always so small for the higher frequency modes that only the first several modes (five in this paper) are used in the analysis.

It is noted that the modal coupling must be considered. Because of the eccentric properties of both the tip-mass and the tip-actuating pulses, the lateral bending vibration will be excited while torsional vibration exists and vice versa. However, the experimental data show that bending modes are hardly recognized in the torsional measurement, and the first torsional mode appears clearly in the bending measurement. So the first torsional mode is included in the analysis of the bending vibration.

From the experiment data it is hard to get any a priori information about the initial conditions of the response, that is, the initial values of A_i and B_i for iteration. Fortunately the initial values of A_i and B_i do not affect the convergency significantly, so they are chosen arbitrarily. However, the initial values of parameters a and b are very important to the convergency. From the results of finite element analysis, we can determine the initial values of equivalent stiffness first, then proceed to reckon the initial values of the parameters a and b.

Iterative accuracy is controlled by the innovation residual of the unknown parameter vector θ, which is defined by

$$e_\theta = \left\{ \frac{1}{P-1} \sum_{i=1}^{p} \left[\theta_n (i) - \theta_{n-1} (i) \right]^2 \right\}^{1/2}$$

where, p the number of the unknowns, $\theta(i)$ the ith element of the unknown parameter vector θ, and n is the number of successive iteration. In the algorithm, $e_\theta < 10^{-7}$ is referred to as the criterion which controls the iteration.

Table 2 shows the comparison of the estimated frequencies obtained from Finite Element Analysis (FEA), Eigensystem Realization Algorithm (ERA) [9] and Distributed Parameter Algorithm (DPA). Most modes are comparable to each other. The fifth bending mode from DPA is extremely higher than that of the other approaches. This is due to inadequacy of the Bernoulli-Euler beam model used. Because the rotary inertia and shear deformation of the beam are neglected, the Bernoulli-Euler beam model produces much higher frequencies in the high frequency range. In order to improve the accuracy for high frequency, Timoshenko beam model is proposed for further investigation.

Figure 4 shows that the reconstructed responses obtained from the estimated parameters and the measured responses have a reasonably good fitness.

CONCLUDING REMARKS

This paper proposes a distributed parameter model for the analysis of the modal characteristics of NASA Mini-MAST truss. Wave equation and Bernoulli-Euler equation have been used to describe the torsional and bending vibrations respectively. Closed-form solutions of the PDE's are derived. By using the Maximum Likelihood Estimation method to provide the optimal match between the experimental data and estimated responses, the coefficients in the PDE's and the parameters dependent on the initial conditions are estimated and the modal properties can be further determined. The results are comparable to those from other approaches. The estimates of bending modes in the higher frequency range is expected to be improved by using

Timoshenko beam model. Because the number of unknown parameters is greatly reduced in the distributed parameter model and the maximum likelihood estimation is feasible based on the derived closed form solutions of the PDE's, the proposed approach is particularly attractive for its less computational burden for the large flexible structures.

REFERENCES

1. J. Y. SHEN, L. W. TAYLOR, JR., and J. K. HUANG, 1990, "An algorithm for maximum likelihood estimation for distributed parameter models of large beam-like structures," 2nd USAF/NASA Workshop On System Identification and Health Monitoring of Precision Space Structures.
2. L. W. TAYLOR, JR., 1989, "Nonlinear and distributed parameter models of the Mini-MAST Truss," 3rd NASA/DoD Controls-Structures Interaction Technology Conference.
3. C. T. SUN and J. N. JUANG, 1986, "Modeling global structural damping in trusses using simple continuum models," *AIAA Journal* 24, No. 1.
4. A. K. NOOR, M. S. ANDERSON and W. H. GREENE, 1978, "Continuum models for beam- and plate-like lattice structures" AIAA/ASME 19th Structures, Structural Dynamics, and Materials Conference.
5. L. W. TAYLOR, JR., 1990, "PDEMOD — computer software for distributed parameter Estimation for flexible spacecraft applied to NASA Mini-MAST Truss experiment," 2nd USAF/NASA Workshop On System Identification and Health Monitoring of Precision Space Structures.
6. H. T. BANKS and D. J. INMAN, 1989, "On damping mechanisms in beams," NASA CR 181904.
7. L. R. ADAMS, 1987, "Design, development and fabrication of a deployable/retractable truss beam model for large space structures application," NASA CR 178287, Astro Aerospace Corporation.
8. K. LIU and R. SKELTON, 1990, "The Q-markov cover and its application to flexible structure identification," School of Aeronautics And Astronautics, Purdue University.
9. R. S. PAPPA, A. SCHENK and C. NOLL, 1990, "ERA modal identification experiences with mini-MAST," 2nd USAF/NASA Workshop on System Identification and Health Monitoring of Precision Space Structures.
10. L. LJUNG, 1987, "System identification: theory for the user," Prentice-Hall.
11. S. TIMOSHENKO, D. M. YOUNG and W. WEAVER, JR., 1974, "Vibration problems in engineering," the 4th Ed. John Wiley & Sons, Inc.
12. W. T. THOMSON, 1972, "Theory of vibration with application," Prentice-Hall, Inc.

FIGURE LEGEND

Fig. 1 Sketch of NASA Mini-MAST Truss

Fig. 2 Equivalent Cantilevered Beam

Fig. 3 Mini-MAST Sensor and Actuator Locations

Fig. 4 Comparison of Reconstructed and Measured Responses

Table 1 Structural Parameters of Equivalent Continuum of NASA Mini-MAST Truss

A. Unadjustable Parameters

Length of the Beam L = 66.24 ft.

X-Coordinate of Bay 10 x_{10} = 36.80 ft.

Radius of Gyration of the Section r = 1.6237 ft.

Mass per Length ρA = 0.1076 slug/ft.

Ratios of Weights:

Bay 10-body/Beam: $\frac{W_{10}}{W_b} = 0.4760$

Tip-body/Beam: $\frac{W_t}{W_b} = 1.4547$

Ratios of Moments of Inertia:

Bay 10-body/Beam: $\frac{J_{10}}{J_b} = 0.6206$

Tip-body/Beam: $\frac{J_t}{J_b} = 0.6206$

B. Adjustable Parameters: Initial Values for Iteration

Longitudinal Stiffness EA = 10,530,000 Lb

Bending Rigidity EI = 27,760,000 Lb.ft.^{2}

Torsional Rigidity GI_p = 1,970,000 Lb.ft.^{2}

Table 2 Comparison of Estimated Frequencies (Hz)

A. Bending Modes

No.	F.E.A.	E.R.A.	D.P.A.
1	0.80	0.86	0.768
2	6.16	6.18	6.637
3	32.06	32.39	29.773
4	44.86	43.23	50.923
5	70.18	67.27	102.973

B. Torsional Modes

No.	F.E.A.	E.R.A.	D.P.A.
1	4.37	4.19	4.527
2	21.57	22.89	21.671
3	39.01	38.06	42.521
4	54.27	51.55	56.509
5	72.87	67.27	70.559

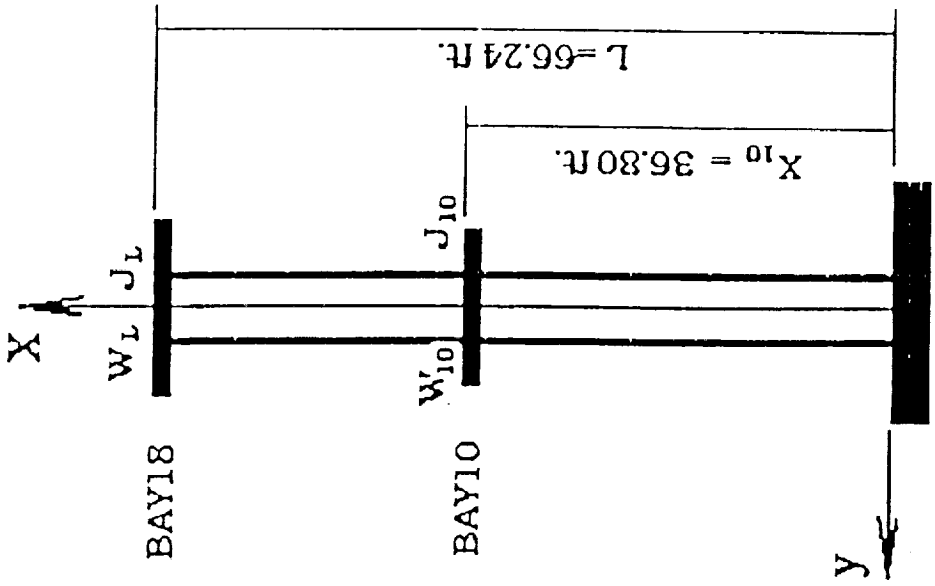

Fig. 2 Equivalent Cantilevered Beam

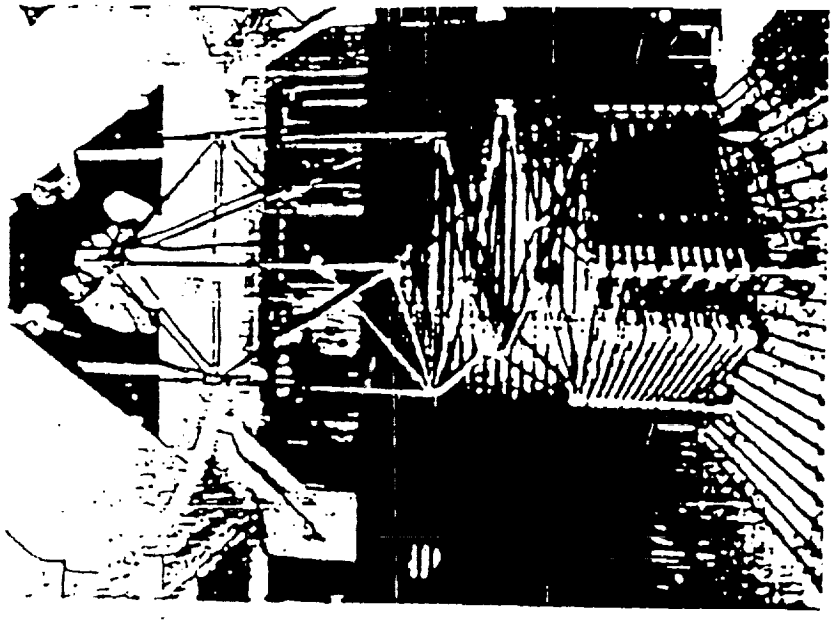

Fig. 1 Sketch of NASA Mini-MAST Truss

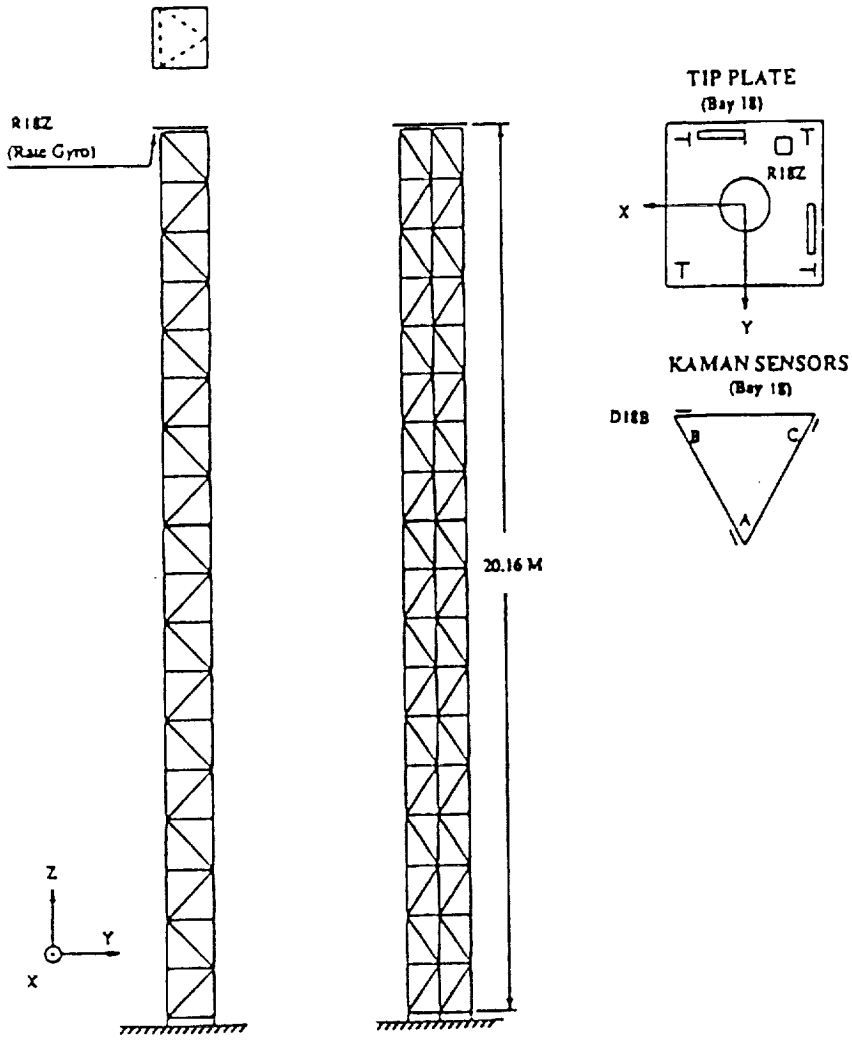

Output No.	Notation	Sensor	Location
y_7	R18Z	Rate Gyro	Bay 18 z axis
y_9	D18B	Displacement Sensor	Bay 18 Corner B

Fig. 3 Mini-MAST Sensor and Actuator Locations

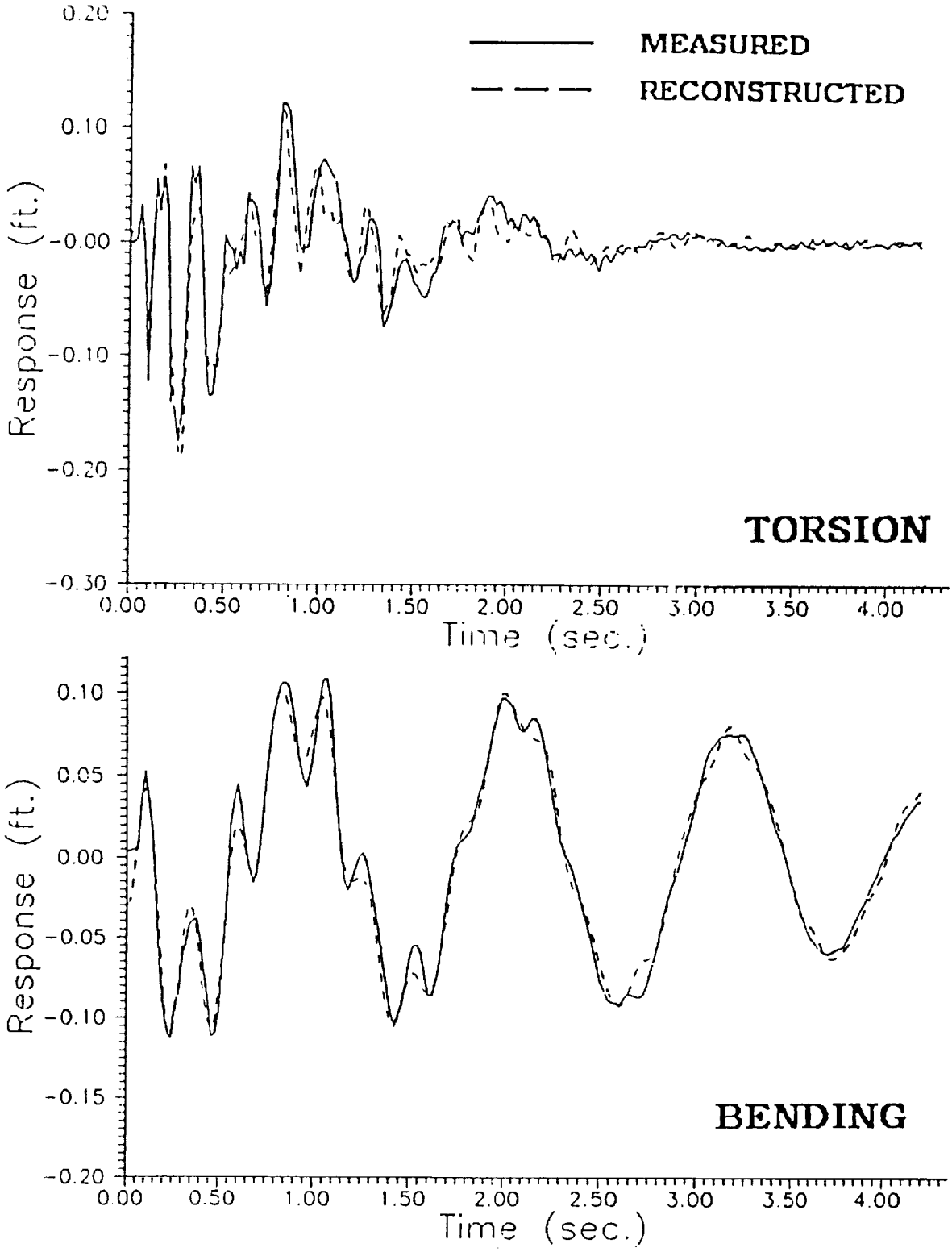

Fig. 4 Comparison of Reconstructed and Measured Responses

APPENDIX A

Solution to the Bernoulli-Euler Beam Equation

In using distributed parameter approach to identify the structural systems, one of the most important procedures is to solve the partial differential equation.

Here, only solution to the Bernoulli-Euler beam equation will be provided. Solution to the torsional vibration equation can be derived by following similar procedures.

The Bernoulli-Euler beam equation describing lateral bending is

$$\frac{\partial^4 y}{\partial x^4} + \frac{1}{a^2}\frac{\partial^2 y}{\partial t^2} = 0 \tag{A.1}$$

where, $a^2 = \frac{EI}{\rho A}$. The general solution to Eq. (A.1) may be expressed as

$$y(x,t) = \sum_i Y_i(x)\left[A_i \cos\omega_i t + B_i \sin\omega_i t\right] \tag{A.2}$$

where, $Y_i(x)$ are the eigenfunctions which are of the form

$$Y_i(x) = C_1 \sin k_i x + C_2 \cos k_i x + C_3 sh\ k_i x + C_4 ch\ k_i x \tag{A.3}$$

Now we derive the specific form of the solution for the equivalent Mini-MAST truss — cantilevered beam with two lumped masses. The procedure consists of three steps as follows.

Step 1 For the right segment, i.e. $x = x_{10} \sim l$.

The PDE for the lateral vibration of the right segment is

$$\frac{\partial^4 y_R}{\partial x^4} + \frac{1}{a^2}\frac{\partial^2 y_R}{\partial t^2} = 0 \tag{A.4}$$

The boundary conditions for the free end ($x = l$) are:

$$\begin{cases} \frac{\partial^2 y_R}{\partial x^2}(l,t) = 0 \\ EI\frac{\partial^3 y_R}{\partial x^3}(l,t) = \frac{W_t}{g}\frac{\partial^2 y_R}{\partial t^2}(l,t) \end{cases} \tag{A.5}$$

After the separation of variables

$$y_R(x,t) = Y_R(x)T(t)$$

899

we have a Y_R – ODE,

$$Y_R''''(x) - k^4 Y_R(x) = 0 \tag{A.6}$$

with B.C.'s

$$\begin{cases} Y_R''(l) = 0 \\ Y_R'''(l) = -\frac{W_t}{W_b} l k^4 Y_R(l) \end{cases} \tag{A.7}$$

The general solution to Eq. (A.6) and the corresponding derivatives are as follows,

$$\begin{cases} Y_R(x) = C_1 \sin kx + C_2 \cos kx + C_3 shkx + C_4 chkx \\ Y_R'(x) = K(C_1 \cos kx - C_2 \sin kx + C_3 chkx + C_4 shkx) \\ Y_R''(x) = K^2(-C_1 \sin kx - C_2 \cos kx + C_3 shkx + C_4 chkx) \\ Y_R'''(x) = K^3(-C_1 \cos kx + C_2 \sin kx + C_3 chkx + C_4 shkx) \end{cases} \tag{A.8}$$

By using the B.C., we have

$$\begin{cases} C_1 = C_3\left(g_1(kl) + 2\frac{W_t}{W_b} kl \cos klshkl\right) + C_4\left(g_3(kl) + 2\frac{W_t}{W_b} kl \cos klchkl\right) \\ C_2 = C_3\left(g_4(kl) - 2\frac{W_t}{W_b} kl \sin klshkl\right) + C_4\left(g_2(kl) - 2\frac{W_t}{W_b} kl \sin klchkl\right) \end{cases} \tag{A.9}$$

where,

$$\begin{cases} g_1(kl) = \cos klchkl + \sin klshkl \\ g_2(kl) = \cos klchkl - \sin klshkl \\ g_3(kl) = \cos klshkl + \sin klchkl \\ g_4(kl) = \cos klshkl - \sin klchkl \end{cases} \tag{A.10}$$

Thus, $Y_R(x)$ and its derivatives can be expressed in terms of the coefficients C_3 and C_4.

$$\begin{cases} Y_R(x) = C_3[h_1(kl)\sin kx + h_4(kl)\cos kx + shkx] \\ \qquad + C_4[h_3(kl)\sin kx + h_2(kl)\cos kx + chkx] \\ Y_R'(x) = C_3K[h_1(kl)\cos kx - h_4(kl)\sin kx + chkx] \\ \qquad + C_4K[h_3(kl)\cos kx - h_2(kl)\sin kx + shkx] \\ Y_R''(x) = C_3K^2[-h_1(kl)\sin kx - h_4(kl)\cos kx + shkx] \\ \qquad + C_4K^2[-h_3(kl)\sin kx - h_2(kl)\cos kx + chkx] \\ Y_R'''(x) = C_3K^3[-h_1(kl)\cos kx + h_4(kl)\sin kx + chkx] \\ \qquad + C_4K^3[-h_3(kl)\cos kx + h_2(kl)\sin kx + shkx] \end{cases} \tag{A.11}$$

where,

$$\begin{cases} h_1(kl) = g_1(kl) + 2\frac{W_t}{W_b} kl \cos klshkl \\ h_2(kl) = g_2(kl) - 2\frac{W_t}{W_b} kl \sin klchkl \\ h_3(kl) = g_3(kl) + 2\frac{W_t}{W_b} kl \cos klchkl \\ h_4(kl) = g_4(kl) - 2\frac{W_t}{W_b} kl \sin klshkl \end{cases} \tag{A.12}$$

Step 2 For the left segment, i.e. $x = 0 \sim x_{10}$.

The PDE for the lateral vibration of the left segment is

$$\frac{\partial^4 y_L}{\partial x^4} + \frac{1}{a^2}\frac{\partial^2 y_L}{\partial t^2} = 0 \tag{A.13}$$

The boundary conditions for the fixed end ($x = 0$) are:

$$\begin{cases} y_L(0,t) = 0 \\ \frac{\partial y_L}{\partial x}(0,t) = 0 \end{cases} \tag{A.14}$$

After the separation of variables

$$y_L(x,t) = Y_L(x)\,T(t)$$

we have a Y_L – ODE

$$Y_L''''(x) - K^4 Y_L(x) = 0 \tag{A.15}$$

with B.C.'s

$$\begin{cases} Y_L(0) = 0 \\ Y_L'(0) = 0 \end{cases} \tag{A.16}$$

The general solution to Eq. (A.15) has the form of

$$Y_L(x) = d_1 \sin kx + d_2 \cos kx + d_3 shkx + d_4 chkx \tag{A.17}$$

By using the B.C., we can express $Y_L(x)$ and its derivatives in terms of the coefficients d_3 and d_4

$$\begin{cases} Y_L(x) = d_3(shkx - \sin kx) + d_4(chkx - \cos kx) \\ Y_L'(x) = d_3K(chkx - \cos kx) + d_4K(shkx + \sin kx) \\ Y_L''(x) = d_3K^2(shkx + \sin kx) + d_4K^2(chkx + \cos kx) \\ Y_L'''(x) = d_3K^3(chkx + \cos kx) + d_4K^3(shkx - \sin kx) \end{cases} \tag{A.18}$$

Step 3 The compatible conditions at the common point, $x = x_{10}$, between the two segments.

I. The lateral displacement must be the same, i.e., $Y_L(x_{10}) = Y_R(x_{10})$. Thus,

$$\begin{aligned} & d_3(shkx_{10} - \sin kx_{10}) + d_4(chkx_{10} - \cos kx_{10}) \\ & = C_3[h_1(kl)\sin kx_{10} + h_4(kl)\cos kx_{10} + shkx_{10}] \\ & + C_4[h_3(kl)\sin kx_{10} + h_2(kl)\cos kx_{10} + chkx_{10}] \end{aligned} \tag{A.19}$$

II. The slope of the center line of the beam must be the same, i.e, $Y'_L(x_{10}) = Y'_R(x_{10})$. Thus

$$\begin{aligned} & d_3(chkx_{10} - \cos kx_{10}) + d_4(shkx_{10} + \sin kx_{10}) \\ & = C_3[h_1(kl)\cos kx_{10} - h_4(kl)\sin kx_{10} + chkx_{10}] \\ & + C_4[h_3(kl)\cos kx_{10} - h_2(kl)\sin kx_{10} + shkx_{10}] \end{aligned} \tag{A.20}$$

III. The bending moment must be the same, i.e, $Y''_L(x_{10}) = Y''_R(x_{10})$. Thus,

$$\begin{aligned} & d_3(shkx_{10} + \sin kx_{10}) + d_4(chkx_{10} + \cos kx_{10}) \\ & = C_3[-h_1(kl)\sin kx_{10} - h_4(kl)\cos kx_{10} + shkx_{10}] \\ & + C_4[-h_3(kl)\sin kx_{10} - h_2(kl)\cos kx_{10} + chkx_{10}] \end{aligned} \tag{A.21}$$

IV. Because of the inertia of the lumped weight W_{10}, the shear has a jump at $x = x_{10}$, i.e.,

$$EIY'''_L(x_{10})T = EIY'''_R(x_{10})T + \frac{W_{10}}{g}Y_L(x_{10})\ddot{T}$$

which yields

$$Y'''_L(x_{10}) = Y'''_R(x_{10}) - \frac{W_{10}}{W_b}lk^4Y_L(x_{10})$$

Thus

$$
\begin{aligned}
&d_3\left(chkx_{10}+\cos kx_{10}\right)+d_4\left(shkx_{10}-\sin kx_{10}\right)\\
&=C_3\left[-h_1(kl)\cos kx_{10}+h_4(kl)\sin kx_{10}+chkx_{10}\right]\\
&+C_4\left[-h_3(kl)\cos kx_{10}+h_2(kl)\sin kx_{10}+shkx_{10}\right]\\
&-\frac{W_{10}}{W_b}kl\left[d_3\left(shkx_{10}-\sin kx_{10}\right)+d_4\left(chkx_{10}-\cos kx_{10}\right)\right]
\end{aligned}
\tag{A.22}
$$

Then a set of equations forms from Eq. (A. 19) to Eq. (A.22)

$$
\begin{cases}
C_3 shkx_{10}+C_4 chkx_{10}-d_3 shkx_{10}-d_4 chkx_{10}=0\\
C_3\left(h_1\sin kx_{10}+h_4\cos kx_{10}\right)+C_4\left(h_3\sin kx_{10}+h_2\cos kx_{10}\right)\\
\quad +d_3\sin kx_{10}+d_4\cos kx_{10}=0\\
C_3\left(h_1\cos kx_{10}-h_4\sin kx_{10}+chkx_{10}\right)+C_4(h_3\cos kx_{10}\\
\quad -h_2\sin kx_{10}+shkx_{10})+d_3\left(\cos kx_{10}-chkx_{10}\right)\\
\quad -d_4\left(\sin kx_{10}+shkx_{10}\right)=0\\
C_3\left(2chkx_{10}\right)+C_4\left(2shkx_{10}\right)+d_3\left[(-2chkx_{10})+\frac{W_{10}}{W_b}kl\left(\sin kx_{10}-shkx_{10}\right)\right]\\
\quad +d_4\left[(-2shkx_{10})+\frac{W_{10}}{W_b}kl\left(\cos kx_{10}-chkx_{10}\right)\right]=0
\end{cases}
\tag{A.23}
$$

The condition for set (A.23) having non-trivial solution is that the determinant of the set (A.23) equals to zero, that is

$$
\mathrm{DET}\begin{vmatrix}
SHX & CHX & -SHX & -CHX\\
h_1SNX+h_4CSX & h_3SNX+h_2CSX & SNX & CSX\\
h_1CSX-h_4SNX+CHX & h_3CSX-h_2SNX+SHX & CSX-CHX & -SNX-SHX\\
2CHX & 2SHX & -2CHX+\frac{W_{10}}{W_b}kl(SNX-SHX) & -2SHX+\frac{W_{10}}{W_b}kl(CSX-CHX)
\end{vmatrix}=0
\tag{A.24}
$$

Actually, Eq. (A.24) is the characteristic equation of the Bernoulli-Euler beam equation used in this paper, from which the eigenvalues K_i will be derived. Solving the characteristic equation by using binary searching technique, we can obtain the eigenvalues K_i,

$$K_i = 0.0172,\ 0.0507,\ 0.1074,\ 0.1405,\ 0.1998,$$

$$0.2258,\ 0.2263,\ 0.2268,\ 0.2278,\ 0.2283, \ldots$$

After determining the eigenvalues K_i's we can solve the set (A.23) for the coefficients C_3, C_4, d_3 and d_4. In fact, there are infinite number of solutions to the set (A.23) because C_3, C_4, $d_3$and d_4 are not totally independent. Assuming the solution to the set (A.23) is

$$\begin{cases} C_3 = \alpha_i C_i \\ C_4 = \beta_i C_i \\ d_3 = r_i C_i \\ d_4 = C_i \end{cases} \tag{A.25}$$

then, from Eqs. (A.11) and (A.18) we have the characteristic functions

$$Y_i(x) = \begin{cases} Y_{L_i}(x) = r_i\left(shk_i x - \sin k_i x\right) + \left(chk_i x - \cos k_i x\right) \\ \qquad\qquad\qquad\qquad\qquad\qquad\qquad\qquad 0 \le x \le x_{10} \\ Y_{R_i}(x) = \alpha_i\left[h_1(k_i l)\sin k_i x + h_4(k_i l)\cos k_i l + shk_i x\right] \\ \qquad +\beta_i\left[h_3(k_i l)\sin k_i x + h_2(k_i l)\cos k_i l + chk_i x\right] \\ \qquad\qquad\qquad\qquad\qquad\qquad\qquad\qquad x_{10} \le x \le l \end{cases} \tag{A.26}$$

By superposition, then, the solution to the PDE should be

$$\begin{aligned} y(x,t) &= \sum_i Y_i(x)\, T_i(t) \\ &= \sum_i Y_i(x)\left[A_i \cos\omega_i t + B_i \sin\omega_i t\right] \end{aligned} \tag{A.27}$$

where, $\omega_i = K_i^2 a$.

When proportional damping is taken into account, the PDE describing damped lateral vibration will be

$$m\frac{\partial^2 y}{\partial t^2} + c\frac{\partial y}{\partial t} + k\frac{\partial^4 y}{\partial x^4} = 0 \tag{A.28}$$

Here, two parameters a and b, which relate the coefficients of the PDE, are defined,

$$\begin{cases} a^2 = \frac{k}{m} = \frac{EI}{\rho A} \\ 2b = \frac{c}{m} \end{cases} \tag{A.29}$$

The substitution of $y(x,t) = \sum_i T_i(t)\,Y_i(x)$ into Eq. (A.28) yields

$$\sum_i \left(m\ddot{T}_i Y_i + C\dot{T}_i Y_i + kT_i Y_i'''' \right) = 0$$

which bears further a set of independent equations under the generalized coordinates $T_i(t)$ by the orthogonality property of the eigenfunctions,

$$m_i\ddot{T}_i + c_i\dot{T}_i + k_i T_i = 0 \tag{A.30}$$

where,

$$m_i = m\int_0^l Y_i^2 dx \qquad \text{generalized mass}$$

$$k_i = k\int_0^l Y_i Y_i'''' dx = m\omega_{n_i}^2 \int_o^l Y_i^2 dx \qquad \text{generalized stiffness}$$

$$c_i = c\int_o^l Y_i^2 dx \qquad \text{generalized damping}$$

Eq. (A.30) can be expressed in modal form

$$\ddot{T}_i + 2\xi_i\omega_{n_i}\dot{T}_i + \omega_{n_i}^2 T_i = 0 \tag{A.31}$$

where,

$$2\xi_i\omega_{n_i} = \frac{c_i}{m_i}$$

$$\omega_{n_i}^2 = \frac{k_i}{m_i}$$

Note that the damping ratio ξ_i is related to the eigenvalue K_i through the parameter a and b. In fact,

$$\xi_i = \frac{1}{2\omega_{n_i}}\frac{c_i}{m_i} = \frac{1}{2\omega_{n_i}}\frac{c}{m} = \frac{b}{ak_i^2} \tag{A.32}$$

Eq. (A.31) turns out to be the equation of motion of a simple mass-spring-dashpot system. Therefore, the ith-component of the response can be expressed as

$$T_i(t) = e^{-\xi_i \omega_{n_i} t}\left(A_i \cos \omega_{d_i} t + B_i \sin \omega_{d_i} t\right) \tag{A.33}$$

where,

$$\xi_i \omega_{n_i} = \frac{c_i}{2m_i} = \frac{c}{2m} = b$$

$$\omega_{d_i} = \omega_{n_i}\sqrt{1-\xi_i^2} = \left(ak_i^2\right)\sqrt{1-\left(\frac{b}{ak_i^2}\right)^2} = \sqrt{\left(ak_i^2\right)^2 - b^2}$$

Thus, $T_i(t)$ can be expressed in terms of parameters a and b,

$$T_i(t) = e^{-bt}\left(A_i \cos t\sqrt{\left(ak_i^2\right)^2 - b^2} + B_i \sin t\sqrt{\left(ak_i^2\right)^2 - b^2}\right) \tag{A.34}$$

By superposition, finally, the solution to the Eq. (A.28) should be

$$\begin{aligned} y(x,t) &= \sum_i Y_i(x)\, T_i(t) \\ &= \sum_i Y_i(x)\, e^{-bt}\left(A_i \cos\sqrt{\left(ak_i^2\right)^2 - b^2} + B_i \sin t\sqrt{\left(ak_i^2\right)^2 - b^2}\right) \end{aligned} \tag{A.35}$$

where, $Y_i(x)$ are the eigenfunctions shown in Eq. (A.26).

SPATIAL OPERATOR APPROACH TO FLEXIBLE MULTIBODY SYSTEM DYNAMICS AND CONTROL

G. Rodriguez

Jet Propulsion Laboratory
California Institute of Technology

SUMMARY

This paper extends to flexible multibody systems the recent [1-6] results of the author on the use of spatially recursive filtering and smoothing techniques to multibody dynamics. The configuration analyzed is that of a mechanical system of flexible bodies joined together by articulated joints. It is established that the composite flexible multibody mass matrix $\mathcal{M}$ can be factored as $\mathcal{M} = (I + \mathcal{K})\mathcal{D}(I + \mathcal{K}^*)$ in which $\mathcal{K}$ is a lower-triangular factor, $\mathcal{D}$ is a diagonal operator, and $\mathcal{K}^*$ is an upper-triangular factor. The operators $(I + \mathcal{K})$ and $\mathcal{D}$ can be constructed by means of a spatially recursive Kalman filter that begins at the tip of the system and proceeds inwardly toward the base. Similarly, the upper- triangular factor $(I + \mathcal{K}^*)$ is constructed by means of a corresponding outward smoothing recursion. The inverse $(I - \mathcal{L}) = (I + \mathcal{K})^{-1}$ of the causal factor $(I + \mathcal{K})$ is also a lower-triangular matrix. This inverse $(I - \mathcal{L})$ and its upper-triangular transpose $(I - \mathcal{L}^*)$ can also be computed by means of filtering and smoothing operations respectively. This means that the inverse $\mathcal{M}^{-1}$ of the mass matrix can be factored as $\mathcal{M}^{-1} = (I - \mathcal{L}^*)\mathcal{D}^{-1}(I - \mathcal{L})$. The foregoing factorization results are used to develop spatially recursive algorithms for multibody system inverse and forward dynamics. The algorithms are what is referred to as Order N in the sense that the total number of arithmetic operations increases only linearly with the number of bodies in the system.

1. INTRODUCTION

The problem of flexible multibody system forward dynamics consists of finding the joint angle accelerations and the flexible body accelerations, given the applied moments at the joints and the forces due to the elastic deformation of the flexible bodies in the system. The closely related problem of inverse dynamics is to find the set of joint moments that must be applied in order to achieve a prescribed set of system accelerations. These problems are particularly important in the simulation and control design for systems which are not readily tested in a ground laboratory. Examples of such systems include future space manipulators (referred to as space cranes) to be used for handling and retrieval of free-flying satellites and space platform modules. Flexible dynamics problems are also encountered in multiarm manipulation of such flexible task objects as thermal blankets, hoses, extensible cables, and spring-loaded mechanisms.

2. PROBLEM STATEMENT

Consider a mechanical system consisting of N flexible bodies numbered $1, \cdots, N$ connected together by N joints numbered $1, \cdots, N$ to form a branch-free kinematic chain. The bodies and joints are numbered in an increasing order that goes from the tip of the

system toward the base. Joint k in the sequence connects bodies k and $k+1$. Joint 0 can be selected at any arbitrary point in body 1.

A typical flexible body k is characterized by a finite-element model consisting of a finite number of nodes defined at the spatial locations i. These locations are expressed in a coordinate system attached to the body. The set of all finite-element nodes for body k is denoted by $\Omega(k)$, and the total number of nodes is N_k.

The finite-element model for body k also involves a mass matrix m_k and a stiffness matrix s_k, which are assumed to be obtained from a stand-alone structural dynamics analysis of this body. It is assumed that the flexible body mass and stiffness matrices are time-independent quantities computed in advance. Alternatively, the flexible body mass and stiffness properties are characterized by pre-computed vibrational modes and the corresponding modal frequencies.

A 6-dimensional displacement at node i of body k is denoted by $u_k(i) = [\alpha(i), x(i)]$ in which $\alpha(i)$ is a 3-dimensional rotation and $x(i)$ is a 3-dimensional translation. These nodal displacements are expressed in a local coordinate frame attached to body k. The corresponding velocities and accelerations are respectively $\dot{u}_k(i)$ and $\ddot{u}_k(i)$ and are also expressed in the same local coordinate frame. The displacement field $u_k = [u_k(1), \cdots, u_k(N_k)]$ produces an elastic force field $f_k = [f_k(1), \cdots, f_k(N_k)]$ which can be computed as $f_k = -s_k u_k$ in terms of the stiffness matrix s_k.

The joints labeled are single-degree-of-freedom joints, which allow rotation along the joint axis only. For these joints, $\hat{h}(k)$ is a unit vector along the axis of rotation; $F(k)$ is the active moment applied about the axis of joint k; $\theta(k)$ is the corresponding joint angle which is positive in the right-hand-sense about $\hat{h}(k)$. The relative angular velocity and acceleration at joint k are denoted by $\dot{\theta}(k)$ and $\ddot{\theta}(k)$.

The objective in forward dynamics is to outline a recursive method for computation of the joint-angle accelerations $\ddot{\theta}(k)$ and the flexible-body nodal accelerations $\ddot{u}_k(i)$ for i in $\Omega(k)$, given the applied moments $F(k)$ and the elastic forces f_k. The objective in inverse dynamics is to compute the set of forces and moments that must be applied in order to achieve a set of prescribed accelerations.

3. STATE SPACE MODEL

The following state space model [1] for propagation of forces, velocities and accelerations makes it easy to express the recursive dynamics algorithms.

The term spatial force refers to a 6×1 vector $X(i)$ whose first three components are pure moments and whose last three components are pure translational forces. Similarly, the term spatial velocity $V(i)$ describes a 6×1 vector of angular and linear velocities. The spatial accelerations $\lambda(i)$ are obtained by appropriate [1] time differentiation of the spatial velocities $V(i)$. If the argument k is used, the corresponding force $X(k)$, velocity $V(k)$, and acceleration $\lambda(k)$ are defined at a typical joint k. If the argument i is used, the corresponding force $X_k(i)$ velocity $V_k(i)$ and acceleration $\lambda_k(i)$ are defined at node i of the body k finite-element model.

The vector $X^+(k)$ is used to represent the spatial force on the "positive" side of joint k. The $+$ superscript indicates that the corresponding variable is evaluated at a point on body $k+1$ immediately adjacent and on the "positive" side, toward the base, of joint k.

The notation $X^-(k)$ is used to represent the force on the "negative", toward the tip, side of hinge k. Similarly, the notation $V^+(k)$ and $V^-(k)$ is used respectively for the spatial velocity on the positive and negative sides of joint k.

To propagate forces, velocities and accelerations between the two typical spatial locations i and k in the multibody system, define the "transition" matrix [1]

$$\phi(k,i) = \begin{pmatrix} U & \tilde{L}(k,i) \\ 0 & U \end{pmatrix} \tag{3.1}$$

in which $L(k,i)$ is the vector from point k to point i; and $\tilde{L}(k,i)$ is the 3×3 matrix equivalent to $L(k,i) \times (\cdot)$. This matrix has the following semi-group properties typically associated with a transition matrix for a discrete linear state space system:

$$\phi(k,m) = \phi(k,i)\phi(i,m); \quad \phi(k,k) = U \tag{3.2}$$

and $\phi^{-1}(k,m) = \phi(m,k)$. This matrix is used in the next section to develop spatial recursions for the kinematics and dynamics of the flexible multibody problem.

4. FLEXIBLE MULTIBODY KINEMATICS

4.1 Kinematics Internal to a Typical Flexible Body

The velocity $V^+(k)$ on the positive side of the joint k and the velocity $V_k(i)$ at nodal point i in body k are related by

$$V_k(i) = \phi^T(k,i)V^+(k) + v_k(i) \quad \text{for all} \quad i \in \Omega(k) \tag{4.1}$$

in which

$$\begin{aligned} v_k(i) &= \phi^T(k,i)H^T(k)\dot{\theta}(k) + \dot{u}_k(i) \qquad i = 1, \cdots, N_{k-1} \\ v_k(i) &= \phi^T(k,i)H^T(k)\dot{\theta}(k) \qquad i = N_k \end{aligned} \tag{4.2}$$

In Eqs. 4.1 and 4.2, $\dot{u}_k(i)$ denotes the relative spatial velocity of the mass element at node i. The set $\Omega(k)$ is the set of all nodes in the finite-element model for body k. Note that the last nodal point N_k in body k is assumed to be rigidly attached to the negative side of joint k. Hence, this point does not undergo an elastic displacement with respect to the joint k. This is reflected in Eq. (4.2).

4.2 Recursive Kinematics for Flexible Multibody System

The sequence of velocities $V^+(k)$ satisfies

LOOP $k = N-1, \cdots, 1$

$$V^+(k) = \phi^T(k+1,k)V^+(k+1) + C^T(k+1,k)v_{k+1}(1) \tag{4.3}$$

END LOOP;

with the terminal condition $V^+(N+1) = 0$. By definition, $v_{k+1}(1)$ is the first 6-dimensional component of the relative velocity vector v_{k+1}, i. e., $v_k = [v_k(1), \cdots, v_k(N)]$. Note also

that $v_{N+1} = 0$. The $6\times 6N$ matrix $C^T(k+1,k)$ is defined as $C^T(k+1,k) = [\phi^T(1,k), \cdots, 0]$. Outward integration of this iterative equation leads to

$$V^+(k) = \sum_{j=k}^{N-1} \phi^T(j,k) C^T(j+1,j) v_{j+1}$$

4.3 Recursive Kinematics Using Spatial Operators

To express the kinematic relationships in Eqs. (4.1)-(4.3) in terms of an equivalent spatial operator [4] notation, define first the spatial operators Φ, h, C, B, and H as

$$\Phi = \begin{pmatrix} I & 0 & \cdots & 0 \\ \phi(2,1) & I & \cdots & 0 \\ \vdots & \vdots & \ddots & 0 \\ \phi(N,1) & \phi(N,2) & \cdots & I \end{pmatrix} \qquad h = [I, 0]$$

$$C = \begin{pmatrix} 0 & 0 & \cdots & 0 & 0 \\ C(2,1) & 0 & \cdots & 0 & 0 \\ \vdots & \vdots & \ddots & 0 & 0 \\ 0 & 0 & \cdots & C(N,N-1) & 0 \end{pmatrix}$$

$$B = diag[B(1), \cdots, B(N)] \quad H = diag[H(1), \cdots, H(N)]$$

in which the spatial operators $B(k)$ are defined as

$$B(k) = [\phi(k,1), \phi(k,2), \cdots, \phi(k,N_k)]$$

Based on this notation, the kinematic relationships in Eqs (4.1)-(4.3) can be expressed as

$$V = B^* V^+ + v \tag{4.4}$$

$$v = B^* H^* \dot{\theta} + h^* \dot{u}; \qquad v = \mathcal{H}^* \dot{X} \tag{4.5}$$

$$V^+ = \Phi^* C^* v \tag{4.6}$$

with $V = [V_1, \cdots, V_N]$, $v = [v_1, \cdots, v_N]$, $\mathcal{H}^* = [h^*, B^* H^*]$, $\dot{X} = [\dot{u}, \dot{\theta}]$, $u = [u_1, \cdots, u_N]$ and $\theta = [\theta_1, \cdots, \theta_N]$. Combination of (4.4) and (4.6) leads to

$$V = (I + B^* \Phi^* C^*) v \tag{4.7}$$

While the kinematic relationships in (4.4)-(4.7) apply to spatial velocities, similar relationships can be derived for the corresponding accelerations by appropriate [1] time differentiation.

5. INVERSE DYNAMICS

RESULT 5.1. *The total kinetic energy in the multibody system can be computed in term of the composite velocity vector* $\dot{X} = [\dot{u}, \dot{\theta}]$ *as*

$$K.E. = (1/2)\dot{X}^* \mathcal{M} \dot{X}$$

in which the system mass matrix $\mathcal{M}$ *is*

$$\mathcal{M} = \mathcal{H}(I + C\Phi B)m(I + B^*\Phi^* C^*)\mathcal{H}^* \tag{5.1}$$

Eqs. (4.4)-(4.7) and (5.1) lead to a recursive inverse dynamics solution consisting of an outward sweep in which a sequence of system accelerations are computed. These accelerations are then multiplied by the appropriate blocks m_k of the mass matrix m in (5.1). Then, an inward recursion is performed to compute the required applied moments. Because of the factorization $\mathcal{M} = \mathcal{H}(I + C\Phi B)m(I + B^*\Phi^* C^*)\mathcal{H}^*$ of the mass matrix $\mathcal{M}$, these two recursions are equivalent to multiplication of the system accelerations $\ddot{X}$ by the composite mass matrix $\mathcal{M}$.

6. MULTIRIGID SYSTEM: A SPECIAL CASE

If the flexible bodies in the system are rigidized, by setting the nodal point velocities to zero, then the flexible body mass matrix of Sec. (5) becomes the multirigid body mass matrix analyzed by the author in [1-4].

Multirigid Body Mass Matrix. *The multirigid body mass matrix*

$$\mathcal{M} = H\Phi M\Phi^* H^* \tag{6.1}$$

in which

$$M = BmB^* = diag[M(1), \cdots, M(N)] \tag{6.2}$$

can be obtained from the flexible body mass matrix by setting the elastic state-to-output operator h *to zero. The diagonal block* $M(k)$ *in Eq. (6.2) is the rigid spatial mass matrix of the rigidized body* k *about joint* k.

Recursive Evaluation of the Multirigid Body Mass Matrix

The elements $m_R(k,j)$ of the mass matrix in (6.1) can be computed by

$$R(0) = 0$$

LOOP $k = 1, \cdots, N$

$$R(k) = \phi(k, k-1)R(k-1)\phi^T(k, k-1) + M(k)$$

$$m_R(k,k) = H(k)R(k)H^T(k)$$

$$x(k) = r(k)H^T(k)$$

Loop $i = k+1, \cdots, N$

$$x(i) = \phi(i, i-1)x(i-1)$$

$$m_R(i,k) = H(i)x(i)$$

End i **Loop;**

END k LOOP;

7. FLEXIBLE SYSTEM MASS MATRIX

The goal of this section is to arrive at a spatially recursive algorithm that computes the flexible multibody system mass matrix by means of an inward recursion from the tip to the base. The approach used to do this is to first establish the identity in (7.1) below.

Result 7.1. *The matrix* $(I+C\Phi B)m(I+B^*\Phi^*C^*)$ *in the flexible multibody system mass matrix* $\mathcal{M}$ *can be expressed as*

$$(I + C\Phi B)m(I + B^*\Phi^*C^*) = r + C\Phi Br + rB^*\Phi^*C^* \tag{7.1}$$

in which $r = m + CRC^*$. *Furthermore, the diagonal matrix* $r = diag[r(1), \cdots, r(N)]$ *is a block-diagonal matrix whose diagonal blocks* $r(k)$ *are given by*

$$r(k) = m(k) + C(k, k-1)R(k-1)C^T(k, k-1) \tag{7.2}$$

Inward Recursion for the Flexible Mass Matrix

$$R(0) = 0$$

LOOP $k = 1, \cdots, N$;

$$r(k) = m(k) + C(k, k-1)R(k-1)C^T(k, k-1)$$

$$\mathcal{M}(k,k) = \mathcal{H}(k)r(k)\mathcal{H}^T(k)$$

$$x(k) = r(k)\mathcal{H}^T(k)$$

Loop $i = k+1, \cdots, N$;

$$x(i) = \phi(i, i-1)x(i-1)$$

$$\mathcal{M}(i,k) = \mathcal{H}(i)x(i)$$

End i **Loop;**

END k LOOP;

Spatial Operator Notation

In spatial operator notation, the above recursions for the diagonal blocks of the mass matrix become

$$r = CRC^* + m; \quad R = BrB^*; \quad r = CBrB^*C^* + m$$

The above results are an extension to flexible multibody systems of the results obtained earlier by the author [1-4] for multirigid body systems.

8. INNOVATIONS FACTORIZATION OF THE MASS MATRIX AND ITS INVERSE

The flexible multibody system mass matrix $\mathcal{M}$ can be factored as

$$\mathcal{M} = (I + \mathcal{K})\mathcal{D}(I + \mathcal{K}^*) \tag{8.1}$$

in which the causal operator $\mathcal{K}$ and the diagonal operator $\mathcal{D}$ are

$$\mathcal{K} = \begin{pmatrix} hC\Phi Bg & hC\Phi G \\ H\Phi Bg & H\phi G \end{pmatrix}; \quad \mathcal{D} = \begin{pmatrix} d & 0 \\ 0 & D \end{pmatrix}$$

The Kalman gain operators g and G are defined in terms of the following Riccati-like equations

$$p = C(P - GDG^*)C^* + m \tag{8.2a}$$

$$P = B(p - gdg^*)B^* \tag{8.2b}$$

$$G = PH^*D^{-1}; \qquad g = ph^*d^{-1}$$

$$D = HPH^*; \qquad d = hph^*$$

Inverse of the Causal Factor $(I + \mathcal{K})$

$$(I + \mathcal{K})^{-1} = I - \mathcal{L} \tag{8.3}$$

in which $\mathcal{L}$ is the causal operator

$$\mathcal{L} = \begin{pmatrix} h\tilde{C}\Psi Bg & h\tilde{C}\psi G \\ H\Psi Bg & H\psi G \end{pmatrix}$$

Some of the spatial operators used in this result are defined as

$$\tilde{B}(k) = B(k)[I - g(k)h(k)]; \qquad \tilde{B} = diag[\tilde{B}(1), \cdots, \tilde{B}(N)]$$

$$\tilde{C}(k, k-1) = C(k, k-1)[I - G(k-1)H(k-1)]$$

$$\tilde{C} = \begin{pmatrix} 0 & 0 & \cdots & 0 & 0 \\ \tilde{C}(2,1) & 0 & \cdots & 0 & 0 \\ \vdots & \vdots & \ddots & \vdots & \vdots \\ 0 & 0 & \cdots & \tilde{C}(N, N-1) & 0 \end{pmatrix}$$

$$\psi(k, i) = \tilde{B}(k)\tilde{C}(k, k-1) \cdots \tilde{B}(i+1)C(i+1, i)$$

$$\psi = \sum_{i=1}^{k-1} \psi(k, i); \qquad \Psi = \sum_{i=1}^{k} \psi(k, i)[I - G(i)H(i)]$$

This states that the causal factor $I + \mathcal{K}$ is causally invertible. Furthermore it states that the inverse $I - \mathcal{L}$ can be computed by means of a spatially recursive Kalman filter. This Kalman filter will be described in more detail in the following section. Here, the immediate objective is to obtain the following factorization for the inverse $\mathcal{M}^{-1}$ of the flexible multibody system mass matrix $\mathcal{M}$. bigskip

Innovations Factorization of the Mass Matrix Inverse.

$$M^{-1} = (I - \mathcal{L}^*)\mathcal{D}^{-1}(I - \mathcal{L}) \tag{8.4}$$

This result states that the inverse of the mass matrix is the product of an anticausal factor, a diagonal operator, and a causal factor. Recall that the equations of motion for the flexible multibody system, disregarding without loss of generality the effects of velocity dependent coriolis and gyroscopic terms, are:

$$M\ddot{X} = \mathcal{F}; \qquad \ddot{X} = M^{-1}\mathcal{F} \tag{8.5}$$

in which $\mathcal{F} = [f, F]$ is a composite vector made up of the elastic forces f and the applied joint moments F.

Use of (8.4) in (8.5) leads to

$$\ddot{X} = (I - \mathcal{L}^*)\mathcal{D}^{-1}(I - \mathcal{L})\mathcal{F}$$

This equation states that the known forces $\mathcal{F}$ must be operated upon by a two-stage filtering and smoothing process in order to obtain the system accelerations $\ddot{X}$. The first operation involves the causal factor $(I - \mathcal{L})$ which can be mechanized by a spatially recursive Kalman filter. The result of the first stage is an innovations process defined as $(I - \mathcal{L})\mathcal{F}$ and a residual acceleration process defined as $\mathcal{D}^{-1}(I - \mathcal{L})\mathcal{F}$. This residual process is operated upon by an outward smoothing computation represented by the anticausal factor $(I - \mathcal{L}^*)$ to obtain the system accelerations $\ddot{X}$. These filtering and smoothing operations are described more completely in the following section.

9. RECURSIVE FORWARD DYNAMICS

Riccati Equation for Articulated Inertias

$$P^+(0) = 0 \tag{9.1}$$

LOOP $k = 1, \cdots, N$;

$$p_k = m_k + C_{k,k-1}P^+(k-1)C^T_{k,k-1} \tag{9.2}$$

$$d_k = h_k p_k^- h_k^T \tag{9.3}$$

$$g_k = p_k^- h_k^T d_k^{-1} \tag{9.4}$$

$$p_k^+ = (I - g_k h_k)p_k^- \tag{9.5}$$

$$P^-(k) = \sum_{i \in \Omega(k)} \sum_{j \in \Omega(k)} \phi(k,i) p_k^+(i,j) \phi^T(k,j) \tag{9.6}$$

$$D(k) = H(k)P^-(k)H^T(k) \tag{9.7}$$

$$G(k) = P^-(k)H^T(k)D^{-1}(k) \tag{9.8}$$

$$P^+(k) = [I - G(k)H(k)]P^-(k) \tag{9.9}$$

END LOOP;

This discrete-step Riccati-like equation computes a sequence of rigid Kalman gains $G(k)$ defined at every joint angle k and a corresponding sequence of flexible body Kalman gains $g_k = g_k(i,j)$ defined for every pair of nodes i,j in body k. This inward recursion is performed simultaneously with a filtering algorithm described below.

INWARD FILTERING: SPATIAL FORCES

$$Z^+(0) = 0 \tag{9.10}$$

LOOP $k = 1, \cdots, N$;

$$z^-(k) = C_{k,k-1}Z^+(k-1) \tag{9.11}$$

$$e_k^- = f_k - h_k z_k \tag{9.12}$$

$$e_k^+ = d_k^{-1} e_k^- \tag{9.13}$$

$$z_k^+ = z_k^- + g_k e_k^- \tag{9.14}$$

$$Z^-(k) = \sum_{i \in \Omega(k)} \phi(k,i) z_k^+(i) \tag{9.15}$$

$$E^-(k) = F(k) - H(k)Z^-(k) \tag{9.16}$$

$$E^+(k) = E^-(k)/D(k) \tag{9.17}$$

$$Z^+(k) = Z^-(k) + G(k)E^-(k) \tag{9.18}$$

END LOOP;

The result of this filtering stage is a sequence of residuals $E^+(k)$ defined at every joint k and a sequence of flexible body residuals $e_k^+(i)$ defined at every nodal element i of every flexible body k.

OUTWARD SMOOTHING: SPATIAL ACCELERATIONS

$$A^+(N) = 0 \tag{9.19}$$

LOOP $k = N, \cdots, 1$;

$$\ddot{\theta}(k) = E^+(k) - G^T(k)A^+(k) \tag{9.20}$$

$$A^-(k) = A^+(k) + H^T(k)\ddot{\theta}(k) \tag{9.21}$$

$$a_k(N_k) = \phi^T(k, N_k) \tag{9.22}$$

$$a_k^+(i) = \phi^T(k, i)a_k(N_k) \tag{9.23}$$

$$\ddot{u}_k(i) = e_k^+(i) - \sum_{j=1}^{N_k-1} g_k^T(j, i)a_k^+(j) \tag{9.24}$$

$$a_k^-(i) = a_k^+(i) + \ddot{u}_k(i) \tag{9.25}$$

$$A^+(k-1) = C^T(k, k-1)a_k^- \tag{9.26}$$

END LOOP;

The result of this smoothing stage is a sequence of joint angle accelerations $\ddot{\theta}(k)$ and flexible body accelerations $\ddot{u}_k(i)$.

PHYSICAL INTERPRETATION

The forward dynamics problem is solved by a spatially recursive Kalman filtering process which begins at the tip of the system and proceeds inwardly toward the base. This filtering algorithm computes: (1) a sequence of spatial forces $z(k)$ at the flexible bodies and $Z(k)$ at the joints; (2) a sequence of residuals $e^+(k)$ and $E^+(k)$; and (3) a sequence of Kalman gains g_k at the flexible bodies and $G(k)$ at the joints. The filtering stage uses as an input the elastic forces $f(k)$ at body k and the applied joint moments $F(k)$ at joint k. The residuals and the Kalman gains are stored for subsequent processing by an outward smoothing stage.

The smoothing stage is an outwardly recursive process which begins at the base of the system and proceeds from body to body toward the tip. The smoother computes a sequence of spatial accelerations a_k at the flexible bodies and $A(k)$ at the joints. The smoother also computes a sequence of relative elastic accelerations $\ddot{u}_k$ at the flexible bodies and joint angle accelerations $\ddot{\theta}(k)$ at the joints.

Riccati Equation

One of the central features of the inward filtering algorithm is the spatial Riccati equation in Eqs. (9.1)-(9.9) which accumulates the outboard spatial inertia as the recursive computations are performed.

This Riccati equation begins at the tip of the system with the initial condition $P^+(0) = 0$ in Eq. (9.1). This initial condition means physically that there is no spatial inertia outboard of this fictitious joint.

Eq. (9.2) is used to add to the body k free-free mass matrix m_k the spatial inertia of a fictitious articulated rigid body which is equivalent to collection of bodies outboard of joint $k-1$. This equivalent inertia is transferred from the joint $k-1$ to the attachment nodal point 1 in body k by the transition operator $C(k, k-1)$.

Eq. (9.3) computes the flexible body k articulated mass matrix. This matrix can be viewed as a reduced-order body k mass matrix. The order reduction occurs because the operator $h(k)$ has the effect of constraining the last nodal point N_k in the finite-element model of body k.

The Kalman gain $g(k)$ in Eq. (9.4) is a $6N \times 6(N-1)$ matrix which is used to compute the projection operator $[I - g(k)h(k)]$. This projection operator, when multiplied in (9.5) by the matrix $p^-(k)$ leads to the updated matrix $p^+(k)$ which has a null space of dimension $N-6$ in the direction of the operator $h(k)$. Eqs. (9.6) transfers the flexible articulated body inertia to an equivalent rigid body mass matrix at joint k.

Eqs. (9.7)-(9.9) are identical to the computations involved in crossing joint k in the multirigid body forward dynamics algorithm in [1]. They involve the following computations: (1) evaluation of the scalar articulated inertia $D(k)$ about joint k. This inertia is the inertia about joint k of the composite body outboard of joint k, with all of the degrees of freedom outboard of joint k being unlocked; (2) computation of the Kalman gain $G(k)$ in Eq. (9.8) to determine the projection operator $[I - G(k)H(k)]$ in Eq. (9.9). When this operator pre- multiplies the rigid-body spatial inertia $P^-(k)$, the updated spatial articulated $P^+(k)$ results. The spatial inertia $P^+(k)$ is that of a fictitious body which has no inertia along the joint k axis.

After crossing the joint k in Eq. (9.9), the algorithm lets $k \rightarrow k+1$ and returns to Eq. (9.2). The process of crossing a flexible body and a joint has been completed.

Filtering

The filtering algorithm in Eqs. (9.10)-(9.18) is a spatially recursive Kalman filter based on an inward sequence which is performed together with the Riccati equation just described. The Kalman filter begins at the tip of the system, the fictitious point "0", with the initial condition $Z^+(0) = 0$ in Eq. (9.10), which indicates that there are no external applied forces at this point. This begins a recursive process which takes as inputs the sequence of elastic forces $f(k)$ and the sequence of applied joint moments $F(k)$. The outputs of this process are a sequence of flexible-body residuals $e^+(k)$ and joint axis residuals $E^+(k)$.

Eqs. (9.11)-(9.13) compute the flexible-body residual $e^+(k)$ at body k. First, Eq. (9.11) determines the spatial force $z^-(k)$ that exists in body k due to the previously determined force $Z^+(k-1)$ at joint $k-1$ reflecting the presence of all of the bodies outboard of this joint. In Eq. (9.11), this force is multiplied by the operator $h(k)$ to obtain the predicted output force $h(k)z^-(k)$. The flexible body innovations $e^-(k)$ in Eq. (9.12) can be viewed as an "error" quantity equal to the difference between the actual force $f(k)$ due to the body stiffness and the predicted force $h(k)z^-(k)$ due to the preceding bodies $1, \cdots, k-1$ outboard of joint $k-1$. The residual acceleration process $e^+(k)$ is computed from $e^-(k)$ by dividing by the articulated spatial mass matrix $d(k)$ which emerges from the Riccati equation. This division is indicated in Eq. (9.13). The flexible body residual $e^+(k)$ has a very interesting physical interpretation. It corresponds to the inertial acceleration that the finite-element nodes in body k would undergo, if the "future" degrees of freedom were locked.

The computation in Eq. (9.14), which determines the updated spatial force distribution $z^+(k)$ in body k, has the effect of unlocking the 6 degrees of freedom associated with the all of the nodal points in body k except the last one.

Eq. (9.15) sums the spatial force estimates $z^+(k)$ at the nodal points in body k and transfers them to joint k. The result of this summation is the 6-dimensional spatial force $Z^-(k)$. This force reflects at joint k the effect of all of the preceding bodies. The next

steps, conducted in Eqs. (9.16)- (9.18), cross or unlock joint k. These steps are identical to that used in the multirigid body algorithms [1] and result in the updated spatial force $Z^+(k)$ on the positive, inward toward the base, of joint k.

At this juncture, the filtering algorithm lets $k \rightarrow k+1$ and returns to Eq. (9.11) to start the computations necessary to cross the next body.

Smoothing

The smoothing process in Eqs. (9.19)-(9.26) is an outward recursion which starts at the base of the system and proceeds outwardly to its tip. The smoothing process produces a sequence of rigid-body spatial accelerations $A(k)$ at the joints and of flexible-body accelerations $a(k)$ at the nodal points of the flexible bodies. It also produces the relative accelerations $\ddot{u}(k)$ at the flexible bodies and the joint-angle accelerations $\ddot{\theta}(k)$ at the joints. The smoother uses as inputs the sequences of residual accelerations $e^+(k)$ and $E^+(k)$. It also uses the Kalman gain sequences $g(k)$ at the flexible bodies and $G(k)$ at the joints.

The outward smoothing sequence begins with the terminal condition $A^+(N) = 0$, which corresponds to the assumption that the base of the system is immobile. Eqs. (9.20) and (9.21) can be viewed as specifying the computations necessary to cross joint k in the outward direction.

Eq. (9.22) computes the spatial acceleration $a_k(N_k)$ of the attachment point N_k. Eq. (9.23) computes the spatial accelerations $a_k^+(i)$ at the internal finite-element nodes of the flexible body k. The "+" indicates that the corresponding acceleration is that of a rigid body frame attached to a rigidized flexible body obtained by setting the elastic displacements to zero. The elastic displacement accelerations at the finite-element nodes are computed by Eq. (9.24). Eq. (9.25) then computes the total inertial accelerations of the finite- element nodes in body k. The spatial acceleration of the first node, also referred as an attachment node, is then propagated by Eq. (9.26) to the positive side of joint $k-1$. At this stage, the algorithm lets $k \rightarrow k-1$ and returns to Eq. (9.20) to begin the computations associated with the next body $k-1$.

Modal Expansions

The above algorithm has been expressed in terms of nodal coordinates to model the flexibility of each of the flexible bodies in the system. In many cases, it is more convenient to use what are typically referred to as modal coordinates. A modal model for a flexible body is obtained by doing a modal or eigenfunction analysis of the finite-element model for the same body. Use of these expansions leads to a spatially recursive forward dynamics algorithm that is almost identical in form to that of (9.1)-(9.26) above, but in which the quantities (displacements, velocities, accelerations, forces, and mass) involved are interpreted in terms of modal coordinates as opposed to the nodal coordinates used in (9.1)-(9.26).

10. CONCLUDING REMARKS

The inverse and forward dynamics problems for flexible multibody systems have been solved using the techniques of spatially recursive Kalman filtering and smoothing. These algorithms are easily developed using a set of identities associated with mass matrix factorization and inversion. These identities are easily derived using the spatial operator algebra

developed by the author. Current work is aimed at computational experiments with the described algorithms and at modeling for control design of limber manipulator systems. It is also aimed at handling and manipulation of flexible objects.

ACKNOWLEDGEMENT

The research described in this publication was carried out by the Jet Propulsion Laboratory, California Institute of Technology, under a contract with the National Aeronautics and Space Administration.

REFERENCES

1. Rodriguez, G., "Kalman Filtering, Smoothing and Recursive Robot Arm Forward and Inverse Dynamics," IEEE Transactions on Robotics and Automation, Dec. 1987.
2. Rodriguez, G., "Recursive Forward Dynamics for Multiple Robot Arms Moving and Common Task Object," IEEE Transactions on Robotics and Automation, Aug. 1989.
3. Rodriguez, G. and K. Kreutz, "Recursive Mass Matrix Factorization and Inversion - An Operator Approach to Open- and Closed-Chain Multibody Dynamics," JPL Publication 88-11, March 1988.
4. Rodriguez, G., K. Kreutz, and A. Jain, "A Spatial Operator Algebra for Manipulator Modeling and Control," IEEE Conf. on Robotics and Automation, May 1989.
5. Rodriguez, G., "Spatial Operator Approach to Flexible Manipulator Inverse and Forward Dynamics," Proceedings of IEEE Conference on Robotics and Automation, May 1990.
6. Rodriguez, G., "Random Field Estimation Approach to Robot Dynamics," IEEE Transactions on Systems, Man and Cybernetics, Sept. 1990.

"A Model for the Three-Dimensional Spacecraft Control Laboratory Experiment"

Yogendra Kakad
University of North Carolina at Charlotte

Fourth NASA Workshop on Computational Control of Flexible Aerospace Systems

Williamsburg, Virginia

A MODEL FOR THE THREE-DIMENSIONAL SPACECRAFT CONTROL LABORATORY EXPERIMENT

Y. P. Kakad

Department of Electrical Engineering
University of North Carolina at Charlotte
Charlotte, NC 28223

In this paper, a model for the three-dimensional Spacecraft COntrol Laboraory Experiment (SCOLE) is developed. The objective behind this method of modeling is to utilize the basic partial differntial equations of motion for this distributed parameter system and not to use the modal expansion in developing the model. The final model obtained is in terms of a transfer function matrix which relates the flexible mast parameters like displacement, slope, shear stress etc. to external forces and moments.

1. INTRODUCTION

It is widely recognized that the future space exploration would require a wide array of very large and flexible spacecrafts with very stringent pointing and vibration suppression requirements. Some of these spacerafts would also be deployed as an assemblage of a number of flexible members. In order to design control systems to meet these requirements, accurate dynamical models of the flexible spacrafts would have to obtained. Generally, the basic dynamical equations are developed in terms of a system of partial differential equations and one common approach is to formaulate solutions of these equations in terms of an infinite modal expansions and use this approach for developing control systems.

In this paper, an attempt is made to work with the basic partial differential equations and by using Laplace Transforms and incorporating boundary condition relationships an alternate modeling scheme is proposed. This methodolgy is based on extensive details documented in reference [1] and is applied to NASA Langley Research Center's SCOLE problem [2,3].

2. NOMENCLATURE

$u_x(t,z)$ Displacement at point z in roll bending

$\theta_x(t,z)$ Slope of beam at point z in roll bending

$M_x(t,z)$ Bending moment at point z in roll bending

$\sigma_x(t,z)$ Shear stress at point z in roll bending

$f_x(t,z)$ External force per unit length in roll bending

I_x Moment of inertia of area about neutral axis in roll bending

B_x Damping in roll bending

$u_x(t,z)$ Displacement at point z in pitch bending

$\theta_y(t,z)$ Slope of beam at point z in pitch bending

$M_y(t,z)$ Bending at beam at point z in pitch bending

$\sigma_y(t,z)$ Shear stress at point z in pich bending

$f_y(t,z)$ External force per unit length in pitch bending

I_y Moment of inertia of area about neutral axis in pitch bending

B_y Damping in pitch bending

$\psi(t,z)$ The angular displacement at z of an element dz of the beam

I_p The polar moment of inertia of the cross-section

ρ_p The mass per unit volume

I_pG The torsional stiffness of the beam

G The shear modulus of the material

I Modulus of elsticity

ρ Mass per unit length

3. METHODOLOGY

The partial differential equations governing the roll bending motion are

$$\frac{\partial u_x}{\partial z} = \theta_x \tag{1}$$

This is obtained from the definition of slope.

$$\frac{\partial \theta_x}{\partial z} = -\frac{1}{(EI)_x} M_x = -\frac{1}{(EI)} M_x \tag{2}$$

This equation is based on beam theory and here $(EI)_x$ and $(EI)_y$ are considered equal and represented by (EI)

$$\frac{\partial M_x}{\partial z} = \sigma_x \tag{3}$$

This is obtained from the definition of bending moment.

$$\frac{\partial \sigma_x}{\partial z} = \rho \frac{\partial^2 u_x}{\partial t^2} - f_x(t,z) \tag{4}$$

This equation is based on Newton's law of motion and the term $f_x(t,z) = -B_x \frac{\partial x}{\partial t}$ if there is no external force per unit length on the beam.

The corresponding equations for pitch bending are

$$\frac{\partial u_y}{\partial z} = \theta_y \tag{5}$$

$$\frac{\partial \theta_y}{\partial z} = -\frac{1}{(EI)_y} M_y \tag{6}$$

$$\frac{\partial M_y}{\partial z} = \sigma_y \tag{7}$$

$$\frac{\partial \sigma_y}{\partial z} = \rho \frac{\partial^2 u_y}{\partial t^2} - f_y(t,z) \tag{8}$$

The following equations describe torsional bending

$$\frac{\partial \psi}{\partial z} = \frac{1}{I_p G} T \tag{9}$$

This is based on torsional flexibility.

$$\frac{\partial T}{\partial z} = \rho I_p \frac{\partial \psi}{\partial t^2} - M_\psi(t,z) \tag{10}$$

This equation is based on Newton's Law of motion and the term $M_\psi(t,z) = -B_\psi \frac{\partial \psi}{\partial z}$ if there is no external torque per unit length of the beam.

Defining the state variables as

$$\begin{bmatrix} q_1 \\ q_2 \\ q_3 \\ q_4 \\ q_5 \\ q_6 \\ q_7 \\ q_8 \\ q_9 \\ q_{10} \end{bmatrix} = \begin{bmatrix} u_x \\ \theta_x \\ M_x \\ \sigma_x \\ u_y \\ \theta_y \\ M_y \\ \sigma_y \\ \psi \\ T \end{bmatrix}, \tag{11}$$

the following equations are obtained

$$\frac{\partial q_1}{\partial z} = q_1$$

$$\frac{\partial q_2}{\partial z} = -\frac{1}{(EI)} q_3$$

$$\frac{\partial q_3}{\partial z} = q_4$$

$$\frac{\partial q_4}{\partial z} = \rho(\frac{\partial^2}{\partial t^2}) q_1 - f_x(t,z)$$

$$\frac{\partial q_5}{\partial z} = q_6$$

$$\frac{\partial q_6}{\partial z} = -\frac{1}{(EI)} q_7 \qquad (12)$$

$$\frac{\partial q_7}{\partial z} = q_8$$

$$\frac{\partial q_8}{\partial z} = \rho(\frac{\partial^2}{\partial t^2}) q_5 - f_y(t,z)$$

$$\frac{\partial q_9}{\partial z} = \frac{1}{I_p G} q_{10}$$

$$\frac{\partial q_{10}}{\partial z} = \rho I_p(\frac{\partial^2}{\partial t^2}) q_9 - M_\psi(t,z)$$

These equations can be expressed in the form

$$\frac{\partial \underline{q}}{\partial z} = F_0 \underline{q} + F_1 \frac{\partial \underline{q}}{\partial t} + F_2 \frac{\partial^2 \underline{q}}{\partial t^2} + \underline{u}(t,z) \qquad (13)$$

Taking Laplace Transforms of the previous matrix-vector equation, the following equation is obtained.

$$\frac{dQ}{dz} = (F_0 + F_1 s + F_2 s^2)\,\underline{Q} - F_1 \underline{q}(0,z) - F_2\,[\,\underline{\dot{q}}(0,z) + s\underline{q}(0,z)\,] + \underline{U}(s,z)$$

$$\frac{dQ}{dz} = (F_0 + F_1 s + F_2 s^2)\,\underline{Q} + \overline{\underline{U}}(s,z) \qquad (14)$$

Here F_1 is a 10 x 10 null matrix. The matrix F_0 is a 10 x 10 matrix with zeros except the following nonzero elements.

$$F_0(21) = 1$$

$$F_0(3,2) = \frac{-1}{(EI)}$$

$$F_0(4,3) = 1$$

$$F_0(7,6) = \frac{-1}{(EI)}$$

$$F_0(8,7) = 1$$

$$F_0(9,9) = \frac{1}{I_p G}$$

The matrix F_2 is also a 10 x 10 matrix with zero entries except for the following elements

$$F_2(4,1) = \rho$$
$$F_2(8,5) = \rho$$
$$F_2(10,9) = \rho\, I_p$$

The equation (14) represents a linear system and this can be solved by using the state-transition matrix as

$$\underline{Q}(s,z) = H(s,z - z_0)\,\underline{Q}(s,z_0) + \int_{z_0}^{z} H(s,z-\xi)\overline{\underline{U}}\,(s,\xi)d\xi \quad . \qquad (15)$$

The SCOLE model is of finite length; i.e. $0 \le z \le L$. Then, at $z = L$,

$$\underline{Q}(s,L) = H(s,L)\,\underline{Q}(s,0) + \int_{0}^{L} H(s,L-\xi)\overline{\underline{U}}\,(s,\xi)d\xi \quad . \qquad (16)$$

To determine $Q(s,L)$ and $Q(s,0)$ which in turn would allow determination of $Q(s,z)$ for any z between 0 and L, ten terminal relations must be specified. These terminal relations can be expressed in the form of ten ordinary differential equations in the following vector-matrix form using linear differential operators.

$$M(D)\,\underline{q}(t,0) + N(D)\,\underline{q}(t,L) = \underline{F}(t) \tag{17}$$

Here, $F(t)$ represents external control forcing functions (the physical inputs like forces on the flexible beam or shuttle moments etc. or linear combinations thereof). Taking Laplace Transforms on both the sides of equation (17), the following vector-matrix equation is obtained.

$$M(s)\,\underline{Q}(s,0) + N(s)\,\underline{Q}(S,L) = \underline{F}(s) \tag{18}$$

The vector $F(s)$ is the sum of the Laplace Transforms of $F(t)$ and any initial condition terms. The termination is said to bo homogeneous if $\underline{F}(s) = \underline{0}$.

It is important to note here that each of the differential equations given in (17) in case of a distributed parameter system may involve quantities at both ends of the distributed system. This represents termination characteristics of a feedback system where quantities at one end are made to depend on quantities at the other. The boundary conditions for SCOLE model without any external forcing functions are given as follows.

At the shuttle end where $z = 0$,

$$(EI)\frac{\partial u_x}{\partial z^2}(0,t) = 0 \quad \textit{Moment} \tag{19a}$$

$$(EI)\frac{\partial u_y}{\partial z^2}(0,t) = 0 \quad \textit{Moment} \tag{19b}$$

$$(EI)\frac{\partial u_x}{\partial z^3}(0,t) = 0 \quad \textit{ShearForce} \tag{19c}$$

$$(EI)\frac{\partial u_y}{\partial z_3}(o,t) = 0 \quad \textit{ShearForce} \tag{19d}$$

$$(I_pG)\frac{\partial \psi}{\partial z}(0,t) = 0 \quad \textit{Torquq} \tag{19e}$$

At the reflector end where $z = L$, the corresponding boundary conditions are

$$(EI)\frac{\partial u_x}{\partial z^2}(L,t) = 0 \tag{20a}$$

$$(EI)\frac{\partial u_y}{\partial z^2}(L,t) = 0 \tag{20b}$$

$$(EI)\frac{\partial u_x}{\partial z^3}(L,t) = 0 \tag{20c}$$

$$(EI)\frac{\partial u_y}{\partial z^3}(L,t) = 0 \tag{20d}$$

$$(I_pG)\frac{\partial \psi}{\partial z}(L,t) = 0 \quad . \tag{20e}$$

In order to obtain a complete representation of the system governed by equations (16) and (18), we substitute (16) into (18) with $z_0 = 0$ and $z = L$;

$$[\, M(s) + N(s)\, H(s,L)\,]\, \underline{Q}(s,0) = \underline{V}(s) \tag{21}$$

where,

$$\underline{V}(s) = \underline{F}(s) - N(s)\int_0^L H(s,L-\xi)\overline{\underline{U}}(s,\xi)d\xi \tag{22}$$

It can be shown that the relationship given in (17) is independent and as a result $[\, M(s) + N(s)H(s)\,]$ is of rank 10 for SCOLE and so has an inverse. Hence, we can write

$$\underline{Q}(s,0) = [\, M(s) + N(s)H(s,L)\,]^{-1}\underline{V}(s) \tag{23}$$

Thus,

$$\underline{Q}(s,z) = H(s,z)\,[\, M(s) + N(s)H(s,L)\,]^{-1}\underline{V}(s) + \int_0^z H(s,z-\xi)\overline{\underline{U}}(s,\xi)d\xi \tag{24}$$

If there are no distributed forcing terms and initial conditions, equation (24) can be written as

$$\underline{Q}(s,z) = H(s,z)\,[\, M(s) + N(s)H(s,L)\,]^{-1}\underline{F}(s) \tag{25}$$

where $F(s)$ is the Laplace transform of the external forcing terms in (16). Hence the matrix of transfer functions from $\underline{F}(s)$ to $\underline{Q}(s,z)$ is given by

$$G(s,z) = H(s,z)\,[\, M(s) + N(s)H(s,L\,]^{-1} \tag{26}$$

NASA

Report Documentation Page

1. Report No.	2. Government Accession No.	3. Recipient's Catalog No.
NASA CP-10065, Part 2		

4. Title and Subtitle	5. Report Date
4th NASA Workshop on Computational Control Of Flexible Aerospace Systems	March 1991
	6. Performing Organization Code
7. Author(s)	8. Performing Organization Report No.
Lawrence W. Taylor, Jr. (Compiler)	
	10. Work Unit No. 506-46-11-01
9. Performing Organization Name and Address	11. Contract or Grant No.
NASA Langley Research Center Hampton, VA 23665-5225	
12. Sponsoring Agency Name and Address	13. Type of Report and Period Covered
National Aeronautics and Space Administration Washington, DC 20546	Conference Publication
	14. Sponsoring Agency Code
15. Supplementary Notes	

16. Abstract

This publication is a collection of papers presented at the Fourth NASA Workshop on Computational Control of Flexible Aerospace Systems. The Workshop was held at the Kingsmill Resort, Williamsburg , Virginia, July 11-13, 1990. The papers address modeling, systems identification, and control of flexible aircraft, spacecraft and robotic systems.

17. Key Words (Suggested by Author(s))	18. Distribution Statement
Large Flexible Spacecraft Control Structural Dynamics	Unclassified - Unlimited Subject Category - 18

19. Security Classif. (of this report)	20. Security Classif. (of this page)	21. No. of pages	22. Price
Unclassified	Unclassified	483	A21

NASA FORM 1626 OCT 86 For sale by the National Technical Information Service, Springfield, Virginia 22161-2171

End date June 20, 1991

NASA-Langley, 1991